RĒZEKNES TEHNOLOĢIJU AKADĒMIJA
Inženieru fakultāte

REZEKNE ACADEMY OF TECHNOLOGIES
Faculty of Engineering

VIDE. TEHNOLOĢIJA. RESURSI

XII starptautiskās zinātniski praktiskās konferences materiāli
2019.gada 20.-22.jūnijs

3.SĒJUMS

ENVIRONMENT. TECHNOLOGY. RESOURCES

Proceedings of the 12th International Scientific and Practical Conference
June 20 – 22, 2019

Volume III

Rēzekne
2019

VIDE. TEHNOLOĢIJA. RESURSI. 12. starptautiskās zinātniski praktiskās konferences materiāli. 2019.gada 20.-22. jūnijs. *1.sējums.* Rēzekne: Rēzeknes Tehnoloģiju akadēmija, 2019. 260 lpp.

ENVIRONMENT. TECHNOLOGY. RESOURCES. Proceedings of the 12th International Scientific and Practical Conference on June 20-22, 2019. *Volume I,* Rezekne: Rezekne Academy of Technologies, 2019. pp. 260.

Rekomendējusi publicēšanai Rēzeknes Tehnoloģiju akadēmijas Zinātnes padome
2019. gada 23. maijā.
Recommended for publication by the Scientific Council of Rezekne Academy of Technologies on May, 23 rd, 2019.

ERDF co-funded project "Funding of international projects in research and innovation at Rezekne Academy of Technologies" No. 1.1.1.5/18/I/012

12.starptautiskās zinātniski praktiskās konferences ''Vide. Tehnoloģija. Resursi'' materiālu trijos sējumos ir pārstāvēti jaunākie pēdējo divu gadu pētījumi vides inženierzinātnē, vides un dabas aizsardzībā, ilgtspējīgā lauksaimniecībā, enerģētikā, materiālzinātnē, mehānikā, metālapstrādē, lāzeru tehnoloģijās, matemātiskajā modelēšanā, elektrotehnikā, vides ekonomikā un vadībā, informācijas tehnoloģijās un sociotehnisko sistēmu modelēšanā, vides izglītībā un ilgtspējīgas attīstības procesos. Krājumā pārstāvēto pētījumu joma ir daudzpusīga un starpdisciplināra, balstīta uz starptautisko zinātnieku kolektīvu sasniegumu rezultātiem. Konferences materiālos iekļauti 173 zinātniskie raksti, kuru autori pārstāv 14 valstis.

Proceedings of the 12th International Scientific and Practical Conference ''Environment. Technology. Resources'' include studies of the last two years in fields of engineering, environmental and nature protection, sustainable agriculture, energy, material science, mechanics, metalworking, laser technologies, mathematical modelling, electrical engineering, environmental economics and management, information technologies and sociotechnical systems modelling, environmental education and sustainable development. The research area presented in the proceedings is comprehensive and cross disciplinary-based, on advances of international researchers. The proceedings comprise 173 scientific papers from 14 countries.

Print ISSN 1691-5402
Online ISSN 2256-070X

Published by Rezekne Academy of Technologies, 2019

Scientific Committee Chairman

Dr.sc.ing. Edmunds Teirumnieks, Rezekne Academy of Technologies, Latvia

Scientific Committee Co-Chairmen

Dr. Walter Leal, Hamburg University of Applied Sciences, Germany
Dr.sc.ing. Andris Martinovs, Rezekne Academy of Technologies, Latvia
Dr.sc.ing. Artis Teilāns, Rezekne Academy of Technologies, Latvia

Scientific Committee

PhD Andres Annuk, Estonian University of Life Sciences, Estonia
Dr. Dragen Antic, University of Nis, Serbia
Dr.oec. Dzintra Atstāja, BA School of Business and Finance, Latvia
DSc. Hristo Ivanov Beloev, Angel Kanchev University of Ruse, Bulgaria
PhD Plamen Bogdanov, Vasil Levski National Military University, Bulgaria
Dr. Xiao Chen, Hefei University, China
Dr.sc.ing. Jurijs Cizovs, Riga Technical University, Latvia
PhD Lubomir Dimitrov, Tehnical University of Sofia, Bulgaria
Dr.-Ing. Horst Exner, Mittweida University of Applied Sciences, Germany
PhD Vladimir Golenkov, Belarusian State University of Informatics and Radioelectronics, Belarus
Dr. Ants Kallaste, Tallinn University of Technology, Estonia
PhD Tsanko Karadzhov, Technical University of Gabrovo, Bulgaria
Dr. Vasily Karasev, Institute of Problems of Mechanical Engineering of Russian Academy of Sciences, Russian Federation
PhD Veiko Karu, Tallinn University of Technology, Estonia
Dipl.-Kfm. Lars Kempt, Chemnitz University of Technology, Germany
Dr. Linas Kliucininkas, Kaunas University of Technology, Lithuania
PhD Egons Lavendelis, Riga Technical University, Latvia
PhD Gilberto Marzano, President of Ecoistituto Udine, Italy
PhD Cristian-Emil Moldoveanu, Military Technical Academy ''Ferdinand I'', Romania
Dr.sc.ing. Vladislav Morozov, Geophysical Centre of the Russian Academy of Sciences, Russian Federation
Dr.geogr. Oļģerts Nikodemus, University of Latvia, Latvia
Dr. Vlastimir Nikolic, University of Nis, Serbia
Dr. Nenad Pavlovič, University of Nis, Serbia
Dr.habil.sc.ing. Igor Plokhov, Pskov State University, Russian Federation
Dr. Svetlana Polukoshko, Ventspils University College, Latvia
PhD Gabriel Raducanu, Air Force Academy Henri Coanda, Romania
Vilnis Rantins, Chairman of the Management Board of the Association of Mechanical Engineering and Metalworking Industries, Latvia
Dr. Anton Rassolkin, Tallinn University of Technology, Estonia
Dr.sc.ing. Andrejs Romanovs, IEEE Latvia Section, Riga Technical University, Latvia
Dr.habil.phys. Vladimir Solovyev, Pskov State University, Russian Federation
PhD Chrysostomos Stylios, Technological Educational Institute of Epirus, Greece
PhD Arita Takahashi, Riga Technical University, Latvia
Dr.sc.ing. Victor Tatarinov, Geophysical Centre of the Russian Academy of Sciences, Russian Federation
Dr.-Ing. Josef Timmerberg, Jade University of Applied Sciences, Germany
Dr. Toomas Vaimann, Tallinn University of Technology, Estonia

Dr.habil.sc.ing Janis Viba, Riga Technical University, Latvia
PhD Constantin-Iulian Vizitiu, Militar Technical Academy ‘’Ferdinand I’’, Romania

Organising Committee Chairman

Dr.habil.geol. Gotfrīds Noviks, Rezekne Academy of Technologies, Latvia

Organizing Commitee

Dr.sc.ing. Egils Ginters, Riga Tehnical University, Latvia
Dr.sc.ing. Pēteris Grabusts, Rezekne Academy of Technologies, Latvia
DSc. Dimitar Grekov, Agricultural University, Bulgaria
PhD Aleksandrs Gorbunovs, Riga Technical University, Latvia
PhD Krzysztof Krakowski, War studies University, Poland
Dr.sc.ing. Ēriks Kronbergs, University of Latvia, Latvia
Dr.sc.ing. Sergejs Kodors, Rezekne Academy of Technologies, Latvia
PhD Egons Lavendelis, Riga Technical University, Latvia
Dr.sc.ing. Lyubomir Lazov, Rezekne Academy of Technologies, Latvia
PhD Līga Mazure, Rezekne Academy of Technologies, Latvia
PhD Magdalena Mitkova, Prof. Assen Zlatarov University Burgas, Bulgaria
Dr.phys. Pāvels Narica, Rezekne Academy of Technologies, Latvia
PhD Valyo Nikolov, Technical University of Sofia, Plovdiv Branch, Bulgaria
Dr.sc.ing. Imants Nulle, Latvia University of Life Sciences and Technologies, Latvia
Dr.geol. Janis Prols, SIA “Geo Consultants”, Latvia
PhD Leonardo Quattrocchi, Confindustria, LUISS Business School, Italy
Dr.geol. Valdis Segliņš, University of Latvia, Latvia
Dr.biol. Artūrs Škute, Daugavpils University, Latvia
Dr.sc.ing. Victor Tatarinov, Geophysical Centre of the Russian Academy of Sciences, Russian Federation

Reviewers

PhD Nikolaj Angelov, Technical University of Gabrovo, Bulgaria
PhD Andres Annuk, Estonian University of Life Sciences, Estonia
PhD Iluta Arbidane, Rezekne Academy of Technologies, Latvia
Dr.oec. Dzintra Atstāja, BA School of Business and Finance, Latvia
Dr.agr. Skaidrīte Būmane, Institute of Food safety, Animal Health and Environment “BIOR”, Latvia
Dr.sc.ing. Jurijs Cizovs, Riga Technical University, Latvia
Dr.sc.ing. Edgars Čubars, Rezekne Academy of Technologies, Latvia
PhD Peteris Daugulis, Daugavpils University, Latvia
PhD Sandra Ezmale, Rezekne Academy of Technologies, Latvia
Dr.sc.ing. Pēteris Grabusts, Rezekne Academy of Technologies, Latvia
PhD Aleksandrs Gorbunovs, Riga Technical University, Latvia
Dr.oec. Elita Jermalajeva, Preili Municipality, Latvia
Dr.sc.ing. Aivars Kaķītis, Latvia University of Life Sciences and Technologies, Latvia
Dr.paed. Ilmārs Kangro, Rezekne Academy of Technology, Latvia
Dr. Vasily Karasev, Institute of Problems of Mechanical Engineering of Russian Academy of Sciences, Russian Federation
Dr.paed. Janis Kapenieks, Riga Technical University, Latvia
Dr.geol. Andris Karpovičs, Rezekne Academy of Technologies, Latvia
PhD Tsanko Karadzhov, Technical University of Gabrovo, Bulgaria

PhD Aivars Kaupuzs, Rezekne Academy of Technologies, Latvia
Dr.sc.ing. Sergejs Kodors, Rezekne Academy of Technologies, Latvia
PhD Egons Lavendelis, Riga Technical University, Latvia
Dr.sc.ing. Lyubomir Lazov, Rezekne Academy of Technologies, Latvia
PhD Angel Lengerov, Technical University of Plovdiv, Serbia
Dr.oec. Lienīte Litavniece, Rezekne Tecnologies Academy, Latvia
Dr.sc.ing. Jānis Locs, Riga Tehnical University, Latvia
Dr.habil.sc.ing. Zigurds Markovics, Riga Technical University, Latvia
Dr.sc.ing. Andris Martinovs, Rezekne Academy of Technologies, Latvia
PhD Gilberto Marzano, President of Ecoistituto Udine, Italy
Dr.habil.sc.ing. Viktors Mironovs, Riga Tehnical University, Latvia
Dr.phys. Pāvels Narica, Rezekne Academy of Technologies, Latvia
Dr.habil.geol. Gotfrīds Noviks, Rezekne Academy of Technologies, Latvia
Dr.sc.ing. Imants Nulle, Latvia University of Life Sciences and Technologies, Latvia
Dr.chem. Sergejs Osipovs, Daugavpils University, Latvia
Dr.sc.ing. Romāns Petričenko, Riga Technical University, Latvia
PhD Desislava Ivanova Petrova, Technical University of Gabrovo, Bulgaria
Dr.habil.sc.ing. Igor Plokhov, Pskov State University, Russian Federation
Dr.Sc.Ing Svetlana Polukoshko, Ventspils University College, Engineering Research Institute "VSRC", Latvia
Mg.sc.ing. Aivars Ratkevičs, Latvia University of Life Sciences and Technologies, Latvia
Dr.habil.math. Andrejs Reinfelds, University of Latvia
Dr.sc.ing. Andrejs Romanovs, IEEE Latvia Section, Riga Technical University, Latvia
Dr.geol. Valdis Segliņš, University of Latvia, Latvia
PhD Irēna Silineviča, Rezekne Academy of Technologies, Latvia
Dr.sc.ing. Andris Skromulis, Rezekne Academy of Technologies, Latvia
Dr.habil.phys. Vladimir Solovyev, Pskov State University, Russian Federation
Dr.geol. Juris Soms, Daugavpils University, Latvia
Dr.sc.ing. Sandis Spolītis, Riga Technical University, Latvia
Dr.agr. Veneranda Stramkale, Latvia University of Life Sciences and Technologies, Institute of Agricultural Resources and Economics, Latvia
PhD Aina Strode, Rezekne Academy of Technologies, Latvia
PhD Gunars Strods, Rezekne Academy of Technologies, Latvia
Dr.biol. Artūrs Škute, Daugavpils University, Latvia
PhD Arita Takahashi, Riga Technical University, Latvia
Dr.sc.ing. Artis Teilāns, Rezekne Academy of Technologies, Latvia
Dr.sc.ing. Edmunds Teirumnieks, Rezekne Academy of Technologies, Latvia
Dr.-Ing. Josef Timmerberg, Jade University of Applied Sciences, Germany
Dr.sc.ing. Mārtiņš Vilnītis, Riga Technical University, Latvia
Dr.sc. ing. Imants Zarembo, Rezekne Academy of Technologies, Latvia
PhD Erika Zubule, Rezekne Academy of Technologies, Latvia
PhD Anda Zvaigzne, Rezekne Academy of Technologies, Latvia

Technical Program Committee Chairman

Mg.sc.chem. Ērika Teirumnieka, Rezekne Academy of Technologies, Latvia

Technical Program Committee

Mg.sc.env. Sintija Augule, Rezekne Academy of Technologies, Latvia
Mg.sc.chem. Inese Bernāne, Rezekne Academy of Technologies, Latvia
Mg.sc.comp. Gundega Bēriņa, Rezekne Academy of Technologies, Latvia

III

Engineering sciences and production technologies

SATURS
CONTENTS

Precision Micromachining of Metals by CuBr Laser

Ivaylo Balchev
Institute of Electronics
Bulgarian Academy of Sciences
Sofia, Bulgaria
ivobalchev@gmail.com

Lyubomir Lazov
Faculty of Engeenering
Rezekne Academy of Technologies
Rezekne, Latvia
lyubomir.lazov@rta.lv

Edmunds Teirumnieks
Faculty of Engeenering
Rezekne Academy of Technologies
Rezekne, Latvia
edmunds.teirumnieks@rta.lv

***Abstract*—The ability to laser machine materials with high resolution and high throughput is critical in advanced manufacturing for a vast array of applications, from photovoltaic cells to bio-compatible micro-components. Copper bromide (CuBr) lasers with their excellent beam quality promised noticeable advantages and improvements in high precision and material processing at the microscale. The application of the CuBr laser as a precision tool for micromachining of different metals has been demonstrated. That good performance was a result of the combination of high power visible radiation, short pulses, and close to the diffraction-limited laser beam divergence with high-speed galvo scanner beam steering.**

Keywords*— *CuBr vapour laser, laser micromachining, precision micromachining

Introduction

The world of laser machining production is divided into micro- and macro-machining. This classification is not based on the size of the work piece but rather the fineness of the impact caused by the laser tool. The lasers system used for micromachining employ normally pulsed beams with an average power of well below several watts while those used for macro machining use generally continuous-wave (CW) laser beams ranging up to several kW.

The excellence attributes of laser radiation combined with a high degree of flexibility, contact-less and wear-less machining, the possibility of high automation as well as easy integration allows using this tool in a wide field of macro machining processes for many materials including silicon, ceramics, metal and polymer.

Lasers for micromachining offer a wide range of wavelengths, pulse duration (from femtosecond to microsecond) and repetition rates (from single pulse to Megahertz). These attributes allow micromachining with high resolution in depth and lateral dimensions.

The field of micro-machining includes manufacturing methods like drilling, cutting, welding as well as ablation and material surface texturing, whereby it is possible to achieve very fine surface structures ranging in the micrometer domain. Such processes require a rapid heating, melting and evaporation of the material. The use of extremely short nano- and pico- and even femtosecond pulse durations helps to minimize the thermal effects such as melting and burr formation thus eliminating the need for any post processing measures [1].

Based on today's approved scan head technologies and software, even processing of three dimensional surfaces is possible. Advantages are simple programmability and the resulting flexibility. In consequence, this process can be easily controlled, permitting a high flexibility.

Compared with traditional mechanical drilling, pulsed laser drilling is characterized by exceptional efficiency, cost-effectiveness, high precision and non-contact processing without tool wear and is particularly suitable for the difficult-to-machine brittle, hard, and flexible materials. With these advantages, it is extensively employed in many industries, including aerospace, automotive, electronics, medical, instrumentation, etc. [2–4]. Pulsed laser drilling is quite a complex process, since materials undergo a series of physical and chemical processes such as heat conduction, melting, boiling, vaporization, and ejection in both liquid and vapour phases, plasma, and even phase explosion [5]. As a thermal ablation process, pulsed laser drilling is inherently associated with thermal defects and poor geometry like recast layer, heat-affected zone, spatter deposition, taper, and circularity, though it can improve the quality of drilling holes by optimizing process parameters such as peak power, pulse duration, pulse frequency, pulse width, repetition rate, focal plane position, and assist gas pressure [6].

High power laser are a widely used in industrial manufacturing applications such as drilling, cutting, welding and surface processing where typically CO_2 and Nd-YAG systems operating in the infrared are used. However, the laser material interactions in many machining cases are more effectively when using lasers operating at shorter wavelengths. For example, micro-machining of many metals is best performed using visible wavelengths. The Cooper Vapour Lasers' has a good place in this area due to visible wavelength, high pulse repetition rate, high peak and average power, good beam quality, short pulse length [7]. When applied to materials processing, the visible wavelength is found to couple well to most materials, the short pulse length causes ablative material removal, and

Print ISSN 1691-5402
Online ISSN 2256-070X
http://dx.doi.org/10.17770/etr2019vol3.4178

the high repetition rate increases the material removal rate [8]. Another advantage of the copper vapour laser is near diffraction-limited operation allowing good focusing and precise spatial control.

In this paper are presented results in the precise micromachining of several metals using laser system based on CuBr master oscillator and power amplifier connected with computer controlled high- speed scanner system. The goal was to find the best conditions for drilling holes of good circular shape, of minimum heat-affected zone (HAZ).

I. MATERIALS AND METHODS

A. Experimental setup

The used laser system is a MOPA (Master Oscillator - Power Amplifier) CuBr laser that generate wavelength 511nm with maximum output power 6W, pulse repetition rate 20kHz, pulse duration 30ns. The master oscillator was formed by a discharge tube placed in an unstable confocal negative-branch resonator with magnification M = 40 and perpendicular optical output through a plane mirror 45-degree tilted, with a small hole (0.5mm) at the center (Fig. 1). The power amplifier was a single pass with the same diameter of the active medium as the oscillator 20mm. The MTS (master timing system) is a computer-controlled tool for synchronizing the laser oscillator and power amplifier [9]. The MTS provides the MOPA power supplies with triggering signals of controlled delay time. Depending on the delay the second laser acts as an amplifier or as an absorber (shutter). The laser beam was focused (spot diameter of about 30μm) by a glass lens (focal length f= 300mm) and directed perpendicularly to the surface of a metal target. The calculated laser fluence at focal spot is 42 J/cm^2.

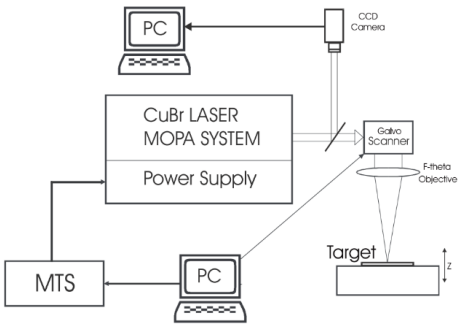

Fig. 1. Schematic of the experimental complex for laser micromachining.

We used Spiricon LBA-300 beam analyser for measuring the profile of the focal spot after focusing with 1m achromatic lens. The obtained intensity distribution was approximated with Gaussian profile. Assuming that, the laser beam diameter is defined at level of 14% of the peak intensity and the dimension of the beam in microns give the divergence in micro radians (Fig. 2). In our case the divergence was approximately 120μrad. In the experiments we used only 14mm of the central part of the laser beam (with diaphragm). It is depends of the input aperture of the scanner. So we lost power but save the divergence and quality of the beam.

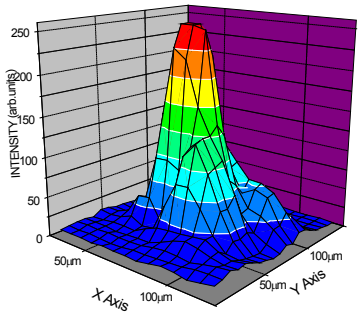

Fig. 2. Spatial distribution of power density at focal point of the laser beam after 1m focusing lens.

Common measure of the beam quality of a laser beam is quality factor M^2 defined by equation (1).

$$M^2 = \frac{\pi\theta D}{4\lambda} \qquad (1),$$

where D is the diameter of the beam, θ – divergence and λ – wavelength. For quality laser material processing is very important to have beam quality factor close to Gaussian beam. In our case it is 2.6 for wavelength 511nm.

B. METHODS

The laser drilling can be done by two ways: by trepanning and by percussion drilling. In the percussion process the laser beam is normally kept still and the hole is punched through the material using multiple pulses. The size and shape of the holes are governed by the size and shape of the focused laser beam (the dimension of the holes is usually the same as the diameter of the beam spot in the focus). The trepanning technique requires a relative beam-target movement during the processing (drill hole cutting, see Fig. 3). In case of trepanning laser drilling the size and shape of holes can be programmed too. In this case, the rotations of the beam spot (or the target) allow making the process as well as the size and shape of holes programmable.

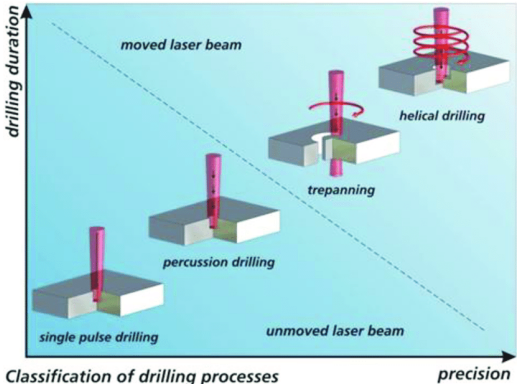

Fig. 3. Classification of drilling processes

Laser percussion and laser trepanning can produce through-holes. The choice comes from the size of hole needed. Laser percussion makes holes of diameter normally less than 50μm. The laser trepanning holes are larger. Laser trepanning is a method by which the laser beam cuts in a circular pattern, taking advantage of high-speed

beam positional scanner. There is a limit to the depth of material that can be cut in a single pass, so a number of passes has to be made. The number of the repetitions is defined as a number of passes around the contour of the hole.

In the most of cases the industry is usually interested in through-holes with a diameter in the range of 50μm up to 1000μm. So we chose the laser trepanning for the realization of precise and reproducible through holes. Another reason for choosing this method is because it allows a fast modification of the processing parameters: scanning speed of the laser focal spot and the number of repetitions. Changing the scanning speed we can control overlapping of the adjacent pulses (see Fig. 4).

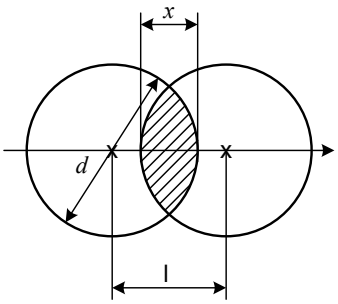

Fig. 4. A schema of the overlapping two consecutive pulses.

Table I shows the scanning speeds employed in order to attain the different overlapping percentages and necessary repetitions to make hole in the foil.

TABLE I. Scanning speeds/overlapping coefficients and number of repetitions needed to drill 100μm hole

Scanning speed, mm/s	**Overlapping coefficient, %**	**Number of repetitions for drilling of 100μm hole in foil thickness of**		
		Al, 100μm	Cu, 150μm	SS316, 150μm
20	97	3	2	6
50	92	6	3	20
100	83	12	5	39
200	67	27	11	88
400	33	55	24	190
600	0	95	70	320
800	-33	200	150	660

Overlapping coefficient of the laser pulses overlapping is a complex factor that gives relation between scanning speed (factor related to the technological process) and pulse repetition rate and laser fluence of laser beam by diameter of focal spot (parameters of the laser). It is defined by the expression

$$k = \frac{x}{d}.100\% = \left(1 - \frac{l}{d}\right).100\% \quad (2),$$

where d is the diameter of focal spot, x is the width of the overlapped area of two consecutive pulses, l - the distance between two consecutive pulses. Taking into account ratio

$$l = \frac{V}{\nu} \quad (3),$$

where V is the scanning speed and ν – pulse repetition rate and making substitution in equation (2) is obtained:

$$k = (1 - \frac{V}{\nu.d}).100\% \quad (4).$$

Negative or zero overlapping coefficients means no overlapping of pulses.

II. Results and discussion

The targets in our experiments were copper, aluminium and stainless steel (SS316) metal foils.

Fig.5 and Fig. 6 presents pictures of drilling of micro holes in Al and Cu using trepanning technique.

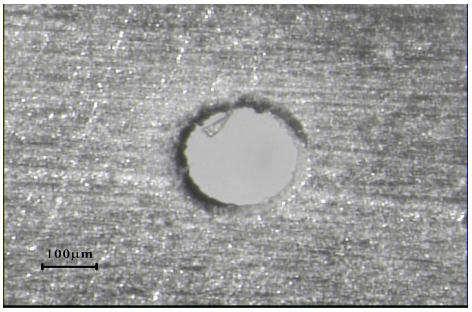

Fig. 5. Al foil, thickness 100μm, scanning speed -20mm/s and number of repetitions – 3.

In this case the edge is clear and sharp and there is no evident thermal distortion. We drilled successful holes also with lower speeds with less repetitions but in this case the HAZ was significant and a small zone of melting materials around the holes was observed. The same unsatisfying results we had for scanner speed more than 600mm/s, i.e. without overlapping of laser pulses. For the drilling the same hole in this case we needed to make a lot of repetitions.

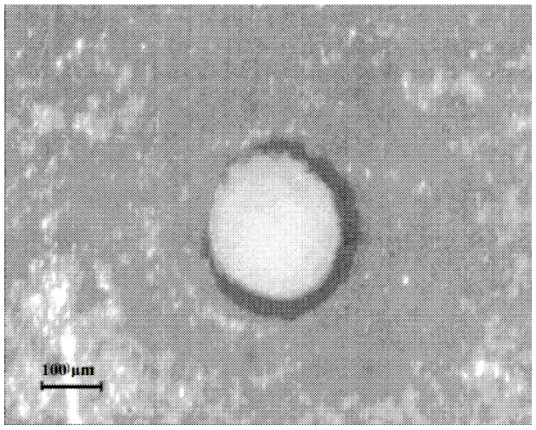

Fig. 6. Cu foil, thickness 150μm, scanning speed - 20mm/s, number of repetitions – 2.

For detailed examination of the holes we used SEM (scanning electronic microscope). Typical holes in aluminium and copper with diameters of 100μm are presented in Fig. 7 and Fig. 8.

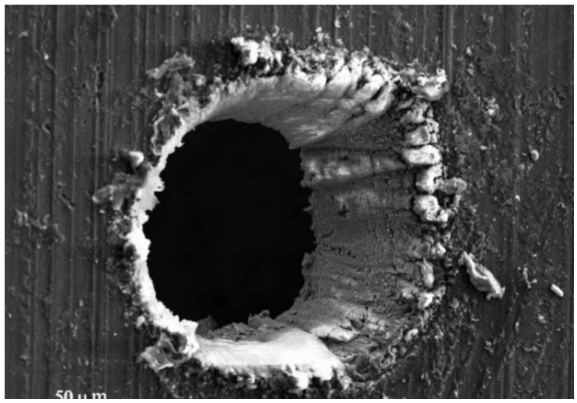

Fig. 7. SEM of the surface of Aluminium foil, thickness 100μm, scanning speed - 20mm/s, number of repetitions – 3.

We found that the trepanning reduces significantly the visible heat-affected zone when the motion velocity of the laser beam spot is more than 50mm/s. By overlapping, the leading edge of the second pulse meets surface temperature higher than the first pulse. So, we have an accumulation temperature effect that conduces to the sample surface high temperature [10].

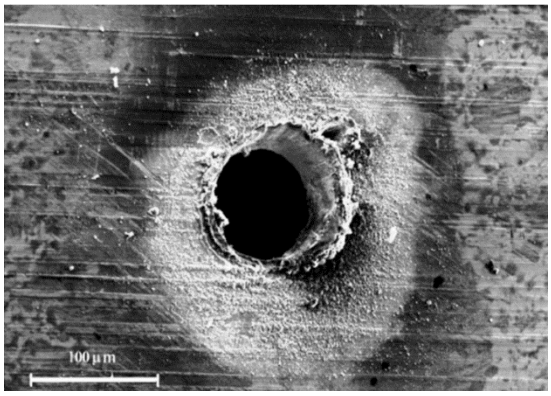

Fig. 8. SEM of the surface of Cupper foil, thickness 150μm, scanning speed - 20mm/s, number of repetitions – 2.

On the other side, the target temperature increase is important because the reflectivity of the metals normally decreases as the surface temperature goes up, and the overall efficiency of the laser processing increases too [11]. This case is presented in the Fig. 7, where the drilling of Al foil is with good efficiency and negligible HAZ. Without overlapping, when the velocity is too high (in our case, more than 800 mm/s), the HAZ is negligible but the efficiency of the drilling decreases sharply (we had to increase greatly the number of repetition cycles) –Table 1.

A series of sieve holes were made in Stainless steel foil. The desire configuration was achieved as 3x3 matrix with distance between the centres of two adjacent holes 200μm. Again was used trepanning technique to drill holes one by one i.e. laser focus sport does not start second hole before finish of first one. Non-spherical shape of holes is due to a technical problem in one axes of xy-galvanometric scanner head (Fig. 9 and Fig. 10).

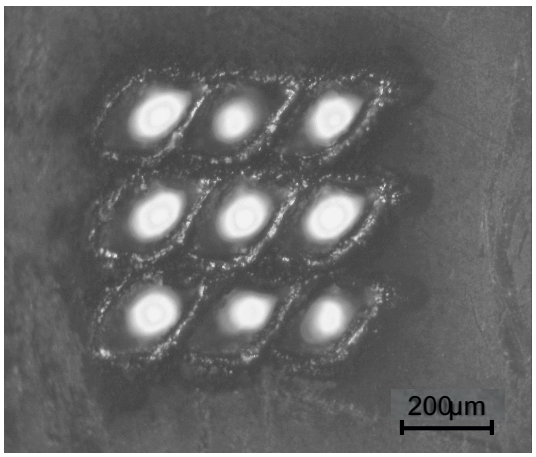

Fig. 9. Sieve on Stainless steel, thickness 150μm, scanning speed 150mm/s, number of repetitions - 65

It has been experimentally found the optimal parameters of trepanning drilling of holes in sieve on stainless steel. The best quality we achieved at scanning speed 50mm/s of laser beam, number of repetitions 20 and pulse repetition rate 20kHz (Fig. 10).

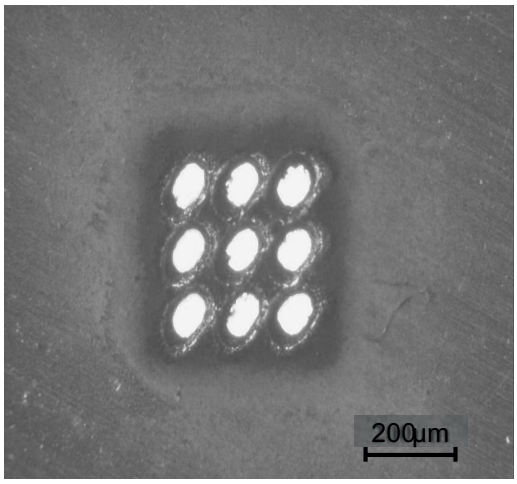

Fig. 10. Sieve on Stainless steel, thickness 150μm, scanning speed 50mm/s, number of repetitions - 20

III. Conclusions

MOPA copper bromide vapour laser system, made in Bulgaria, combined with computer controlled xy - galvanometric scanner was used to investigate process of laser drilling of micro holes using trepanning of aluminium, copper and stainless steel metal foils. Although the quantity of removed material per pulse is small for these processes, the high repetition rate of CuBr laser allows material processing at high speeds.

The experimental results show that our system is a good tool for high - speed laser drilling and cutting. The trepanning method for drilling or cutting with kilohertz repetition rates laser pulses allows better control of high-speed machining with good quality.

References

[1] W. Steen and J. Mazumder, "Laser Material Processing," Springer-Verlag London, 2010, pp. 131–198.

[2] S. Mishra, V. Yadava, "Laser beam micromachining (LBMM) – a review," Opt. Lasers Eng., vol. 73, pp. 89–122, 2015.

[3] D. Ganguly, B. Acherjee, A. Kuar, S. Mitra, "Hole characteristics optimization in Nd:YAG laser micro-drilling of zirconium oxide by grey relation analysis," Int. J. Adv. Manuf. Technol., vol. 61, pp. 1255–1262, 2012.

[4] R. Biswas, A. Kuar, S. Sarkar, S. Mitra, "A parametric study of pulsed Nd:YAG laser micro-drilling of gamma-titanium aluminide," Opt. Laser Technol., vol. 42(1), pp. 23–31, 2010.

[5] Y. M. Zhang, Z. H. Shen, X.W. Li "Modeling and simulation on long pulse laser drilling processing," Int. J. Heat Mass Transf., vol. 73, pp. 429– 437, 2014.

[6] M. Ghoreishi, "Statistical analysis of repeatability in laser percussion drilling." Int. J. Adv. Manuf. Technol.", vol. 29, pp. 70–78, 2006.

[7] N. V. Sabotinov, "Pulsed Metal Vapour Lasers," NATO ASI Series 1ed, vol. 5, C. E. Little and N. V. Sabotinov Eds., Springer Netherlands, Kluwer Academic Press, 1996, pp. 113–124.

[8] J. S. Lash and R. M. Gilgenbach, "Copper vapour laser drilling of copper, iron and titanium foils in atmospheric pressure air and argon," Rev. Sci. Instrum. 64, 1993, pp. 3308–3313.

[9] H. W. Bergmann, C. Korner, M. Hartmann and R. Mayerhofer, "Pulsed Metal Vapour Lasers," NATO ASI Series 1/5, Kluwer Academic Press, 1996, pp. 317–330.

[10] H. Lei, L. Lijun, "A study of laser cutting engineering ceramics", Optics & Laser Technology, vol. 31, pp. 531–538, 1999.

[11] G. Andra, E. Glauche, "Real time investigation of the interaction of a CuBr laser beam with solid surfaces" Appl. Surf. Sci. 109/110 133–136, 1997.

Environment. Technology. Resources. Rezekne, Latvia
Proceedings of the 12th International Scientific and Practical Conference. Volume III, 18-23

Visualization Approaches for Stirred Tank Bioreactors

Armands Bušs
Institute of General Chemical Engineering
Riga Technical University
Riga, Latvia
armands.buss@rtu.lv

Normunds Jēkabsons
Institute of Physics
University of Latvia
Salaspils, Latvia
normunds@jesystems.eu

Artūrs Šuleiko
JSC Biotehniskais centrs
Latvian State Institute of Wood Chemistry
Riga, Latvia
arturs.suleiko.00@rpg.lv

Dagnija Loča
Institute of General Chemical Engineering
Riga Technical University
Riga, Latvia
dagnija.loca@rtu.lv

Juris Vanags
JSC Biotehniskais centrs
Latvian State Institute of Wood Chemistry
Riga, Latvia
juris.vanags@rtu.lv

***Abstract*— Computational Fluid Dynamics (CFD) is the analysis of fluid behaviour employing numerical solution methods. Using CFD it is possible to analyse simple and complex fluid-gas, fluid-fluid or fluid-solid interactions. Fluid dynamics is described with laws of physics in the form of partial differential equations also known as Navier-Stokes equations. Sophisticated CFD solvers transform these laws into algebraic equations which are solved by numerical methods. In this paper Ansys CFX and Fluent analysis systems as research methods are used to visualize flow patterns in a stirred tank bioreactor. The results obtained are informative and can be used to improve the yield of biomass. CFD analysis can save time and aid fluid system designing process. This approach is cheaper and faster compared to conventional build-and-test process. However, it should be noted that CFD analysis results are as accurate as the level of skill possessed by a CFD engineer therefore there are still place for hands-on testing. Authors have developed a stirred tank model and visualized flow patterns. The research presents experimental computation methods and the model setup key parameters. The developed model allows to predict flow patterns inside stirred systems and evaluate efficiency of the mixing process by analysing parameters such as velocity field, turbulence eddy frequency, shear strain rate and power input.**

Keywords*— Ansys CFX/Fluent, CFD, bioreactor, stirred tank.

I. Introduction

Stirred tank bioreactors are used to produce a variety of products across several industries. Many ingredients for the food industry are made through fermentation [1]. For instance, bioreactors are used in the manufacture of antibiotics (e.g., penicillin, lovastatin). Bioethanol has gained importance as a viable alternative fuel, and it is made from fermented agricultural products and waste (e.g., potato starch, wheat, sugar beet). Cell-culture bioreactors lie at the heart of the processes used to produce large-molecule, protein-based therapeutics. Therefore, the importance of scale-up of bioreactors for meeting higher demands of quantity and efficiency of production becomes paramount. Design, construction, and evaluation of bioreactors for larger scale production can be costly and time consuming endeavour. Some critical limiting factors are fluid mechanics effects (e.g., non-ideal mixing, nutrient and oxygen distribution, mass transfer). Thus before building a large scale system it is wise to investigate and visualize a smaller system. The investigation tool used in this research is Ansys CFX simulation software.

Computational fluid dynamics (CFD) refers to solving transport equations for fluid flow, heat and mass transfer quantities using numerical methods. The approach frames a 3-dimensional model and fills the fluid region with large number of finite volumes that are all connected to each other in a form of finite volume (or finite element) mesh. On each one of the mesh elements, momentum, the basic conservation of mass and heat transfer is solved. The underlying equations that govern the solution are called Navier-Stokes equations [2]Japan. Computational fluid dynamics was applied for simulations of a three-dimensional fluidized bed to study the effectiveness of various turbulence models coupled with multiphase models in replicating hydrodynamic profiles within the fluidized bed. For bubbling fluidization, the shear stress transport (SST where the global conservation of the mentioned quantities above is satisfied.

In simple words, CFD models quite complex unit operations as a network of well-mixed compartments that adapt to the boundaries of fluid flow geometry. When set up properly this approach works on any conventional geometry, including sliding and moving parts on a very fundamental level. The number of mixed compartments can be small or large providing that the fine spatial resolution of flow represents related processes occurring within the basic steps in process. The main benefit of this modelling approach is increased process understanding

Print ISSN 1691-5402
Online ISSN 2256-070X
http://dx.doi.org/10.17770/etr2019vol3.4077

and insight into a unit operation from modelling perspective. CFD technology has been and still is widely used in the automotive and aerospace industries. It entered the chemical industries in the middle of nineties along with development of more accessible simulation software that can be run on a PC. The principle "make it right the first time" is desired outcome for many industries as it offers that competitive edge and saves resources. Therefore, modeling fits in as a virtual laboratory before more or less expensive prototypes are built. In the past two decades, CFD has seen increased interest in the fermentation and bioprocessing area, where insight into fluid flow and related phenomena (e.g., turbulence) can assist in risk management associated with mixing zones in bioreactors.

This research investigates a 5L working volume laboratory stirred vessel (298 K, 1 atm) setup with double custom build magnetically coupled Rushton impellers (Fig. 1) and a cell-culture fluid that resembles physical properties of water.

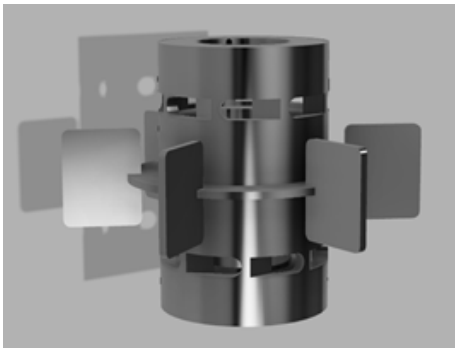

Fig. 1. Magnetically coupled impeller designed and rendered in Autodesk Fusion 360.

In this research we are answering and explaining the following questions:

1. What is the flow pattern and average liquid velocity in bulk liquid?
2. What is average water turbulence eddy frequency in bulk liquid?
3. What is minimum fluid velocity in a laminar region inside a thin slit between the shaft and rotor?
4. What is the smallest turbulence length scale (eddy size) in bulk liquid?
5. What is the shear strain rate in the liquid?

To answer these questions, we use numerical modelling approach as experimental setup is hardly constructible and due to lack of specialised equipment not possible.

The key setup values are arranged in TABLE I.

TABLE I.

Stirred tank geometry parameters		
Baffle width	0.160	[m]
Impeller blade heigth	0.020	[m]
Impeller blade width	0.016	[m]
Impeller blades	6	[-]
Impeller diameter	0.078	[m]
Number of baffles	3	[-]
Shaft diameter	0.019	[m]
Shaft length	0.450	[m]
Tank diameter	0.155	[m]
Tank height	0.350	[m]

II. MATERIALS AND METHODS

Ansys CFX a high-performance computational fluid dynamics (CFD) software tool is used to visualize and answer the questions above. As well as Fluent, CFX is recognized for its outstanding accuracy, robustness and speed when simulating turbomachinery (e.g., pumps, fans, turbines and stirred tanks). In the core of CFX is a cell vertex finite volume code similar to Fluent but with more modern look and feel GUI.

The geometry and mesh of the reactor was drawn in SpaceClaim 3D modelling software and Ansys mesh generator. The mesh consists of tetragonal elements in the liquid region and hex-dominant elements in the air region. The near wall inflation was set to five layers with growth rate of 1.2 and transition ratio 0.77. The mesh consists of 498624 elements and contain 101552 nodes. Under setup section the analysis type was set to steady-state with three distinct domains: air (above fluid), rotor (two rotating domains for impellers) and the stationary fluid domain. The solver control was set to continuity equation class with high resolution advection scheme and first order turbulence numeric. The residual type was set to target value 1E-5. Free surface standard isothermal homogenous k-epsilon turbulence model with scalable wall function was chosen to model the fluid behaviour. The surface tension coefficient was set to 0.072 N/m with continuum surface force and free surface interphase transfer. In boundary conditions the rotating domain has continuous fluid morphology and initial rotational speed of 200 revolutions per minute (Fig. 3).

The model contains two distinct interface regions between: 1) bulk liquid and air above; 2) bulk liquid and rotating domain. The top of the vessel has open boundary condition. The interface model was set to general connection and the frame change (mixing model) was set to frozen rotor. After completing the setup steps the model was executed in platform MPI local parallel run mode using 4 partitions of CPU.

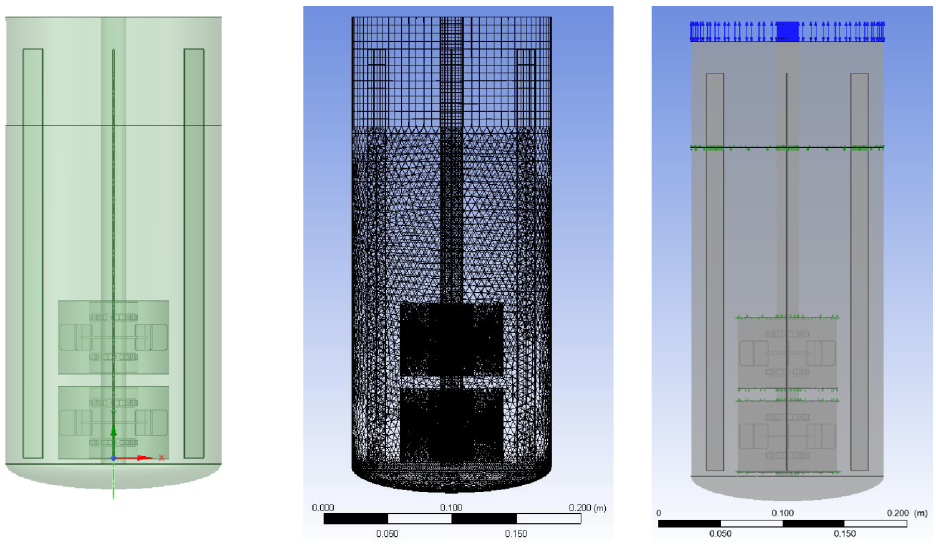

Fig. 2. Geometry, mesh and boundary condition setup profiles.

RESULTS AND DISCUSSION

The flow velocity profile contains the liquid fraction, section lines and vector field with corresponding velocity values when it is stirred at 200 revolutions per minute. The flow pattern corresponds to the one that radial impellers are expected to create. Higher velocity streams are directed towards the wall forming vortexes that travel upwards and downwards creating intense turbulence regions (Fig. 4).

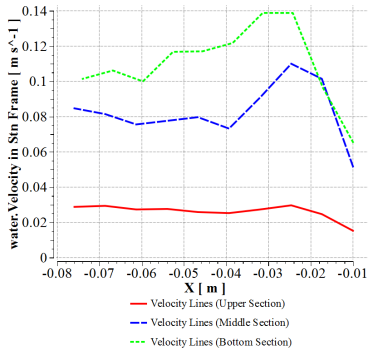

Fig. 3. Liquid velocity along section lines.

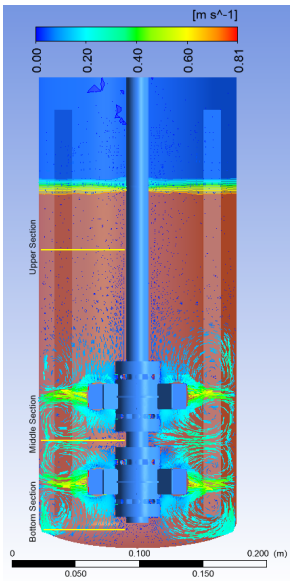

Fig. 4. Velocity profile (XY plane) with vector field and liquid volume fraction (@200 rpm).

Section lines indicate how velocity propagates along the lines (Fig. 3). The upper section has the lowest velocity value which was expected as there is no impeller present suggesting sharp drop of velocity in non-agitated regions.

An interesting region is the thin slit between the shaft and the impeller typical for magnetically coupled rotors (Fig. 5).

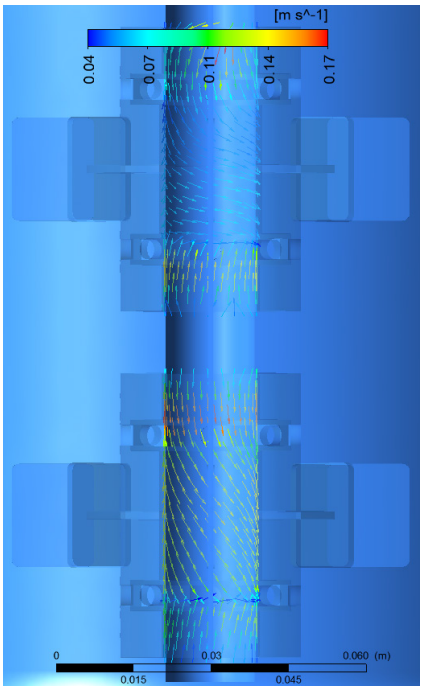

Fig. 5. Thin slit profile between the shaft and the impeller (XY plane, @200 rpm).

In this region flow is predominantly laminar and judging from the vector lines occurs in both directions but mainly downwards suggesting that the intended effect of impeller holes was achieved. The reason for implementing holes was to minimize undesirable flow stagnation. The liquid velocity according to CFD results in this region along the vertical axis is in a range of 0.04 to 0.17 m/s. The slit between the rotor and stationary shaft is 1 mm wide. The rotors are hold in place effectively by magnetic force that originates from a smaller rotating shaft

containing neodymium magnets (grade N42, 1.280 T) within the stationary shaft. The height of each rotor is 55 mm. This essentially gives a hollow cylinder with the same height of 55 mm and wall thickness of 1 mm. The cross-section area (A) of such geometric entity (ring) can be determined by equation below:

$$A_{hc}=\pi t(d+t) \qquad (1)$$

Where, *t* is the slit thickness and *d* is stationary shaft diameter. Substituting the numbers this gives value of 3.14*1 mm*(18 mm+1 mm) = 60 mm^2 = 60E-6 m^2. If liquid velocity in the slit is 0.04 m/s or 40 mm/s according to low end from CFD results (Fig. 5) this would give the volumetric flow rate 0.04 m/s * 60E-6 m^2 = 2.4E-6 m^3/s. Assuming that the liquid inside reactor is homogenous, the whole bulk of the liquid would pass through the slit opening on average in 5E-3 m^3/2.4E-6 m^3/s = 2083 s or 35 min. This indicates that each cell has high probability being exposed to strong magnetic fields between NdFeB magnets (grade N42, 1.28 T, 318 kJ/m^3) during the 35 min mixing time. Cell contact time with 1.28 T could be estimated by dividing rotor height with flow velocity which gives 55 mm / 40 mm/s =1.4 s. Studies of magnetic field effects on cells are limited [3]such as visual photoreceptor and chloroplast membranes, in a homogeneous magnetic field of about 10 kG. While it is not possible to orient the individual constituent molecules with such a field because of thermal fluctuation, these ordered structures can be oriented as a whole by virtue of summing the anisotropy over a large number of mutually oriented molecules. While the magneto-orientation effect seems to require the use of unphysiologically strong magnetic fields, certain birds apparently have highly sensitive sensors to detect the geomagnetic field for the purpose of orientation and navigation. However, the advances in this latter field were made mainly in the behavioral studies; the magnetosensors and the neural mechanisms remain elusive. A number of candidates of the sensors are evaluated. We suggest that pecten oculi, which is unique to avian eyes, should not be overlooked for its possible role as a magneto-sensor based on the magneto-orientation effect. Birds primarily use a static (DC, [4]cell metabolic activity and ability to form biofilms by E. coli and S. aureus. Liquid cultures of the bacteria were exposed to the RMF (RMF frequency f = 1-50 Hz, RMF magnetic induction B = 22-34 mT, time of exposure t = 60 min, temperature of incubation 37 °C, [5]ATCC 43300, Enterococcus faecalis, ATCC 29212, Streptococcus mutans ATCC 35668 and conclusions vary among researchers.

Turbulence eddy frequency contour (or rotations per second for a typical turbulent eddy) represents high turbulence regions which are most intense in the impeller area and to some extent on the surface where the air and liquid phases come in contact (Fig. 6). The area directly under the impeller and above upper rotor is a lot less turbulent suggesting that mixing in this zone is less effective.

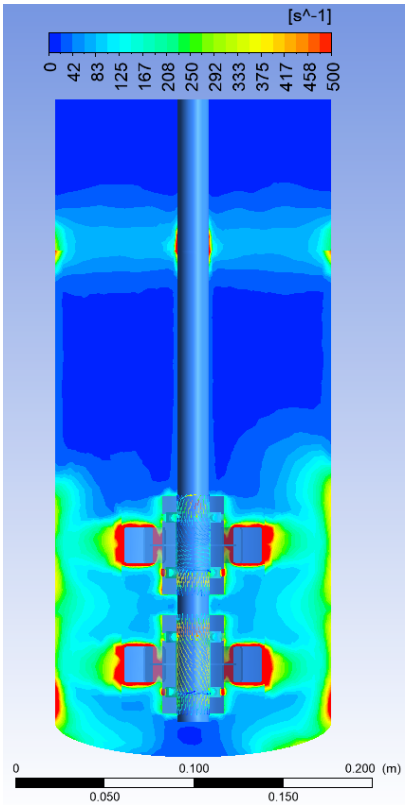

Fig. 6. Turbulence eddy frequency contour (XY plane, @200 rpm).

The smallest turbulence length scale η can be determined by the following expression [6]:

$$\eta = \left(\frac{\nu^3}{\varepsilon}\right)^{1/4} \qquad (2)$$

Where, ν is s the kinematic viscosity of the fluid and ε is the average rate of dissipation of turbulence kinetic energy (per unit mass). The expression above is called Kolmogorov length scale and was first proposed by A. Kolmogorov (1941). This is the smallest scale (eddy size) in turbulent flow. Below Kolmogorov scale turbulent kinetic energy is dissipated as heat and viscosity becomes dominant. This means if eddy size approaches the cell size then significant cell damage is likely to occur within such medium. Similar theory exists that relates the idea above but uses different variables is called Taylor length scale, which is sometimes called the turbulence length scale [7]. This microscale is named after G.I. Taylor (1915). The Taylor microscale is the intermediate length scale at which fluid viscosity significantly affects the dynamics of turbulent eddies in the flow. This length scale is traditionally applied to turbulent flow which can be characterized by a Kolmogorov spectrum of velocity fluctuations. Below the Taylor microscale the turbulent motions are subject to strong viscous forces and kinetic energy is dissipated into heat.

Reynolds number in a stirred tank can be calculated by the following expression [8]the average shear rate γ in the fluid is a function of the rotational speed N of the impeller, as follows:γ = constant ṡ N (laminar flow:

$$\mathrm{Re} = \frac{\rho N D^2}{\mu} \quad (3)$$

Where, ρ is liquid density (1000 kg/m3), μ is liquid dynamic viscosity (0.001 kg.m-1.s-1), D is impeller diameter (0.078 m) and N is impeller angular velocity expressed in s-1 (200/60 s =3.3 s-1). The length scale is related to Reynolds number Re by the following expression [9]:

$$\eta = D\mathrm{Re}^{-3/4} \quad (4)$$

From (3) at 200 rpm or 3.3 s-1 Re equals 20280 and from (4) η is equal to 46 μm. Most eukaryotic cells are within 10-20 μm size range [10] suggesting that mixing regime even at 200 rpm could endanger certain cells but not necessarily destroy them.

In early studies of animal cell cultures, the concern of "shear sensitivity" has been often mentioned [11]. Given the native state of animal cells with all of the mechanical and nutrient support, this concern is understandable, and is further highlighted by lack of cell wall in comparison to the typical microorganisms used in fermentation. The only separation of the animal cell from the surrounding fluid is the plasma membrane consisting of phospholipids, triglycerides, cholesterol, and transmembrane proteins. Therefore, knowing the shear rate is something to consider dealing with delicate cell-cultures. Shear rate is the rate at which a fluid is sheared or "worked" during flow. In more technical terms, it is the rate at which fluid layers move past each other. Shear rate is determined by both the geometry and speed of the flow. CFD indicates shear rate maximum at 1063 s-1 which corresponds to 1063s-1*0.001 Pa.s = 1.063 Pa = 10.63 dyne/cm2 shear stress (Fig. 7). Some authors report even 2 Pa shear stress as damaging for mammalian cells [12].

Mixing process is associated with agitation input power. Different type of impellers has different power rates at the same angular velocity. Power Number Np is a dimensionless parameter used for estimating the power input P by the agitating turbine [8].

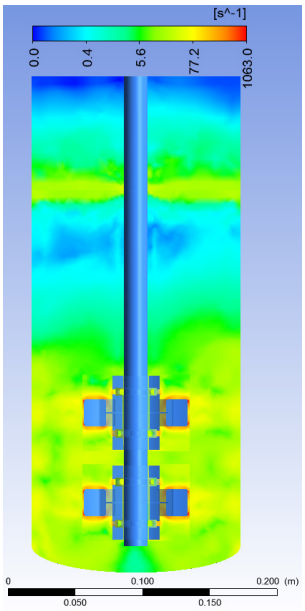

Fig. 7. Shear strain rate (log scale, XY plane, @200 rpm).

The same reactor setup was simulated at 500 and 1000 rpm. The obtained values are represented in TABLE II.

TABLE II.

Revolutions per minute [rpm]	Average stirred tank characteristic variables depending on rpm					
	Re number (x1000)	Turbulence length scale [μm]	Bulk liquid velocity [cm/s]	Thin slit liquid velocity [mm/s]	Eddy frequency in bulk liq. [1/ds]	Shear strain rate @ impellers [1/s]
200	20	46	16	66	35	167
500	51	23	38	99	102	445
1000	101	14	75	180	300	903

Power number is usually plotted vs Reynolds number Re. From our experimental setup the power numbers obtained are shown in TABLE III. Power numbers were calculated by the following equation [8]:

$$Np = \frac{P}{\rho N^3 D^5} \quad (5)$$

Calculated *Re* and *Np* number are ploted in Fig. 8. The best fit line can be approximated as a power function with negative power: $y=4E7x^{-1.44}$.

TABLE III.

Revolutions per minute [rpm]	Experimental power input with corresponding *Re* at 100-1000 rpm		
	Input power experimental [W]	Corresponding Reynolds number [-]	Corresponding Power number [-]
100	1.17	10140	87.75
150	1.65	15210	36.56
200	2.37	20280	22.13
250	3.35	25350	16.04
300	4.43	30420	12.27
350	5.90	35490	10.30
400	7.46	40560	8.72
450	9.33	45630	7.66
500	11.05	50700	6.61
550	12.67	55770	5.70
600	14.33	60840	4.96
650	15.59	65910	4.25
700	17.52	70980	3.82
750	20.26	76050	3.59
800	23.37	81120	3.42
850	27.06	86190	3.30
900	29.88	91260	3.07
1000	37.91	101400	2.84

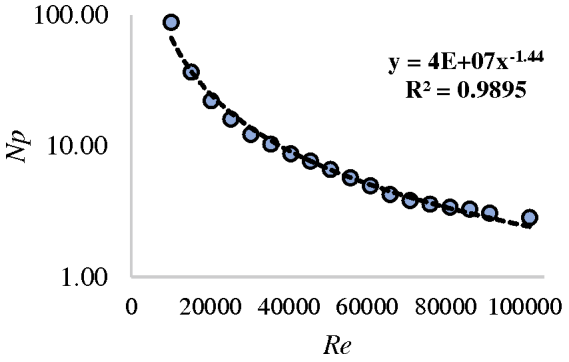

Fig. 8. Power number *Np* versus Reynolds number *Re*: experimental.

The best fit function can be further used for *Np* estimation and hence the power requirement, providing the setup has similar aspect ratio as in this research. However, more experimental work could be done to verify the last statement.

III. Conclusions

The hydrodynamics of stirred tank bioreactor was studied predominantly using CFD and experimental results. The CFD calculations indicate that flow velocity, turbulent eddy frequency and shear rate are largest in the close proximity of the impeller and smallest underneath the impeller and above upper impeller. According to CFD the impeller holes appear to be beneficial and assist to the flow direction in the thin slit region thus minimizing the flow stagnation in this region. As the mixing rate increases so does the apoptosis risk to cell-based fermentation cultures. 200 rpm regime is considered reasonably safe while 1000 rpm regime is likely damaging to eukaryotic cell cultures due to high shear rate and turbulent length scale (14 μm) that is close to the cell dimensions. CFD results provide valuable insight into the working bioreactor flow physics in the way that would be impossible or hardly possible with experimental setup. Furthermore, CFD modelling can help in identifying most desirable bioreactor work regime settings to suit the needs of delicate fermentation systems.

Acknowledgements

This work has been supported by European Regional Development Fund within the project "Influence of the magnetic field initiated stirring on biotechnological processes" No. 1.1.1.1/16/A/144.

References

[1] K. M. Dhanasekharan and J. L. Kokini, "Design and scaling of wheat dough extrusion by numerical simulation of flow and heat transfer," *J. Food Eng.*, vol. 60, no. 4, pp. 421–430, 2003.

[2] J. Liang and E. W. C. Lim, "Evaluation of RANS Turbulence Models, les and des for CFD Simulations of Bubbling, Turbulent and Core-Annular Fluidization," *J. Chem. Eng. Japan*, vol. 51, no. 8, pp. 646–663, 2018.

[3] F. T. Hong, "Magnetic field effects on biomolecules, cells, and living organisms," *BioSystems*, vol. 36, no. 3, pp. 187–229, 1995.

[4] K. Fijałkowski, P. Nawrotek, M. Struk, M. Kordas, and R. Rakocz, "The effects of rotating magnetic field on growth rate, cell metabolic activity and biofilm formation by staphylococcus aureus and Escherichia coli," *J. Magn.*, vol. 18, no. 3, pp. 289–296, 2013.

[5] M. Konopacki and R. Rakoczy, "The analysis of rotating magnetic field as a trigger of Gram-positive and Gram-negative bacteria growth," *Biochem. Eng. J.*, vol. 141, no. 15, pp. 259–267, 2019.

[6] C. Johnson, V. Natarajan, and C. Antoniou, "Verification of energy dissipation rate scalability in pilot and production scale bioreactors using computational fluid dynamics," *Biotechnol. Prog.*, vol. 30, no. 3, pp. 760–764, 2014.

[7] S. Tavoularis and U. Karnik, "Further experiments on the evolution of turbulent stresses and scales in uniformly sheared turbulence," *J. Fluid Mech.*, vol. 204, pp. 457–478, 1989.

[8] J. A. Sánchez Pérez, E. M. Rodríguez Porcel, J. L. Casas López, J. M. Fernández Sevilla, and Y. Chisti, "Shear rate in stirred tank and bubble column bioreactors," *Chem. Eng. J.*, vol. 124, no. 1–3, pp. 1–5, 2006.

[9] V. N. Vlachakis, P. P. Vlachos, D. P. Telionis, M. R. Brady, and R. H. Yoon, "Turbulence Characteristics in a Rushton Stirring Vessel: A Numerical Investigation," in *ASME 2006 2nd Joint U.S.-European Fluids Engineering Summer Meeting Collocated With the 14th International Conference on Nuclear Engineering*, 2008, pp. 19–26.

[10] D. A. Guertin and D. M. Sabatini, "Cell Size Control," *Encyclopedia of Life Sciences*. pp. 1–10, 2005.

[11] W. Hu, C. Berdugo, and J. J. Chalmers, "The potential of hydrodynamic damage to animal cells of industrial relevance: Current understanding," *Cytotechnology*, vol. 63, no. 5, p. 445, 2011.

[12] T. Tanzeglock, M. Soos, G. Stephanopoulos, and M. Morbidelli, "Induction of mammalian cell death by simple shear and extensional flows," *Biotechnol. Bioeng.*, vol. 104, no. 2, pp. 360–370, 2009.

Combined Technology of Electro-Spark Alloying and Thermal Diffusion Boriding of Steel

Vladimir Dashkevich
Belarusian National Technical University
Minsk, Belarus
Vladimir_dvl@tut.by

Yulia Usherenko
Belarusian National Technical University
Minsk, Belarus
osher_yu@mail.ru

Igor Matvienko
Belarusian National Technical University
Minsk, Belarus
volhamirabella@mail.ru

Victor Ivashko
Belarusian National Technical University
Minsk, Belarus
vsivashko@bntu.by

***Abstract*—The process of thermal diffusion boriding is well known and used throughout the world. It has a number of unique properties, such as high hardness and wear resistance under abrasive wear conditions. Continuous boride layers have increased brittleness, which is related with the elastic properties of borides. In this work, we studied the features of the formation of surface layers onlow-carbon steels after electro-spark alloying, and not by continuous processing of the entire surface of the steel, but only sections and subsequent thermal diffusion boriding from powder medium. Such complex technology enables to form discrete regular and irregular layers, which have a number of advantages, in particular, reduced brittleness. The structure and phase composition of the combined coating growth kinetics of the diffusion layer during the thermal diffusion boriding, are investigated. The creation of the considered composite layers with FeB and Fe_2B phases with reduced brittleness will significantly expand their area of application, for example, for working conditions with moderate impact loads.**

***Keywords*—Electro-spark, boriding, steel.**

I. Introduction

Currently accumulated a wealth of scientific and practical experience in the application of boriding. Traditionally, the diffusion layer after boriding consists of two phases: on the outer surface of the product there is a high-boron FeB phase, below a low-boron Fe_2B, and then a transition zone, represented by a solid solution of boron in α-Fe [1, 2]. In addition, between the diffusion layer and the base can form an intermediate layer of cementite (borocementite), which is formed when carbon is pushed back into the product. One of the main problems of boride layers retaining their active use - increased brittleness. The brittleness of boride layers is studied in numerous works, for example, in the works of Krukovich [3]. Traditional ways to reduce the brittleness of the layer are: additional alloying of the layer, obtaining single-phase layers, softening heat treatment, obtaining boride eutectics, etc. Along with them, an effective technique for improving the performance of a thermal diffusion boride layer is to change its morphology, to obtain a discrete structure using surface pretreatment [4].

In this paper, we consider a variant of the combined treatment consisting in preliminary electro-spark alloying (ESA) and subsequent thermal diffusion boriding.

II. Materials and methods

When applying ESA coatings, the ENPOUR-121 installation (Russia) was used, the electrode material - technical copper. Processing parameters: current I <0.5 A; voltage U = 220 V; vibration frequency 10 ... 20 s^{-1} (turbo mode). After applying the electro-spark coating, thermal diffusion boriding in a powder medium was carried out during furnace heating, in an airtight container with a fusible bolt. Processing mode: temperature 920 ° C, time 1 h.

For carrying out the process, an electric shaft furnace with residential heaters is used. As a saturating mixture, the powder environment developed by the Belarusian National Technical University was used, which was obtained by the metal-thermal method of the Besto-Bor brand (Belarus). The saturating medium used gives special competitive advantages of the boriding enhancement technology.

Metallographic studies of the samples obtained after processing were carried out on a Leica microscope with magnification from 200 to 500 times. Microstructural studies were performed on transverse microsections, etched in special metallographic reagents. Microhardness measurements were performed on a PMT-3 instrument with loads of 0.49 N and 0.98 N.

Results and discussion

When combining two technological processes of hardening, it is necessary to take into account the materials used and the resulting structures. For the case under consideration, the coatings formed during the electric-spark treatment can be divided into two groups:

Print ISSN 1691-5402
Online ISSN 2256-070X
http://dx.doi.org/10.17770/etr2019vol3.4149

1 — coatings that intensify the diffusion process of the element, in our case boron, and 2 - barrier coatings that partially or completely suppress the diffusion process of the element into the interior of the product. The most promising direction of the combination of the combination under consideration is the possibility of obtaining regular coatings consisting of boride sections isolated from each other by fragments of an electric spark coating. Therefore, in this paper, we considered the case of barrier coatings, in particular, steel samples obtained by ESA copper electrode.

During the formation of areas of boride needles separated from each other by fragments of another coating obtained, for example, ESA, there is a partial compensation of elastic deformations in the layer due to adjacent zones and, as a consequence, a decrease in brittleness.

The specificity of the electric-spark processing makes it possible to simply form the processing not of the entire surface, but of sections, for example, forming a periodic (regular) profile in the form of lines parallel to each other. Moreover, the step between the treatment sites can vary widely, contributing to the formation of layer structures of different morphology. In our case, the distance between the areas treated by ESA was about 2 mm (fig. 1). By varying the pitch and modes of the preliminary electric-spark treatment, the prerequisites for controlling the layer structure are created.

Thus, processing performed by the following scheme:

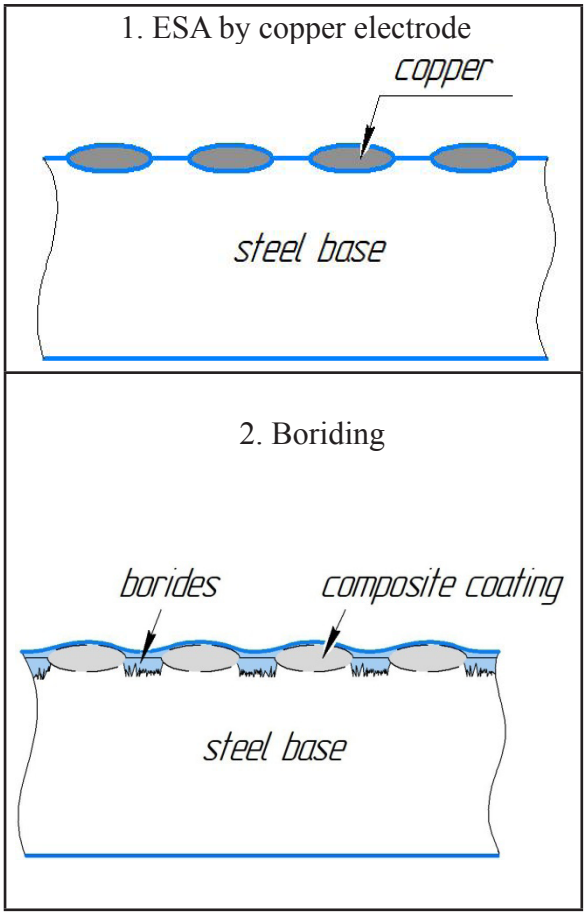

Fig. 1. Scheme of coating obtaining with a combination of ESA and boriding

As noted earlier, copper was chosen because it prevents the through diffusion of boron. It is known that boron does not form compounds with copper, and the solubility of boron in copper is extremely low (0.06% wt.) [5]. When copper is applied by the ESA method, sparking occurs on the surface and part of the copper electrode is transferred to the surface, while copper partially mixes with the base metal, a defective structure is formed, which is only partially impermeable to boron atoms [6]. During the subsequent boriding, a conglomerate of iron and copper borides is formed, and the borides are mainly represented by the low-boron phase Fe_2B (fig. 2).

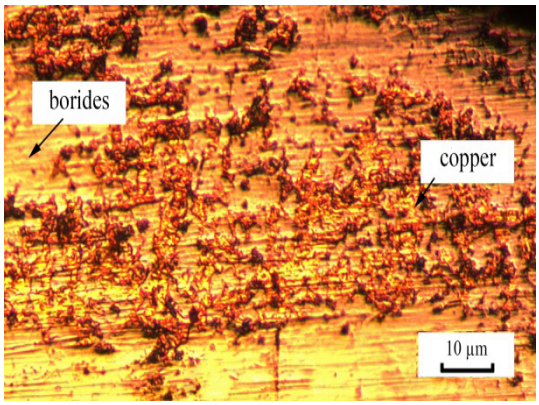

Fig. 2. The microstructure of the area with a composite coating, obtained by preliminary copper ESA

As a result of complex processing structure formed with distinct areas of classical boride layer and the areas of the composite coating formed by preliminary copper ESA (fig. 3).

It should be noted that the transition zone of the two areas of the structure is quite sharp. The microhardness of the boride area is 14000 - 15000 MPa, the area of composite coating varies in wide range from 1500 to 1400 MPa.

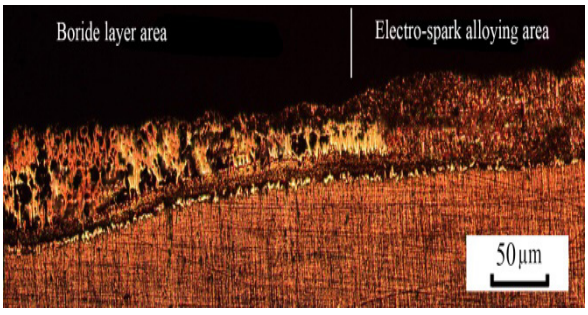

Fig. 3. Microstructure of the coating consisting of a boron layer and a composite coating

The application of the copper coating by the method of ESA contributes to the separation of the total layer during the subsequent boriding to the areas of the boride layer and the areas of the composite coating based on iron and copper borides. Moreover, copper in the structure is represented as separate dispersed inclusions with sizes of about 5 ... 20 microns (fig. 2). Such structure is sufficient and promising for parts working in friction pairs, in this case copper can partially act as a lubricant.

It has been established that the microhardness of the

obtained boride areas corresponds to the microhardness of the layers obtained under the classical processing conditions, including in the zone approaching the transition, and is 14 000 - 15 000 MPa.

One of the most important criteria that is crucial for the effective use in production is the fragility of the obtained thermal diffusion layers. Obviously, the resulting structure of the diffusion layer will reduce brittleness and a tendency to shear at high contact pressures and shock loads [3, 7].

The characteristic of brittleness was evaluated by the cleavage stress, as well as the total score of brittleness.

The cleavage stress is an integral characteristic of the fragility of the layer, spontaneously taking into account the physical and mechanical properties of the borides themselves, the phase composition, the phase ratio, their dispersion and mutual arrangement in the layer and on the surface, the stress state of the layer and its plasticity. The greater the value of the cleavage stress, the less brittleness, and therefore the layer is more plastic [3, 8].

The brittleness score was determined based on the microhardness measurement method. This characteristic is a qualitative indicator of fragility and is similar to the method used to assess the fragility of nitrided layers.

As a result of investigations it was found that the brittleness of the considered complex coating is reduced. The brittleness determined in areas with a composite layer structure, determined by the cleavage stress, is reduced in 1.5 times relative to traditional boriding (table 1).

TABLE I. CHARACTERISTIC OF BRITTLES

Processing type	**Brittleness rate**	
	Cleavage stress, MPa	**The total score of brittleness Z100**
Boriding (two-phase)	280	35
ESA +boriding	420	26

Note that there is no clear correlation between the values of brittleness in certain different ways, but the general trends for all research options remain.

III. CONCLUSIONS

Thus, the application of a copper coating by the ESA method enables the separation of the total layer during the subsequent boriding to the zone of the boride layer and the zone of composite coating. In areas with a composite coating obtained by preliminary ESA, boron diffusion slows down, due to which lower iron borides are predominantly formed, which have a higher ductility. Due to the appearance of copper inclusions in the structure, in which the elastic modulus is much less than that of borides, some reduction and relaxation of internal stresses in the layer is possible, which affects the overall brittleness of the boride layer.

The creation of the considered binary composite layers based on boron can significantly reduce the fragility of the resulting layers and, accordingly, expand their area of application, for example, for working conditions with moderate impact loads.

REFERENCES

[1] LG. Voroshnin, L.S. Lyakhovich, Boronizing of Steel, Metallurgy, Moscow, 1978 (in Russian).
[2] M. Kulka, Current trends in boriding: Techniques: Springer Nature, Switzerland, 2019.
[3] Krukovich M.G., Prusakov B.A, Sizov I.G. Plasticity of Boronized Layers: Springer International Publishing AG, Switzerland, 2016.
[4] M.A. Béjar, W. Schnake, W. Saavedra J.P. Vildósola, Surface hardening of metallic alloys by electrospark deposition followed by plasma nitriding, Journal of Materials Processing Technology 176 (1-3), pp. 210-213. June 2006.
[5] O.A. Bannyh, M.E. Drica, Phase diagrams of binary and multicomponent iron-based systems: A Handbook, Moskow: Metallurgy, 1986 (in Russian).
[6] A.E. Gitlevich, V.V. Mikhailov, N.Ya. Parkansky, V.M. Revutskiy, Electrospark alloying of metal surfaces, Chisinau: Shtiintsi Publishing House, 1985 (in Russian).
[7] C. H. Xu, Wei Gao,Y.L. Yang, Superplastic boronizing of a low alloy steel – microstructural aspects, Journal of Materials Processing Technology. Vol. 108 (3), pp. 349-355, Jan. 2001.
[8] V. F. Protasevich, V. V. Melnichenko, Some features of microhardness and micro-brittleness of boride layers, Journal of Foundry Production and Metallurgy. Vol. 4 (36), pp. 145-147, 2005 (in Russian).

Method for Measuring Motion Parameters of Moving Objects

Dimitar Dichev
Department of Machine and Precision Engineering Technical University of Gabrovo
Gabrovo, Bulgaria
dichevd@abv.bg

Iliya Zhelezarov
Department of Machine and Precision Engineering
Technical University of Gabrovo
Gabrovo, Bulgaria
izhel@tugab.bg

Tsanko Karadzhov
Department of Machine and Precision Engineering
Technical University of Gabrovo
Gabrovo, Bulgaria
Karadjov_st@abv.bg

Nikolay Madzharov
Department of Electronics
Technical University of Gabrovo
Gabrovo, Bulgaria
madjarov@tugab.bg

Dimitar Diakov
Department of Precision Engineering and Measurement Instruments
Technical University of Sofia
Sofia, Bulgaria
diakov@tu-sofia.bg

***Abstract*—The paper considers a new method for measuring the angular deviations of moving objects. A specific measuring system is proposed to measure ship roll, pitch, heel and trim. The system consists of two measurement channels operating in parallel. The first channel is built on the position properties of a physical pendulum so as to build the base vertical. The second channel ensures the dynamic accuracy of the system. The principal of operation of the second channel involves correction of the signals from the first channel by using information obtained from linear MEMS accelerometers. To increase system measurement accuracy, a signal processing module is used through the Kalman filter algorithm.**

Keywords*— *Kalman filter; dynamic error; gyro-free measuring system; roll, pitch, heel, trim.

I. Introduction

The dynamic accuracy of measuring instruments and systems mounted on moving objects considerably depends on the intensity of the linear and angular accelerations acting upon them and mainly caused by the fluctuations of the object. Meanwhile the basic parameters of the interference effects and the quantities being measured vary within wide ranges and depend on a number of factors which are determined by the specific moving object and its motion medium. In this respect, there is a great variety available for state-of-the-art means of transport (ships, aircrafts, road transport, etc.).

The above mentioned substantially complicates the development of measuring systems that possess the required accuracy for the whole range of variations of the interference effects and the quantities being measured. This holds true for instruments measuring parameters such as roll, pitch, heel and trim which characterize the ship motion. Namely, the problems related to measuring those parameters are covered by the present study.

A distinguishing feature of the measuring instruments presented in this paper is that they operate under conditions of dynamic effects caused by the motion of the moving objects or by the fluctuations of the ships, aircrafts and road means of transport, as well as by the vibrations in the place where the measuring instruments have been positioned [1] - [3]. Those motions result in producing inertial forces and moments which act upon the measuring instruments thus causing a dynamic error in the measurement result. [4].

To reduce the influence of inertial forces and moments in current measuring instruments, gyro-stabilized systems are mainly used. They model the reference coordinate system in relation to which the position of the moving object upon its rotation with respect to its mass centre and its motion along with its mass centre is measured, as well as the set direction of motion is kept. [5] - [8]. This complicated model for reproducing the direction of the vertical leads to a number of disadvantages such as a complex design resulting in a bigger instrumental error, low reliability under extreme conditions, need for special systems ensuring the operation of the gyro-vertical, larger dimensions, higher price of the instrument or system, etc. [9], [10].

Thus, the present paper proposes a new method for developing measuring instruments and systems which define the parameters of moving objects. That method is able to overcome the drawbacks of the current measuring instruments since, on one hand, it is based on a considerably simplified mechanical module, and on the other hand, on the advanced achievements in the area of nanotechnologies, microprocessor and computer equipment.

A specific measuring system has been developed in compliance with the basic principles of the proposed method so as to measure ship roll, pitch, heel and trim.

II. Description of the measuring method

The general concept of the proposed method is presented by means of a block diagram shown in Fig. 1. The

Print ISSN 1691-5402
Online ISSN 2256-070X
http://dx.doi.org/10.17770/etr2019vol3.4131

block diagram consists of a main measurement channel, an additional channel, interfaces to be connected to a computer and software modules for processing and presenting measurement information. The main channel is designed to measure the current values of the quantities being measured.

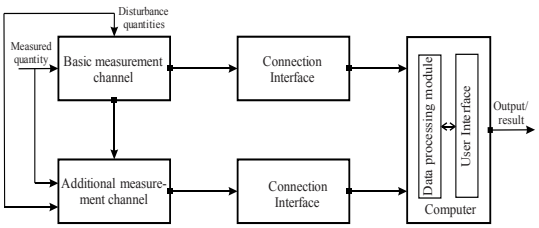

Fig.1. Block diagram illustrating the principle of modeling of measuring systems

Due to its simplified design and lack of stabilization systems, the signal at the channel output contains a dynamic error caused by the deviation of the physical pendulum from the astronomical vertical. The procedure for obtaining the measurement information required for defining the current values of the dynamic error is performed in the additional channel (Fig. 1). The latter operates in parallel with the main one, which makes possible the elimination of the dynamic error from the measurement result in real time. The design of the additional channel and the type of the constituent devices are specified according to the model chosen to determine the current values of the dynamic error and the correction algorithm of the signal from the main measurement channel.

III. Measuring system for defining ship roll, pitch, heel and trim

To illustrate the features of the proposed method, the characteristics of a specific measuring system built in compliance with the above concept are considered. The system has been developed to measure ship roll, pitch, heel and trim.

The block diagram of the system is shown in Fig. 2. The main measurement channel consists of a mechanical module intended to provide gyro-free modelling of the local vertical and a system for recording the angles of the heel and trim, which includes two code photoelectric converters mounted along the respective measurement axis. The design model of the mechanical module of the main measurement channel (Fig. 3) has been developed according to the block diagram in Fig. 2.

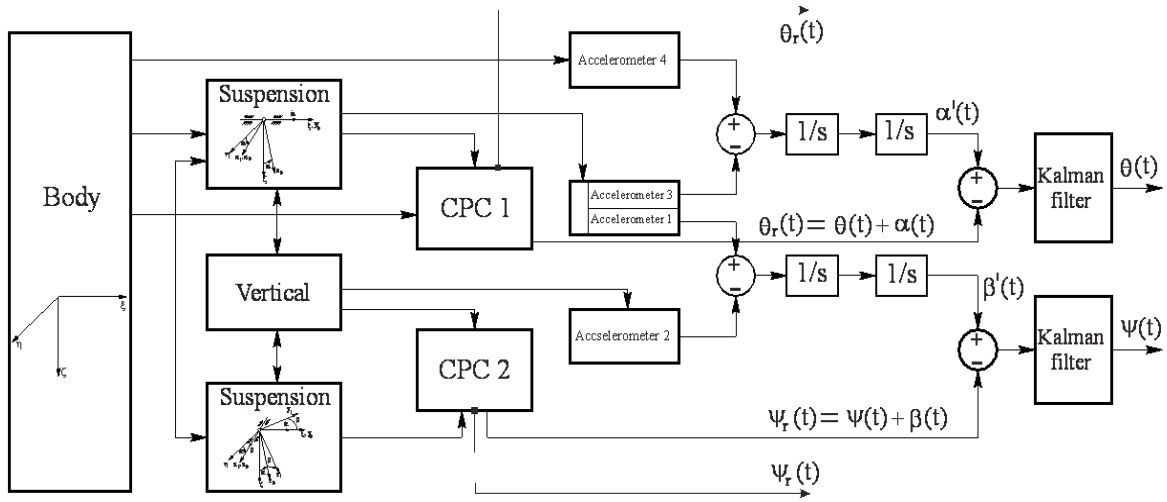

Fig.2. Operating diagram of the measuring system

The development of the main measurement channel is focused on a simplified technical implementation of the vertical in the form of a physical pendulum. Therefore, this comparatively easy technical implementation of the mechanical module, which consists of a small number of components, results in reducing the magnitude of the instrumental error.

The body of the mechanical module is permanently connected to the ship. A 2-degree-of-freedom physical pendulum reproducing the device vertical is mounted on the body by means of a suspension system (Fig. 3). The latter consists of an outer and inner frame, connected in series by cylindrical joints. A physical pendulum is attached to the inner frame. The two frames have inter perpendicular axes of rotation, which intersect at one point. The measurement information about the heel and trim angles is obtained from two code photoelectric converters (CPC1 and CPC2), mounted on the respective measurement axis.

The measurement accuracy in dynamic mode is ensured by an additional channel for determining the dynamic error. It consists of two pairs of identical MEMS accelerometers used for measuring the linear acceleration. The accelerometers are mounted respectively on the body of the mechanical module, on the first cylindrical joint (two accelerometers), and on the physical pendulum. The first two accelerometers are mounted in such a way that their measurement axes are sensitive to the accelerations generated by the roll whereas the measurement axes of the other two accelerometers are sensitive to the accelerations generated by the pitch. This scheme of mounting of the MEMS sensors ensures the sensitivity of the first accelerometer of each sensor pair to all accelerations generated by the roll and pitch. Every second accelerometer is sensitive not only to the accelerations of the first sensor but also to those generated by the pendulum motion with respect to its degree of freedom. This makes possible the development of a procedure involving the subtraction of

the signals from the first and second accelerometer of each sensor pair where the output signals are proportional to the accelerations generated by the pendulum motion with respect to its degree of freedom. By means of a data processing algorithm a double integration of the accelerations is performed, where signals defining the pendulum deviations from the vertical with respect to its two degrees of freedom are obtained.

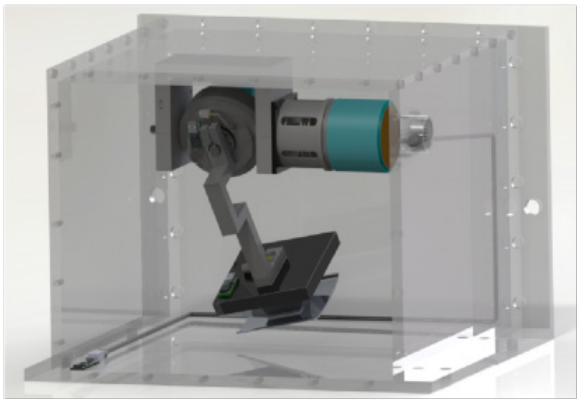

Fig.3. Design model of the main measurement channel

Because the device body is permanently fixed to the ship and its measurement axes are sensitive to ship fluctuations with respect to the heel θ and trim ψ , the measurement information on the change of those quantities is obtained at CPC1 and CPC2 outputs. That information is recorded with respect to the time coordinate in the form of functions $\theta_r(t)$ and $\psi_r(t)$. The instability of the physical pendulum in the inertial space leads to a dynamic error in the result whose characteristics are defined by functions α(t) and β(t). The latter are formed by the pendulum deviations from the ideal astronomic vertical emerging along the two measuring coordinates of the device. In this case the values obtained from the two measurement channels are equal to the sums of the desired signals and the respective dynamic errors, i.e. $\theta_r(t) = \theta(t) + \alpha(t)$; $\psi_r(t) = \psi(t) + \beta(t)$, where θ(t) and ψ(t) are the signals determining the true values of the heel and trim along the time coordinate.

Due to the presence of interference sources of random characteristics, additional secondary processes of unpredictable behavior and possible occurrence of errors as a result of system conversion processes, additional errors may occur thus considerably reducing accuracy when defining the dynamic error [11] - [14]. Therefore, in order to eliminate the influence of the above listed sources, adaptive algorithms (such as Kalman filter) need to be introduced in the measurement procedure [15] - [17]. They make possible the automatic adjustment of the measuring system when searching for optimal solutions according to the minimum mean square criterion. In this sense, the result from the precise solution of the algorithmic synthesis problem can be formulated by target inequalities of the form

$$\varepsilon_{\alpha_{de}}(t) - \alpha(t) \le q_{äîï}\ ; \quad \varepsilon_{\beta_{de}}(t) - \beta(t) \le q_{äîï}\ , \quad (1)$$

where $\varepsilon_{\alpha_{de}}(t)$, $\varepsilon_{\beta_{de}}(t)$ - the dynamic errors obtained as a result at the output of the adaptive filters; *α(t)*, *β(t)* – the true values of the respective dynamic error; $q_{доп}$ – admissible deviation.

IV. Mathematical model of the measuring system

The measuring system can be developed only on the basis of a complete and precise mathematical model because this model is used to determine the main dependences of the parameters of the measuring system, the quantities being measured, and the influence quantities in a form appropriate for the analysis of the required characteristics.

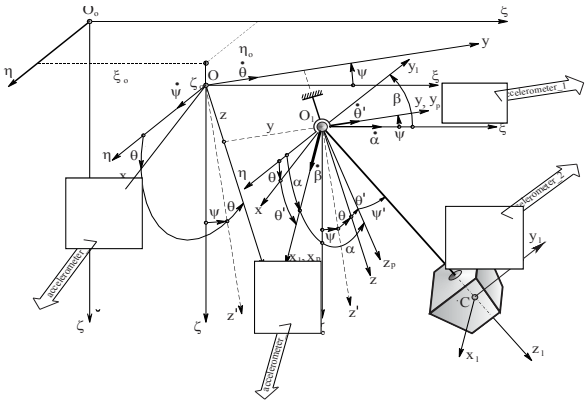

Fig.4. Diagram of the dynamic system moving object - measuring instrument

The differential equations are worked out on the basis of the design model and the diagram showing the arrangement of the accelerometers. The dynamic system is shown in fig. 4. Ship motions are defined as angular and linear fluctuations of a rigid body around or along with its centre of gravity. The moving object (the ship) to which the coordinate system O*xyz* is connected moves randomly with respect to the reference system $O_o\xi\eta\zeta$. A measuring instrument is mounted on the ship and its sensitive element (a physical pendulum) is connected to coordinate system $Cx_1y_1z_1$. The suspension point O_1 of the instrument sensor coincides with the diametral plane of the ship and its position with respect to the centre of gravity of the moving object O is defined by the *z* and *y* coordinates.

The position of the moving object with respect to the reference system $O_o\xi\eta\zeta$ is set by the three coordinates of its centre of gravity O - ξ_o, η_o, ζ_o and the matrix $A = \|a_{ij}\|$ (*i,j=1,2*) of the given angle cosines of the trim *ψ* and the heel *θ*, defining the angular displacement between the axes of the systems $O_o\xi\eta\zeta$ and Oxyz. The dynamic system consists of two bodies - a physical pendulum which is free to rotate with respect to the coordinate axes O_1x_1 and O_1y_1, and an accelerometer mounted in the centre of gravity C of the physical pendulum. The accelerometer inertial body of a mass m_2 stays at an equilibrium position in relation to the y_1 coordinate by means of two horizontal springs of an elastic constant c.

Therefore, the system has three degrees of freedom and the generalized coordinates are, respectively, *α, β* and y_1. The *α* and *β* coordinates define the angular

displacement of the physical pendulum from the vertical in relation to, respectively, O_1y_1 and O_1x_1 axes whereas y_1 determines the relative motion of the inertial mass m_2. By means of coordinate β the inertial component of the dynamic error for the measurement channel under consideration is defined. The latter determines the trim values of a ship.

After performing the required mathematical operations and reducing the obtained equations to a simplified form by linearizing the quantities that define the motion of the system points and including only small first-order quantities, the following system of differential equations is obtained:

$$\begin{vmatrix} \left(J_{y_1} + m_1.l^2\right).\ddot{\alpha} + k_\alpha.\dot{\alpha} + m_1.g.l.\alpha = \\ = m_1.l.\ddot{\eta}_o - \left(J_{y_1} + m_1.l.z\right).\ddot{\theta}; \\ \left(J_{x_1} + m_1.l^2\right).\ddot{\beta} + k_\beta.\dot{\beta} + m_1.g.l.\beta = \\ = -m_1.l.\ddot{\xi}_o - \left(J_{x_1} + m_1.z.l\right).\ddot{\psi}; \\ m_2.\ddot{y}_1 + k_{y_1}.\dot{y}_1 + c.y_1 = \\ = -\frac{1}{2}m_2.\left(l.\ddot{\beta} + \ddot{\xi}_0 + z.\ddot{\psi}\right), \end{vmatrix} \quad (2)$$

where k_α, k_β and k_{y1} are damping factors along the three generalized coordinates α, β and y_1; l – the length of the physical pendulum.

The third equation in (2) defines the link between the readings of the accelerometer mounted on the physical pendulum and the quantities entering at the input of the instrument. A differential equation representing the motion of the sensitive element of the second accelerometer can be easily worked out from this equation, taking into account the identical design characteristics of the two sensors and the fact that this accelerometer is not sensitive to the motion of the physical pendulum. Then the differential equation sought will be:

$$m_2 \cdot \ddot{y}_p + k_{y_p} \cdot \dot{y}_p + c \cdot y_p = -\frac{1}{2} m_2 \cdot \left(\ddot{\xi}_0 + z \cdot \ddot{\psi}\right), \quad (3)$$

where y_p is the coordinate of the motion of the sensitive element of the second accelerometer.

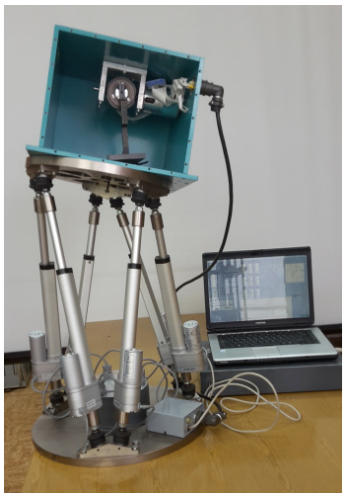

Fig.5. Photos from the experiments

In this case the difference between the readings of the two accelerometers will be proportional to the function $\ddot{\beta}(t)$, by means of which we can easily determine the quantity β(t) defining the dynamic error. However, additional interferences are accumulated to the $\ddot{\beta}(t)$ signal. They can be easily identified if equations (2) are reduced to a form which consists of first- and second-order quantities. Then on the right side of the third differential equation from (2) functions $\ddot{\xi}_o \cdot \beta$ and $y \cdot \ddot{\psi} \cdot \beta$ appear and they are superposed on signal $\ddot{\beta}(t)$. Although the values of those functions are formed as small second-order quantities with respect to $\ddot{\beta}(t)$, they cause an additional error when determining quantity $\beta(t)$. Hence, they should be eliminated from the signal before the final formation of function $\beta(t)$. In this case the use of Kalman filter, whose location in the measurement procedure is given in the block diagram in fig. 2, is very relevant.

V. Experiments and results

To carry out the experiments, the required stand equipment has been developed. It possesses reference properties and makes possible the implementation of all metrological tasks related to checks, calibration, definition of dynamic characteristics and investigation of dynamic accuracy. The equipment is in the form of a 6-degree-of-freedom hexapod and photos from the experiments are shown in fig. 5.

To illustrate the quality of the measuring system, the results from the investigation of the channel measuring the ship pitch and trim are presented in fig. 6. The figure shows: the reference motion of the hexapod operating platform $\psi(t)$; the recorded signal before Kalman filter $\psi_{bk}(t)$; the pitch measurement result obtained at the output of Kalman filter $\psi_{bk}(t)$; the dynamic error $\varepsilon_{\beta_{de}}(t)$. Figure 5 indicates that the measuring system possesses high measurement accuracy in dynamic mode, since error $\varepsilon_{\beta_{de}}(t)$ does not exceed *4%* of the variation range of the quantity being measured. Similar results are obtained upon investigating the second measurement channel (measuring roll and heel). In static mode the system operates at approximately two times higher accuracy because of its simplified design diagram, which is used in the mechanical module for modeling the vertical.

VI. Conclusions

The proposed measurement concept is designed for developing gyro-free measuring systems that determine the parameters of moving objects. This modelling approach overcomes the disadvantages of the existing measuring instruments since it is based, on one hand, on a very simplified mechanical module, and on the other hand, on the advanced achievements in the area of nanotechnologies, microprocessor and computer equipment.

The high dynamic accuracy of the proposed measuring system is ensured by an additional measurement channel operating in parallel with the main channel. The metrological procedures in the additional channel are based on an appropriate correction algorithm using signals from linear MEMS accelerometers.

The experimental results confirm the effectiveness

of the proposed measurement concept in relation to the dynamic accuracy of systems measuring moving objects. As a result of the operation of the additional channel and the Kalman algorithm the accuracy characteristics of the measuring system under conditions of dynamic influences are improved to a great extent. This can be implemented without using expensive elements and stabilization systems.

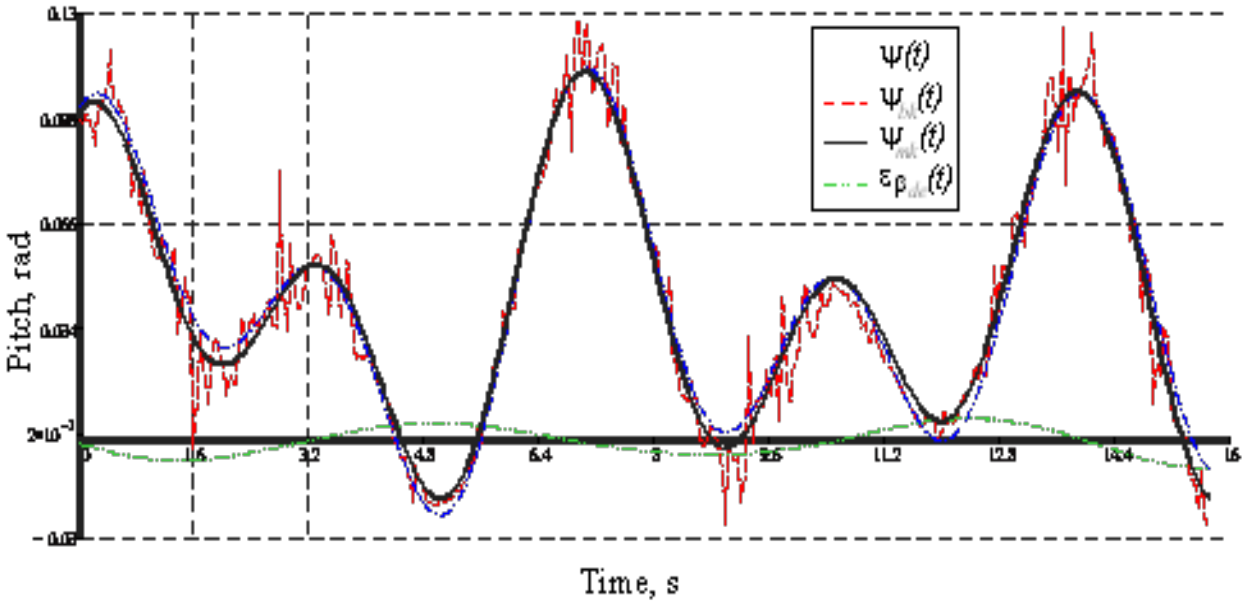

Fig.6 Experimental results

Acknowledgment

This work was supported by the European Regional Development Fund within the OP "Science and Education for Smart Growth 2014 - 2020", Project CoC "Smart Mechatronic, Eco- And Energy Saving Systems And Technologies", № BG05M2OP001-1.002-0023.

References

[1] H. Pan, S. Tian and P. Ye, "An Adaptive Synthesis Calibration Method for Time-Interleaved Sampling Systems" in Metrol. Meas. Syst., Vol 17, issue 3, 2010, pp. 405-414.
[2] L. Song, Z. Chen, Y. Mao, Z. Dong and Z. Xiang, "Error Mitigation Algorithm Based on Bidirectional Fitting Method for Collision Avoidance of Unmanned Surface Vehicle", in Polish Maritime Research, Vol. 25, issue 4, 2018, pp. 13-20.
[3] D. Borkowski and S. Barczentewicz, "Power Grid Impedance Tracking with Uncertainty Estimation Using Two Stage Weighted Least Squares", in Metrol. Meas. Syst., Vol. 21, issue 1, 2014, pp. 99-110.
[4] D. Dichev, F. Kogia, H. Nikolova and D. Diakov, "A Mathematical Model of the Error of Measuring Instruments for Investigating the Dynamic Characteristics", in Journal of Engineering Science and Technology Review, Volume 11, Issue 6, 2018, pp. 14-19.
[5] R. Zhu, D. Sun, Z. Zhou and D. Wang, „A linear fusion algorithm for attitude determination using low cost MEMS-based sensors", in Measurement, Vol. 40, issue 3, 2007, pp. 322–328.
[6] J-O. Nilsson and I. Skog, "Inertial Sensor Arrays - A Literature Review", presented at 24th European Navigation Conference, IEEE, Finland, 2016, pp. 1-10.
[7] I. Malakov, V. Zaharinov and V. Tzenov, "Size Ranges Optimization", in Procedia Engineering, Vol. 100, 2015, pp. 791-800.
[8] I. Malakov, T. Georgiev, V. Zaharinov, A. Tzokev and V. Tzenov, "Demand modeling for the optimization of size ranges", presented at 26th DAAAM International Symposium, Vienna, Austria, 2015, pp. 0435-0444.
[9] D. Dichev, F. Kogia, H. Koev and D. Diakov, "Method of Analysis and correction of the Error from Nonlinearity of the Measurement Instruments", Journal of Engineering Science and Technology Review, Vol. 9, Issue 6, 2016, pp. 116-121.
[10] A. Volosnikov and E. Yurasova, "Dynamic Measurement Error Evaluation and Minimization based on FIR-filter", presented at 2018 Global Smart Industry Conference (GloSIC), Chelyabinsk, Russia, 2018, pp. 1-7.
[11] D. Dichev, H. Koev, T. Bakalova and P. Louda, "A Model of the Dynamic Error as a Measurement Result of Instruments Defining the Parameters of Moving Objects", in Measurement Science Review, Vol. 14, issue 4, 2014, pp. 183-189.
[12] E. Yurasova and A. Volosnikov, "Dynamic measurement errors correction adaptive to noises of a sensor", Series on Advances in Mathematics for Applied Sciences, vol. 89, 2018, pp. 427-438.
[13] H. Pan, S. Tian and P. Ye, "An Adaptive Synthesis Calibration Method for Time-Interleaved Sampling Systems", in Metrol. Meas. Syst., Vol. 17, issue 3, 2010, pp. 405-414.
[14] M. Jiang, J. Luo, D. Jiang, J. Xiong, H. Song and J. Shen, "A cuckoo search-support vector machine model for predicting dynamic measurement errors of sensors", in IEEE Access, Vol. 4, 2016, pp. 5030-5037
[15] K. Ormandzhiev, S. Yordanov and S. Stoyanov, "Synthesis of Fuzzy Controller for Cross-Flow Water Turbine", in Information Technologies and Control, Vol. 15, issue 1, 2017, pp. 9-16.
[16] Y. Zhang, C. Peng, D. Mou, M. Li and W. Quan, "An Adaptive Filtering Approach Based on the Dynamic Variance Model for Reducing MEMS Gyroscope Random Error", in Sensors, Vol. 18, issue 11, 2018, pp. 1-14.
[17] M. Jiang, L. Jiang, D. Jiang, J. Xiong, J. Shen, S. H. Ahmed, J. Luo and H. Song, "Dynamic Measurement Errors Prediction for Sensors Based on Firefly Algorithm Optimize Support Vector Machine", in Sustainable Cities and Society, Vol. 35, 2017, pp. 250-256.

Environment. Technology. Resources. Rezekne, Latvia
Proceedings of the 12th International Scientific and Practical Conference. Volume III, 32-36

Use of CO_2 Laser for Marking and Clearing of Textile Materials for Manufacture of Military Equipment

Dolchinkov Nikolay Todorov
National Military University „Vasil Levski", Veliko Tarnovo, Bulgaria
National Research University "Moscow Power Engineering Institute", Moscow, Russia Veliko Tarnovo, Bulgaria
n_dolchinkov@abv.bg

Lazov Lyubomir
Rezekne Academy of Technologies, Faculty of Engineering)
Address: Atbrivosanas aleja 115,)
Rezekne, LV-4601, Latvia
llazov@abv.bg

Ivanov Jordan Shterev
National Military University „Vasil Levski", Veliko Tarnovo, Bulgaria
Veliko Tarnovo, Bulgaria
jshterev@abv.bg

Lilyanova Stelena Dimitrova
National Military University „Vasil Levski", Veliko Tarnovo, Bulgaria
Veliko Tarnovo, Bulgaria
stelena.lilqnova@abv.bg

Antons Pacejs
Rezekne Academy of Technologies, Faculty of Engineering)
Address: Atbrivosanas aleja 115,)
Rezekne, LV-4601, Latvia
antons.pacejs@rta.lv

***Abstract*— In the last decades, a large application has been found by lasers in marking and cutting on textiles, plexiglass, wood, metals and other materials. These items apply to both the military and the economy of the countries of the world. A group of Bulgarian students from the National Military University Vasil Levski, led by Dr. Nikolay Dolchinkov, conducted a research with a group of TAR under the leadership of Prof. Lubomir Lazov at the Laser Center in Rezekne at the end of 2018. The report shows the achieved results and the relevant analyzes. Graphically and tabularly, the dependence of the depth of the markings and the cut-off of the power and speed of the used CO_2 laser are presented.**

***Keywords*— cutting, laser, marking, research, textil.**

I. Introduction

Laser technologies are one of the most widespread these days. In the early 1960s, the first laser was discovered and its practical application in the industry began to develop. Over time, laser technology has become increasingly important in many sectors of the economy, both in the European Union and in the world.

The advent of laser technology in textiles industry has established a new innovative solution, which successfully prevents some of the weaknesses in the conventional technologies. Lasers are being used in Laser Marking (Only the surface of fabric is processed, fading), Laser Engraving (Controlled cutting to depth). It has been used extensively as the replacement of some conventional dry processes like sand blasting, hand sanding, destroying, and grinding etc., which are potentially harmful and disadvantageous for the environment [2].

Since the practical opening of the laser in the early 1960s, it has continuously improved and contributed to the development of industrial production - automotive, aircraft construction, shipbuilding, machine building in Bulgaria and the world. Swallowing is the most important parameter of the material being processed when it interacts with the laser. For each configuration, swallowing is given as a combination of the following laser parameters: wavelength, drop angle, polarization of laser radiation, and material emission (shape), surface geometry and temperature. The greater the ultimate intake, the greater the laser radiation used in the laser marking process.There is a many ways in which laser cutting technology can be used within the field of textiles too [6]. In this we presente some results from this area.

The aim of the experiments at the Technological Academy Resets, on the basis of analyzing the parameters (velocity and power) change, is to improve the marking and cutting of polymethylmethacrylate (PMMA) products, to obtain data that would be useful in optimizing the production lines using laser technologies for processing PMMA. The studies conducted show the application of laser marking and cutting. The optimal parameters of the laser device were found to perform a 9.5 mm thick PMMA quality cut. At the same time, results were obtained for making markings by removing a certain volume of material.

II. Equipment And Experimental Establishment

Our study examines the dependencies of the technological parameters of cutting and marking for the quality of the processes. Laser marking is an important process in modern production [4]. The last few years have become increasingly popular. Marking is a process of impacting the laser on the surface layer of the material. During the marking, a process of absorption of the laser radiation from the material takes place. Unlike marking, the energy absorbed at the cut is many times larger and leads to ablation by ablation.

Print ISSN 1691-5402
Online ISSN 2256-070X
http://dx.doi.org/10.17770/etr2019vol3.4201

There are various factors that affect the quality of the markings. Some of them are: contrast, homogeneity, clarity and sharpness of the image contour, positioning accuracy, wear resistance, lack of additional products around the impact area. In laser cutting, the factors that affect it are divided into three main groups:

- parameters related to the laser source
- parameters related to the properties of the material
- parameters related to the technological process.

The common advantages of all laser marking techniques are [1]:

- permanent, high quality marks;
- high efficiency and low operation cost;
- good accessibility, even to irregular surface;
- non-contact marking and no special working environmental needed;
- easy to automate and integrate (using computer-controlled movement of the beam or sample);
- precise beam positioning and a beam highly localised energy transfer to the workpiece;
- high reproducibility and high speed ;
- contamination - free.

The quality of a mark is assessed by its legibility characteristics such as mark contrast, mark width, mark depth, and microstructures. The characteristics are usually evaluated using complementary techniques such as optical microscopy, ultrasonics microscopy, electron microscopy, surface roughness measurement. In beam deflected marking, the line width is mainly determined by the focused beam spot size, which varies between 20 - 100 μm. Other parameters: scanning speed, power density and material properties also affect the line width. [1].

The main factors that influence the contrast of laser marking are [7,8,10]:

- optical characteristics: power density, pulse energy (pulse lasers only), pulse duration of the laser beam, frequency, overlap factor;
- thermophysical characteristics: marking speed, laser beam pitch, laser beam defocus, number of repetitions, volumetric density of the absorbed energy.

The marking and engraving on fabric with a composition of 65/35% CO / polyester ± 3% determined according to EN ISO 1833 quantitative chemical standard with CO_2 laser was investigated and analysed [8, 9]. For this purpose, an experimental methodology was developed, which concludes in the following:

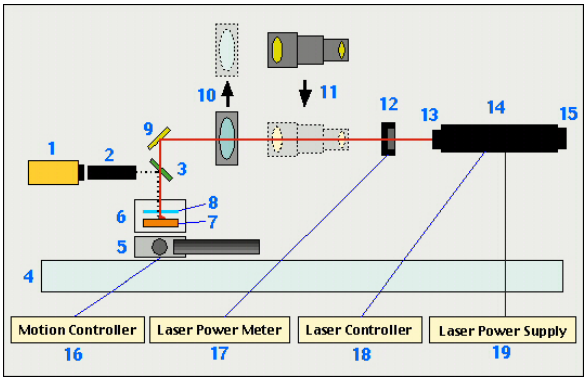

Fig.1. Scheme of the experimental setting[14]

Fig. 1 shows more precisely the schematic diagram of CO_2 laser. It includes also the working area, fully reflecting mirror, intransperant mirror, then anodes and cathodes, the lens and the focus point [15].

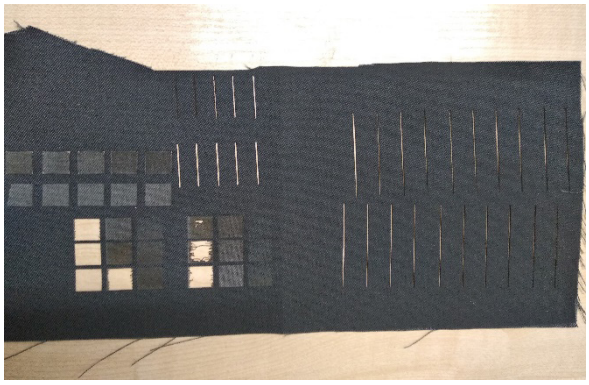

Fig.2. Scheme of the matrix

The marking and engraving on fabric with a composition of 65/35% CO / polyester ± 3% determined according to EN ISO 1833 quantitative chemical standard with CO_2 laser was investigated and analysed [8]. For this purpose, an experimental methodology was developed, which concludes in the following: a matrix of 9 squares with 1x1 cm is created. The power of the laser beam is in the range of 2-26W and its speed is in the range of 100x350 mm/s. A schematic of the six-square matrix after experiments is shown in Fig. 2 and 3.

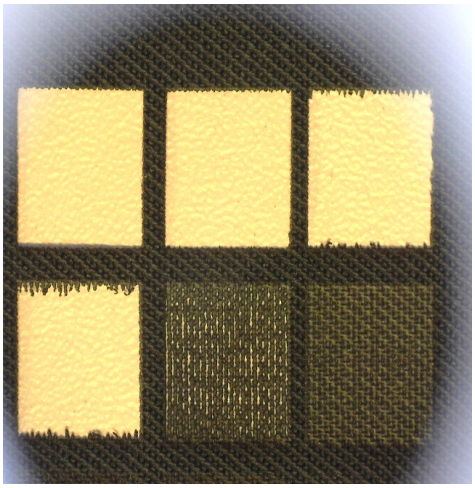

Fig.3. Scheme of the matrix

We investigate the possibility of marking and engraving on CO_2 laser plates. For this purpose, an experimental methodology was developed, which concludes in the following:

- a matrix of 9 squares with dimensions 1: 1 cm was created. Speed and power range in the range of 2-26 Watts and 100-350mm/sec. The scheme of the matrix is shown in Fig. 2

Experimental data were obtained using a Dino-lite AM4515ZTL digital microscope having the following 1.3 MPx result, 10-140X magnification and polarization.

Fig. 5 shows the variation of speed and power P for 2 W, 10 W and 26 W and the resulting linear energy density.

Each processing area (each square) is implemented with the raster scan method [13]. The line-to-line step

is 0.1mm. The processing areas and the processing quality were analyzed by means of a AM4515ZTL digital microscope manufactured by DINO-LITE:

https://www.dino-lite.eu/index.php/en/products/microscopes/long-working-distance with 1.3 MPx resolution, 10-140X zoom and polarizer. Total 28 treatment zones were investigated. From all the experiments we can draw the following conclusions [12]:

- a good cutting of the material is obtained with the following parameters: constant power 26 watts and speed ranging from 100-200 mm/s, with linear energy densities correspondingly 0.26, 0.17 and 0.13 J/mm.
- the quality marking is obtained in the range of LED values of $5*10^{-2}$, $3,8*10^{-2}$ J/mm for a power of 10 W where the velocity varies in the range of 200-260 mm/s. The remaining marking areas have a slight contrast that is between 5% and 10%. Contrast measurements are performed using the Color Contrast Analyzer version: 2.5.0.0. [11,12]. On Figure 4 are given photo of marked areas with good contrast.

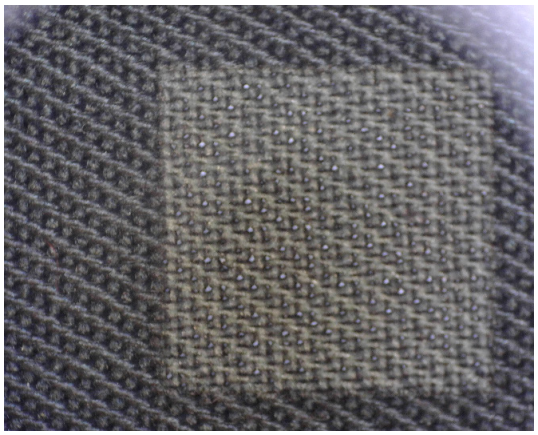

Fig. 4 Photo of marked areas with good contrast.

The main factors that influence the contrast of laser marking are [3,7]:

Each processing area is implemented by the raster scan method. The line-to-line step is 0.1mm. Processing areas and processing quality were analyzed with the help of a digital microscope AM4515ZTL Total 50 processing areas were analyzed.

III. LASER CUTTING

The possibility of laser cutting on a CO_2 laser is investigated [5]. For this purpose, an experimental methodology has been developed which consists of the following:

Lines of length 4 cm are applied to the textile at different speeds and power processing. Power ranges from 2-20 W, and the speed is 10-55 mm/s. Two sets of experiments with 10 lines were made. In one series the power was maintained constant - 10 W, and the speed varied in the range of 10-55 mm/s. In the second series the speed is constant 10 mm/s and the power varies in the range of 2-20 W – fig. 2. The thickness of the textile is 0.41 mm [9].

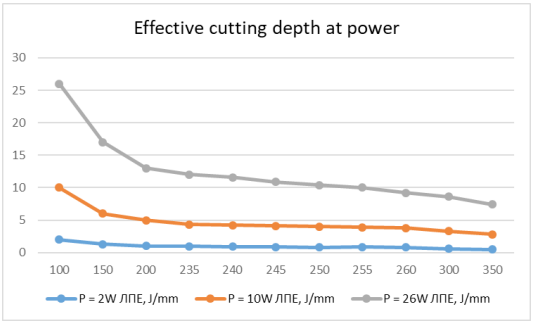

Fig 5: Effective cutting depth at power

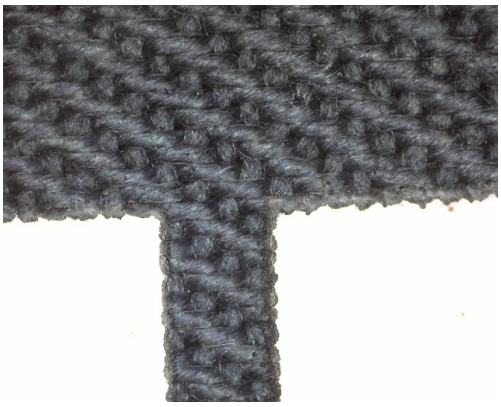

Fig 6. Cutting with good contrast quality

The microscopic analysis of the shear lines shows that a good shear of the fabric is present on all 18 incisions in the range of LED (0.2-2 J/mm for a constant rate of 10 mm/s and 1-0.22 J/mm for a constant power 10 W) - Fig. 5. Quality cutting of the textile, and for two of the experiments at 0.2 J/mm and 0.18 J/m LED for a constant power of 10 W, a shear limit was found. The threshold of destruction is shown on Fig. 6.

The experimental data obtained at the laser beam power at 10 w are shown in Table 1. In which the width of the hole in the material is shown, the heat-affected zone (COP), the Line Energy Density (LED), and the Effective Shear Depth (ESD).

Power density is a function of the focused laser size (laser power per unit area, W/cm^2). This is different from the raw output power of the laser. Focused laser beam size for each focal length lens and laser wavelength is a function of laser beam bias controlled by the laser configuration, the size of the aperture for mode selection, and the magnification of the expansion beam (collimator beam expander).

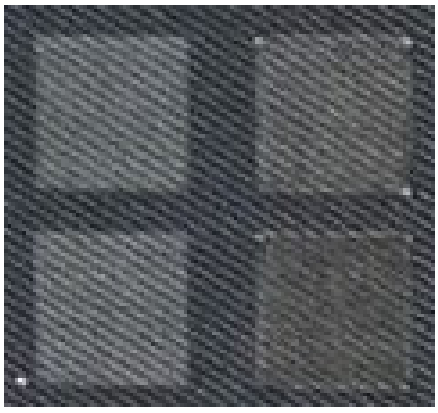

Fig 7. Marked areas with good contrast quality

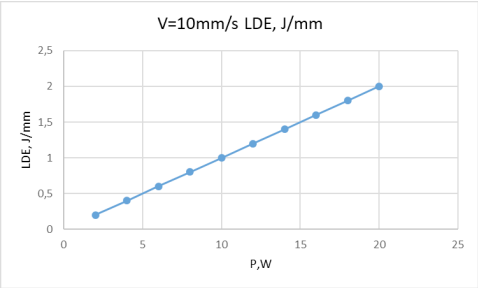

Fig 8: Laser marking parameters

Frequency of repetition of pulses (by acoustic-optical Q switch) and peak power density are critical parameters in forming the markings and achieving optimal contrast and velocity. High peak power at low frequency rapidly increases surface temperature, evaporates material while minimizing heat in the substrate. As the pulse repetition increases, lower peak power results in minimal evaporation, but generates more heat. The beam speed (the laser beam speed through the work surface) is also a critical factor.

Fig 8 and 9 gives the optimal laser marking parameters.

Good marking of the material (nearly 50%) is obtained with the following technological parameters: power 10-20-30 watts at a speed of 25-30 mm/s

Good marking through the material is obtained with the following technological parameters: power 10W 20W 30W 40W at a speed of 30-10mm/s.

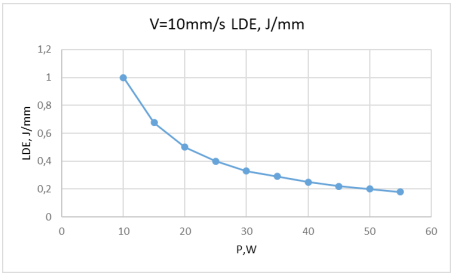

Fig 9: Laser marking parameters

The possibility of laser cutting on a CO_2 laser is also studied. For this purpose several cuts were made with different parameters. A 4 cm (4 cm) line has been placed on the fabric at various processing capacities and speeds. Power ranges from 2 to 20W and speeds from 10 to 55mm / sec. Two series of experiments with 10 lines were made. In the first series the power was maintained constant - 10W, and the speed varied in the range of 20 to 50mm / s. In the second series the speed was preserved - 10mm / s, and the power varies from 2 to 20W.

Microscopic analysis of shear lines shows that a good shear of the fabric is obtained in 18 of the experiments conducted.

V. CONCLUSION

From the conducted study and the analyzed experimental data, the following conclusions can be drawn:

1. A good shear of the material is obtained with the following parameters: constant power 26 watts (9%) and speed ranging from 100-200mm / s. In the first zone, the LPE is 0,1; in the second zone - 0.06 and in the third zone is 0.05
2. Good marking by lightening of the material (nearly 50%) is obtained with the following process parameters: these are shown in Table 2 (with blue color). The rest have a slight contrast that is between 5% and 10%. The quality mark is obtained in the range of 5 * 10^{-2} to 3.8 * 10^{-2}. The speed changes in the range of 200-260mm / s and the power is retained.
3. Microscopic analysis of the shear lines shows that a good shear of the fabric was obtained in 18 of the 50 experiments conducted.
4. The data obtained will serve as a basis for further research on dual-use fabrics. In further studies, similar experiments will be made on fabrics with other content and thickness of matter, comparisons will be made and the best choice will be made for making different purpose clothing.
5. The data obtained can be analyzed and, on the basis of the results obtained, estimates will be made for the possibility of laser cutting and marking of these articles.

For all textile materials and for leather materials, marking, engraving and cutting can be successfully applied. The choice of laser process is determined by the desired final result.

In this research, the laser applications for and textile processing are analyzed. The advantages of laser technology in textile fields were pointed. The linear energy density during marking and cutting by the laser beam was introduce.

References

[1] Adelina Han, Dinu Gubencu, Analysis of The Laser Marking Technologies, Nonconventional Technologies Review – no.4/ 2008.

[2] Angelova Y., Lazov L., Mezinska S., Rezene, Latvia, Innovative Laser Technology in Textile Industry: Marking and Engraving, Technical University of Gabrovo, Bulgaria, Rezekne Academy of Technologies, Faculty of Engineering, Rezekne, Latvia Proceedings of the 11th International Scientific and Practical Conference. Volume III, 15-21.

[3] Drago N., Villoresi P., Graziano Bertogli, Laser technologies: a step forward for small and medium Enterprises, International Centre for Science and High Technology, Trieste, http://capacitydevelopment.unido.org/wp-content/uploads/2014/11/10.-Laser-technologies-a-step-forward-for-small-and-medium-enterprises.pdf, 2008.

[4] Dolchinkov N., Shterev Y., St. Lilianova, D. Boganova, M. Peneva, L. Linkov, D. Nedialkov, Exploring the possibility of laser cutting with CO2 laser on felt in the range from 1W to 26W power, International scientific journal: Industry 4.0 Issue 1/2019, ISBN 2534-8582, стр. 29-31.

[5] Lazov L.., Angelov N., The 50th anniversary of laser, Technical University of Gabrovo, Bulgaria, 2010.

[6] Lazov L,, H. Deneva, E. Teirumnieka, Study of Auxiliary Gas Pressure on Laser Cutting Technology, Environment. Technology. Resources, Rezekne, Latvia Proceedings of the 11th International Scientific and Practical Conference. Volume III, 159-162

[7] Lazov L., E. Teirumnieks, Application of laser technology in the army, Proceedings of International Scientific Conference "Defense Technologies", Faculty of Artillery, Air Defense and Communication and Information Systems, Shumen, Bulgaria, 2018

[8] Shterev Y., N. Dolchinkov, St. Lilianova, D. Boganova, M. Peneva, L. Linkov, D. Nedialkov, Examining the possibility Of marking and engraving of textiel using CO_2 laser, International journal for science Machines, Technologies, Materials 12/2018 стр 491-493

[9] Lazov L., Dngelov N., Scanning the contrast in function of velocity in laser marking of samples of steel, International Scien-

tific Conference, GABROVO, 2010.
[10] Petrov N., Optimization of the marking process with laser radiation of samples of tool steel, dissertation, Gabrovo, 2011.
[11] https://www.dino-lite.eu/index.php/en/products/microscopes/long-working
[12] https://www.lasercuttingshapes.com/felt/
[13] https://www.pinterest.com/eleeneelab/laser-cut-felt/
[14] http://digitalcommons.unl.edu/tsaconf/index.2.html
[15] https://www.bing.com/images/search?q

*Note: This article is presented with the assistance of project BG05M2OP001-2.009-0001, Support for the development of human resources and the research potential of the National Military University "Vasil Levski" for its assertion as a modern knowledge center.

Study of Cutting and Labeling of Polymethylmethacrylate Using a CO2 Laser

Dolchinkov Nikolay Todorov
National Military University „Vasil Levski", Veliko Tarnovo, Bulgaria
National Research University "Moscow Power Engineering Institute", Moscow, Russia
Veliko Tarnovo, Bulgaria
n_dolchinkov@abv.bg

Lazov Lyubomir
Rezekne Academy of Technologies, Faculty of Engineering)
Address: Atbrivosanas aleja 115,)
Rezekne, LV-4601, Latvia
llazov@abv.bg

Ivanov Jordan Shterev
National Military University „Vasil Levski", Veliko Tarnovo, Bulgaria
Veliko Tarnovo, Bulgaria
jshterev@abv.bg

Nedyalkov Deyan Dimitrov
National Military University „Vasil Levski", Veliko Tarnovo, Bulgaria
Veliko Tarnovo, Bulgaria
ddned@abv.bg

Linkov Lyubomir Ivanov
National Military University „Vasil Levski", Veliko Tarnovo, Bulgaria
Veliko Tarnovo, Bulgaria
kubratovec@gmail.com

***Abstract* — Progress in direct laser marking when processing plastics with unmatched quality of markings, contrast and speed. This article presents the latest generation of laser materials and laser equipment systems. When properly applied, laser marking can provide quality for production and add value to the appearance and function of the product.**

Describe the parameters influencing the depth of the laser marking of polymethylmethacrylate (PMMA) products. Experimental results are presented for determining the quality of cuts on the polymer surface at specific parameters - power and speed.

Keywords — cutting, laser, marking, pleksiglas, research.

I. Introduction

Polymethyl methacrylate, widely known under the trade name Plexiglas, is a synthetic thermoplastic transparent polymer. It is also found under the trademarks lemacryl, perpsex, plastid, acrylate, acrylate, acrylate, etc., also called organic glass, acrylic glass or acrylic (fig. 1) [14].

It was created in 1928 and was sold in 1933 by Rohm and Haas Company [15].

Plexiglas is used as an alternative to glass. It has the following properties:

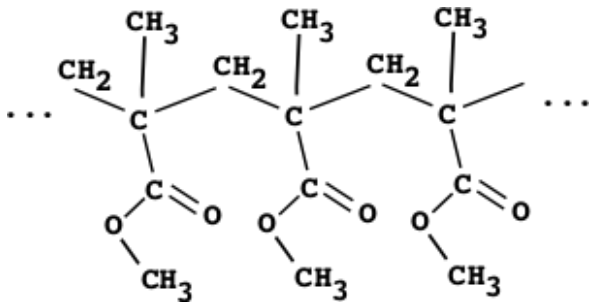

Fig.1. Structure of the polymer [14]

lighter: its density (1190 kg / m3) is approximately twice as low as that of the glass;

resistant to external influences (humidity, cold, etc.);

softer than the glass and therefore more scratch-sensitive;

when heated above 100 ° C becomes plastic and lends itself to molding;

it is easily processed with metal cutting and woodworking machines and tools;

perfectly cut and engraved with a laser;

passes ultraviolet rays and X-rays, but filters infrared rays; passes less light (92-93% vs. 99%) from the glass [9];

is not resistant to the effects of organic solvents [1, 14].

Deliberating upon the question which innovation changed the world, many scientists would answer that it was the laser. Soon after its invention in 1960 it attracted the attention of many scientists from all over the world [6,12].

Laser sources emit radiations with wavelengths in a wide spectral range - from ultraviolet, visible and infrared to continuous and pulsed modes. Some of the laser technologies are: laser marking, cutting, engraving, welding, drilling of holes and many others [2].

Laser devices are the core technology in instruments performing vital functions in many industries including transportation, healthcare, and telecommunications [4]. Laser marking and laser cutting technology are now widely associated with plastics.

The most common mechanism of surface reaction is thermal chemical "carbonization" or "charring". First, the charging process occurs when the absorbed energy increases the local temperature of the material around the subject of absorption, high enough to cause thermal decomposition of the polymer [13]. While this may lead to burning of the polymer in the presence of oxygen, the limited supply of oxygen inside the substrate results in polymerization of the polymer to produce a black or dark

Print ISSN 1691-5402
Online ISSN 2256-070X
http://dx.doi.org/10.17770/etr2019vol3.4203

contrast to light.

The aim of the experiments at the Technological Academy Resets, on the basis of analyzing the parameters (velocity and power) change, is to improve the marking and cutting of polymethylmethacrylate (PMMA) products, to obtain data that would be useful in optimizing the production lines using laser technologies for processing PMMA. The studies conducted show the application of laser marking and cutting. The optimal parameters of the laser device were found to perform a 9.5 mm thick PMMA quality cut. At the same time, results were obtained for making markings by removing a certain volume of material.

II. EQUIPMENT AND EXPERIMENTAL ESTABLISHMENT

The wavelength (energy) is important. The materials have to absorb the laser energy if a good marking effect is to occur. The more plastic materials are able to absorb the laser energy at a wavelength of 1064 nm (which is the infrared band - Nd:YAG). Here is used CO2, which is important because of different wavelength and the results.

Gas laser CHANXAN CW 1325 CO2 active, 1-150 watts power, 1-400 mm / s, laser beam wavelength 10.6 mm, maximum marking area: 2500 x 1300 mm, maximum laser size focal spot is 100 mm and water cooling system was used.

The surface power density SPD of the laser beam is determined by:

$$SPD = \frac{P}{S}$$

where P is the power of laser beam and S is the area of the laser beam section in focus. Laser control was performed using the RdWorks software [7,10].

In relation to the influence of the laser beam on the plastic, the linear energy density LED of the laser [8] beam is defined on a unit length depending on the velocity:

$$LED = \frac{P}{v}$$

where P is the power of laser beam and v is the speed of laser beam movement on the plastic [11].

The focusing system controls the laser beam spot direction is important system part. The area diameter of the focused laser beam defined marking line width and the real marking efficiency and the penetrating depth of the laser beam. The diameter depends of the lens focal length and the of the laser beam deviation.

Polymethylmethacrylate (PMMA) is a transparent thermoplastic material that is light and stable. As a multifunctional material used in a wide range of applications. The thickness of the plexiglass used is 10 mm.

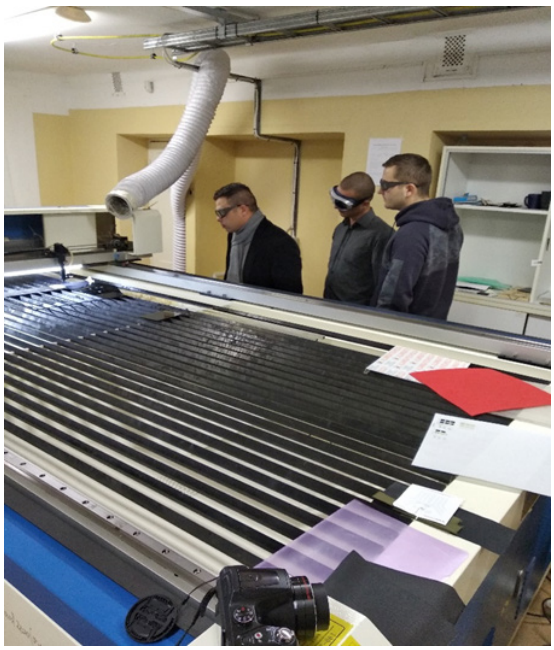

Fig.2. The laser used for the experiments

Fig. 2 This figure is an image of the laser used during our experiment. Marking and cutting of the plexiglass was done at the laser center of the Rezekne Technological Academy

Experimental data were obtained using a Dino-lite AM4515ZTL digital microscope having the following 1.3 MPx result, 10-140X magnification and polarization (fig. 3).

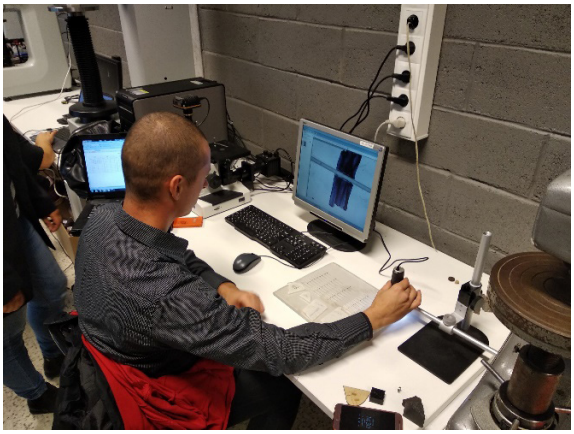

Fig 3. Operating the electronic microscope

We investigate the possibility of marking and cutting the CO_2 laser material. For this purpose, an experimental methodology was developed, which concludes in the following:

- A matrix of 50 lines was created. Speed and power range in the range of 10-50 watts and 5-30mm/s. The scheme of the matrix is shown in Fig. 4.

The main factors that influence the contrast of laser marking are [3,4,5,6]:

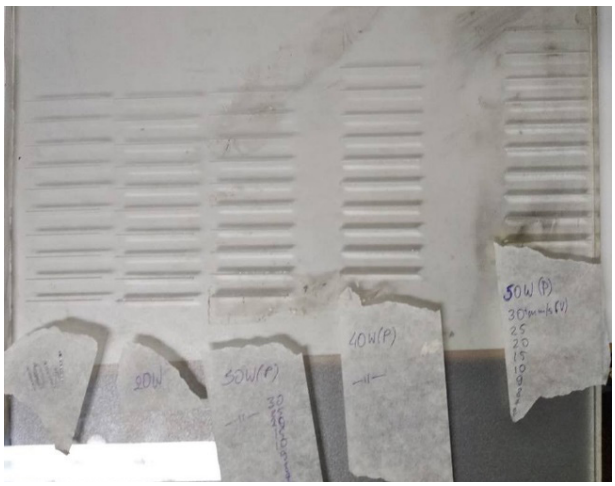

Fig. 4. Matrix

Each processing area is implemented by the raster scan method. The line-to-line step is 0.1mm.

Processing areas and processing quality were analyzed with the help of a digital microscope AM4515ZTL Total 50 processing areas were analyzed.

III. Laser Cutting

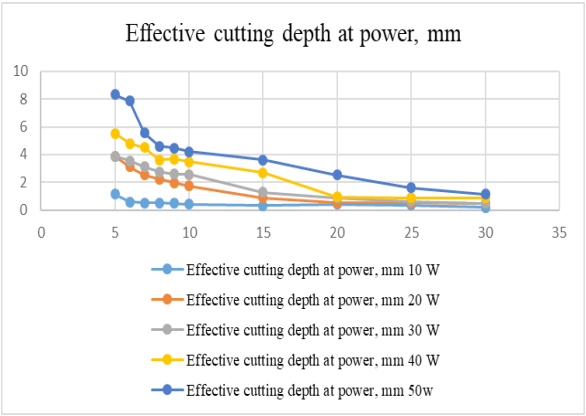

Fig 5: Effective cutting depth at power

The experimental data obtained at the laser beam power at 10 w are shown in figure 5. In which the width of the hole in the material is shown, the heat-affected zone (COP), the Line Energy Density (LED), and the Effective Shear Depth (ESD).

Power density is a function of the focused laser size (laser power per unit area, W/cm^2). This is different from the raw output power of the laser. Focused laser beam size for each focal length lens and laser wavelength is a function of laser beam bias controlled by the laser configuration, the size of the aperture for mode selection, and the magnification of the expansion beam (collimator beam expander).

Frequency of repetition of pulses (by acoustic-optical Q switch) and peak power density are critical parameters in forming the markings and achieving optimal contrast and velocity. High peak power at low frequency rapidly increases surface temperature, evaporates material while minimizing heat in the substrate. As the pulse repetition increases, lower peak power results in minimal evaporation, but generates more heat. The beam speed (the laser beam speed through the work surface) is also a critical factor.

Table 2 gives the optimal laser marking parameters.

Good marking of the material (nearly 50%) is obtained with the following technological parameters: power 10-20-30 watts at a speed of 25-30 mm/s

Good marking through the material is obtained with the following technological parameters: power 10W 20W 30W 40W at a speed of 30-10mm/s.

TABLE 2
OPTIMAL LASER MARKING PARAMETERS

Speed, mm/s	Width, mm	COP, mm	LED, mm	ESD, mm
5	0,675	0.029	2,000	1,145
6	0,653	0.029	1,667	0,579
7	0,576	0.30	1,429	0,525
8	0,561	0.029	1,250	0,767
9	0,543	0.029	1,111	0,512
10	0,535	0.046	1,000	0,417
15	0,511	0.045	0,667	0,338
20	0,514	0.046	0,500	0,406
25	0,478	0.054	0,400	0,350
30	0,448	0.055	0,333	0,188

Figure 5 shows a qualitative marking of the material at a power of 20w and a speed of 25mm/s.

Fig.5. qualitative marking of the material at a power of 20w and a speed of 25mm/s.

Figure 6 shows a quality cut of the material at a power of 50w and a speed of 5mm / s. Figure 7 shows the threshold of destruction,

Each processing area (line) is implemented by the raster scan method. The line-to-line step is 0.1mm. In Fig. the processing area and the parameters for each zone are shown.

Qualitative shear of the material results in the following parameters constant power 50W and 40W and velocity ranging from 5-7mm / s. In the first zone, the LPE is; in the second zone and in the third zone is 0.13J / mm.

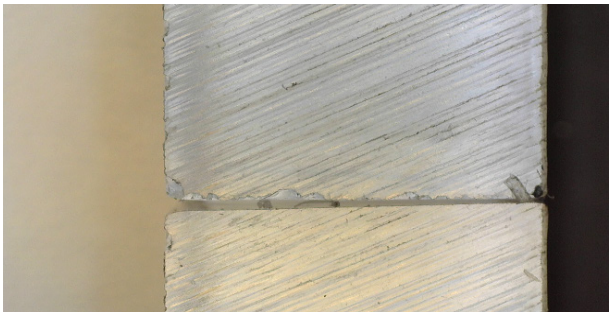

Fig.6. Quality cut of the material at a power of 50w and a speed of 5mm / s

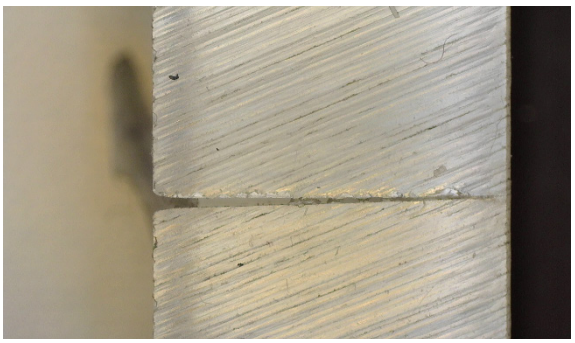

Fig.7. The threshold of destruction

V. CONCLUSION

From the conducted study and the analyzed experimental data, the following conclusions can be drawn:

1. Quality cut of the material is achieved with the following parameters: for white and red felt - permanent power 50W and 40W and speed ranging from 5-7mm / s. In the first zone, the LPE is; in the second zone and in the third zone is 0.13J / mm.
2. Good marking by lightening of the material is obtained with the following technological parameters
   Power 10 -20-30-40 at a speed of 30-10 mm / s.
3. For laser cutting of plexiglass, best cut parameters are obtained at a power of 40 - 50 watts and a speed of 5 - 7 mm / s. When power is increased, the cut-off line is better outlined without residual unevenness, but this will lead to unnecessary energy consumption and no practical value. When the thickness of the material is reduced, less laser power is required to obtain a full cut.
4. Low power cuts of the laser beam result in incomplete shearing. We then see a mark on a certain depth of the material depending on the applied power. From our research we can select laser power and speed to obtain a mark of different depth depending on the desired depth of engraving or marking.
5. The 9.5 mm thick Plexiglas test material is suitable for laser marking and engraving. It is convenient for laser cutting with medium power lasers and good shear quality. It can be used to make billboards, souvenirs and others that can be used in both military and civilian industries.
6. The results obtained can serve as a basis for further studies with similar materials, and the data obtained can be used practically when working with the CO_2 laser materials tested. This study can be continued using materials of a similar structure and finding the best ingredient of the Plexiglas for performing qualitative marking.

References

[1] Angelova Y., Lazov L., Mezinska S., Rezene, Latvia, Innovative Laser Technology in Textile Industry: Marking and Engraving, Technical University of Gabrovo, Bulgaria, Rezekne Academy of Technologies, Faculty of Engineering, Rezekne, Latvia Proceedings of the 11th International Scientific and Practical Conference. Volume III, 15-21.

[2] Grigiryants A., I. Shiganov, A. Misyurov. Technological processes of laser processing, ed. MGTU them. N. Bauman, Moscow, 2006

[3] Dolchinkov N., Shterev Y., St. Lilianova, D. Boganova, M. Peneva, L. Linkov, D. Nedialkov, Exploring the possibility of laser cutting with CO2 laser on felt in the range from 1W to 26W power, International scientific journal: Industry 4.0 Issue 1/2019, ISBN 2534-8582, стр. 29-31.

[4] Eichler, J., L. Dünkel, Eppich Die Strahlqualität von Lasern - Wie bestimmt man Beugungsmaßzahl und Strahldurchmesser in der Praxis?, Laser Technik Journal 1 (2004), Nr. 2

[5] Lazov L.., Angelov N., The 50th anniversary of laser, Technical University of Gabrovo, Bulgaria, 2010.

[6] Lazov L., E. Teirumnieks, Application of laser technology in the army, Proceedings of International Scientific Conference "Defense Technologies", Faculty of Artillery, Air Defense and Communication and Information Systems, Shumen, Bulgaria, 2018

[7] Lazov L,, H. Deneva, E. Teirumnieka, Study of Auxiliary Gas Pressure on Laser Cutting Technology, Environment. Technology. Resources, Rezekne, Latvia Proceedings of the 11th International Scientific and Practical Conference. Volume III, 159-162

[8] Lazov L.., Angelov N. Optimization of laser marking with the help of simulation models, International Scientific Conference, Gabrovo, 2010.

[9] Lazov L., Angelov N., Scanning the contrast in function of velocity in laser marking of samples of steel, International Scientific Conference, Gabrovo, 2010.

[10] Petrov N., Optimization of the marking process with laser radiation of samples of tool steel, dissertation, Gabrovo, 2011.

[11] Shterev Y., N. Dolchinkov, St. Lilianova, D. Boganova, M. Peneva, L. Linkov, D. Nedialkov, Laser marking and cutting of plexiglas with CO_2 , International journal for science Machines, Technologies, Materials 4/2018 стр 494-496.

[12] https://www.laserfelt.com/

[13] http://chris-reilly.org/blog/how-to-laser-cut-felt/

[14] http://digitalcommons.unl.edu/tsaconf/index.2.html

[15] https://bg.wikipedia.org/wiki/Полиметилметакрилат

*Note: This article is presented with the assistance of project BG05M2OP001-2.009-0001, Support for the development of human resources and the research potential of the National Military University "Vasil Levski" for its assertion as a modern knowledge center.

Comparison of the Long-Term Properties in Compression of Different Size Foamed Concrete

Rihards Gailitis
Faculty of Civil Engineering
Riga Technical University
Riga, Latvia
rihards.gailitis@edu.rtu.lv

Andina Sprince
Faculty of Civil Engineering
Riga Technical University
Riga, Latvia
andina.sprince@rtu.lv

Leonids Pakrastins
Faculty of Civil Engineering
Riga Technical University
Riga, Latvia
leonids.pakrastins@rtu.lv

Genadijs Shakhmenko
Faculty of Civil Engineering
Riga Technical University
Riga, Latvia
genadijs.sahmenko@rtu.lv

Tomass Kozlovskis
Faculty of Civil Engineering
Riga Technical University
Riga, Latvia
t.kozlovskis@gmail.com

***Abstract*—Foamed concrete has been used as a building material since the early 1920s. In the beginning, it was used as an insulation material with very low density. Since then there have been attempts to make this material more load-bearing and structural. In the present-day foamed concrete is being used in soil reinforcement, manufacturing of building blocks and other sorts of construction materials. [1]**

The aim of this article is to determine long-term properties and strength of foamed concrete specimens as well as compare the results between two differently sized foamed concrete specimens.

The size of creep and shrinkage specimens were Ø46x190 mm and Ø75x180 mm. The creep properties of the specimens were determined by loading them with 20% of the ultimate stress value. [2]

The compressive strength, creep and specific creep of specimens were determined as well as specimen size factor to creep deformations.

Keywords*—Foamed concrete, long-term properties, creep and shrinkage deformations.

I. Introduction

Typically, foamed concrete is considered to be lightweight, low strength concrete with good thermal insulating properties. [7]. Foamed concrete is a cellular cementitious material obtained by introducing foam in the cement matrix. This introduction gains development of air voids within the microstructure of the material, thus contributing to advantages in properties such as low self-weight, low thermal conductivity, good acoustic absorption, increased fire resistance and workability. Due to this, it is widely used as an exterior insulating material, cavity filling, shock absorption barrier, and fire insulation material. On the other hand, structural voids also reduce the strength of material [3,4,9]. It has been well recognized that the compressive strength of foamed concrete decreases as the porosity of the material increases. Because the mechanical properties of a material are mainly affected by its pore structure, its void features are considered in many previous studies [6].

Foamed concrete, conventionally described by the density of 280-1800 kg/m^3, thus a lightweight material. The density of the cellular (foamed) concrete can be controlled by adding a specific amount of foam into the slurry of water and cement, with and without the addition of aggregate. Foam stability is a very important factor for foamed concrete. Unstable foam can cause segregation and uneven density through the material. However, it is relatively difficult to control foam stability because it is affected by various parameters such as foam agent, foam achieving technology, water/cement ratio, and others. Usually, surfactant, protein, synthetic, metal powders and hydrogen peroxide are used as a foaming agent [4,7-9,12].

In relevant literature, a common strategy to increase the strength of foamed concrete without worsening the characteristics associated with low densities is to add different kinds of fibers to the cementitious matrix [3].

Creep is an important quality of concrete since it affects the deformation and stress distribution within the concrete structures. Investigations on concrete creep have lasted for over a hundred years and the findings are considerable.

It has been reported that the factors, affecting concrete creep, are mixture proportion, curing age, environmental temperature, and relative humidity, and applied stress level [5,11].

The aim of this article is to determine and compare the strength and long-term properties of foamed concrete, by observing specimens of two different sizes. In addition, possible reasons for differences in strength and long-term properties shall be noted.

II. Materials and methods

Two types of cylindrical specimens were prepared: Ø46x190 mm length and Ø75x180 mm. Specimens had two different foamed concrete mix, that is shown in Table I [10].

Print ISSN 1691-5402
Online ISSN 2256-070X
http://dx.doi.org/10.17770/etr2019vol3.4093

TABLE I.
TABLE I. FOAMED CONCRETE MIXES

Ingredients	Units	Specimen type	
		Ø75x180 ***mm***	Ø46x190 ***mm***
Cement CEM I 42.5N	kg/m^3	350	240
Quartz sand 0/0.5 mm	kg/m^3	125	300
Quartz sand 0/0.3 mm	kg/m^3	75	-
Foam agent (Tukums) mixed together with 0.35l H_2O	kg/m^3	1.8	1.05
PP fibers	kg/m^3	1.25	0.3
Metakaolin LMK, kg	kg/m^3	25	-
Micro silica Elkem 971 U	kg/m^3	15	8
Water	kg/m^3	225	80
Plastificator Stachema	kg/m^3	4	3.098
W/C		0.643	0.333

Compression strength of foamed concrete was determined according to EN 12390-3:2009. The tests were performed 7 and 28 days after specimens were made. A compression machine with the accuracy of ± 1% was used and the rate of loading was 0.7 MPa/sec. (see Fig.1).

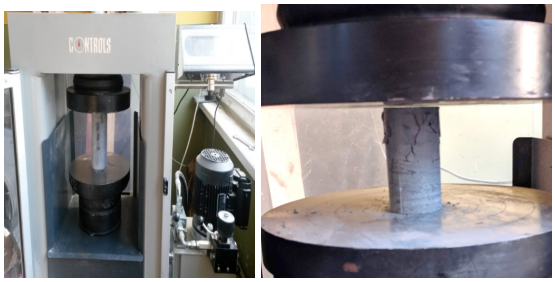

Fig. 1. Specimen compressive strength test.

For creep deformation and shrinkage tests, 6 aluminium plates (10x15 mm) were glued to each specimen in pairs. Afterward, to those plates deformation indicators were attached (see Fig.2 and Fig.3).

Fig. 2. Specimens prepared for creep testing.

Fig. 3. Specimens prepared for shrinkage testing.

The creep was measured for foamed concrete specimens subjected to a uniform compressive load, which was constant through all the creep test [2]. Meanwhile, the shrinkage test was also performed to register deformations caused by foamed concrete shrinkage. Afterward, shrinkage deformation values were subtracted from creep test results in order to evaluate only the load impact on the specimens.

During creep tests, specimens were loaded with 20% of the ultimate compressive load, which was determined in compression strength tests. Specimens were loaded gradually by adding 25% of the determined load value. Specimens were kept in creep lever test stands (see Fig.4 and Fig.5), loaded under constant load for 53 days.

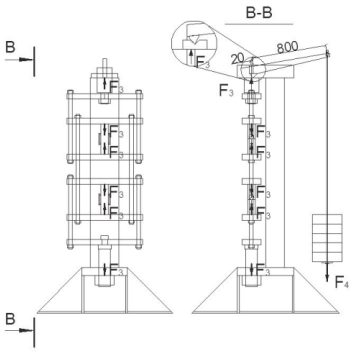

Fig. 4. Creep lever test stand [2].

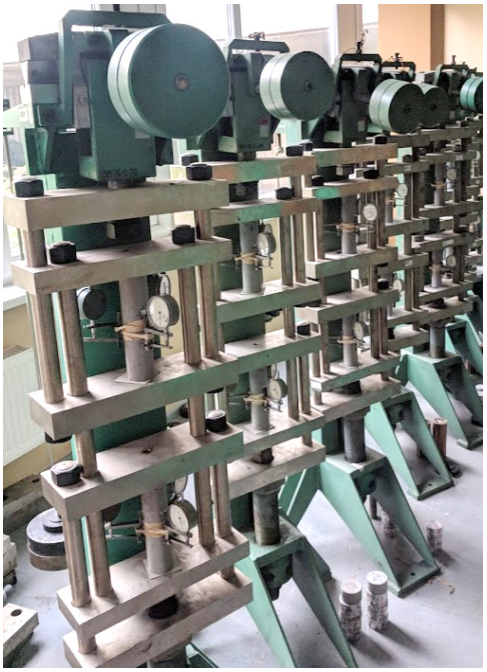

Fig. 5. Creep lever test stands with foamed concrete specimens inserted.

III. Results and discussion

The tests to determine compressive strength, creep deformations and specific creep was done.

The density for specimens is shown in Table II.

TABLE II. Foamed concrete specimen densities

Specimen type	Average density, kg/m³
Ø46x190 mm, 28 days old	1276.89
Ø75x180 mm, 7 days old	1097.24
Ø75x180 mm, 28 days old	1096.23

Compressive strength values of foamed concrete specimens 7 and 28 days after specimens were made are shown in Table III.

TABLE III. Foamed concrete compressive strength

Specimen type	Average compressive load, kN	Average compressive strength, MPa
28 days old Ø46x190 mm	13.80	8.32
7 days old Ø75x180 mm	17.54	4.56
28 days old Ø75x180 mm	36.20	9.41

From Fig.6 it is visible that for both types of cylindrical specimen absolute deformation values show small difference, with a slight increase to Ø46x190 mm specimens from 11th to 33rd day.

Foamed concrete specimens total creep deformations in Fig.6 are shown with shrinkage values subtracted.

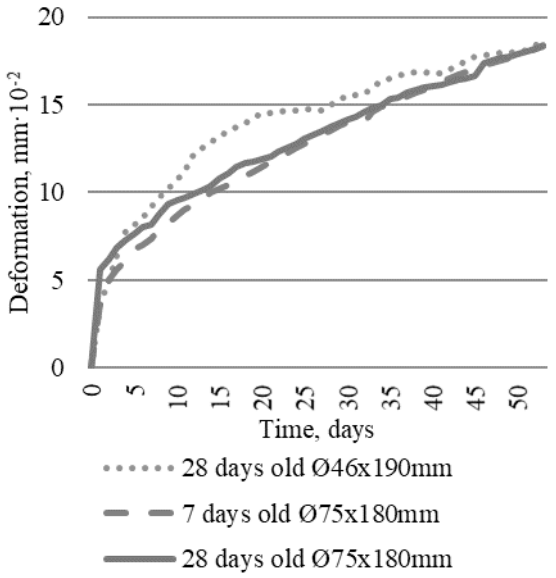

Fig. 6. Foamed concrete specimen total deformations.

Due to different sizes of the test specimens, absolute creep values are not relevant to be taken into account in order to evaluate materials ability to creep. Therefore, specific creep values were calculated to obtain more objective results.

Specific creep value is calculated: relative creep deformation divided by applied stress value. This method excludes circumstances such as the difference in the specimen geometry as well as differences in applied stress levels [2].

Specific creep can be calculated using the following equation:

$$X_{cr}(t,t_0) = \frac{\varepsilon_{cr}(t,t_0)}{\sigma} = \frac{\varepsilon_{kop}(t) - \varepsilon_{sh}(t) - \varepsilon_{el}(t,t_0)}{\sigma} = \frac{1}{E_{cr}(t,t_0)} \quad (1)$$

$\chi_{cr}(t,t_0)$ is a specific creep,
$\varepsilon_{cr}(t,t_0)$ is a creep strain,
$\varepsilon_{kop}(t)$ is a total strain,
$\varepsilon_{sh}(t)$ is shrinkage strain,
$\varepsilon_{el}(t,t_0)$ is elastic strain,
σ is the compressive stress,
$E_{cr}(t,t_0)$ is the modulus of creep

Specific creep can be measured as micro-strains to megapascal.

From Fig.7 it is apparent that 7 days old Ø75x180 mm specimens show almost twice as big specific creep as the 28 days old Ø75x180 mm specimens. The 28 days old Ø46x190 mm specimens show slightly increased specific creep, compared to the 28 days old Ø75x180 mm specimens.

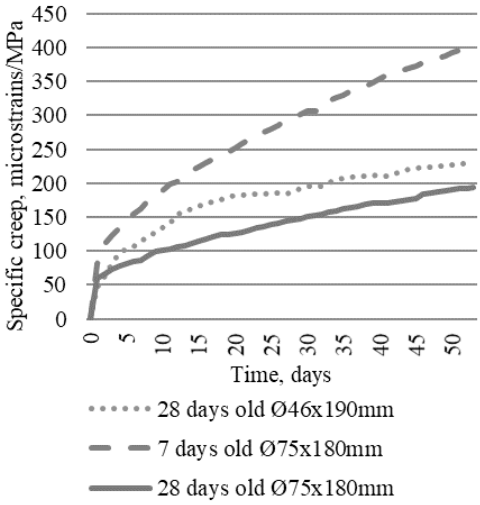

Fig. 7. Foamed concrete specimen specific creep.

IV. Conclusions

The creep properties of differently sized foamed concrete specimens were determined by performing 53 days long creep test. Also, compressive strength has been determined during this test. According to results that have been obtained, the following conclusions can be drawn:

- From Fig.7 it is determined, the specimens with bigger diameter has relatively lower specific creep. The 7 days old Ø75x180 mm specimens show twice as big specific creep as the 28 days old Ø46x190 mm specimens. Comparing 28 days old specimens, more likely to creep (with higher specific creep values) are Ø46x190 mm specimens (difference by 17%). This increase in specific creep can be related to specimen compressive strength., 28 days old Ø75x180 mm specimens have 12% higher compressive strength than Ø46x190 mm specimens.
- In 28 days after creating the test specimens, larger specimens are 14% less dense than smaller specimens, whereas the difference in compressive strength is not significant. The compressive strength of Ø75x180 mm specimen is only 12% higher than

small specimen compressive strength.

- Creep deformations for Ø75x180 mm specimens loaded on 7th or 28th day are almost similar. The only difference in creep deformations is in earlier test stages when there is a small increase in creep deformations for specimens loaded 30 days after they were made.
- Absolute creep deformations for Ø46x190 mm and Ø75x180mm specimens slightly differ. Larger creep deformations have been registered over 11th to 33rd day of testing for Ø46x190 mm specimens. From these results, it can be determined that linear relevance between applied stresses and creep deformations, that in stress level of 20% from the ultimate stress value has to be linear, better appears to be happening for Ø75x180 mm specimens. All in all, it has to be mentioned that in linear creep testing RILEM TC 107-CSP recommendation (suggests to use creep specimens with dimensions ratio of 1/4 regarding cylinder diameter and length/ height) is relative and achieved deformations values will be similar to dimension ratio of 1/2 (cylinder diameter to length/ height).

V. Acknowledgments

This research is funded by the Latvian Council of Science, project 'Long-term properties of innovative cement composites in various stress-strain conditions', project No. lzp-2018/2-0249.

References

[1] Y. H. Mugahed Amran, N. Farzadnia, A.A. Abang Ali. Properties and applications of foamed concrete; a review. Construction and Building Materials 101, 2015. – pp 990-1005.

[2] A. Sprince Methodology For Determination of Long Term Properties and Crack Development Research in Extra Fine Aggregate Cement Composites. PhD Thesis—Rīga: [RTU]. 2015.—70–77. lpp, 172.p.

[3] D. Falliano, D. De Domenico, G. Ricciardi, E. Gugliandolo. Compressive and flexural strength of fiber-reinforced foamed concrete: Effect of fiber content, curing conditions and dry density. Construction and building materials 198, 2019 -pp 479-493.

[4] H.Suleyman Gokce, D. Hatungimana, K. Ramyar. Effect of fly ash and silica fume on hardened properties of foam concrete. Construction and building materials 194, 2019 -pp 1-11.

[5] S. Liang, Y. Wei. Methodology of obtaining intrinsic creep property of concrete by flexural deflection test. Cement and Concrete Composites 97, 2019 -pp 288-299.

[6] T. T. Nguyen, H. H. Bui, T. D. Ngo, G. D. Nguyen. Experimental and numerical investigation of influence of air-voids on the compressive behaviour of foamed concrete. Materials & Design 130, 2017 -pp 103-119.

[7] T. T. Nguyen, H. H. Bui, T. D. Ngo, G. D. Nguyen, M. U. Kreher. A micromechanical investigation for the effects of pore size and its distribution on geopolymer foam concrete under uniaxial compression. Engineering Fracture Mechanics 209, 2019 -pp 228-244.

[8] S.Ghorbani, S. Ghorbani, Z. Tao, J. de Brito, M. Tavakkolizadeh. Effect of magnetized water on foam stability and compressive strength of foam concrete. Construction and Building Materials 197, 2019 -pp 280-290.

[9] T. Li, Z. Wang, T. Zhou, Y. He, F. Huang. Preparation and properties of magnesium phosphate cement foam concrete with H_2O_2 as foaming agent. Construction and Building Materials 205, 2019 -pp 566-573.

[10] RILEM TC 107-CSP: Creep and shrinkage prediction models: principles of their formation. Measurement of time-dependent strains of concrete. Materials and structures/Matériaux et Constructions, Vol. 31, October 1998, -pp 507-512. [Online]. Available: https://www.researchgate.net/publication/280141856_RILEM_TC_107-CSP_CREEP_AND_SHRINKAGE_PREDICTION_MODELS_PRINCIPLES_OF_THEIR_FORMATION_Recommendation_Measurement_of_time-dependent_strains_of_concrete. [Accessed: March 3, 2019.].

[11] A. M. Neville (2002) Creep of Concrete and Behaviour of Structures. Concrete International No.5., 2002 -pp 52-55

[12] L. F. Kazanskaya, O.M. Smirnova. Supersulphated Cements with Technogenic Raw Materials. International Journal of Civil Engineering and Technology, 9(11), 2018, pp.3006–3012.

Effect of Carbon Nanotubes on the Electrical Properties of the Polymeric Composites

S. Gango
Department of Physics, Faculty of Physics and Mathematics, Pskov State University,
Lenin Square 2, 180000 Pskov, Russia

E. Ilin
International Scientific Center of Thermophysics and Energetic Limited Liability Company,
Inzhenernaya 24, 630090 Novosibirsk, Russia

V. Solovyev
Department of Physics, Faculty of Physics and Mathematics, Pskov State University,
Lenin Square 2, 180000 Pskov, Russia

K. Gusev
Department of Physics, Faculty of Physics and Mathematics, Pskov State University,
Lenin Square 2, 180000 Pskov, Russia

M. Predtechensky
International Scientific Center of Thermophysics and Energetic Limited Liability Company,
Inzhenernaya 24, 630090 Novosibirsk, Russia

S. Trifonov
Department of Physics, Faculty of Physics and Mathematics, Pskov State University,
Lenin Square 2, 180000 Pskov, Russia

***Abstract* – Experimental study of single-wall carbon nabotubes (CNT) effect on the electrical properties of polymeric composite materials based on epoxy matrix has been carried out. Direct-current (DC) as well as alternating-current (AC) electrical conductivity of nanocomposites with different CNT concentrations have been investigated in the temperature interval from 293 K to 373 K. Measurements of Seebeck coefficient confirm n-type conductivity of composite with CNTs.**

Percolation threshold of the composite material under study has been estimated. It has been found that addition of single-wall CNT at low concentration causes hysteresis of current-voltage characteristics and the temperature dependences of electrical conductivity as well as its anisotropy in the samples under study. No noticeable frequency dependence of the AC electrical conductivity has been found in the frequency range from 100 Hz to 300 kHz.

Keywords – polymeric composites, carbon nanotubes, electrical conductivity.

I. Introduction

Carbon nanotubes (CNT) have a great influence not only on mechanical but also on electrical properties of polymeric composites [1 – 5]. Due to the large aspect ratio of CNT, even a small amount of doping (at a level of 0.01 – 0.1%) is enough to increase the electric conductivity of the material by many orders of magnitude when CNT concentration exceeds the percolation threshold [5].

Electrical properties of CNT / polymer composites depend upon many factors including aspect ratio, type and geometry of CNTs, their concentration, spatial distribution and orientation, state of the contact between adjacent nanotubes as well as between CNT guest substance and polymer host matrix [4, 5].

Nonhomogeneous distribution of CNTs inside the volume of composite material leads to the large scatter of measured electrical characteristics of the sample under study. Thus, there exists a strong dependence of electrical properties of CNT / polymer composites on their preparation experimental procedure.

In this work, electrical properties of polymeric composite materials CNT / epoxy based on host epoxy matrix with glass fibers and single-wall CNT guest substance has been studied.

II. Materials and Methods

Methods of the samples' preparation and their structure were described in detail in [6].

The temperature dependences of the electrical characteristics of the samples with graphite electrodes in the temperature interval from 293 K to 373 K were obtained upon continuous heating or cooling with a rate of 1 to 2 degrees per minute. Alternating-current (AC) conductivity was measured by an E7-13 impedance meter at the frequency of 1 kHz. Direct current (DC) measurements were carried out by micro ammeters F195 and M95 or multimeter APPA 605. Frequency dependence of the AC electrical conductivity has been analyzed by admittance bridge MPP 300 in the frequency range 100 Hz – 300 kHz.

Thermal electromotive force of the samples under study was measured by pulse method proposed in [7].

III. Results and Discussion

Fig. 1 shows SEM image of the glass fibers arrangement in epoxy-based composite under study containing carbon nanotubes [6]. One can assume that CNTs inside the composite material are partly oriented in parallel to these glass fibers.

Fig. 2 confirms this assumption, demonstrating noticeable anisotropy of direct-current (DC) specific electrical conductivity σ of *CNT / epoxy* composite: $\sigma_{\parallel} : \sigma_{\perp} \approx 2$, i.e., electrical conductivity along glass fibers is about two times larger than that across them.

Such anisotropy of conductivity (or electrical resistance) was observed earlier in other experimental works (especially at low content of CNT additive) and received a theoretical explanation [5]. The reason for this is that at a low concentration of the additive, the percolation network containing a small number of

Print ISSN 1691-5402
Online ISSN 2256-070X
http://dx.doi.org/10.17770/etr2019vol3.4053

Published by Rezekne Academy of Technologies.

conduction channels changes significantly as a result of giving the nanotubes even a small ordering, since this significantly affects the structure of the percolation network (at a low content of the additive, even weak anisotropy increases the number of percolation paths).

It should be noted that one can approximate the current-voltage characteristics of *CNT / epoxy* composite by a power law $I = U^{m}$, where $m \geq 1$ (Fig. 3). When direct current flows across the glass fibers, $m = 1$ in all the investigated voltage diapason (Fig. 2, curve 1). Direct current flowing along glass fibers obeys Ohm's law only for small values of applied voltage (Fig. 2, curve 2).

Besides the pronounced nonlinearity, attention is also drawn to hysteresis of the current-voltage characteristics measured in the longitudinal direction, and the magnitude of the current on the descending branch of the hysteresis loop exceeds the corresponding value on the ascending branch at the same voltage (Fig. 2, curve 2). This result can be presumably associated with the formation of new conducting channels near the ends of nanotubes, where the electric field strength reaches values sufficient for the local breakdown of the thin layers of the dielectric surrounding the nanotubes. It is noted in the literature [8] that internal discharges are a common phenomenon for polymers; in the systems containing nanotubes, the probability of such processes obviously should increase.

Formation of new conducting paths may also occur as a result of sample heating. Therefore, the weak temperature dependence of the electrical conductivity of the nanocomposites under study often also demonstrates hysteresis (Fig. 4).

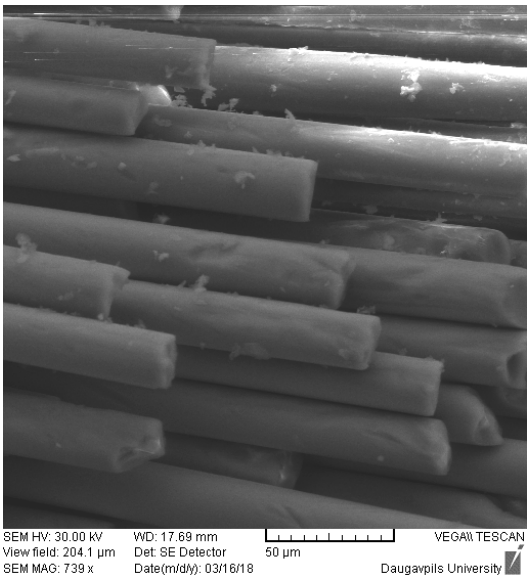

Fig. 1. SEM image of the glass fibers arrangement in epoxy-based nanocomposite containing carbon nanotubes [6].

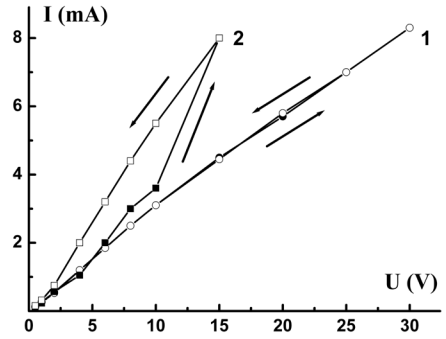

Fig. 2. Current-voltage characteristics of *CNT / epoxy* composite. Direct current flows across (curve 1) and along (curve 2) glass fibers. Arrows indicate forward and reverse directions of voltage changes.

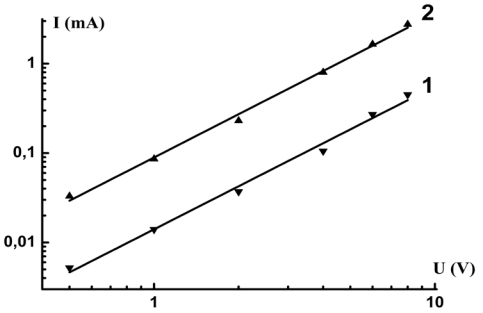

Fig. 3. Direct current-voltage characteristics of the nanocomposite samples under study with different CNT concentration values in polymer matrix: 0.02 wt. % (curve 1) and 0.08 wt. % (curve 2), respectively.

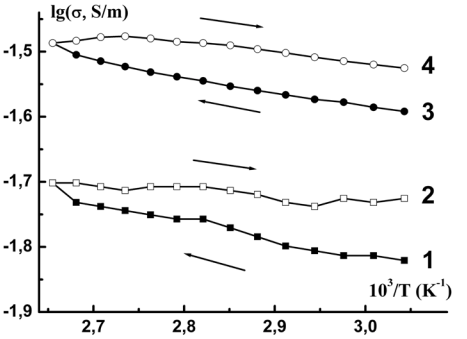

Fig. 4. Arrhenius temperature dependences of the specific electrical conductivity of nanocomposite sample under study with CNT concentration value in polymer matrix W = 0.08 wt. %. Direct current (curves 1, 2) and alternating current (curves 3, 4) flow across glass fibers. Arrows indicate heating (curves 1, 3) and cooling (curves 2, 4) of the sample.

We did not observe any significant frequency dependence of the AC conductivity of *CNT / epoxy* composites under study in the frequency range from 100 Hz to 300 kHz. Frequency independence of the electrical conductivity of such systems is associated [5] with the presence of a large number of percolation junctions in the samples, which provides a sufficiently high conductivity at concentrations of nanotubes above the percolation threshold W_0.

The value of this percolation threshold $W_0 \approx (0.001 - 0.01)\,\text{wt.\%}$ can be estimated from the concentration dependence of the DC electrical conductivity (Fig. 5), which obeys the power law [5]:

$$\sigma = A(W_{CNT} - W_0)^{t},$$

where t is the critical index (for the *CNT / epoxy* composites under study $t \approx 1$).

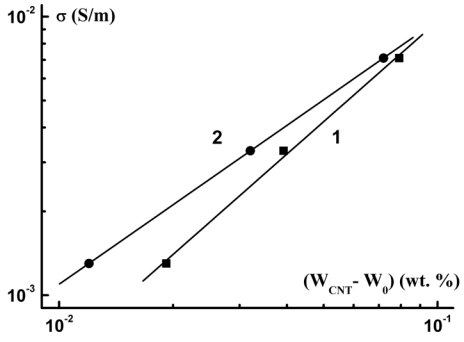

Fig. 5. Dependences of the DC specific electrical conductivity σ of CNT / epoxy composite under study on the CNT concentration W_{CNT} near the percolation thresholds $W_{01} \approx 0.001$wt.% (curve 1) and $W_{02} \approx 0.001$wt.% (curve 2) in double logarithmic scale.

Our investigations of the thermoelectric properties of the *CNT / epoxy* composite samples under study confirm *n*-type conductivity of composite with CNTs. Thus, the addition of CNTs leads to the formation of 3D conductive network within the dielectric matrix, hence the typical conductivity mechanism is observed (tunnelling of electrons from one filler to another [4]).

IV. Conclusions

Addition of carbon nanotubes (CNT) has a great effect on electrical properties of polymer-based composites due to the percolation processes even at a very low doping level.

Anisotropy and hysteresis of electrical conductivity of the *CNT / epoxy* composite samples under study have been experimentally observed. These results have been attributed to the peculiarities of conducting paths formation in the percolation network.

Electronic mechanism of the *CNT / epoxy* nanocomposites conductivity has been confirmed by the measurements of Seebeck coefficient sign of the samples under study.

Acknowledgements

Authors are grateful to Dr. V. Gerbreders and Dr. A. Ogurcovs (G. Liberts' Innovative Microscopy Centre, Daugavpils University, Latvia) for obtaining SEM images of the *CNT / epoxy* composite samples under study.

References

[1] C. P. Poole, Jr., F. J. Owens, *Introduction to nanotechnology.* Wiley-Interscience, 2003.
[2] Yiu-Wing Mai and Zhong-Zhen Yu, Eds., *Polymer nanocomposites.* Cambridge, England: Woodhead Publishing Limited, 2006.
[3] C. Leopold, T. Augustin, T. Schwebler, J. Lehnann, W. V. Liebig, B. Fiedler, "Influence of carbon nanoparticle modification on the mechanical and electrical properties of epoxy in small volumes", Journal of Colloid and Interface Science, vol. 506, pp. 620–632, 2017.
[4] A. A. Moosa, A. Ramazani, M. N. Ibrahim, "Effects of carbon-nanotubes on the mechanical and electrical properties of epoxy nanocomposites", International Journal of Current Engineering and Technology, vol. 5, pp. 3253–3258, 2015.
[5] A. V. Eletskii, A. A. Knizhnik, B. V. Potapkin, J. M. Kenny, "Electrical characteristics of carbon nanotube doped composites", Uspekhi Fizicheskikh Nauk, vol. 185, pp. 225–270, 2015.
[6] K. Gusev, V. Gerbreders, A. Ogurcovs, V. Solovyev, "Structure and mechanical properties of polymeric composites with carbon nanotubes", Environment. Technology. Resources: Proceedings of the 12th International Scientific and Practical Conference, Rezekne, Latvia, vol. 3, pp. 48-51, 2019.
[7] S. E. Gango, V. N. Markov, V. G. Solov'ev, "A cell for measuring the thermal electromotive force of microscopic samples by a pulse method", Instruments and Experimental Techniques, vol. 41, pp. 858–859, 1998.
[8] T. Blythe, D. Bloor, *Electrical properties of polymers*. Cambridge, England: University Press, 2005.

Environment. Technology. Resources. Rezekne, Latvia
Proceedings of the 12th International Scientific and Practical Conference. Volume III, 48-51

Structure and Mechanical Properties of Polymeric Composites with Carbon Nanotubes

K. Gusev
Department of Physics, Faculty of Physics and Mathematics, Pskov State University,
Lenin Square 2, 180000 Pskov, Russia

V. Gerbreders
G. Liberts' Innovative Microscopy Centre, Daugavpils University,
Vienibas Street 13,LV-5400 Daugavpils, Latvia

A. Ogurcovs
G. Liberts' Innovative Microscopy Centre, Daugavpils University,
Vienibas Street 13,LV-5400 Daugavpils, Latvia

V. Solovyev
Department of Physics, Faculty of Physics and Mathematics, Pskov State University,
Lenin Square 2, 180000 Pskov, Russia

***Abstract* – Experimental investigations of single-wall carbon nanotubes (CNT) effect on the mechanical properties of polymeric composite materials based on epoxy matrix have been carried out. It has been found that addition of CNT at low concentration dramatically increases tensile strength (20 – 30 per cent growth) and Young's modulus of the samples under study.**

Structure of polymeric composites with CNT was characterized by atomic force microscopy (AFM) and scanning electron microscopy (SEM). AFM images of the samples under study confirm strong interaction between polymeric matrix and nano-additives, demonstrating intimate contact between CNT and epoxy surroundings which is of great importance for composite material reinforcement.

Dependences of tensile strength and those of Young's modulus on CNT concentration are discussed using micromechanics models for nanocomposites.

Keywords – polymeric composites, carbon nanotubes, mechanical properties.

I. Introduction

Due to the high values of tensile strength and Young's modulus combined with the large aspect ratio and giant surface area single wall carbon nanotubes (CNT) with small weight fraction are shown to be the most promising nanoparticle fillers for improving mechanical properties of polymeric composites widely using in many industries [1 – 4].

Different energy dissipating and thus tensile strength increasing mechanisms at the CNT have been proposed. Among these mechanisms are nanotube pull-out, nanoparticle-matrix debonding and nanotube breakage [3]. In particular, the bonds between the CNTs and polymer chains enable a stress transfer between the host matrix (polymer) and guest substance (CNTs). This mechanism decreases the rate of crack formation, redirects cracks and restricts the mobility of the main chain of the epoxy resin leading to an increase of the Young's modulus [4].

On the other hand, researchers used multi-walled CNTs in order to improve the interfacial properties between carbon fibers and epoxy matrix in multicomponent composite materials [5]. In this case, it was concluded that the Van der Waals force combination and the mechanical interlock increase the internal friction of carbon fiber – epoxy matrix and limit the movement of the interface of the composite, which plays an important role in the enhancement of interface interaction.

It should be emphasized that in general, the level of interaction between matrix and fillers ("nanoadhesion") [6 – 8] is of great importance for composite material reinforcement.

In this work, mechanical properties of epoxy-based multicomponent composite material containing glass fibers and single-wall CNT nano-additives have been studied. Structural investigations of CNT / epoxy composite under study confirm strong interaction between host matrix and guest substance, demonstrating intimate contact between CNT and epoxy surroundings which is of great importance for composite material reinforcement (noticeable **g**rowth of tensile strength and Young's modulus of composite material when compared with check sample without adding CNTs).

II. Materials and Methods

We prepared *CNT / epoxy* nanocomposite based on ED-20 epoxy resin, hardener and concentrate (paste) TUBALL MATRIX from OCSiAL (Novosibirsk, Russia), containing single wall carbon nanotubes (CNT) with a length $L > 5$ microns and diameter $d = (1.6 \pm 0.4)$ nm. The technology of composite materials preparation included the following stages:

1. Weighing the estimated amount of the paste TUBALL MATRIX containing 10 mass. % CNT, on AXIS A6N 200 analytical balance.
2. Weighing the calculated amount of epoxy resin.
3. Hand mixing of the compound with the help of a stirrer in order to prevent the accumulation of concentrate (to obtain positive results, mixing of

Print ISSN 1691-5402
Online ISSN 2256-070X
http://dx.doi.org/10.17770/etr2019vol3.4052

the binder was carried out in a cylindrical vessel with a flat bottom).

4. Mixing with a suspended mechanical mixer (2000 rpm for 20 minutes).
5. Quality control of the resulting mixture using a glass rod. The mixture was distributed in a thin layer on a white sheet of paper. If the "smear" was homogeneous, without signs of roughness, the mixture was considered prepared for the introduction of the hardener. Otherwise, the stirring was continued.
6. Adding the calculated amount of hardener immediately after mixing in order to polymerize the compound as soon as possible and prevent CNT agglomeration.

Finally, cylindrical rods with a diameter $d = (10 \pm 1)$ **m** containing *CNT / epoxy* and glass fibers with a diameter of 24 μm and concentration 85 vol. % were fabricated at the "Polycomposite" firm (Pskov, Russia). Experimental study of mechanical characteristics of the samples has been carried out in the laboratory of this firm branch using the universal testing machine H300KU-0050 «Tinius Olsen Ltd».

Structure of nanocomposites under study was characterized by «VEGA // LMU Tescan» Scanning Electronic Microscope (SEM, see Fig. 1) and "PARK NX10" atomic force microscope (AFM, see Fig. 2).

III. Results and Discussion

During this work, 7 types of compounds with TUBALL MATRIX paste and a check sample (without adding CNT) were prepared.

The results of the experimental study of physical and mechanical characteristics of the samples obtained using the universal testing machine H300KU-0050 "Tinius Olsen Ltd" are given in table 1.

TABLE I

PHYSICAL AND MECHANICAL CHARACTERISTICS OF POLYMERIC COMPOSITES

Sample number	Paste type	Mass CNT concentration W_{CNT},%	Tensile strength σ, MPa	Young's modulus *E*, GPa
Glass fibers	–	–	1970	78.8
Check composite sample	–	0	1103	51.6
1	MATRIX 301	0.04	1456.0	54.2
2	MATRIX 301	0.08	1412.0	53.9
3	MATRIX 301	0.02	1333.0	53.5
4	MATRIX PD 0072	0.04	1380.0	53.6
5	MATRIX PD 0072	0.08	1252.5	52.4
6	MATRIX PD 0073	0.04	1445.0	53.8
7	MATRIX PD 0073	0.08	1300.0	54.8

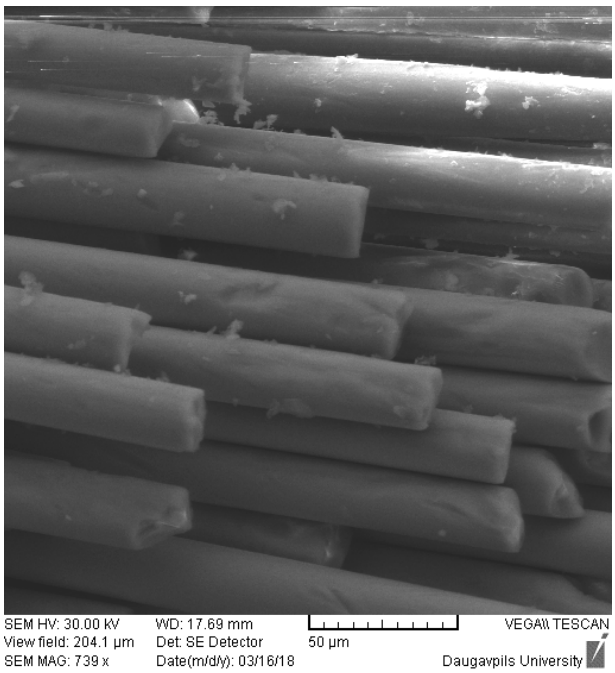

Fig. 1. SEM image of the glass fibers arrangement in epoxy-based nanocomposite containing carbon nanotubes.

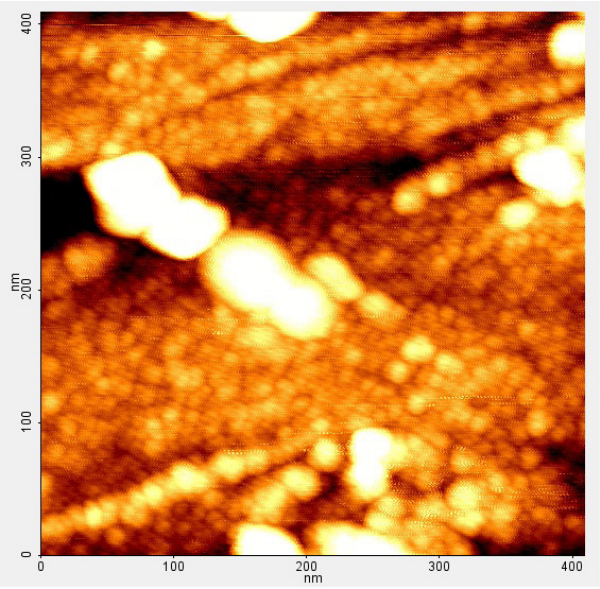

Fig. 2. AFM image of CNT interacting with polymeric matrix in *CNT / epoxy* composite.

One can consider these experimental results taking into account classical Kelly and Tyson theory [9, 10] which predicts the tensile properties of a fiber-reinforced material from the mechanical properties of fiber and

matrix. According to this theory, when very strong continuous fibers with volume fraction V_f are embedded in a matrix which has a yield stress for plastic flow very much less than the breaking stress of the fibers, the tensile strains in fiber and matrix are taken to be equal and we have

$$\sigma_c = \sigma_f V_f + \sigma_m (1 - V_f), \quad (1)$$

where $\sigma_c, \sigma_f, \sigma_m$ are the values of the tensile strength of composite, fiber, and matrix, respectively.

Similarly, in the elastic range one can write:

$$E_c = E_f V_f + E_m (1 - V_f), \quad (2)$$

where E_c, E_f, E_m are the values of the Young's modulus (modulus of elasticity) of composite, fiber, and matrix, respectively.

Taking into consideration that in our case $\sigma_f > \sigma_m$ and $E_f > E_m$, one can obtain:

$$\sigma_c \approx \sigma_f V_f \quad (3) \text{ and } \quad E_c \approx E_f V_f. \quad (4)$$

Thus, we can estimate expectative values of $\sigma_c \approx 1680$ MPa and $Ec \asymp 67GPa$ for $Ef \asymp 85$ $\sigma_f \approx 1970$ MPa and $Ef \asymp 78.8GPa$.

As can be seen from table 1, corresponding experimental values for the check composite sample (without nanotubes) are much less than these ideal theoretical predictions. However, after addition of CNTs into epoxy matrix (which has to bear stress when the strain of the composite is such that the fibers are strained to their ultimate tensile strain [9]) the deviation of experimental results from theoretical limits becomes much smaller (for the tensile strength this deviation can drop from 50% to 15%). Thus, addition of carbon nanotubes strengthens matrix under stress, therefore this matrix becomes strong enough to provide adequate load transfer to the glass fibers.

For CNT-reinforcement of composite material the applied load must be transferred from polymer to nanotubes by means of shear forces at the nanotube / epoxy interface. Hence, matrix has to bear rather high tangential strength without breakdown. One can suppose that addition of CNT enhances both normal and tangential components of matrix limit mechanical stress. In order to propose micromechanical mechanism of this effect one can estimate a CNT critical length [9-12]:

$$L_c = \frac{\sigma_{CNT} d}{2\tau}, \quad (5)$$

where $d = (1.6 \pm 0.4)\,nm$ – CNT diameter for the samples under study, $\sigma_{CNT} \asymp 37GPa$ – mean value for CNT tensile strength and $\tau \asymp 10MPa$ – typical value for interfacial shear strength in CNT / polymer nanocomposites [11]. Substituting these values into formula (5) one obtains $L_c \approx 3\,\mu m < L$. Thus, in our *CNT / epoxy* nanocomposite the length of nanotubes exceeds the critical value; hence, the epoxy matrix is able to load CNTs to their fracture stress (at $L < L_c$ the CNT is pulled out of matrix before its failure [10]).

Fig. 2 demonstrates some interesting characteristic features of the interaction between nanotubes and polymeric matrix in CNT / epoxy composite. One can see that CNTs in epoxy matrix are not similar to the freely moving "hair in pie"; due to the strong CNT – epoxy interaction, spherical polymeric nanoparticles on the nanotube look like the beads on the thread. In our opinion, this type of mechanical interaction between modified corrugated (covered with polymeric "nanoballs") CNTs and host epoxy matrix within composite material is analogous to the behavior of corrugated armature in reinforced concrete.

It should be noted that increasing the filler concentration leads to the significant reduction of mechanical characteristics of composite material due to the agglomeration of the additives [6, 7, 13]. This tendency can be clearly seen from Fig. 3, demonstrating concentration dependence of the Young's modulus enhancement effect in the nanocomposite under study. The graph shows that at low concentrations of CNTs $W_{CNT} < 0.04$wt.% one can approximate experimental data by theoretically expected [14] dependence

$$\frac{E_c}{E_0} = 1 + A \cdot W_{CNT}^{0.5}, \quad (6)$$

but afterwards the Young's modulus of the nanocomposite (E_c) begins to decrease with increasing CNT concentration probably due to the beginning of the agglomeration process.

Tensile strength of the nanocomposites under study demonstrates the similar behavior (see table 1).

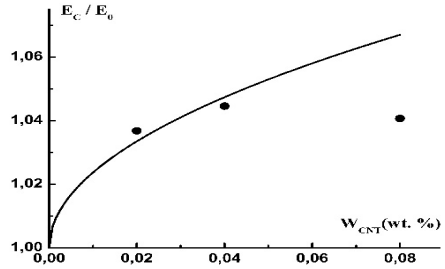

Fig. 3. Ratio of the mean value of the Young's modulus of the nanocomposite, E_c to that of the check composite sample (without CNTs), E_0 versus CNT percentage, W_{CNT}. Circles: experimental data; solid line: theoretical curve (formula (6)).

IV. Conclusions

Engineering of mechanical properties of epoxy-based multicomponent composite material has been achieved via the addition of single-wall carbon nanotubes (CNTs) at low concentration to the epoxy matrix.

Samples under study demonstrate mechanical enhancement effect due to the strong interaction between CNT guest substance and host epoxy matrix.

Acknowledgements

The authors thank OCSiAL (Novosibirsk, Russia) for

the support of high-quality CNT.

The authors are grateful to Prof. V. V. Ostashev and Prof. A. I. Vanin for fruitful discussions.

References

[1] C. P. Poole, Jr., F. J. Owens, Introduction to nanotechnology. Wiley-Interscience, 2003.

[2] Yiu-Wing Mai and Zhong-Zhen Yu, Eds., Polymer nanocomposites. Cambridge, England: Woodhead Publishing Limited, 2006.

[3] C. Leopold, T. Augustin, T. Schwebler, J. Lehnann, W. V. Liebig, B. Fiedler, "Influence of carbon nanoparticle modification on the mechanical and electrical properties of epoxy in small volumes", Journal of Colloid and Interface Science, vol. 506, pp. 620–632, 2017.

[4] A. A. Moosa, A. Ramazani, M. N. Ibrahim, "Effects of carbon-nanotubes on the mechanical and electrical properties of epoxy nanocomposites", International Journal of Current Engineering and Technology, vol. 5, pp. 3253–3258, 2015.

[5] C. Xiao, Y. Tan, X. Wang, L. Gao, L. Wang, Z. Qi, «Study of interfacial and mechanical improvement of carbon fiber / epoxy composites by depositing multi-walled carbon nanotubes on fibers», Chemical Physics Letters, vol. 703, pp. 8–16, 2018.

[6] G. V. Kozlov, "Structure and properties of particulate-filled polymer nanocomposites", Uspekhi Fizicheskikh Nauk, vol. 185, pp. 35–64, 2015.

[7] B. Pukanszky, "Influence of interface interaction on the ultimate tensile properties of polymer composites", Composites, vol. 21, pp. 255-262, 1990.

[8] Y. Zare, K. Y. Rhee, "Multistep modeling of Young's modulus in polymer / clay nanocomposites assuming the intercalation / exfoliation of clay layers and the interphase between polymer matrix and nanoparticles", Composites: Part A, vol. 102, pp.137–144, 2017.

[9] A. Kelley, G. J. Davies, "The principles of the fibre reinforcement of metals", Metallurgical Reviews, vol. 10, pp. 1-77, 1965.

[10] A. Kelly, W. R. Tyson, "Tensile properties of fibre-reinforced metals: Copper / tungsten and copper / molybdenum", Journal of the Mechanics and Physics of Solids, vol. 13, pp. 329-350, 1965.

[11] Y. Zare, "Effects of interphase on tensile strength of polymer / CNT nanocomposites by Kelly-Tyson theory", Mechanics of Materials, vol. 85, pp. 1–6, 2015.

[12] V. Lutz, J. Duchet-Rumeau, N. Godin, F. Smail, F. Lortie, J. F. Gerard, "Ex-PAN carbon fibers vs carbon nanotubes fibers: From conventional epoxy based composites to multiscale composites", European Polymer Journal, vol. 106, pp. 9–18, 2018.

[13] A. K. Mikitaev, G. V. Kozlov, «The structural model of strength of nanocomposites poly(methyl methacrylate) / functionalized carbon nanotubes», Materials Physics and Mechanics, vol. 24, pp. 187–193, 2015.

[14] A. Mikitaev, G. Kozlov, G. Zaikov, Polymer Nanocomposites: Variety of Structural Forms and Applications. New York: Nova Science Publishers, 2008.

Environment. Technology. Resources. Rezekne, Latvia
Proceedings of the 12th International Scientific and Practical Conference. Volume III, 52-59

Modelling and Investigation of the Dependence of Superhydrophobic Properties of Nanosurfaces on the Topology of Microchannels

Sharif E. Guseynov
Faculty of Science and Engineering, Liepaja University; Institute of Fundamental Science and Innovative Technologies, Liepaja University
Liepaja, Latvia
"Entelgine" Research & Advisory Co., Ltd.
Riga, Latvia
sh.e.guseinov@inbox.lv

Jkaterina V. Aleksejeva
Institute of Fundamental Science and Innovative Technologies, Liepaja University
Liepaja, Latvia
Riga Secondary School 34
Riga, Latvia
jekaterina.v.aleksejeva@gmail.com

***Abstract*—In the Cassie-Baxter state anisotropic superhydrophobic surfaces have high lubricating properties. Such superhydrophobic surfaces are used in medical implants, aircraft industry, vortex bioreactors etc. In spite of the fact that quantitative understanding of fluid dynamics on anisotropic superhydrophobic surfaces has been broadened substantially for last several years, there still are some unsolved problems in this field. This work investigates dynamics of a liquid on unidirectional superhydrophobic surfaces in the Cassie-Baxter state, when surface texture is filled with gas and, consequently, the liquid virtually is located on some kind of an air cushion. Energy of the interphase boundary liquid-gas is much smaller than energy of the interphase boundary solid-liquid, that is why the contact angle at wetting such surfaces differs a lot from the Young contact angle and depends on contact area ratio of liquid-gas and liquid-solid in visible contact of liquid and surface. Considering difference in energy obtained if we slightly shift the three-phase contact line, expression for macroscopic equilibrium contact angle, which describes the Cassie-Baxter state, can be deduced. In the work the design formula for computing local-slip length profiles of liquid on the considered superhydrophobic surfaces is obtained.**

***Keywords*—Cassie-Baxter state, local-slip length, mathematical modelling, superhydrophobic surface**

I. Introduction

During last 25-30 years breakthrough progress in nano- and microtechnology, as well as aspiration to miniaturize physical, chemical, biological, pharmaceutical, electronic, bioengineering systems and processes with tight deterministic control at each stage of synthesis and functioning aroused heightened interest to micro-hydrodynamics and nano-hydrodynamics that are often called micro-fluidics and nano-fluidics, respectively (for instance, see [5]-[13] and relative references given there). In the framework of micro- and nano-hydrodynamics, the behaviour of small volumes (with order of micro- and nanoliter) and flows of fluid in slender channels with diameter of micron scale, in which the laws of fluid flow differ significantly from the laws of classical hydrodynamics [14]: surface effects, which play an negligibly small role in classical hydrodynamics are crucial in micro-fluidics and nano-fluidics, and the skill of controlling these effects allows to optimize fluid flow in slender channels (see [15]-[21] and respective references given there). One of these controlled surface effects is slippage effect in pressure-driven fluid flow past superhydrophobic stripes (see [22]-[26] and respective references given there). Superhydrophobic surfaces combine natural hydrophobicity and roughness which results in almost complete nonwetting: on such surfaces, the contact angle is larger than 150° and, due to weak interaction forces ($\frac{W_{\text{adhesion}}}{W_{\text{cohesion}}} = 1$, where W_{adhesion} is the reversible thermodynamic work of adhesion, W_{cohesion} is the work of cohesive forces) and high surface tension value, the so-called "lotus effect" occurs – a drop of liquid takes a spherical shape and reduces the contact area with a superhydrophobic surface, or the so-called "rose petal effect" – a drop of liquid is firmly held on a vertical surface and looks as if it were pinned to the surface (for instance, see [3], [4], [27]-[33] and respective references given there). While studying hydrodynamics of a fluid flowing past gas stripes of unidirectional superhydrophobic surfaces, an important task is to manage the process of stabilizing gas bubbles inside the cavities of such surfaces. The importance of this problem is due to the fact that superhydrophobic surfaces in the Cassie-Baxter state (sometimes also in the Wenzel state) can have exceptional lubricating properties [34]-[36] and generate secondary flows, transverse to the direction of the applied pressure gradient [37]-[39]. To achieve these lubricating properties, a controlled transition from superhydrophobic surfaces with a disordered texture to superhydrophobic surfaces with an ordered texture

Print ISSN 1691-5402
Online ISSN 2256-070X
http://dx.doi.org/10.17770/etr2019vol3.4171

is required [40]. The wettability of the material, as well as its ability to repel water or hold a drop due to its strong adhesion to the solid surface, play a crucial role in such micro- and nanotechnologies and nanomaterials as vortex bioreactors, immersion lithography, dipping coating, inkjet printing, wear-resistant implant for human joint replacements, biological microelectromechanical systems, microscale thermalphysic devices, etc. [3]-[13], [41]. As shown in [42], if the liquid penetrates into the stripes of the nanostructured surface and fills them, then the Wenzel state occurs, which is characterized by

hydrophilicity $\theta \in \left(0, \frac{\pi}{2}\right)$

(with a probability of ≤0.7 [3], [4], [43]), or hydrophobicity

$\theta \in \left(\frac{\pi}{2}, \frac{2\cdot\pi}{3}\right]$

(with a probability of ≤0.5), high hydrophobicity $\theta \in \left(\frac{2\cdot\pi}{3}, \frac{5\cdot\pi}{6}\right]$ (with a probability of ≤0.2), superhydrophobicity $\theta \in \left(\frac{5\cdot\pi}{6}, \pi\right)$

(with a probability of ≤0.1). As noted in [30], the "rose petal effect" is manifested when, despite the high hydrophobicity of the surface, only large-scale roughnesses of surface are completely filled with liquid, and small-scale roughnesses of surface are only partially filled and air always remains in them, i.e. the fluid is actually located on a gas cushion. With the maximum slope of the surface above which a drop of liquid begins to slide or roll down, the advancing wetting angle of a liquid drop is much larger than its receding wetting angle in the Wenzel state, and the difference between these angles, called wetting hysteresis $\Delta\theta$, is huge. If the surface property of superhydrophobicity is manifested not only for a

large wetting angle $\left(\theta \geq \frac{5\cdot\pi}{6}\right)$, but also for small

wetting hysteresis $\Delta\theta \leq 10°$, then this means that Cassi-Baxter state is present. According to [44], [45], a wetting hysteresis $\Delta\theta < 1°$, and $\Delta\theta < 1°$, respectively, is characteristic for the Cassie-Baxter state. In the state of Cassi-Baxter, liquid droplets are located both on the upper sections of the thin micron-scale slender channels and on the gas bubbles in their voids: the droplets are not able to force the bubbles out of these voids. Due to baseline adhesiveness of interaction of the contacting surfaces drops of liquid quickly slide or roll down from the surface already for the inclination angle $\alpha \approx 4°$ and take with them pollution, which ensures self-cleaning of the surface with the "lotus effect" (the "lotus effect") [46], i.e. there is a Cassie-Baxter sliding state [33] and, therefore, there is a mixed state – the Wenzel-Cassie-Baxter state [47]. In order to achieve the state of superhydrophobicity of nanostructured surfaces with the "lotus effect", they are modified by additionally depositing water-repellent coatings on them in the form of ultra-fine layers of compounds with low surface free energy [44], [46], [48]. In the work [40], the possibility of creating of high-hydrophobic nanostructured zinc oxide (ZnO) layers without any water-repellent coatings were experimentally demonstrated by means of pulsed electrodeposition from aqueous solutions: authors experimentally revealed the conditions for deposition of high-hydrophobic nanostructured zinc oxide layers characterized by the "rose petal effect" with specific morphology, optical properties, crystal structure and texture. Nevertheless, Cassie-Baxter state is, as a rule, unstable and prone to full or partial transformation to the Wenzel state under the external influences, for example, under the influence of pressure, heating, vibration or expulsion of drop [45].

In conclusion of this section, we emphasize that despite the impressive success achieved in the study of the mechanism of synthesis and control of superhydrophobicity of micro- and nanostructured surfaces (it is impossible not to note the stupendous theoretical and experimental achievements of Dr.Sc. Math.&Phys. O.I.Vinogradova (O.I.Vinogradova) and/or her numerous students from the Laboratory of Physical Chemistry of Modified Surfaces, A.N.Frumkin Institute of Physical Chemistry and Electrochemistry, Russian Academy of Sciences [18]-[20], [36]-[39], [49], [50], [67]; for more information, see [51]), problems of finding and synthesizing the best nanorelief of surfaces to maximize their superhydrophobic properties; the problem of the synthesis of coatings, possessing both superhydrophobic and superhydrophilic properties, as well as the problem of improving the adhesive and mechanical properties of such coatings and increasing their operational life; the problem of maintaining superhydrophobicity when exposed to the external environment; etc. problems are not yet fully resolved. The authors of this work believe that, along with the scientific reasons (mathematical, physical, chemical reasons), technological nature, etc., the reason for the insufficient learnedness of the above and other relevant problems is also the failure to use the powerful theory of inverse and ill-posed problems in studying these problems. As far as the authors know, at the moment the application of this apparatus in micro- and nano-fluidics, in particular, to the problem of determining dependence of nano-surfaces' superhydrophobic properties on the topology of micro-channels, is just absent: one of options of application of theory of inverse and ill-posed problems is reducing the original direct problem (i.e. the problem of determining the superhydrophobic properties of a surface by given source data and by known controlled influences on this surface as well as on the corresponding processes taking place) to the parametrized inverse problem, in which according to the desired superhydrophobic surface properties (as if these properties are already achieved and, consequently, they are the given properties; obviously that these desired properties must firstly be mathematically formalized) it is required to find the feasible interval values of sought-for parameters (here we understand sought-for parameters as those controlled effects on the surface and on the processes taking place, owing to which the surface is superhydrophobic). This kind of reducing original direct problems to parameterized inverse problems (coefficient

inverse problems, boundary inverse problems, inverse identification problems, etc.) is a quite typical approach when solving wide classes of applied problems in the field of mathematical physics (for instance, see [52]-[54] and respective references given there); as shown in [55], [56], this approach can also be successfully applied in the field of mathematical economics, as well as in technical diagnostics [57]-[60].

II. Dynamics of fluid in the attractive field along the superhydrophobic surface with a point source

As it is known [1], the influence of surface heterogeneity on the measured contact angle can be taken into account based on the relation

$$\cos(\theta) = \sum_{i=1}^{3} s_i \cdot \cos(\theta_{i0}), \qquad (1)$$

where s_i is portion of area of i-th type smooth sections on the surface of the considered material, characterized by a macroscopic contact angle θ_{i0}.

Here the type of surface area means the type of isotherm of disjoining pressure, which, in its turn, is determined by the nature of surface forces acting in a three-phase system solid-liquid-gas. If the smooth section of the surface of the material in question is of the first type, then the value of the integral in the equation

$$\cos(\theta_{10}) = 1 + \frac{\left(P(h)\cdot h\right)\Big|_{h=h_{e.d.}}}{\sigma_{1,s.t.}} + \frac{\int\limits_{h\geq h_{e.d.}} P(h)\,dh}{\sigma_{1,s.t.}}, \qquad (2)$$

will be positive, and then such an isotherm characterizes three-phase systems, in which complete wetting takes place. In (2) by $h_{e.d.}$ we denote equilibrium depth of wetting thin film with disjoining pressure equal to capillary pressure in a drop; $P(h)$ is disjoining pressure; $\sigma_{1,s.t.}$ is the surface tension of a liquid, dependence on the temperature T which is calculated by the empirical formula $\sigma_{1,s.t.} \approx \sigma_0 \cdot \left(1 - \frac{T}{T_{c.t.}}\right)^{\frac{11}{9}}$,

which has shown itself working well for liquids with simple molecules, but it can also be used approximately for most of other liquids; if the fluid is water, it is recommended to use the interpolation formula

$$\sigma_{1,s.t.} \approx 0.235 \cdot \left(1 - \frac{T}{T_{c.t.}}\right)^{1.256} \cdot \left(1 - 0.625 \cdot \frac{T_{c.t.} - T}{T_{c.t.}}\right),$$

where $T_{c.t.}$ critical temperature, σ_0 is determined on the basis of experiments with a fixed value of temperature [43],[61].

If the smooth section of the surface of the considered material is of the second type, then the integral value in equation (2) will always be negative: in three-phase systems with a second kind isotherm a "sitting" drop of liquid will be in equilibrium with a "dry" substrate free from liquid molecules. For three-phase systems with a third kind isotherm there is a balance between a drop of liquid and a substrate covered with a wetting film; if the value of the integral in equation (2) is positive, then complete wetting can be established, if the value of this integral is negative, then incomplete wetting takes place. Large contact angles for liquid droplets on hydrophobic and superhydrophobic surfaces can be achieved in three-phase systems characterized by isotherms of the first and second kinds, and for this, a necessary condition is the presence in such three-phase systems significant forces of attraction, for example, structural forces.

Let is consider the isothermal dynamics of a thin film along a horizontal superhydrophobic surface with two orthogonal main directions of the sliding tensor in a field of gravity. Assuming that the linear scales of fluid flow far exceed the scale of micro- or nano-inhomogeneity of a surface, we can assume that the surface is a flat surface with a given slip condition. We will assume that the mass of the fluid continuously enters the surface microchannels from a localized linear source with negligibly small dimensions, and, it is assumed that the volume $V(t)$ of linear source power is set. Now let us introduce Cartesian coordinate system with origin in the source in such way that axis OX is directed along the underlying surface from the source, axis OY is directed perpendicular to axis OX, gravity force is directed down perpendicular to underlying surface. Then, within the framework of the assumptions made, the dynamics of slow fluid flows in microchannels of a superhydrophobic surface can be represented by the following model, which contains Navier-Stokes equations and continuity equation:

$$\begin{cases} \dfrac{\partial \vartheta_x}{\partial t} = \nu\Delta\vartheta_x + \nu\dfrac{\partial}{\partial x}\left(\dfrac{\vartheta_x}{x}\right) - \dfrac{1}{\rho}\dfrac{\partial p}{\partial x} - \vec{\vartheta}\nabla\vartheta_x, \\ \dfrac{\partial \vartheta_y}{\partial t} = \nu\Delta\vartheta_y + \dfrac{\nu}{x}\dfrac{\partial \vartheta_y}{\partial x} - \dfrac{1}{\rho}\dfrac{\partial p}{\partial y} - \vec{\vartheta}\nabla\vartheta_y - g, \\ \vartheta_x + x\nabla\cdot\vec{\vartheta} = 0, \end{cases} \qquad (3)$$

where $\vec{\vartheta} = \vec{\vartheta}\left(\vartheta_x(t,x,y), \vartheta_y(t,x,y)\right)$ is fluid velocity vector field; $p = p(x,y)$ is fluid pressure in the microchannel; $\rho = \rho(x,y)$ is fluid density; ν is kinematic viscosity of liquid; g is gravitational acceleration; t is time; operators Δ and ∇ are Laplacian and gradient, respectively;

vector operator $\nabla\cdot\vec{\vartheta} = \dfrac{\partial \vartheta_x}{\partial x} + \dfrac{\partial \vartheta_y}{\partial y}$ is divergence.

Obviously, for the mathematical completeness of model (3), it is necessary to add the corresponding initial and boundary conditions: in the present paper we will neither discuss the methods of construction nor the concrete forms of these conditions.

If we introduce designation $\varepsilon = \dfrac{h}{l} = 1$ (ε is the relative thickness of the microchannel, by h we denote microchannel characteristic thickness, by l we denote characteristic longitudinal scale on which the dynamics of a thin film is considered) and make substitutions in (3) (for convenience, the symbols of new substitutions will remain the same)

$$x : hx;\ \ y : hy;\ \ t : \frac{l}{u}t;\ \ \vec{\vartheta} : u\vec{\vartheta};\ \ p : \frac{ul\nu\rho}{h^2}p, \qquad (4)$$

where u means the longitudinal local velocity of

component ϑ_x in a thin film (this value can be physically interpreted also as a measure of the displacement of the cross-sectional area of a thin film), then we obtain the following system:

$$\begin{cases} \varepsilon^3 \operatorname{Re}\dfrac{\partial \vartheta_x}{\partial t} = \varepsilon\Delta\vartheta_x + \varepsilon\dfrac{\partial}{\partial x}\left(\dfrac{\vartheta_x}{x}\right) - \dfrac{\partial p}{\partial x} \\ -\varepsilon^2 \operatorname{Re}\vec{\vartheta}\nabla\vartheta_x, \\ \varepsilon^3\dfrac{\partial \vartheta_y}{\partial t} = \Delta\vartheta_y + \dfrac{\varepsilon}{x}\dfrac{\partial \vartheta_y}{\partial x} - \dfrac{\partial p}{\partial y} \\ -\varepsilon^2 \operatorname{Re}\vec{\vartheta}\nabla\vartheta_y - \dfrac{\varepsilon^3 \mathrm{l}\operatorname{Re}}{u^2}g, \\ \vartheta_x + x\nabla\cdot\vec{\vartheta} = 0, \end{cases} \tag{5}$$

where $\operatorname{Re} = \dfrac{u\mathrm{l}}{\nu}$ is Reynolds number, which does not have to be small, but the value $\varepsilon^2 \operatorname{Re}$ is supposed to be small enough.

Depending on the order of smallness of neglected terms of equations, containing $\varepsilon = 1$, from the mathematical model (5), one can obtain various asymptotic models of the theory of Stokesian flows with point disturbances, which arise when studying various technological processes and objects (for instance, see [61], [62] and respective references given there). For example, if in (5) we neglect the terms of the equations containing the magnitude of the first and higher orders, then we find that the fluid pressure in the thin film does not change along the underlying surface from the source, nor does the microchannel depth.

Let us return to the substitutions (4), with the help of which the transition from model (3) to model (5) was made. Actually, longitudinal local velocity u of component ϑ_x in a thin film is not a priori known value and, moreover, is not a constant [24], since in real conditions the physical properties of the medium and processes are significantly different from the properties of an ideal model in which you can operate with assumptions like "unbounded medium", "incompressible fluid", etc. The desire to present a longitudinal local velocity by a constant is quite understandable: this simplifies and simplifies the simulated process and the constructed mathematical model, in which you can focus on quantitative and/or qualitative studies of other unknown parameters and functions that are considered by some reasons within the specific problem studied. In this work we omitting the course of derivation, offer the following nonlinear equation for finding longitudinal local velocity $u = u(t,x,y)$:

$$\frac{\partial^2 u}{\partial t^2} + \frac{\mu\rho}{2h}\left(\frac{\partial u}{\partial t}\right)^2 = a^2\Delta u, \tag{6}$$

where $a = \sqrt{gh}$; μ is friction coefficient; nonlinear term $\dfrac{\mu\rho}{2h}\left(\dfrac{\partial u}{\partial t}\right)^2$ of the equation characterizes total friction force per unit area.

It is easy to make sure that the value $-h\vec{e}\nabla u \overset{def}{\equiv} \delta$, where $\vec{e} = (1,1)$, characterizing the increase in the level of liquid in the microchannel, satisfies homogeneous linear wave equation $\dfrac{\partial^2\delta}{\partial t^2} = a^2\Delta\delta$. The idea of solving a nonlinear equation (6) is set out below (perhaps there are more elegant ideas). Imagine the solution of (6) as $u(t,x,y) = f_1(\varphi_1) + f_2(\varphi_2)$, where $\varphi_1 = \dfrac{at+x}{at-x}$ and $\varphi_2 = \dfrac{at+y}{at-y}$, $f_1(\cdot)$ and $f_2(\cdot)$ are still unknown functions. It is not hard to make sure that

$$\frac{1}{a}\frac{\partial u}{\partial t} = \frac{1-\varphi_1}{at-x}f_1'(\varphi_1) + \left(\frac{1-\varphi_2}{at-y}\right)^2 f_2'(\varphi_2), \tag{7}$$

$$\begin{aligned} \frac{1}{a^2}\frac{\partial^2 u}{\partial t^2} &= \left(\frac{1-\varphi_1}{at-x}\right)^2 f_1''(\varphi_1) - \frac{2(1-\varphi_1)}{(at-x)^2}f_1'(\varphi_1) \\ &+ \left(\frac{1-\varphi_2}{at-y}\right)^2 f_1''(\varphi_2) - \frac{2(1-\varphi_2)}{(at-y)^2}f_2'(\varphi_2), \end{aligned} \tag{8}$$

$$\frac{\partial^2 u}{\partial x^2} = \left(\frac{1+\varphi_1}{at-x}\right)^2 f_1''(\varphi_1) + \frac{2(1+\varphi_1)}{(at-x)^2}f_1'(\varphi_1), \tag{9}$$

$$\frac{\partial^2 u}{\partial y^2} = \left(\frac{1+\varphi_2}{at-y}\right)^2 f_1''(\varphi_2) + \frac{2(1+\varphi_2)}{(at-y)^2}f_2'(\varphi_2). \tag{10}$$

Taking into account (7)-(10) in (6) allows us to obtain the following linear ordinary differential equation with respect to $\dfrac{1}{f_j'(\varphi_j)}$, $j = 1,2$:

$$\left(\frac{1}{f_j'(\varphi_j)}\right)' - \frac{1}{\varphi_j f_j'(\varphi_j)} + \frac{\mu\rho}{8h}\left(\varphi_j + \frac{1}{\varphi_j} - 2\right) = 0. \tag{11}$$

Solving the linear equations (11), we get the formula

$$f_j(\varphi_j) = -\frac{8h}{\mu\rho}\int \frac{d\varphi_j}{\varphi_j^2 + \varphi_j - 2\varphi_j\ln\varphi_j - 1}, \; j = 1,2, \tag{12}$$

in which the integral, unfortunately, is not calculated analytically. By applying a numerical integration method to this integral, we can determine approximate expressions for the functions

$f_1\left(\dfrac{at+x}{at-x}\right)$ and $f_2\left(\dfrac{at+y}{at-y}\right)$ and, consequently,

to find the desired longitudinal local velocity of component ϑ_x of fluid velocity vector field in a thin film using the formula $u = f_1 + f_2$.

Dynamics of fluid in nanochannel of structured superhydrophobic surface and sliding phenomena

For the mathematical description of transport phenomena on a superhydrophobic surface with microrelief, in stripes of which the liquid, solid and gaseous phases occur, it is necessary to determine the physical mechanisms of sliding on the surface and formulate the corresponding boundary conditions (for instance, see [24], [25] and respective references given there). As mentioned in the introduction, sliding takes place if the value of the tangential component of the velocity vector at the interphase boundary is not zero. The simplest model of sliding phenomena suggests that tangential force acting per unit of surface area S, is proportional to the sliding velocity: $\vartheta_{sl.}\big|_S = \mu\tau\big|_S$, where $\vartheta_{sl.}$ is this sliding velocity; τ stands for shear stress, μ stands for friction coefficient. This condition is called Navier sliding condition. For Newtonian fluid Navier sliding condition can be written in the form $\vartheta_{tan.}\big|_S = L_{sl.}\left.\dfrac{\partial\vartheta}{\partial y}\right|_S$, called Navier boundary condition, where $\vartheta_{tan.}$ is tangential velocity on the cavity wall; $L_{sl.} = \eta\mu$ is the sliding length that characterizes the distance at which the velocity profile is extrapolated to zero, η stands for dynamic viscosity; $L_{sl.} = 0$ corresponds to boundary condition of adhesion, at which the relative velocity of the liquid on the solid wall is zero; $L_{sl.} \to \infty$ corresponds to the boundary condition of the absence of friction, at which plug-like flow takes place with zero speed gradient. Since fluid dynamics at the interface with a solid surface can be considered at different scales, as a rule (as a rule), three different types of sliding at the interphase boundary are distinguished: internal/molecular sliding; apparent sliding; effective sliding.

Internal sliding model suggests movement of molecules in the near-wall layer, and it cannot lead to large values of $L_{sl.}$.

The apparent sliding model suggests formation of a gas cushion or a low viscosity liquid film near the solid wall. The seeming sliding is supported by a higher shear rate in the low viscosity layer compared to the shear volume rate. The apparent sliding length is defined as

$$L_{app.sl.} = \varepsilon\left(\frac{\eta}{\eta_\varepsilon} - 1\right) \approx \frac{\langle h_{\text{sulcus}}\rangle\eta}{\eta_\varepsilon},$$

where η_ε is viscosity of interphase boundary (i.e. viscosity of the above mentioned gas cushion or liquid film); $\langle h_{\text{sulcus}}\rangle$ is averaged (in the sense of surface mean value) depth of the sulci. It should be emphasized that for all appearance simplicity, the apparent sliding model reflects the formation of rarefied gaseous layer near the hydrophobic wall and makes it possible to better understand the influence of the interface region structure on the phase transfer transport phenomena) [25].

The effective sliding model assumes the formation of a stable gas phase in the stripes of microrelief of the surface in the Cassie-Baxter state, and allows you to replace the actual non-uniform surface with a homogeneous smooth plane, showing the same hydrophobic properties as real surface. This approach allows, in addition to increasing the sliding length, also to find solutions to problems and analyze complex systems, without requiring time-consuming calculations of the local velocity field of the fluid to be performed. The effective sliding length is defined as the boundary condition. $\left\langle \vartheta\big|_S \right\rangle = L_{eff.}\left\langle \left.\dfrac{\partial\vartheta}{\partial y}\right|_S \right\rangle$, where $\langle\cdot\rangle$ denotes mean value for surface S and characterizes the sliding intensity of a fluid over a smooth surface with a sliding length $L_{eff.}$. One of the first experimental studies of the effective sliding length of a Newtonian fluid was performed in Department of Mechanical and Industrial Engineering, University of Massachusetts [63], [64] using example of a flow in a microchannel with a rectangular cross section and a superhydrophobic coating on the bottom wall: surfaces with periodic sets of microbars or parallel sulci were used as a superhydrophobic coating with a surface portion of liquid-gas plots in the range 0.5÷0.9; the height of microchannels ranged in 76÷264 μm; it was found that an increase in the surface fraction of the gas sections and the height of the microchannel leads to an increase in the sliding length, the maximum value of which was more than 20 μm with 0.9 surface fraction of the gas sections. The obtained experimental results are consistent with the results of theoretical studies in [65]-[67].

As mentioned in the introduction, with a high surface portion of the gas sections, the stability of the Cassie-Baxter state can be broken, resulting in liquid penetrating into the gaseous stripes [42]. Therefore, with the flow of fluid in the microchannel, in addition to the general thermodynamic stability criteria:

- stability criterion for a system with constant volume and entropy: only processes with a decrease in internal energy can spontaneously occur in the system, and consequently a stable state with a minimum of internal energy is stable;
- stability criterion for a system with constant pressure and entropy: only processes with a decrease in enthalpy can occur spontaneously in the system, and, therefore, the state with minimum enthalpy is stable;
- stability criterion for a system with constant volume and temperature: only processes with a decrease in free energy can spontaneously occur in the system. Therefore, only a state with a minimum of free energy

is stable;

– stability criterion for a system with constant temperature and pressure: only processes with a decrease in the thermodynamic potential can spontaneously occur in the system, and therefore the state with a minimum of the Gibbs thermodynamic potential is stable,

it is also necessary to take into account the balance of forces acting on the liquid-gas interface. The stability of the Cassie-Baxter state for an isotropic texture in the form of microbars set is ensured by the fulfillment of the inequality [68], [69]

$$2\sigma_{s.t.}\sqrt{\pi\left(1-r_{gas}\right)}\cos\left(\theta\right)\le r_{gas}T\Delta p, \qquad (13)$$

where $\sigma_{s.t.}$ is the surface tension of a liquid (72 mN/m for water at 25°C); r_{gas} denotes surface portion of microchannel gas plots (i.e. the percentage of the surface that is perfect slip:

$r_{gas}=\dfrac{h}{T}$, h is slip size); θ stands for contact angle; T is period of microbars of the texture; $\Delta p = p_{g.} - p_{l.}$ is the pressure difference in gas and liquid (see Fig. 1, [68]). The stability of the Cassie-Baxter state for anisotropic texture in the form of parallel sulci is ensured by the fulfillment of inequality

$$2\sigma_{s.t.}\cos\left(\theta\right)\le r_{gas}T\Delta p. \qquad (14)$$

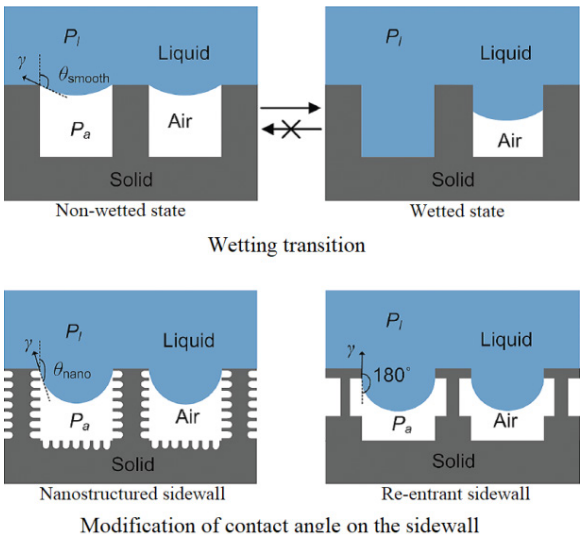

Fig. 1. Illustration of wetting transition on superhydrophobic surfaces.

As can be seen from (13) and (14), provided that Cassie-Baxter state remains stable, the maximum possible value of the surface portion r_{gas} of gas plots is inversely proportional to increment of values Δp and T, and, conversely, increases together with the value of contact angle. According to the results of [70], for $\theta = 120°$ and for varying the pressure difference in gas and liquid Δp in the range 200÷300 Pa effective sliding length $L_{eff.}$ for an isotropic texture in the form of a microbars set with a period T in the range 50÷250 μm and with surface portion $r_{gas} = 0.993$ of microchannel gas plots is equal to 94 μm; and for anisotropic texture in the form of parallel grooves (parallel sulci) with a surface portion $r_{gas} = 0.976$ of gas plots the effective sliding length $L_{eff.}$ is equal to 185 μm (for the same range of Δp and T).

Now let us briefly describe the basis of the theoretical analysis of the effective sliding length: a theoretical analysis allows making the quantitative assessment of the influence of various factors on the effective sliding length, to explain the experimental results, find the optimal texture structure of a superhydrophobic surface with a stable Cassie-Baxter state. Consider a surface with an anisotropic texture in the form of parallel sulci and make the following assumptions: (1) there is a wide channel, h ? T; (2) ideal liquid sliding conditions are fulfilled on the liquid-gas interphase surfaces; (3) liquid-gas interfaces are flat. Then the following relations hold [65], [66], [69]:

$$L_{eff.}^{\mathrm{P}}=\frac{RT}{\pi}\ln\left(\sec\left(\frac{\pi r_{gas}}{2}\right)\right),\ \forall r_{gas}>0,\ \forall T<2\pi, \qquad (15)$$

where $L_{eff.}^{\mathrm{P}}$ is an effective sliding length for a longitudinal fluid flow along the furrow of the surface texture; R is size of the microsystem (R is radius (or average radius) if the sulcus is of cylindrical shape);

$$L_{eff.}^{\perp}:\ \frac{RT}{2\pi}\ln\left(\sec\left(\frac{\pi r_{gas}}{2}\right)\right)\ \text{as}\ T\to 0,\ r_{gas}\ \text{fixed}, \qquad (16)$$

where $L_{eff.}^{\perp}$ is an effective sliding length for a transverse fluid flow along the furrow of the surface texture;

$$L_{eff.}^{\perp}:\ \frac{r_{gas}}{4\left(1-r_{gas}\right)}\ \text{as}\ T\to+\infty,\ r_{gas}\ \text{fixed};$$

$$L_{eff.}^{\perp}:\ \frac{Rr_{gas}}{4}\ \text{as}\ r_{gas}\to 0,\ T\ \text{fixed};$$

$$L_{eff.}^{\perp}:\ \frac{1}{4\left(1-r_{gas}\right)}\ \text{as}\ r_{gas}\to 1,\ T\ \text{fixed};$$

$$L_{eff.}^{\mathrm{P}}:\ \frac{RT\pi r_{gas}^{2}}{4}\ \text{as}\ r_{gas}\to 0;$$

$$L_{eff.}^{\mathrm{P}}:\ \frac{RT}{\pi}\ln\left(1-r_{gas}\right)\ \text{as}\ r_{gas}\to 1.$$

From (15) and (16) it follows that under certain conditions it can be said that the asymptotic values of $L_{eff.}^{\mathrm{P}}$ and $L_{eff.}^{\perp}$ differ approximately twice: $L_{eff.}^{\mathrm{P}}\approx 2L_{eff.}^{\perp}$ when $T\to 0$, and $r_{gas}\in\left(0,2\pi\right)$ is fixed.

If the fluid flows at an arbitrary angle to the texture axis, then it is necessary to consider the effective sliding length as a tensor value $\hat{L}_{eff.}=\left\{L_{j,k}^{eff.}\right\}$, and to note that Navier sliding condition has the following form:

$$\left\langle \hat{\vartheta}_i\Big|_S \right\rangle = \sum_{j,k} L_{j,k}^{eff.} \vec{n}_k \left\langle \frac{\partial \hat{\vartheta}_j}{\partial y_k}\Big|_S \right\rangle,$$

where $\left\langle \hat{\vartheta}_i\Big|_S \right\rangle$ is i-th component of the average sliding speed on a superhydrophobic surface with a texture in the form of parallel sulci; $\vec{n}_k$ denotes k-th components of the outer normal $\vec{n}$ to surface S.

In this case, instead of the effective sliding length, we can talk about the tensor of the effective sliding length, which can be represented as a symmetric positive definite matrix:

$$\hat{L}_{eff.} = \begin{pmatrix} L_{11}^{eff.} & L_{12}^{eff.} \\ L_{21}^{eff.} & L_{22}^{eff.} \end{pmatrix} \geq L_0 > 0,\ L_{12}^{eff.} = L_{21}^{eff.}.$$

It is obvious that if $L_{11}^{eff.} \neq L_{22}^{eff.}$, then this matrix will be guaranted diagonalized:

$$\hat{L}_{eff.} = \begin{pmatrix} L_{eff.}^{\parallel} & 0 \\ 0 & L_{eff.}^{\perp} \end{pmatrix},$$

that is more convenient to use: knowing $L_{eff.}^{\parallel}$ and $L_{eff.}^{\perp}$ (the essence of which are the eigenvalue of the tensor $\hat{L}_{eff.}$), it is easy to calculate the effective sliding length tensor when flowing at an arbitrary angle to the texture axis.

III. Conclusion

In the present work, the dynamics of a liquid on unidirectional superhydrophobic surfaces in the Cassie-Baxter state is studied, when surface texture is filled with gas and, consequently, the liquid virtually is located on some kind of an air cushion. The model describing the dynamics of slow fluid flows in microchannels of a superhydrophobic surface is formulated. Besides, in the paper, an approach (one of many possible approaches) for finding the sought-for longitudinal local velocity of one of the components of the fluid velocity vector field in a thin film: the nonlinear equation and the idea of its analytical solution are proposed. Finally, in the work, the design formula for computing local-slip length profiles of liquid on the considered superhydrophobic surface is obtained.

References

[1] A. B. D. Cassie and S. Baxter, "Large contact angles of plant and animal surfaces," Nature, vol. 155, pp. 21-22, 1945.
[2] S. Baxte and A. B. D. Cassie, "The water repellency of fabrics and a new water repellency test," Journal of the Textile Institute Transactions, vol. 36, no. 4, pp. 67-90, 1945.
[3] Sh. E.Guseynov, J. V. Aleksejeva, A. Jansone, and D. Kuma, "Formation of the hydrophobic surface of the ball-shaped titanium head of the human hip joint endoprosthesis by direct laser irradiation," Journal of New Materials, Compounds and Applications, vol. 1, no. 1, pp. 65-93, 2017.
[4] U. Zaimis, Sh. E. Guseynov, "Scientifically substantiated guidelines for physico-mathematical modelling of laser surface-treatment of wear-resistant implants for human joint replacements," The 11th International Scientific and Practical Conference "Environment. Technology. Resources", June 15-17, 2017, Rezekne, Latvia, Vol. 3, pp. 350-356, 2017.
[5] Y. H. Ghallab and W. Badawy, Lab-on-a-chip: Techniques, Circuits, and Biomedical Applications. Boston: Artech House, 2010, xv+154 p.
[6] N. T. Nguyen and S. T. Wereley, Fundamentals and Applications of Microfluidics. Boston: Artech House, 2006, xiv+471 p.
[7] K. E. Herold, and A. Rasooly, Lab-on-a-Chip Technology. Vol. 1: Fabrication and Microfluidics. Norfolk: Caister Academic Press, 2009, xiv+410 p.
[8] K. E. Herold and A. Rasooly, Lab-on-a-Chip Technology. Bol. 2: Biomolecular Separation and Analysis. Norfolk: Caister Academic Press, 2009, xii+300 p.
[9] J. Lichtenberg and H. Baltes, Advanced Micro & Nanosystems. Vol 1: Enabling Technology for MEMS and Nanodevices. –Weinheim: Wiley-VCH Verlag, 2004, xii+427 p.
[10] C. L. Rice and R. Whitehead, "Electrokinetic Flow in a Narrow Cylindrical Capillary," Journal of Physical Chemistry, vol. 69, no. 11, pp. 4017-4024, 1965.
[11] T. M. Squires and S.R.Quake, "Microfluidics: Fluid physics at the nanoliter scale," Reviews of Modern Physics, vol. 77, no. 3, pp. 977-1026, 2005.
[12] H. A. Stone, A. D. Stroock, and A. Ajdari, "Engineering Flows in Small Devices: Microfluidics Toward a Lab-on-a-Chip," Annual Review of Fluid Mechanics, vol. 36, pp. 381-411, 2004.
[13] G. M. Whitesides, "The origins and the future of microfluidics," Nature, vol. 442, pp. 368-373, 2006.
[14] H. Bruus, Theoretical Microfluidics. Oxford: Oxford University Press, 2008, xvi+346 p.
[15] B. Ramos-Alvarado, S. Kumar, and G. P. Peterson, "Hydrodynamic slip in silicon nanochannels," Physical Review E, vol. 93, no. 3, pp. 3117-3125, 2016.
[16] D. M. Huang, Ch. Sendner, D. Horinek, R. R. Netz, and L. Bocquet, "Water Slippage versus Contact Angle: A Quasiuniversal Relationship," Physical Review Letters, vol. 101, no. 22, pp. 6101-6105, 2008.
[17] P. Joseph, C. Cottin-Bizonne, J.-M. Benoit, C. Ybert, C. Journet, P. Tabeling, and L. Bocquet, "Slippage of water past superhydrophobic carbon nanotube forests in microchannels," Physical Review Letters, vol. 98, no. 15, pp. 6104-6108, 2006.
[18] O. I. Vinogradova and G. E. Yakubov, "Surface roughness and hydrodynamic boundary conditions," Physical Review E, vol. 73, no. 4, pp. 5302-5306, 2006.
[19] O. I. Vinogradova, "Slippage of water over hydrophobic surfaces," International Journal of Mineral Processing, vol. 56, no. 1-4, pp. 31-60, 1999.
[20] O. I. Vinogradova, "Drainage of a thin liquid film confined between hydrophobic surfaces," Langmuir, vol. 11, no. 6, pp. 2213-2220, 1995.
[21] A. Ajdari, "Electroosmosis on inhomogeneously charged surfaces," Physical Review Letters, vol. 75, no. 4, pp. 755-758, 1995.
[22] A. M. J. Davis and E. Lauga, "Hydrodynamic friction of fakir-like superhydrophobic surfaces," Journal of Fluid Mechanics, vol. 661, pp. 402-411, 2010.
[23] C. H. Choi, U. Ulmanella, J. Kim, C. M. Ho, and C. J. Kim, "Effective slip and friction reduction in nanograted superhydrophobic microchannels," Physics of Fluids, vol. 18, no. 8, pp. 71051-71059, 2006.
[24] A .I.Ageev, "Viscous fluid flow along the super-hydrophobic surfaces," PhD thesis, Lomonosov Moscow State University, Moscow, Russia, 2015, 117 p.
[25] A. V. Belyayev, "Hydrodinamical and electrokinetic flows nearby the super-hydrophobic surfaces," PhD thesis, Lomonosov Moscow State University, Moscow, Russia, 2012, 125 p.
[26] J.-L. Barrat and L. Bocquet, "Large slip effect at a nonwetting fluid-solid interface," Physical Review Letters, vol. 82, no. 23, pp. 4671-4674, 1999.
[27] A. Lafuma and D. Quere, "Superhydrophobic states," Nature Materials, vol. 2, no. 7, pp. 457-460, 2003.
[28] S. S. Latthe, A. B. Gurav, Ch. Sh. Maruti, and Sh. Vhatkar, "Recent Progress in Preparation of Superhydrophobic Surfaces: A Review," Journal of Surface Engineered Materials and Advanced Technology, vol. 2, no. 2, pp. 76-94, 2012.
[29] M. Nosonovsky and B. Bhushan, "Superhydrophobic Surfaces and Emerging Applications: Non-Adhesion, Energy, Green Engineering," Current Opinion in Colloid & Interface Science, vol. 14, no. 4, pp. 270-280, 2009.
[30] Y. Y. Yan, N. Gao, and W. Barthlott, "Mimicking natural superhydrophobic surfaces and grasping the wetting process: A review on recent progress in preparing superhydrophobic surfaces," Advances in Colloid and Interface Science, vol. 169, no. 2, pp. 80-105, 2011.

[31] M. T. Z. Myint, G. L. Hornyak, and J. Dutta, "One pot synthesis of opposing "rose petal"' and "lotus leaf" superhydrophobic materials with zinc oxide nanorods," Journal of Colloid and Interface Science, vol. 415, pp. 32-38, 2014.
[32] Z. Guo, W. Liu, and B.-L. Su, "Superhydrophobic surfaces: From natural to biomimetic to functional," Journal of Colloid and Interface Science, vol. 353, no. 2, pp. 335-355, 2011.
[33] D. Quer´e, "Drops at Rest on a Tilted Plane," Langmuir, vol. 14, no. 8, pp. 2213-2216, 1998.
[34] L. Bocquet and J. L. Barrat, "Flow boundary conditions from nano- to micro-scales," Soft Matter, The Royal Society of Chemistry, vol. 3, pp. 685-693, 2007.
[35] J. P. Rothstein, "Slip on superhydrophobic surfaces," Annual Review of Fluid Mechanics, vol. 42, no. 1, pp. 89-109, 2010.
[36] O. I. Vinogradova and A. L. Dubov, "Superhydrophobic textures for microfluidics," Mendeleev Communications, vol. 22, no. 5, pp. 229-236, 2012.
[37] F. Feuillebois, M. Z. Bazant, and O. I. Vinogradova, "Transverse flow in thin superhydrophobic channels," Physical Review E, vol. 82, no. 5, pp. 5301-5305, 2010.
[38] S. Schmieschek, A. V. Belyaev, J. Harting, and O. I. Vinogradova, "Tensorial slip of super-hydrophobic channels," Physical Review E, vol. 85, no. 1, pp. 6324-6335, 2012.
[39] J. Zhou, A. V. Belyaev, F. Schmid, and O. I. Vinogradova, "Anisotropic flow in striped superhydrophobic channels," Journal of Chemical Physics, vol. 136, no. 19, pp. 4706-4717, 2012.
[40] N. P. Klochko, K. S. Klepikova, V. R. Kopach, G. S. Khrypunov, Y. O. Myagchenko, E. E. Melnychuk, V. M. Lyubov, and A. V. Kopach, "Hydrophobicity control of nanostructured zinc oxide layers produced by pulsed electrodeposition," Semiconductors/Physics of the Solid State, vol. 50, no. 3, pp. 357-368, 2016.
[41] H. B. Eral, D. J. C. M.'t Mannetje, and J. M. Oh, "Contact angle hysteresis: a review of fundamentals and applications," Colloid and Polymer Science, vol. 291, no. 2, pp. 247-260, 2013.
[42] C. N. C. Lam, R. Wu, D. Li, M. L. Hair, and A. W. Neumann, "Study of the advancing and receding contact angles: liquid sorption as a cause of contact angle hysteresis," Advances in Colloid and Interface Science, vol. 96, no 1-3, pp. 169-191, 2002.
[43] U. Zaimis, J. V. Aleksejeva, R. Aleksejevs, and Sh. E. Guseynov, "Hydrophilic nanostructure formation on the titanium surface by direct laser irradiation," International Scientific Journal "Machines. Technologies. Materials", vol. 11, no. 8, pp. 407-412, 2017.
[44] X.-T. Zhang, O. Sato, and A. Fujishima, "Water Ultrarepellency Induced by Nanocolumnar ZnO Surface," Langmuir, vol. 20, no. 14, pp. 6065-6067, 2004.
[45] B. Bhushan and Y. C. Jung, "Natural and biomimetic artificial surfaces for superhydrophobicity, self-cleaning, low adhesion, and drag reduction," Progress in Materials Science, vol. 56, no. 1, pp. 1-108, 2011.
[46] X. Zhang, F. Shi, J. Niu, Y. Jiang, and Z. Wang, "Superhydrophobic surfaces: from structural control to functional application," Journal of Materials Chemistry, vol. 18, no. 6, pp. 621-633, 2008.
[47] N. Gao, Y. Y. Yan, X. Y. Chen, and D. J. Mee, "Superhydrophobic surfaces with hierarchical structure," Materials Letters, vol. 65, no. 19, pp. 2902-2905, 2011.
[48] B. Bhushan, Y. C. Jung, and K. Koch, "Micro-, nano- and hierarchical structures for superhydrophobicity, self-cleaning and low adhesion," Philosophical Transactions, Series A: Mathematical, Physical, and Engineering Sciences, vol. 367, no. 1894, pp. 1631-1672, 2009.
[49] E. S. Asmolov, A. L. Dubov, T. V. Nizkaya, A. J. C. Kuehne, and O. I. Vinogradova, "Principles of transverse flow fractionation of microparticles in superhydrophobic channels," Lab on a Chip, vol. 15, no. 13, pp. 2835-2841, 2015.
[50] T. V. Nizkaya, E. S. Asmolov, and O. I. Vinogradova, "Advective superdiffusion in superhydrophobic microchannels," Physical Review E, vol. 96, no. 3, pp. 3109-3116, 2017.
[51] Laboratory of Physical Chemistry of Modified Surfaces, A.N. Frumkin Institute of Physical Chemistry and Electrochemistry, Russian Academy of Sciences. |Online|. Available: http://nanofluidics.phys.msu.ru/. |Accessed: Feb. 23, 2019|.
[52] J. V. Beck, B. Blackwell, and C. St. Clair Jr., Inverse Heat Conduction: Ill-Posed Problems. New York: Wiley & Sons Publishing, 1985, xvii+308 p.
[53] A. Repaci and M. T. Vacca, "Parameter Identification By Solution of Inverse Problem Referred to Mathematical Models of Continuum Physics," Mathematical and Computer Modelling, vol. 13, no. 2, pp. 79-84, 1990.
[54] J. F. Acker, B. Berkels, et al., "Inverse Problems and Parameter Identification in Image Processing," in Mathematical Methods in Signal Processing and Digital Image Analysis. Understanding Complex Systems (Eds.: R. Dahlhaus, J. Kurths, P. Maass, and J. Timmer), 2008, pp. 111-151.
[55] Sh. E. Guseynov, R. Aleksejevs, J. V. Aleksejeva, and Y. S. Gasimov, "Evaluating attractiveness of the group of the Central and the Eastern European Countries by using index approach for strategic decision making process related to expansion of financial service markets," Advanced Mathematical Models & Applications, vol. 2, no. 3, pp. 167-214, 2017.
[56] Sh. E. Guseynov, R. Aleksejevs, J. V. Aleksejeva, and R. Guseinovs, "Determining countries' potentials for successful export of luxurious and banking services," The 11th International Scientific and Practical Conference "Environment. Technology. Resources", June 15-17, 2017, Rezekne, Latvia, vol. 3, pp. 83-88, 2017.
[57] Sh. E. Guseynov, A. I. Urbah, and S. A. Andreyev, "On one Approach for Stable Estimate of Technical System Efficiency," The 10th International Scientific and Practical Conference "Environment. Technology. Resources", June 18-20, 2015, Rezekne, Latvia, vol. 3, pp. 100-108, 2015.
[58] Sh. E. Guseynov, J. V. Aleksejeva, and S. A. Andreyev, "On one regularizing algorithm for comprehensive diagnosing of apparatus, engines and machinery," International Journal of Advanced Materials Research, pp. 254-257, 2015.
[59] S. A. Andreyev and Sh. E. Guseynov, Regularizing Algorithms for Diagnosing: Applied to Gas Turbine Engines in Operation. Saarbrücken: LAP Publishing, 2013, 116 p.
[60] S. M. Yunusov, V. P. Labendik, and Sh. E. Guseynov, Monitoring and Diagnostics of Aircraft Gas Turbine Engines: Improvement of Models and Methods for Diagnosis of Gas Path of Gas Turbine Engines. Saarbrücken: LAP Publishing, 2014, 204 p.
[61] H. Schlichting, Boundary-Layer Theory. New York: McGraw-Hill, 1979, xxii+817 p.
[62] A. Oron, S. H. Davis, and S. G. Bankoff, "Long-scale evolution of thin films," Reviews of Modern Physics, vol. 69, no. 3, pp. 931-980, 1997.
[63] J. Ou, B. Perot, and J. P. Rothstein, "Laminar drag reduction in microchannels using ultrahydrophobic surfaces," Physics of Fluids, vol. 16, no. 12, pp. 4635-4643, 2004.
[64] J. Ou, B. Perot, and J. P. Rothstein, "Direct velocity measurements of the flow past drag-reducing ultrahydrophobic surfaces," Physics of Fluids, vol. 17, no. 10, pp. 3606-3616, 2005.
[65] J. R. Philip, "Integral properties of flows satisfying mixed no-slip and no-shear conditions," Journal of Applied Mathematics and Physics, vol. 23, no. 6, pp. 960-968, 1972.
[66] E. Lauga and H. A. Stone, "Effective slip in pressure-driven Stokes flow," Journal of Fluid Mechanics, vol. 489, pp. 55-77, 2003.
[67] A. V. Belyaev and O. I. Vinogradova, "Effective slip in pressure-driven flow past superhydrophobic stripes," Journal of Fluid Mechanics, vol. 652, pp. 489-499, 2010.
[68] C. Lee and C.-J. Kim, "Maximizing the Giant Liquid Slip on Superhydrophobic Microstructures by Nanostructuring Their Sidewalls," Langmuir, vol. 25, no. 21, pp. 12812-12818, 2009.
[69] S. A. Vagner, "Numerical modeling of the flow characteristics of pseudo-plastic polymer fluids in microchannels," PhD thesis, Institute of Problems of Chemical Physics, Chernogolovka, Russia, 2018, 141 p.
[70] C. Lee, C.-H. Choi, and C.-J. Kim, "Structured Surfaces for a Giant Liquid Slip," Physical Review Letters, vol. 101, no. 6, pp. 4501-4517, 2008.

Environment. Technology. Resources. Rezekne, Latvia
Proceedings of the 12th International Scientific and Practical Conference. Volume III, 60-69

On a 3D Initial-Boundary Value Problem for Determining the Dynamics of Impurities Concentration in a Horizontal Layered Fine-Pore Medium

Sharif E. Guseynov
Faculty of Science and Engineering
Institute of Fundamental Science and Innovative Technologies
Liepaja University
Liepaja, Latvia
"Entelgine" Research & Advisory Co., Ltd.
Riga, Latvia
sh.e.guseinov@inbox.lv

Ruslans Aleksejevs
Faculty of Mechanics and Mathematics
Lomonosov Moscow State University
Moscow, Russia
aleksejevs.ruslans@gmail.com

Jekaterina V. Aleksejeva
Institute of Fundamental Science and Innovative Technologies
Liepaja University
Riga Secondary School 34
Riga, Latvia
jekaterina.v.aleksejeva@gmail.com

***Abstract*—In the present paper, we propose an analytical approach for solving the 3D unsteady-state boundary-value problem for the second-order parabolic equation with the second and third types boundary conditions in two-layer rectangular parallelepipedic domain.**

Keywords*— *unsteady-state diffusion equation, initial-boundary value problem, Robin boundary condition, analytical method.

I. Introduction

In the present paper, we propose an analytical approach for solving the 3D unsteady-state boundary-value problem for the second-order parabolic equation with the third type boundary conditions in two-layer rectangular parallelepipedic domain. Such type problems arise in particular at study of metal concentration dynamics in the peat blocks (for instance, see [1]-[5] and respective references given in these). Mathematical statement of the considered problem is taken from the article [1], where the problem was solved by combination of the two approaches: firstly, the averaging method in the vertical direction (i.e. in height) and two horizontal directions (i.e. in width and in length), and, then, the obtained 2D problems have been solved by the standard/classical analytical methods. As opposed to the combinational approach suggested in [1], in the present paper, we do not use approximation methods at all (basically, result of application of the averaging method always is approximate).

II. Mathematical formulation of problem

Denote by Ω_{ix} i-th $(i=1,2)$ layer of two-layer peat block, which has shape of rectangular parallelepiped:

$$\Omega_{ix} \overset{def}{\equiv} \left\{ x=(x_1,x_2,x_3) \in \mathbb{R}^3 \mid x_j \in \left[0, L_j\right],\ j=1,2; \right.$$
$$\left. (i-1)H_1 \le x_3 \le (i-1)(L_3-H_1)+H_1 \right\},\ i=1,2.$$

Now we formulate a mathematical model describing the dynamics of metal concentration in a two-layer peat block: it is required to find functions $c_i(x,t): \Omega_{ix} \times [0,t_{END}] \to \mathbb{R}^1$, $(i=1,2)$, which satisfy

- diffusion equations with sources

$$\frac{\partial c_i(x,t)}{\partial t} = \sum_{j=1}^{3} D_{ij} \frac{\partial^2 c_i(x,t)}{\partial x_j^2} + f_i(x,t), \quad (1)$$
$$(x,t) \in \operatorname{int}\Omega_{ix} \times (0,t_{END}],\ (i=1,2);$$

- initial conditions

$$c_i(x,t)\big|_{t=0^+} = c_{i0}(x),\ x \in \Omega_{ix},\ (i=1,2); \quad (2)$$

- the following boundary conditions given:
  - at the trailing wall in the form of von Neumann condition

$$\left.\frac{\partial c_i(x,t)}{\partial x_1}\right|_{x_1=0^+} = c_{i1}(x_2,x_3,t), \quad (3)$$
$$(x/\{x_1\},t) \in \Omega_{ix/\{x_1\}} \times [0,t_{END}],\ (i=1,2);$$

  - at the front wall in the form of Robin condition

$$\left[D_{i1} \frac{\partial c_i(x,t)}{\partial x_1} + \lambda_{i1} c_i(x,t) \right]\Big|_{x_1=L_1^-} = a_{i1}(x_2,x_3,t), \quad (4)$$
$$(x/\{x_1\},t) \in \Omega_{ix/\{x_1\}} \times [0,t_{END}],\ (i=1,2);$$

  - at the left-side wall in the form of von Neumann condition

$$\left.\frac{\partial c_i(x,t)}{\partial x_2}\right|_{x_2=0^+} = c_{i2}(x_1,x_3,t), \quad (5)$$
$$(x/\{x_2\},t) \in \Omega_{ix/\{x_2\}} \times [0,t_{END}],\ (i=1,2);$$

Print ISSN 1691-5402
Online ISSN 2256-070X
http://dx.doi.org/10.17770/etr2019vol3.4172

– at the right-side wall in the form of Robin condition

$$\left[D_{i2}\frac{\partial c_i(x,t)}{\partial x_2}+\lambda_{i2}c_i(x,t)\right]\Big|_{x_2=L_2^-}=a_{i2}(x_1,x_3,t),\quad (x/\{x_2\},t)\in\Omega_{ix/\{x_2\}}\times[0,t_{END}],\ (i=1,2); \tag{6}$$

– at the lower (by $i=1$) and the upper (by $i=2$) bases in the form of Robin condition

$$\left[D_{i3}\frac{\partial c_i(x,t)}{\partial x_3}+(2i-3)\lambda_{i3}c_i(x,t)\right]\Big|_{x_3=(i-1)^+L_3^-}=a_{i3}(x_1,x_2,t),\quad (x/\{x_3\},t)\in\Omega_{ix/\{x_3\}}\times[0,t_{END}],\ (i=1,2); \tag{7}$$

- matching conditions given at the bedding interface [6]

$$\left((i-1)(D_{13}-1)+1\right)\frac{\partial^{i-1}c_1(x,t)}{\partial x_3}\Big|_{x_3=H_1^-}=\left((i-1)(D_{23}-1)+1\right)\frac{\partial^{i-1}c_2(x,t)}{\partial x_3}\Big|_{x_3=H_1^+},\quad (x/\{x_3\},t)\in\Omega_{ix/\{x_3\}}\times[0,t_{END}],\ (i=1,2); \tag{8}$$

- all 12 consistency conditions linking the initial and boundary functions from the constraints (2) (7).

In the mathematical model (1)(8) it is assumed that all numerical parameters $L_i>0\ (i=\overline{1,3})$, $H_i>0\ (i=1,2)$, $D_{ij}>0\ (i=1,2;\ j=\overline{1,3})$, $\lambda_{ij}>0\ (i=1,2;\ j=\overline{1,3})$ $t_{END}>0$, and all functions except functions $c_1(x,t)$ and $c_2(x,t)$, which stand for the desired metal concentrations, respectively, in the first and second layers of the peat block, are a priori given.

Remark 1. If in the mathematical model (1)(8) we assume that: (a) $c_{i1}(g)=c_{i2}(g)\equiv 0,\ (i=1,2)$, (b) boundary functions $a_{ij}(g),\ (i=1,2;\ j=\overline{1,3})$ do not depend on time t, then the model (1)(8) will completely coincide with the mathematical model (1.1) from [1], in which the physical interpretations of all the initial data - numerical parameters and functions are exhaustively described. Therefore, in this paper we will not describe the physical meaning of the initial numerical parameters and functions of the model (1)(8): they have the same meaning as in [1]. End of Remark 1.

The mathematical model (1)(8) can be solved by two different approaches. The first approach is a more universal approach for solving wide classes of initial-boundary value problems in layered regions with layers, whose physical, chemical, etc. characteristics are different. The main idea of the first approach is to reduce the mathematical model (1)(8) to the Fredholm integral equation of the first kind, and the subsequent procedure for applying Tikhonov's regularization method to the obtained integral equation [7], [8]. In view of the strict requirements for the maximum volume of articles, in this paper we will not consider the necessary procedures for performing the first approach. The essence of the second approach consists of applying method of separation of variables and constructing the Green's function (for instance, see [6] that is one of the best mathematical textbooks ever written). This method of solving initial problems (a Cauchy problem, when the region in which the process is studied is an unbounded region), boundary-value problems (in the case when the steady-state process is studied, or the process is studied at a time sufficiently far from the initial moment of the process) and initial-boundary value problems is a more "traditional" approach in the sense that this technique is, firstly, thoroughly studied in almost all courses of equations of mathematical physics and/or partial differential equations, and, secondly, is widely used in the study of various kinds of mathematical models described in the language of initial, boundary and initial-boundary problems for partial differential equations, in particular, for hyperbolic, parabolic and elliptic types of differential equations. In this paper, the second approach is chosen as the analytical method for solving the mathematical model (1)(8) – the method of separation of variables and construction of the corresponding Green's function.

III. Application of the method of separation of variables, and construction of the corresponding Green's functions

So, let us consider the initial-boundary value problem (1)(8), and try to find its solution by applying the method of separation of variables. To do this, we first formulate, as is customary in the method of separation of variables [6], two auxiliary boundary-value problems - the problem AP1 and the problem AP2, in each of which the equation is homogeneous.

A. Formulation of two auxiliary boundary-value problems

Auxiliary problem AP1. It is required to find the function $0\not\equiv c_1(x,t):\Omega_{1x}\times[0,t_{END}]\to$ ¡ [1] that satisfies:

- homogeneous equation

$$\frac{\partial c_1(x,t)}{\partial t}=\sum_{j=1}^{3}D_{1j}\frac{\partial^2 c_1(x,t)}{\partial x_j^2},\quad (x,t)\in\operatorname{int}\Omega_{1x}\times(0,t_{END}], \tag{9}$$

- heterogeneous initial condition

$$c_1(x,t)\big|_{t=0^+}=c_{10}(x),\ x\in\Omega_{1x}, \tag{10}$$

- homogeneous boundary conditions

$$\frac{\partial c_1(x,t)}{\partial x_1}\Big|_{x_1=0^+}=0,\ (x/\{x_1\},t)\in\Omega_{1x/\{x_1\}}\times[0,t_{END}], \tag{11}$$

$$D_{11}\frac{\partial c_1(x,t)}{\partial x_1}\Big|_{x_1=L_1^-}+\lambda_{11}c_1(x,t)\big|_{x_1=L_1^-}=0,\quad (x/\{x_1\},t)\in\Omega_{1x/\{x_1\}}\times[0,t_{END}], \tag{12}$$

$$\left.\frac{\partial c_1(x,t)}{\partial x_2}\right|_{x_2=0^+}=0,\ \left(x/\{x_2\},t\right)\in\Omega_{1x/\{x_2\}}\times[0,t_{END}], \tag{13}$$

$$\left.D_{12}\frac{\partial c_1(x,t)}{\partial x_2}\right|_{x_2=L_2^-}+\lambda_{12}c_1(x,t)\big|_{x_2=L_2^-}=0,\quad \left(x/\{x_2\},t\right)\in\Omega_{1x/\{x_2\}}\times[0,t_{END}], \tag{14}$$

$$\left.D_{13}\frac{\partial c_1(x,t)}{\partial x_3}\right|_{x_3=0^+}-\lambda_{13}c_1(x,t)\big|_{x_3=0^+}=0,\quad \left(x/\{x_3\},t\right)\in\Omega_{1x/\{x_3\}}\times[0,t_{END}], \tag{15}$$

- as well as two conditions

$$c_1(x,t)\big|_{x_3=H_1^-}=c_2(x,t)\big|_{x_3=H_1^+},\quad (x_1,x_2,t)\in[0,L_1]\times[0,L_2]\times[0,t_{END}], \tag{16}$$

$$\left.D_{13}\frac{\partial c_1(x,t)}{\partial x_3}\right|_{x_3=H_1^-}=\left.D_{23}\frac{\partial c_2(x,t)}{\partial x_3}\right|_{x_3=H_1^+},\quad (x_1,x_2,t)\in[0,L_1]\times[0,L_2]\times[0,t_{END}], \tag{17}$$

where the function $c_2(x,t)$ is defined in the domain $\Omega_{2x}\times[0,t_{END}]$ and is a nontrivial solution of the problem AP2 stated below.

Auxiliary problem AP2. It is required to find the function $0\not\equiv c_2(x,t):\Omega_{2x}\times[0,t_{END}]\to ¡^1$ that satisfies:

- homogeneous equation

$$\frac{\partial c_2(x,t)}{\partial t}=\sum_{j=1}^{3}D_{2j}\frac{\partial^2 c_2(x,t)}{\partial x_j^2},\quad (x,t)\in\operatorname{int}\Omega_{2x}\times(0,t_{END}], \tag{18}$$

- heterogeneous initial condition

$$c_2(x,t)\big|_{t=0^+}=c_{20}(x),\ x\in\Omega_{2x}, \tag{19}$$

- homogeneous boundary conditions

$$\left.\frac{\partial c_2(x,t)}{\partial x_1}\right|_{x_1=0^+}=0,\quad \left(x/\{x_1\},t\right)\in\Omega_{2x/\{x_1\}}\times[0,t_{END}], \tag{20}$$

$$\left.D_{21}\frac{\partial c_2(x,t)}{\partial x_1}\right|_{x_1=L_1^-}+\lambda_{21}c_2(x,t)\big|_{x_1=L_1^-}=0,\quad \left(x/\{x_1\},t\right)\in\Omega_{2x/\{x_1\}}\times[0,t_{END}], \tag{21}$$

$$\left.\frac{\partial c_2(x,t)}{\partial x_2}\right|_{x_2=0^+}=0,\left(x/\{x_2\},t\right)\in\Omega_{2x/\{x_2\}}\times[0,t_{END}], \tag{22}$$

$$\left.D_{22}\frac{\partial c_2(x,t)}{\partial x_2}\right|_{x_2=L_2^-}+\lambda_{22}c_1(x,t)\big|_{x_2=L_2^-}=0,\quad \left(x/\{x_2\},t\right)\in\Omega_{2x/\{x_2\}}\times[0,t_{END}], \tag{23}$$

$$\left.D_{23}\frac{\partial c_2(x,t)}{\partial x_3}\right|_{x_3=L_3^-}+\lambda_{23}c_2(x,t)\big|_{x_3=L_3^-}=0,\quad \left(x/\{x_3\},t\right)\in\Omega_{2x/\{x_3\}}\times[0,t_{END}]. \tag{24}$$

B. Partial investigation of the first auxiliary boundary-value problem

First of all, we note that the use of the phrase "partial research" in the titles of the current and next subsections is related to the interconnectedness of the auxiliary problems AP1 and AP2: as it will be seen in subsections B and C of this section, a full research of AP1 is impossible without research of AP2, and vice versa.

So, first consider the AP1 problem, a non-trivial solution of which will be sought in the form

$$c_1(x,t)=X_{11}(x_1)X_{12}(x_2)X_{13}(x_3)T_1(t), \tag{25}$$

where the essence of the requirements $X_{1j}(x_j)\not\equiv 0,\ j=\overline{1,3}$ and $T_1(t)\not\equiv 0$ is obvious.

Taking into account representation (25) in the equation (9), we get

$$\frac{T_1'(t)}{T_1(t)}=\sum_{j=1}^{3}D_{1j}\frac{X_{1j}''(x_j)}{X_{1j}(x_j)}. \tag{26}$$

Since the left side of equality (26) depends only on the time variable t, and the right side depends only on spatial variables $x=(x_1,x_2,x_3)$, equality (26) is possible only if both sides of it are equal to the same constant, which we will denote by $-\mu_1$, without making any assumptions regarding the sign of the constant μ_1. So, instead of (26) we can write the following two equations:

$$T_1'(t)+\mu_1 T_1(t)=0, \tag{27}$$

$$\sum_{j=1}^{3}D_{1j}\frac{X_{1j}''(x_j)}{X_{1j}(x_j)}+\mu_1=0. \tag{38}$$

First we deal with equation (28), and then we return to equation (27). Alternately differentiating equation (28) with respect to variables x_1, x_2 and x_3, we obtain $\frac{d}{dx_j}\left(D_{1j}\frac{X_{1j}''(x_j)}{X_{1j}(x_j)}\right)=0,\ \forall j=\overline{1,3}$, from which it follows that $D_{1j}\frac{X_{1j}''(x_j)}{X_{1j}(x_j)},\ \forall j=\overline{1,3}$ are constants: $D_{1j}\frac{X_{1j}''(x_j)}{X_{1j}(x_j)}=\mu_{1j},\ \forall j=\overline{1,3}$, where $\mu_1=\sum_{j=1}^{3}\mu_{1j}$, i.e. new constants μ_{11}, μ_{12}, μ_{13} are constituent constants of the

initial constant μ_1, appearing in equations (27) and (28). So, we obtained the following homogeneous equations of the same type:

$$D_{11}X_{11}''(x_1)+\mu_{11}X_{11}(x_1)=0, \tag{29}$$

$$D_{12}X_{12}''(x_2)+\mu_{12}X_{12}(x_2)=0, \tag{30}$$

$$D_{13}X_{13}''(x_3)+\mu_{13}X_{13}(x_3)=0, \tag{31}$$

which are related only by the fact that $\mu_1=\sum_{j=1}^{3}\mu_{1j}$. As the constant's μ_1 sign still is unknown to us, we also have no information about constants' μ_{11}, μ_{12}, μ_{13} signs.

Further, the substitution of (25) to the boundary conditions (11)(15) gives us the following boundary conditions:

- for the function $X_{11}(x_1)$ two boundary conditions:

$$\begin{cases} X_{11}'(0)=0, \\ D_{11}X_{11}'(L_1)+\lambda_{11}X_{11}(L_1)=0; \end{cases} \tag{32}$$

- for the function $X_{12}(x_2)$ again two boundary conditions:

$$\begin{cases} X_{12}'(0)=0, \\ D_{12}X_{12}'(L_2)+\lambda_{12}X_{12}(L_2)=0; \end{cases} \tag{33}$$

- for the function $X_{13}(x_3)$ one boundary condition:

$$D_{13}X_{13}'(0)-\lambda_{13}X_{13}(0)=0. \tag{34}$$

Consequently, the combination of equation (29) and boundary conditions (32), the combination of equation (30) and boundary conditions (33), and finally the combination of equation (31) and boundary condition (34) generate the following three SturmLiouville problems [9], [10], the first two of which are complete problems (in the sense that they have a complete formulation: each of them has a second-order ordinary differential equation and two boundary conditions are given), and the third problem is an incomplete problem (one boundary condition is missing):

$$\begin{cases} D_{11}X_{11}''(x_1)+\mu_{11}X_{11}(x_1)=0,\ x_1\in(0,L_1), \\ X_{11}'(0)=0, \\ D_{11}X_{11}'(L_1)+\lambda_{11}X_{11}(L_1)=0; \end{cases} \tag{35}$$

$$\begin{cases} D_{12}X_{12}''(x_2)+\mu_{12}X_{12}(x_2)=0,\ x_2\in(0,L_2), \\ X_{12}'(0)=0, \\ D_{12}X_{12}'(L_2)+\lambda_{12}X_{12}(L_2)=0; \end{cases} \tag{36}$$

$$\begin{cases} D_{13}X_{13}''(x_3)+\mu_{13}X_{13}(x_3)=0,\ x_3\in(0,H_1), \\ D_{13}X_{13}'(0)-\lambda_{13}X_{13}(0)=0. \end{cases} \tag{37}$$

We will have to solve all three SturmLiouville problems in turn (35)(37): our goal is to find their non-trivial solutions $X_{1j}(x_j)\not\equiv 0,\ j=\overline{1,3}$.

It is not difficult to show that in the case, when $\mu_{11}\le 0$, the problem (35) has only a trivial solution. Therefore, in problem (35) only the case $\mu_{11}>0$ should be considered, and in this case the general solution of the problem (35) is the following function

$$X_{11}(x_1)=A_{11}\cos\left(\sqrt{\frac{\mu_{11}}{D_{11}}}x_1\right),\ x_1\in[0,L_1], \tag{38}$$

where A_{11} is an arbitrary constant.

Function $X_{11}(x_1)$, $x_1\in[0,L_1]$, defined by formula (38), is called eigenfunction of the SturmLiouville problem (for instance, see [9] as well as [6]), and it corresponds to the eigenvalue $\mu_{11}=D_{11}\left(\frac{\alpha_1}{L_1}\right)^2>0$, where α_1 is a positive root of the transcendental equation

$$\alpha_1 tg(\alpha_1)=\frac{\lambda_{11}L_1}{D_{11}}. \tag{39}$$

Since the transcendental equation (39) has an infinite number of solutions, we can say that the SturmLiouville problem (35) has an infinite number of eigenvalues

$$\mu_{11n}=D_{11}\left(\frac{\alpha_{1n}}{L_1}\right)^2>0, \tag{40}$$

to which the following eigenfunctions correspond

$$X_{11n}(x_1)=A_{11n}\cos\left(\sqrt{\frac{\mu_{11n}}{D_{11}}}x_1\right),\ x_1\in[0,L_1], \tag{41}$$

and each of them is determined with precision to an arbitrary constant A_{11n}. In (41) number α_{1n} is n-th $(n\in\mathbb{N})$ positive root of the transcendental equation (39), and, hereinafter, speaking of the ordinal numbers of the positive roots of the transcendental equation, we will mean their ordering in non-decreasing order: $\alpha_{11}\le\alpha_{12}\le\alpha_{13}\le\ldots$

Because of the fact that the SturmLiouville problem (36) differs from the problem (35) only by the coefficients D_{12} and λ_{12}, we can write, fully following the results of the study of the problem (35) obtained above, that the eigenfunctions of the SturmLiouville problem (36) are the functions

$$X_{12m}(x_2)=A_{12m}\cos\left(\sqrt{\frac{\mu_{12m}}{D_{12}}}x_2\right),\ x_2\in[0,L_2], \tag{42}$$

where A_{12m} are some constants; $\mu_{12m}=D_{12}\left(\frac{\beta_{1m}}{L_2}\right)^2>0$ are eigenvalues, β_{1m} is m-th

$(m \in ¥)$ positive root of the transcendental equation

$$\beta_1 tg(\beta_1) = \frac{\lambda_{12} L_2}{D_{12}}. \quad (43)$$

Now we investigate the incomplete SturmLiouville problem (37). It is easy to check that when $\mu_{13} > 0$ (in the case of $\mu_{13} \le 0$ problem (37) has only trivial solution) incomplete problem (37) has general solution

$$X_{13}(x_3) = A_{13}\left\{\sin\left(\sqrt{\frac{\mu_{13}}{D_{13}}}x_3\right) + \frac{\sqrt{\mu_{13} D_{13}}}{\lambda_{13}}\cos\left(\sqrt{\frac{\mu_{13}}{D_{13}}}x_3\right)\right\}, \; x_3 \in [0, H_1], \quad (44)$$

which is called the SturmLiouville incomplete problem eigenfunction (37) corresponding to the eigenvalue μ_{13} (not yet found); A_{13} is an arbitrary constant. To find eigenvalue $\mu_{1,3}$, we should refer to conditions (16), (17), in which another function is involved – the desired function $c_2(x,t), (x,t) \in \Omega_{2x} \times [0, t_{END}]$ of auxiliary problem AP2. In other words, to find the eigenvalues and the corresponding eigenfunctions of the incomplete SturmLiouville problem (37), we will need to investigate the auxiliary problem AP2, which we will do in subsection C of this section.

Recall that in the course of studying the AP1 problem (still unfinished), we found out that all the eigenvalues of problems (35)(37) of SturmLiouville are positive. Therefore, the constant μ_1 from (27) and (28), which is the sum of these eigenvalues, is also positive:

$$0 < \underbrace{\mu_{1nm}}_{\mu_1} = \mu_{11n} + \mu_{12m} + \mu_{13} = D_{11}\left(\frac{\alpha_{1n}}{L_1}\right)^2 + D_{12}\left(\frac{\beta_{1m}}{L_2}\right)^2 + \mu_{13}, \; \forall n, m \in ¥, \quad (45)$$

where α_{1n} and β_{1m} are n-th $(n \in ¥)$ and m-th $(m \in ¥)$ positive roots of the transcendental equations (39) and (43), respectively; constituent constant $\mu_{13} > 0$, which is the eigenvalue of the incomplete SturmLiouville problem (37), has not yet been found (it means that the eigenfunction $X_{13}(x_3), x_3 \in [0, H_1]$, having a formal representation in the form (44) and corresponding to this eigenvalue, is not uniquely determined).

C. Partial investigation of the second auxiliary boundary-value problem

We will look for nontrivial solution of the AP2 problem in the following form

$$c_2(x,t) = X_{21}(x_1) \cdot X_{22}(x_2) \cdot X_{23}(x_3) \cdot T_2(t), \quad (46)$$

where meaning of requirements $X_{2j}(x_j) \not\equiv 0, \; j = \overline{1,3}$ and $T_2(t) \not\equiv 0$ is obvious. By analogy with the previous subsection B, given the representation (46) in equation (18), we obtain

$$T_2'(t) + \mu_2 T_2(t) = 0, \quad (47)$$

$$\sum_{j=1}^{3} D_{2j} \cdot \frac{X_{2j}''(x_j)}{X_{2j}(x_j)} + \mu_2 = 0, \quad (48)$$

where μ_2 is the same constant μ_1 as in equations (27), (28), i.e. $\mu_2 = \mu_1$ (for convenience, we will use the notation μ_2, knowing that $\mu_2 = \mu_1$).

First we deal with equation (48), and then we return to equation (47). We already know that constants μ_1 and μ_2 in equations (28) and (48) coincide. However, we do not have the right to require that in three homogeneous equations of the same type

$$D_{21} X_{21}''(x_1) + \mu_{21} X_{21}(x_1) = 0, \quad (49)$$

$$D_{22} X_{22}''(x_2) + \mu_{22} X_{22}(x_2) = 0, \quad (50)$$

$$D_{23} X_{23}''(x_3) + \mu_{23} X_{23}(x_3) = 0, \quad (51)$$

which directly follow from equation (48) (see the transition procedure from equation (28) to equations (29) (31)), constants μ_{21}, μ_{22} and μ_{23}, whose sum gives μ_2 $\left(\text{i.e. } \mu_2 = \sum_{j=1}^{3} \mu_{2j}\right)$, coincide with the previous constituent constants μ_{11}, μ_{12}, μ_{13} (values μ_{11} and μ_{12} are already determined, and value μ_{13} will be determined in this subsection). The reason for this circumstance (i.e. the fact that $\mu_1 = \mu_2$, but $\mu_{1j} \not\equiv \mu_{2j}, \; j = \overline{1,3}$) is due to the fact that the coefficients D_{1j} $\left(j = \overline{1,3}\right)$ in equations (29)(31) differ from the corresponding coefficients D_{2j} $\left(j = \overline{1,3}\right)$ in equations (49)(51). In other words, in the equations (49) (51) constants μ_{21}, μ_{22}, μ_{23}, where $\sum_{j=1}^{3} \mu_{2j} = \mu_2$, are still unknown constants and need to be determined. Finally, we note that equations of the same type (49)(51) are related only by the fact that $\mu_2 = \sum_{j=1}^{3} \mu_{2j}$. Further, the substitution of representations (46) to the boundary conditions (20)(24) gives us the following boundary conditions:

- for function $X_{21}(x_1)$ two boundary conditions:

$$\begin{cases} X_{21}'(0) = 0, \\ D_{21} X_{21}'(L_1) + \lambda_{21} X_{21}(L_1) = 0; \end{cases} \quad (52)$$

- for function $X_{22}(x_2)$ again two boundary conditions:

$$\begin{cases} X_{22}'(0) = 0, \\ D_{22} X_{22}'(L_2) + \lambda_{22} X_{22}(L_2) = 0; \end{cases} \quad (53)$$

- for function $X_{23}(x_3)$ one boundary condition:

$$D_{23}X'_{23}(L_3)+\lambda_{23}X_{23}(L_3)=0. \tag{54}$$

Consequently, the appropriate combination of equations (49)(51) and boundary conditions (52)(54) again give us the following three SturmLiouville problems, the first two of which are complete problems, and the third problem, just like problem (37) is not a complete problem:

$$\begin{cases} D_{21}X''_{21}(x_1)+\mu_{21}X_{21}(x_1)=0,\ x_1\in(0,L_1), \\ X'_{21}(0)=0, \\ D_{21}X'_{21}(L_1)+\lambda_{21}X_{21}(L_1)=0; \end{cases} \tag{55}$$

$$\begin{cases} D_{22}X''_{22}(x_2)+\mu_{22}X_{22}(x_2)=0,\ x_2\in(0,L_2), \\ X'_{22}(0)=0, \\ D_{22}X'_{22}(L_2)+\lambda_{22}X_{22}(L_2)=0; \end{cases} \tag{56}$$

$$\begin{cases} D_{23}X''_{23}(x_3)+\mu_{23}X_{23}(x_3)=0,\ x_3\in(H_1,L_3), \\ D_{23}X'_{23}(L_3)+\lambda_{23}X_{23}(L_3)=0. \end{cases} \tag{57}$$

Almost completely following the reasoning from subsection B in the study of problems (35) and (36), with respect to complete problems (55) and (56) of SturmLiouville, we can assert the following statements without detailed derivation:

- The complete problem (55) of SturmLiouville has eigenvalues

$$\mu_{21k}=D_{21}\left(\frac{\alpha_{2k}}{L_1}\right)^2>0,\ k\in ¥, \tag{58}$$

to which the following eigenfunctions correspond

$$X_{21k}(x_1)=A_{21k}\cos\left(\sqrt{\frac{\mu_{21k}}{D_{21}}}x_1\right),\ x_1\in[0,L_1], \tag{59}$$

and each of them is determined with precision to an arbitrary constant A_{21k}. In (59) number α_{2k} is k-th $(k\in ¥)$ positive root of the transcendental equation

$$\alpha_2 tg(\alpha_2)=\frac{\lambda_{21}L_1}{D_{21}}. \tag{60}$$

- The complete problem (56) of SturmLiouville has eigenvalues

$$\mu_{22p}=D_{22}\left(\frac{\beta_{2p}}{L_2}\right)^2>0,\ p\in ¥, \tag{61}$$

to which the following eigenfunctions correspond

$$X_{22p}(x_2)=A_{22p}\cos\left(\sqrt{\frac{\mu_{22p}}{D_{22}}}x_2\right),\ \forall x_2\in[0,L_2], \tag{62}$$

and each of them is determined with precision to an arbitrary constant A_{22p}. In (62) number β_{2p} is p-th $(p\in ¥)$ positive root of the transcendental equation

$$\beta_2 tg(\beta_2)=\frac{\lambda_{22}L_2}{D_{22}}. \tag{63}$$

Now let us study the incomplete SturmLiouville problem (57). It is easy to check that when $\mu_{23}>0$ (in the case of $\mu_{23}\le 0$ problem (57) has only trivial solution) the general solution of (57) is function

$$X_{23}(x_3)=A_{23}\left\{\sin\left(\sqrt{\frac{\mu_{23}}{D_{23}}}x_3\right)\right. \\ \left.-\cos\left(\sqrt{\frac{\mu_{23}}{D_{23}}}x_3\right)tg\left(\sqrt{\frac{\mu_{23}}{D_{23}}}L_3+\theta\right)\right\},\ x_3\in[H_1,L_3], \tag{64}$$

where A_{23} is an arbitrary constant; $\theta=arctg\left(\frac{\sqrt{\mu_{23}D_{23}}}{\lambda_{23}}\right)$.

Function $X_{23}(x_3)$, defined by formula (64), is called the eigenfunction of the incomplete SturmLiouville problem (57) corresponding to the eigenvalue μ_{23}. Recall that in the course of studying the AP2 problem (still unfinished), we found out that all the eigenvalues of problems (55)(57) of SturmLiouville are positive. Therefore, the constant μ_2 from (47) and (48), which is the sum of these eigenvalues, is also positive:

$$0<\underbrace{\mu_{2kp}}_{\mu_2}=\mu_{21k}+\mu_{22p}+\mu_{23} \\ =D_{21}\left(\frac{\alpha_{2k}}{L_1}\right)^2+D_{22}\left(\frac{\beta_{2p}}{L_2}\right)^2+\mu_{23},\ \forall k,p\in ¥, \tag{65}$$

where α_{2k} and β_{2p} are k-th $(k\in ¥)$ and p-th $(p\in ¥)$ positive roots of the transcendental equations (60) and (63), respectively; constituent constant $\mu_{23}>0$, which is eigenvalue of incomplete SturmLiouville problem (57), is still unknown (it means that the eigenfunction $X_{23}(x_3)$, $x_3\in[H_1,L_3]$, having a formal representation in the form (64) and corresponding to this eigenvalue, is not uniquely determined).

So, within the framework of the study of auxiliary problems AP1 and AP2, by this time the eigenvalues μ_{13} and μ_{23}, remain uncertain and, therefore, same thing can be said about their corresponding eigenfunctions $X_{13}(x_3)$, $x_3\in[0,H_1]$ and $X_{23}(x_3)$, $x_3\in[H_1,L_3]$; in addition, it is necessary to clarify the choice of constants $A_{11n}\ (n\in ¥)$, $A_{12m}\ (m\in ¥)$, A_{13}, $A_{21k}\ (k\in ¥)$, $A_{22p}\ (p\in ¥)$, A_{23}; finally, it is required to find functions $T_1(t)$ and $T_2(t)$, which satisfy equations (27) and (47).

D. Using the matching conditions, and the complete solving the both auxiliary problems

Recall that in the course of studying the auxiliary problems AP1 and AP2, we did not use matching conditions (16) and (17), and now it is time to use these conditions to find eigenvalues μ_{13} and μ_{23}, and redefine the corresponding eigenfunctions $X_{13}(x_3)$, $x_3\in[0,H_1]$ and $X_{23}(x_3)$, $x_3\in[H_1,L_3]$, formally represented by formulas (44) and (64)), respectively. For this purpose, we first note that if equality

$$\underbrace{T_1(t)\prod_{j=1}^{3}X_{1j}(x_j)}_{c_1(x,t)}=\underbrace{T_1(t)\prod_{j=1}^{3}X_{2j}(x_j)}_{c_2(x,t)}$$

holds for $\forall x_j\in[0,L_j]$, $j=1,2$, $\forall t\in[0,T_{END}]$ and $\forall x_3\in(H_1-\varepsilon,H_1+\varepsilon)$, $0<\varepsilon=1$, then it means that $X_{13}(x_3)=CX_{23}(x_3)$, $0<\forall\varepsilon=1$, where $C\neq 0$ is an arbitrary constant, which for convenience we choose as $\frac{A_{13}}{A_{23}}$, i.e. $C=\frac{A_{13}}{A_{23}}$ (such a choice of a constant is legitimate because of its arbitrariness, and, moreover, nothing will change from such (or other) choice). Now, having this fact, substituting representations (25) and (46) to matching conditions (16) and (17), we obtain

$$A_{23}X_{13}(x_3)\big|_{x_3=H_1^-}=A_{13}X_{23}(x_3)_{x_3=H_1^+},$$
$$A_{23}D_{13}X'_{13}(x_3)\big|_{x_3=H_1^-}=A_{13}D_{23}X'_{13}(x_3)\big|_{x_3=H_1^+}.$$

Taking into account formulas (44) and (64) in these two equalities, after performing the necessary calculations and transformations, gives us the following results: the desired eigenvalue μ_{23} from the SturmLiouville problem (57) are found by the formula

$$\mu_{23}=D_{23}\left(\frac{\gamma}{H_2}\right)^2>0, \tag{66}$$

and then the desired eigenvalue μ_{13} from the SturmLiouville problem (37) is calculated by the formula

$$\mu_{13}=\mu_{21}+\mu_{22}+\mu_{23}-\mu_{11}-\mu_{12}, \tag{67}$$

whose right side contains already found eigenvalues of SturmLiouville problems (35), (36), (55), (56).

In the formula (66) parameter γ is positive root of the transcendental equation

$$\frac{\sqrt{D_{23}\gamma^2+\xi}}{\gamma}tg\left(\gamma+arctg\left(\frac{D_{23}\gamma}{H_2\lambda_{23}}\right)\right)=g(\gamma), \tag{68}$$

$$g(\gamma)=\frac{D_{23}}{\sqrt{D_{13}}}\frac{\sqrt{D_{13}(D_{23}\gamma^2+\xi)}+H_2\lambda_{13}tg\left(\frac{H_1}{H_2}\sqrt{\frac{D_{23}\gamma^2+\xi}{D_{13}}}\right)}{\sqrt{D_{13}(D_{23}\gamma^2+\xi)}tg\left(\frac{H_1}{H_2}\sqrt{\frac{D_{23}\gamma^2+\xi}{D_{13}}}\right)-H_2\lambda_{13}},$$

$$\xi=H_2^2(\mu_{21}+\mu_{22}-\mu_{11}-\mu_{12}).$$

Since the transcendental equation (68) has an infinite number of solutions, we arrive at the following results:

- The SturmLiouville problem (57) has an infinite number of eigenvalues

$$\mu_{23q}=D_{23}\left(\frac{\gamma_q}{H_2}\right)^2,\ q\in\text{¥},$$
$$q=q(n,m,k,p),\ \forall n,m,k,p\in\text{¥}, \tag{69}$$

to which the following eigenfunctions correspond

$$X_{23q}(x_3)=\sin\left(\sqrt{\frac{\mu_{23q}}{D_{23}}}x_3\right)$$
$$-tg\left(\sqrt{\frac{\mu_{23q}}{D_{23}}}L_3+arctg\left(\frac{\sqrt{\mu_{23q}D_{23}}}{\lambda_{23}}\right)\right)\times \tag{70}$$
$$\times\cos\left(\sqrt{\frac{\mu_{23q}}{D_{23}}}x_3\right),\ x_3\in[H_1,L_3];$$

in (69) number $\gamma_q=\gamma_{q(n,m,k,p)}$ is q-th $(q\in\text{¥})$ positive root of the transcendental equation (68);

- The SturmLiouville problem (37) has an infinite number of eigenvalues

$$\mu_{13nmkpq}=\mu_{21k}+\mu_{22p}+\mu_{23q}-\mu_{11n}-\mu_{12m},$$
$$q=q(n,m,k,p),\ \forall n,m,k,p\in\text{¥},$$

to which the following eigenfunctions correspond

$$X_{13nmkpq}(x_3)=\frac{\sqrt{\mu_{13nmkpq}D_{13}}}{\lambda_{13}}\cos\left(\sqrt{\frac{\mu_{13nmkpq}}{D_{13}}}x_3\right)$$
$$+\sin\left(\sqrt{\frac{\mu_{13nmkpq}}{D_{13}}}x_3\right),\ x_3\in[0,H_1]. \tag{71}$$

So, within the framework of the study of auxiliary problems AP1 and AP2, two sub-problems remain unfinished: the problem of finding functions $T_1(t)$ and $T_2(t)$, for whose solution one, first of all, needs to clarify/redefine formulas (45) and (65) for constants μ_1 and μ_2; problem of choosing constants A_{11n} $(n\in\text{¥})$, A_{12m} $(m\in\text{¥})$, A_{21k} $(k\in\text{¥})$ and A_{22p} $(p\in\text{¥})$, which appear in formulas (41), (42), (59) and (62), respectively. We start by clarifying/redefining formulas (45) and (65) for constants μ_1 and μ_2. Since constants μ_1 and μ_2 coincide, then it is sufficed to clarify the formula (45) for the constant μ_1 only:

$$0<\underbrace{\mu_{1nmkpq}}_{\mu_1=\mu_2\equiv\mu}=D_{21}\left(\frac{\alpha_{2k}}{L_1}\right)^2+D_{22}\left(\frac{\beta_{2p}}{L_2}\right)^2$$
$$+D_{23}\left(\frac{\gamma_q}{H_2}\right)^2-D_{11}\left(\frac{\alpha_{1n}}{L_1}\right)^2-D_{12}\left(\frac{\beta_{1m}}{L_2}\right)^2 \tag{72}$$

Now we clarify the problem of choosing constants A_{11n} $(n\in\text{¥})$, A_{12m} $(m\in\text{¥})$, A_{21k} $(k\in\text{¥})$ and A_{22p} $(p\in\text{¥})$, which appear in formulas (41), (42), (59) and (62), respectively. For this we use the fact that the system of eigenfunctions of the SturmLiouville problem forms an orthogonal system with some weight on the segment. Therefore, we can state that the system of functions $\{X_{11n}(x_1)\}_{n\in\text{¥}}$, $\{X_{12m}(x_2)\}_{m\in\text{¥}}$, $\{X_{21k}(x_1)\}_{k\in\text{¥}}$, $\{X_{22p}(x_2)\}_{p\in\text{¥}}$, represented by formulas (41), (42), (59), (62), respectively, are orthogonal systems on segments $[0,L_1]$, $[0,L_2]$, $[0,L_1]$, $[0,L_2]$, respectively. One of the

reasonable constraints on choice of constants $A_{11n}\ (n\in ¥)$, $A_{12m}\ (m\in ¥)$, $A_{21k}\ (k\in ¥)$, $A_{22p}\ (p\in ¥)$, which appear in formulas (41), (42), (59), (62), respectively, is the requirement of orthonormality of systems $\left\{X_{11n}(x_1)\right\}_{n\in ¥}$, $\left\{X_{12m}(x_2)\right\}_{m\in ¥}$, $\left\{X_{21k}(x_1)\right\}_{k\in ¥}$, $\left\{X_{22p}(x_2)\right\}_{p\in ¥}$ of eigenfunctions. Another option (very simple, but less reasonable) of choosing constants is simply equating them to some number, for example, to 1. In this paper, we choose the first option:

$$X_{11n}(x_1)=\sqrt{\frac{\lambda_{11}}{D_{11}}+\frac{\mu_{11n}}{\lambda_{11}}}\sin\left(\sqrt{\frac{\mu_{11n}}{D_{11}}}x_1\right), \quad (73)$$

$\forall x_1\in[0,L_1],\ \forall n\in ¥.$

$$X_{12m}(x_2)=\sqrt{\frac{\lambda_{12}}{D_{12}}+\frac{\mu_{12m}}{\lambda_{12}}}\sin\left(\sqrt{\frac{\mu_{12m}}{D_{12}}}x_2\right), \quad (74)$$

$\forall x_2\in[0,L_2],\ \forall m\in ¥.$

$$X_{21k}(x_1)=\sqrt{\frac{\lambda_{21}}{D_{21}}+\frac{\mu_{21k}}{\lambda_{21}}}\sin\left(\sqrt{\frac{\mu_{21k}}{D_{21}}}x_1\right), \quad (75)$$

$\forall x_1\in[0,L_1],\ \forall k\in ¥.$

$$X_{22p}(x_1)=\sqrt{\frac{\lambda_{22}}{D_{22}}+\frac{\mu_{22p}}{\lambda_{22}}}\sin\left(\sqrt{\frac{\mu_{22p}}{D_{22}}}x_2\right), \quad (76)$$

$\forall x_2\in[0,L_2],\ \forall p\in ¥.$

Now we can proceed to solving the last problem in the framework of the study of auxiliary problems AP1 and AP2 – the problem of finding functions $T_1(t)$ and $T_2(t)$ from equations (27) and (47), respectively. If we consider equations (27) and (47) only from the position of time $t\in[0,t_{END}]$, rather than from the position of spatial variables, the solution of these equations is the function $T(t)=Be^{-\mu\cdot t}$, where B is some coefficient that is not yet defined. Since number $\mu(=\mu_1=\mu_2)$ is determined by finally found formula (72), we can write

$$T_{nmkpq}(t)=B_{nmkpq}e^{-\mu_{nmkpq}\cdot t},\ \forall n,m,k,p,q\in ¥, \quad (77)$$

where coefficients B_{nmkpq} are to be determined taking into account spatial variables.

To satisfy conditions (10) and (19), in the formula (77) for the layer Ω_{1x} there should be its own distinctive coefficients B_{1nmkpq}, and for the layer Ω_{2x} there should be its own distinctive constants B_{2nmkpq}. Taking into account formula (73) for $X_{11n}(x_1)$, formula (74) for $X_{12m}(x_2)$, formula (71) for $X_{13nmkpq}(x_3)$, formula (75) for $X_{21k}(x_1)$, formula (76) for $X_{22p}(x_2)$, formula (70) for $X_{23nmkpq}(x_3)$, formula (77) for $T_{nmkpq}(t)$ in representations (25) and (46), we obtain the following formula for the desired functions $c_1(x,t)$, where $(x,t)\in\Omega_{1x}\times[0,t_{END}]$, and $c_2(x,t)$, where $(x,t)\in\Omega_{2x}\times[0,t_{END}]$:

$$c_1(x,t)=\sum_{n,m,k,p,q=1}^{+\infty}B_{1nmkpq}e^{-\mu_{nmkpq}\cdot t}X_{1nmkpq}(x), \quad (78)$$

where $X_{1nmkpq}(x)=X_{11n}(x_1)X_{12m}(x_2)X_{13nmkpq}(x_3)$, $x_1\in[0,L_1]$, $x_2\in[0,L_2]$, $x_3\in[0,H_1]$, $t\in[0,t_{END}]$, system of functions $\left\{X_{1nmkpq}(x)\right\}_{n,m,k,p,q\in ¥}$ is an orthogonal system;

$$c_2(x,t)=\sum_{n,m,k,p,q=1}^{+\infty}B_{2nmkpq}e^{-\mu_{nmkpq}\cdot t}X_{2nmkpq}(x), \quad (79)$$

where $X_{2nmkpq}(x)=X_{21k}(x_1)X_{22p}(x_2)X_{23nmkpq}(x_3)$, $x_1\in[0,L_1]$, $x_2\in[0,L_2]$, $x_3\in[H_1,L_3]$, $t\in[0,t_{END}]$, system of functions $\left\{X_{2nmkpq}(x)\right\}_{n,m,k,p,q\in ¥}$ is an orthogonal system.

Obviously, the function $c_1(x,t)$, determined by the formula (78), satisfies all homogeneous boundary conditions (11)(15) of the auxiliary problem AP1, since they are satisfied by all members of the quadruple series in the right-hand side (78); similarly function $c_2(x,t)$, determined by the formula (79), satisfies all homogeneous boundary conditions (20)(24) of the auxiliary problem AP1, since they are satisfied by all members of the quadruple series in the right-hand side (79); in addition, these functions satisfy the matching conditions (16), (17), since functions $X_{13nmkpq}(x_3)$ and $X_{23nmkpq}(x_3)$, which are contained in each member of the quadruple series of (78) and (79), respectively, automatically satisfy the matching conditions (16), (17) – functions $X_{13nmkpq}(x_3)$ and $X_{23nmkpq}(x_3)$ were determined owing to the conditions (16), (17). Therefore, it remains to enforce functions $c_1(x,t)$ and $c_2(x,t)$ to satisfy the initial conditions (10) and (19), respectively.

The sought-for function $c_1(x,t)$, which is determined by formula (78), to satisfy initial condition (10), we obtain:

$$c_{10}(x)=\sum_{n,m,k,p,q=1}^{+\infty}B_{1nmkpq}X_{1nmkpq}(x). \quad (80)$$

Analogously, the sought-for function $c_2(x,t)$ determined by formula (79) to satisfy the initial condition (19), we obtain:

$$c_{20}(x)=\sum_{n,m,k,p,q=1}^{+\infty}B_{2nmkpq}X_{2nmkpq}(x). \quad (81)$$

Let us by turns apply to (80) and (81) one of the fundamental theorems of mathematical physics – Steklov's Theorem on decomposability of any twice continuously differentiable function into absolutely and uniformly convergent series by orthogonal system of eigenfunctions of the SturmLiouville problem (first strictly proved in

[11]; see also [10]): for $\forall n,m,k,p,q \in ¥$ there take place

$$B_{1nmkpq} = \frac{\int\limits_{\Omega_{1x}} c_{10}(y) X_{1nmkpq}(y)\,dy}{\int\limits_{\Omega_{1z}} X^2_{1nmkpq}(z)\,dz} = \frac{\int\limits_0^{L_1} dy_1 \int\limits_0^{L_2} dy_2 \int\limits_0^{H_1} c_{10}(y) X_{1nmkpq}(y)\,dy_3}{\int\limits_0^{L_1} dz_1 \int\limits_0^{L_2} dz_2 \int\limits_0^{H_1} X^2_{1nmkpq}(z)\,dz_3}, \quad (82)$$

$$B_{2nmkpq} = \frac{\int\limits_{\Omega_{2y}} c_{20}(y) X_{2nmkpq}(y)\,dy}{\int\limits_{\Omega_{2z}} X^2_{2nmkpq}(z)\,dz} = \frac{\int\limits_0^{L_1} dy_1 \int\limits_0^{L_2} dy_2 \int\limits_{H_1}^{L_3} c_{20}(y) X_{2nmkpq}(y)\,dy_3}{\int\limits_0^{L_1} dz_1 \int\limits_0^{L_2} dz_2 \int\limits_{H_1}^{L_3} X^2_{2nmkpq}(z)\,dz_3}. \quad (83)$$

It is not difficult to prove [6] that the function $c_1(x,t)$ defined by formulas (78), (82) is a continuously differentiable function by a variable t in the interval $[0,t_{END}]$ and twice continuously differentiable function by variable x for the layer Ω_{1x}, which satisfies the equation (9). Similarly, a function $c_2(x,t)$, defined by formulas (79), (83) is a continuously differentiable function for a variable in a segment and a twice continuously differentiable function (twice differentiable function) for a variable t for the layer Ω_{2x}, which satisfies equation (18). Thus, the functions $c_1(x,t)$ and $c_2(x,t)$ are continuous functions for $\Omega_{1x} \times [0,t_{END}]$ and $\Omega_{2x} \times [0,t_{END}]$, respectively, and since these functions satisfy the matching conditions (16), (17), they are considered to be solutions of auxiliary problems AP1 and AP2, respectively. Thus, the study of auxiliary problems AP1 and AP2 is entirely completed, and now we can proceed to finding a solution for the original problem (1)-(8).

E. Solving the original problem (1)(8)

Obviously, substituting (82) in (78) and (83) in (79), we get the following representations for the functions $c_1(x,t), \forall (x,t) \in \Omega_{1x} \times [0,t_{END}]$ and $c_2(x,t), \forall (x,t) \in \Omega_{2x} \times [0,t_{END}]$:

$$c_1(x,t) = \int\limits_{\Omega_{1y}} G_1(x,y,t) c_{10}(y)\,dy, \quad (84)$$

$$G_1(x,y,t) = \sum_{n,m,k,p,q=1}^{+\infty} e^{-\mu_{nmkpq} t} \frac{X_{1nmkpq}(x) X_{1nmkpq}(y)}{\int\limits_{\Omega_{1z}} X^2_{1nmkpq}(z)\,dz}, \quad (85)$$

$$c_2(x,t) = \int\limits_{\Omega_{2y}} G_2(x,y,t) c_{20}(y)\,dy, \quad (86)$$

$$G_2(x,y,t) = \sum_{n,m,k,p,q=1}^{+\infty} e^{-\mu_{nmkpq} \cdot t} \frac{X_{2nmkpq}(x) X_{2nmkpq}(y)}{\int\limits_{\Omega_{2z}} X^2_{2nmkpq}(z)\,dz}, \quad (87)$$

which are a more compact form for auxiliary problems AP1 and AP2 solutions, respectively. Each of the above introduced functions $G_j(x,y,t)$, $j=1,2$ is a well-known and deeply studied Green's function [6], [10], [13], [14]. Our goal in this subsection is the analytical construction of the solution to the original problem (1)(8), using the Green's functions $G_j(x,y,t)$, $j=1,2$. As you will be able to see below, after completing the study of auxiliary problems AP1, AP2, there is no difficulty in finding an analytical solution to the original problem (1)-(8): a more or less difficult part of the research for the problem considered in this paper is the study of auxiliary problems AP1 and AP2.

Let us formulate a new auxiliary problem, naming it NAP1: it is required to find solutions to the inhomogeneous equation (which coincides with equation (1) for $i=1$)

$$\frac{\partial c_1(x,t)}{\partial t} = \sum_{j=1}^{3} D_{1j} \frac{\partial^2 c_1(x,t)}{\partial x_j^2} + f_1(x,t),$$
$$(x,t) \in \operatorname{int} \Omega_{1x} \times (0,t_{END}],$$

which satisfies the zero-initial condition

$$c_1(x,t)\big|_{t=0^+} = 0,\ x \in \Omega_{1x}$$

and zero-boundary conditions (11)-(15) of the auxiliary problem AP1.

The desired solution of the NAP1 is the function

$$c_1(x,t) = \int\limits_0^t d\tau \int\limits_{\Omega_{1y}} G_1(x,y,t-\tau) f_1(y,\tau)\,dy, \quad (88)$$

where the function $G_1(x,y,t-\tau)$ is the same Green function (85), in which instead of the argument t there is an argument $t-\tau$.

Now let us formulate a new auxiliary problem NAP2: it is required to find solutions to the inhomogeneous equation (which coincides with equation (1) at $i=2$)

$$\frac{\partial c_2(x,t)}{\partial t} = \sum_{j=1}^{3} D_{2j} \frac{\partial^2 c_2(x,t)}{\partial x_j^2} + f_2(x,t),$$
$$(x,t) \in \operatorname{int} \Omega_{2x} \times (0,t_{END}],$$

which satisfies the zero-initial condition

$$c_2(x,t)\big|_{t=0^+} = 0,\ x \in \Omega_{2x}$$

and to zero-boundary conditions (20)-(24) of the auxiliary problem AP2.

The desired solution of the NAP2 is the function

$$c_2(x,t) = \int\limits_0^t d\tau \int\limits_{\Omega_{2y}} G_2(x,y,t-\tau) f_2(y,\tau)\,dy, \quad (89)$$

where the function $G_2(x,y,t-\tau)$ is the same Green's function (87), in which instead of the argument t there is an argument $t-\tau$.

Thus, the following functions that contain the

corresponding right-hand sides of (84), (88) and (86), (89), give us a solution to problem (1)-(8) provided that $c_{j1}(x_2,x_3,t)\equiv 0$, $a_{j1}(x_2,x_3,t)\equiv 0$, $c_{j2}(x_1,x_3,t)\equiv 0$, $a_{j2}(x_1,x_3,t)\equiv 0$, $a_{j3}(x_1,x_2,t)\equiv 0$ for $\forall j=1,2$:

$$c_j(x,t)=\int\limits_{\Omega_{jy}} G_j(x,y,t)c_{j0}(y)\,dy + \int\limits_0^t d\tau \int\limits_{\Omega_{jy}} G_j(x,y,t-\tau)f_j(y,\tau)\,dy,\ \ j=1,2 \tag{90}$$

Therefore, to complete our study, it remains to find a solution to problem (1)-(8), provided that $f_j(x,y,t)\equiv 0$ and $c_{j0}(x)\equiv 0$ for $\forall j=1,2$, and then, add the solution found to the right side of the formula (90). To achieve this, it is necessary to use the multiplicative property of the Green functions as well as the properties of the Dirac delta function [14], [15]:

- function $c_1(x,t)$, which is defined as

$$\begin{aligned} c_1(x,t)&=\int_0^t d\tau\int_0^{L_2} dy_2\int_0^{H_1} G_1(x,y,t-\tau)\big|_{y_1=0}\frac{-c_{11}(y_2,y_3,\tau)}{D_{11}}dy_3\\ &+\int_0^t d\tau\int_0^{L_2} dy_2\int_0^{H_1} G_1(x,y,t-\tau)\big|_{y_1=L_1}a_{11}(y_2,y_3,\tau)\,dy_3\\ &+\int_0^t d\tau\int_0^{L_1} dy_1\int_0^{H_1} G_1(x,y,t-\tau)\big|_{y_2=0}\frac{-a_{11}(y_1,y_3,\tau)}{D_{12}}dy_3\\ &+\int_0^t d\tau\int_0^{L_1} dy_1\int_0^{H_1} G_1(x,y,t-\tau)\big|_{y_2=L_2}a_{12}(y_1,y_3,\tau)\,dy_3\\ &+\int_0^t d\tau\int_0^{L_1} dy_1\int_0^{L_2} G_1(x,y,t-\tau)\big|_{y_3=0}\frac{-a_{13}(y_1,y_2,\tau)}{D_{13}}dy_2, \end{aligned} \tag{91}$$

is a solution to problem (1)-(8) at $i=1$ under conditions $f_1(x,t)\equiv 0$, $c_{10}(x)\equiv 0$ (i.e. with homogeneous equation (1), zero initial condition (2), and non-zero boundary conditions (3)-(7));

- function $c_2(x,t)$, which is defined as

$$\begin{aligned} c_2(x,t)&=\int_0^t d\tau\int_0^{L_2} dy_2\int_{H_1}^{L_3} G_2(x,y,t-\tau)\big|_{y_1=0}\frac{-c_{21}(y_2,y_3,\tau)}{D_{21}}dy_3\\ &+\int_0^t d\tau\int_0^{L_2} dy_2\int_{H_1}^{L_3} G_2(x,y,t-\tau)\big|_{y_1=L_1}a_{21}(y_2,y_3,\tau)\,dy_3\\ &+\int_0^t d\tau\int_0^{L_1} dy_1\int_{H_1}^{L_3} G_2(x,y,t-\tau)\big|_{y_2=0}\frac{-a_{11}(y_1,y_3,\tau)}{D_{22}}dy_3\\ &+\int_0^t d\tau\int_0^{L_1} dy_1\int_{H_1}^{L_3} G_2(x,y,t-\tau)\big|_{y_2=L_2}a_{22}(y_1,y_3,\tau)\,dy_3\\ &+\int_0^t d\tau\int_0^{L_1} dy_1\int_0^{L_2} G_2(x,y,t-\tau)\big|_{y_3=L_3}\frac{-a_{23}(y_1,y_2,\tau)}{D_{23}}dy_2, \end{aligned} \tag{92}$$

is a solution to problem (1)-(8) at $i=2$ under conditions $f_2(x,t)\equiv 0$, $c_{20}(x)\equiv 0$ (i.e. with homogeneous equation (1), zero initial condition (2), and non-zero boundary conditions (3)-(7)).

Thus, the function $c_1(x,t)$, which is obtained by summing the right parts of formulas (90) (at $j=1$) and (91), describes the desired dynamics of the concentration of metal substances in the first layer of a two-layer peat block, the function $c_2(x,t)$, which is obtained by summing the right parts of formulas (90) (at $j=2$) and (92) describes the desired dynamics of the concentration of metal substances in the second layer of a two-layer peat block. The construction of the analytical solution of the problem (1)-(8) is entirely completed.

IV. Conclusion

In this paper, it is studied the problem of determining the dynamics of the concentration of metal substances in a two-layer anisotropic peat block. The work examines in detail the well-known variables separation method for constructing an analytical solution for a mathematical model of the studied problem. It is shown that the main difficulty is only the solution of interrelated auxiliary problems AP1 and AP2, which are obtained from the original mathematical model under the conditions that there are no sources in both layers, and that all boundary conditions are homogeneous

References

[1] E. Teirumnieka, I. Kangro, E. Teirumnieks, and H. Kalis, "The analytical solution of the 3D model with Robin's boundary conditions for 2 peat layers," The 10th International Scientific and Practical Conference "Environment. Technology. Resources", vol. III, June 18-20, 2015, Rezekne, Latvia, pp. 186-192. |Online|. Available: http://journals.ru.lv/index.php/ETR/article/view/618/714. |Accessed: March 15, 2017.

[2] I. Kangro, H. Kalis, A. Gedroics, E. Teirumnieka, and E. Teirumnieks, "On mathematical modelling of metals distributions in peat layers," Journal of Mathematical Modelling and Analysis, vol. 19, no. 4, pp. 568-588, 2014.

[3] E. Teirumnieka, E. Teirumnieks, I. Kangro, H. Kalis, and A. Gedroics, "The mathematical modelling of Ca and Fe distribution in peat layers," The 8th International Scientific and Practical Conference "Environment. Technology. Resources", vol. II, June 20-22, 2011, Rezekne, Latvia, pp. 40-47, 2011.

[4] H. Orru and M. Orru, "Sources and distribution of trace elements in Estonian peat," Journal of Global and Planetary Change, vol. 53, no. 4, pp. 249-258, 2006.

[5] P. A. Brown, S. A. Gill, and S. J. Allen, "Metal removal from wastewater using peat," Journal of Water Research, vol. 34, no. 16, pp. 3907-3916, 2000.

[6] A. N. Tikhonov and A. A. Samarsky, Equations of Mathematical Physics. New York: Dover Publications, 1990, xvi+765 p.

[7] A. N. Tikhonov and V. Ya. Arsenin, Solution of Ill-posed Problems. Washington: Winston & Sons, 1977, xiii+258 p.

[8] S. A. Andreyev and Sh. E. Guseynov, Regularizing algorithms for diagnosing: Applied to gas turbine engines in operation. Monograph. Saarbrücken: LAP Publishing, 2013, 116 p.

[9] M. A. Al-Gwaiz, Sturm-Liouville Theory and its Applications. London: Springer-Verlag, 2008, x+264 p.

[10] B. M. Levitan and I. S. Sargsyan, Sturm-Liouville and Dirac Operators. Dordrecht: Kluwer Academic Publications, 1991, xi+350 p.

[11] V. A. Steklov, Fundamental Problems of Mathematical Physics. Moscow: Science, 1983, 432 p.

[12] V. A. Il'in and E. G. Poznyak, Fundamentals of Mathematical Analysis, Part II. Moscow: Science, 1980, 448 p.

[13] A. A. Abrikosov, L. P. Gor'kov, and I. E. Dzyaloshinsky, Methods of Quantum Field Theory in Statistical Physics. Englewood Cliffs: Prentice-Hall, 1963, xv+352 p.

[14] L. S. Levitov and A. V. Shitov, Green's Functions: Problems with Solutions. Moscow: FizMatLit, 2002, 252 p.

[15] V. M. Babich, V. B. Kapilevich, S. G. Mikhlin, G. I. Natanson, P. M. Riz, L. N. Slobodetsky, and M. M. Smirnov, Linear Equation of Mathematical Physics. Moscow: Science, 1964, 368 p.

Environment. Technology. Resources. Rezekne, Latvia
Proceedings of the 12th International Scientific and Practical Conference. Volume III, 70-73

Development of a Parametric Program for Processing a Hyperbolic Surface on a Lathe Machine

Tsvetan Kaldashev
Technical university of Sofia
Sofia, Bulgaria
email: kaldashev.cvetan@abv.bg

***Abstract*—This paper discusses the development of a parametric (macro) program for processing a hyperbolic surface on a CNC lathe machine. Analytical dependences have been used to develop the macro program, as a result of which the CNC (computer numerical control) automatically calculates the coordinates of the intermediate points of the tool trajectory. The WHILE cycle operator is used to run the tool. Macro program functionality has been verified in a virtual environment using Vericut.**

Keywords—CNC, hyperbola, parametric (macro) program.

I. Introduction

Parametric programming, in addition to CNC commands and functions, also involves the use of variables, arithmetic actions, trigonometric and other functions, algorithmic structure building, system variables, CNC external linking and control devices "to" and "from" via interface variables [4]. This considerably expands the capabilities of CNC machines by allowing the development of parametric programs for processing of typical surfaces and the creation of a technological library, significantly simplified programs for approximating movements on curves other than a circle (and in general different from those in the basic language) , which have an analytical description and others. Variables, as in any algorithmic language, are used to store and subsequently use the values that are changing in the course of the program. Using variables makes the program more flexible than using ordinary subroutines. The variables are identified by their name, formed by the "hash mark" - #, followed by a number or a formula. The variables are user and system variables (Table 1). The first set of variables (user) can be used by the developer at random, and the second group (system) represents fixed-term variables, most commonly related to the CNC system job records. When constructing algorithmic structures, the GOTO unconditional transition operators, conditional IF operator and WHILE [1] cycle operator are used.

TABLE I.

Type of variables	Function	Designation
User variables	Local	#1 ÷ #33
	Common	#100 ÷ #149 #500 ÷ #509
System variables	with special purpose	#1000 ÷ #1015 #1100 ÷ #1115 #1000 ÷ #1015 #1032 ÷ #1132 #2xxx #3000 #3003 ÷ #3005 #4001 ÷ #4120 #5xxx

II. Parametric program for processing hyperbolic surface

The need of developing a parametric program for treating a hyperbolic surface results from the fact that rolling rolls are required to be processed for rolled periodically. In the process of employment, the hyperbolic surface is worn out and its profile deviates from the set, which affects the end product.

Hyperbola is a planar curve of second order and consists of two branches having two focuses (f1 and f2) and asymptotes [3] (Figure 1). The asymptotic intersection is a center of symmetry for the hyperbola. The axis of the hyperbola, called the main axis, coincides with the x-axis. Its vertices have coordinates (a, 0) and (-a, 0). Parametric equations of the hyperbolic branch corresponding to x> 0 are:

$$X = \frac{\alpha}{coc(\alpha)} \qquad (1)$$

$$Y = b - \tan(\alpha)$$

As a is the length of the main axis coinciding with the axis x (Figure 1), and e is the length of the minor axis coinciding with the y axis.

Print ISSN 1691-5402
Online ISSN 2256-070X
http://dx.doi.org/10.17770/etr2019vol3.4037

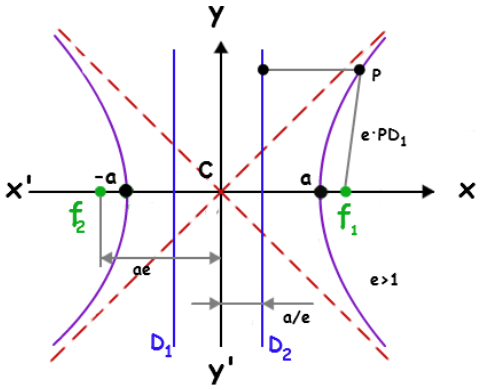

Fig. 1. Hyperbola [2]

The processing of a hyperbolic surface can be accomplished using a CAD / CAM system, where a 3D model is created in advance, from which the control programs are generated. In figure 2 is shown a window where the parametric equation of hyperbola is recorded, as a result of which the system automatically constructs the curve.

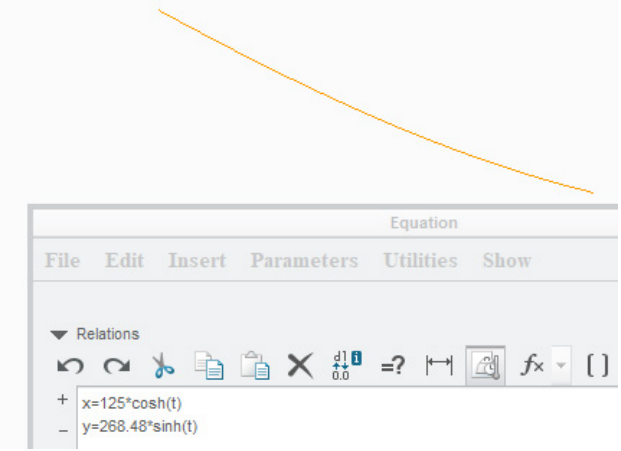

Fig. 2. Construction of hyperbola in parametric equation using the tool Equation

The PTC Creo CAD / CAM system uses the Equation tool. For curve construction is used parametric equation of hyperbola with hyperbolic functions.

After the construction of the hyperbolic curve using the Revolve tool, the CAD model of the workpiece is created. Figure 3 shows the final 3D model.

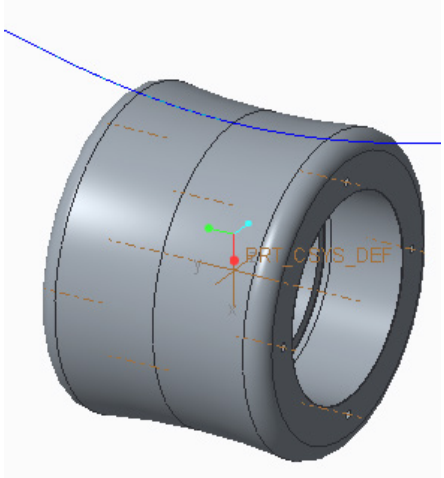

Fig. 3. 3D model of detail

The development of instrumentation transitions for the treatment of the hyperbolic surface is carried out in the CAM environment of PTC Creo. Figure 4 shows the clean instrumental transition for the workpiece. As already mentioned, the CNC does not have a second-order surface interpolator, which means that the curve should be approximated with straight lines.

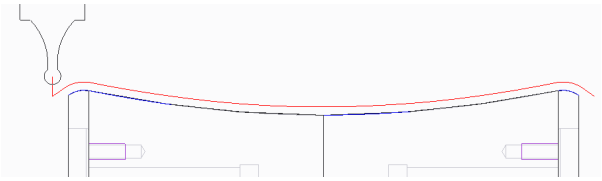

Fig. 4. Tool path

Accuracy can be controlled with the Tolerance parameter so that the hyperbolic surface of the workpiece is processed with the least possible deviation from the curve. This means that the smaller the value set in the Tolerance parameter, the deviation from the curve will be less, but on the other hand it will affect the volume of the control program - it will increase.

In order to avoid the aforementioned processing problems, a good solution is to develop a parametric program, thus the CNC will automatically calculate the coordinates of the workpiece contour with precision to the CNC input increment. The program has the algorithm shown in figure 5.

As the input data, the main axle length coinciding the X axis (#100), the length of the minor axis (#101), in the case coinciding with the Z axis, the increment of the angle reduction (#102), the initial (#103) and the final (#104) angles associated with the hyperbola treatment and the overall length of the workpiece (# 108).

In order to be able to process the workpiece it is necessary to have the working coordinate system positioned symmetrically in relation to its length (Figure 6). Therefore, two portions of the hyperbola are conventionally indicated in figure 6 with first and second stretches. Each of the plots is L / 2 long.

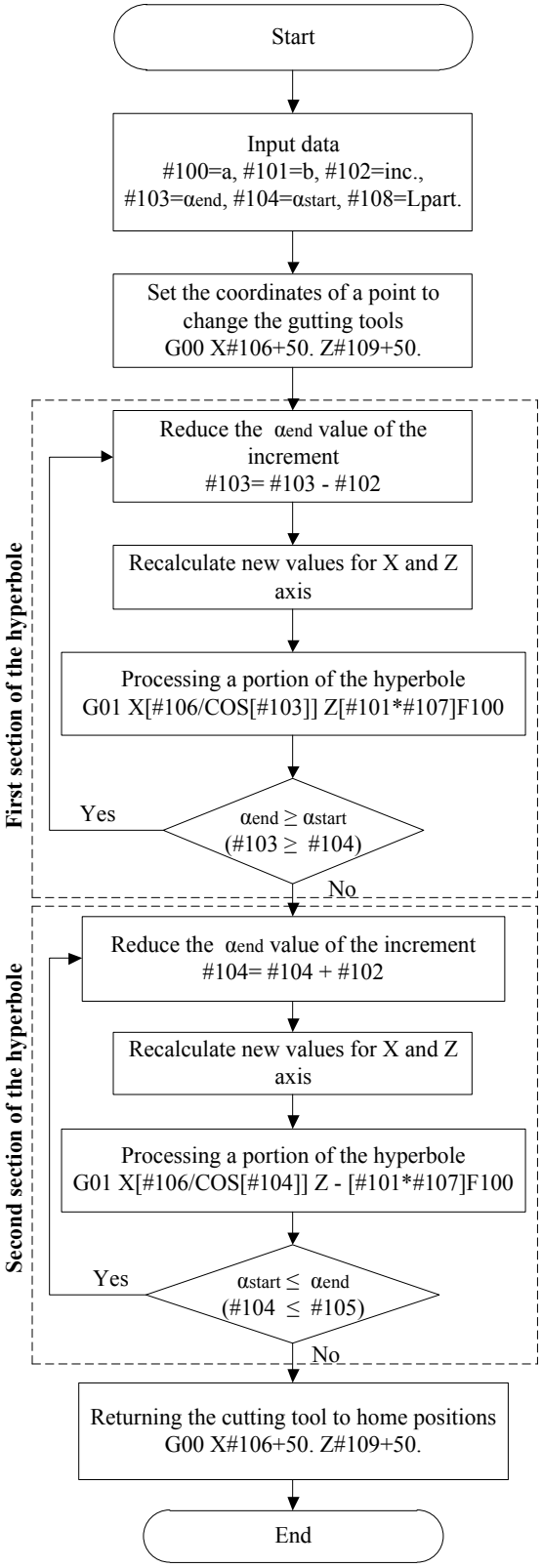

Fig. 5. Block diagram of the parametric (macro) program

Parametric equation (1) of the hyperbola is used in developing the parametric program. Two operators are used for the WHILE cycle, the first being used to handle the first section of the hyperbola and the second for the second section of the hyperbola.

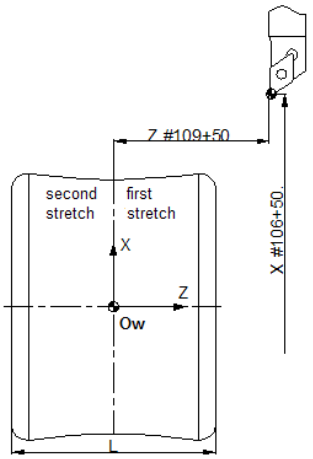

Fig. 6. Annotation of some variables used in the parametric program

The parameter program has the following structure:

```
#100=100. (Stojnost za A=)
#101=202.4 (Stojnost za B=)
#108=196. (Daljina na detaila)
#109=#108/2
#102=0.2 (Inkrement)
#103=40. (Kraen agal na krivata)
#104=0.   (Nachalen agal na krivata)
#105=#103
#106=#100*2
#107=SIN[#103]/COS[#103]  (TAN)
T0606
G55 X#106+50. Z#109+50.
S500 M03
G00 X[#106/COS[#103]] Z[#101*#107]
WHILE[#103GT#104]DO1
#107=SIN[#103]/COS[#103]  (TAN)
G01 X[#106/COS[#103]] Z[#101*#107]
F0.15
#103=#103-#102
END1
WHILE[#104LT#105]DO2
#107=SIN[#104]/COS[#104]  (TAN)
G01 X[#106/COS[#104]] Z-[#101*#107]
F0.15
#104=#104+#102
END2
G00 Z150.
G00 X[#106/COS[#103]] Z[#101*#107]
G00 Z150.
M30
```

The parametric program was verified in a virtual environment using Vericut. In figure 7 is a screen of the simulation with the developed macro program.

In order to assess whether it is correct, if there is a deviation of the surface from the theoretical examination, the AutoDiff tool is used. It is used to automatically detect the differences between the resulting model as a result of the simulation and the one generated by the control programs. As a result of the analysis no difference was found (Figure 8 - No Differences) from where it can be concluded that the macro program is efficient.

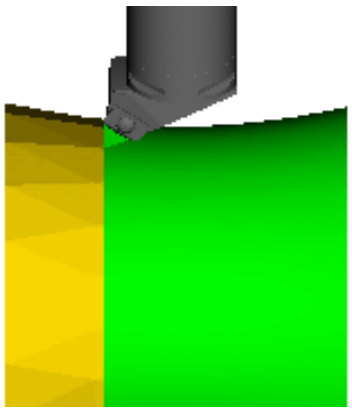

Fig. 7. Simulation in Vericut of the parametric program developed

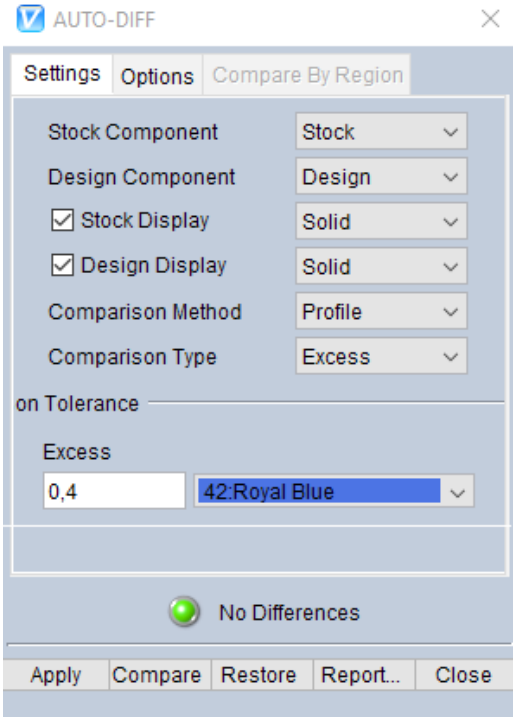

Fig. 8. Analysis with the AutoDiff tool

III. Conclusion

The parametric program developed has been verified in a Vericut virtual environment. An analysis of the Auto-Diff tool has been made from which it can be concluded that the program is work efficient.

References

[1] Ben Groves, Macro B programming manual

[2] www.tutorvista.com, visited on 30.07.2018 г.

[3] www.wikipedia.org, visited on 30.07.2018 г.

[4] Hadjiiski P., Programming of CNC machine tools, TU-Sofia, 2010 г., ISBN 978-954-438-865-2

Environment. Technology. Resources. Rezekne, Latvia
Proceedings of the 12th International Scientific and Practical Conference. Volume III, 74-76

Developing lathes postprocessor generating cycles of processing grooves

Tsvetan Kaldashev
Technical university of Sofia
Sofia, Bulgaria
email: kaldashev.cvetan@abv.bg

***Abstract*—This article explores the possibility of developing a post-processor generating circles for radial and facsimile grooves in PTC Creo environments using a generalized postprocessor G-POST and a specialized language FIL (Factory Interface Language). The proposed development approach can also be applied to post-processor generating cycles for rough and fine turning (G71, G72 and G70).**

Keywords— CNC, postprocessor, canned cycle

Introduction

After the development of instrumental transitions to process the workpieces using CAM systems, it is necessary to generate a CN program for a particular machine and control system. For this purpose, it is necessary to perform post-processing, i. e. to transform the CL Data file [4] into the NC program. Here is the CAD/CAM system PTC Creo and the generalized postprocessor G-POST. It is based on an existing postprocessor that creates another new postprocessor [3] for the particular machine and the control system. G-Post offers the opportunity to create post-processors for different types of machines: lathes, milling machines, turning centers, wire EDMs, etc. G-POST uses the information from CL Data File, created by PTC Creo, which is the only input for it. In cases where the created postprocessor does not have the necessary functions or cycles to manage the particular machine using the FIL (Factory Interface Language), they can be created and described with the tools and commands in the language.

As is known in CNC lathe machines are used repetitive cycles. They shorten the production time and the length of the NC program, and that the process can be managed directly by the CNC without the need to regenerate the NC program. The G74 cycle is used to process wide front groove with a narrower tool and holes whose axes coincide with the axis of rotation of the workpiece. Its scheme of operation is shown in Fig. 1. Cycle G74 has the following format [1]:

G74 R(e);

G74 X(U) Z(W) P(Δi) Q(Δk) R(Δd) F(f),

where e - retraction amount; X - X-coordinate of point B; U - distance between point A and B (incremental); Z - Z-coordinate of point C; W-distance between point A and pint C; Δi - distance in the X-axis direction; Δk - distance in the Z-axis direction; Δd - relief amount of the tool at the cutting bottom; f – federate.

If the values in addresses X (U) and P are equal to 0, then this cycle is used for drilling.

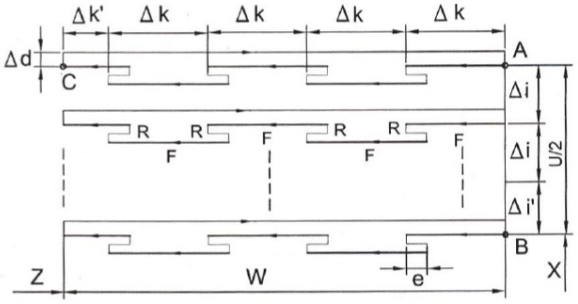

Fig. 1. Working scheme of cycle G74

Similar to Cycle G74 is Cycle G75, which is used to handle broad radial grooves with a narrower tool. The schema and cycle format are similar to the G74.

I. Development of the postprocessor generating cycles G74 and G75

When developing postprocessors generating cycles G74 and G75 the following stages are [5]:

1. Create a Manufacturing User Define Feature (MUDF) that contains all of the technological information such as distance in the X-axis direction (Δi), distance in the Z-axis direction (Δk), federate (F), creating a tool path;

2. Describe the cycle in G-POST using the FIL language.

Manufacturing User Define Feature has the task of retrieving and writing the values necessary for defining cycles G74 and G75. To load the relevant parameters in the Tool Motions window, the cycle definition is written as a CL command:

For Cycle G74

CYCLE/FACE,RETRACT,&PULLOUT_DIST:FID_224,XAXIS,&PECK_DEPTH:FID_224,ZAXIS,&STEP_OVER,FEED,&CUT_FEED:FID_224

For Cycle G75

CYCLE/RADIUS,RETRACT,&PULLOUT_DIST:FID_216,XAXIS,&PECK_DEPTH:FID_216,ZAXIS,&STEP_OVER,FEED,&CUT_FEED:FID_216

The meaning of the parameters in the CL command for the two cycles are as follows:

PULLOUT_DIST - retraction of the tool from the surface

Print ISSN 1691-5402
Online ISSN 2256-070X
http://dx.doi.org/10.17770/etr2019vol3.4186

being processed;
PECK_DEPTH - depth of workflow cutout for chip breaking;
These parameters are standard for the PTC Creo system and are used in the development of instrument transitions.
The transverse displacement of the tool both on the X axis and on the Z axis depends on the width of the plate and the nose radius. Different widths are used for different grooves sizes, meaning that the transverse displacement will change. For this purpose, this displacement is calculated from the tool width and the nose radius by dependence (1):

step_over=0.6(tool_width-2*nose_radius)* (1)

This dependency is recorded in the Relations window where the tool_width and nose_radius parameter values are internal parameters for the PTC Creo system and it automatically retrieves them from the selected tool which is doing the proccesing.

After recording the cycles as a CL command, a MUDF is created where, with its help, the instrumental transitions are created more quickly, enhances the productivity of work with CAM system, thus not passing through all stages of creating a technological operation (fig. 2).

In order to create tool transitions for grooves processing, only the workpiece, the machined geometry, the machine, the start and the end points (for automatic tool change) must be defined in advance. These several steps are sufficient to insert a MUDF that automatically creates the instrument transition and loads the cutting mode parameters. In this case, MUDF is used as a template that carries all the technological information, but the user can set (change) different cutting tools and modes than those in the template.

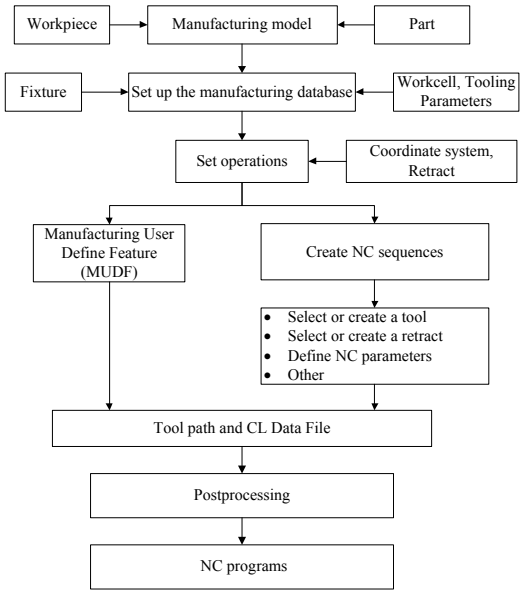

Fig. 2. Block diagrame for creating a lathe operation using MUDF

For postprocessor development, G-POST and FIL are used to describe the cycles pre-recorded as a CL command. To process CL records CYCLE/FACE ..., CYCLE/RADIUS.... the following FIL record is used:

```
CIMFIL/ON,CYCLE
CTYPE=POSTF(7,4)
CASE/CTYPE
WHEN/ICODEF(FACE)
G74=1
RET=POSTF(7,6)
XDEPTH=POSTF(7,8)
ZSTEP=POSTF(7,10)
FED=POSTF(7,12)
XX=POSTF(26,5,5,1)
WHEN/ICODEF(RADIUS)
G75=1
RET=POSTF(7,6)
XDEPTH=POSTF(7,8)
ZSTEP=POSTF(7,10)
FED=POSTF(7,12)
XX=POSTF(26,5,5,1)
WHEN/OTHERS
XX=POSTF(26,5,5,0)
ENDCAS
XX=POSTF(13)
CIMFIL/OFF
```

This FIL record is used to take the values of the CL Data file for the respective cycle (G74 or G75) and set them to RET (retract distance), XDEPTH (peck_depth), ZSTEP (step_over), FED (cut_feed). After assigning the variables values with command XX = POSTF (26,5,5,1) goes directly to a GOTO motion record. This command works like IF - THEN - ELSE or CASE - WHEN operators to find a specific subtype [2]. The GOTO movement record has saved the G74 and G75 output format. The motion track has the following structure:

```
CIMFIL/ON,GOTO
XX=POSTF(13)
IF(G74.EQ.1) THEN
G74=0
CURX=POSTF(7,6)*2
CURZ=POSTF(7,8)
XX=POSTF(14)
XX=POSTF(14)
LASTZ=POSTF(7,8)
LASTX=POSTF(7,6)*2
XX=POSTF(25,1)
DO/ENDO2,ILOOP=1,10
ILOOP=1 $$ infinite loop
DMY=POSTF(14) $$ Get next CL (TAPERD)
CLC=POSTF(7,2)  $$ $FCLASS, 2d
parameter of record
SCL=POSTF(7,3) $$ $FSUBCL, 3rd
parameter of record
IF(CLC.EQ.2000.AND.SCL.
EQ.(ICODEF(CYCLE))) THEN
MOD=POSTF(7,5)
ILOOP=21 $$ Exit the loop
ELSE
XX=POSTF(13) $$ Process
ENDIF
ENDO2) CONTIN $$ End of DO loop
XX=POSTF(25,0)
IF(MOD.EQ.ICODEF(OFF))THEN
```

```
POSTN/OUT,G,74,R,RET
POSTN/T,G,74,X,LASTX,Z,LASTZ,P,XDEPTH
,Q,ZSTEP,F,FED
ENDIF
ENDIF
IF(G75.EQ.1)THEN
G75=0
CURX=POSTF(7,6)*2
CURZ=POSTF(7,8)
.....
.....
POSTN/OUT,G,75,R,RET
POSTN/T,G,75,X,LASTX,Z,LASTZ,P,XDEPTH
,Q,ZSTEP,F,FED
ENDIF
CIMFIL/OFF
```

In the GOTO record, an initial check is made whether a G74 cycle command has been received and if the IF (G74.EQ.1) THEN condition is met, the CURX, CURZ, LASTZ, and LASTX variables are assigned respectively for start and end coordinates of the X and Z axis path. With the DO / Loop function, the remaining CL records are processed until a CYCLE record is found, then the MOD variable is assigned the cycle state value. An IF statement verifies whether the end of the cycle is reached and whether the condition is filled with a record of the type POSTN/OUT,G,74,R,RET

P O S T N / O U T , G , 7 4 , X , L A S T X , Z,LASTZ,P,XDEPTH,Q,ZSTEP,F,FED

a cycle G74 is generated. Similarly, a command G75 is generated.

After the postprocessor has been developed, a control program for the workpiece shown in Fig. 3. In Fig. 4 shows the program where it was generated for a 3mm wide tool.

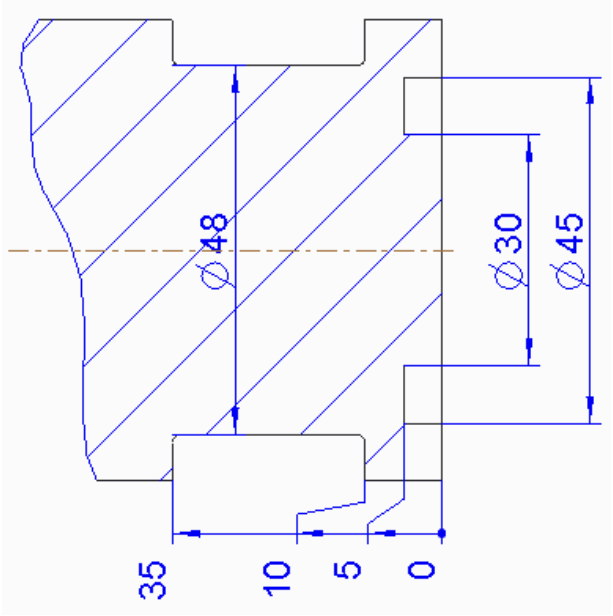

Fig. 3. Part

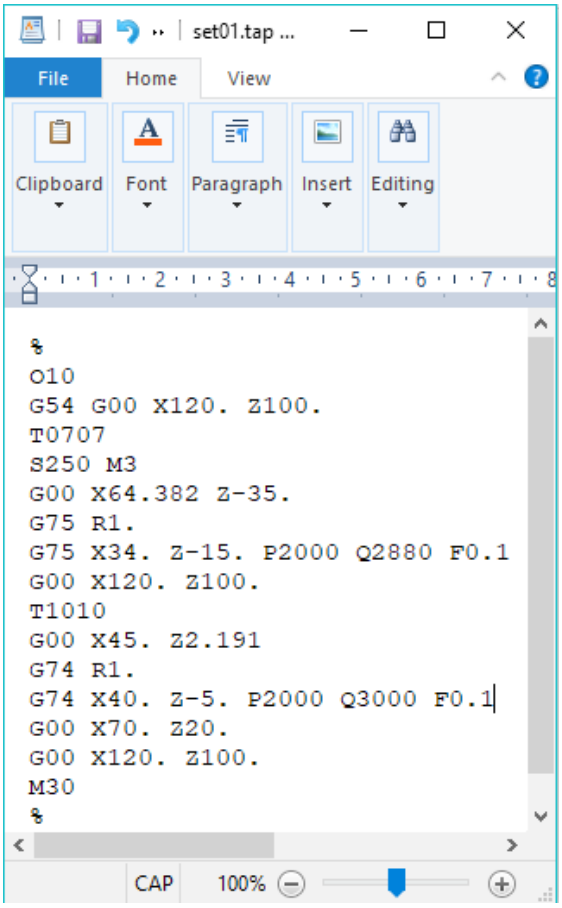

Fig. 4. Generated NC program

II. Conclusion

1. Developed and tested experimentally postprocessor generating cycles for processing radial and front grooves, which has its practical advantages;

2. This approach to the development cycles for lathes can be applied to generate control programs using cycles G70 and G71, G76.

III. References

[1] Doosan Puma series, Programming manual, MXTTPGE68;

[2] FIL Help V6.6;

[3] HJ. Patthi Bin Hussain, Zhu Yuesheng, Murthy Rallapalli and J.Mahmud, Development of Post Processor for Dual-Spindle Turning Center, Applied Mechanics and Materials, 2014, Vols. 541-542, pp 804-807, ISSN 1662-7482;

[4] Čuboňová, N., Postprocessing of cl data in CAD/CAM system edgecam using the constructor of postprocessors, Manufacturing Technology, Vol. 13, Iss. 2, 2013, pp 158-164, ISSN 1213-2489;

[5] Hadjiiski, P. I., Kaldashev, T. P., Creation of lether postprocessor generate repeated cycle in an environment of Pro/Engineer, International scientific conference-FIT 2012, pp. 245-249, 2012, Bulgaria, ISBN 978-954-438-994-9.

Method for Measuring Error Establishment in 5-Axis Milling Machines with a Touch Probe

Tsvetan Kaldashev
Technical university of Sofia
Sofia, Bulgaria
email: kaldashev.cvetan@abv.bg

Abstract*—The present paper proposes a method for measuring and compensating for error establishment. The measurement is done with a touch probe and the measuring program is a macro program. A mathematical model was developed to experimentally determine the error of non-alignment of the axis of rotation of the workpiece with the physical axis of rotation of mass C. A virtual approach to compensate for the error of establishment by using a postprocessor for the particular machine was also proposed.

***Keywords*— milling machine, measuring, touch probe, CNC.**

I. Introduction

The use of touch probes greatly expands the capabilities of CNC machines. Their use reduces machine setup time, which increases accuracy. These measurement processes are fully automated. The measurement method consists in the fact that measurement is actually carried out by the CNC machine tracking system, and the measuring head only perceives the controllable magnitude. Impact on measurement accuracy is the precision of the machine's measuring system, scattering when the touch probe is working and its moving speed at the touch.

The leading manufacturers of CNC Fanuc, Sinumerik, Heidenhain and others. Offer dialogue cycles to measure and compensate for the set-up error. In Fanuc, command G54.4 is available [3].

II. Method for measuring error establishment

As an example, be considered a rotary die for sanitary absorbents (figure 1). Typical of them is that they have a higher productivity than those with reciprocating movement. The production of these tools is carried out on 4 and 5 axis CNC milling machines [5]

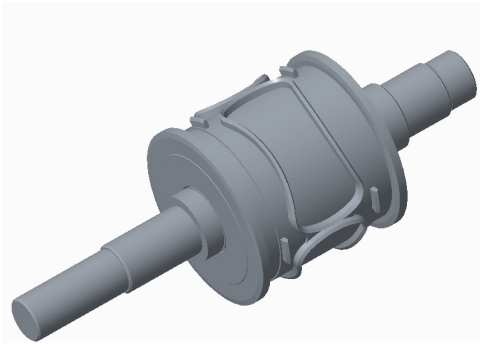

Fig. 1. Rotary die

After milling, the knives are hardened and the cutting contour is grinded with high-speed spindles with abrasive tapered head, mostly made of ultra-hard materials. The ultimate requirement is to achieve a long life of the contour. In the process of operation, the tool is worn out, which necessitates restoration of its cutting ability. This is done by grinding the outer cylindrical surface of a grinding machine where the setting is carried out between centers and the grinding on the side surface of the cutting contour is carried out on a machining center with a bearing on the bearing in a chuck. As a result of the change of the technological base, set-up errors are obtained, which must be compensated in order to obtain a uniform width of the cutting track. Significant influence on the precision of machining is due to the radial beating errors and the failure of the axis of the workpiece with the axis of rotation of the C axis. To measure these errors, a method is used to measure the touch probe in mass position A = 90° (figure 2). The surfaces to which the radial beating is measured are the two supporting boards 1 and 2 of the workpiece. Measurement is performed through an angular pitch of 10° on the C axis when it was at the point of the machine.

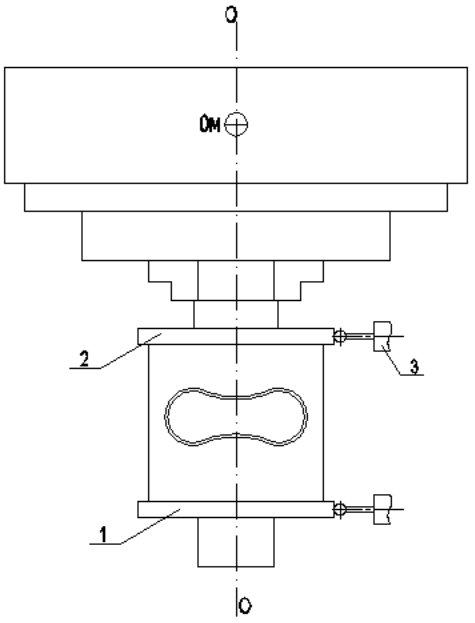

Fig. 2. *Measuring radial beating with touch probe*

Print ISSN 1691-5402
Online ISSN 2256-070X
http://dx.doi.org/10.17770/etr2019vol3.4190

Measuring motion is on axis Z. The program on which the measurement is performed is a macro program. It is organized so that the minimum value of radial beating ρmin is found within 180°. The instruction in DNC mode displays the measured minimum value and the angle Cρmin, which is measured relative to the machine's point of reference. For the determination of the maximum beating ρmax, the workpiece is rotated at 180° to the minimum beating angle, where the value is determined by measurement. Analogously, the values of ρmin, Cρmin, ρmax and ρmax for the second section are determined. The algorithm for the measurement is shown in figure 3. At the start, there is a check for calibration of the touch probe. The calibration is done with another macro program, where a bearing is pressed into the machine body as a reference. In the table 1 shows the measured values for one full part of the workpiece.

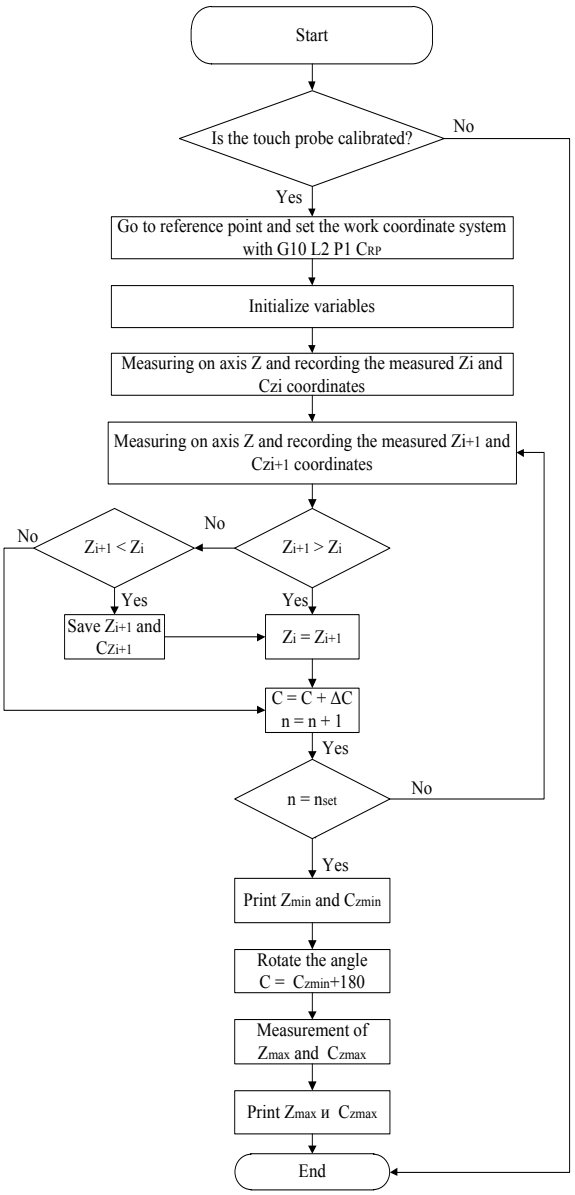

Fig. 3. *Algorithm measuring program*

In figure 4 shows the distribution of the radial beating of the workpiece relative to the axis of rotation of C axis.

TABLE I.

Angle of rotation on axis C [°]	Measured value along the Z axis [mm]	Angle of rotation on axis C [°]	Measured value along the Z axis [mm]	Angle of rotation on axis C [°]	Measured value along the Z axis [mm]
10	79.838	130	79.681	250	79.8
20	79.83	140	79.683	260	79.814
30	79.815	150	79.683	270	79.826
40	79.795	160	79.683	280	79.846
50	79.783	170	79.69	290	79.853
60	79.765	180	79.696	300	79.858
70	79.749	190	79.707	310	79.87
80	79.734	200	79.725	320	79.873
90	79.72	210	79.735	330	79.871
100	79.705	220	79.752	340	79.87
110	79.695	230	79.768	350	79.858
120	79.685	240	79.789		

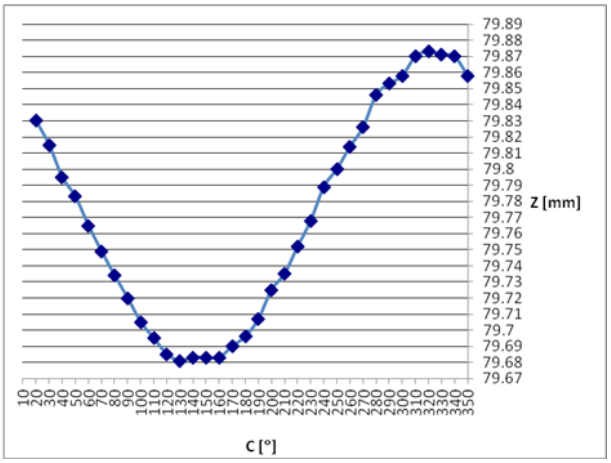

Fig. 4. *The distribution of the radial beating of the workpiece relative to the axis of rotation of the C axis*

Measurement was performed at a feed rate of 30 mm / min, where the scattering of the result remained constant [4], [2].

After measuring the error [1] it is possible to compensate it. The detection error can be compensated by using the postprocessor for the particular machine being machined or in a manufacturing model to create a coordinate system rotated relative to the machine with rotation equivalents equivalent to the error. To calculate the error of non-alignment of the axis of the workpiece with the axis of rotation C axis, Microsoft Excel is used where the mathematical model of the error is introduced. Thus, after measurement with a touch probe, the minimum and maximum beating values and the angle at which they are measured are introduced into the mathematical model. On the basis of the analytical dependencies in the mathematical model the matrix giving the relation between the axis of rotation of the workpiece and the axis of rotation of the mass C is obtained. The values obtained are introduced into the matrix of generalized post-processor G-POST (figure 5).

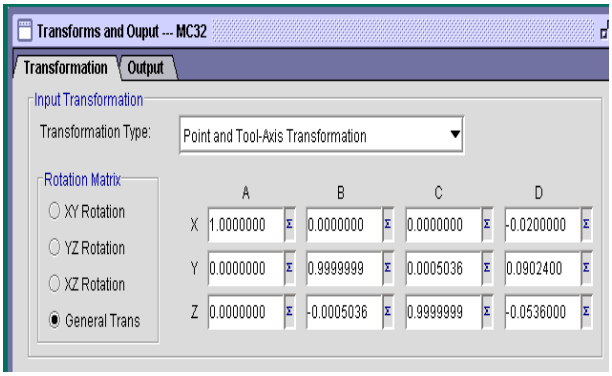

Fig. 5. *Transforms and Output page of the generalized postprocessor G-POST with input compensation values*

With the proposed method of measuring and compensating for the error of establishment, the grinding of the cutting edge of a rotating knife in a virtual environment (Vericut) was performed. The values with which the test was made are actually measured on the measuring headpiece according to the algorithm shown in figure 3. In table 2 shows the measured radial beating values for the supporting board 1 and the supporting board 2 (figure 2) and the angle at which they are measured relative to a reference point of the machine.

TABLE II.

	Supporting board 1	**Supporting board 2**
	Measured values, mm	
ρmin	0. 01	0.02
Cρmin	170	140
ρmax	0.16	0.03
Cρmax	350	320

After processing the workpiece in Vericut, the deviation (marked with a yellow color as a narrow strip) is seen as a result of the set-up error (figure 6). From figure 6 it is seen that as a result of the error, sections of the cutting contour are obtained where it is highly sharpened and sections in which it has a certain width. This is unacceptable in terms of the working ability of the instrument above certain limits.

The set-up error value is entered into the G-POST generalized postprocessor matrix, and then a control program is generated with the tool trajectory equidistant to the error. With the generated control programs, a "grinding" was performed on the side surfaces of the cutting track in Vericut's environment. In fig. 7 shows the result after processing the workpiece with a compensated set-up error with the postprocessor. From Fig. 7 it is seen that a relatively uniform width of the cutting track is obtained.

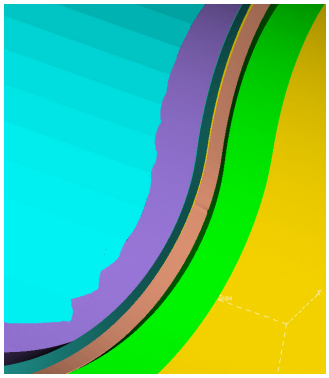

Fig. 6. *Deviation of the width of the cutting path due to error of establishment of the workpiece*

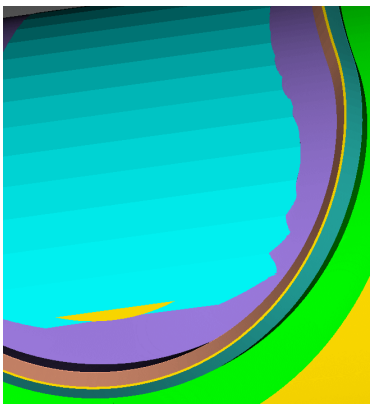

Fig. 7. *The result of compensating the error in establishment with a postprocessor*

After error compensation and grinding on the side surfaces of the cutting contour, a two-section measurement is performed with the X-Caliper tool to determine the width of the cutting track. The results of the measurements are shown in table 3, and the sections in which the measurement in figure 8.

TABLE III.

Section	**Point**	**Measure value, mm**
I - I	1	0,279
	2	0,28
II - II	3	0,25
	4	0,13

The measured value at point 4 shows a difference due to incorrect setting of the rotation angle relative to the machine reference point. The task is solved by recalculating the angle C on the axis, which is set as offset in the offset of the operating coordinate systems relative to the machine's pivot. The study, which is shown, refers to the most unfavorable case - a curvilinear contour located on a cylindrical surface, where on these measured values are accumulated some inconsistencies with the angle at the tip of the cone tool.

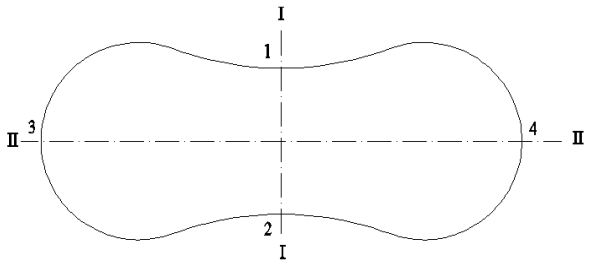

Fig. 8. *Determination of the size b in different sections of the cutting contour*

III. Conclusion

1. An approach is proposed to measure the detection error in 5-axis machines using the touch probe;
2. An approach is proposed to conpensate the postprocessor error for the particular machine;
3. The set-up error compensating approach has been verified in a virtual environment (Vericut) where it is determined that the deviation in the width of the cutting track falls within the accepted limits.

References

[1] Angel Lengerov, Galina Nikolcheva, Julieta Kaleycheva, Lyubomir Lazov, Computer control the accuracy of the parts processed on cnc machine tools based on statistical process control, ,Vide. Tehnologija. Resursi- Environment, Technology, Resources 3, pp.179-182, 2017;

[2] Dimitrov D., Karachorova V., Nenov G., Research the possibilities of the method for determining the tolerances in geometric precision of machining center, Machines Technologies Materials, Issue 3, 2017, pp. 118-120, ISSN Print 1313-0226;

[3] Fanuc Series 30i/31i/32i-Model B, Operator Manuals for machining center system;

[4] Graham T. Smith, CNC machining technology 3, Part programming technique, Springer Verlag, London, 1993, ISBN 978-1-4471-17-48-3;

[5] Hadzhiyski P., Knives for rotary dies with variable geometry, Journal "Engineering and automations problems", 2011, p. 131-135, ISSN 0234-6206;

Study of Error Establishment in Milling Machines with 5 Axes

Tsvetan Kaldashev
Technical university of Sofia
Sofia, Bulgaria
email: kaldashev.cvetan@abv.bg

Petar Hadjiiski
Technical university of Sofia
Sofia, Bulgaria
email: phad@tu-sofia.bg

***Abstract*—This report examines the accuracy of rotary die processing on a 5 axes machine and a special bolt-disk system. Faults that affect the accuracy and their measurement and reduction within acceptable limits are analyzed. As a result of the measurement, a virtual model of the radial beating of the workpiece relative to the actual axis of rotation of the machine was developed.**

Keywords— CNC, milling machine, error detection, 5 axis.

I. Introduction

When machining rotationally symmetrical details on 4 and 5 axis milling machines, setting is most often done in a chuck. As a result, there are set-up errors related to the radial and axial beating of the machine masses. These errors, as well as machine positioning errors, have a significant effect on the accuracy of processing [1], [2], [5]. With modern CNCs, different commands are available, with which some of these errors can be compensated. In the Fanuc CNC, the G54.2 [3] command is used, which sets the position of the workpiece set on a circular axis as a support compensation for the tool. Thus, when rotating the circular axis, the CNC automatically receives the current compensation of the device based on the angular displacement of the mass and creates a suitable coordinate system of the workpiece (figure1). Once the support compensation is established, the coordinate system of the workpiece is created dynamically regardless of the position of the rotary mass. The new position of the coordinate system of the workpiece is obtained by adding the fitting compensation to the initial set offset by a reference point of the machine.

For older CNCs, the offset of the set-up error is performed using devices where the radial beating error is measured with an indicator clock.

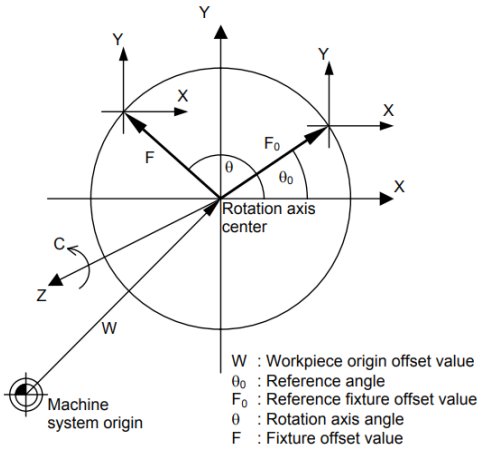

Fig. 1. Rotary table dynamic fixture offset

II. Study of Error Establishment with Fixture

The workpiece alignment device consists a disk with a bolt system 1 and 2 (Figure 2) located on the flange of the chuck 3 at a central angle of 90 degree. The bolts 1 are used to secure the chuck to the rotating mass C. Bolts 2 are in contact with the mass of the machine, thereby pushing the chuck (rotating it around a point located at 180 degree relative to the bolt used for adjustment). In this way, the axis of the workpiece is displaced relatively to the axis of rotation of the mass C, while the radial beating becomes as small as possible.

As an example will be discussed detail - knife for a rotary die for a sanitary absorbents. In these details, the width of the cutting blade (Figure 3), which is finally obtained by grinding the side surfaces 1 and 2 of the cutting contour [4], is of great importance. The mounting is made on the bearing and the front face of the shaft (Figure 4).

Print ISSN 1691-5402
Online ISSN 2256-070X
http://dx.doi.org/10.17770/etr2019vol3.4187

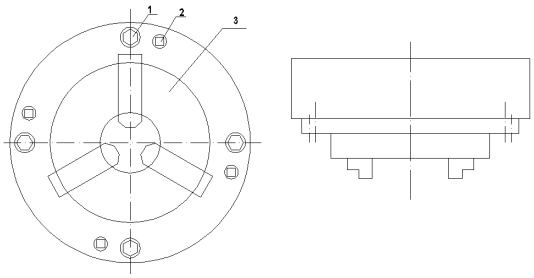

Fig. 2. Workpiece alignment tool

As a result, a base error arises due to the in organized base shifting. It appears because before the machine detail is found, it is grinded between the centers of a grinding machine on the cylindrical surface “A” on which lies the cutting contour “B”. Once a piece is found in the chuck of the machine, an error occurs due to the non-alignment of the axis of the workpiece 1-1 with the axis of rotation of the mass C. On the other hand, there is a mass positioning error A -.

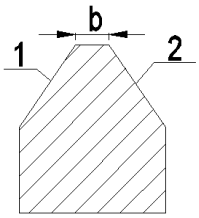

Fig. 3. Cutting width b

As a result of the beating, the axis of the workpiece 1-1 makes a precession around the axis of the machine O-O. As a result, the radial and frontal rolling of the cylindrical surface “A”, on which is located the cutting contour “B” having a trapezoidal section (Figure 3), has a significant impact on the precision of processing of the workpiece.

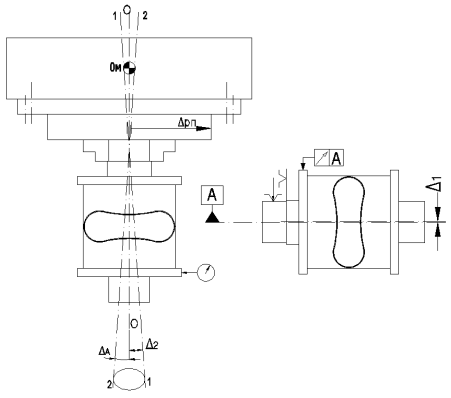

Fig. 4. Errors in establishing detail rotary die

The cutting capability of the contour sections is determined by the width b of the cutting track, and it must change for the time between two resharpenings in the bmin to bmax range. The maximum permissible width so that cuts are obtained is bmax and bmin is the minimum width allowed so that no breakage occurs and a resource is provided between two resharpenings. In order to reduce the impact of the settlement error caused by a shifting in the bases, it is necessary to work on a method to compensate it for a full turnover. After setting the machine detail, the radial beating is measured with an indicator clock set in the spindle of the machine. Measurement is carried out at A axis position of 90° (Figure 5).

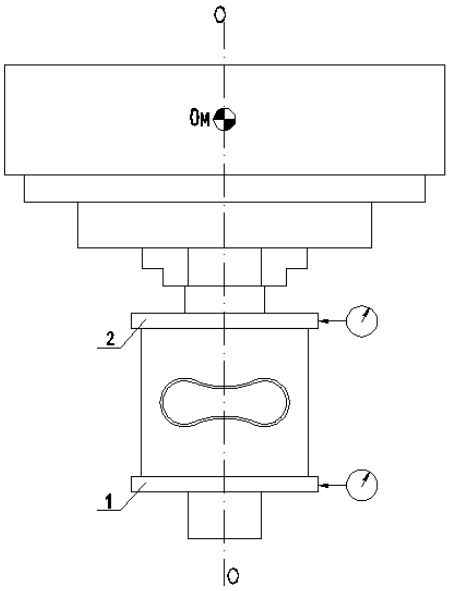

Fig. 5. *Measuring radial beating with an indicator*

For the surfaces to which the radial beating is taken, the two supporting boards 1 and 2 are selected. Measurement was performed at 30° C on axis C. In Table 1 shows the measurement results.

TABLE I.

Angle of rotation on axis C, [°]	Radial beating, mm	
	Supporting board 1	*Supporting board 2*
0	0	-0.06
30	0.05	-0.08
60	0.1	-0.1
90	0.13	-0.09
120	0.12	-0.08
150	0.09	-0.06
180	0.04	0.03
210	-0.02	0.05
240	-0.06	0.07
270	-0.08	0.07
300	-0.07	0.06
330	-0.04	0.03
360	0	-0.06

With the measured radial beating values, a virtual error model in the PTC Creo CAD system has been developed to determine how the axis of the work surface is displaced relative to the real axis of rotation of axis C (Figure 6).

The center of the supporting board 1 is constructed by passing a straight line connecting two points corresponding to the maximum and minimum radial beating. The center point is the center of the circle with a radius equal to the radius of the tool (supporting boards).

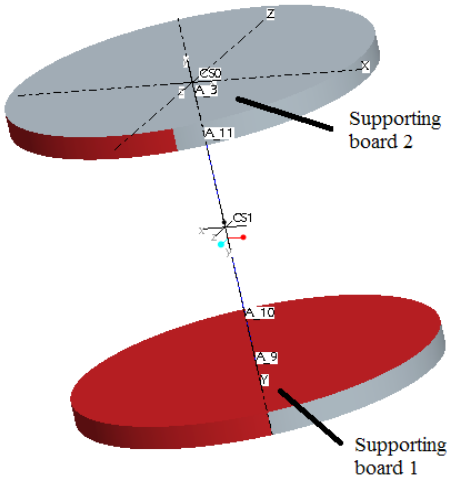

Fig. 6. Beating the workpiece to the real axis of the machine

Similarly, the center of the circle for the supporting board 2 is built. The red color of the supporting board shows the actual C axis position on the machine, and the gray shows the beating of the workpiece relative to the same axis. Once the two centers have been built, a line is drawn to connect them. The angle between the two axes, which is 0.02º (0° 1' 12"), was measured with the toolbox. In Figure 7 shows the displacement of the workpiece axis due to the beating for the supporting boards 1 and 2.

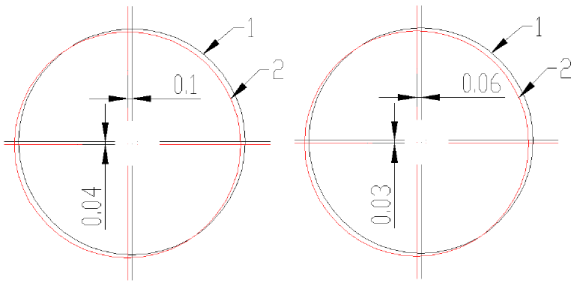

Fig. 7. Displacement of the workpiece axis due to the beating for the supporting boards 1 and 2

After the tool is centered (radial bevel reduction) with the chuck and flange assembly with the bolt system, the radial bevel is reduced to 0.06 mm for the supporting board 1 and 0.04 mm for the supporting board 2. After repositioning the tool on the side surface on an instrumental microscope, the dimension b of the cutting track for the three cutting edges located at a central angle of 120 ° in the sections shown in Figure 8.

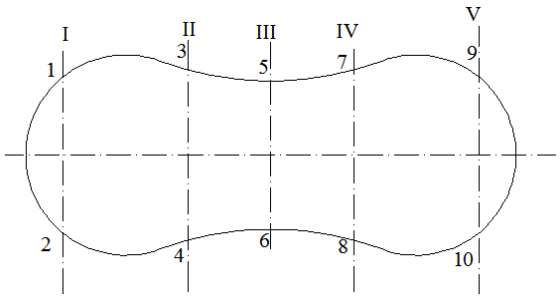

Fig. 8. *Determination of the size b in different sections of the cutting contour*

Table 2 gives the measured values of the b dimension of the cutting track.

TABLE II.

№	Section	I		II		III		IV		V	
	Point	*1*	*2*	*3*	*4*	*5*	*6*	*7*	*8*	*9*	*10*
1		0.4	0.3	0.35	0.25	0.3	0.3	0.3	0.3	0.3	0.45
2		0.3	0.3	0.25	0.2	0.3	0.2	0.4	0.2	0.35	0.3
3		0.4	0.4	0.3	0.3	0.3	0.3	0.3	0.3	0.4	0.3

III. Conclusion

From Table 2, it can be seen that at 0.06 mm for supporting board 1 and 0.04 mm for supporting board 2, the error that occurs on the width of the cutting track is within 0.2 mm. The highest accuracy is obtained by processing the second loop where a relatively uniform width of the cutting track is obtained. The results obtained are acceptable to a certain extent, but this necessitates subsequent finishing in order to achieve a uniform width of the cutting track.

References

[1] Angel Lengerov, Galina Nikolcheva, Julieta Kaleycheva, Lyubomir Lazov, Statistical control of accuracy at machining ,Vide. Tehnologija. Resursi-Environment, Technology, Resources 3, pp. 183-187, 2017;

[2] Erik L.J. Bohez, Compensating for systematic errors in 5-axis NC machining, Computer-Aided Design, Volume 34, Issue 5, pages 347-420, 2002, DOI 10.1016/S0010-4485(01)00111-7;

[3] Fanuc Series 30i/31i/32i-Model B, Operator Manuals for machining center system;

[4] Hadzhiyski P., Knives for rotary dies with variable geometry, Journal "Engineering and automations problems", 2011, p. 131-135, ISSN 0234-6206;

[5] Wahid Khan, Abdul & Chen, Wuyi, A methodology for systematic geometric error compensation in five-axis machine tools. The International Journal of Advanced Manufacturing Technology, 2011, DOI: 10.1007/s00170-010-2848-3

Environment. Technology. Resources. Rezekne, Latvia
Proceedings of the 12th International Scientific and Practical Conference. Volume III, 84-87

Investigation on Tribological Behavior of Ductile Cast Irons with Nanosized Particles

Julieta Kaleicheva
Faculty of Industrial Technology
Technical University of Sofia
Sofia, Bulgaria
jkaleich@tu-sofia.bg

Valentin Mishev
Faculty of Industrial Technology
Technical University of Sofia
Sofia, Bulgaria
v_mishev@tu-sofia.bg

Manahil Tongov
Faculty of Industrial Technology
Technical University of Sofia
Sofia, Bulgaria
tongov@tu-sofia.bg

***Abstract*—The work in this study is focused on investigation of the tribological behavior of ductile cast iron with nanosized particles: titanium nitride TiN; titanium nitride 30% + titanium carbonitride 70% (30%TiN+70%TiCN). The ductile cast iron composition is: Fe-3,55C-2,67Si-0,31Mn-0,009S-0,027P-0,040Cu-0,025Cr-0,08Ni-0,06Mg wt%. Before the addition to the melt nanosized particles were coated with nickel by the electroless nickel deposition method EFFTOMNICKEL .The nickel coating on the nanosized particles ensures their wetting in the melt as well as their uniform distribution into the cast. The optical and quantity metallographic observations and wear test are performed to study the influence of the nanoparticle additives on the cast iron tribological properties. It is observed that the quantity proportion changes between pearlite, ferrite and graphite phase in the cast iron structure. The graphite shape is retained the same, but the nanosized additives decrease the average diameter of the graphite spheres Dmid and increase the quantity of the graphite phase in the structure of ductile cast irons. The cast iron wear resistance in the presence of nanosized additives of (TiN+TiCN) and TiN increases to 55–69% in comparison to wear resistance of the cast iron without nanoparticles.**

***Keywords*—nanosized particles, microstructure, hardness, wear resistance, ductile cast iron.**

I. Introduction

The grey cast iron antifriction properties and wear resistance are well known and depend on the graphite presence in the cast iron structure. At the same quality of the graphite phase (shape, size, quantity and distribution) the wear resistance of the cast iron depends on the structure of the metal base. The graphite characteristics and the metal base structure define the mechanical properties, which could be changed by thermal processing and alloying, as well as the tribological properties of the grey cast iron [1]–[6]. In a small quantity the nanosized additives to the melt change the graphite morphology from flake-like to vermicular-like [7] and the matrix structure, which increases the wear resistance [7]–[12].

The aim of this study was to investigate the influence of different nanosized additives on the graphite characteristics, metal base microstructure and tribological properties of ductile cast iron samples.

II. Materials and methods

The samples from ductile cast iron with additives of nanosized particles: titanium nitride TiN; titanium nitride 30%TiN + titanium carbonitride 70%TiCN are investigated. The composition of ductile cast iron is: Fe-3,55C-2,67Si-0,31Mn-0,009S-0,027P-0,040Cu-0,025Cr-0,020Ni-0,039Mg wt%. The quantity of the nanosized additives into the cast iron is 0,01 wt %. The electroless nickel coating is deposited on the nanopowders prior to the casting by EFTTOM-NICKEL Method [13]. Nickel coating deposited on the nanosized particles improves their wetting and uniform distribution in the moulding volume.

The microstructure of cast iron samples is observed by means of the optical metallographic microscope GX41 OLIMPUS. The samples were treated with 2 % HNO_3 - C_2H_5OH solution before the examination. The microhardness of the coating was determined by Brinell Method. The quantity metallographic analysis is performed by „Olympus MicroImage" Software and the data for an average diameter Dmid of the graphite grains, their roundness as well the volume parts of graphite, pearlite and ferrite are received.

The experimental testing of the wear is performed in conditions of a fixed abrasive by a cinematic scheme „pin - disc" using method and a device for an accelerated testing. The device functional diagram is shown in Fig. 1.

The tested cylindrical sample 3 (body) is fixed in a loading head 6 as its frontal surface contacts with the abrasive surface 2 of a horizontal disc 1 (antibody). The antibody 2 rotates with a constant angular speed around its vertical axis. The cycle's number is accounted with a cyclometer 5. The device allows alteration of the sliding speed changing the disc angular speed from a control unit and trough changing of the distance between the rotation axis of the antibody 1 and the axis of the sample 3 toward the rotation axis of the disc.

The abrasive surface 2 of the antibody 1 is formed by impregnate corundum 60% harder then the tested materials. The used impregnate material in this study is Smirdex 330, Duraflex P80, 117SV.

Print ISSN 1691-5402
Online ISSN 2256-070X
http://dx.doi.org/10.17770/etr2019vol3.4181

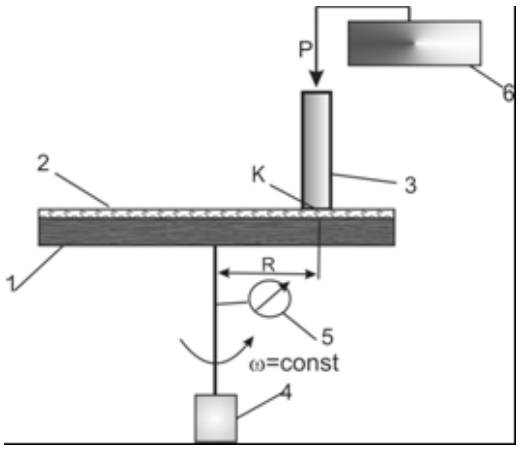

Fig. 1. Functional scheme of a device for wear testing of ductile cast iron samples with nanosized additives in a fixed abrasive

The methodology includes the following operations:

- Preparation of same cylindrical samples 3 with an equal surface roughness avoiding structural and physical and chemical changes of the samples surface. The sample dimensions are: base radius r=4mm and height 20mm;
- Measuring of the weight of the sample before and after a determinate friction road S by an analytical balance WPS 180/C/2 précised to 0,1[mg]. The samples are treated with a special solution to neutralize the static electricity before the testing;
- The sample 3 is mounted in a loading head, the desired normal load P and friction road S is assigned by a cycle counter 5;
- The absolute massive wear m [mg] is measured as a difference between a sample mass before and after a definite cycle number N (friction road S).

Test basic parameters:

1. Absolute massive wear m, [mg] - difference between the samples weight before and after appointed number of friction road S ;
2. Massive wear rate dm/dt [mg/min] - the lost weight of the sample surface for a minute;
3. Absolute intensity of the linear wear i - this is the lost thickness of the surface layer for a one friction cycle. It is a dimensionless number, which could be calculated by the formula having in mind the lost weight:

$$i = \frac{m}{\rho . A_a . S} \tag{1}$$

where: ρ is the density of the sample material ρ=7,8.103 [kg/m3], *Aa* is the nominal interaction contact surface, *S* is a friction road calculated by the number of cycles of the contact interaction N by the formula:

$$S = 2.\pi.R.N \tag{2}$$

where R=42 [mm];

4. Absolute wear resistance I - it is determined as a reciprocal value of the wear intensity and respectively it is a dimensionless number etc.

$$I = \frac{1}{i} = \frac{\rho . A_a . S}{m} \tag{3}$$

The specific wear resistance I_S is a number presenting the friction road in meters, covered by 1 square millimeter contact ground in which 1mg ground material is lost. The dimension respectively is [m.mm2/mg];

5. Nominal contact pressure Pa [N/cm2] is the normal load P, distributed per a unit of a nominal (geometrical) contact surface etc.

$$p_a = \frac{P}{A_a} \tag{4}$$

In Table 1 the value of some basic test parameters are shown.

Table 1. Test parameters

Parameters	Value
Nominal contact pressure, Pa	0,21.10^6 [Pa]
Average speed of sliding, V	26,38 [cm/s]
Nominal contact surface, A_a	50,24 [mm^2]
Density ρ	7,8.10^3 kg/m^3]

Results and discussion

The structure of the tested cast irons consists from ferrite, pearlite and graphite (Figs 2,3 and 4). The quantitative metallographic analysis is performed to evaluate the nanosized additives influence on the graphite quantity, size and morphology, as well as on the volume ratio of ferrite and pearlite (Table 2). Analyses are made for three random fields of metallographic section, and average value is given. The nanosized additives in spheroidal graphite cast iron do not alter the graphite shape. They decrease the average diameter of the graphite spheres Dmid only from 11,00 to 10,52μm. The nanosized additives cause an increase in the quantity of the graphite phase in the range 35÷94% compared to cast irons without nanoparticles (Table 2).

SEM analysis of the fracture of the impact destructed cast iron samples with nanosized additives, show the nanoparticles presence in the graphite [11]. These results and that achieved from the quantity metallographic analysis prove the modified influence of the nanoparticles on the graphite phase in the cast iron samples.

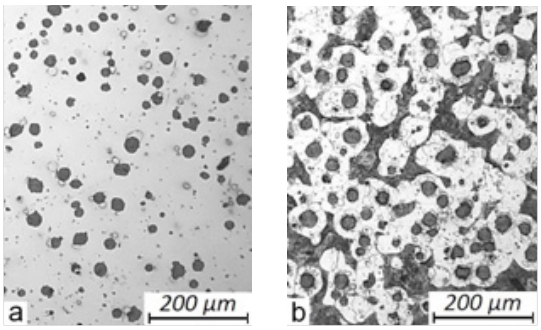

Fig. 2. Microstructure of not developed (a) and developed in 2% solution of HNO3 + ethyl alcohol (b) ductile cast iron samples without nanoparticles.

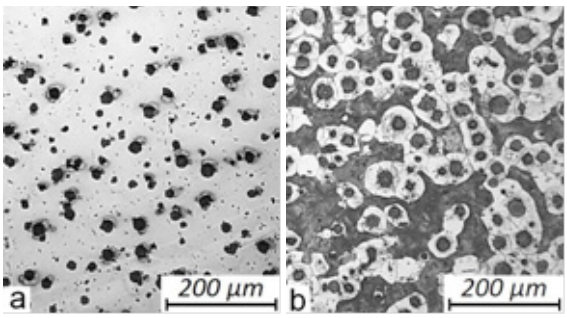

Fig. 3. Microstructure of not developed (a) and developed in 2% solution of HNO3 + ethyl alcohol (b) ductile cast iron samples with nanoparticles of TiN.

In this study the wear of three pieces of ductile cast iron samples is investigated (Table 3). The ductile cast iron samples hardness with and without nanoparticles varies from 165 to 185 HB (Table 2).

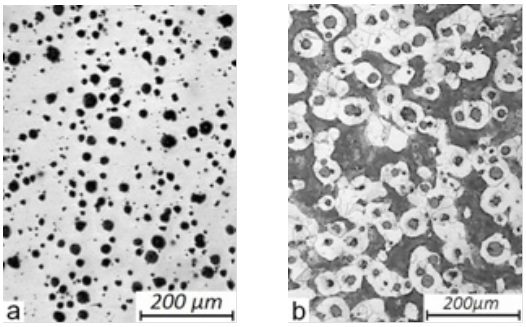

Fig. 4. Microstructure of not developed (a) and developed in 2% solution of HNO3 + ethyl alcohol (b) ductile cast iron samples with nanoparticles of (TiN+TiCN)

The experimental results for the massive wear m, wear rate dm/dt , absolute intensity of wear i and absolute wear resistance I of the samples and their alteration in a contact interaction time are received (Table 3).

For an assessment of the base structure wear resistance should have in mind its ability of changing as a result of the complicated processes during the operation. It is observed the micro geometry change, significant residual stresses, reinforcing of the surface layers trough the formation of sliding bands in the materials with a stable structure (after casting, improving and normalization) during the exploitation. During the exploitation of materials with a metastable structure (martensite, bainite, and residual austenite) it is observed structural and phase transformations in the surface layer and the wear resistance is defined by the intensity of formation and properties of the secondary structures. Graphite in the grey iron structure is an important factor for their wear bearing. There is no adhesion wear in some sections of the contact surface during a dry friction. The reason is the presence of graphite in the structure, which possess a lubricating ability and it appears to be a lubricating material. It is specified the wear resistance of the cast irons on a pearlite base is inversely proportional to the average distance between the graphite grains at given conditions (contact pressure and sliding speed).

When the distance between graphite grains decreases the protective properties of the surface carbon layer are improved and cast iron wear resistance increases.

In the presented study the tested cast iron with and without nanomodifiers possess an equilibrium ferrite – pearlitic base structure. Nanosized particles change the pearlte-ferrite proportion. The microstructure tests by optical and quantity metallographic analysis show that nanosized additives increase the graphite quantity and decrease the distance between graphite grains without changing the graphite shape. The intensity of wear of the cast irons with nanoparticles decrease, the wear resistance increases – with 69% for the cast iron with TiN additive and with 55% for the cast iron with (TiN + TiCN) additives (Table 3).

Table 2.

Nanoadditives, graphite characteristics, graphite, pearlite and ferrite quantity

№ of the sample	Nanosized particles	D_{mid} µm	Roundness	Volume part of: [%]			Hardness HB
				graphite	pearlite	ferrite	
1	-	11,00	1,59	8,44	32,12	59,44	185
2	*TiN*	10,64	1,49	11,36	34,28	54,36	165
3	*TiN+TiCN*	10,52	1,28	16,36	25,36	58,28	180

Table 3.

Test results for massive wear *M*, wear rate *DM/DT,* intensity of wear *I* and wear resistance *I.*

Friction road, *S* [m]		**140**	**280**	**420**	**560**	**659**
Cycles number, *N*		**500**	**1000**	**1500**	**2000**	**2500**
Time, *t* [min]		**2,35**	**4,7**	**7,05**	**9,4**	**11,75**
Massive wear, *m* [mg]	sample 1	18,3	24,5	28,2	30,8	32
	sample 2	8,2	10,8	15,5	18	19
	sample 3	10	12,9	15,5	19,2	20,8
Wear rate, *dm/dt* [mg/min]	sample 1	7,79	5,21	4	3,28	2,72
	sample 2	3,49	2,3	2,2	1,91	1,62
	sample 3	4,25	2,74	2,2	2,04	1,77

Intensity of wear, *i*	sample 1	$0{,}071.10^{-6}$	$0{,}095.10^{-6}$	$0{,}109.10^{-6}$	$0{,}119.10^{-6}$	$0{,}124.10^{-6}$
	sample 2	$0{,}032.10^{-6}$	$0{,}042.10^{-6}$	$0{,}06.10^{-6}$	$0{,}07.10^{-6}$	$0{,}075.10^{-6}$
	sample 3	$0{,}039.10^{-6}$	$0{,}05.10^{-6}$	$0{,}06.10^{-6}$	$0{,}074.10^{-6}$	$0{,}08.10^{-6}$
Wear resistance, *I*	sample 1	$14{,}08.10^{6}$	$10{,}53.10^{6}$	$9{,}17.10^{6}$	$8{,}4.10^{6}$	$8{,}06.10^{6}$
	sample 2	$31{,}25.10^{6}$	$23{,}80.10^{6}$	$16{,}67.10^{6}$	$14{,}29.10^{6}$	$13{,}6.10^{6}$
	sample 3	$25{,}64.10^{6}$	20.10^{6}	$16{,}67.10^{6}$	$13{,}5.10^{6}$	$12{,}5.10^{6}$

Conclusions

The tribological properties, microstructure and hardness of unalloyed ductile cast iron without and with nanosized additives are investigated. The nanosized particles change the quantity proportion between pearlite, ferrite and graphite in the cast iron structure. Nanoadditives of (TiN+TiCN) and TiN in the ductile cast irons have a modifying effect on the graphite phase. They reduce the average diameter of the graphite grains. The graphite shape doesn't change but its quantity increases, the distance between the graphite grains decreases, which have an effect on the cast iron wear behavior. The wear resistance of the ductile cast irons with nanosized additives of (TiN+TiCN) and TiN increases by 55-69% compared with this one of the same cast iron composition without nanoparticles.

References

[1] A.S.M.A. Haseeb, Md.A. Islam and Md.M.A. Bepari, "Tribological behavior of quenched and tempered, and austempered ductile iron at the same hardness level", Wear, 244, pp.15–19, 2000.

[2] Y. Sahin, M. Erdogan and V. Kilicli, "Wear behavior of austempered ductile irons with dual matrix structures", Mater. Sci. Eng., A 444, pp. 31–38, 2007.

[3] F. Iacoviello and O. DiBartolomeo, "Damaging micromechanisms in ferritic-pearlitic ductile cast irons", Mater. Sci. Eng., A 478, pp. 181–186, 2008.

[4] C. Fragassa, N. Radovic, A. Pavlovic and G. Minak, "Comparison of Mechanical Properties in Compacted and Spheroidal Graphite Irons", Tribology in Industry, Vol. 38, No 1, pp. 45-56, 2016.

[5] W. Xu, M. Ferry and Y. Wang, "Influence of alloying elements on as cast microstructure and strength of gray iron", Mater. Sci. Eng., A 390, pp. 326–333, 2005.

[6] K. Hirasata, K. Hayashi and Y. Inamoto, "Friction and wear of several kinds of cast irons under severe sliding conditions", Wear, 263, pp. 790–800, 2007.

[7] Y. Wang, Z. Pan, Z. Wang, X. Sun and L. Wang, "Sliding wear behavior of Cr–Mo–Cu alloy cast irons with and without nanoadditives", Wear 271, pp. 2953– 2962, 2011.

[8] J. Li, M. Chen, H. Gao and Y. Zhao, "Structures and Properties of Cast Irons Reinforced by Trace Addition of Modified SiC Nanopowders",Chinese Journal of Chemical Physics, Vol.20, No 6, pp. 625-631, 2007.

[9] J. Kaleicheva, "Wear Behavior of Austempered Ductile Iron with Nanosized Additives", Tribology in Industry, Vol. 36, No 1, pp. 74-78, 2014.

[10] J. Kaleicheva, V. Mishev, G. Avdeev, Z. Karaguiozova and B. Dineva, Influence of Nanoadditives on the Structure and Properties of Austempered Ductile Irons, in Proceedings of the European Conference on Heat Treatment and 21st IFHTSE Congress, 12-15 May, 2014, Munich, Germany, pp. 537-543, 2014.

[11] J. Kaleicheva, V. Mishev, Z. Karaguiozova, G. Nikolcheva and A. Miteva. "Effect of nanoadditives on the wear behavior of spheroidal graphite cast irons", Tribology in Industry, Vol. 39, No 3, pp. 294-301, 2017, doi: 10.24874/ti.2017.39.03.03

[12] J. Kaleicheva and V. Mishev, Wear Resistance of Austempered Ductile Iron with Nanosized Additives, in 9th International Conference on Tribology Balkantrib'17, IOP Conf. Series: Mater. Sci. Eng. 295, Article number 012034, 2018 doi:10.1088/1757-899X/295/1/012034

[13] G. Gavrilov G. and C. Nicolov, Electroless Nickel and Composite Coatings, Sofia: Tehnika, 1985.

Environment. Technology. Resources. Rezekne, Latvia
Proceedings of the 12th International Scientific and Practical Conference. Volume III, 88-91

Tribological Properties and Microstructure of Electroless Nickel Coatings Reinforced with Nanoparticles

Julieta Kaleicheva
Faculty of Industrial Technology
Technical University of Sofia
Sofia, Bulgaria
jkaleich@tu-sofia.bg

Zdravka Karaguiozova
Space Research and Technology Institute
Bulgarian Academy of Sciences
Sofia, Bulgaria
karazuzi@yahoo.com

lentin Mishev
Faculty of Industrial Technology
Technical University of Sofia
Sofia, Bulgaria
v_mishev@tu-sofia.bg

***Abstract* — Composite nickel coatings composed of Ni; Ni + TiN are studied. The method for elecrtroless nickel deposition EFFTOM-NICKEL with TiN nanosized strengthening particles (50nm) is applied. The coatings are deposited on austempered ductile iron (ADI) samples. The composition of cast iron samples is: Fe-3,63C-2,59Si-0,30Mn-0,010S-0,034P-0,53Cu wt. %. The samples are put under isothermal hardening at 900°C for an hour and isothermal retention at 290 °C for 2 hours with the aim to receive a lower bainite structure. The wear resistance experimental testing is carried out using Taber-Abraser test machine by disk to disk classical method. The microstructure observations of the coatings and padding are performed using an optical microscope GX41 OLIMPUS also the coatings' microhardness by Knoop Method is examined. The wear resistance, microstructure, thickness and microhardness of the as plated and thermally processed at 290°C for 6 hours coatings are defined.**

Keywords* — *titanium nitride, electroless nickel coating, wear resistance, microhardness, lower bainite.

Introduction

The simplicity of electroless plating technology and its ability to produce high quality coatings is the reason for their popularity in surface modification and significant impact on numerous industrial applications. Nickel is a preferred metal in this method for producing coatings. Nickel coatings have excellent corrosion and wear resistance and high microhardness [1]. The necessity for the materials surface properties improvement launched the idea of the various second phase particles incorporation in the electroless nickel coatings in the 1960s [2] and led to the development of electroless nickel composite coatings. The electroless composite coating is formed by the co-deposition and settlement of particles on the surface of the work piece, and the subsequent envelopment of these particles by the matrix material as it is deposited. There is no molecular bonds between the particles and metal matrix [3]. The soft or hard particles are used for the co-deposition process. Several factors influence their incorporation in the electroless Ni–P matrix including, particle size and shape, relative density of the particle, particle charge, inertness of the particle, the concentration of the particles in the plating bath, the method and degree of the agitation, the compatibility of the particle with the matrix, and the orientation of the part being plated [4]. In [5] the authors outline the improvement in surface properties offered by such composite coatings and their significant impact on numerous industrial applications securing a more prominent place in the surface engineering of the metals and alloys. Thus composite coatings constitute a new class of materials which are mostly used for mechanical and tribological applications. Among these materials, nickel deposits incorporating hard ceramic particles such as silicon carbide SiC, combine anti-corrosion properties (due to the presence of nickel), with mechanical and tribological performances (due to the presence of particles of SiC). [6] studying the mechanical (hardness) and tribological (friction resistance and wear) properties of the co-deposits concludes that increasing the size or the rate of SiC particles incorporated lead to an increase in both the hardness of the films and friction coefficient when sliding against a steel ball. Author's research [7] on the mechanism of incorporation of reinforced ZrO2, TiO2, and Al2O3 particles on 6061 aluminium alloy and on the effect of different composites on the mechanical properties of the deposit such as hardness and wear resistance proved once again that the reinforced particles as well as the heat treatment provide satisfactory improvement in hardness and wear resistance of the deposits.

Improving the properties of low-cost materials is a good opportunity to expand their application areas. Electroless nickel coatings are such an opportunity for the improvement of the cast irons surface properties [8]. The study in this work utilized electroless nickel (EN) and cathodic arc deposition (CAD) technologies with lower processing temperature to treat austempered ductile iron (ADI). The test results show that microstructures of ADI did not deteriorate after EN and CAD surface treatments. Moreover, both the EN and CAD-DLC (diamond-like carbon) coatings are identified to be amorphous type and they could be well deposited on the ADI substrate. The duplex coated DLC/EN-ADI show the highest hardness (1312 HV0.05), followed by DLC-ADI (1088 HV0.05),

Print ISSN 1691-5402
Online ISSN 2256-070X
http://dx.doi.org/10.17770/etr2019vol3.4182

EN-ADI (409 HV0.05) and then uncoated ADI (396 HV0.05). In the case of corrosion resistance, all the coated specimens are better than that of the uncoated one in 3,5wt.% NaCl aqueous solution, and the sequence is DLC/EN-ADI > EN-ADI > DLC-ADI >ADI.

In recent years, physical vapor deposition (PVD) technique using lower processing temperature has been widely adopted to coat various films, such as diamond-like carbon (DLC), CrN, TiN etc., on the engineering material for surface modification. In particular, DLC film possesses excellent mechanical properties such as high hardness and low friction coefficient. Electroless nickel (EN), another lower temperature coating process, has also a wide field of application such as the industrial components and machine parts. The purpose of the study [9] is to investigate the effect of EN and PVD–DLC surface coatings on mechanical behaviors of ADI, especially the tensile and fatigue properties.

This study is focused on the investigation of nanosized strengthening TiN particles influence on the tribological properties, microstructure and microhardness of composite nickel coatings, deposited on austempered ductile iron (ADI) samples, copper alloyed.

Materials and methods

A. Materials and heat treatment

The EFTTOM-NICKEL technology for electroless nickel plating developed at TU of Sofia [10] is applied to obtain composite coatings with nanosized strengthening TiN particles (50nm).

The composite coatings are deposited on copper alloyed austempered ductile iron (ADI) samples.The composition of cast iron samples is: Fe-3,63C-2,59Si-0,30Mn-0,010S-0,034P-0,53Cu wt.%. The cast iron samples are put under prior to the plating process. The heat treatment consists of heating at 900°C for an hour and subsequent isothermal retention at 290°C for 2 hours. The result is to obtain ductile cast iron with a lower bainite structure (Fig. 1).

Two types of coatings are investigated: electroless nickel coating Ni and composite nickel coating with nanosized titanium nitride Ni+TiN (Table 1).

Some of the samples are heat treated at 290°C for 6 hours after coating deposition for the coatings' adhesion improvement and microhardness increase.

The microstructure of the padding and the coatings and the coatings' thickness are defined by means of an optical metallographic microscope GX41 OLIMPUS. The microhardness testing of the coatings is examined by Knoop method under 20g load (Table1).

Table 1 Composition, heat treatment, microhardness and thickness of coatings

№	Composition	Heat treatment	Microhardness HK0,02	Thickness, [μm]
1	Ni	-	538	10
2	Ni	290°C, 6h	950	10
3	Ni + TiN	-	588	8
4	Ni + TiN	290°C, 6h	1020	8

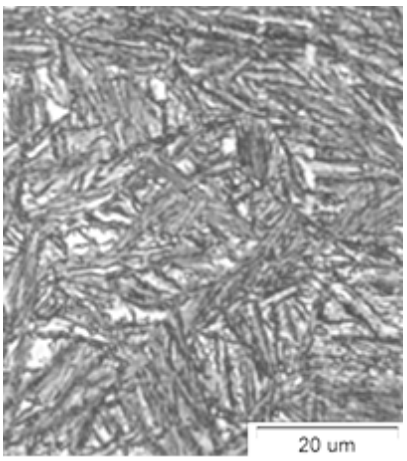

Fig.1. Microstructure of the austempered ductile iron sample without coating

B. Device and method for wear resistance testing

The experiments on the wear resistance of nickel coatings are carrying out using a classic design "back-to-back" disc on a TABER ABRASER test machine 503, modified in accordance with the developed by the authors' method. The device design is shown on Fig. 2.

The ring shaped sample 1 (solid) with a coating 2 is fixed on a horizontal disc 3, which is moved by an electric motor 4 with a constant angular speed w. The antibody 5 is a disc from a special abrasive material CS10. The desire normal load P in the contact surface is set through a mounted in the antibody axle, which is operated by a special device. In this way the body 1 and antibody 5 are fixed on two cross axes. Upon the constant angular speed w=const of the sample 1 and upon constant nominal contact pressure Pa=const the friction in the contact surface K keeps a constant rotation speed of the antibody 5.

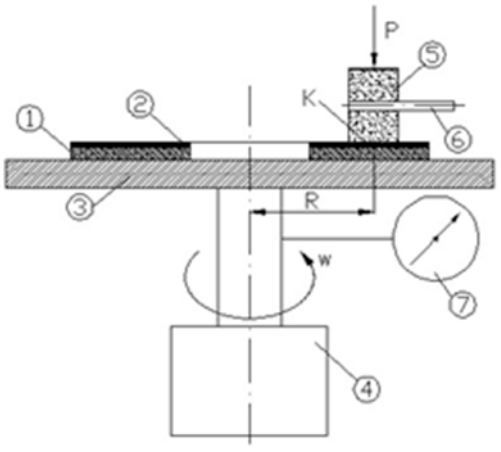

Fig.2. TABER-ABRASER test machine

The test method description:

- All samples with the same ring shape and size, before the coating process are subjected to a mechanical treatment, namely grinding and polishing to ensure an equal surface roughness Ra=0,4μm. This is a binding requirement for the reliability of the wear testing, because the electroless coatings "copy" the samples surface by the plating process.
- When choosing the integral parameter "massive wear" the weight of the sample is weighed before

and after a determinate number of the disc rotation by an analytical balance WPS 180/C/2 précised to 0,1mg. The samples are treated with a special solution to neutralize the static electricity before the weighting.

- Sample 1 is fixed on a horizontal disc 3 and by the lever system the desire normal load P is set. The friction road L is determined by the number of cycles N, accounted with a cyclometer 7.

Test basic parameters are:

- absolute massive wear m[mg] - this is a coating lost weight in the process of the wear, estimated as a difference between the samples weight before and after the appointed number of friction cycles.
- speed of massive wear ṁ [mg/min] - the lost weight of the coating for a minute.
- intensity of wear i - this is the lost coating thickness for an one friction cycle. The result is a dimensionless number, which could be calculated by the formula having in mind the lost weight:

$$i = \frac{m}{\rho . A_a . L} \quad (1)$$

where:

- ρ is the coating density - ρ=7,8.10^3 [kg/m3];
- Aa is the nominal interaction contact surface - Aa =26,10^{-6} [m2];
- L is the friction road, estimated by the number of cycles N:

$$L=2.\pi.R.N \quad (2)$$

where:

-R is the distance between the rotation axis of the bearing disc and the mass center of the contact place between the sample 1 and the contra body 5 (Fig. 1).

- absolute wear resistance I - this is a dimensionless number and is determined as a reciprocal value of the wear intensity, namely

$$I = \frac{1}{i} = \frac{\rho . A_a . L}{m} \quad (3)$$

- nominal contact pressure Pa ,[N/cm^2] is the normal load, per the contact interaction surface Aa, i.e.

$$P_a = \frac{P}{A_a} \quad (4)$$

- comparative index of wear resistance εie what means the ratio between the wear resistance of the tested sample Ii and the wear resistance of a sample-standard Ie, i.e it is a dimensionless number, indicating how many times the wear resistance of the tested sample is higher compared to the sample-standard under the same contact interaction conditions:

$$\varepsilon_{ie} = \frac{I_i}{I_e} \quad (5)$$

The parameters of the contact interaction are presented in Table 2.

Table 2 Test Parametars

Nominal contact surface A_a , [m^2]	26.10^{-6}
Nominal contact pressure Pa ,[N/cm^2]	47,15
Average speed of sliding V, [cm/s]	17,90

Results and discussion

The coatings' thickness is between 8÷10μm (Table 1). The microhardness HK0,02 test results of the coatings are presented in Table 1. The heat treatment of the coatings at 290°C for 6 hours leads to the coatings' microhardness twice increase.

Electroless Ni-coatings show amorphous structure in an as-plated state. The coatings' structure becomes crystalline after heat treatment at 290oC, 6h. The diffraction patterns of the samples prove the presence of Ni3P phase in the coatings' structure [12].The heat treatment at 290oC, 6h leads to a crystal formation of Ni3P phase, which is dispersed and increases the microhardness of the coatings [11], [12]. The introduced nano- and microparticles in coatings deposited by various methods further increase their microhardness [13].

The coatings' microstructure appears as a white strip following the sample relief (Figs 3 and 4). The padding microstructure of the cast iron, obtained at a low temperature isothermal retention in the bainitic field consists of a lower bainite (Figs 1, 3 and 4).

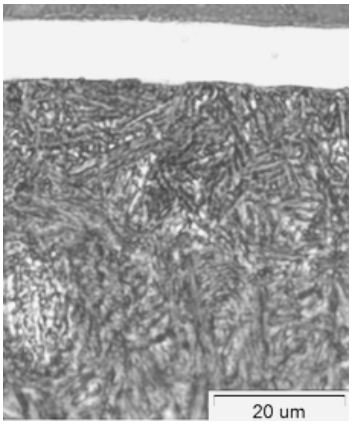

Fig.3. Microstructure of the austempered ductile iron sample with coatings Ni after heat treatment at 290°C, 6 h

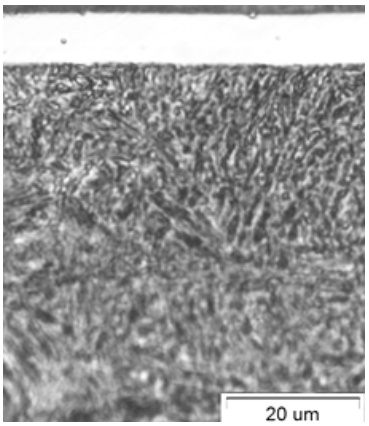

Fig.4. Microstructure of the austempered ductile iron sample with coating Ni+TiN after heat treatment at 290°C, 6 h

The experimental results received for the massive wear *m* for the different coatings during the contact interaction are presented in Table 3.

Table 3 Massive wear variation in time.

№	2,5 [min]	5 [min]	7,5 [min]	10 [min]	12,5 [min]	15 [min]
1	3,2	5,1	6,0	6,7	7,9	8,9
2	3,8	4,7	6,9	8,0	9,8	10,5
3	2,7	3,8	4,3	5,3	6,0	6,9
4	1,5	2,8	4,0	4,6	4,9	5,2

The experimental results received for the massive wear rate *ṁ* dependence on the friction road L for the different coatings are presented in Table 4.

Table 4 Massive wear rate variation in friction road

№	26,85 [m]	53,70 [m]	80,55 [m]	107,4 [m]	134,25 [m]	161,1 [m]
1	1,28	1,02	0,80	0,67	0,63	0,59
2	1,52	0,94	0,92	0,80	0,78	0,70
3	1,08	0,76	0,57	0,53	0,48	0,46
4	0,60	0,56	0,53	0,46	0,39	0,35

Table 5 presents experimental results of the coatings' massive wear *m* in contact interaction t=15min, the massive wear rate *ṁ*, also the wear intensity value *i* and absolute wear resistance *I*. The samples' wear intensity *i* and wear resistance *I* are calculated at the friction road L=161,1 [m].

Table 5 Wear intensity and wear resistance in friction road L=161,1 m.

№	***m*** **[mg]**	ṁ **[mg/min]**	**Wear intensity *i***	**Wear resistance *I***
1	8,9	0,59	$2,72.10^{-7}$	$0,37.10^{7}$
2	10,5	0,7	$3,2.10^{-7}$	$0,31.10^{7}$
3	6,9	0,46	$2,11.10^{-7}$	$0,47.10^{7}$
4	5,2	0,34	$1,6.10^{-7}$	$0,63.10^{7}$

The analysis of the wear resistance value (Fig .5) shows the sample 4 with Ni+TiN coating with heat treatment at 290°C, 6h possesses higher wear resistance ($I = 0,63.10^{7}$) than this one of the sample 3 with the same coating but without heat treatment ($I = 0,47.10^{7}$). The measured higher microhardness of the Ni+TiN coating with heat treatment at 290°C, 6h (1020 HK0,02) compared to this one of the same coating without heat treatment (588 HK0,02) corresponds to higher wear resistance (Table 1 and Fig. 5). The lack of correlation between the microhardness and wear resistance of the coatings of pure Ni (samples 1 and 2) could be attributed to the low adhesion between the coating and the padding This could be explained with the graphite presence in the iron microstructure.

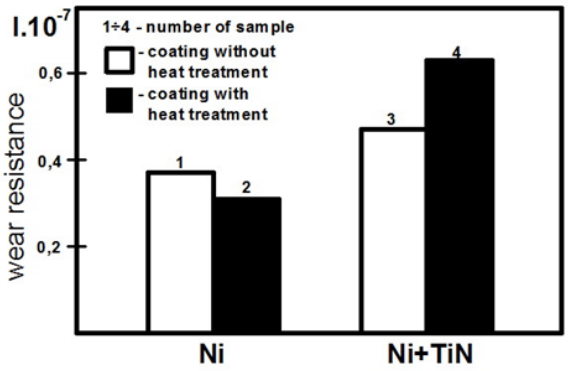

Fig.5. Wear resistance I of the coatings composition Ni (samples 1 and 2) and composition Ni+TiN (samples 3 and 4), deposited on the austempered ductile iron samples.

Conclusions

It is found out that the electroless nickel coatings' microhardness with composition nickel Ni and nickel + nanosized titanium nitride (50nm) Ni+TiN deposited on austempered ductile iron samples is twice higher after heat treatment at 290°C, 6 h than this one of the coatings without heat treatment.

It is found that heat treated at 290°C, 6 h composite nickel coatings composition nickel + nanosized titanium nitride (50nm) Ni+TiN posses 34% higher wear resistance than this one of the same coatings without heat treatment.

References

1. F. Mindivan, H. Mindivan and C. Darcan, "Electroless Ni–B Coating of Pure Titanium Surface for Enhanced Tribocorrosion Performance in Artificial Saliva and Antibacterial Activity," Tribology in Industry, vol. 39, No. 2, pp. 270-276, 2017, doi: 10.24874/ti.2017.39.02.15
2. W. Metzger and Th. Florian, "The Deposition of Dispersion Hardened Coatings by Means of Electroless Nickel," The Int. Journal of Surf. Eng. and Coatings, vol. 54, issue 1, pp. 174-177, 1976.
3. F.N. Hubbell, "Chemically Deposited Composites—A New Generation of Electroless Coatings," The Int. Journal of Surf. Eng. and Coatings, vol. 56, issue 1, pp. 65-69, 1978.
4. W.F. Sharp, "Properties and applications of composite diamond coatings," Wear, vol. 32, issue 3, pp. 315-325,1975.
5. J. Balaraju, S. Narayanan and S. Seshadri, "Electroless Ni–P composite coatings," Journal of Appl. Electrochemistry, vol. 33, issue 9, pp 807–816, 2003.
6. A. Grosjeana, M. Rezrazia, J. Takadoumb and P. Berçota, "Hardness, friction and wear characteristics of nickel-SiC electroless composite deposits," Surf. and Coatings Tech., vol. 137, issue 1, pp. 92-96, 2001.
7. Z Abdel Hamid and M.T. Abou Elkhair, "Development of electroless nickel–phosphorous composite deposits for wear resistance of 6061 aluminum alloy," Mat. Lett., vol. 57, issue 3, pp. 720-726, 2002.
8. Cheng-Hsun Hsu, Jung-Kai Lu and Rung-Jie Tsai, "Characteristics of duplex surface coatings on austempered ductile iron substrates," Surf. and Coat. Tech., vol. 200, issues 20-21, pp. 5725-5732, 2006.
9. Cheng-Hsun Hsu, Jung-Kai Lu and Rung-Jie Tsai, "Effects of low-temperature coating process on mechanical behaviors of ADI," Mat. Sc. and Eng., A, vol. 398, issues 1-2, pp. 282-290, 2005.
10. G. Gavrilov and C. Nicolov, Electroless Nickel and Composite Coatings. Sofia: Tehnika, 1985.
11. Z. Karaguiozova, J. Kaleicheva, V. Mishev and G. Nikolcheva, "Enhancement in the tribological and mechanical properties of electroless Nickel-nanodiamond coatings plated on iron," Tribology in Industry, vol. 39, No 4, pp. 444-451, 2017, doi: 10.24874/ti.2017.39.04.03
12. A. Mukhopadhyay, S. Duari, T.K. Barman and P. Sahoo, "Evaluation of Tribological Properties and Optimization of Electroless Ni-P-W Coating under Dry Condition using Grey Fuzzy Analysis," Tribology in Industry, vol. 39, No. 1, pp. 50-62, 2017, doi: 10.24874/ti.2017.39.01.06
13. T. Simeonova, M. Tongov and G. Avdeev, "Microstructure and properties of NiCrBSiC Overlay Coatings Deposited By The Plasma Scanning Process," WIT Trans.on the Built Env. vol. 137, pp. 553-564, dos: 10.2495/HPSM140511

Environment. Technology. Resources. Rezekne, Latvia
Proceedings of the 12th International Scientific and Practical Conference. Volume III, 92-94

Investigation of the Corrosion Behaviour of Aluminium Alloy in Selected Environments

Kalina Kamarska
Technical University–Sofia, Branch
Plovdiv
Department of Mathematics,
Physics,Chemistry
Plovdiv, Bulgaria
e-mail:kamarska@tu-plovdiv.bg

***Abstract*—The corrosion behaviour of aluminium alloy EN AW-2011 was investigated in selected environments of various electrolytes using gravimetric technique. The results showed that, under the conditions employed in the present work, the corrosion rate of this alloy depends on the specific ions present in solution. The corrosion resistance of aluminium alloy EN AW-2011 is higher in solutions of acids and salts containing sulfate and nitrate ions than in these consisting chloride ions.**

Keywords—aluminium alloy EN AW-2011, corrosion resistance.

I. Introduction

Aluminium alloy EN AW-2011 is construction material widely used in the automotive industry, aircraft and chemical industries as screw machine products, appliance parts and trim, ordnance, automotive, electronic, fasteners, hardware, machine parts [1]. During its exploitation, in natural or technological environments as electrolytic media, it is in contact with aggressive components and interacting with them is progressively destroyed.

Corrosion of metals is the spontaneous chemical destruction of metals under the effect of their environment [2]. The corrosion study of aluminium and aluminium alloys is of immense technological importance due to their growing industrial application.

The corrosion behaviour of aluminium alloys depends on the chemical resistance of oxide layer of Al_2O_3, the characteristics of the parent metal, the chemical composition and the number of the alloying elements [3], [4]. The environments that contain aggressive ions, such as chloride, activate the corrosion process, impair the stability and integrity of the passive layer [5].

In recent years the environmental factors affecting the corrosion behaviour of aluminium and its alloys in salt solutions [6] - [9] and acid solutions [10] - [12], have very often been studied.

The aim of the present investigation is to study the corrosion behaviour of aluminium alloy EN AW-2011 under exposure to selected environments of different acids and salts containing chloride, nitrate and sulfate ions and measure corrosion rate using gravimetric technique.

II. MATERIALS AND METHODS

The experiments were performed with samples aluminium alloy EN AW-2011 with an exposed area of 8.54 cm^2. For the corrosion tests, a 1M solutions of various electrolytes such as HCl, HNO_3, H_2SO_4, NaCl, $NaNO_3$ and Na_2SO_4 were used at room temperature (≈ 25°).

Before immersion in solution, the experimental samples were washed in detergent for five minutes and then rinsed with distilled water and dried. The dried samples were weighed with an analytical balance Acculab ATILON an accurate to ± 0,0001g and then were immersed in 100 ml of test solution of 1 M HCl. The system was lightly covered with parafilm. The same process was repeated at different of 1 M solutions of HNO_3, H_2SO_4, NaCl, $NaNO_3$ and Na_2SO_4. The first weight loss of each coupon was determined after 4 h and after that every 192 h of exposure. The maximum period of exposure was 768 h. After immersion period the samples were cleaned by brushing them under the stream of water using a fibre-bristle brush to remove the corrosion products. Then the samples were rinsed with tap water, dried under a stream of air, and weighed. For each of the immersion period the corrosion rate (K*m*) of alloy were determined using the following equation:

$$Km = m_1 - m_2 / S.10^{-2}\ g/m.h \quad (1),$$

where

m_1 is the weight of the sample, g; m_2 is the weight of the sample after the corrosion test, g; S is the area of the sample, m and t is the test time, h.

III. RESULTS AND DISCUSSION

The gravimetric technique is has proved to be useful in monitoring the corrosion of aluminium alloy in selected environments of different electrolytes. Corrosion of EN AW-2011 was detected in each of the immersion solution as indicated by the weight loss data. The results of obtained are processed by this method and presented in table (Table I and Table II).

Print ISSN 1691-5402
Online ISSN 2256-070X
http://dx.doi.org/10.17770/etr2019vol3.4191

Table I.

Corrosion rate of aluminium alloy EN AW-2011 in 1M salt solutions

Solution, 1M	4 h	192 h	384 h	576 h	768 h
	Km, *g/m.h*	Km, *g/m.h*	Km, *g/m.h*	Km, *g/m.h*	Km, *g/m.h*
NaCl	0,14	0,020	0,023	0,020	0,014
$NaNO_3$	0,09	0,004	0,020	0,014	0,013
Na_2SO_4	0,06	0,002	0,001	0,010	0,010

Table II.

Corrosion rate of aluminium alloy EN AW-2011 in 1M acid solutions

Solution, 1M	4 h	192 h	384 h	576 h	768 h
	Km, *g/m·h*	Km, *g/m.h*	Km, *g/m.h*	Km, *g/m.h*	Km, *g/m.h*
HCl	0,67	0,16	0,24	0,20	0,20
HNO_3	0,30	0,26	0,40	0,36	0,37
H_2SO_4	0,14	0,27	0,46	0,45	0,47

The corrosion rate (Km) derived as per equation (1), is plotted against exposure time immersed in aqueous solutions of salts (Fig. 1) and acids (Fig. 2).

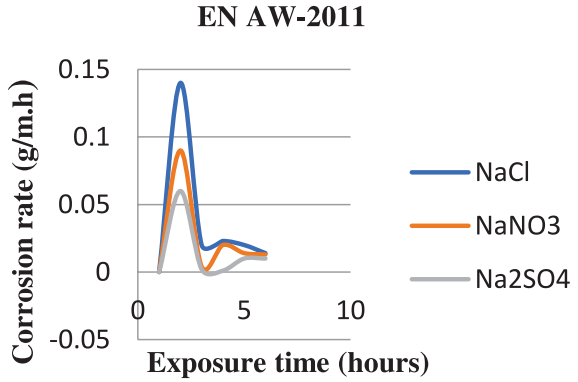

Fig. 1 Corrosion rate of aluminium alloy EN AW-2011 immersed in 1M salt solutions

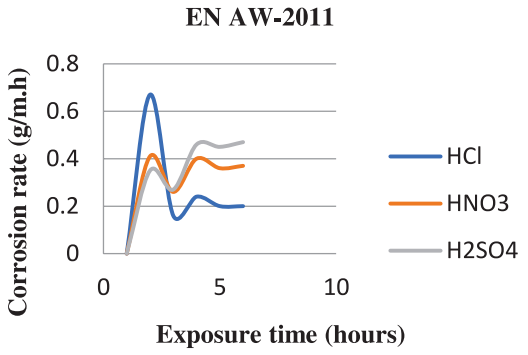

Fig. 2 Corrosion rate of aluminium alloy EN AW-2011 immersed in 1M acid solutions

Observation of the graphs shows as initial increase in corrosion rate of aluminium alloy EN AW-2011 with respect to time. During the first four hours of immersion in solutions of acid (HCl, HNO_3, H_2SO_4) and salt (NaCl, $NaNO_3$ and Na_2SO_4) the gaphs achieve the maximum level followed by a sudden decrease in corrosion rate of aluminium alloy. This figure shows that, after 192 hours the corrosion rate increased slightly and stays constant till 768 hours of exposure in test environments.

The behaviour of this process can be attributed to the formation of the protective layer on the alloy surface and increase in corrosion rate with respect to time. Increase in corrosion rate ceases with the formation of the protective oxide layer [13]. When exposed to environment with aggressive ions this oxide layer breaks down at definite sites causing corrosion on the aluminium surface. The corrosion rate of aluminum alloys depends on the specific ions present in solution.

Solutions of most inorganic salts cause insignificant corrosion of aluminum alloys at room temperature [14]. EN AW-2011 showed better corrosion resistances in salt solutions containing sulfate (Na_2SO_4) and nitrate ($NaNO_3$) ions even after 768 h of immersion. It showed high corrosion rate in NaCl environment and is found the increasing trend of weight loss.

In acid solution mechanism of dissolution of aluminium and its alloys is as follows [15]:

$Al + H_2O \rightarrow AlOH_{(ads)} + H^+ + e^-$

Aluminium alloys most resistant to solutions dilute in sulfuric acid and nitric acid bit hydrochloric acid solutions is definitely corrosive to this alloy. In acid solutions, chlorides greatly stimulate attack of the protective layer [14] and it showed very high corrosion rate.

Alloy EN AW-2011showed better corrosion resistances in H_2SO_4 as compared to HNO_3 even after 768 h of immersion.

The results obtained in this work also showed that, in the conditions employed in the present work, the corrosion rate in solutions of acids (HCl, HNO_3, H_2SO_4) was higher than of the samples immersed in solutions of salts (NaCl, $NaNO_3$, Na_2SO_4). Furthermore, as shown in the Fig. 2 the corrosion rate of the samples immersed in 0,1M solutions of HCl showing the highest corrosion rate. This was followed by the aluminium alloy immersed in 0,1M solutions of HNO_3 and H_2SO_4.

Comparison of the corrosion rate of EN AW-2011 from weight loss analysis showed that the solutions of acids and salts consisting sulfate and nitrate ions are found to be less aggressive to the alloy showing relatively less corrosion rates than these consisting the chloride ions. The maximum corrosion rate in presence of chloride ions is indicative of the high penetrating power of these aggressive ions into the barrier oxide layer [16]. Nitrate ions shown the moderate weight loss in presence of these acids and salts. Sulfate ion in the solution appears to impart passivity to the alloy and reduced corrosion rates. The presence of sulfate ion in the medium is probably to produce aluminium sulfates which are less soluble than the other aluminium salts formed in presence of nitrate and chloride ions and may effectively retard the surface degradation [17].

IV. CONCLISIONS

The present study on corrosion behaviour of

aluminium alloy EN AW-2011 reveals susceptibility of corrosion in selected environments of various electrolytes of 1M HCl, HNO_3, H_2SO_4, NaCl, $NaNO_3$ and Na_2SO_4.

The results obtained in this work showed that, in the conditions employed in the present study, during the first hours of immersion the corrosion rate achieves the maximum level. The corrosion resistance of this alloy depends on the specific ions present in solution and is more in the acid and salt environments containing sulfate and nitrate ions than in the solutions consisting chloride ions.

V. References

[1] J. R. Davis, Alloying: Understanding the Basics. Ohio: ASM International, 2001.
[2] V. S. Bagotsky, Fundamentals of electrochemistry. Hoboken, NJ: John Wiley, 2006.
[3] R. Rachev, Corrosion and protection of metals, Sofia: Novi znania, 2000.
[4] J. Esquivel and R. Gupta, "Corrosion Behaviour and Hardness of Al–M (M: Mo, Si, Ti, Cr) Alloys, "Acta Metall. Sin. (Engl. Lett.), vol.30, pp. 333-341, Feb. 2017.
[5] I. Huang, "Uniform Corrosion and General Dissolution of Aluminium Alloys 2024-T3, 6061-T6, and 7075-T6, "M.S. thesis, The Ohio State University, Columbus, Ohio, USA, 2016.
[6] R. Ambat and E. Dwarakadasa, "Studies on the influence of chloride ion and pH on the electrochemical behaviour of aluminium alloys 8090 and 2014, "J. Appl. Electrochem., vol.24, pp. 911-916, Sept.1994.
[7] V. Guillaumin and G.Mankowski, "Localized corrosion of 2024 T351 aluminium alloy in chloride media, " Corros Sci., vol. 41, pp. 421-438, July, 2000.
[8] A.Mazhar, S. Arab, E. Noor, "The role of chloride ions and pH in the corrosion and pitting of Al-Si alloys, "J. Appl. Electrochem., vol. 31, pp. 1131-1140, May, 2001.
[9] J. Datta, C. Bhattacharya, S. Bandyopadhyay, "Influence of Cl^-, Br^-, NO_3^- and SO_4^{2-} ions on the corrosion behaviour of 6061 Al alloy , "Bul. Mater. Sci., vol. 28, pp 253–258, June, 2005.
[10] N. Obi-Egbedi, I. Obot, S. Umoren, " Spondias mombin L. as a green corrosion inhibitor for aluminium in sulphuric acid: Correlation between inhibitive effect and electronic properties of extracts major constituents using density functional theory, " Arab. J. Chem., vol. 5, pp. 361–373, Sept. 2012.
[11] L. Nnanna, I. Anozie, A. Avoaja, C. Akoma, E. Eti, "Comparative study of corrosion inhibition of aluminium alloy of type AA3003 in acidic and alkaline media by Euphorbia hirta extract, " Afr. J. Pure Appl. Chem. vol.5, 265–271, Aug. 2011.
[12] D. Prabhu and R. Padmalatha, "Studies of corrosion of aluminium and 6063 aluminium alloy in phosphoric acid medium, " International Journal of Chem. Tech Research, vol. 5, 2690-270, Jan. 2013.
[13] R, Tolulope Loto and A, Adeleke, "Corrosion of Aluminum Alloy Metal Matrix Composites in Neutral Chloride Solutions, " J Fail. Anal. and Preven., vol. 16, pp. 874-885, July, 2016.
[14] E. Ghali, "Aluminum and Aluminum Alloys," in Uhlig's Corrosion Handbook, Second Edition, R.W. Revie, Ed. Wiley, Hoboken, 2000, pp. 677-715.
[15] I. Obot, N. Obi-Egbedi, S. Umoren, E. Ebenso, "Synergistic and antagonistic effects of anions and Ipomoea invulcrata as green corrosion inhibitor for aluminium dissolution in acidic medium, "Int. J. Electrochem. Sci., vol. 5, pp. 994–1007, July, 2010.
[16] L. Tomcsanyi, K. Varga, I. Bartik, G. Horanyi, E. Maleczki, "Electrochemical study of the pitting corrosion of aluminium and its alloys—II. Study of the interaction of chloride ions with a passive film on aluminium and initiation of pitting corrosion, " Electrochim. Acta, vol. 34, pp. 855-859, June, 1989.
[17] S. Pyun, S. Moon, S. Ahn, S. Kim, "Effects of Cl^- ,NO_3^- **and** SO^{2-} **ions on anodic dissolution of pure aluminum in alkaline solution**, " Corros. Sci., vol. 41, pp. 653-667, Apr. 1999.

Special Hperbolic Type Approximation for Solving of 3-D Two Layer Stationary Diffusion Problem

Ilmārs Kangro
Faculty of Engineering
Rezekne Academy of Technologies
Rezekne, Latvia
ilmars.kangro@rta.lv

Harijs Kalis
Institute of Mathematics and Computer sciences
University of Latvia
Riga, Latvia
harijs.kalis@lanet.lv

Ērika Teirumnieka
Faculty of Engineering
Rezekne Academy of Technologies
Rezekne, Latvia
Erika.Teirumnieka@rta.lv

Edmunds Teirumnieks
Faculty of Engineering
Rezekne Academy of Technologies
Rezekne, Latvia
Edmunds.Teirumnieks@rta.lv

***Abstract*—In this paper we examine the conservative averaging method (CAM) along the vertical z-coordinate for solving the 3-D boundary-value 2 layers diffusion problem. The special parabolic and hyperbolic type approximation (splines), that interpolate the middle integral values of piece-wise smooth function, is investigated. With the help of these splines the problems of mathematical physics in 3-D with respect to one coordinate are reduced to problems for system of equations in 2-D in every layer. This procedure allows reduce also the 2-D problem to a 1-D problem and the solution of the approximated problem can be obtained analytically. As the practical application of the created mathematical model, we are studying the calculation of the concentration of heavy metal calcium (Ca) in a two-layer peat block.**

Keywords*—conservative averaging method, finite-difference method, diffusion problem, special splines.

Introduction

The boundary value problems (BVP) described by PDE with piece-wise coefficients in multi-layered domains are currently the subject of studies [4]. The interest is often caused by problems in itself, but even more interesting are their solutions: mainly numerical ones, because analytical solutions can only be obtained in the ordinary sense (without changing the number of dimensions of the boundary-value problem) in the simplest cases [2]. The article deals with a universal method for solving the second order of partial differential equations – a consider conservative averaging method (CAM), the essence of which is a reduction in the number of dimensions of a given BVP, with a view to obtaining analytical expressions (formulas) of the solution. The further solution of the BVP includes a repeated reduction in the number of dimensions or applying of numerical methods to solve the acquired BVP. The unknown function is replaced by the approximated solution – the special spline with two different functions, which interpolate the middle integral values of piece-wise smooth function. The functions of the hyperbolic type spline are created and used with parameters that have to be chosen in the appropriate way to decrease the error of approximation of the solution. It should be noted that, in limit case when the parameters of spline function tends to zero we have the integral parabolic spline, obtained from A.Buikis [3]. The 2-D boundary value problem obtained by the conservative averaging method (CAM) was solved numerically using the finite-difference method in the case of parabolic and hyperbolic splines. A test example, a solution to the given 3-D boundary value problem, was created for numerical approbation of the averaging method, where the unknown function was a solution to the corresponding 1-D boundary value problem for two ODEs. The solution of ODEs' could be obtained both analytically (exact solution) and numerically by the averaging method using parabolic type and hyperbolic type splines. This in turn allowed a comparison of the analytical solution with the obtained numerical solutions.

Materials and methods

1.The Mathematical Model

The process of diffusion is considered in 3-D parallelepiped

$$\Omega = \{(x,y,z): 0 \le x \le l, 0 \le y \le L, 0 \le z \le Z\}$$

. The domain Ω consists of two layer medium. We will consider the stationary 3-D problem of the linear diffusion theory for multilayered piece-wise homogenous materials of N layers in the form $\Omega_i = \{(x,y,z): x \in (0,l)\ \ y \in (0,L)\ \ z \in (z_{i-1}, x_i)\}, i = \overline{1,N}$ where $H_i = z_i - z_{i-1}$ is the height of layer

Print ISSN 1691-5402
Online ISSN 2256-070X
http://dx.doi.org/10.17770/etr2019vol3.4079

$\Omega_i, z_0 = 0, z_N = Z$. The distribution of concentrations $c_i = c_i(x,y,z)$ in every layer Ω_i at the point $(x,y,z) = \Omega_i$ should be calculated by solving the following partial differential equation(PDE):

$$D_{ix}\partial^2 c_i/\partial x^2 + D_{iy}\partial^2 c_i/\partial y^2 + D_{iz}\partial^2 c_i/\partial z^2 + f_i(x,y,z) = 0, \quad (1.1)$$

D_{ix}, D_{iy}, D_{iz} are constant diffusion coefficients, $c_i = c_i(x,y,z)$ - the concentrations functions in every layer, $f_i(x,y,z)$ - the fixed sources functions. The values c_i and the flux functions $D_{iz}\partial c_i/\partial z$ must be continuous on the contact lines between the layers $z = z_i, \overline{i = 1, N-1}$:

$$c_i\big|_{z_i} = c_{i+1}\big|_{z_i}, \quad D_{iz}\partial c_i/\partial z\big|_{z_i} = D_{(i+1)z}\partial c_{(i+1)}/\partial z\big|_{z_i} \quad (1.2)$$

where $\overline{i = 1, N-1}$. The layered material is bounded above and below with the plane surfaces $z = 0, z = Z$ with fixed boundary conditions in following form:

$$D_{1z}\partial c_1(x,y,0)/\partial z = 0, \quad c_N(x,y,Z) = C_a(x,y), \quad (1.3)$$

or $c_1(x,y,0) = C_0(x,y), \quad c_N(x,y,Z) = C_a(x,y), \quad (1.4)$

$C_0(x,y)$, $C_a(x,y)$ are the given concentration-functions.

We have two forms of fixed boundary conditions in the x,y directions: 1) The periodical conditions by $x = 0, x = l$ (1.5):

$c_i(0,y,z) = c_i(l,y,z)$, $\partial c_i(0,y,z)/\partial x = \partial c_i(l,y,z)/\partial x$,

2) The symmetrical conditions by $y = 0, y = L$ (1.6): $\partial c_i(x,0,z)/\partial y = \partial c_i(x,L,z)/\partial y = 0$.

We will use the CAM and the finite difference (FD) method to solve the problem (1.1)-(1.6). These procedures allow reduce the 3-D problem to some 2-D boundary-value problem (BVP) for the system of partial differential equations with circular matrix in the x-direction.

2.The conservative averaging method with parabolic splines

The equation of (1.1) are averaged along the heights H_i of layers Ω_i and quadratic integral splines along z coordinate in the following form one used [3]

$$c_i(x,y,z) = C_i(x,y) + m_i(x,y)(z - \bar{z}_i) + e_i(x,y)G_i\left((z - \bar{z}_i)^2/H_i^2 - 1/12\right), \quad (2.1)$$

$G_i = H_i/D_{iz}$, $\bar{z}_i = (z_{i-1} + z_i)/2$. m_i, e_i, C_i - the unknown coefficients of the spline-function,

$C_i(x,y) = H_i^{-1}\int_{z_{i-1}}^{z_i} c_i(x,y,z)dz$ - the average values of $c_i, i = \overline{1,N}$.

After averaging the system (1.1) along every layer Ω_i we obtain

$$D_{ix}\partial^2 C_i/\partial x^2 + D_{iy}\partial^2 C_i/\partial y^2 + 2H_i^{-1}e_i + F_i(x,y) = 0, \quad (2.2)$$

$C_i(x,y) = H_i^{-1}\int_{z_{i-1}}^{z_i} c_i(x,y,z)dz$ - the average values of $f_i, i = \overline{1,N}$. From (1.1), (2.1) using boundary conditions (1.3) we can determine the unknown functions m_i, e_i. Therefore, from (2.2) we obtain the system of N partial differential equations (PDE), where the boundary conditions for C_i are determined from (1.4)-(1.5) in the x,y-directions for averaged values

$$C_i(0,y) = C_i(l,y), \ \partial C_i(0,y)/\partial x = \partial C_i(l,y)/\partial x \quad (2.3)$$

$$\partial C_i(x,0)/\partial y = \partial C_i(x,L)/\partial y = 0. \quad (2.4)$$

In the case $N = 2$ (two layers) we have (2.5):

$$e_1 = \left(9C_2 - (12 + 3/k)C_1 - 3C_a + (6 + 3/k)C_0\right)/(2G_2 + 2G_1),$$

$$e_2 = \left(9C_1 - (12 + 3k)C_2 + (6 + 3k)C_a - 3C_0\right)/(2G_2 + 2G_1),$$

$k = G_1/G_2$.

We have from (2.2) the following system of two PDE

$$\begin{cases} D_{1x}\partial^2 C_1(x,y)/\partial x^2 + D_{1y}\partial^2 C_1(x,y)/\partial y^2 + \\ 2H_1^{-1}e_1(x,y) + F_1(x,y) = 0, \\ D_{2x}\partial^2 C_2(x,y)/\partial x^2 + D_{2y}\partial^2 C_2(x,y)/\partial y^2 + \\ 2H_2^{-1}e_2(x,y) + F_2(x,y) = 0. \end{cases} \quad (2.6)$$

After resolving (2.6), the concentration functions $c_i = c_i(x,y,z)$ shall be obtained

$$c_1(x,y,z) = C_1(x,y) + m_1(x,y)(z - H_1/2) + e_1(x,y)G_1\left((z - H_1/2)^2/H_1^2 - 1/12\right), z \in [0, H_1]$$

$$c_2(x,y,z) = C_2(x,y) + m_2(x,y)(z - (2H_1 + H_2)/2) + e_2(x,y)G_2\left((z - (2H_1 + H_2)/2)^2/H_2^2 - 1/12\right), z \in [H_1, Z].$$

From (1.3) it is obtained

$$m_1(x,y) = e_1(x,y)/(3D_{1z}) + 2(C_1(x,y) - C_0(x,y))/H_1,$$

$$m_2(x,y) = -e_2(x,y)/(3D_{2z}) + 2(C_a(x,y) - C_2(x,y))/H_2$$

3.The conservative averaging method with hyperbolic type splines in 2 layers

The equation of (1.1) is averaged along the heights H_i of layers Ω_i using the hyperbolic type splines. Applying averaged method with respect to z we use the approximate solution with two fixed parametrical functions $f_{i1}, f_{i2}, i = \overline{1,2}$

$c_i(x,y,z) = C_i(x,y) + m_i(x,y) f_{i1}(z - \bar{z}_i) + e_i(x,y) + f_{i2}(z - \bar{z}_i)$,

$C_i(x,y) = H_i^{-1} \int_{z_{i-1}}^{z_i} c_i(x,y,z) dz$ - the averaged values, according to the definition of the spline function

$\int_{z_{i-1}}^{z_i} f_{i1}(z) dz = \int_{z_{i-1}}^{z_i} f_{i2}(z) dz = 0$,

$\bar{z}_i = (z_{i-1} + z_i)/2, z \in [z_{i-1}, z_i]$,

$f_{iz1} = \dfrac{0.5 H_i \sinh(a_i (z - \bar{z}_i))}{\sinh(0.5 a_i H_i)}$,

$f_{iz2} = \dfrac{\cosh(a_i (z - \bar{z}_i)) - A_i}{8 \sinh^2(0.5 a_i H_i)}$,

$A_i = \dfrac{0.5 \sinh(0.5 a_i H_i)}{a_i L / 2}, i = \overline{1,2}$.

$a_i > 0$ are fixed parameters (unknown). It should be noted if parameters a_i tend to zero then the integral parabolic spline from [3] is obtained in the limit case. The unknown functions $m_i(x,y)$ $e_i(x,y)$ we can determined from boundary conditions at $z = 0, z = Z$:

$d_{iz} = 0.5 H_i a_i \coth(0.5 a_i H_i)$

$k_{iz} = 0.25 a_i \coth(0.25 a_i H_i)$

$C_1 - 0.5 m_1 H_1 + e_1 b_{1z} = C_0$

$C_2 + 0.5 m_2 H_2 + e_2 b_{2z} = C_a$

$b_{iz} = \dfrac{\cosh(0.5 a_i H_i) - A_i}{8 \sinh^2(0.25 a_i H_i)}$

$D_{1z}(m_1 d_{1z} + e_1 k_{1z}) = D_{2z}(m_2 d_{2z} - e_2 k_{2z})$

$C_1 + 0.5 m_1 H_1 + e_1 b_{1z} = C_2 - 0.5 m_2 H_2 + e_2 b_{2z}$,

$m_1 = 2(C_1 + b_{1z} e_1)/H_1$.

Thus we have a system of 2 algebraic equations for determining $e_i, i = \overline{1,2}$:

$b_{11} e_1 + b_{12} e_2 = b_3 C_a + b_4 C_0 - b_3 C_2 - b_4 C_1$

, $b_{21} e_1 + b_{22} e_2 = 2C_2 - 2C_1 - C_a + C_0$, where

$b_{11} = b_4 b_{1z} + k_{1z}$, $b_{12} = b_3 b_{2z} + D_{21} k_{2z}$, $b_{21} = 2 b_{1z}$

, $b_{22} = -2 b_{2z}$, $b_3 = 2 D_{21} d_{2z} / H_2$, $b_4 = 2 d_{1z} / H_1$,

$D_{21} = D_{2z} / D_{1z}$.

The solution for e_1, e_2 is:

$e_1 = b_{17} C_1 + b_{18} C_2 + d_4 C_a + d_6 C_0$

, $e_2 = b_{27} C_1 + b_{28} C_2 + d_5 C_a + d_7 C_0$, where

$b_{17} = (-b_4 b_{22} + 2 b_{12})/\det$, $b_{18} = (-b_3 b_{22} - 2 b_{12})/\det$

, $b_{27} = (b_4 b_{21} - 2 b_{11})/\det$, $b_{28} = (b_3 b_{21} + 2 b_{11})/\det$

, $d_4 = (b_3 b_{22} + b_{12})/\det$, $d_6 = (b_4 b_{22} - b_{12})/\det$,

$d_5 = -(b_3 b_{21} + b_{11})/\det$, $d_7 = (-b_4 b_{21} + b_{11})/\det$,

$\det = b_{11} b_{22} - b_{21} b_{12}$.

The 2-D boundary-value problem is in following form:

$$\begin{cases} \dfrac{\partial}{\partial x}\left(D_{1x} \dfrac{\partial C_1}{\partial x}\right) + \dfrac{\partial}{\partial y}\left(D_{1y} \dfrac{\partial C_1}{\partial y}\right) + b_5 e_1 + F_1 = 0, \\ \dfrac{\partial}{\partial x}\left(D_{2x} \dfrac{\partial C_2}{\partial x}\right) + \dfrac{\partial}{\partial y}\left(D_{2y} \dfrac{\partial C_2}{\partial y}\right) + b_6 e_2 + F_2 = 0, \\ \dfrac{\partial c_{iz}(0,y)}{\partial x} = \dfrac{\partial c_{iz}(x,0)}{\partial y} = 0, c_{iz}(l,y) = c_{iz}(x,L) = 0, \end{cases} \quad (3.1)$$

where $b_5 = 2 D_{1z} k_{1z} / H_1$, $b_6 = 2 D_{2z} k_{2z} / H_2$.

4.The finite-difference method for two layers with parabolic type splines

We consider an uniform grid $(N_x \times (N_y + 1))$ [7],

$$\omega_h = \left\{ \begin{array}{l} (x_i, y_j), x_i = h_x, y_j = (j-1) h_y, i = \overline{1, N_x}, \\ j = \overline{1, N_y + 1}, N_x h_x = l, N_y h_y = L \end{array} \right\}.$$

Subscripts (i, j) refer to x, y indices; the mesh spacing in the x_i, y_j directions is h_x, h_y . For two layers ($N = 2$) we can the PDEs (2.6) rewritten in following vector form:

$$D_x \partial^2 C / \partial x^2 + D_y \partial^2 C / \partial y^2 - AC + F = 0 \quad , \quad (4.1)$$

where D_x, D_y are the 2 order diagonal matrices with elements D_{1x}, D_{2x} and D_{1y}, D_{2y} . A is the matrix of second order, C is the 2nd order vectors-column with elements C_1, C_2 and F is the 2 order vectors-column with following elements :

$$\begin{pmatrix} F_1 - \left(\left(6 + 3k^{-1}\right) C_0 - 3C_a\right)/(H_1 d_1) \\ F_1 + \left((6 + 3k) C_a - 3C_0\right)/(H_2 d_1) \end{pmatrix}^T ,$$

$$A = \frac{1}{d_1} \begin{pmatrix} \left(12 + 3k^{-1}\right)/H_1 & -9/H_1 \\ -9/H_2 & (12 + 3k)/H_2 \end{pmatrix} ,$$

$(d_1 = G_2 + G_1)$. The equation (4.1) with periodical conditions (2.4) for vector function C in the uniform grid (x_i, y_j) is replaced by vector difference equations of second order approximation in 3- point stencil [1]:

$$\boldsymbol{A} \ W_{j-1} - \boldsymbol{C} \ W_j + \boldsymbol{B} \ W_{j+1} + F_j = 0 , \quad (4.2)$$

where W_j are vectors-column

$\left(W_j \approx \left(C_{1,j}, C_{2,j}, ..., C_{N_x,j}\right)^T\right)$, F_j are vectors-column with elements $\left(F_{1,j}, F_{2,j}, ..., F_{N_x,j}\right)^T, \overline{j = 2, N_y}$

, $AA, CC, BB = AA$ are the block- matrices of second

order with the elements of the circular symmetric matrix with $N_x = M$ -order in the following form (it is possible to define the circular matrix with the first row that is in the form $A = [a_1, a_2, ..., a_M]$):

$$\boldsymbol{A} = \begin{pmatrix} [D_{1y}/h_y^2, 0, ..., 0] & 0 \\ 0 & [D_{2y}/h_y^2, 0, ..., 0] \end{pmatrix},$$

$$\boldsymbol{C} = \begin{pmatrix} \boldsymbol{c}_1 & \boldsymbol{c}_2 \\ \boldsymbol{c}_3 & \boldsymbol{c}_4 \end{pmatrix},$$

where the circular matrices $\boldsymbol{c}_1, \boldsymbol{c}_2, \boldsymbol{c}_3, \boldsymbol{c}_4$ are

$$cc_1 = \begin{bmatrix} 2(D_{1x}/h_x^2 + D_{1y}/h_y^2) + (12 + 3k^{-1})/(H_1 d_1), -D_{1x}/h_x^2, \\ 0, ..., 0, -D_{1x}/h_x^2 \end{bmatrix}$$

$$cc_2 = [-9/(H_1 d_1), 0, ..., 0], \quad cc_3 = [-9/(H_2 d_1), 0, ..., 0],$$

$$cc_4 = \begin{bmatrix} 2(D_{2x}/h_x^2 + D_{2y}/h_y^2) + (12 + 3k)/(H_2 d_1), \\ -D_{2x}/h_x^2, 0, ..., 0, -D_{2x}/h_x^2 \end{bmatrix}.$$

The boundary conditions (2.4) are replaced by difference equations of first order approximation:

$$C(x, h_y) = C(x, 0) + O(h_y^2), \quad C(x, L) = C(x, L - h_y) + O(h_y^2).$$

5.The finite-difference method for two layers with hyperbolic type splines

The vector F and matrix A in (4.1) are

$$F_1 + b_5 d_4 C_a + b_5 d_6 C_0, \; F_2 + b_6 d_5 C_a + b_6 d_7 C_0,$$

$$A = \begin{pmatrix} a_{11} & a_{12} \\ a_{21} & a_{22} \end{pmatrix}, \text{ where}$$

$$a_{11} = -b_5 b_{17}, \; a_{12} = -b_5 b_{18}, \; a_{21} = -b_6 b_{27},$$

$$a_{22} = -b_6 b_{28}.$$

The circular matrices $\boldsymbol{c}_i$ are $a_{22} = -b_6 b_{28}$

$$cc_1 = \begin{bmatrix} 2(D_{1x}/h_x^2 + D_{1y}/h_y^2) + a_{11}, \\ -D_{1x}/h_x^2, 0, ..., 0, -D_{1x}/h_x^2 \end{bmatrix},$$

$$cc_2 = [a_{12}, 0, ..., 0], \quad cc_3 = [a_{21}, 0, ..., 0],$$

$$cc_4 = \begin{bmatrix} 2(D_{2x}/h_x^2 + D_{2y}/h_y^2) + a_{22}, \\ -D_{2x}/h_x^2, 0, ..., 0, -D_{2x}/h_x^2 \end{bmatrix}.$$

We use $a_1 = 15, a_2 = 13$.

6. The numerical methods

The vectors-column W_j from (4.2) is calculated on Thomas algorithm [9] in the matrix form using MATLAB.

$$W_j = X_j W_{j+1} + Y_j = 0, \; j = N_y(-1)1, \quad (6.1)$$

where X_j, Y_j are corresponding matrices and vectors, obtaining of following expressions (6.2):

$$X_j = (\boldsymbol{C}_j - \boldsymbol{A}_j X_{j-1})^{-1} \boldsymbol{B}_j,$$

$$Y_j = (\boldsymbol{C}_j - \boldsymbol{A}_j X_{j-1})^{-1} (\boldsymbol{A}_j Y_j + F_j), \quad j = 2(1) N_y$$

Here $X_1 = E$, v, $W_{\overline{N}+1} = (E - X_{\overline{N}})^{-1} Y_{\overline{N}}$, $(\overline{N} = N_y)$,

where $E = \begin{pmatrix} [1, 0, ..., 0] & 0 \\ 0 & [1, 0, ..., 0] \end{pmatrix}$.

The inverse matrix of $A = \begin{pmatrix} A_1 & A_2 \\ A_3 & A_4 \end{pmatrix}$ is $B = A^{-1}, (BA = AB = E)$, $B = \begin{pmatrix} B_1 & B_2 \\ B_3 & B_4 \end{pmatrix}$, where

$$B_4 = (A_4 - A_3 A_1^{-1} A_2)^{-1}, \quad B_2 = -A_1^{-1} A_2 B_4,$$

$$B_1 = (A_1 - A_2 A_4^{-1} A_3)^{-1}, \; B_3 = -A_4^{-1} A_3 B_1.$$

The others operations with circular matrices and vectors of the second order can be easy obtain [6].

Results and discussion

1. Approbation of numerical algorithms

The special solution in the form $c_1(x, y, z) = g_1(z) \cos(\pi y / L) \sin(2\pi x / l)$, $c_2(x, y, z) = g_2(z) \cos(\pi y / L) \sin(2\pi x / l)$ of the PDE (1.1) was designed, where functions $g_1(z)$ $g_2(z)$ was the solution of the following boundary value problem for two ODE (for boundary condition (1.3)):

$$g_1''(z) - a_1^2 g_1(z) = 0, \; g_1(0) = 0, \; g_2''(z) - a_2^2 g_2(z) = 0$$

$$, g_2(Z) = 1, \; g_1(H_1) = g_2(H_1), \quad (7.1)$$

$D_{1z} g_1'(H_1) = D_{2z} g_2'(H_1)$, where

$$a_1 = \pi \sqrt{\left(\frac{4D_{1x}}{l^2} + \frac{D_{1y}}{L^2} \right) / D_{1z}},$$

$$a_2 = \pi \sqrt{\left(\frac{4D_{2x}}{l^2} + \frac{D_{2y}}{L^2} \right) / D_{2z}}.$$

The analytical solution of boundary-value problem of ODEs (7.1) is [5]:

$$g_1(z) = P_1 \sinh(a_1 z), \quad (7.2)$$

$g_2(z) = P_2 \cosh(a_2 z) + P_3 \sinh(a_2 z)$, where the constants are:

$$P_1 = \frac{P_2 \cosh(a_2 H_1) + P_3 \sinh(a_2 H_1)}{\sinh(a_1 H_1)},$$

$$P_2 = \frac{1 - P_3 \sinh(a_2 Z)}{\cosh(a_2 Z)},$$

$$P_3 = \frac{\cosh((a_1 - a_2)H_1)a_1 D_{1z}}{\sinh(a_2 H_2 + a_1 H_1)a_2 D_{2z}} + \frac{\sinh(a_1 H_1)\sinh(a_2 H_1)(a_1 D_{1z} - a_2 D_{2z})}{\sinh(a_2 H_2)\cosh(a_1 H_1)(a_1 D_{1z} - a_2 D_{2z})}.$$

Based on the literature source [4], it can be proofed that the solution to the BVP (7.1), obtained by hyperbolic spline function, coincides with the analytical (exact) solution (7.2) of the BVP (7.1).

2. Some numerical results

Measurements of peat samples for the determination of heavy metals – iron and calcium concentrations were carried out in the swamp of the Vilani municipality Knavu swamp. Peat analyses have been performed with the OPTIMA 2100 MS ICP/OES Spectrometer of the inductively associated plasma optic emission spectrometer of the Perkin Elmer firm in the laboratories of the Geotechnology and Eco-Industrial Research Centre of Rezekne Academy of Technologies [8]. We consider the metal concentration in the 2 layered peat blocks Ω with following measure:

$L = l = 1m$, $H_1 = 1m$, $H_2 = 1.5m$,

$Z = H_1 + H_2 = 2.5m$.

On the top of the earth $(z = Z)$ we have the measured concentration $c[mg/kg]\times 1000$ of calcium (Ca) in the following points in the (x, y) plane:

$c(0.1, 0.2) = 0.62$, $c(0.5, 0.2) = 0.57$,

$c(0.9, 0.2) = 0.43$, $c(0.1, 0.8) = 0.51$,

$c(0.5, 0.5) = 0.43$, $c(0.9, 0.5) = 0.64$,

$c(0.1, 0.5) = 0.58$, $c(0.5, 0.8) = 0.44$,

$c(0.9, 0.8) = 0.72$.

This date are smoothing by 2D interpolation with MATLAB operator, using the spline function. We use following diffusion coefficients in the layers:

$D_{1z} = 10^{-3}$, $D_{2z} = 5\cdot 10^{-4}$, $D_{1x} = D_{2x} = 10^{-4}$,

$D_{1y} = D_{2y} = 10^{-5}$. We can see the distribution of concentration c in the (x, y) plane for Ca at $z = H_1$ for hyperbolic (Fig. 1) and parabolic (Fig. 2) spline.

We can see the distribution of concentration c in the (x, y) plane for Ca at $z = H_1$ for hyperbolic (Fig. 1) and parabolic (Fig. 2) spline, in the Fig. 3 – the averaged concentration C_2 within the second layer for hyperbolic spline, in the Fig. 4 – concentration's c curves at $y = L/2$ for hyperbolic spline.

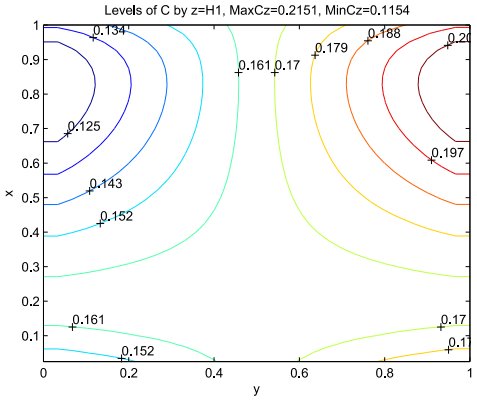

Fig. 1. Levels of c at $z = H_1$ for hyperbolic spline.

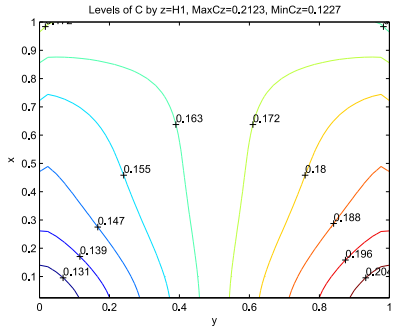

Fig. 2. Levels of c at $z = H_1$ for parabolic spline.

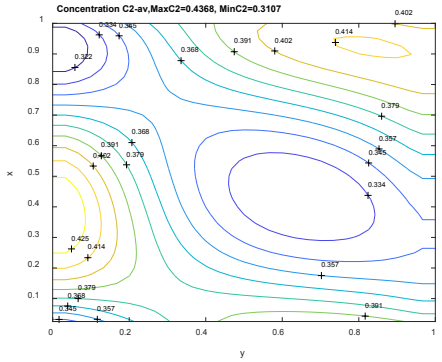

Fig. 3.The averaged concentration C_2 within the second layer for hyperbolic spline.

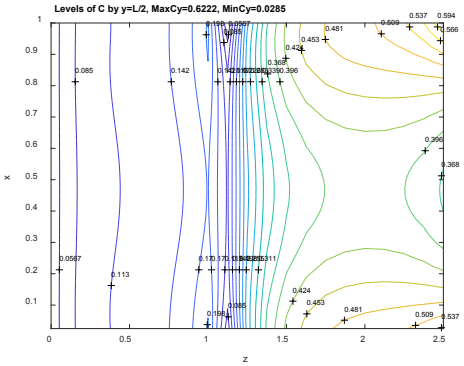

Fig. 4. Concentration's c curves at $y = L/2$ for hyperbolic spline.

Conclusions

1. The 3D diffusion problem in N layered domain described by a boundary value problem of the system of PDEs with piece-wise constant diffusion coefficients are approximated on the boundary value problem of a system of N PDEs. The last mentioned system is solved due to the finite difference method.
2. For reducing the 3D diffusion problem to 2D boundary value problem of a system of PDEs the conservative averaging method (CAM) along the vertical z-coordinate by using parabolic type splines and newly designed special hyperbolic and type splines is studied.
3. The calculation process compared the effectiveness of the parabolic and hyperbolic splines usage for 3D diffusion problem reduction to 2D boundary value problem and resulted in higher accuracy of the approximated solution directly with hyperbolic type splines.
4. A Test example has been created allowed a comparison of the analytical (exact) solution of the 1-D BVP with the numerically obtained solutions of parabolic type splines and hyperbolic type splines, to assess their accuracy. It was found that the solution obtained by hyperbolic splines functions coincided with the analytical solution of the 1-D problem under consideration. This indicates the usefulness of the further usage of the CAM for solving BVP problems with the hepl of hyperbolic type splines compared to the previously widely used parabolic type splines.
5. The theoretical and practical problem studied makes it possible to obtain an engineering algorithm for mathematical modelling mass transfer processes in multilayered domain.
6. The results of the numerical experiments can give some new physical conclusions about the distribution of metals concentration in different layered peat blocks.

References

[1] .N. S. Bahvalov, N. P. Zhitkov and G. M. Kobelhkov, Numerical methods. M.: Nauka, 1987 (in Russian).

[2] J. Bear, Hydraulic of groundwater. Mc.Graw-Hill Inc., 1979.

[3] A. Buikis, "The approximation with splines for problems in layered systems," in Acta Universitatis Latviensis, Vol. 592, Riga, 1994, pp. 135-138 (in Latvian).

[4] A. Buikis, "The analysis of schemes for the modelling same processes of filtration in the underground, " in Acta Universitatis Latviensis, Vol. 592, Riga, 1994, pp. 25-32 (in Latvian).

[5] C. Henry Edwards and David E. Penny, Differential equations and boundary value problems, computing and modelling. Pearson, Prentice Hal, third edition, 2008 (in Russian).

[6] H. Kalis, A. Buiķis,A. Aboltins and I. Kangro, "Special Splines of Hyperbolic Type for the Solutions of Heat and Mass Transfer 3-D Problems in Porous Multi-Layered Axial Symmetry Domain," Mathematical Modelling and Analysis, vol. 22, issue 04, pp. 425-440, 2017.

[7] A. A. Samarskij, Theory of finite difference schemes. M.: Nauka, 1977 (in Russian).

[8] Ē. Teirumnieka, M., Kļaviņš and E. Teirumnieks, "Major and trace elements in peat from bogs of east Latvia," in Mires and Peat /Ed. Māris Kļaviņš, Riga: University of Latvia Press, 2010, pp. 115-124.

[9] J. W.Thomas, Numerical partial differential equations. Finite difference methods. New-York: Springer-Verlag, Inc., 1995.

Environment. Technology. Resources. Rezekne, Latvia
Proceedings of the 12th International Scientific and Practical Conference. Volume III, 101-104

Contactless Measuring of Temperature with Differential Photo Receiver

Tsanko Karadzhov
Department of Mechanical and Precision Engineering
Technical University of Gabrovo
Gabrovo, Bulgaria
karadjov_s@abv.bg

Dimcho Pulov
Department of Mechanical and Precision Engineering
Technical University of Gabrovo
Gabrovo, Bulgaria
pulov@mail.bg

Nikolay Angelov
Department of Pysics, Chamistry and Ecology
Technical University of Gabrovo
Gabrovo, Bulgaria
angelov_np@abv.bg

***Abstract*—A method for contactless temperature measurement has been created with two photo receivers with different spectral sensitivity. An algorithm for processing the signals from both receivers of a single-chip microprocessor system has been developed. An optical system for the LWIR diapason of the spectrum is proposed.**

Keywords — differential photo receiver, temperature, method, IR diapason, lens design.

I. Introduction

Temperature is one of the basic parameters to be measured and controlled in modern manufacture. It is increasingly important to acquire contactless methods for temperature measurement based on the registration of the thermal radiation of objects.

Planck law, Wien law, Rayleigh-Jeans law and Stefan-Boltzmann law are known to determine the magnitude and spectral distribution of the energetic luminosity of the heated object in terms of its temperature. These laws are used to solve the forward problem. Pyrometry is one area of science which solves the inverse problem - to find temperature of objects by the magnitude or by the spectral distribution of the energy flux emitted by them.

Two basic methods can be used to solve this problem. First method (radiation) – temperature is determined by the magnitude of the optical flux emitted by the object. Second method (method of spectral ratio) – temperature is determined by the spectral characteristics of the optical flux emitted by the object [1], [4].

At present radiation pyrometers are the largest group of non-contact temperature measurement devices. However, they have a few significant limitations. The main limitation is the dependence of the flux falling on the pyrometer from two unknown quantities: the actual temperature of the object T_{obj} (to be measured) and its emissivity coefficient ε.

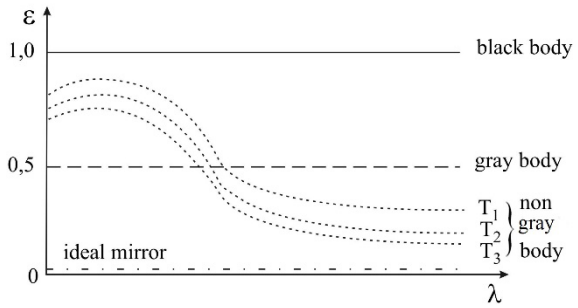

Fig. 1. Emissivity coefficient of different bodies

Emissivity coefficient of all bodies can be varied from 0% for ideal mirrors and up to 100% for black bodies (fig. 1).

Most of the measured objects are "non-gray" bodies. Therefore, their emissivity coefficient depends on the wavelength λ. In addition, the emissivity coefficient depends on the temperature of the object T_{obj}. Therefore $\varepsilon = f(\lambda, T)$. This implies uncertainty in the measurement results and difference ΔT between the actual temperature of the object T_{obj} and the measured one T_{meas} ($T_{meas} = T_{obj} - \Delta T$). The dependence

$$T_{obj} = \frac{T_{meas}}{\sqrt[4]{\varepsilon(T)}}, \text{ or } \frac{\Delta T}{T_{obj}} = 1 - \sqrt[4]{\varepsilon(T)}$$

is valid for radiation pyrometers where $\varepsilon(T)$ is the integral emissivity coefficient in the operational spectral diapason of device $\Delta\lambda$.

$$\text{If } \varepsilon(T) = 100\%, \text{ then } \frac{\Delta T}{T} = 0;$$

$$\varepsilon(T) = 85\%, \text{ then } \frac{\Delta T}{T} = 4\%;$$

$$\varepsilon(T) = 40\%, \text{ then } \frac{\Delta T}{T} = 20\%;$$

As can be seen, the error due to the unknown emissivity coefficient can be great. Therefore the value

Print ISSN 1691-5402
Online ISSN 2256-070X
http://dx.doi.org/10.17770/etr2019vol3.4132

$\varepsilon(T)$ of the object being measured is introduced to radiation pyrometers.

The actual value of the coefficient $\varepsilon(T)$ is determined by the equation

$$\varepsilon(T) = \frac{\int_{\Delta\lambda} \varepsilon(\lambda, T) s(\lambda) R_{bb}(\lambda, T) d\lambda}{\int_{\Delta\lambda} s(\lambda) R_b(\lambda, T) d\lambda},$$

where $\varepsilon(\lambda, T)$ is a spectral emissivity coefficient of the object, $s(\lambda)$ - spectral sensitivity of the photo receiver used in the pyrometer, $R_{bb}(\lambda, T)$ - spectral density of the energetic luminosity of an black body (BB).

There is ambiguity in determining the coefficient $\varepsilon(T)$ due to its complex dependence on λ and T. Therefore it is practically impossible to enter this coefficient correctly when using radiation pyrometers and the error in temperature measurement can reach tens of percent [3].

Pyrometers of spectral ratio (PSR), which are the subject of the present paper, have no such limitations.

The purpose of the present paper is to introduce a two-spectral pyrometer (dual spectrum pyrometer or pyrometer of spectral ratio) in order to increase the accuracy of contactless temperature measurement as compared to the commonly used radiation pyrometers.

The goal set can be reached by accomplishing the following tasks:

- Choice and development of a functional block chart of the pyrometer;
- Development of a basic electrical circuit diagram of the pyrometer;
- Development of a device control algorithm.

II. EXPOSITION

1. The essence of the two-spectral method

The method consists in measuring the ratio of the signals from the controlled object for two narrow spectral ranges and comparing it with the ratio of the signals for the same spectral range (diapason), but obtained for an black body (fig. 2).

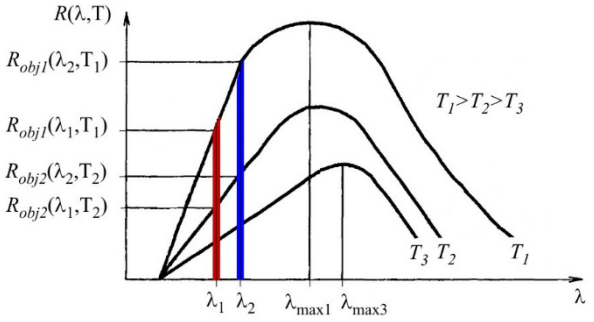

Fig. 2. The essence of the spectral method

The temperature measured T_{meas} is numerically equal to the temperature of the BB (black body) where the ratio of the spectral densities $R_{bb}(\lambda, T)$ for two narrow spectral ranges is equal to the same ratio, but for the controlled object at its actual temperature T_{obj}.

Therefore, the ratio between the electrical signals at the output of the two photo receivers can be expressed as follows:

$$\frac{u_1}{u_2} = \frac{R_{bb}(\lambda_1, T_{meas})}{R_{bb}(\lambda_2, T_{meas})} = \frac{R_{obj}(\lambda_1, T_{obj})}{R_{obj}(\lambda_2, T_{obj})} = \frac{R_{bb}(\lambda_1, T_{obj})\varepsilon_{\lambda_1}}{R_{bb}(\lambda_2, T_{obj})\varepsilon_{\lambda_2}}. \quad (1)$$

In (1) the spectral densities R will be expressed by the law of Wein, which is valid for the short wavelength range of the spectrum (under the condition that $\lambda \cdot T < C_2$).

$$R(\lambda, T) = C_1 \lambda^{-5} \exp^{-\frac{C_2}{\lambda T}} \quad (2)$$

From (1) and (2) an equation can be obtained for the relationship between the actual and the measured object temperature

$$\frac{1}{T_{obj}} - \frac{1}{T_{meas}} = \frac{\lambda_1 \lambda_2}{C_2(\lambda_2 - \lambda_2)} \ln(\varepsilon_1 / \varepsilon_2). \quad (3)$$

From (3) follows that:

- For gray bodies $T_{obj} = T_{meas}$. Certain bodies that are in two close spectral diapasons can be accepted as gray;
- For non-gray bodies the correct determination of T_{obj} depends not on the absolute value of the refractive index, but on the ratio $\varepsilon_1 / \varepsilon_2$. This ratio is more stable when changing the external conditions by changing the absolute value of the integral emissivity coefficient $\varepsilon(T)$ used in radiation pyrometers.

2. Choice and development of a function circuit diagram of a two-spectral pyrometer.

The function circuit of the two-spectral pyrometer can be created in two variants depending on the means of signal generation in the two spectral diapasons. In the first case a beam splitting device and two separate photo receivers are used. In the second case one tandem structured photo receiver ("sandwich" type) is used. In the latter case no beam splitting device is used. There is a different dependence of the current in dark environment from the temperature for the two spectral diapasons. This will increase the measurement error. For this reason, the circuit with two separate photo receivers and a beam splitting device is used in the developed pyrometer.

Fig. 3 shows the function circuit of the developed two-spectral pyrometer. The heated object emits a flux in a hemisphere. Part of the flux falls on the pyrometer's lens and focuses on the beam splitting device.

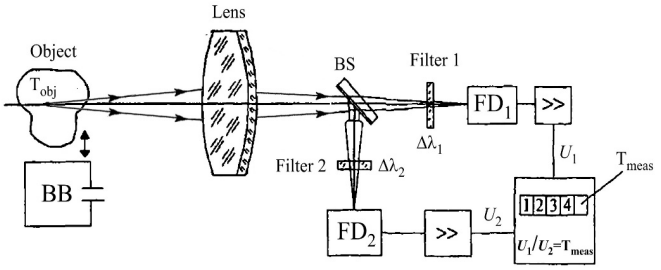

Fig. 3.

The lens is an achromatic doublet AC254-100-B-ML from the Thorlabs catalog. The beamsplitter is an interference filter which partially passes and partially reflects the radiation. About of beamsplitter was selected a translucent sheet BSW11 from the *Thorlabs* catalog. It is made of quartz glass (Fused Silica) and divides the optical flow in a 50:50 ratio. The device divides the optical signal between the two photo receivers. Each photo receiver has a light filter. Two identical silicone photodiodes are selected as photo receivers *Hamamatsu S2386.* As filters from the catalog of Thorlabs are selected accordingly: filter 1 - FB900-10 (Center Wavelength *CW=900nm*; Full Width Half Max *PWHM=10nm* and filter 2 - FB1000-10 (*CW=1000nm;PWHM=10nm)*. The photodiodes produce electrical signals proportional to the optical flux. These signals are amplified in an electronic processing unit, and then their ratio is determined which is subsequently converted to a value of the measured temperature of the controlled object T_{meas} .

3. Development of basic electrical circuit of the two-spectral pyrometer.

Fig. 4 shows the basic electrical circuit of the device. Silicon photodiodes are used as photo receivers.

The photoelectric current I_{ph} through the photodiodes is transformed into a voltage by means of feedback amplifiers LM258:

$$U_0 = I_{ph} \cdot R_f \quad (4)$$

where U_0 is the voltage at the output of the amplifier, R_f - feedback resistance.

The feedback of the operational amplifier is selected so as to use the entire measurement range of the analog-to-digital converter of the controller.

The 8-bit PIC18F452 microcontroller which has a 10-bit analog-to-digital converter is used to control the device operation. The controller has a sufficient number of input-output ports and a sufficient amount of program memory where the control program can be located.

The threshold voltages that determine the measurement range of the converter are respectively V_{REF}=0 V and V_{REF}+ = 5 V. The input analog signal to ADC is expressed as 2^{10} or 1024 levels. The increase in voltage is determined by the formula:

$$\Delta U = \frac{V_{REF+}}{2^{10}} = \frac{5}{1024} = 4{,}883\ mV \quad (5)$$

The device functional circuit consists of two measuring channels. The voltage from the outputs of the current-to-voltage converters is fed to two analog inputs of the controller RA0/AN0 and RA1/AN1. The inputs switch. At any moment of time voltage is measured at one input only.

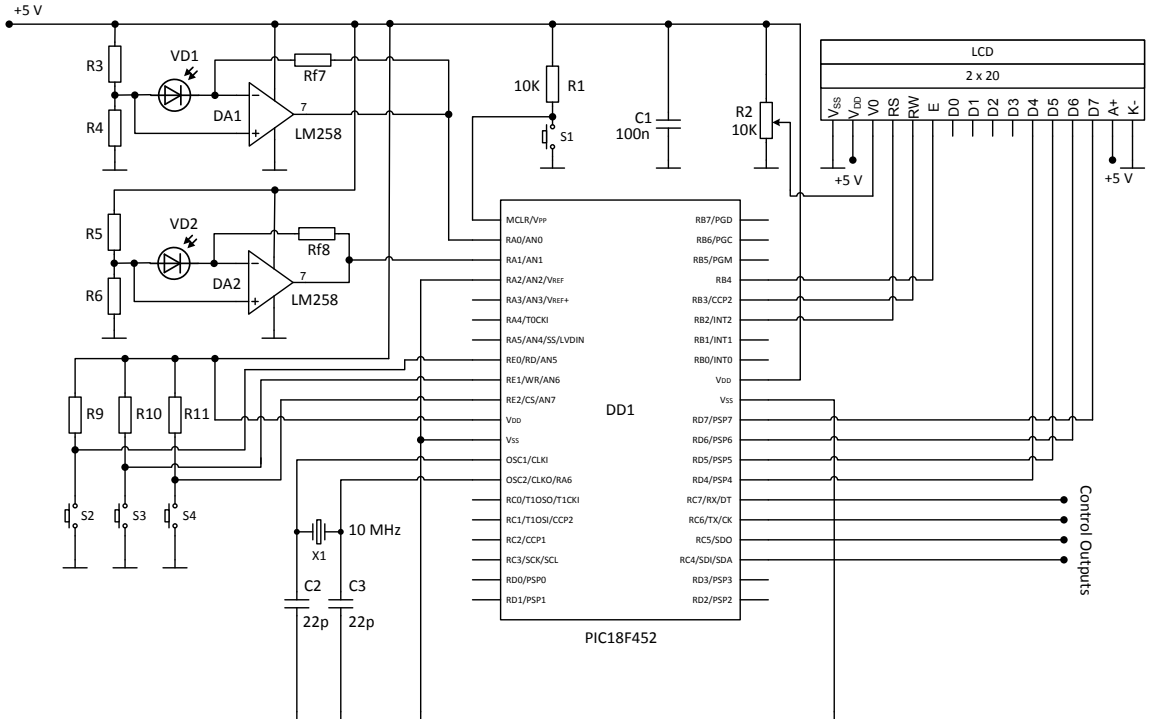

Fig. 4.

4. Development of a block chart of the program algorithm.

The block chart of the control program algorithm is shown in fig. 5. [7]. First, the controller is initialized, constants and variables are defined and corresponding cells from the data memory are reserved for them. The next stage of the block chart is related to determining the I/O ports to be used. Digital inputs, analog inputs and digital outputs are determined. PIC18F452 has 4 internal module timers. Only Timer 0 is used. It sets time lags in the program which are used to synchronize the operation of the microcontroller and the alphanumeric LCD. Next, an initialization of the display is performed. The master program is a continuous loop, which stops only when the voltage measurement from the ADC (analog-to-digital converter) has been completed.

The processing of the result of each measurement takes place in a subroutine, which starts when an ADC break occurs.

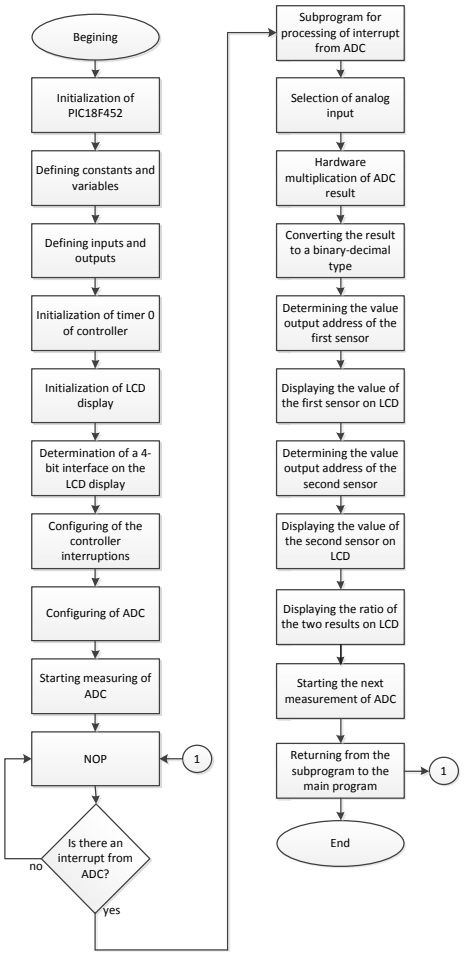

Fig. 5. Control program algorithm

Subroutine for processing ADC break

At the beginning of the subroutine an analog input for the next measurement is selected. The result of the previous measurement is then processed, which includes – hardware multiplication of the measurement value by a preset constant. The ratio U_1 / U_2 between the voltages measured in the two channels is determined. The result is converted from hexadecimal to binary-decimal code.

The second stage of the subroutine is related to outputting the measurement results on an LCD display. First, the output addresses are defined, it means - to determine in which position to display each digit from the result, including the decimal points. The values of the calculations are then displayed. Finally, a subsequent measurement is started in the subroutine and then returning to the master program takes place.

Connecting to the microcontroller and controlling the LCD display

The display used is a two-line, alphanumeric, liquid crystal display, with 20 characters per line. It is a smart display with its own control scheme – LCD driver hd44780. The display has a total of 16 ports to enable power supply and connection to an external microcontroller. For controlling the LCD module a control bus is used comprising RS, R/W, E ports which are correspondingly connected to microcontroller ports RB2, RB3, RB4 initialized as digital outputs. The data bus of this type of display consists of 8 ports. The microcontroller communicates with the LCD module by means of the data bus. In this case a mode is selected for this communication to take place using 4-bit interface. The DB4, DB5, DB6, DB7 display ports are initialized as inputs and correspondingly connected to the microcontroller's RD4, RD5, RD6, RD7 ports which are initialized as outputs. At the beginning of the program, initialization of the display takes place, which selects the following:

- 4-bit interface;
- two-line mode;
- character format 5x8 dots;
- incrementing the address counter by one unit when in read/record mode

III. Conclusion

A two-spectral pyrometer with two identical silicon photodiodes and a beam splitter has been developed. The use of this circuit reduces the influence of external conditions on the measurement error. The device is intended for high temperature measurements ranging from 700 ºC to 1500 ºC. The spectral diapasons of the two channels are separated by narrowband filters, thus increasing the accuracy of the measurement.

References

[1] Lisiyenko V.G., Shleymovich YE.M., Ladygichev M.G., Sannikov S.P., Shchelokov Ya.M. Temperatura: teoriya, praktika, eksperiment. Spravochnoye izdaniye: V 3-kh tomakh. T.1, kniga 2 – M.: Teplotekhnik, 2009 – 340 s.

[2] Frunze A.V. Vliyaniye metodicheskikh pogreshnostey pirometra na vybor pribora, Fotonika – 2012. - № 3 – S.46-51; № 3 – S.56-60.

[3] Frunze A.V. Pirometry spektral'nogo otnosheniya: preimushchestva, nedostatki i puti ikh ustraneniya, Fotonika – 2009. -№ 4 – S.32-37.

[4] Belen'kiy A.M., Dubinskiy M.Yu., Ladygichev M.G., Lisiyenko V.G., Shchelokov Ya.M. Izmereniye temperatury: teoriya, praktika, eksperiment. Spravochnoye izdaniye: V 3-kh tomakh. T.2 – M.: Teplotekhnik, 2007 – 736 s.

[5] A. Sala, Radiant properties of materials, Elsevier Publishing, Oxford, 1986.

[6] Lyubomir Lazov, Nikolay Angelov, Numerical experiments for determining of laser inducion temperature fields, Turkish Journal of Physics, 37, 212-218, Turkey, 2013

[7] Karadzhov, Ts. V., I. S. Balabanova, M. S. Slavov, Multi-channel electronic device for temperature monitoring. Elektrotechnica & Elektronica, Vol. 48. No 1-2/2013, ISSN 0861-4717.

[8] Chrzanowski, K., Non-Contact Thermometry. Measurement Errors. SPIE Polish Chapter, Warsaw, 2001

Fractal Properties of Microplasma Breakdown and Structural Heterogeneity of Semiconductor Materials

Samuil Khanin
Herzen State Pedagogical University of RussiaSt.Petersburg, Russia
antodinik@gmail.com

Antonina Shashkina
St.Petersburg State University of Film and Television
St.Petersburg, Russia
shashkinaas@yandex.ru

***Abstract*—This work presents experimental results on the study of current-voltage characteristics and oscillograms of microplasma pulses of the p-n-junction avalanche breakdown. Based on the latter, the pulse duration distributions are determined. As a result, it is shown that microplasma noise has fractal properties. The latter form the basis of avalanche breakdown types developed classification. The correlation between the fractal dimension of microplasma noise and structural inhomogeneities of functional semiconductor structures is revealed.**

Keywords— avalanche breakdown, microplasma, p-n-junction, fractal, structural defect, semiconductor structure.

I. INTRODUCTION

Avalanche breakdown of real semiconductor structures is strongly localized and has microplasmic character [1, 2]. Breakdown localization usually occurs in places of various defects. These may be vacancies, dislocations, inclusions of another phase, inhomogeneities in the distribution of alloying impurities, amphoteric impurities. Dislocations [1] are the most significant here. Close to dislocation there are areas of compression and expansion of crystal lattice, which effects the width of band gap. Moreover, dislocations are centers of impurity association, and they create enhanced diffusion channels for the latter. Accordingly, the probability that carrier generating avalanche will appear in defect area is higher than for defect-free area. The concentration of charge carriers in enhanced diffusion channel is higher, and the effective thickness of depleted layer is respectively lower. As a result, the field strength locally increases, breakdown voltage decreases, microplasmas are formed. Current flowing through microplasma channel is short pulses appearing and disappearing in random times [1, 2]. In the previous works [2-4] we obtained first indications that temporal distribution of microplasma pulses is random, and at the same time has self-similarity property. The discovered properties require additional studies, including those aimed at identifying correlation between the observed time distributions in the context of fractal approach and structural inhomogeneities of semiconductor materials, which is the subject of this work.

II. MATERIALS AND METHODS

As a follow-up to the works [2-4] we investigated gallium phosphide *p-n*-junctions used particularly in LEDs with red emission AJI102AM (GaP:ZnO). Semiconductor structures were supplied with constant reverse voltage (supply voltage) from 10 to 19 V. Signal received at the resistance in series connection with *p-n*-junction was amplified and fed to analog-to-digital converter (ADC). Further processing of signal from ADC was carried out using Matlab mathematical package.

Supply voltage was controlled through programming, with spacing increment of about 0.005 V until first microplasma appeared. After that, the rate of tension growth decreased, though it was increased until next microplasma appeared. The process continued until reverse current pulses disappeared and its changes started being monotonous, i.e. semiconductor switched to developed avalanche breakdown mode [4, 5]. At the same time, the signal was recorded in the computer memory and displayed in real time on the screen in Matlab window. The proposed method was applied to 300 semiconductor structures.

The obtained quantitative data were used to construct inverse branch of current-voltage curve (I–V curve) for each studied sample, showing breaks and fractures associated with avalanche current unstable nature. With specially developed software for each point of I–V curve, it was possible to record and characterize the oscillogram of pulse current – dependence of voltage on time, with voltage dropping with resistance connected in series with *p-n*-junction.

The obtained oscillograms confirmed self-similar nature of avalanche current pulses set through reverse biased *p-n*-junction. Fractal dimension of different semiconductor structures at different breakdown voltages was determined.

Algorithm for calculating fractal dimension D using Hausdorff's formula was implemented in Matlab [6]:

Print ISSN 1691-5402
Online ISSN 2256-070X
http://dx.doi.org/10.17770/etr2019vol3.4051

$$D = \lim_{dT \to 0} \frac{\ln n}{\ln\left(1/dt\right)},$$

where *dt* is the length of the extracted segment of the investigated time series, *n* is the number of iterations. Using wavelet analysis [7], local extrema moments of signal values along Y axis were determined. As a result we obtained a number of extrema values and a number of corresponding time moments (number of points on X axis). At the first iteration we selected a segment equal to half the length of the investigated time series. Its beginning was combined with the first point of the series. The segment "overlapped" a number of points. Then the beginning of the segment was combined with next nearest nonoverlapped point. Then we determined the number of overlaps. At the second iteration: we divided the segment in half, and counted number of series overlaps similarly. Then we did *i* number of steps. As a result, we got dependence of number of overlaps *n* on length of used segment *dt*, and plotted dependence *ln(n)* against *ln(1/dt)* (Fig.1). Using least square method we made a trend line and defined tangent of its inclination angle, which is equal to *D*. Meanwhile we established that the value of fractal dimension significantly depends on reverse voltage supplied to a sample.

To obtain additional information on the structure of semiconductor structures we recorded and analyzed I–V curve direct branches.

III. RESULTS AND DISCUSSION

Fig. 2-4 represent indicative oscillograms of pulse current, analysing which we can classify avalanche breakdown by fractal properties. We can distinguish the following types of avalanche breakdown:

Type B (basic) is characterized by long current pulses of same amplitude, fractal properties are distinct (dimension is usually up to 0,6-0,7) (Fig. 2).

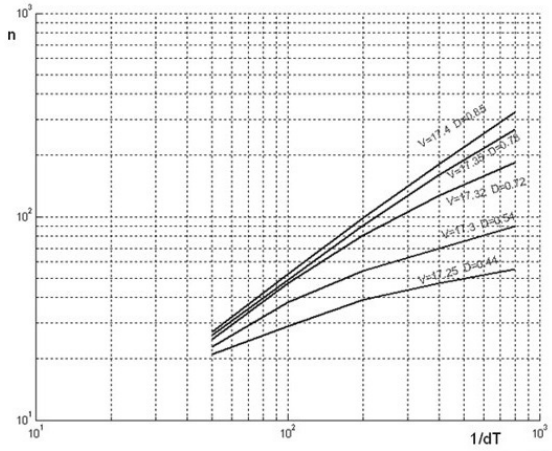

Fig. 1. Fractal dimension curves

Type C (chaotic) is characterized by chaotic change in duration and amplitude of microplasma noise (absence of significant pulses) and weaker fractal properties (fractal dimension is close to 1) compared to type B (Fig. 3).

Type S (secondary) is close to type B, though pulses are very short, numerical value of fractal dimension is intermediate between values of fractal dimensions of type C and type B (Fig. 4). One may note that type B breakdown can regenerate into type S breakdown. Such samples are noticed to have increased series resistance.

Materials science, condensed matter physics and other sciences have general hierarchy of real structures: macrostructure, mesostructure, microstructure [8]. At all three levels, with load on a sample, there are processes of self-organization in structure. Emergence and resorption of microplasmas is a process that takes place at microlevel, and it can be regarded as fluctuations between two stationary states. These fluctuations are determined by changes in parameters at microlevel, which depend on macroparameters, most important of which is temperature [9-11]. Therefore, presence of fractal properties (self-similarity properties) and multi-level amplitude of current pulses indicate that in avalanche breakdown several competing factors act simultaneously, and they must be considered together in analysis of avalanche breakdown mechanisms of *p-n*-junction. These factors are: dependence of concentration, mobility of charge carriers, mean free path on temperature and field value.

Feedbacks common to self-organizing processes were reflected in the developed simulation mathematical model. Within the model processes taking place in *p-n*-junction were presented as dynamic positive (contributing to development of breakdown) and negative (suppressing breakdown) feedbacks, which allowed to take into account the most important factors affecting avalanche formation during microplasma noise analysis. The theoretical values of fractal dimension calculated using the model showed good correspondence to the values obtained during the experiment. Thus, we verified the classification.

Let us turn to the main goal of this work – establishing correlation between fractal dimension of microplasma noise and structural inhomogeneities of semiconductor structures. As is known, defectiveness degree of structure can be judged by analysis of I–V curve direct branch [12]. Excess currents (in our case above 10^{-12}A) on it with displacements less than 1V are associated with tunneling, which can occur in the area of extended defects (dislocations, packaging defects, etc.) and local heterogeneities of composition. In this case, the coefficient of nonideality (which is part of the Shockley equation for the diode) is much more than two [12].

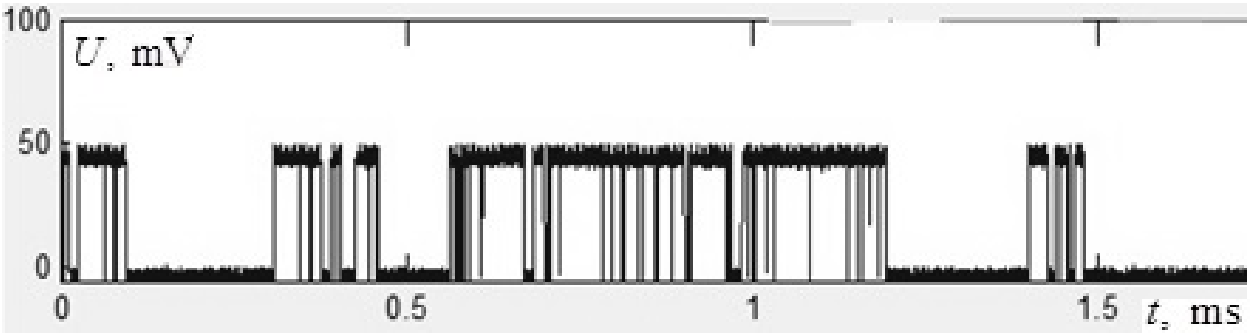

Fig. 2. Oscillogram of pulse current through reverse biased *p-n*-junction at avalanche breakdown type B

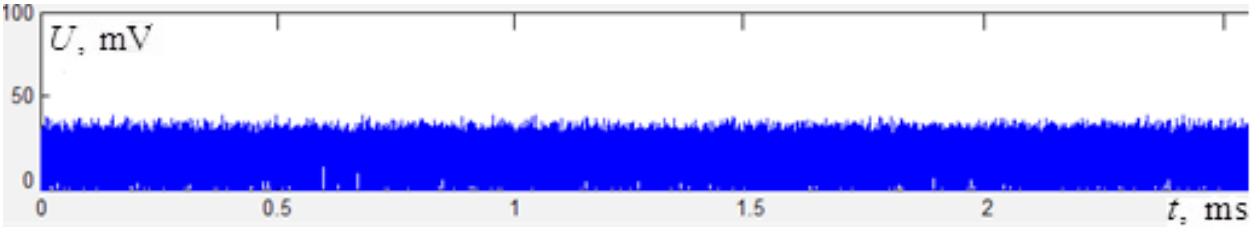

Fig. 3. Oscillogram of pulse current through reverse biased *p-n*-junction at avalanche breakdown type O

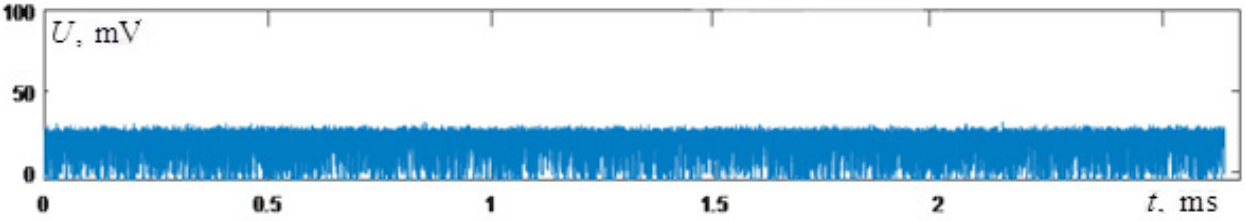

Fig. 4. Oscillogram of pulse current through reverse biased *p-n*-junction at avalanche breakdown type A

As the experiment shows, most of the type B devices have tunnel component at displacements less than 1V on I–V curve straight branch (Fig. 5), on type C and S structures such components are practically not detected in the same voltage range (Fig. 6).

We defined the value of direct current at which yellow glowing appears in LEDs based on the studied structures. According to the results of these studies we found that most LEDs made on the basis of group B structures begin to emit in yellow spectrum at current values close to 120 mA, whereas for LEDs of group S and C glow appears at current values above 200 mA. This may be due to a large number of defects that contribute to formation of microplasmas in avalanche breakdown. Traditional methods cannot effectively detect such defects.

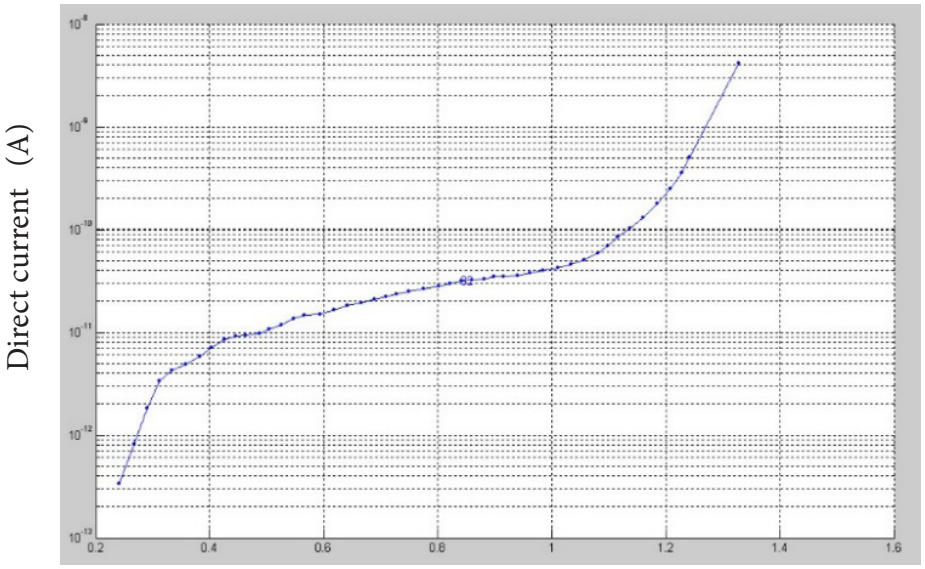

Fig. 5. I–V curve direct branch at avalanche breakdown type B

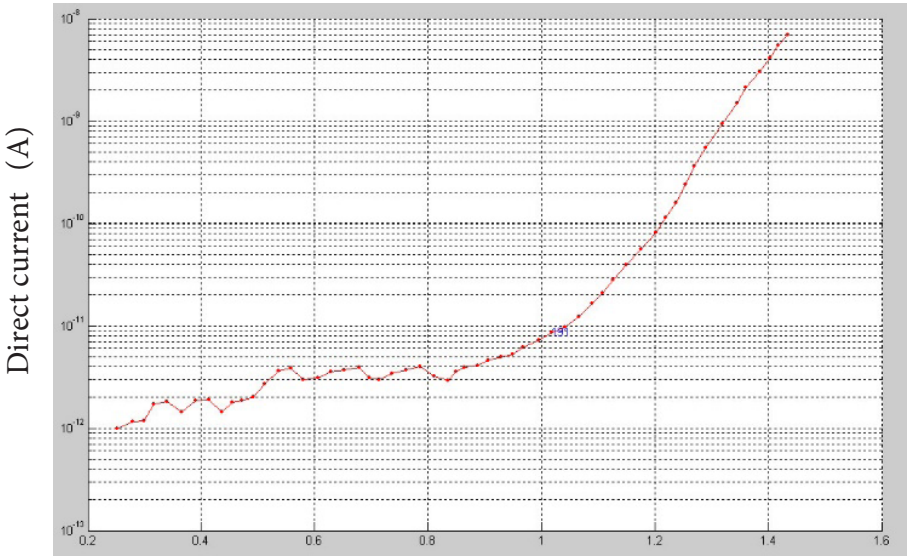

Fig. 6. I–V curve direct branch at avalanche breakdown type S

Summarizing the above, we can conclude that the applied experimental method for analysis of fractal properties can be used as a basis for nondestructive control method of structural inhomogeneities in development and production of semiconductor devices.

IV. CONCLUSIONS

Our analysis showed that microplasma noise has fractal properties. Based on the latter we developed an avalanche breakdown types classification. The obtained data confirm that the semiconductor structure sample belongs to one or another classification group. Thus, we found that strongly pronounced fractal properties may indicate the presence of a large number of defects in semiconductor structure. Based on this we propose nondestructive control method for semiconductor devices.

REFERENCES

1. *Grekhov I.V., Serezhkin U.N.* Avalanche breakdown of p-n-junction in semiconductors [Text]. – L.: Energia, Leningrad department, 1980. p.152
2. *Vorotkov M.V., Skvortsov N.N., Shashkina A.S.* Fractal properties of microplasma noise // Innovative technologies in media education. Materials of III All-Russia research and practical conference, March 27-28, 2015. Issue 3. SPb: SPbGUKIT, 2015. Pp. 65-71.
3. *Shashkina A.S., Krivosheikin A.V., Skvortsov N.N., Vorotkov M.V.* Fractal properties of avalanche breakdown of LED // STB SPbPU. Physicomathematical sciences. 2016. №4 (253) 2016. Pp. 85-93.
4. *Shashkina A.S., Krivosheikin A.V., Skvortsov N.N., Vorotkov M.V.* Avalanche breakdown of p-n-junction in radiotechnics // Scientific and technical bulletin for information technology, mechanics and optics. 2016. Vol. 16. № 5. Pp. 864–871.
5. Ivanov P.A., Potapov A.S., Samsonova T.P., Grekhov I.V. Current–voltage characteristics of high-voltage 4H-SiC p^+–n_0–n^+ **diodes in the avalanche breakdown mode** // Semiconductors. 2017. T. 51. № 3. Pp. 374-378.
6. Feder E. Fractals. — M: MIR, 1991. — Pp. 254.
7. Shchitov I.N., Galkina V.G. Introduction in signal theory. Part 3. Wavelet transform. SPb: SPbGUKIT publishing house, 2012. p.99
8. Tushinskiy L.I. Synergetical basis for structures classification and evolution in modern material sciences // Fractals and applied synergetics 2005: Collection of articles. – M: Interkontakt-Nauka, 2005.
9. Schoell, E. Self-organisation in semiconductors. Nonequillibrium phase junctions in semiconductors due to generation-recombination processes. / E. Schoell − M.: Mir, 1991. − p.464
10. Kuznetsov V. S., Kuznetsov P. A. To the question of spatial self-organisation of current free carrier in strong electric fields // Materials for electronic technology. 2012. №3.
11. *Skvortsov N.N., Shashkina A.S.* Avalanche breakdown self-organisation in LEDs // Papers of VII All-Russia conference «Irreversible processes in nature and technics». BMSTU, January, 27-29 Moscow, 2015. Part II, pp. 46-48.
12. W. Shockley, W.T. Read. Phys. Rev., 87, 835 (1952)

Electric Energy Generation in Autonomous Energy Supply Module Having Rotary Expansion Engine

Andrei Khitrov
Electric drive and automation systems department
Pskov State University
Pskov, the Russian Federation
khitrov.aa@gmail.com

Alexander Khitrov
Electric drive and automation systems department
Pskov State University
Pskov, the Russian Federation
khitrov-pscov@mail.ru

Alexander Ilyin
Electric drive and automation systems department
Pskov State University
Pskov, the Russian Federation
al.ilyin@yandex.ru

Yulia Domracheva
Electric drive and automation systems department
Pskov State University
Pskov, the Russian Federation
juli-politeh@yandex.ru

Dmitriy Fedorov
Electric drive and automation systems department
Pskov State University
Pskov, the Russian Federation
dmitriy-fedorov-2012@mail.ru

***Abstract*—The development of autonomous energy supply systems is among the priority ways of scientific and technological growth in the Russian Federation. The autonomous energy supply module providing the consumer with heat, electric power, hot and cold water can contain the different variants of the electric power subsystem. This paper considers three different variants of building the electric power subsystem for the rotary expansion engine used as a driving machine whereas the permanent magnet synchronous machine is used as a generator. Also the designed structure of 30 kW electric power supply subsystem is regarded.**

Keywords*—autonomous energy supply module, permanent magnet machines, power converters, variable speed system.

I. Introduction

The priority area of scientific and technological growth in the Russian Federation includes the transition to environmentally clean and resource-saving energy sector, forming new power sources and ways of storing and transporting energy [1]. As a part of that, creating autonomous energy supply plants is an actual task. This problem is particularly urgent in regions having no centralized energy supply: no heat, electricity, cold and hot water (For example, in the northern regions where the extending of the centralized power supply lines is not cost-effective [2]). The autonomous energy supply module allows to solve the problems of providing consumers with necessary energy resources [3]. The autonomous energy supply module can be located in the immediate area surrounding consumers, which allows to reduce losses associated with the transportation of electric and thermal energy.

The autonomous energy supply module contains steam generator (steam boiler) having the required power and working on natural gas and (or) other types of fuel. Also the module includes the low-speed rotary expansion engine of a new type, the electric generator having electric energy converting system (which meets the requirements of the state standard [4]) and other units that provide the consumer with heat, hot and cold water.

The low-speed rotary expansion engine is used as a steam engine for driving the shaft of the electric generator. The engine of this type provides the smooth rotation of the output shaft with almost constant output torque depending on the temperature and the pressure of the working fluid of the steam generator [5].

In autonomous electric power plants having low-speed engine (up to 750 rpm) it is difficult to design a generating system based on the industrial synchronous generator (SG) having electromagnetic excitation, without using in such a system the electric or the mechanical multiplication. Maintaining the shaft speed in the range of fluctuations no more than 10% in synchronous generators is carried out by automatic excitation controllers. At rated speeds of 1500 or 3000 rpm such a problem is not so acute and is easier to solve. But in all cases an electric energy generating system is not operational if the speed significantly deviates: both because of the changes in technological process (variation of the heat carrier parameters) or because of the need to control electric energy consumption in order to save the fuel.

The choice of the electric machine for the autonomous power plant is presented by the authors in [6]. It is shown that the application of the permanent magnet synchronous machine (PMSM) is perspective for reducing mass and dimensional characteristics of the power plant.

This paper considers the technical solutions for creating the electric power subsystem of the autonomous energy supply module whereas the PMSM is used as a starter-generator.

Print ISSN 1691-5402
Online ISSN 2256-070X
http://dx.doi.org/10.17770/etr2019vol3.4038

II. Electric power subsystem concepts

Autonomous electric power plants continue to be evolved and improved. Various autonomous power supply systems are being advanced by their composition and by their power, and their control systems are being improved. Such systems containing electric generators often produce electric energy working at the variable speed of the generator shaft.

They must convert the alternating voltage having the variable frequency to the voltage having the quality indicators for the general purpose industrial systems [4].

One of the tasks for the autonomous energy supply module is providing the consumers with three-phase voltage having constant frequency whereas the speed of the rotary expansion engine is variable. The real task is developing the autonomous electric power plant having the power up to 30kW as a subsystem of the energy supply module with the rotary expansion engine having variable shaft speed from 300 to 750 rpm. The electric power subsystem must be able to control the output power to provide the effective operating modes.

The analysis of the currently existing autonomous electric power systems allows to conclude that constructing the electric subsystem of the autonomous energy supply module can be based on three concepts.

Concept I.

The first basic concept is using the SG having electromagnetic excitation, with the automatic excitation controller and the standard frequency converter (Fig. 1). Such concept is applied in diesel generator sets [7].

In the systems presented in Fig. 1 the output parameters meet the requirements of the state standard [4] generally if the speed fluctuates into the range of 10-15% (0.85-1.1 of n_{IN} (rpm)).

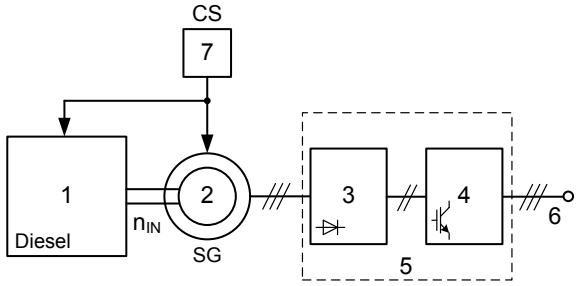

Fig. 1. Diesel generator set

Fig. 1 shows the following units: 1 – diesel engine; 2 – synchronous generator (SG); 3 – rectifier; 4 – voltage inverter; 5 – frequency converter; 6 – electric power system outputs; 7 – control system (automatic excitation controller).

In the case of the autonomous energy supply module being designed the speed could not be lower than 650 rpm. Since the SG at the low electric load is forced to work having constantly higher speed, it results in the higher fuel consumption. Electric power quality depends on the voltage inverter applied and the supplementary filters and compensating devices completing the power plant. If the voltage at the generator output is reduced lower than the acceptable level, the standard frequency converter switches off its outputs due to the error of losing the input voltage. After the outputs were blocked operating can be continued only if the voltage is increased to the level required.

The problem is also complicated with the fact that electrical corporations and firms mainly produce SG having the rated speed of 1500 and 3000 rpm. Therefore there is a need for the mechanical transmission (reduction gear, chain or belt drive, etc) between the shaft of the SG and the shaft of the driving engine (e.g. the diesel engine in Fig.1) for keeping the acceptable voltage level at the input of the rectifier at the lower speeds (<750 rpm).

Concept II.

The second basic concept is using the power step-up transformer (voltage multiplicator) at the output of the electric generator. Ideally it should be the regulating booster transformer having the possibility of boosting the voltage if the speed is below the acceptable level.

Applying such concept essentially increases mass and dimensional characteristics of the autonomous energy supply module (e.g. a standard transformer of the TC type having a power of 30 kVA weighs more than 250 kg and has a specific power less than 0.2 kVA/kg).

The structure of converting the mechanical energy from the engine shaft in this case is shown in Fig. 2. The stator windings of the SG are connected according to Δ-connection or Y-connection.

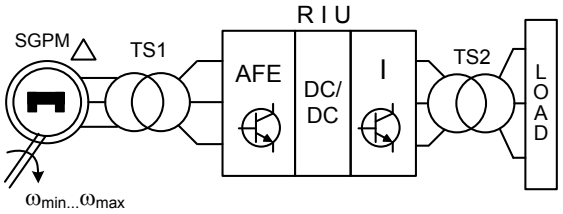

Fig. 2. The power system structure containing the step-up transformer and rectifier-inverter unit

Fig. 2 shows the following units: TS1 – step-up transformer; RIU – rectifier-inverter unit that can include the uncontrolled or the controlled rectifier (AFE), boost or buck converters of the DC voltage (DC/DC) and the output voltage inverter (I); TS2 – output isolating transformer.

Concept III.

The third basic concept is using the SG or SGPM (synchronous generator with permanent magnets) and modular electronic power converters as part of the RIU without the mechanical or electric multiplicators (Fig. 3). The units shown in Fig. 3 have the same designations as in Fig. 2; TS – output isolating transformer. This technical solution, in spite of its higher cost, has the best mass and dimensional characteristics and is promising for the autonomous electric power plants having variable speed of a driving engine. Moreover, where necessary, the SGPM (PMSM) can be used for the starter mode of the steam generator or of the wind power plant with a vertical axis of rotation (Darrieus or Savonius wind turbine type).

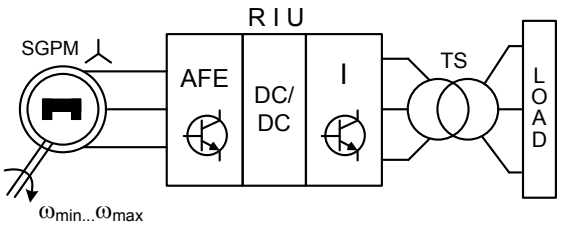

Fig. 3. The basic concept for the autonomous energy supply module without the mechanical or electric multiplicator

At the first start the power plant is in the starter mode for spinning and bringing to the required aerodynamic performance. After that the power plant should be driven into the generator mode. Such wind power plants have various advantages over the wind plants with a horizontal axis of rotation: operating with the wind of any direction, no need in wind orientation system, reduced mass and dimensional characteristics of the engine. Such systems can be closely established near the autonomous energy supply module container and serve as an auxiliary power supply system for the module (including the function of recharging the accumulator batteries contained in the autonomous energy supply module).

III. 30 kW System design

Fig. 4 shows the designed structure and the composition for the 30kW electric subsystem of the autonomous energy supply module.

The module contains the following basic units and systems:

1. Accumulator batteries unit (AB) consisting of 5 batteries (lead-acid helium sealed) and charger 1 controlling the charging process (individually for each battery) and limiting the charging current.
2. Power converters (controlled units) for providing the auxiliaries of the autonomous energy supply module and monitoring the output power changes and fluctuations.
   - UZ1 – inverter for controlling the start of the REE – rotary expansion engine (an additional option if required). It is implemented on the base of the standard 3kW frequency converter having the ability to be connected to the 48V DC-bus (e.g. Unidrive SP 1402) or using DC/AC converter 48V DC/3x380V AC of 3 kW power. The module can be equipped with the supercapacitor (e.g. LSUM048R6C) and the charger 2.
     Instead of using UZ1 the soft starter device can be applied (e.g. MCT-331H of SPC Bitek, The Russian Federation [8]). In this case it is connected to output of the UZ2 inverter.
   - UZ2 – inverter for creating the local three-phase 380 V AC network. 4kVA inverter UZ2 is supplied from input DC voltage 48-60V.
   - UZ3 – electric network inverter having the input DC voltage +24V and the output single-phase AC voltage 220V, 50 Hz. The AC/DC converters forming the stabilized voltages of the needed values for supplying low power electric devices and sensors are connected to the output of UZ3.
   - UZ4 – rectifier-inverter unit (RIU) with output isolating transformer TS2 of 30 kVA power. The composition of the RIU is determined by the type of an electric generator of the autonomous power plant.
3. Generator unit on the base of SG or SGPM (e.g. SGPM of the LSRPM 250SE type, Leroy Somer [9]) having the power of 31 kW, the speed of 710 rpm and the embedded speed sensor (encoder EN) and air cooling system.
4. Autonomous power energy module control system (APEM CS) with sensors and auxiliary units. The control system is intended for controlling the operating modes of the power energy module.

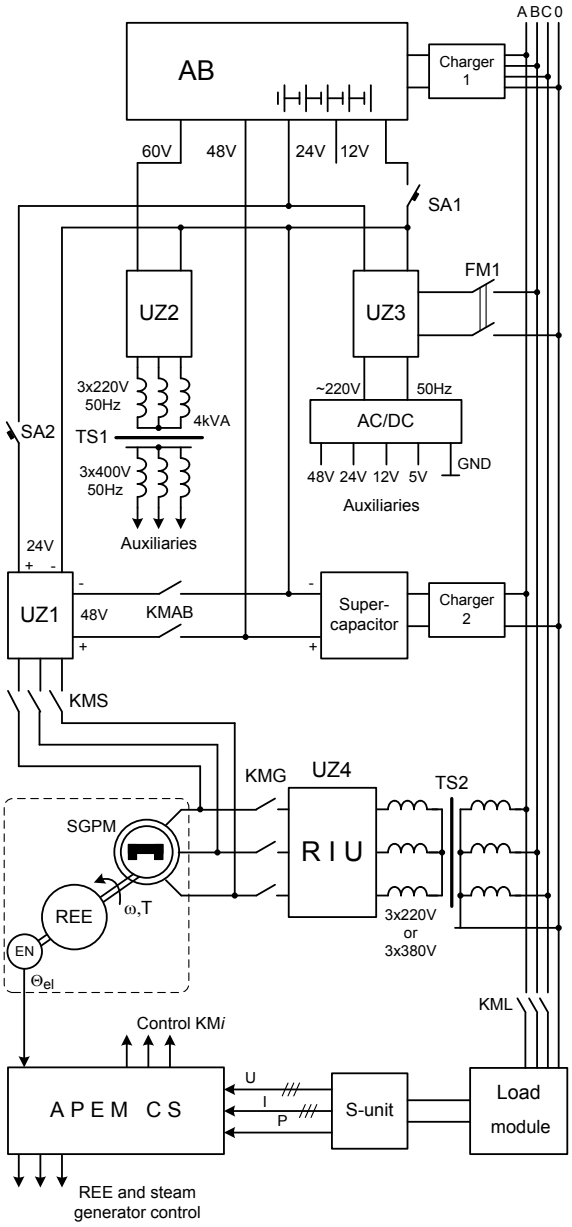

Fig. 4. 30kW autonomous energy supply module electric subsystem

The signals of the output variables states (output AC network variables: currents, voltages, power consumption) from the sensors unit (S-unit) and the generator shaft speed from the generator unit come to the input of the

APEM CS. The output signals of the APEM CS are the signals of regulating the switching equipment and connecting the load module for balancing the autonomous electric network load. Also the output variables of the APEM CS are the control signals for the steam generator for providing the effective and energy-saving operating modes.

5. Switching and protection equipment.

- SA1 – switch for connecting the AB unit (DC contactor 100V, 60A).
- SA2 – switch (circuit breaker or contactor 30V, 1A) for supplying the auxiliaries of the UZ1 inverter.
- FM1 – single-phase circuit breaker or AC contactor. It is being connected after switching to the autonomous supply of the auxiliaries from the own network. FM1 prevents the discharge of the AB unit.
- KMAB – DC contactor for connecting 48V DC voltage from the output of the AB unit or the supercapacitor to the input of the UZ1 inverter.
- KMS – switch (3x380V AC contactor, 10A) for connecting the stator winding of the SGPM to three-phase voltage for the idle start of the REE. Then the engine reaches the nominal conditions at the «light» operating mode till the speed is 600-700 rpm.
- KMG – switch (3x380V AC contactor, 50A) for connecting the output of SGPM to the RIU after the starting procedure was completed and the KMS switch was switched off.
- KML – AC contactor for connecting the load module.

Fig. 5 shows the module structure of the power circuit as a technical solution for the RIU. Such solution may be effective for the autonomous energy supply module [10] – [12]:

1. Three-step principle of converting the electric energy from the SGPM. The structure of the RIU based on this principle includes the uncontrolled or the controlled (active) rectifier – module 1, the boost DC/DC converter operating at the high frequency (more than 10kHz) – module 2, the inverter of the required power having the input control of the DC voltage (450-600V) and the sensorless vector control mode – module 3. The DC voltage multiplication factor of the module 2 is in the range from 2 to 3,5. The output of the RIU is connected to filter F or an isolating transformer (which is more preferable). The power circuit of the rectifier, the DC/DC converter and the inverter can be manufactured as separate complete devices. There can be two separate control systems for the DC/DC converter and the inverter or single combined control system for two modules.
2. The autonomous energy supply module of this type has optimal mass and dimensional characteristics for the output power given, and these characteristics mostly depend on the applied SGPM and the implemented control principle of the RIU [6]. The module can provide the power control without electric power sensors if the calibration curves of the power plant (the steam generator and the rotary expansion engine at the rated shaft speed) are known in advance.

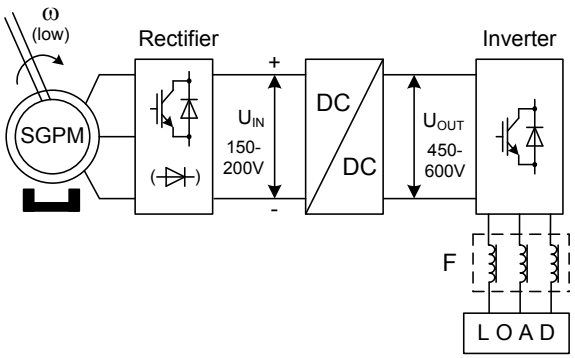

Fig. 5. Module structure of the power circuit

The ready-made technical solutions analysis made by the authors allows to note that currently there are no high power DC/DC converters manufactured by the industrial companies for integrating into the systems with frequency converters having an option of connecting to the DC-bus.

There are no various options for purchasing the inverters with input DC voltage and output three-phase AC voltage that are not complete standard frequency converters in the market of electric products in the Russian Federation. Such technical decisions are available at the markets for the solar power systems. E.g. the inverter Omega 11kW (solar inverter for the power water pump [13]) of Master-Power (Spain) having the input DC voltage range from 250V to 800V and the output three-phase AC voltage of 380V.

Scientific articles and patents [12], [14] confirm the relevance of the solution of the technical problem in designing autonomous electric power plants of various power and of different purposes with variable speed of a driving engine and controlling output electric power for efficiency increasing.

IV. Conclusion

The designed electric power subsystem of 30kW power for the autonomous energy supply module is given in this article.

The synchronous generator with permanent magnets (SGPM) is recommended to be applied as an electric generator within the autonomous energy supply module.

The structures including SGPM without using electric or mechanical multiplicators have the limited possibilities of regulating the output voltages. It requires designing the special type of the rectifier-inverter unit (RIU) of the module type including the rectifier (controlled or uncontrolled) module, the boost DC/DC converter and the inverter having an option of connecting to the DC-bus.

References

[1] Decree of the President of the Russian Federation of 01.12.2016, No. 642. About the Strategy for the Scientific and Technological Development of the Russian Federation. 25 p. (In Russian).

[2] Mikhalap S.V., Khutornoy A.N. Alternative power supply for northern rural settlements. *Promyshlennaya energetika*. [Industrial Energy Magazine]. №10, 2018. pp. 46-52. (In Russian).

[3] Khitrov A.I., Khitrov A.A. Electric machine switch system as part

of the cogeneration power plant. *Elektroprivody peremennogo toka: Trudy mezhdunarodnoy shestnadtsatoy nauchno-tekhnicheskoy konferentsii*. [Proc. 16-th Int. Conf. «AC Electric Drives»]. Yekaterinburg, Ural Federal University named after the first President of Russia B. N. Yeltsin. 2015. pp.218-219. (In Russian).

[4] State Standard 32144-2013. Electric Energy. Electromagnetic compatibility. Standards of quality of electric energy in general-purpose power supply systems. (In Russian).

[5] Lukyanov Y.N., Perminov A.L. and oth. *Rotornaya rasshiritelnaya mashina*. [Rotary expansion machine]. Patent RF № 2619391. 15.05.2017. (In Russian).

[6] Khitrov A.I., Khitrov A.A. Justification of electric machine choice for autonomous electric low-power supply system working with low-speed variable speed engine. *Vestnik Pskovskogo gosudarstvennogo universiteta. Seriya «Tekhnicheskie nauki»*. [PskovSU journal. «Technical science» series]. Vol. 7, 2018. pp. 57-71. (In Russian).

[7] Khvatov O.S., Darenkov A.B., Tarasov I.M. Diesel generator power station with variable shaft speed. *Vestnik IGEU*. [Ivanovo State Energetic University Journal]. Vol. 2. 2010. (In Russian). pp. 53-56. (In Russian).

[8] Scientific Production Company «Bitek». Soft starters / electronic starters. [Online]. Available: http://bitek-e.ru/softstart.htm [Accessed: Febr. 19, 2019].

[9] Permanent magnet synchronous motor 3 to 350 kW - 1500 to 5500 rpm. [Online]. Available: http://acim.nidec.com/ motors/leroy-somer/products/permanent-magnet-synchronous-motors/ lsrpm-dyneo [Accessed: Febr. 19, 2019].

[10] Khitrov A.I., Khitrov A.A., Veselkov E.L. Three-phase inverter for autonomous electric power supply low-power systems *Vestnik Pskovskogo gosudarstvennogo universiteta. Seriya «Tekhnicheskie nauki»*. [PskovSU journal. «Technical science» series]. Vol 2, 2015. pp.70-79. (In Russian).

[11] Khitrov A.A., Khitrov A.I. Investigations of Electric Power Quality in Autonomous Low Power Plant. Environment. Technology. Resourses. Proceeding of the 11th International Scientific and Practical Conference. Rezekne, Latvia. June 15-17, 2017. Volume III. pp.136-139.

[12] Plokhov I.V., Khitrov A.A., Khitrov A.I. *Starter-generatornaya ustanovka dlya avtonomnoy sistemy elektrosnabzheniya na baze rotorno-lopastnogo dvigatelya s vneshnim podvodom teploty.* [Starter-generator set for autonomous power supply system for external combustion rotary-vane engine]. Patent RF №144521. 27.08.2014. (In Russian).

[13] Omega. Solar Inverter for Water Pump. User manual. [Online]. Available: http://www.masterbattery.es/manuales/ Omega_ Water_Pump.pdf [Accessed: Febr. 21, 2019].

[14] Darenkov A.B. *Avtonomnaya elektrostantsiya peremennogo toka.* [Isolated alternating current electric power station]. Patent RF № 2666903. 13.09.2018. (In Russian).

Environment. Technology. Resources. Rezekne, Latvia
Proceedings of the 12th International Scientific and Practical Conference. Volume III, 114-118

Extraction of Biologically Active Components from Freshwater Sapropel

Aneka Klavina
Institute of Occupation Safety and Environmental Health
Riga Stradins university
Riga, Latvia
aneka.klavina@rsu.lv

Agris Auce
Institute of Occupation Safety and Environmental Health
Riga Stradins university
Riga, Latvia
a@aa.lv

Ivars Vanadzins
Institute of Occupation Safety and Environmental Health
Riga Stradins university
Riga, Latvia
ivars.vanadzins@rsu.lv

Alise Silova
Scientific Laboratory of Biochemistry
Riga Stradins university
Riga, Latvia
alise.silova@rsu.lv

Linda Dobkevica
Institute of Biology
University of Latvia
Riga, Latvia
linda.eglite@lu.lv

***Abstract*—Sapropel has been used for different purposes - in agriculture as fertilizer, in construction as building material, in cosmetic products, in balneology also in medicine and pharmaceuticals as bioactive component. Previously sapropel has been commonly used in raw form and there is no general accepted method or standard method for obtaining sapropel extract. However, most extraction methods follow the same path. Currently, there are few extraction methods using several extractants for obtaining bioactive components from raw sapropel.**

The most commonly used extractant is alkaline solution. When sapropel is subjected to alkaline environment, the humic and fulvic acids, together with some lipids, vitamins and sugar, present in the raw sapropel become soluble, however other organic and mineral content present in the sapropel remain solid. Alkaline extraction is followed by filtration and water present in the aqueous mixture is evaporated off.

Latvian freshwater sapropel can be used as raw material for obtaining sapropel extract and use it as remedy. But the main question for sapropel usage in medicine, balneology and pharmacy is to develop quality criteria for raw sapropel and its extracts. The quality criteria should include minimum requirements for biologically active substance concentration, pH values, antioxidants as well as physical characteristics.

In future studies the differences in extract characteristics of the various deposit sites, as well as the stability of the extracts under different storage conditions should be defined; also, there is need for a common approach to develop method of extraction process for active substances from sapropel and analysis procedures of its extract.

***Keywords*—antioxidants, extraction, freshwater sapropel, fulvic acid, humic acid, sapropel**

I. Introduction

Sapropel has long been used as a remedy in medicine and veterinary medicine, having a positive effect on the health [1], [2]

Sapropel biological and biochemical structure and composition varies strongly depending on its origin. Its characteristics are determined by organic, mineral and biological compounds that can have a multitude of effects on skin [3]. Sapropel has a high heating capacity that makes it useful for topical applications in medicine and rehabilitation. It is proposed that the medical effects are due to its high heating capacity and a mixture of chemical elements, hormones, various organic acids and vitamins (C, B1, B2, B5, B6, B9, B12, E, D and P) found in sapropel [2], [4]being included in most of ancient Mediterranean/European medical texts and currently used to prepare therapeutic hot-muds (peloids.

Previously sapropel has been used in raw form and there is no general accepted method or standard method for obtaining extracts of its active components. There are number of extraction methods using several extractants for obtaining bioactive components from raw sapropel and most of the extraction methods follow the same path [5].

Extraction is a principal process for recovery and separation of biologically active compounds from nature materials. Extraction converts complex matrix into suitable ingredients for pharmaceuticals, medicine, cosmetics and analytical procedures [6].

Literature suggest different extraction methods for obtaining biological active substances from sapropel. Most popular is solid-liquid extraction (SLE) with alkaline solution [7]. There are recent reports for sapropel extract using microwave-assisted extraction (MAE), ultrasound-assisted extraction (UAE), supercritical fluid extraction (SFE) and hydrostatic pressure extraction (HHPE) [6]–[8]. All these techniques have proven effectiveness in extraction form natural matrices and could be used as extraction methods for raw sapropel. Also all methods have followed principles of maximizing the yield of extraction, can be adapted for industry and have procedures to avoid impurities [6].

The first step of extraction process is isolation of active components from cells by using physical and chemical processes [9]. Choice for appropriate cell disruption process depends on sapropel sediments, that consist of

Print ISSN 1691-5402
Online ISSN 2256-070X
http://dx.doi.org/10.17770/etr2019vol3.4135

crystalline skeleton like sand and clay, and residues of water organisms – flora, fauna; it all makes colloidal mud solution, which has complex cellular matrix [10]. In case of sapropel extract, cell disruption usually is done by drying samples before solid-liquid extraction process.

II. Materials and methods

A. Sapropel samples

In this work the sapropel samples were extracted from 5 lakes in eastern Latvia. Lakes were selected by analysing the Latvian lake database (*ezeri.lv*) [11], containing official geological survey of Latvia lakes. The sapropel deposits depth, lakes coordinates, history of agriculture next to lake were considered in the selection of the lakes. The sapropel was obtained from 5 lakes: Audzelu lake (*Audzeļu ezers*), Dunaklu lake (*Dūnākļu ezers*), Ivusku lake (*Ivušku ezers*), Zeilu lake (*Zeiļu ezers*), and Little Kivdalova lake (*Mazais Kivdalovas ezers*) in Latgale region of Latvia.

The extraction of sapropel from the lakes was performed during the winter time when the surface of the lakes is frozen. Prior to the sample collection the thickness of the proper sediment layer was determined and the depth of sapropel deposit was established for each of the lakes as well as within each of the lakes by taking probes in several locations. To select a well-composed sapropel layer for further laboratory analyses the samples were taken from three different depths of sapropel sediment at each extraction point and up to eleven different points through lake coordinates (fig.1). During the sample collection procedure 21 samples were obtained from each for the lakes that resulted in 105 sapropel samples in total.

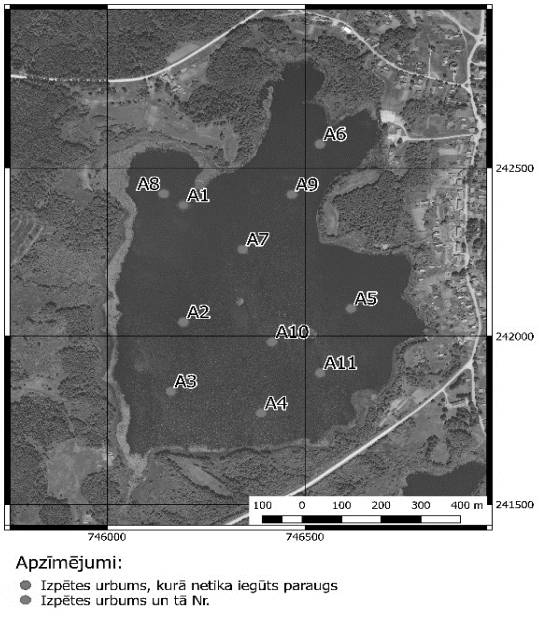

Fig. 1. Sapropel sample coordinates in Audzelu lake (A1 – A11 sample taking points)

Preservation of sapropel samples. All sapropel samples were kept in closed plastic containers without oxygen access to oxygen in order to prevent oxidation of the sapropel and its active components. The sediments were refrigerated and kept at **4°**C; in these conditions' samples were stored from 4 to 8 months before extraction process and analysis.

The storage temperature of 4°C was selected as it most closely resembled the natural water temperature at the bottom of the lake during the winter time.

B. Extraction of active componenets from Sapropel

For the extraction of active components from the sapropel samples the alkaline method was selected. Extract was obtained from each of the samples (n=56). Solid-liquid extraction process with 2% NaOH solution was used for the extraction of humic and fulvic acids from the sapropel samples. Sapropel sample with NaOH solution was stirred for 24 h, and then mixture was centrifuged at 5000 rmp for 30 min, and then filtrated. Filtrate was acidified with 5 N H_2SO_4 solution till pH 2 and centrifuged again. Filtrate was separated from solid particles, and both liquid extract and solid extract were stored at 4°C before use.

After sodium hydroxide solution was added pH level rises from neutral to pH 10, all chemical cell disruption processes began, stirring helps with mixing base alkaline solution with sapropel; colloidal mixture is formed. After centrifugation, sand particles and insoluble matter precipitates and is discarded. When acid was added humic acids molecules precipitated from the solution and stay in solid form; fulvic acid remains in the solution. The extraction process results in two forms of extract: solid, crystalline phase; main part of which is humic acids, and the liquid that contains high concentration fulvic acid solution.

C. Characterisation of the sapropel extract

For the characterisation of the sapropel extracts there are no generally accepted guidelines as it is usually the case for many plant extracts. In general the minimal quality indicators for plant extracts are the concentration of active substances, pH values, visual inspection, and raw material quality. The same principles were applied to the characterisation of the sapropel extracts.

Sapropel extracts were characterised by organic carbon content (TOC), humic acid (HA) and Fulvic acid (FA) concentration, pH level, and antioxidant level.

Total organic carbon, HA and FA were determined using spectrometric method.

Sapropel pH level was determined using distillated water (volumetric ration sample: water - 1:2.5).

To determine antioxidants the following methods were used: DPPH radical method, Folin-Ciocalteu method for determination of the total phenolic content and total antioxidants status were calculated.

The total phenolic content in sapropel extract was determined spectrophotometrically according to Folin-Ciocalteu method [12]we will determine the antioxidant properties of methanolic extract of propolis from Ghardaia and Khanchla provinces of Algeria and will correlate the values with total levels of polyphenolic compounds. Methods: The total polyphenol contents of methanolic extract of propolis were measured by using Folin-Ciocalteu spectrophotometric method. Thereafter, the antioxidant properties of these polyphenols were

determined by using the 2,2-diphenyl-1-picrylhydrazyl (DPPH. This method is based on the reaction of phenol in sapropel extract with Folin-Ciocalteu reagent. The content of phenolic compounds of the extract was expressed as gallic acid equivalents. The gallic acid was used to set up a standard curve. All the samples were analyzed in triplicates.

The total free radical scavenging capacity of sapropel extract was determined using the stable DPPH radical, which has absorption maximum at 515 nm. The radical solution was prepared by dissolving 2.4 mg DPPH in 100 ml methanol, a test sample (5µl) was added to methanolic DPPH. Also, absorption of blank sample (without antioxidant) was measured. A calibration curve was plotted with DPPH scavenged versus concentration of Trolox equivalent (TE mmol/L) [13], [14]. All samples were determined as triplicates.

Total antioxidant status (TAS) in samples was measured using Randox Total Antioxidant status kit (Randox Laboratories Ltd.) adapted to the RX Daytona automated chemistry analyzer (Randox Laboratories Ltd) [15]

ABTS® [2,2'-azino-bis(3-ethylbenzothiazoline-6-sulphonic acid)] incubated with H_2O_2 and peroxidase (metmyoglobin), generated the ABTS® radical cation. It has a relatively stable colour of green and blue, which absorbs at 600 nm. The antioxidants present in the sample prevent the formation of the cation; therefore the colour is proportional to its concentration. The result was expressed in milimoles of Trolox equivalent (TE mmol/L) of the sample solution.

III. Results and discussion

A. Sapropel samples

The location of balneologically usable sapropel layer in the studied lakes was found to be from 2.0 to 9.0 m from the surface of the sediment layer exact depth depending on the lake and the position of the measurement point in the lake. Actual thickness and location of the balneologically usable sapropel layer varied depending on the depth of the lake and the degree of the decomposition of organic matter in the lakes. If the depth is less than 1.5 m from the surface of the sediment layer, sapropel sediments are not fully developed and thus were not used in this study. Organoleptically testing the colour of samples it was found that sapropel colour varies from greenish yellow till black. Green and yellow coloured sapropel usually relates to high silica content and is found in moraine landscape lakes; black coloured sapropel has high organic matter and is found in lakes with low mineral content; brown and dark green sapropel is mixed type and its origin comes from lakes plankton, higher plants and sometimes its connected with peat layers [1]. Sapropel sample pH level is around 7 – 8 it means that these sapropel sediments has high mineral content [16]. The characteristics of the research areas are shown in table I.

TABLE I. THE CHARACTERISTICS OF THE RESEARCH AREAS

Lake name	Characteristics			
	Lake surroundings	Sapropel colour	The depth of the sapropel layer, m	pH
Audzelu	Small village forest	Black	2.65 – 11.4	7.14
Ivusku	Agricultural land	Brown	2.2 – 10.4	7.96
Dunaklu	Towns suburb, has an island	Greenish yellow	0.9 – 9.5	7.56
Zeilu	Forest, agricultural land, cemetry	Dark green	4.0 – 9.5	7.82
Little Kivdalova	Agricultural land, farmstead	Dark brown	1.7 – 11.2	7.27

B. Sapropel extract

All 105 sapropel samples were tested for the presence of heavy metal residues and pesticides. Almost all of the samples tested had the level of heavy metal and pesticides below the level accepted for medical use, 56 samples were selected for the extraction of humic and fulvic acids.

In literature it is reported that the concentration of humic and fulvic acids in the sapropel extract varies due to differences in the chemical structure of humic substances (HS) and physical availability of the organic matter associated with mineral in sapropel [17].

Extraction performed with sodium hydroxide the yielded approximately is 22 -28 g of humic acids and 5 - 9 g fulvic acids from one-kilogram dried sapropel. Outcome of acids is calculated in dried extract form, for fulvic acids excess liquid was evaporated. Humic acids, fulvic acids and total organic carbon, extracted from one g sapropel from each of the lakes are shown in fig. 2; median values of HA, FA and TOC were calculated to show average values of each lake. The highest difference between the sapropel from different lakes is in the yield of the fulvic acids where the highest and lowest values differs by more than 80%, while the total organic carbon is more uniform with the difference between lowest and highest values less being less than 30%. Results show that the highest organic acid concentration is in Audzelu lake and Little Kivdalova lake. The high organic acid concentration in these lakes can be related to the way sapropel forms in these lakes. In both lakes the sapropel sediments are organic sapropel with lower mineral content and with lover pH values.

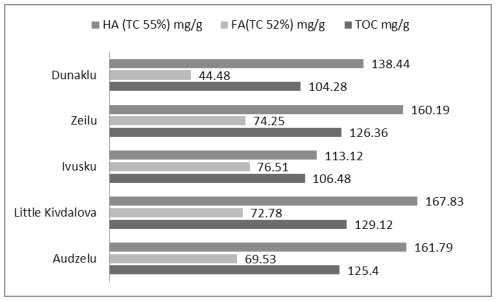

Fig. 2. Concentration of humic acid (HA), fulvic acid (FA) and total organic carbon (TOC) in each lake, mg/g.

It is reported in [18], [19] that not only the color of sapropel sediments can vary, but also the color of extracted HS can be different, indicating the degree of humification and HA and FA concentration in the extracts. Color of extracts was from light yellow to dark brow. Extracts from Dunaklu and Ivusku lake were yellow but extracts from Audzelu and Little Kivdolova lakes were darker almost black and it correlates with HA and FA concentration.

The concentration of humic and fulvic acids in sapropel extract are higher in organic sapropel, it also is related to the age of sapropel layers as the formation of bioactive substances, mineralisation of lakes and degradation of organic matter all influences the concentration of HA and FA in sapropel [3], [20].

In the analysis of the extracts the antioxidant level was measured. Antioxidant levels were calculated for each sapropel layer, there was no significant difference in antioxidant concentration of each sapropel extract from various layer, so median concentration of antioxidants was calculated to show average findings from each lake. It was found that antioxidant level is considerably higher in organic sapropel extracts from the lakes Audzelu, Little Kivdalovu and Zeilu. The difference between the highest and the lowest values is almost threefold for the total antioxidant level. The reason for so drastic differences in the antioxidant levels between different lakes is not fully understood. It seems that the antioxidant level does not correlate with the level of humic and fulvic acids

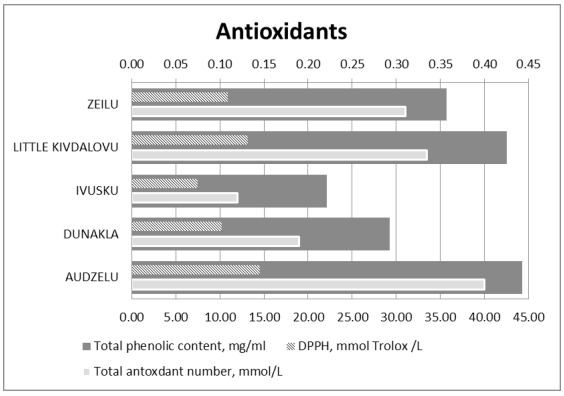

Fig. 3. Antioxidant level in sapropel extract from each lake.

One trend is that one of the lakes – Dunaklu lake gives considerably lower both antioxidant and humic and fulvic acids levels. However, Ivusku lake with the lowest antioxidant levels is high in fulvic acid level. More studies of different samples from the sediments in the same lake might be needed to better understand the variations of these parameters in the sapropel extracts obtained from different sources. The antioxidant measurement results are shown in fig.3 for each lake.

IV. CONCLUSION

Balneologically usable sapropel was found in all studied lakes. The most suitable lake as a source of sapropel was found to be Audzelu lake. It is easy reachable, because of the small village next to it, it has high humic and fulvic acids concentration and it shows the highest antioxidant level.

The concentration of humic and fulvic acids and the antioxidant levels varies strongly between different lakes. In the studied samples the concentration of humic and fulvic acids do not correlate with the antioxidant level.

The difference in humic acid levels between different lakes is much less pronounced than the difference in the fulvic acid and antioxidant levels.

In cases where higher fulvic acids and or antioxidant level are desirable it is important to select correct lake for the raw sapropel extraction since the fulvic acid content and antioxidant level varies strongly between the lakes.

ACKNOWLEDGMENTS

This research was supported by „Analysis of characteristics of medical sapropel and its usage for medical purposes and elaboration of industrial extraction methods", project No. 1.1.1.1/16/A/165.

REFERENCES

[1] K. Stankeviča and M. Kļaviņš, "Sapropelis un tā izmantošanas iespējas," *Mater. Sci. Appl. Chem.*, vol. 29, no. 29, p. 109, 2014.

[2] R. Sánchez-Espejo, C. Aguzzi, P. Cerezo, I. Salcedo, A. López-Galindo, and C. Viseras, "Folk pharmaceutical formulations in western Mediterranean: Identification and safety of clays used in pelotherapy," *J. Ethnopharmacol.*, vol. 155, no. 1, 2014.

[3] M. Orru, M. Übner, and H. Orru, "Chemical properties of peat in three peatlands with balneological potential in Estonia," no. Wollina 2009, pp. 43–49, 2011.

[4] E. S. Trofimova, M. V Zykova, A. A. Ligacheva, E. Y. Sherstoboev, V. V Zhdanov, M. V Belousov, M. S. Yusubov, S. V Krivoshchekov, M. G. Danilets, and A. M. Dygai, "Influence of Humic Acids Extracted from Peat by Different Methods on Functional Activity of Macrophages in Vitro," vol. 162, no. 6, pp. 741–742, 2017.

[5] A. Fioravanti, S. Tenti, C. Giannitti, N. A. Fortunati, and M. Galeazzi, "Short- and long-term effects of mud-bath treatment on hand osteoarthritis: A randomized clinical trial," *Int. J. Biometeorol.*, 2014.

[6] T. Belwal, S. M. Ezzat, L. Rastrelli, I. D. Bhatt, M. Daglia, A. Baldi, H. P. Devkota, I. E. Orhan, J. K. Patra, G. Das, C. Anandharamakrishnan, L. Gomez-Gomez, S. F. Nabavi, S. M. Nabavi, and A. G. Atanasov, "A critical analysis of extraction techniques used for botanicals: Trends, priorities, industrial uses and optimization strategies," *TrAC - Trends Anal. Chem.*, vol. 100, no. 2018, pp. 82–102, 2018.

[7] G. L. Ryzhova, M. A. Tyunina, and K. A. Dychko, "Determination of fatty acids in products of the vibromagnetic treatment of sapropel by chromatography-mass spectrometry," *J. Anal. Chem.*, vol. 68, no. 8, pp. 736–742, 2013.

[8] C. C. Xu, B. Wang, Y. Q. Pu, J. S. Tao, and T. Zhang, "Advances in extraction and analysis of phenolic compounds from plant materials," *Chin. J. Nat. Med.*, vol. 15, no. 10, pp. 721–731, 2017.

[9] J. M. Roux, H. Lamotte, and J. L. Achard, "An Overview of Microalgae Lipid Extraction in a Biorefinery Framework," *Energy Procedia*, vol. 112, no. October 2016, pp. 680–688, 2017.

[10] O. Y. Strus, "Study of sapropel extracts from Prybych natural deposits," *J. Chem. Pharm. Res.*, vol. 7, no. 6, pp. 133–137, 2015.

[11] "Latvian lakes datubase: ezeri.lv," *Datubase*. [Online]. Available: https://www.ezeri.lv/database/. [Accessed: 04-Mar-2019].

[12] A. Rebiai, T. Lanez, and M. L. Belfar, "Total polyphenol contents, radical scavenging and cyclic voltammetry of algerian propolis," *Int. J. Pharm. Pharm. Sci.*, 2014.

[13] M. Tarnawski, K. Depta, D. Grejciun, and B. Szelepin, "HPLC determination of phenolic acids and antioxidant activity in concentrated peat extract - A natural immunomodulator," *J.*

Pharm. Biomed. Anal., vol. 41, no. 1, pp. 182–188, 2006.

[14] W. Brand-Williams, M. E. Cuvelier, and C. Berset, "Use of a free radical method to evaluate antioxidant activity," *LWT - Food Science and Technology*. 1995.

[15] N. J. Miller, C. Rice-Evans, M. J. Davies, V. Gopinathan, and A. Milner, "A novel method for measuring antioxidant capacity and its application to monitoring the antioxidant status in premature neonates.," *Clin. Sci.*, 1993.

[16] G. A. Leonova, V. A. Bobrov, S. K. Krivonogov, A. A. Bogush, V. A. Bychinskii, A. E. Mal'tsev, and G. N. Anoshin, "Biogeochemical specifics of sapropel formation in Cisbaikalian undrained lakes (exemplified by Lake Ochki)," *Russ. Geol. Geophys.*, vol. 56, no. 5, pp. 745–761, May 2015.

[17] A. Javanshah and A. Saidi, "Determination of Humic Acid by Spectrophotometric Analysis in the Soils," pp. 19–23, 2016.

[18] G. D. S. Tserenpil, O. Ugtakhbayar, S. G. Shevchenko, L. V Kliba, and M. G. Voronkov, "Characterization and organic compounds in peloids from Mongolia," 2009.

[19] G. P. Alexandrova, G. Dolmaa, B. G. Sukhov, and D. Regdel, "A new humic acid remedy with addition of silver nanoparticles," vol. 13, pp. 7–11, 2012.

[20] A. Whitbread, "Soil organic matter: its fractionation and role in soil structure," *Soil Org. Matter Manag. Sustain.*, 1995.

Research of Laser Marking and Engraving on Brass Alloy 260

Dainis Klavins
Faculty of Engineering
Rezekne Academy of Technologies
Rēzekne, Latvia
dainis.klavins@rta.lv

Lyubomir Lazov
Faculty of Engineering
Rezekne Academy of Technologies
Rēzekne, Latvia
lyubomir.lazov@rta.lv

Antons Pacejs
Faculty of Engineering
Rezekne Academy of Technologies
Rēzekne, Latvia
antons.pacejs@rta.lv

Ritvars Revalds
Faculty of Engineering
Rezekne Academy of Technologies
Rēzekne, Latvia
ritvars.revalds@rta.lv

Edgars Zaicevs
Faculty of Engineering
Rezekne Academy of Technologies
Rēzekne, Latvia
edgars.zaicevs@rta.lv

***Abstract*—Brass Alloy 260 is widely used in mechanical engineering (odometer contacts, radiator cores), electrical engineering (electrical connectors, screw shells), plumbing (bathroom fixtures), consumers (watch parts, buttons, lamps) etc. The paper presents an analysis of the laser marking and engraving process. The ability Rofin powerline f20 laser system to engrave on Brass Alloy 260 is described. Recommendations are given on choosing the right parameters for laser marking and engraving of Brass Alloy 260 products.**

Keywords— laser engraving, laser marking, Brass Alloy 260, Brass Alloy laser marking, laser marking analysis.

I. INTRODUCTION

The need for different types of information to be placed on different products has increased in recent years. The most common information on products is related to the manufacturer. A serial number of the product or item, information about the manufacturer, manufacturer's logo, etc. Specific material for marking is brass alloy which is widely used in many areas including military area, where the need for marking has increased. Ammunition marking is necessary for public safety and stronger ammunition control. [2],[4]

Information can be placed in direct text (letters, numbers, and images) or encrypted (barcode or QR code). Different marking methods are used based on the type of material used and production needs. Manufacturing companies devote their efforts and resources to the development of different marking methods for specific needs.

Various marking methods are widely used in industries and fields: shock-mechanical; electro erosion; electrochemical; screen printing; pad printing; anodizing; thermal painting; powder coating; ink printing; labeling; laser marking etc. Each of them has its own place in different specific productions. As the materials used in production change, the requirements for their marking change.

Historically used marking methods become unprofitable or unusable. Like shock-mechanical marking method can't be used on brittle materials.[1] Laser marking successfully replace older marking methods and provide the following benefits:

- the ability to mark various types of materials - metals, semiconductors and dielectrics;
- contactless method;
- minimal heat-affected zone;
- high wear resistance;
- accuracy;
- high contrast;
- high labor productivity;
- high information density;
- flexibility; marking of hard-to-reach places;
- no additional processing;
- the possibility of marking in the movement; integration into automated lines;
- ensuring high protection of information; environmentally friendly process.
- possibility of marking on assembled products, like ammunition cartridges (Fig.1). [5], [6]

Fig. 1. Brass ammunition cartridge laser marking. [2]

As we have many different materials used in production, we must choose the right laser system that meets our marking needs. There are different types of laser systems on the market that have a wide range of applications:

- Gas laser – Helium-Neon, Argon, Krypton, Carbon dioxide, Nitrogen.
- Solid-state laser – Rubin, Neodymium: Glass, Neodymium, Alexandrite.
- Diode laser – GaAlAs/GaAs, InGaAsP/InP, InGaAlAs. [3]

Print ISSN 1691-5402
Online ISSN 2256-070X
http://dx.doi.org/10.17770/etr2019vol3.4167

II. OBJECTIVE OF THE STUDY

The objective of the paper is to analyze marking possibilities on Brass Alloy 260 using the 20W fiber laser system *Rofin powerline f20*.

Research is made for company that manufactures several types of Brass Alloy 260 products. Goal is to create a system and marking technology and integrate it in one of the production stages with the following requirements:

- The mark should be clear and legible;
- After chemical treatment, the mark can't be significantly damaged;
- The marking area is up to 10x50 mm;
- Up to 16 symbols are placed in the marking area;
- Marking speed should be at least 2 products per second.

III. MATERIALS AND EQUIPMENT

A. MATHERIALS

Brass alloy has been used for many centuries for locks, plumbing valves (Fig.2), bearings and musical instruments. [A7]. Brass is an alloy of copper and zinc. Changes in proportions of zinc and copper leads to different material properties.

There are 3 types of commonly used brass alloys:

- Cartridge Brass (Brass alloy 260) – areas of application: plumbing tools, automotive manufacturing, ammunition (Fig.1) components etc.
- Brass C330 – wide usage in plumbing for good bending and welding ability.
- Brass C360 - Leaded brasses are known for resistance to atmospheric corrosion. [A7]

Fig. 2. Brass Laser Marking with Fiber Laser [A8]

Brass alloy 260 consist of copper and zinc. Where Coper is approx. 70%, zinc is approx. 30% and other components are less than 0.15%.

TABLE I. COMPONENT ELEMENTS PROPERTIES [A9]

Copper, Cu	68.5 - 71.5 %
Iron, Fe	<= 0.050 %
Lead, Pb	<= 0.070 %
Other, total	<= 0.15 %
Zinc, Zn	28.5 - 31.5 %

Brass alloy is a highly reflective material. Therefore, many laser systems are not suitable for marking this material (Fig.3).

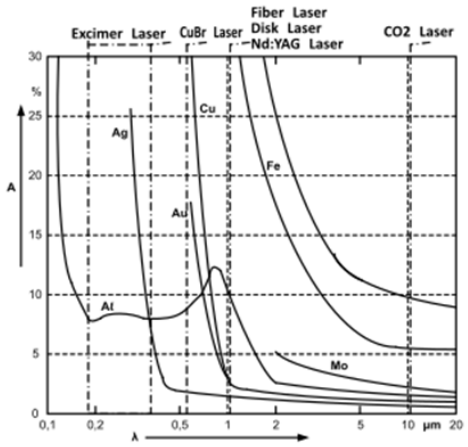

Fig. 3. Various material electromagnetic radiation absobrtion [%] depending on emited wavelength [μm].

B. LASER SYSTEM

The fiber laser system *Rofin powerline f20* was used in the study.

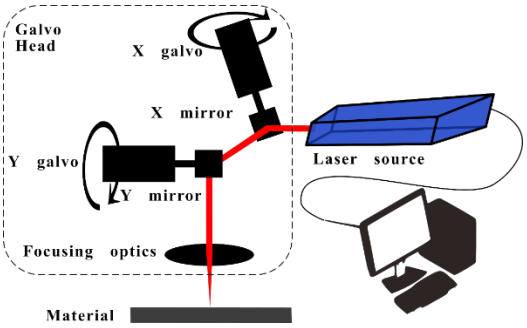

Fig. 4. Schematic view of *Rofin powerline f20* experimental set-up

Rofin powerline f20 laser system technical parameters can be observed in Table II. and schematic view of experimental set-up could be observed in Fig.4

TABLE II. *ROFIN POWERLINE F20* TECHNICAL PARAMETERS

Symbol	Name	Values range	Units
v	Scan speed	1 — 20000	mm/s
Δf	Defocus	-10 — +10	mm
P	Avarege power	0 — 20	W
f	Impulse frequency	20 — 50	kHz
τ	Impulse length	4 - 200	ns
	Working range	300x300	mm
	Focal spot size	20	μm
λ	Wavelength	1064	nm
Laser type		diode pumped fiber Yb;	
Operating mode		impulse	

C. MESUREMENT DEVICES

In the beginning of experiments laser system adjustments were made in pulse mode. The average output power was measured on an OPHIR F150A-BB-26 instrument (Table 3). Results are represented as power as a function from k_p (Fig5). This graph is important as in laser system software must be defined coefficient k_p not power directly.

TABLE III. POWER MEASUREMENT SENSOR OPHIR F150A-BB-26 SPECIFICATIONS

Absorber Type	**Broadband**
Spectral Range [µm]	0.19 - 20
Aperture diameter [mm]	26
Power Range [W]	0,05 - 150
Power Noise Level [mW]	3
Max Average Power Density [kW/cm2]	12
Max Energy Desnity [J/cm2]	10
Power Accuracy [+/-%]	3
Cooling	fan

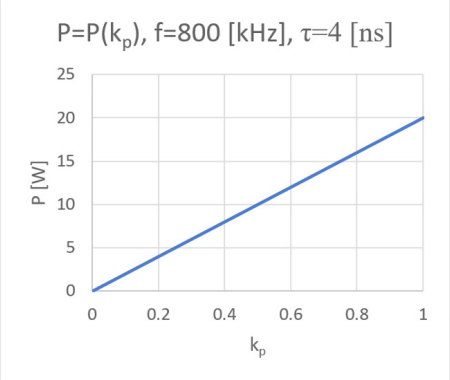

Fig. 5. Mapping of values of power regulation coefficient k_p [%] to laser mean power P [W] with a constant pulse repetition frequency f = 800 [kHz].

"Lext" 3D Laser Measuring Microscope OLS 5000 was used in this study for laser processing impact on the material e.g. in this case after laser processing we measured the width and depth of laser beam influence on the material.

Measurements were made using MPLFNN10XLEXT lens with 236x zoom and following technical data was given from manufacturer:

- Z measurement pitch: 2µm
- Z axis measurement accuracy: 0.15+L/20µm
- X and Y axis resolution: +/- 1.5%

IV. METHODS OF MEASUREMENT

Effects on area of laser impact - heating, melting or evaporation depends on the energy that is absorbed by material. For understanding Energy absorption in more detail following formulas was used:

- Linear Pulse Energy

$$LPE = \frac{P}{v}, [J/mm] \quad (1)$$

The LPE dimension is numerically equal to the absorbed energy per unit length in the laser marking area.

- Linear Pulse Density

$$LPD = \frac{f}{v}, \quad (2)$$

The LPD dimension is numerically equal to the number of pulses fallen to a unit length.

- Effective energy

$$E_{ef} = LPE \ LPD, \quad (3)$$

The E_{ef} dimension gives the amount of absorbed energy of the laser radiation per unit area of the laser impact area. From formulas (1), (2) and (3) formula a shorter version could be obtained (4).

$$E_{ef} = \frac{Pf}{v^2}, \quad (4)$$

V. RESULTS AND DISCUSSIONS

The experiments in this study were grouped in three main directions:

- Investigation of the duration of laser pulses on the width and depth of the lines marked on the samples;
- Investigation of the effect of the processing speed on the geometry of the marked line (width, depth);
- Examination of the influence of the power density on the marking (width and line depth)

During each of these series of experiments, the remaining technological parameters were kept constant.

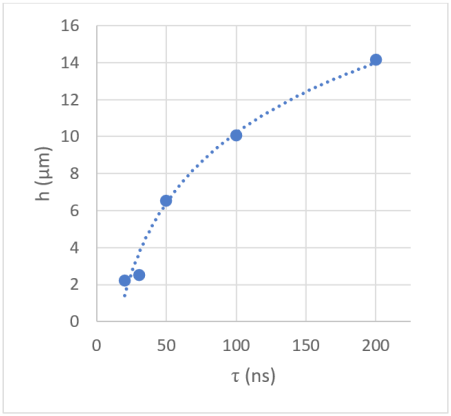

Fig. 6. Graph shows depth changes as a function from impulse length h=h(τ). Variable parameter is τ. All other parameters are constant: f= 2 [kHz], k_p = 80 [%], v=20 [mm/s]. k_p – mean power [%]; τ – pulse duration [ns]; f – pulse frequency [kHz]; v – marking speed [mm/s]

A nonlinear increase in the depth of the mark is observed for the entire investigated pulse duration range (Fig.6). The curve is part of a parabola. The rate of increase in depth is:

- 0.10 µm/ns for the range $\tau \in [20, 100]$ ns;
- 0.04 µm/ns for the range $\tau \in [100, 200]$ ns.

In the first pulse duration range, the marking depth is changing significantly faster than in the second.

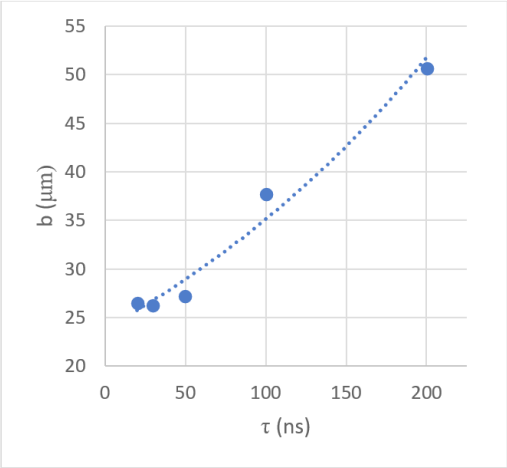

Fig. 7. Graph shows width changes as a function from impulse length b=b(τ). Variable parameter is τ. All other parameters are constant: f= 2 [kHz], k_p = 80 [%], v=20 [mm/s].

A nonlinear increase in the width of the mark is observed for the entire investigated pulse duration range (Fig. 7). The curve is part of a concave parabola. The rate of increase in width is:

- 0.023 µm/ns for the range τ Є [20, 50] ns
- 0.13 µm/ns for the range τ Є [50, 200] ns.

In the first pulse duration range, the marking width is changing significantly faster than in the second.

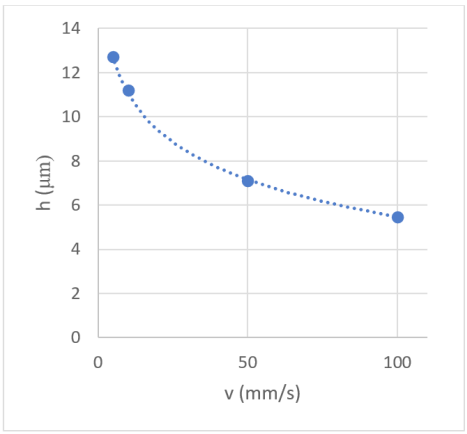

Fig. 8. Graph shows depth changes as a function from marking speed h=h(v). Variable parameter is τ. All other parameters are constant: f= 2 [kHz], k_p = 80 [%], τ=200 [ns].

The depth of the marking decreases non-linearly with increasing the span speed v Є [5, 100] mm / s (Fig.8). The rate of decrease in depth is:

- 0.139 µm/(mm/s) for the range v Є [5, 50] mm/s;
- 0.026 µm/(mm/s) for the range v Є [50, 100] mm/s.

The results are in line with the theory of speed influence on the laser marking process of metals.
The same non-linearity is observed for marking width changes as a function from marking speed (Fig.9).
The rate of decrease in width is:

- 0.93 µm/(mm/s) for the range v Є [5, 50] mm/s;
- 0.033 µm/(mm/s) for the range v Є [50, 100] mm/s.

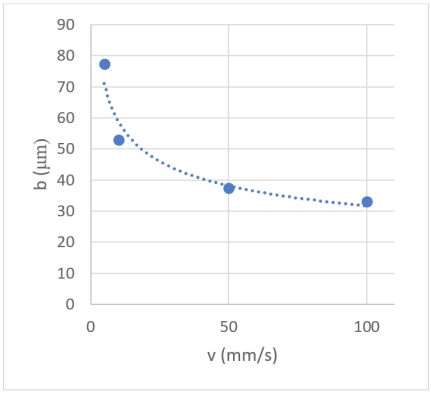

Fig. 9. Graph shows width changes as a function from marking speed b=b(v). Variable parameter is τ. All other parameters are constant: f= 2 [kHz], k_p = 80 [%], τ=200 [ns].

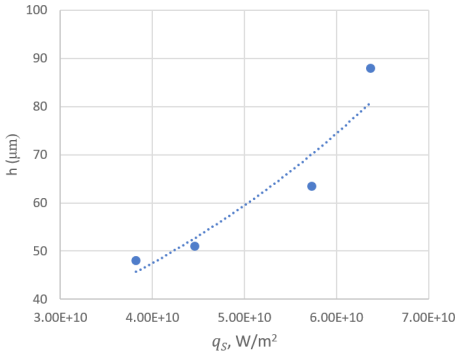

Fig. 10. Graph shows depth changes as a function from power density h=h(q_s). All other parameters are constant: f= 2 [kHz], v = 5 [mm/s], τ=200 [ns].

A nonlinear increase in the depth of the mark is observed for the entire investigated power density range (Fig.10).

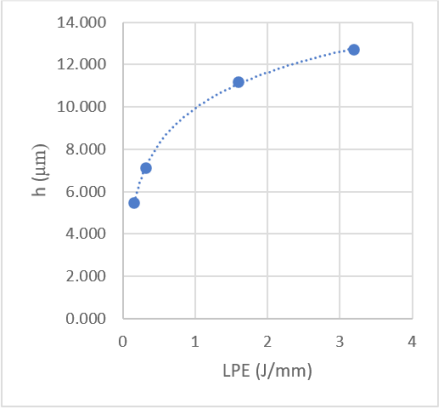

Fig. 11. Graph shows depth changes as a function from linear pulse energy. All other parameters are constant: f= 2 [kHz], v = 5 [mm/s], τ=200 [ns], P=18 [W].

A nonlinear increase in the depth of the mark is observed for the entire investigated linear pulse energy

range (Fig.11). The rate of increase in depth is:

- 3.984 µm/(J/mm) for the range LPE Є [0.16, 1.6] J/mm;
- 0.925 µm/(J/mm) for the range LPE Є [1.6, 3.2] J/mm.

In the first pulse duration range, the marking depth is changing significantly faster than in the second.

VI. CONCLUSION

More and more companies and manufacturers need to mark new materials where classical marking methods become more difficult to apply. Laser marking provides new opportunities to process different materials. Each material has its own specific characteristics, so it is necessary for each technology to choose the most optimal and efficient laser system.

The need for our research is new requirements for the manufacturer to mark each product by including the marking system in the production line. The material used in the production is Brass Alloy 260.

With our chosen F20 fiber laser system, samples with variable parameters of the laser system were marked. The depth and width of the mark were analyzed.

The depth and width of the marking lines were analyzed as a function of the laser parameters, the results obtained were good and meet the user requirements.

Further research will focus on analyzing other parameters related to markup quality, such as contrast, and more. Their dependence on changing laser parameters. Research will also be done with other laser systems having a variable wavelength. It will also assess the performance and economic efficiency of the new technology.

REFERENCES

[1]. "Great Impressions. Ruger turns to lasers to make its mark", Shot Business Daily, Day 2, January 16, 2013. www.telesis.com/pdf/shotdaily_2_2013_Ruger_TTI_Article.pdf

[2]. "Ammunition Control Practicies in Latin America and the Caribbean", UNLIREC, 2018. http://www.unlirec.org/Documents/Amm_Contro_Practices.pdf

[3]. CO2 Laser, Technical documentation, TRUMPF 02/2007 http://www.iconmachinetool.com/education/Library_Laser_CO2_Laser.pdf

[4]. Giacomo Persi Paoli, Ammunition Marking, Small Arms Survey Issue Brief, Number 3, December 2012 http://www.smallarmssurvey.org/fileadmin/docs/G-Issue-briefs/SAS-IB3-Ammunition-Marking.pdf

[5]. L. Lazov, N. Angelov, Principal factors determining quality of markings on metals and alloys. International Scientific Conference AMTECH- 2007, Gabrovo, Vol. I (2007) 102−10].

[6]. L. Lazov, H. Deneva, P. Narica, Laser Marking Methods. Environment. Technology. Resources, Rezekne, Latvia Proceedings of the 10th International Scientific and Practical Conference. 2015. Volume I, 108-115.

Environment. Technology. Resources. Rezekne, Latvia
Proceedings of the 12th International Scientific and Practical Conference. Volume III, 124-128

Unidirectional Braking Energy Recovery System for Elevators

Kaspars Kroics
Institute of Industrial Electronics and Electrical Engineering
Riga Technical University
Riga, Latvia
kaspars.kroics@rtu.lv

***Abstract*—The paper discusses design of energy storage based energy recovery system for elevators. The main element of such system is unidirectional DC-DC converter to control energy flow to supercapacitor or li-ion battery based energy storage. The paper gives explanation of selection of the converter topology and some design considerations. The test results of experimental prototype on a developed test bench are presented in the paper.**

***Keywords*—DC-DC converter, supercapacitors, energy efficiency, electrical drive, isolated converter.**

I. Introduction

Energy efficiency of an elevator can be improved by storing the regenerated braking energy produced during descending of heavy loads and ascending of light loads. The proposed solution is to integrate DC-DC converter together with supercapacitors into one module and retrofit existing electrical drive system of the elevator to increase energy efficiency. The structure of the energy recovery system is shown in Fig. 1. Such system makes the elevator system energy efficient.

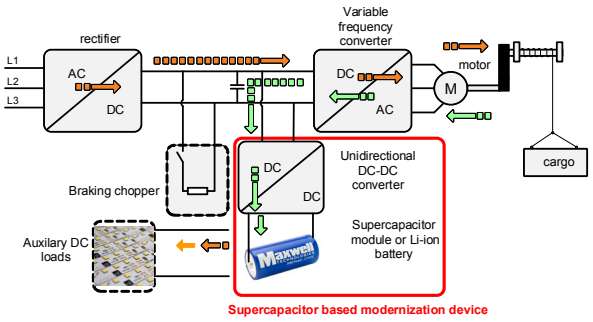

Fig. 1. The application of supercapacitor based retrofit device in elevator or lifting device system.

To utilize low voltage energy storage unidirectional DC-DC converter is required. The stored energy later can be used to supply auxiliary DC loads such as LED lightening and elevator control system. Induction motor or permanent magnet motor together with frequency converter is used more frequently to drive elevator mechanisms. If the motor is pushed rotating faster than the synchronous speed, then it will move to regenerative braking mode and generate electricity. The braking energy still is wasted as heat in braking resistors in more than 90 percent of all installed elevators [1]. By useful utilizing of this energy could be stored from 20 to 40% of electrical energy. In other cases regenerative variable frequency drives are used that supplies braking energy back into AC grid. If there are no electrical loads into shared facilities electricity should be supplied back to the utility network. The price for this electricity is low, therefore, payback time of regenerative drive system can be much longer as in case with a local storage with a DC-DC converter – one example is shown in Fig. 2.

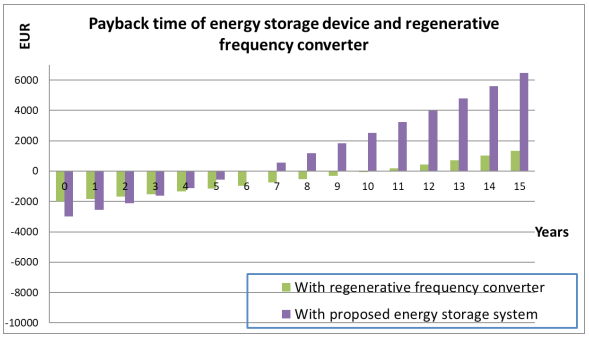

Fig. 2. Payback period of regeneretive AC drive and energy storage system.

In the example shown in Fig. 2 consumption of the elevator is equal to 7000 kWh, energy savings 40% and electricity price in Latvia. The approximate price of the regenerative variable frequency converter is equal to 2000 EUR but price of proposed energy storage system – 3000 EUR. Taken into consideration that price of electricity purchased from the grid operator is at least 3 times higher than price for electricity delivered back to grid operator the payback time of energy storage system can be much shorter although the initial investments is higher.

The central part of the proposed solution is unidirectional power electronic converter which should detect braking mode and provide optimal power flow to the storage. It is important to reduce the current ripple and improve the efficiency of the converter. One of possibility is to use multilevel interleaved DC-DC converter topology. In such way it is possible to improve efficiency as low voltage transistors have better parameters and reduce current ripple as the currents are shifted in phase and therefore current ripples are much lower.

Print ISSN 1691-5402
Online ISSN 2256-070X
http://dx.doi.org/10.17770/etr2019vol3.4173

Interleaving control schemes of the DC-DC converters more and more often are used in the converter applications, especially, in the converters that require high power capability and high performance. Benefits of such control methods include reduction of size, losses and cost of the input and output filter, reduction of current stress of the DC bus capacitor, improved dynamic performance and increase in the power capacity of the converters. Interleaved DC-DC converters are used in various applications: as voltage regulation modules [2], [3] renewable applications [4], [5], [6], [7], [8], traction applications [9]–[14] and in the other application areas. In this case benefit from utilizing interleaved topology is possibility to reduce the size and losses in output inductors.

II. DC-DC Converter Description

As a converter topology for particular application input-series output-parallel (ISOP) configuration is selected that consists of two modular DC-DC converters connected in series at the input and in parallel at the output (Fig. 3), enabling the use of high switching frequency MOSFETs with low voltage ratings, which leads to a higher power density and a high conversion efficiency. As output current ripple frequency is twice of the switching frequency, size and costs of the output filter can be reduced. The voltage of both legs of the converter due to unequal values of passive components and delays in control signals may differ. If this issue is solved without changing the control system, the control of the converter can be realized as for conventional DC-DC converter just signals should be shifted in phase by 180 degrees.

If in the ISOP the converter balancing of the voltages of both legs is not provided, the difference in currents through transistors causes misbalance of the capacitors voltage and this will lead to failure. The difference of currents of both legs can be caused by unequal inductances of the inductors, transformers, unlike parameters of semiconductors or different duty cycle, especially, in the transient process. Misbalance in the voltage causes larger current in the leg with higher voltage so slow process of stabilization will take place, but mostly it is not enough to keep voltage of the capacitor in the desired level. Therefore, it is necessary to find a solution to prevent the situation when voltage of the capacitor reaches dangerous value and damages semiconductors or passive elements. of the capacitor reaches dangerous value and damages semiconductors or passive elements.

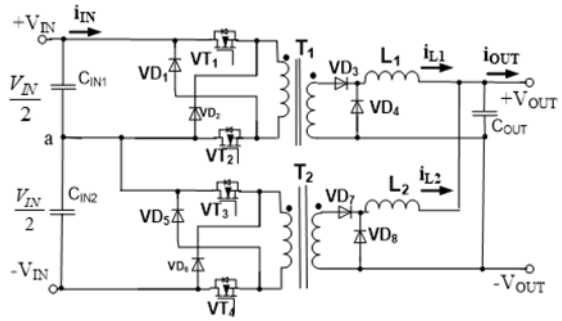

Fig. 3. Schematics of ISOP forward DC-DC converter.

Fig. 4 shows structure of the proposed transformer which consists of round ferrite core and three windings. Number of turns of the secondary winding and balancing winding are equal to 27. For the balancing winding wire with cross sectional area equal to 0,2 mm2 is used. For the secondary winding litz wire with cross sectional area equal to 7 mm^2 is used. The balancing resistor in series with balancing winding must be selected according to desired rapidity of voltage balancing process. Should be considered that resistor with low resistance leads to higher current therefore cross sectional area of the balancing winding must be increased if it is required faster balancing process. In the particular case balancing resistor has value around 800 Ohm. The power losses in this circuit is low therefore compact balancing resistor can be used with power of less than watt, additional balancing windings can be created by using wire with small cross-sectional area.

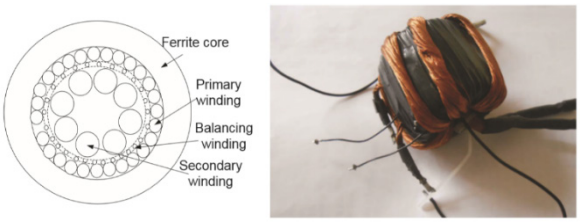

Fig. 4. The transformer for ISOP converter configuration with integrated balancing winding.

Fig. 5 shows the oscillograms with voltage balancing process. The voltage equalization circuit is not provided to hold equal voltages in all conditions. The main task of the balancing winding is to ensure that voltage does not reach dangerous value. In particular case there is voltage shifting margin of safety equal to 70 volts as maximum allowed voltage of the input capacitor is equal to 350 V. And other task is equate voltages when misbalance current is over.

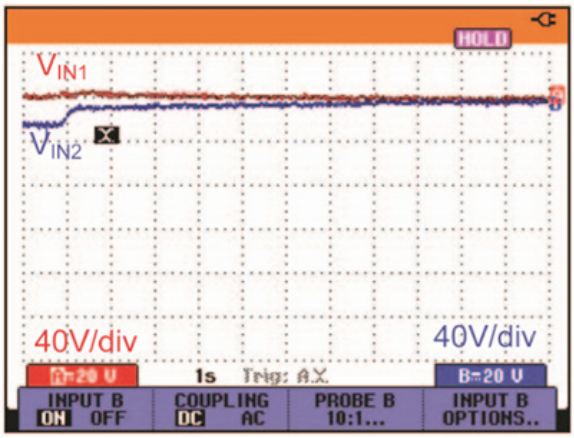

Fig. 5. The process of voltage balancing.

In the oscillograms shown in the Fig. 5 during first moment the converter works with full load but in mode with small duty cycle therefore voltage balancing circuit cannot fully compensate misbalance current but the voltage stays in the safety margin. After reducing of the load balancing circuit equalize both voltages. The oscilogram is measured in the short circuit and no load conditions in which the voltage equalizing process is the worst as duty cycle in these modes is small. But even in the following

conditions balancing circuit works satisfactorily. More detailed description of the balancing circuit design and working principle can be found in [15]–[17]

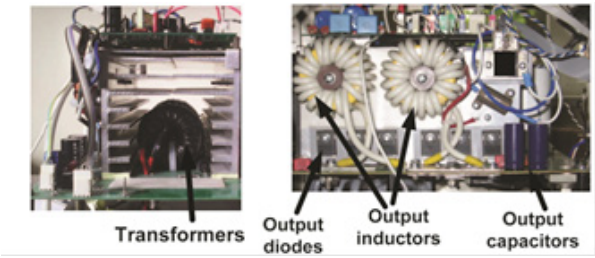

Fig. 6. The hardware realization of the ISOP DC-DC converter.

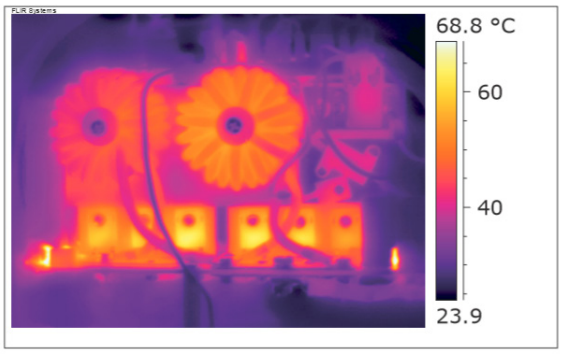

Fig. 7. The thermal image of the converter working at full load.

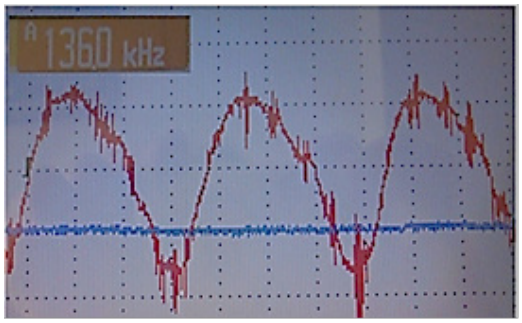

Fig. 8. Output current ripple (blue line) and current ripple in the inductor (red line).

The ISOP converter is designed for input voltage 600 V DC and output voltage from 0-30 volts, output current 100 A. The control of the converter is realized by using DSP microcontroller. Fig. 6 shows hardware of the converter, for transformer design it is used N87 material two ring ferrite cores to increase effective cross sectional area of the core. For inductor it is used metal powder cores. Output diodes are connected 3 in parallel to minimize power losses. Input capacitors have high value as converter also was tested far from the 3 phase rectified AC power DC bus, this value can be significantly reduced. The transformer based drivers were designed to drive MOSFET transistors. To cool down the semiconductors and magnetic elements the converter is equipped with radiator and electric fan. As can be seen in Fig. 7 the temperature of the converter elements does not exceed critical values under nominal load. In Fig.8 are shown current ripples in the output inductor of one phase and summary output current, Due to interleaved topology these ripples can be eliminated fully by using relatively small output capacitor therefore size and price of the converter can be reduced.

III. Design of Test Bench to Emulate Energetic Processes of Elevator

The energy recovery system that includes unidirectional DC-DC converter and series connection of supercapacitors is connected to the DC link of the traction drive simulator. The DC-DC converter operates in a step-down mode and provides supercapacitor or Li-ion battery charging, after that the stored energy is slowly discharged by powering auxiliary DC loads.

Fig. 9 shows hardware of the developed test bench – in this case ABB VFDs and braking resistors are used and CEO electric motors are used. The test bench control system is developed to test on test bench bi-directional DC-DC converter for energy recovery application in elevator system.

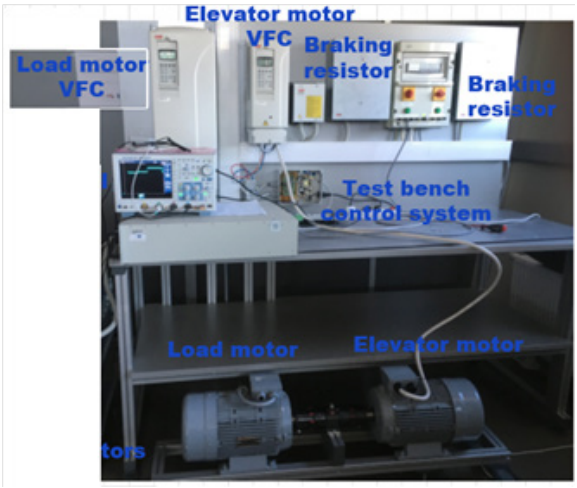

Fig. 9. Hardware implementation of the test bench.

In case of elevator the out of balance torque can be referred to the motor as follows:

$$M = \frac{m_{o.b.} \cdot g \cdot D}{2 \cdot i \cdot \eta}, \quad (1)$$

where $m_{o.b.}$ – out of balance mass (considering counterweight);

g - is the acceleration due to gravity;

D- is the diameter of the sheave in m;

i is the reduction ratio of the gearbox;

η is the efficiency of the installation.

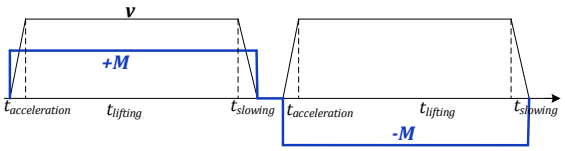

Fig. 10. The analog reference control signals send to the VFDs in case of elevator emulation.

As the acceleration equal to 0.8-1.0 m/s^2 is acceptable and is set in settings of VFD of the elevator motor there is no need to calculate inertia of the system. Fig. 10 shows control signals to VFDs in case of elevator. The elevator motor VFD is controlled by providing speed reference signal to VFD analog input (black curve in Fig. 10). The elevator motor accelerates to the constant speed and then keeps constant speed till it slows down with a desired slow down time. The load emulation motor VFD is controlled by providing analogue torque reference signal

(blue curve in Fig. 10). During the braking mode the control system generates negative torque reference signal to load emulation VFD. Other alternative can be reversing rotational speed of the elevator VFD and provide positive moment – it is more close to real elevator but from the energy flow point of view there is no difference therefore in particular application rotational speed is selected only in one direction.

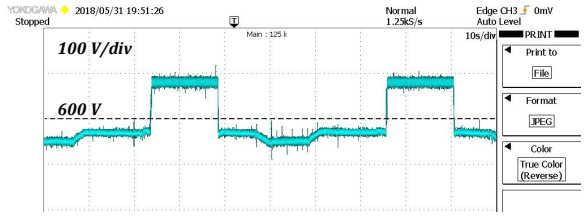

Fig. 11. Voltage of DC bus during two cycles implemented on test bench.

Fig. 11. shows DC bus voltage of elevator motor VFD, it is possible clearly indicate the braking time of period when the voltage goes up till the braking chopper operating voltage. During the lifting mode the voltage drops down. More detailed description of the development of test bench can be found in [18].

IV. Experimental Analysis of Energy Recovery System

The particular converter is designed to control input voltage at 600 V DC level. If the elevator system is in the braking mode, the DC bus voltage increases as can be seen in Fig. 11 and converter control loop is designed in a such a way to regulate DC bus voltage equal to 600 V DC. As can be seen in Fig. 12 such voltage regulation works well and it is possible to charge battery with a braking power that in other case will be lost in the braking resistor. The output voltage of the converter is from 0–30 volts, nominal output current 100 A. The control of the converter is realized by using DSP microcontroller.

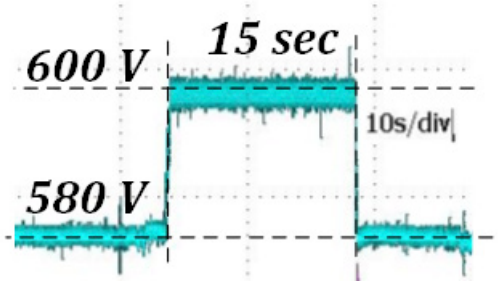

Fig. 12. DC bus voltage during charge mode of the battery.

The efficiency of the converter is approximately 90 percent but it is possible efficiency improvement by using semiconductors with better parameters and by implementing soft-switching circuits.

Conclusions

In the paper proposed method to improve energy efficiency of the elevators by using unidirectional DC-DC converter and energy storage. Developed DC-DC converter have efficiency around 90 percent but the benefit is that such converter is inexpensive and therefore payback time of energy storage system will be shorter.

To test energy recovery system test bench was developed that allows experimental testing of energy storage system in laboratory. The experimental results show proper operation of the energy storage system, further goal is the efficiency improvement of the converter without significant increasing price of electronics components used to develop such converter. Also integration of such system in solar DC power system can be as one of the further goals.

References

[1] "Energy-efficient elevators and escalators in Europe: An analysis of energy efficiency potentials and policy measures - ScienceDirect." [Online]. Available: https://www.sciencedirect.com/science/article/pii/S0378778811006530. [Accessed: 28-Feb-2019].

[2] P.-L. Wong, P. Xu, P. Yang, and F. C. Lee, "Performance improvements of interleaving VRMs with coupling inductors," IEEE Transactions on Power Electronics, vol. 16, no. 4, pp. 499–507, Jul. 2001.

[3] Y. Panov and M. M. Jovanovic, "Design considerations for 12-V/1.5-V, 50-A voltage regulator modules," IEEE Transactions on Power Electronics, vol. 16, no. 6, pp. 776–783, Nov. 2001.

[4] D. Arnaudov and S. Vuchev, "Multiphase converters for charging of energy storage elements," in 2016 XXV International Scientific Conference Electronics (ET), 2016, pp. 1–3.

[5] J. Zakis, D. Vinnikov, and L. Bisenieks, "Some design considerations for coupled inductors for integrated buck-boost converters," in 2011 International Conference on Power Engineering, Energy and Electrical Drives, 2011, pp. 1–6.

[6] J. Shen, K. Rigbers, and R. W. D. Doncker, "A Novel Phase-Interleaving Algorithm for Multiterminal Systems," IEEE Transactions on Power Electronics, vol. 25, no. 3, pp. 741–750, Mar. 2010.

[7] K. Kroics, J. Zakis, and U. Sirmelis, "Multiphase interleaved DC-DC converter with directly and inversely coupled inductors," in 2016 57th International Scientific Conference on Power and Electrical Engineering of Riga Technical University (RTUCON), 2016, pp. 1–6.

[8] K. Kroics, A. Sokolovs, U. Sirmelis, and L. Grigans, "Interleaved series input parallel output forward converter with simplified voltage balancing control," in PCIM Europe 2016; International Exhibition and Conference for Power Electronics, Intelligent Motion, Renewable Energy and Energy Management, 2016, pp. 1–8.

[9] M. A. Shrud, A. Bonsbaine, A. S. Ashur, R. Thorn, and T. Benmusa, "Modeling and simulation of automotive interleaved buck converter," in 2009 44th International Universities Power Engineering Conference (UPEC), 2009, pp. 1–5.

[10] J. Czogalla, J. Li, and C. R. Sullivan, "Automotive application of multi-phase coupled-inductor DC-DC converter," in 38th IAS Annual Meeting on Conference Record of the Industry Applications Conference, 2003., 2003, vol. 3, pp. 1524–1529 vol.3.

[11] M. Hirakawa et al., "High power DC/DC converter using extreme close-coupled inductors aimed for electric vehicles," in The 2010 International Power Electronics Conference - ECCE ASIA -, 2010, pp. 2941–2948.

[12] D. Arnaudov, N. Hinov, S. Vuchev, and I. Nedyalkov, "Modeling of Multiphase Converter for Charging of Energy Storage Elements," in PCIM Europe 2017; International Exhibition and Conference for Power Electronics, Intelligent Motion, Renewable Energy and Energy Management, 2017, pp. 1–7.

[13] V. Brazis, K. Kroics, and L. Grigans, "Scientific Laboratory Platform for Testing the Electric Vehicle Equipped with DC Drive," Latvian Journal of Physics and Technical Sciences, vol. 51, no. 5, Jan. 2014.

[14] K. Kroics and J. Zakis, "Electronic Ballast for Gas Discharge Lamp Based on Input-Series Output-Series Resonant Converter," in PCIM Europe 2017; International Exhibition and Conference for Power Electronics, Intelligent Motion, Renewable Energy and Energy Management, 2017, pp. 1–7.

[15] K. Kroics, U. Sirmelis, and V. Brazis, "Voltage balance control of two-level DC-DC converter," in Engineering for rural development, 2015, pp. 402-407.

[16] K. Kroics, J. Zakis, A. Suzdalenko, and G. Gaigals, "A simplified approach to input voltage balancing for series connected isolated DC-DC converters," in 2016 18th European Conference on Power Electronics and Applications (EPE'16 ECCE Europe), 2016, pp. 1–10.

[17] U. Sirmelis, L. Grigans, K. Kroics, and J. Zakis, "Isolated DC/dc converter based voltage measuring system for series connected supercapacitor cells," in 2015 9th International Conference on Compatibility and Power Electronics (CPE), 2015, pp. 443–446.

[18] K. Kroics, "Development of Induction Motor Based Test Bench for Supercapacitor Braking Energy Recovery System Testing," in 2018 IEEE 59th International Scientific Conference on Power and Electrical Engineering of Riga Technical University (RTUCON), 2018, pp. 1–5.

[19] K. Kroics, J. Zakis, A. Suzdalenko, and G. Gaigals, "A simplified approach to input voltage balancing for series connected isolated DC-DC converters," in 2016 18th European Conference on Power Electronics and Applications (EPE'16 ECCE Europe), 2016, pp. 1–10.

Method for Preliminary Estimation of the Critical Power Density in Laser Technological Processes

Lyubomir Lazov
Faculty of Engineering
Rezekne Academy of Technologies
Rezekne, Latvia
llazov@abv.bg

Nikolay Angelov
Department of Physics, Chemistry and Ecology
Technical University of Gabrovo
Gabrovo, Bulgaria
angelov_np@abv.bg

Edmunds Teirumnieks
Faculty of Engineering
Rezekne Academy of Technologies
Rezekne, Latvia
edmunds.teirumnieks@rta.lv

***Abstract*—For a number of new laser technology processes, it is essential to plan an experimental plan for primary experimental engineering activities in terms of quality. The assessment of the critical power density to reach the melting or evaporation temperature of the surface with a suitable theoretical model is an important stage in the development of a particular manufacturing technology. With the help of numerical experiments, this report provides a method for pre-examining the influence of wavelength on the laser technological process. The calculations are performed with a specialized program, running MATLAB. A series of temperature fields were obtained at a change in power density and wavelength at laser impact for concrete types of structural steel. The temperature dependence of the optical and thermo-physical characteristics of the material is also reporded. The analysis is made for laser technology complexes working with lasers emitting in the ultraviolet, visible, near and distant infrared areas. For these wavelengths the critical power density of melting and evaporation is determined.**

Keywords*—laser processing of materials, numerical experiments, temperature fields, structural steel, wavelength, power density.

I. Introduction

The specific properties of laser radiation, such as high monochromaticity, low distortion, coherence, as well as the possibility of achieving high energy density (respectively power density) in the processing area are the main arguments for the successful industrial application of laser sources over the last 58 years. Laser sources generate radiations with wavelength in a wide spectral range, from ultraviolet, visible and infrared, working in continuous and pulsed mode. Today, lasers are widely used in a number of areas of industrial production such as automotive, aircraft, shipbuilding, machine building and more. For marking, engraving, cutting, welding, drilling of holes, thermal annealing, measurements of linear and angular quantities. Other areas of life in which lasers have entered in recent years include communications, medicine, research, agriculture, the food industry, advertising, military, and so on.

Laser technological processes are complex to realising and depend on a number of factors. Some of them are power density, speed, frequency, pulse duration, impact time, pulse power, pulse energy, defocus, number of repetitions, absorption capacity of the material, depth of penetration, etc. For each technological process, material, and laser, preliminary studies must be performed to clarify the role of all factors and to optimize the process [1 - 4] - fig. 1.

The influence of some factors (fill factor, power, velocity and frequency) is investigated for optimizing the marking of barcodes on aluminum surfaces using the Nd: YAG laser [5].

The role of frequency on the process of marking stainless steel products with the Nd: YAG laser has been investigated, and the working interval for quality marking, has been determined [6].

In [7] analyzes the effect of power, velocity, defocustion, pressure and flow of the auxiliary gas on cutting process with CO_2 laser.

In [8] is considered the receiving of seamless laser welds of low carbon and stainless steel sheets. The influence of speed and power on the process is investigated. Technological tables have been compiled with optimal parameters for the studied steels.

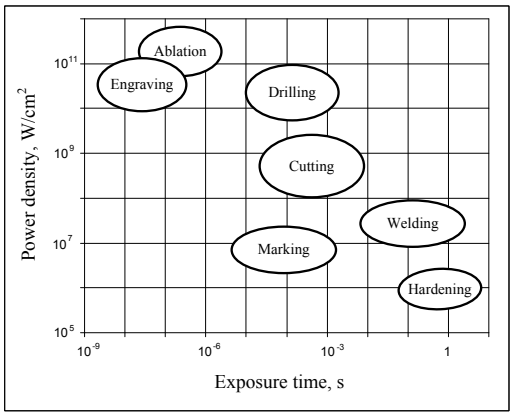

Fig. 1. Diapasons of the power density and time of impact for basic laser technological processes

Research on the determination of optimal technological parameters is mandatory when introducing laser technologies into practice, as the processes are complex and involve a number of processes of the interaction

Print ISSN 1691-5402
Online ISSN 2256-070X
http://dx.doi.org/10.17770/etr2019vol3.4140

of the radiation with the substance (the materials being processed). They can generally be divided into two stages. First stage theoretical studies are related to modeling and simulations of process. The second stage is experimental for determining and achieving the qualitative criteria, pledged in the technology.

The purpose of the publication is to investigate the influence of the laser radiation density and the rate of processing to reach of critical power densities of melting and evaporation for concrete materials (samples) from the industry.

II. EXPOSITION

A number of laser technology processes such as hardening, alloying, welding, cladding, marking, engraving, etc. are carried out in the intervals between the temperatures of: quenching $T_н$, melting T_m and evaporation T_v of the treated materials – fig. 2.

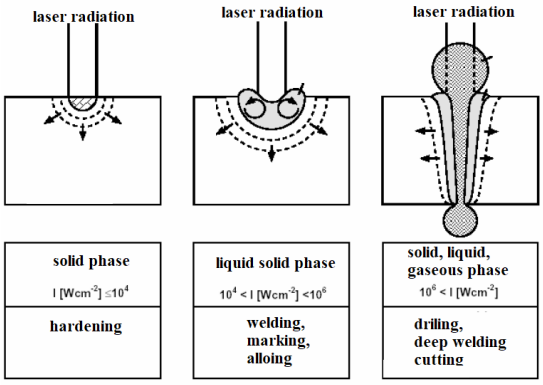

Fig. 2. Mechanism of interaction of the laser radiation with the substance for the different processes

Preliminary numerical experiments and model simulations and analyzes were performed for three types of laser systems and two types of materials.

Laser technological systems

The researches are for laser technological systems with a CuBr laser (operating in the visible area), a fiber laser (operating in the near infrared area), a CO_2 laser (operating in the far infrared area). In the Table I are showed some parameters of these systems. The fiber laser has higher radiation quality and higher efficiency compared to the other two lasers. All three laser systems have high positioning accuracy and good repeatability.

TABLE I. BASIC PARAMETERS OF TECHNOLOGICAL SYSTEMS WITH CUBR LASER, FIBER LASER AND CO_2 LASER

Laser parameter	CuBr laser	Fiber laser	CO_2 laser
Wavelength λ, μm	0,511	1, 062	10,6
Power P, W	20,0	40,0	100
Frequency ν, kHz	20,0	20	50
Pulse duration τ, ns	30	250	250
Pulse energy E_p, mJ	1,00	2,00	2,00
Pulse power P_p, kW	33,3	8,00	8,00
Beam quality M^2	< 1,7	< 1,1	10,0
Positioning accuracy, μm	2,5	2,5	2,5
Efficiency, %	10	40	20

Materials

Numerical experiments refer to samples of structural steels C45 and 18ChGT. They are widely used in the industry [9]. C45 is used for making gears, crankshafts and camshafts, sprockets, spindles, sealants, cylinders, cams and other parts that are normalized, improved and subjected to surface heat treatment requiring increased strength. From steel 18ChGT are produced improved or cemented important details, which require increased strength, as well as high surface hardness, which require increased strength, as well as high surface hardness, operating under impact loads. n the Table II and Table III are showed the temperature dependence of some parameters of the studied steels. They are characterized by high coefficients of thermal conductivity and thermal diffusivity.

TABLE II. TEMPERATURE DEPENDENCE OF CERTAIN PARAMETERS OF CONSTRUCTION STEEL C45.

Legend: k – coefficient of thermal conductivity, ρ – density, c – specific heat capacity, a – coefficient of thermal diffusivity.

T, K	k, W/(m.K)	ρ, kg/m³	c, J/(kg.K)	a, m²/s
293	49	7826	457	$1,37.10^{-5}$
373	48	7799	473	$1,35.10^{-5}$
473	47	7769	494	$1,22.10^{-5}$
573	44	7735	515	$1,10.10^{-5}$
673	41	7698	536	$9,94.10^{-6}$
773	39	7662	583	$8,73.10^{-6}$
873	36	7625	578	$8,17.10^{-6}$
973	31	7587	611	$6,69.10^{-6}$
1073	27	7595	720	$4,94.10^{-6}$
1173	26	7565	708	$4,85.10^{-6}$

TABLE III. TEMPERATURE DEPENDENCE OF CERTAIN PARAMETERS OF CONSTRUCTION STEEL 18CHGT.

T, K	k, W/(m.K)	ρ, kg/m³	c, J/(kg.K)	a, m²/s
293	37	7800	485	$9,78.10^{-6}$
373	38	7773	495	$9,88.10^{-6}$
473	38	7743	508	$9,66.10^{-6}$
573	37	7709	525	$9,14.10^{-6}$
673	35	7672	537	$8,50.10^{-6}$
773	34	7636	567	$7,85.10^{-6}$
873	31	7599	588	$6,94.10^{-6}$
973	30	7561	626	$6,34.10^{-6}$
1073	29	7569	705	$5,43.10^{-6}$

Numerical experiments

To determine the critical values of the power density of melting q_{Scrm} and evaporation q_{Scrv}, numerical experiments with the program TEMPERATURFELD3D [10] were carried out. It is a specialized program for obtaining temperature fields in the area of laser impact. The calculations refer to the examined technological systems with CuBr laser, fiber optic laser, CO_2 laser [11-13] and structural steels C45 and 18ChGT. The temperature dependence of some parameters of steels (according to Table II and Table III) is recorded.

- **for CuBr laser**

In Fig. 3 and Fig. 4 are presented graphics of the dependencies of the critical power densities of melting q_{Skpm} and evaporation q_{Skpv} from the speed for steels C45 and 18ChGT. From the obtained results, the following

conclusions can be drawn:

- The critical power densities of melting and evaporation increment non-linearly with increasing of speed for structural steels C45 and 18ChGT with speed in the interval $v \in [20; 100]$ mm/s;
- The rate of increase in critical power density of melting is

for interval $v \in [20; 60]$ mm/s
$7{,}55.10^8$ (W/m^2)/(mm/s) for steel C45;
$8{,}82.10^8$ (W/m^2)/(mm/s) for steel 18ChGT;
for interval $v \in [60; 100]$ mm/s
$5{,}18.10^8$ (W/m^2)/(mm/s) for steel C45;
$6{,}12.10^8$ (W/m^2)/(mm/s) for steel 18ChGT;

- The rate of increase in critical power density of evaporation is

for interval $v \in [20; 60]$ mm/s
$12{,}0.10^8$ (W/m^2)/(mm/s) for steel C45;
$14{,}2.10^8$ (W/m^2)/(mm/s) for steel 18ChGT;
for interval $v \in [60; 100]$ mm/s
$8{,}25.10^8$ (W/m^2)/(mm/s) for steel C45;
$9{,}75.10^8$ (W/m^2)/(mm/s) for steel 18ChGT;

- For structural alloy steel 18ChGT, the critical values of power densities of melting and evaporation density are about 17% greater than for structural carbon steel C45. The reasons for this are the higher melting and evaporation temperatures of steel 18ChGT.

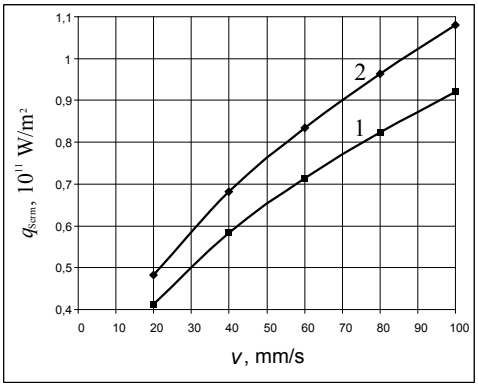

Fig. 3. Graphics of dependence of critical power density of melting from speed for CuBr laser for: 1 – steel C45; 2 – steel 18ChGT

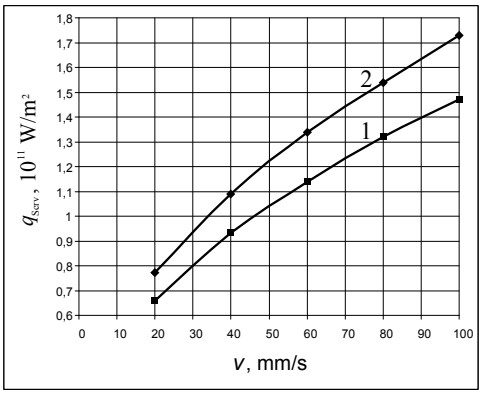

Fig. 4. Graphics of dependence of critical power density of evaporation from speed for CuBr laser for: 1 – steel C45; 2 – steel 18ChGT

- **for fiber laser**

In Fig. 3 and Fig. 4 are showed graphics of the dependencies of the critical power densities of melting q_{Skpm} and evaporation q_{Skpv} from the speed for steels C45 and 18ChGT From the obtained graphics, it follows:

- The critical power densities of melting and evaporation increment non-linearly with increasing of speed for both steels;
- The rate of increase in critical power density of melting is

for interval $v \in [20; 60]$ mm/s
$0{,}94.10^9$ (W/m^2)/(mm/s) for steel C45;
$1{,}09.10^9$ (W/m^2)/(mm/s) for steel 18ChGT;
for intrval $v \in [60; 100]$ mm/s
$0{,}64.10^9$ (W/m^2)/(mm/s) for steel C45;
$0{,}75.10^9$ (W/m^2)/(mm/s) for steel 18ChGT;

- The rate of increase in critical power density of evaporation is

for interval $v \in [20; 60]$ mm/s
$1{,}52.10^9$ (W/m^2)/(mm/s) for steel C45;
$1{,}74.10^9$ (W/m^2)/(mm/s) for steel 18ChGT;
for interval $v \in [60; 100]$ mm/s
$1{,}02.10^9$ (W/m^2)/(mm/s) for steel C45;
$1{,}25.10^9$ (W/m^2)/(mm/s) for steel 18ChGT;

- For structural alloy steel 18ChGT, the critical values of power densities of melting and evaporation density are about 17% greater than for structural carbon steel C45. The explanation is the same as with the CuBr laser;
- Higher values of critical power densities of melting and evaporation for the fiber laser compared to the CuBr laser are because the radiation in visible area is better absorbed from the steels from that in the near-infrared area.

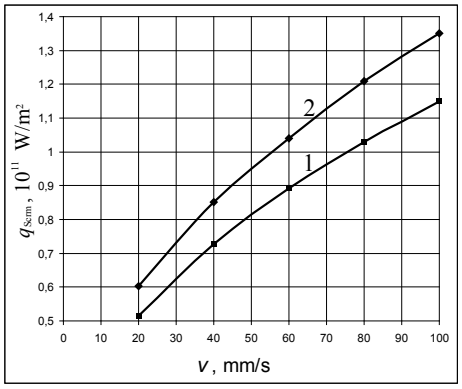

Fig. 5. Graphics of dependence of critical power density of melting from speed for fiber laser for: 1 – steel C45; 2 – steel 18ChGT

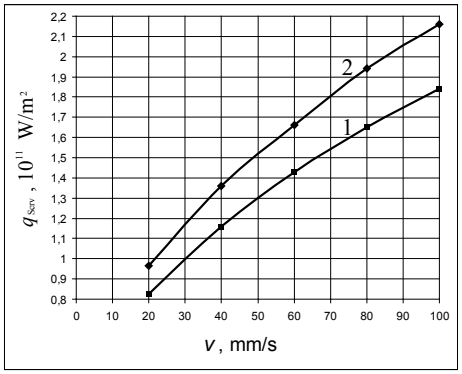

Fig. 6. Graphics of dependence of critical power density of evaporation from speed for fiber laser for: 1 – steel C45; 2 – steel 18ChGT

- **for CO_2 laser**

From the numerical experiments obtained, the dependencies of the critical power densities of melting q_{Scrm} and evaporation q_{Scrv} from the speed for steels C45 and 18ChGT (Fig. 7 and Fig. 8) were presented. The following conclusions can be drawn:

- The critical power densities of melting and evaporation increment non-linearly with increasing of speed for both studied steels;
- The rate of increase in critical power density of melting is

for interval $v \in [20; 60]$ mm/s
$1{,}32.10^9$ (W/m^2)/(mm/s) for steel C45;
$1{,}54.10^9$ (W/m^2)/(mm/s) for steel 18ChGT;
for interval $v \in [60; 100]$ mm/s
$0{,}90.10^9$ (W/m^2)/(mm/s) for steel C45;
$1{,}08.10^9$ (W/m^2)/(mm/s) for steel 18ChGT;

- The rate of increase in critical power density of evaporation is

for interval $v \in [20; 60]$ mm/s
$2{,}10.10^9$ (W/m^2)/(mm/s) for steel C45;
$2{,}48.10^9$ (W/m^2)/(mm/s) for steel 18ChGT;
for interval $v \in [60; 100]$ mm/s
$1{,}45.10^9$ (W/m^2)/(mm/s) for steel C45;
$1{,}70.10^9$ (W/m^2)/(mm/s) for steel 18ChGT;

- For structural alloy steel 18ChGT, the critical values of power densities of melting and evaporation density are greater than for structural carbon steel C45.;
- Critical power densities upon impact to CO_2 laser Критичните плътности на мощността при въздействие с CO_2 лазер are considerably larger than the other two lasers – with about 40% greater than fiber laser and about 75% greater than those for a CuBr laser.

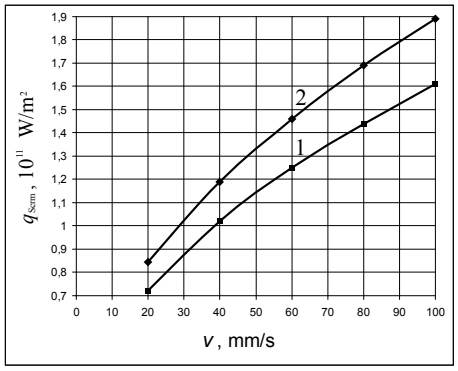

Fig. 7. Graphics of dependence of critical power density of melting from speed for CO2-laser for: 1 – steel C45; 2 – steel 18ChGT

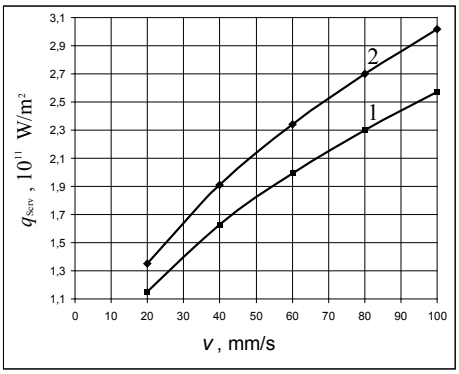

Fig. 8. Graphics of dependence of critical power density of evaporation from speed for CO_2- laser for: 1 – steel C45;

Fig. 9. 2 – steel 18ChGT

Summary

The pre-operating intervals of the power density for the laser technological processes hardening, marking and welding by melting for the three lasers and the two structural steels are given in Table IV.

THE PRE-OPERATING INTERVALS OF THE POWER DENSITY FOR THE LASER TECHNOLOGICAL PROCESSES HARDENING, MARKING AND WELDING BY MELTING

	Steel	**C45**	**18ChGT**
Laser	**Speed**		
CuBr laser	20	$4{,}12.10^{10} \div 6{,}59.10^{10}$	$4{,}82.10^{10} \div 7{,}72.10^{10}$
	40	$5{,}83.10^{10} \div 9{,}32.10^{10}$	$6{,}82.10^{10} \div 1{,}09.10^{11}$
	60	$7{,}14.10^{10} \div 1{,}14.10^{11}$	$8{,}35.10^{10} \div 1{,}34.10^{11}$
	80	$8{,}24.10^{10} \div 1{,}32.10^{11}$	$9{,}64.10^{10} \div 1{,}54.10^{11}$
	100	$9{,}21.10^{10} \div 1{,}47.10^{11}$	$1{,}08.10^{11} \div 1{,}73.10^{11}$
Fiber laser	20	$5{,}15.10^{10} \div 8{,}24.10^{10}$	$6{,}03.10^{10} \div 9{,}62.10^{10}$
	40	$7{,}28.10^{10} \div 1{,}16.10^{11}$	$8{,}52.10^{10} \div 1{,}36.10^{11}$
	60	$8{,}92.10^{10} \div 1{,}43.10^{11}$	$1{,}04.10^{11} \div 1{,}66.10^{11}$
	80	$1{,}03.10^{11} \div 1{,}65.10^{11}$	$1{,}21.10^{11} \div 1{,}94.10^{11}$
	100	$1{,}15.10^{11} \div 1{,}84.10^{11}$	$1{,}35.10^{11} \div 2{,}16.10^{11}$
CO_2 laser	20	$7{,}21.10^{10} \div 1{,}15.10^{11}$	$8{,}44.10^{10} \div 1{,}35.10^{11}$
	40	$1{,}02.10^{11} \div 1{,}63.10^{11}$	$1{,}19.10^{11} \div 1{,}91.10^{11}$
	60	$1{,}25.10^{11} \div 1{,}99.10^{11}$	$1{,}46.10^{11} \div 2{,}34.10^{11}$
	80	$1{,}44.10^{11} \div 2{,}30.10^{11}$	$1{,}69.10^{11} \div 2{,}70.10^{11}$
	100	$1{,}61.10^{11} \div 2{,}57.10^{11}$	$1{,}89.10^{11} \div 3{,}02.10^{11}$

The pre-operating intervals of the power density for the laser technological processes ablation, marking by evaporation, engraving, drilling and cutting of thin sheets for the three lasers and the two structural steels are given in Table V.

TABLE IV. THE PRE-OPERATING INTERVALS OF THE POWER DENSITY FOR THE LASER TECHNOLOGICAL PROCESSES ABLATION, MARKING BY EVAPORATION, ENGRAVING, DRILLING AND CUTTING OF THIN SHEETS

	Steel	**C45**	**18ChGT**
Laser	**Speed**		
CuBr laser	20	$6{,}59.10^{10} \div 2{,}08.10^{11}$	$7{,}72.10^{10} \div 2{,}08.10^{11}$
	40	$9{,}32.10^{10} \div 2{,}08.10^{11}$	$1{,}09.10^{11} \div 2{,}08.10^{11}$
	60	$1{,}14.10^{11} \div 2{,}08.10^{11}$	$1{,}34.10^{11} \div 2{,}08.10^{11}$
	80	$1{,}32.10^{11} \div 2{,}08.10^{11}$	$1{,}54.10^{11} \div 2{,}08.10^{11}$
	100	$1{,}47.10^{11} \div 2{,}08.10^{11}$	$1{,}73.10^{11} \div 2{,}08.10^{11}$
Fiber laser	20	$8{,}24.10^{10} \div 3{,}18.10^{11}$	$9{,}62.10^{10} \div 3{,}18.10^{11}$
	40	$1{,}16.10^{11} \div 3{,}18.10^{11}$	$1{,}36.10^{11} \div 3{,}18.10^{11}$
	60	$1{,}43.10^{11} \div 3{,}18.10^{11}$	$1{,}66.10^{11} \div 3{,}18.10^{11}$
	80	$1{,}65.10^{11} \div 3{,}18.10^{11}$	$1{,}94.10^{11} \div 3{,}18.10^{11}$
	100	$1{,}84.10^{11} \div 3{,}18.10^{11}$	$2{,}16.10^{11} \div 3{,}18.10^{11}$
CO_2 laser	20	$1{,}15.10^{11} \div 3{,}60.10^{11}$	$1{,}35.10^{11} \div 3{,}60.10^{11}$
	40	$1{,}63.10^{11} \div 3{,}60.10^{11}$	$1{,}91.10^{11} \div 3{,}60.10^{11}$
	60	$1{,}99.10^{11} \div 3{,}60.10^{11}$	$2{,}34.10^{11} \div 3{,}60.10^{11}$
	80	$2{,}30.10^{11} \div 3{,}60.10^{11}$	$2{,}60.10^{11} \div 3{,}60.10^{11}$
	100	$2{,}57.10^{11} \div 3{,}60.10^{11}$	$3{,}02.10^{11} \div 3{,}60.10^{11}$

III. CONCLUSION

The obtained critical power densities of melting and evaporation and pre-operating intervals of power density for the investigated technological processes help to plan real experiments in the study of concrete laser technological processes. The results will be in help of:

- operators of laser industrial processes in the industry who will use the pre-operating intervals of power

density in their work;

- engineers-technologists to optimize specific technological processes and to be able to quickly implement new products on which to implement laser technologies.

Similar studies can be made to investigate the impact of other basic technological factors (pulse energy, impulse power, impulse response, pulse duration, defocusing, etc.) onto processes of laser processing.

References

[1] Sobotova, L., Demec P. (2015), Laser Marking of Metal Materials, Modern Machinery Science Journal, December 2015, 808-812
[2] Valiulin A., Gorniy S., Grechco Y., Patrov M., Yudin K., Yurevich V. Lazerna markirovka materialov. Nauchno-technicheskij zhurnal Fotonika, 2007, 3, pp 16-22 (in Russian)
[3] Angelov N. Optimizacija na procesa markirane s lazerno lychenie na obrazci ot instrumentalna stomana. Disertacionen trud za pridobivane na stepen doktor. TU-Gabrovo, 2011 (in Bulgarian)
[4] Pauli, G., The Method behind the Mark, Small Arms Survey, Number 1, December 2010
[5] Jianmei Li, Aiqun Wang, Yusong Wuab, ZhuoMa, Xinxin Fang, LiangTao, Experimental investigation and mathematical modeling of laser marking two-dimensional barcodes on surfaces of aluminum alloy, Journal of Manufacturing Processes, Volume 21, January 2016, pp 141-152
[6] Qi, J., K. Wang, Y. Zhu (2003), A study on the laser marking process of stainless steel, Journal of Materials Processing Technology, 2003, 20 August, Volume 139, Issues 1-3, 273-276
[7] Senthilkumar, V., Laser cutting process – A Review International Journal of Darshan Institute on Engineering Research & Emerging Technologies, Vol. 3, No. 1, 2014
[8] Blecher, J., T. Palmer, T. Debroy, Mitigation of Root Defect in Laser and Hybrid Laser-Arc Welding, Welding Journal, 94(3),73-82, March 2015
[9] www.splav-kharkov.com/main.php
[10] Belev I. Sreda za presmyatane na lazerno inducirani temperaturni poleta. Diplomna rabota, TU-Gabrovo, 2009 (in Bulgarian)
[11] www.pulsligth.net
[12] www.axsys.de
[13] www.spilasers.com

Environment. Technology. Resources. Rezekne, Latvia
Proceedings of the 12th International Scientific and Practical Conference. Volume III, 134-136

Methodology for Automatic Determination of Contrast of Laser Marking for Different Materials

Lyubomir Lazov
Faculty of Engineering
Rezekne Academy of Technologies
Rezekne, Latvia
llazov@abv.bg

Edmunds Teirumnieks
Faculty of Engineering
Rezekne Academy of Technologies
Rezekne, Latvia
edmunds.teirumnieks@rta.lv

Nikolay Angelov
Department of Physics, Chemistry and Ecology
Technical University of Gabrovo
Gabrovo, Bulgaria
angelov_np@abv.bg

Erika Teirumnieka
Faculty of Engineering
Rezekne Academy of Technologies
Rezekne, Latvia
erika.teirumnieka@rta.lv

***Abstract*—A new methodology for determining and optimizing the contrast of the technological laser marking process has been developed. It can evaluate the quality of the markings regardless of the type of material and the type of laser system.**

To perform the test analysis, a specialized test field is programmed, which including the change of two of the main parameters influencing the marking process: the linear energy density (LED) and the linear density of the pulses (LDI). Marking of a test field consisting of squares of a certain size is done by means of a raster marking method with a constant step between the lines.

The results are processed with a digital camera and specialized software. The maximum blackening is compared with the background of all fields and is juxtaposed with the effective energy needed to obtain a certain contrast. Several consecutive iterations are made, with each of the following experiments excluding the variants with least contrast. Thus, the study consistently brings the result to a minimum working area of the basic technological parameters, providing the user's desired contrast of the marking.

The developed author's method of automatically determining the contrast of the laser marking reduces the time for preliminary experimental research and gives a reliable and subjectively absent way of qualitatively marking different types of industrial products.

Keywords*—method, laser marking, software, digital camera, contrast, linear energy density, linear density of the pulses.

I. INTRODUCTION

Laser marking is a technological process in which a number of mutual connected physical phenomena and effects participate, and with interaction of laser radiation with material. These processes are connected with each other in many cases, i.e. they interact with each other. In order to manage the qua-lity and the results of technology process, it is necessary to know these processes, as well as to know the principles connecting them. This knowledge is also necessary for successful monitoring of technological process in on-line regime and for selection of appropriate device for creating of technological systems. Laser processing occurs in space and time and represents an impact of radiation on the material. Therefore, there is a need to explore the quantity of absorbed energy of laser radiation in substrate and its impact on the material. Fig. 1 presents the principal scheme of energy balance of laser impact on metals and alloys. This gives us a notion of complexity of interaction of laser radiation with material and connections between these phenomena and processes.

As a result of interaction, electromagnetic energy is transformed in thermal energy. The efficiency of the entire process is strongly impacted by the losses that are a result of scattering and reflection.

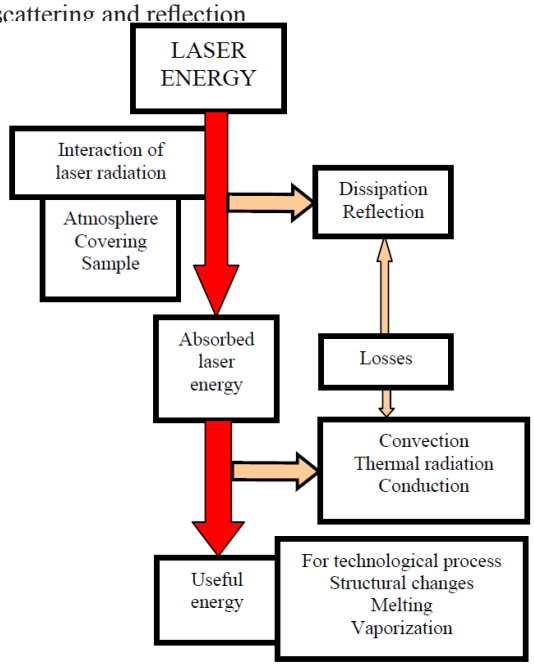

Fig. 1. Principal scheme of energy balance of laser impact

Print ISSN 1691-5402
Online ISSN 2256-070X
http://dx.doi.org/10.17770/etr2019vol3.4143

Only actually absorbed quantity has a direct impact on the technology method and the result of the processing. It is clear that with regards to the technological method of melting, vaporizing or structural changes in the material, only a part of that energy makes a real contribution, because the losses appear as a result of convection, heat radiation and thermal conductivity.

We may examine the absorbed energy as a degree of efficiency η_A of total laser energy that falls onto the material, i.e. that is a part of falling energy which really participates in processing (structural changes, melting, vaporization in the unit volume).

In certain references it is defined as a percentage of the total energy falling onto the material, necessary

for concrete processing. Under certain simplifications, if we ignore the conditions of working zone (convection, heat radiation and thermal conductivity) we assume that it is energy absorbed by the material.

II. EXPOSITION

A. Theoretical aspects

Contrast is a key factor for determining laser marking quality [1-5]. There are several parameters that affect laser marking contrast. According to [6, 7] they can be grouped in the following way:

- Parameters related to laser source – surface density of laser radiation power q_S, pulse energy Ep, frequency of pulse repeating ν, duration of pulses τ;
- Parameters related to material properties – optical and thermo-physical characteristics;
- Parameters related to the manufacturing technology process – marking speed v, step Δx, number of repeatition N, defocusing Δf.

Other parameters include the coefficient of overlapping k_{ov}, a complex parameter which depends both on laser parameters and those of the manufacturing technology process $k_{ov} = f(v, v, d)$, where d is the diameter of the work spot.

A number of magnitudes influence the laser marking process of steels. Some of the magnitudes influencing the process are of a complex nature. As such, linear energy density, linear power density, linear pulse density, volumetric energy density, fill factor, and overlap coefficient, can be indicated.

Linear density of energy E_l is a complex magnitude associated with laser parameters and technological parameters. Determined by the formula

$$E_l = \frac{P}{v}, \quad (1)$$

where P is the power of the falling laser radiation, v – marking speed.

The magnitude of a linear energy density is numerically equal to the absorbed energy per unit length in the laser marking area.

Linear energy density should have a value that allows the material in the processing area to melt or evaporate. It is also decisive in order to obtain a good quality marking, respectively, with good contrast..

Linear pulse density I_l is a complex magnitude associated with laser and technological parameters. It obtains from the expression

$$I_l = \frac{\nu}{v}, \quad (2)$$

where ν is the frequency of following the pulses.

The magnitude of the linear density of the pulses is numerically equal to the number of impulses fallen to a unit length.

Effective energy E_{ef} is a complex magnitude associated with laser parameters and technological parameters.

It is defining with the expression

$$E_{ef} = E_l I_l. \quad (3)$$

The magnitude E_{ef} gives the absorbed energy of the laser radiation per unit area of the laser impact area.

After replacing (1) and (2) in (3), it is obtained

$$E_{ef} = \frac{P\nu}{v^2} \quad (4)$$

What obtains in the zone of laser impact - heating, melting or evaporation depends on the energy that is absorbed in it.

B. Methodology of experimental studies

The implementation of the individual stages of the experimental research methodology can be described in the following example:

The laser marking process for steel CT80 is investigating. It is with widely using in the industry. It is used to make tools that work in conditions that do not cause cutting edge edges: milling cutters, countersinks, axes, chisels, chisels, longitudinal and disk saws, grooving rollers, kerners, screwdrivers, combined pliers, side cutters [8]. A laser technology system with a fiber laser is used to conduct the experiments [9, 10]. The more important parameters of the system are given in Table I. The fiber laser emits in the near infrared area and operates in pulse mode. It has high beam quality and its pulse frequency changes over a wide diapason. The system has high positioning accuracy and good repeatability.

TABLE I. Basic Parameters Of Technological Systems With Cubr Laser And Fiber Laser

Parameter	Value
Wavelength λ, μm	1, 062
Power P, W	30,0
Frequency ν, kHz	10 ÷ 50
Pulse duration τ, ns	250
Pulse energy E_p, mJ	0,60 ÷ 3,00
Pulse power P_p, kW	2,40 ÷ 12,0
Beam quality M^2	< 1,1
Positioning accuracy, μm	2,5
Efficiency, %	40

Stages

- *A test field consisting of squares with a side of 5 mm, is compiled (Fig. 2);*

A test field consisting of 100 squares with a side of 5 mm is realized, arranged in 10 rows and 10 columns.

- *The intervals of change of the linear energy density and the linear density of the pulses are determined;*

Based on our previous research on the laser laser marking process and formulas (1) and (2), preliminary intervals for the linear pulse density I_l and the linear energy density E_l are defined:

I_l Є [3,33.10^5; 7,83.10^5] m^{-1} and

E_l Є [183, 333] J/m .

- *The squares are marking raster;*

Through the laser technology system, the squares with different values of the linear density of impulses and the linear density of the energy are marked. A raster marking method is applied, with step Δx being maintained constant Δx = 50 μm.

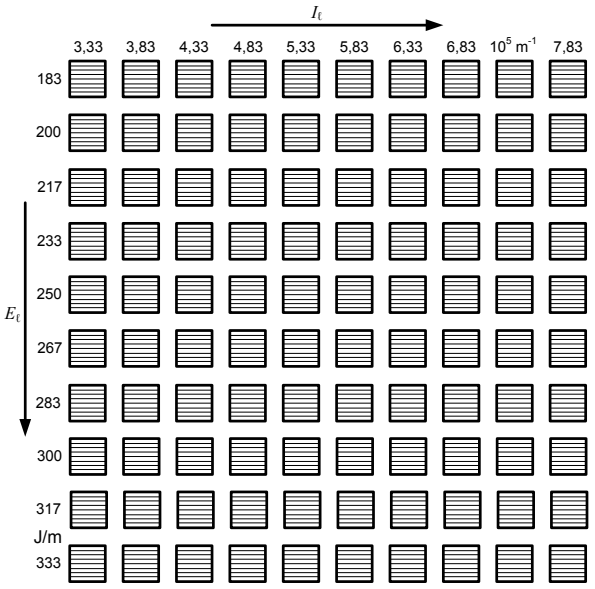

Fig. 2. Test field for conducting of the experiments

- *The contrast of the marking are determined;*

For measuring contrast k^* a methodology was used prescribed by the Bulgarian State Standard 16383:1986.

Contrast k^* is determined in percentage through a reference scale of grey color either in relative units or in percents. A black and white photo is made in the marking zone for the purpose of contrast measuring. By comparing the investigated image with the reference scale a value N_x in the range between 0 (black) and 255 (white) is selected. A reference number N_f is set for the background (that is the image on the surface around the marked zone). Contrast k_x^* is defined by way of linear interpolation from the expression

$$k_x^* = \frac{N_f - N_x}{N_f}.100\% \cdot \qquad (5)$$

- *Reducing the intervals of the studied magnitudes;*

The obtained markings are investigated by determining the contrast of each square with a camera.

Fields with less contrast are excluded, and new experiments are performed by narrowing the investigated intervals for the linear energy density and the linear pulse density.

- *The iterations are repeated until optimal contrast of the laser marking is achieved.*

Working intervals of linear energy density and linear pulse density are determined.

III. CONCLUSION

The process of laser marking is the subject of research by a number of authors.

In recent years, laser marking of 1D and 2D barcodes on the products has increased considerably. The marking of this type is applied directly to the product. It allows to automate the process of reporting and controlling production, to protect the product from forgery. With laser technology for marking of barcodes achieve a high density of inflicted information. For this type of marking, it is particularly important to achieve an optimal contrast ratio relative to the basic background of the sample and the surface of the material.

The methodology proposed and considered by us will be useful for the operators of laser systems to reach the desired optimal technological parameters more quickly.

REFERENCES

[1] Velotti, C., A. Astarita, C. Leone, S. Genna , F. Minutolo, A. Squillace, Laser marking of titanium coating for aerospace applications, Procedia CIRP 41, 2016, pp. 975 – 980
[2] Sobotova, L. P. Demec, P. Laser marking of metal materials. *Modern Machinery Science Journal*, 2015, pp. 808-812.
[3] Valiulin A., Gorniy S., Grechco Y., Patrov M., Yudin K., Yurevich V. Lazerna markirovka materialov. Nauchno-technicheskij zhurnal Fotonika, 2007, 3, pp 16-22 (in Russian).
[4] Jianmei Li, Aiqun Wang, Yusong Wuab, ZhuoMa, Xinxin Fang, LiangTao, Experimental investigation and mathematical modeling of laser marking two-dimensional barcodes on surfaces of aluminum alloy, *Journal of Manufacturing Processes*, Volume 21, January 2016, pp 141-152.
[5] Han A., D. Gubencu, Analysis of the Laser Marking Technologies, *Nonconventional Technologies Review*, № 4, 2008, pp. 17-22.
[6] Lazov L., Angelov N. Vliyaniye na nyakoi faktori vyrhu procesa na lazerno markirane na izdeliya ot metali i splavi. mezhdunarodna nauchna konferenciya UNITEH`11. Gabrovo, 18-19 noembri 2011 (in Bulgarian)
[7] Angelov N. Optimizacija na procesa markirane s lazerno lychenie na obrazci ot instrumentalna stomana. Disertacionen trud za pridobivane na stepen doktor. TU-Gabrovo, 2011 (in Bulgarian)
[8] www.splav-kharkov.com/main.php
[9] www.axsys.de
[10] www.spilasers.com

Preliminary Numerical Analysis for the Role of Speed onto Laser Technological Processes

Lyubomir Lazov
Faculty of Engineering
Rezekne Academy of Technologies
Rezekne, Latvia
lyubomir.lazov@rta.lv

Nikolay Angelov
Department of Physics, Chemistry and Ecology
Technical University of Gabrovo
Gabrovo, Bulgaria
angelov_np@abv.bg

Edmunds Teirumnieks
Faculty of Engineering
Rezekne Academy of Technologies
Rezekne, Latvia
edmunds.teirumnieks@rta.lv

Erika Teirumnieka
Faculty of Engineering
Rezekne Academy of Technologies
Rezekne, Latvia
erika.teirumnieka@rta.lv

***Abstract*—Studying the impact of speed on a number of laser processes such as marking, engraving, cutting, welding and others is crucial for the optimization of these technological processes. The processing speed, along with the frequency of laser pulses and their duration, also determines the time of action in the processing area and hence the absorbed quantity of electromagnetic energy. Based on numerical experiments with specialized software TEMPERATURFELD3D, the report analyzes the temperature variation in the processing area as a function of speed. The researches were analyzed for processing with two types of lasers emitting in the visible and infrared areas of the electromagnetic spectrum and two types of steels (tool and structural). From the course of the obtained temperature fields the dependence of temperature on the speed at two power densities was obtained. The obtained results help to make a preliminary assessment the speed work intervals for the processes as laser marking, laser engraving, laser cutting, laser welding and others. In this way, it is assisted in building an optimal concept for the passing of a particular technological process in function of the laser source, the material and the type of the technological operation.**

***Keywords*—laser technological processes, numerical experiments, laser, steel, temperature, speed, power density**

I. Introduction

Laser technologies has been undergoing rapid development in recent decades. New types of lasers with high-quality of radiation, high reliability and high efficiency were constructed. This has allowed to be extended the diapason of lasers in many industries spheres. In particular, laser process processes such as marking, engraving, cutting, welding, drilling of holes, tempering, annealing, overlaying, etching, scribing and others are continuously expanding their positions [1 - 7]. In addition, the need for systematic analysis and solutions to the engineering problems that arise during their introduction into production increases. In each case, research should be done to optimize the process and to determine the operating intervals of the basic technological parameters [8 – 10]. Numerical calculations with appropriate software or real experiments are used. Thus, technological tables for each particular process, type of laser and material can be obtained.

The purpose of the publication is to study the influence of velocity at constant power densities for CuBr laser and fiber laser on samples of structural steel for basic technological processes (marking, cutting, welding, engraving).

Studies will be conducted in the following areas:

- Receiving temperature fields in the laser impact area for different speeds and power densities for samples of steels C35 and 50G;
- Analysis of graphical dependencies of temperature from speed for two power densities for the investigated lasers and materials.
- Evaluating the results from the perspective of the materials surveyed;
- Assessment of the role of processing with both types of lasers - CuBr laser and fiber laser;
- Determination of working intervals of processing speed for two fixed power densities to achieve the desired temperature regimes.

II. EXPOSITION

Laser technology processes are complex and their implementation depends on many factors. Factors influencing laser technological processes can be grouped into three groups (Figure 1) associated with:

- properties of the material - optical properties (reflection coefficient, absorption capacity, absorption coefficient, depth of penetration) and thermo-physical properties of the material (coefficient of thermal conductivity, specific heat capacity, coefficient of thermal diffusivity, heat diffusion length);
- laser source - laser beam wavelength, laser beam quality, laser beam power, power density, frequency, pulses duration, impulse energy,

Print ISSN 1691-5402
Online ISSN 2256-070X
http://dx.doi.org/10.17770/etr2019vol3.4154

impulse power;

- technological process - speed, step, defocusing, number of repetitions.

These basic factors are within certain physical dependencies. They are important for understanding the physical essence of processes [8, 9].

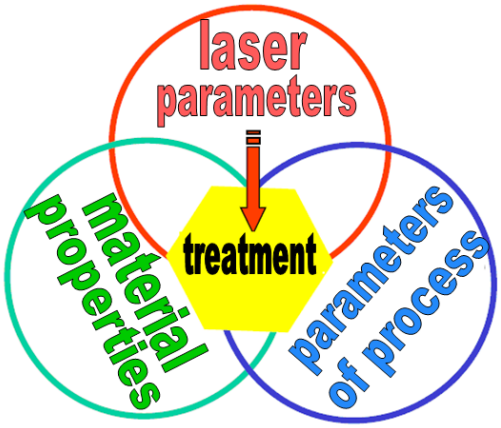

Fig. 1. Basic groups of factors that affect of laser technological processes

The speed v is one of the most important parameters of the technological processes. The time of impact on the sample and the energy that is absorbed in the material in the impact area, depends from its.

For example, the energy E absorbed in the impact area - a square with a side d (d is diameter of the working spot) is directly related to the processing speed

$$E = \frac{APd}{v}, \quad (1)$$

where A is the absorption capacity of the material, P – power of laser radiation.

The speed of technological processes can be consider in several aspects: on the one hand, the speed should be such that the technological process itself takes place at the maximum possible high performance and efficiency; on the other hand, it must be optimal for the technological process within the quality criteria. Between these two trends, a balance must be found in order to obtain optimal technological parameters to achieve good product quality.

Power density and speed are basic magnitudes that influence technological processes. They are related to the temperature of the material surface in the impact area.

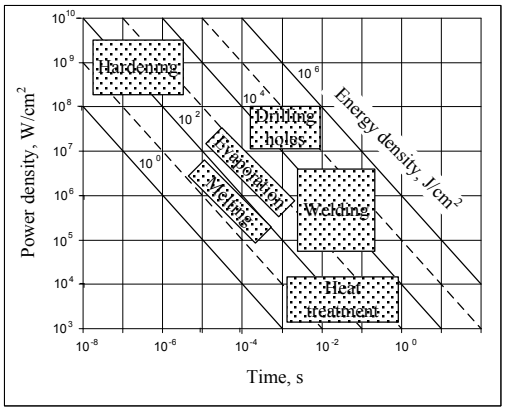

Fig. 2. Relationship between power density and time for some technological processes

The phenomenological (thermophysical) approach to laser exposure to materials requires determining the optimum temperature for each process. As can be seen from Fig. 2, it depends mainly on two factors: the power density

$$q_s = P / S \quad (1)$$

where S is the area at which it is absorbed by the surface of the material, and time of impact t.

The ratio between temperature T and the power density q_S can be determined by the thermal conductivity equation

$$\frac{\partial T}{\partial t} - a\Delta T = \frac{Q(x, y, z)}{\rho c} \quad (2)$$

where $\Delta = \frac{\partial^2}{\partial x^2} + \frac{\partial^2}{\partial y^2} + \frac{\partial^2}{\partial z^2}$ is the operator of Laplace, $Q(x, y, z)$ - volume density of the absorbed light flux, a - coefficient of thermal conductivity, ρ - density, c- specific heat capacity.

To solve equation (2) it is necessary to set 1 initial condition, 6 boundary conditions and determine $Q(x, y, z)$.

$$T = f\begin{bmatrix} Aq \\ \rho, c, a, R, \alpha \\ x, y, z, t \end{bmatrix}. \quad (3)$$

The heat conduction equation has no analytical solution and numerical methods are used to obtain the temperature fields in the laser impact area. In addition, numerical experiments with the appropriate software should take into account the temperature dependencies of the coefficient of heat conductivity , the specific heat capacity and the coefficient of thermal difusivity.

A. Software

A program TEMPERATURFELD3D is used to conduct numerical experiments [11]. It specializes in calculating temperature fields for laser impact on various materials. It is suitable for technological processes laser marking, laser engraving, laser cutting, laser welding, laser drilling and others. The dynamic model of the program is chosen for the laser marking process. The main program window then opens (Fig. 3). There is a possibility to store data and results from previous numerical experiments.

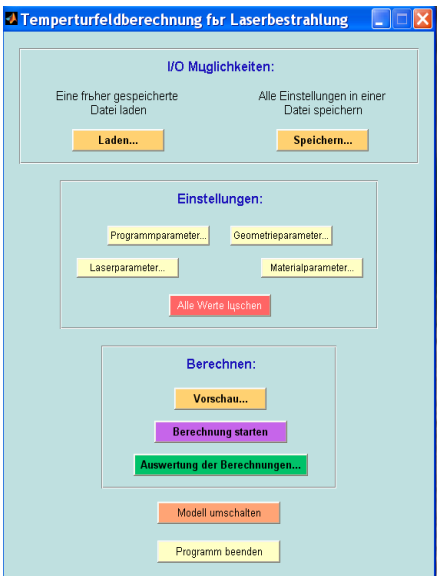

Fig. 3. Basic window of the software Temperaturfeld3D

When performing a specific numerical experiment input data is entered:

- Program parameters;
- Geometric parameters;
- Laser parameters and process parameters;
- Material parameters.

The next step is to perform the calculation. The obtained results can be displayed after opening the „Output Data" window. It includes (Fig. 4):

- Approximating the results;
- Animation of the whole process;
- Temperature profile of the material at a time;
- Profile of maximum temperature;
- Dependence of temperature from time;
- Temperature change in depth of the material.

Fig. 4. Window „Output Data" of the software Temperaturfeld3D

B. Laser technological systems

The researches concerns for two technological systems with CuBr laser and fiber laser [12 – 14]. The first laser generates radiation in the visible area and the second laser in the near infrared area. Both lasers work in pulse mode. The CuBr laser has a very high impulse power, and the fiber laser has a very high beam quality (near the ideal) and a high efficiency. Laser systems have high positioning accuracy and good repeatability. They maintain robust process parameters throughout the entire production process.

TABLE I. Basic Parameters Of Technological Systems With Cubr Laser And Fiber Laser

Laser Parameter	CuBr laser	Fiber laser
Wavelength λ, μm	0,511	1,062
Power P, W	20,0	40,0
Frequency ν, kHz	20,0	20
Pulse duration τ, ns	30	250
Pulse energy E_p, mJ	1,00	2,00
Pulse power P_p, kW	33,3	8,00
Beam quality M^2	< 1,7	< 1,1
Positioning accuracy, μm	2,5	2,5
Efficiency, %	10	40

C. Materials

Numerical experiments are for structural steels C35 and 50G [15]. From structural steel C35 are produced axles, cylinders, crankshafts, washers, spindles, sprockets, rods, wheels, sleepers, shafts, seals, discs and other low strength items that experience small mechanical stresses. The structural alloy steel 50G is used to make friction discs, shafts, sprockets, splines, washers, displacement rollers, bearing bushings, elbows, spindles, flywheel wheels, crankshafts of diesel engines and gas engines, and other details that require increased strength and durability [15]. Both steels have high coefficients of thermal conductivity and thermal diffusivity.

TABLE II. Temperature Dependence Of Certain Parameters Of Construction Steel C35.

Legend: k – coefficient of thermal conductivity, ρ – density, c – specific heat capacity, a – coefficient of thermal diffusivity.

***T*, K**	***k*, W/(m.K)**	ρ, kg/m³	**c, J/(kg.K)**	**a, m²/s**
293	50	7826	453	$1{,}41.10^{-5}$
373	49	7804	469	$1{,}34.10^{-5}$
473	49	7771	490	$1{,}29.10^{-5}$
573	47	7737	511	$1{,}19.10^{-5}$
673	44	7700	532	$1{,}07.10^{-5}$
773	41	7662	553	$9{,}68.10^{-6}$
873	38	7623	578	$8{,}62.10^{-6}$
973	35	7583	611	$7{,}55.10^{-6}$
1073	29	7600	708	$5{,}39.10^{-6}$
1173	28	7549	699	$5{,}30.10^{-6}$

TABLE III. Temperature Dependence Of Certain Parameters Of Construction Alloy Steel 50G.

***T*, K**	***k*, W/(m.K)**	ρ, kg/m³	**c, J/(kg.K)**	**a, m²/s**
293	43	7810	477	$1{,}15.10^{-5}$
373	42	7776	487	$1{,}09.10^{-5}$
473	41	7745	500	$1{,}06.10^{-5}$
573	38	7714	517	$9{,}52.10^{-6}$
673	36	7681	533	$8{,}79.10^{-6}$
773	34	7648	559	$7{,}95.10^{-6}$
873	31	7615	584	$6{,}97.10^{-6}$
973	29	7582	609	$6{,}28.10^{-6}$
1073	28	7577	676	$5{,}47.10^{-6}$

D. Numerical experiments

Multiple numerical experiments were conducted to determine the temperature fields in the impact area for the two lasers and the two steels. The speed varied within the interval $v \in [20; 110]$ mm/s with step 10 mm/s as the power density maintained constant. In the first series of experiments is $q_{S1} = 9{,}35.10^{10}$ W/m², and in the second – $q_{S2} = 1{,}08.10^{11}$ W/m². The temperature dependence of some parameters of steels (according to Table II and Table III) is recorded. In Fig. 4 shows temperature fields in the impact area for structural carbon steel C35 Both temperatures in the central processing area are higher than the melting temperature.

a)

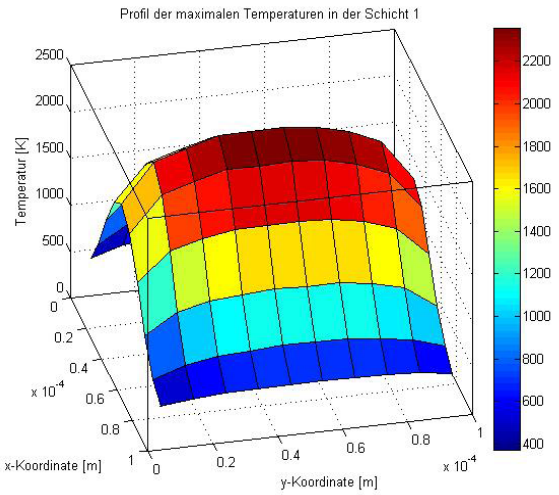

b)

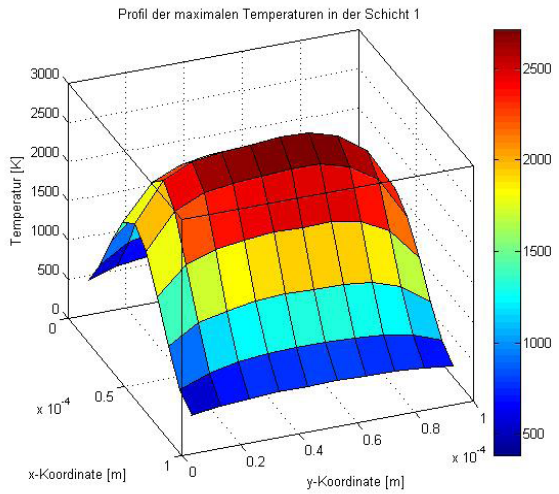

Fig. 5. Температурно поле на образец от конструкционна стомана С35 за скорост $v = 60$ mm/s и плътности на мощността: а) $q_{S1} = 9{,}35.10^{10}$ W/m²; b) $q_{S2} = 1{,}08.10^{11}$ W/m²

for CuBr laser

In Fig. 6 and Fig. 7 are presented graphics of the dependencies of the temperature from the speed for steels C35 and 50G. From the obtained results, the following conclusions can be drawn:

- The temperature decreases non-linearly with increasing of speed throughout the entire study interval for both steels;
- The temperature reduction rate for steel C35 is

with CuBr laser for steel C35		
***v*, mm/s**	***q*, W/m²**	ΔT/ ***Δv*,** K/ (mm/s)
20 ÷ 30	$9{,}35.10^{10}$	**23,5**
20 ÷ 30	$1{,}08.10^{11}$	**27,0**
60 ÷ 110	$9{,}35.10^{10}$	**15,7**
60 ÷ 110	$1{,}08.10^{11}$	18,0
with CuBr laser for steel 50G		
20 ÷ 30	$9{,}35.10^{10}$	**20,6**
20 ÷ 30	$1{,}08.10^{11}$	**23,7**
60 ÷ 110	$9{,}35.10^{10}$	**13,7**
60 ÷ 110	$1{,}08.10^{11}$	**15,8**

- For structural carbon steel C35, the temperature is about 14% greater than for structural alloy steel 50G. The reasons for this are the higher absorption of steel 50G.

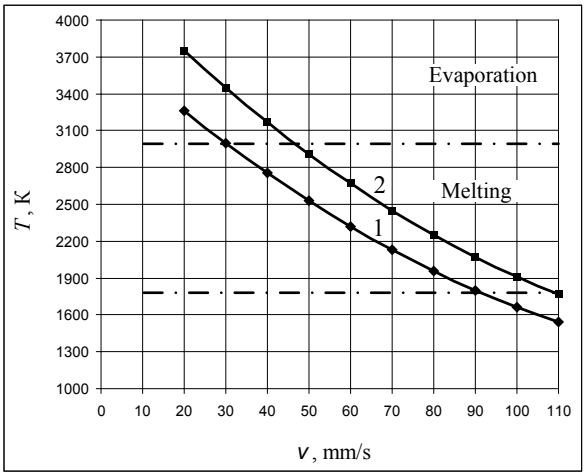

Fig. 6. Graphics of dependence of temperature from speed for structural carbon steel C35 for power density: 1 – $q_{S1} = 9{,}35.10^{10}$ W/m²; 2 – $q_{S2} = 1{,}08.10^{11}$ W/m² .

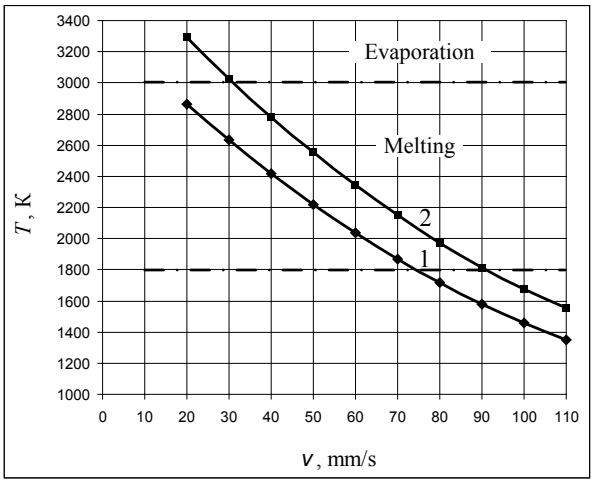

Fig. 7. Graphics of dependence of temperature from speed for structural alloy steel 50G for power density: 1 – $q_{S1} = 9{,}35.10^{10}$ W/m²; 2 – $q_{S2} = 1{,}08.10^{11}$ W/m² .

for fiber laser

In Fig. 8 and Fig. 9 are presented graphics of the

dependencies of the temperature from the speed for steels C35 and 50G. From the obtained graphics, it follows:

- The temperature decreases non-linearly with increasing of speed throughout the entire study interval for both steels;
- The temperature reduction rate for steel C35 is

with fiber laser for steel C35		
***v*, mm/s**	***q*, W/m²**	**ΔT/*Δv*, K/(mm/s)**
20 ÷ 60	$1{,}16.10^{11}$	**26,3**
20 ÷ 60	$1{,}36.10^{11}$	**30,0**
60 ÷ 110	$1{,}16.10^{11}$	**18,4**
60 ÷ 110	$1{,}36.10^{11}$	**26,2**
with fiber laser for steel 50G		
20 ÷ 60	$1{,}16.10^{11}$	**22,6**
20 ÷ 60	$1{,}36.10^{11}$	**26,3**
60 ÷ 110	$1{,}16.10^{11}$	**15,5**
60 ÷ 110	$1{,}36.10^{11}$	**18,0**

- For structural carbon steel C35, the temperature is about 14% greater than for structural alloy steel 50G.
- For the same speeds and power densities, the sample temperature in the impact area for CuBr laser is higher than that for fiber laser.. Higher values of temperatures for the CuBr laser compared to the fiber laser are because the radiation in visible area is better absorbed from the steels from that in the near-infrared area;

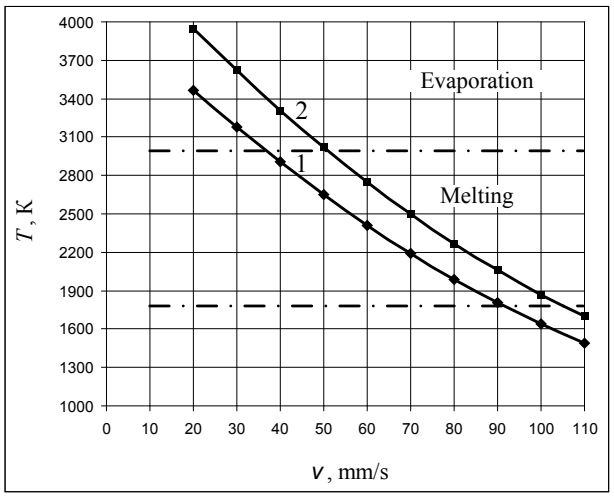

Fig. 8. Graphics of dependence of temperature from speed for structural carbon steel C35 for power density: 1 – q_{S1} = $1{,}16.10^{10}$ W/m²; 2 – q_{S2} = $1{,}36.10^{11}$ W/m² .

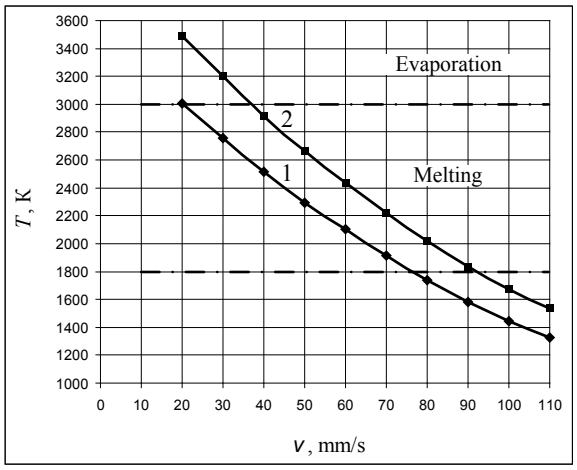

Fig. 9. Graphics of dependence of temperature from speed for structural alloy steel 50G for power density: 1 – q_{S1} = $1{,}16.10^{11}$ W/m²; 2 – q_{S2} = $1{,}36.10^{11}$ W/m² .

E. Preliminary working intervals of speed

For the realization of the processes marking by melting and welding, the temperature of the sample in the impact zone must be between the melting point and the evaporation temperature. For process processes marking by evaporation, engraving and cutting, the temperature in the impact zone must be higher than the temperature of evaporation.

From the obtained results, preliminary working intervals of the speed for marking by melting and welding were determined (see Fig. 5 – 9):

with CuBr laser for steel C35		**with fiber laser for steel C35**	
***v*, mm/s**	***q*, W/m²**	***v*, mm/s**	***q*, W/m²**
30 ÷ 90	$9{,}35.10^{10}$	**35 ÷ 84**	$1{,}16.10^{10}$
47 ÷105	$1{,}08.10^{11}$	**47** ÷105	$1{,}36.10^{11}$
with CuBr laser for steel 50G		**with fiber laser for steel 50G**	
20 ÷75	$9{,}35.10^{10}$	**20 ÷ 77**	$1{,}16.10^{10}$
52 ÷ 103	$1{,}08.10^{11}$	**37 ÷ 92**	$1{,}36.10^{11}$

For marking by evaporation, engraving and cutting, the preliminary working intervals of the speed are (see Fig. 5 – 9):

with CuBr laser for steel C35		**with fiber laser for steel C35**	
***v*, mm/s**	***q*, W/m²**	***v*, mm/s**	***q*, W/m²**
20 ÷ 30	$9{,}35.10^{10}$	**20 ÷ 35**	$1{,}16.10^{11}$
20 ÷ 47	$1{,}08.10^{11}$	**20 ÷ 52**	$1{,}36.10^{11}$
with CuBr laser for steel 50G		**with fiber laser for steel 50G**	
20 ÷ 30	$1{,}08.10^{11}$	20 ÷ 37	$1{,}36.10^{11}$

Smaller intervals of the speed of steel G50 compared to steel C35 are due to the higher melting and evaporation temperatures of the first steel.

III. CONCLUSION

The obtained results will be useful for operators of laser systems to reach the desired optimal technological parameters more quickly. These numerical experiments contribute to significantly reducing the time created in actual production settings. These numerical experiments help to better coordinate the theoretical models of the interaction of laser radiation with specific technological processes related to the melting and evaporation of the materials in the processing area. Experiments are planned to continue to investigate and the impact of other factors influencing the quality of specific technological processes. The aim is to create a basis of technology tables to support pilot real-world experiments in the implementation of new technologies related to the laser processing of different types of materials and ultimately the creation of new products.

References

[1] Jianmei Li, Aiqun Wang, Yusong Wuab, ZhuoMa, Xinxin Fang, LiangTao, Experimental investigation and mathematical modeling of laser marking two-dimensional barcodes on surfaces of aluminum alloy, Journal of Manufacturing Processes, Volume 21, January 2016, pp 141-152

[2] Valiulin A., Gorniy S., Grechco Y., Patrov M., Yudin K., Yurevich V. Lazerna markirovka materialov. Nauchno-technicheskij zhurnal Fotonika, 2007, 3, pp 16-22 (in Russian)

[3] Dutta Majumdar, J., Laser material processing, International Materials Reviews,56(5-6), November 2011, pp. 341-388

[4] Grigoryan A.G., Shiganov I.N., Misyurov A.I. Technologicheskiye processy lazernoy obrabotki. MGTU im. N.E.Baumana, 2006, pp 665 (in Russian)

[5] Senthilkumar, V., Laser cutting process – A Review International Journal of Darshan Institute on Engineering Research & Emerging Technologies, Vol. 3, No. 1, 2014

[6] Dyuli U. Lazernaya technologiya I analiz materialov. Mir, Moskva, 1986 (in Russian)

[7] Murzin S., Ilyuchin V. Lazerniye technologii obrabotki materialov. SGAU, Samara, 2006 (in Russian)

[8] Zakayukina L., Bannov V. Vidy i parametri processa lazernoy rezki. Novie informacionniye technologii v avtomatizirovannih sistemah. IPM im. M.Keldisha. Moskva, 2016, pp 163 – 167 (in Russian)

[9] Lazov L., Angelov N. Osnovi factori, opredyelyaschi kachestvo na markirovkata na metali i splavi. Mezhdunarodna nauchna konfirenciya Amteh`07. Gabrovo, 23-24 noemvri 2007, tom I, pp 102-107 (in Bulgarian)

[10] Angelov N. Optimizaciya na procesa markirane s lazerno lichenie na obrazci ot instrumentalna stomana. Disertacionen trud za pridobivane na stepen doktor. TU-Gabrovo, 2011 (in Bulgarian)

[11] Belev I. Sreda za presmyatane na lazerno inducirani temperaturni poleta. Diplomna rabota, TU-Gabrovo, 2009 (in Bulgarian)

[12] www.pulsligth.net

[13] www.axsys.de

[14] www.spilasers.com

[15] www.splav-kharkov.com/main.php

Study of Laser Cutting and Marking on The Filt with the Help of a CO_2-Laser

Lazov Lyubomir
Rezekne Academy of Technologies, Faculty of Engineering)
Address: Atbrivosanas aleja 115,)
Rezekne, LV-4601, Latvia
llazov@abv.bg

Dolchinkov Nikolay Todorov
National Military University „Vasil Levski", Veliko Tarnovo, Bulgaria
National Research University "Moscow Power Engineering Institute", Moscow, Russia
Veliko Tarnovo, Bulgaria
n_dolchinkov@abv.bg

Ivanov Jordan Shterev
National Military University „Vasil Levski", Veliko Tarnovo, Bulgaria
Veliko Tarnovo, Bulgaria
jshterev@abv.bg

Peneva Madlen Nikolaeva
National Military University „Vasil Levski", Veliko Tarnovo, Bulgaria
Veliko Tarnovo, Bulgaria
merianp98@gmail.com

Bojhanova Denitsa Angelova
National Military University „Vasil Levski", Veliko Tarnovo, Bulgaria
Veliko Tarnovo, Bulgaria
denica_a_b@abv.bg

***Abstract*— Describe the parameters influencing the depth of the laser marking of textile products. Experimental results are presented to determine the quality of cuts on felt surfaces of different colors at specific parameters - power and speed. Approximately 100 extras were made on two materials with a change in laser power and speed. As a result, the optimal results for cutting and marking a felt are shown.**

Keywords*— *cutting, filt, laser, marking, research.

I. Introduction

The felt is a soft fabric which is made not by weaving but by pressing under steam or hot water and felting of animal fibers. A 100% synthetic fiber felt felt felted as well as felt from a combination of animal, vegetable or artificial fibers.

Felting is probably the oldest form of fabrication known to mankind before weaving and knitting.

Today traditional felting is still practiced by the nomadic tribes in Asia, producing mats, tents and clothing. Because of its qualities such as strength, heat and sound insulation, the felt is used in the textile industry, but also in machine-building, woodworking and others.

Most commonly this material is used for the production of articles, useful for households, for example, sealing in various branches of industry - machine-building, paper-pulp industry, also as an insulating material, for polishing, etc. Often, the felt also serves as an upholstery on different surfaces. However, because it is thick cutting intricate patterns and structures into felt is difficult to do by hand. Precise cutting is usually done by means of an industrial mashine cutter. Using a laser to cut felt is great choose.

The laser has moved in 58 years from "a solution looking for a problem" to a key technology that contributes to major sectors of the world economy. Laser devices are the core technology in instruments performing vital functions in many industries including transportation, healthcare, and telecommunications [4].

Laser marking and laser cutting technology is now widely associated with textiles and in particular with felt [3,5,13,15]. In this paper we present some experimental results from this area.

After researches were made, we found out that the main factor for the difference in laser cutting on white and red felt is the difference in the color of the material. Another factor is its thickness – of the white felt it is 0.63 mm. and for the red felt – 0.67 mm.

There are different kind of lasers which are:

-depending on the spectral field: CO_2 laser, Nd:YAG, ruby laser, excimer laser

-depending on the active middle: solid-state, gas, liquid and semiconductor

-depending on the power: low-powered (under 100 W), middle-powered (100-500 W), powered (1 kW- 100 kW), over-powered (over 100 kW).

-depending on the possibility to change the frequency: with fixed frequency; with possibility to change the frequency [17].

II. Experimental setting

The possibility of marking and engraving on a standard felt in two colors - red and white with CO_2 laser was studied. For this purpose, an experimental methodology has been developed, which concludes in the following:

a matrix of 9 squares with 1: 1 cm (10x10mm) is created. The speed and power range in the range of 100?50 mm/s and 2, 10 and 26 W. The matrix scheme is shown in the figures:

Gas laser CHANXAN CW 1325 CO2 active, 1-150 watts power, 1-400 mm / s, laser beam wavelength 10.6 mm, maximum marking area: 2500 x 1300 mm, maximum

Print ISSN 1691-5402
Online ISSN 2256-070X
http://dx.doi.org/10.17770/etr2019vol3.4202

laser size focal spot is 100 mm and water cooling system was used – Fig 1 [10].

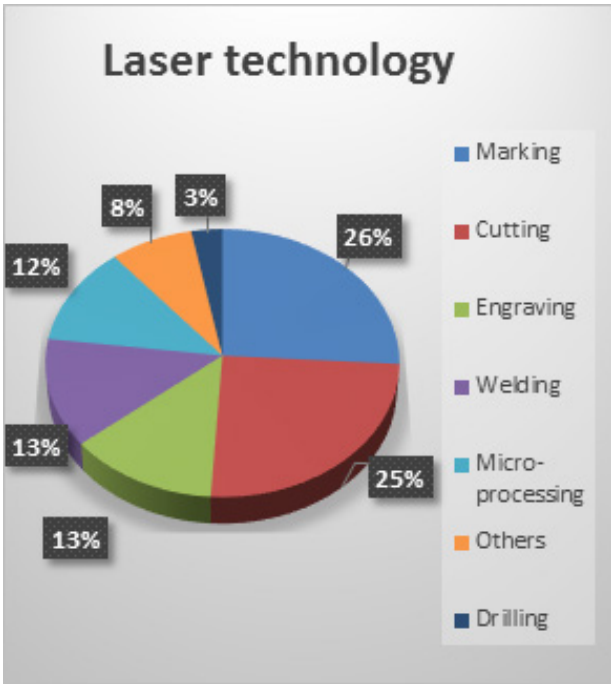

Fig.1. Percentage of Laser used technologies

The area of laser marking and cutting is showed on the figure. A considerable amount of heat is emitted in the marking and cutting processes, so the working area is cooled with air.

The surface power density SPD of the laser beam is determined by:

$$SPD = \frac{P}{S}$$

where P is the power of laser beam and S is the area of the laser beam section in focus. Laser control was performed using the RdWorks software [8, 14].

There are many methods of part or product marking, including labels, ink systems, mechanical engraving and embossing, chemical and dry etching. Each has its use, but laser marking is growing more and more popular. The utilization of laser engraving of metals is shown in the Fig.1 where we can compare it with other marking systems in the part production.

III. LASER MARKING

The common advantages of all laser marking techniques are [1]:

- permanent, high quality marks;
- high efficiency and low operation cost;
- good accessibility, even to irregular surface;
- non-contact marking and no special working environmental needed;
- easy to automate and integrate (using computer-controlled movement of the beam or sample);
- precise beam positioning and a beam highly localised energy transfer to the workpiece [6];
- high reproducibility and high speed ;
- contamination - free.

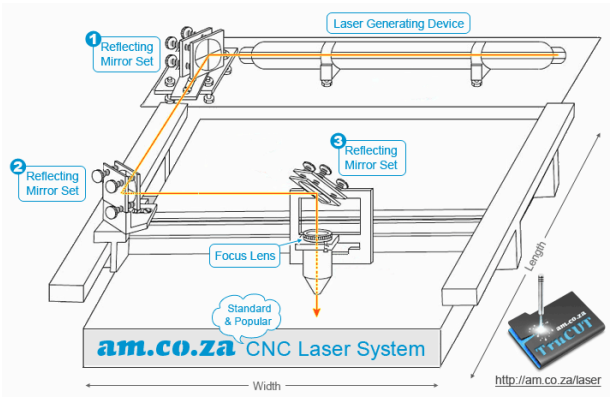

Fig.2 Laser system

Fig.2. shows the scheme of the laser that we use for the experiment and on it we are able to see the different part of CO_2 laser, including Laser Generating Device, 3xReflecting Mirror Set and Focus Lens [11,12].

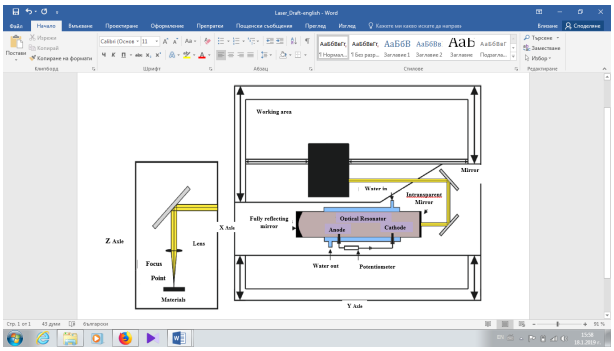

Fig.3. Schematic diagram of CO_2 laser

Fig. 3 shows more precisely the schematic diagram of CO_2 laser. It includes also the working area, fully reflecting mirror, intransperant mirror, then anodes and cathodes, the lens and the focus point [2, 9,16].

Fig.4. The laser used for the experiments

Fig. 4 This figure is an image of the laser used during our experiment. It is located in the laser center of the Technological Academy in Rezekne and under it under the supervision of Professor Lubomir Lazov the markings on the research field were carried out.

The abbreviation LASER comes from Light Amplification by Stimulated Emission of Radiation. The quality of a mark is assessed by its legibility characteristics such as mark contrast, mark width, mark depth, and microstructures. The characteristics are usually evaluated using complementary techniques such as optical microscopy, ultrosonics microscopy, electron microscopy, surface roughness measurement. In beam deflected marking, the line width is mainly determined by the focused beam spot size, which varies between 20 - 100 μm. Other parameters: scanning speed, power density and material properties also affect the line width. [1].

In relation to the influence of the laser beam on the fabric, the linear energy density LED of the laser beam is defined on a unit length depending on the velocity:

$$LED = \frac{P}{v}$$

where P is the power of laser beam and *v* is the speed of laser beam movement on the felt [2,7].

TABLE 1. LED PARAMETERS

№	V, mm/s	P=2W	P=10W	P=26W
		LED, J/mm	LED, J/mm	LED, J/mm
1	100	0,02000	0,10000	0,26000
2	150	0,01333	0,06667	0,17333
3	200	0,01000	0,05000	0,13000
4	250	0,00800	0,04000	0,10400
5	300	0,00667	0,03333	0,08667
6	350	0,00571	0,02857	0,07429

In Table 1 is shown the linear energy density dependences of power P for 2 W, 10 W and 26 W and the variation of the speed 100, 150, 200, 250, 300 and 350 mm/s [2].

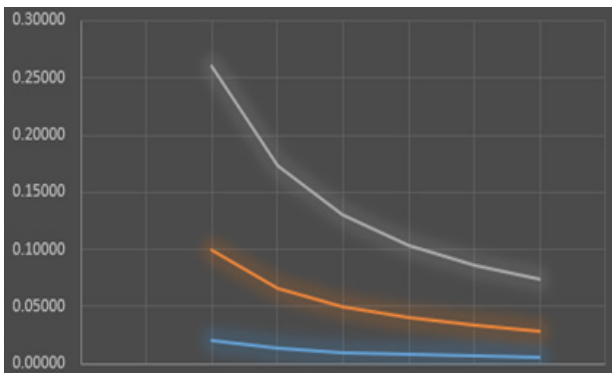

Fig 5. Graphic of changing of LED

In Fig.5 the graphic shows the changing of LED parameters as a result of the interaction between the speed and power.

Each processing area (each square) is implemented with the raster scan method. The line-to-line step is 0.1mm. The processing areas and the processing quality were analyzed by means of a AM4515ZTL digital microscope manufactured by DINO-LITE:

https://www.dino-lite.eu/index.php/en/products / microscopes/long-working-distance with 1.3 MPx resolution, 10-140X zoom and polarizer.

The diagrams of the square matrices after experiments are shown on Fig 6. The Markings 7, 8, 9 in Figure show respectively the energy of 2 W, 10 W, 26 W in percent, which is used for the interaction with a felt.

IV. LASER CUTTING

- The possibility of laser cutting on a CO_2 laser is investigated. For this purpose, an experimental methodology has been developed which consists of the following:
- The processing areas and the processing quality with the help the microscope have been analyzed. Altogether, 90 processing areas were investigated. From the experiments made, the following conclusions can be drawn:
- a quality cut of the material is obtained with the following parameters: for white and red felt - a constant power of 26 W (9%) and a speed ranging 100, 150 and 200 mm/s and the LEDs are 0.26 J/mm, 0.17 J/mm 0.13 J/mm - Fig. 4. Quality cutting of the felt.;
- about the same power 26 W and a speed ranging 250, 300 and 350 mm/s and LEDs are 0.104 J/mm, 0.08667 J/mm 0.0749 J/mm the cutting is not full;

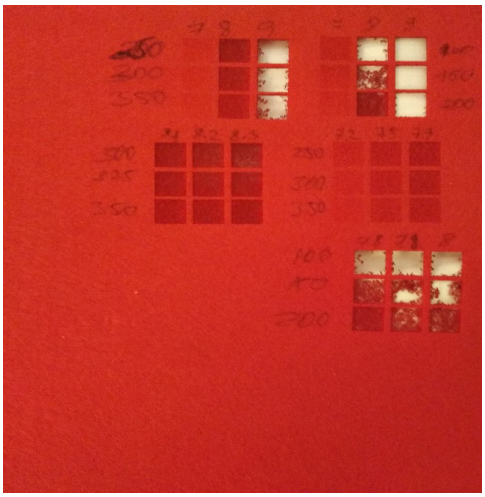

Fig.6. The diagrams of the square matrices

- good marking by lightening of the material (nearly 50%) is obtained with the following process parameters: P = 2W and V = 250, 300 and 300 mm/s, and the LEDs are 0.008, 0.00667 and 0.00571 as shown in the table 1 - Fig. 8. Red and white felt. Contrast measurements are performed using the Color Contrast Analyzer version: 2.5.0.0. [14];
- about the same power 2 W and a speed ranging 100, 150 and 200 mm/s and the LEDs are 0.20 J/mm, 0.01333 J/mm and 0.010 J/mm the marking is not so good, it is nearby cutting red and white felt;

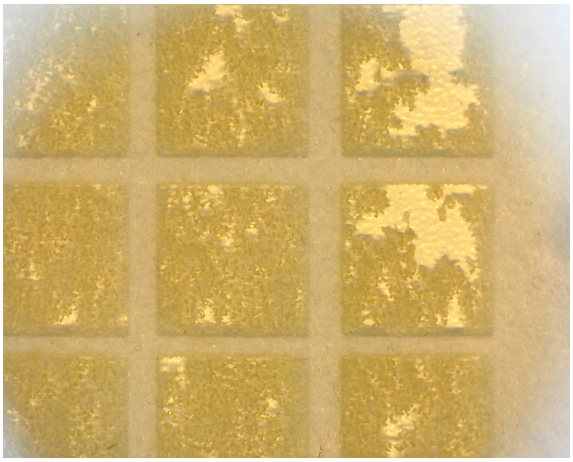

Fig.7. White felt under microscope

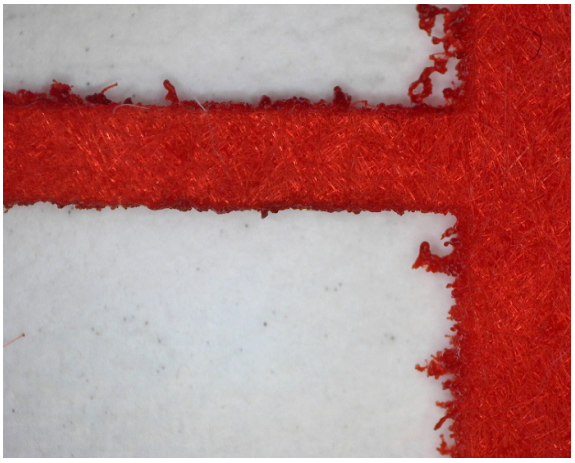

Fig. 8. Cutting of the felt.

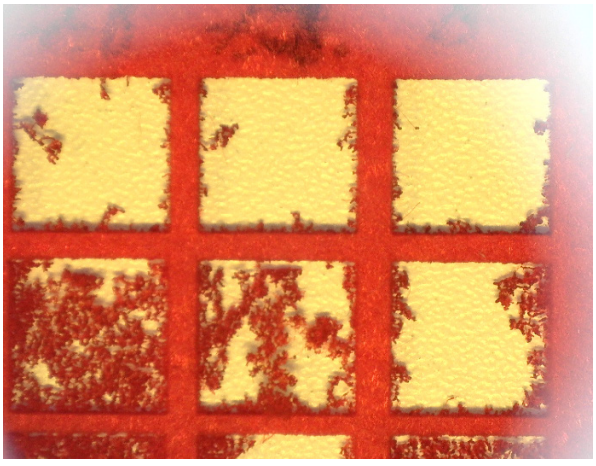

Fig. 9. Cutting of the felt.

- About power 10 W and speed 100, 150, 200 mm/s of laser beam the red felt and white felt have less partial cutting (less destroying felt) and the LEDs are 0.1, 0.06667, 0.0.50;
- About power 10 W and speed 250, 300 and 350 mm/s of laser beam the red felt and white felt have less partial cutting (less destroying felt) and the LEDs are 0.04, 0.03333, 0.02857;
- About the next areas from all 90 processing areas can say the same analogy.

V. CONCLUSION

For all felt materials marking, engraving and cutting can be successfully applied. The choice of laser process is determined by the desired final result.

In this research, the laser applications for and felt processing are analyzed. The advantages of laser technology in felt fields were pointed. The linear energy density during marking and cutting by the laser beam was introduce.

With the help of a robotic automated line, the making of marking and cutting of felt results in the production of an obtained, attractive commercial product [2].

The results in the end of the research are:

1. During the laser cutting on the white felt one of the best parameters of cutting are made in the power of 9 W and speed of 100 mm/s where the cutting is precise. With the increasing of the speed to 150 and 200 mm/s the cutting line becomes better, without any mustaches. Unfortunately, this will bring waste of energy.

2. As for the red felt best results in laser cutting are between 100-150 mm/s and power of 9 W, but for the speed of 200 mm/s and the same power, we are able to see some mustaches left.

3. When we use less power of laser beam there is imperfect cutting. Then we observe laser marking, but not cutting, which depends on the power used for the experiment.

4. The researching felt material is not suitable for laser marking because of its structure is not appropriate for quality work. It is good for laser cutting with low power and the quality is perfect.

5. The results from this experiment can be used as a base for future projects with similar materials and the data base can be practically used during working with CO_2 laser.

References

[1] Dave Ahearn, ONR Laser Power Jumps 10 Fold; Further 10 - Fold Leaps Seen, Defense Today, August 4, 2004, p. 4

[2] Dolchinkov N., Shterev Y., St. Lilianova, D. Boganova, M. Peneva, L. Linkov, D. Nedialkov, Exploring the possibility of laser cutting with CO_2 laser on felt in the range from 1W to 26W power, International scientific journal: Industry 4.0 Issue 1/2019, ISBN 2534-8582, стр. 29-31.

[3] Lamberson S. E., The airborne laser, Proc. SPIE, Gas Chem. Lasers, vol. 2702, pp. 2702-1_2 702 - 6, Mar. 1996

[4] .Lazov L., E. Teirumnieks, Application of laser technology in the army, Proceedings of International Scientific Conference "Defense Technologies", Faculty of Artillery, Air Defense and Communication and Information Systems, Shumen, Bulgaria, 2018

[5] Lazov L,, H. Deneva, E. Teirumnieka, Influence of Defocus Position on Laser Cutting Process in Sheet Steel, Environment. Technology. Resources, Rezekne, Latvia Proceedings of the 11 th International Scientific and Practical Conference. Volume III, 163-167,

[6] Lazov, L., H. Deneva. Investigation on the Influence of the Process Parameters Power and Velocity to Laser Cutting of Lamellae. Journal of the Technical University - Sofia, Plovdiv branch, Bulgaria, Fundamental Sciences and Applications, Vol. 21, Book 2, 2015, ISSN 1310-8271.

[7] Lazov L., Angelov N., Scanning the contrast in function of velocity in laser marking of samples of steel, International Scientific Conference, Gabrovo, 2010.

[8] Petrov N., Optimization of the marking process with laser radiation of samples of tool steel, dissertation, Gabrovo, 2011.

[9] Shterev Y., N. Dolchinkov, St. Lilianova, D. Boganova, M. Peneva, L. Linkov, D. Nedialkov, Examining the possibility Of marking and engraving of textiel using CO_2 laser, International journal for science Machines, Technologies, Materials 12/2018 стр 491-493

[10] https://www.laserfelt.com/

[11] http://chris-reilly.org/blog/how-to-laser-cut-felt/

[12] https://www.epiloglaser.com/resources/sample-club/felt-place-mat-cutting.htm

[13] https://www.lasercuttingshapes.com/felt/

[14] https://www.pinterest.com/eleeneelab/laser-cut-felt/

[15] http://digitalcommons.unl.edu/tsaconf/index.2.html

[16] https://developer.paciellogroup.com/resources/contrastanalyser

[17] https://rdworks.software.informer.com

*Note: This article is presented with the assistance of project BG05M2OP001-2.009-0001, Support for the development of human resources and the research potential of the National Military University "Vasil Levski" for its assertion as a modern knowledge center.

Environment. Technology. Resources. Rezekne, Latvia
Proceedings of the 12th International Scientific and Practical Conference. Volume III, 148-150

Experimental Studies of Roughness by Surface Plastic Deformation on Flat Surfaces

Angel Lengerov
Technical University – Sofia, Plovdiv Branch
Department of Mechanical Engineering and Technologies
Plovdiv, Bulgaria
e-mail: anlen@tu-plovdiv.bg

***Abstract*—The article presents experimental studies of the roughness by surface plastic deformation (SPD) on flat surfaces of steel 45. A dispersion analysis was used to study the influence of various factors on the surface quality. From the experimental studies and the dispersion analysis made, a graphical interpretation of the main effects was obtained. Graphical visualizations of the roughness pattern after SPD on the processed surfaces were obtained. Overlapping sinusoidal movements of the deforming spherical element were realized.**

***Keywords*—surface plastic deformation, roughness, flat surfaces.**

I. Introduction

The loss of machinability of the machine parts usually occurs after the surface layer has been destroyed. It has been found that the functional purpose of various machine-building products depends to a large extent on the qualitative indicators of the surfaces.

One of the simplest and most common methods for controlling a wide range of Surface Layer Quality Parameters is the finishing treatment by surface plastic deformation (SPD).

One of the ways to improve the quality of production is the use of surface plastic deformation processing methods [1]. The advantage of the SPD is a capability to combine effects of finishing and strengthening treatment. In the literature, there is a wide variety of methods for finishing by surface plastic deformation, having a number of specific features [3] – [4]. The most complete and systematic methods for surface elastic deformation are discussed in [2]. In [5] prepared a review of the methods of plastic deformation of matrices and punches.

At the same time, there is no scientifically based methodology allowing the selection of optimal working conditions to ensure the specified quality of the parts.

The purpose of the present work is to perform experimental studies to determine the influence of the geometrical, technological and energetic parameters of the surface plastic deformation on the roughness of the machining surfaces.

II. General Regulations

In order to study the influence of the technological parameters of the SPD process on the roughness of the processed surfaces, a number of experimental studies were carried out.

The flat surfaces of steel 45 with chemical composition according to Table 1 are face milling [6]. Sinusoidal overlapping movements with a ball deforming tool have been realized by changing the process parameters of the SPD process.

Table 1 Chemical compositionab of steel 45

C	Si	Mn	P	S	Cr	Ni
%	%	%	%	%	%	%
0,45	0,26	0,63	0,035	0,040	0,20	0,20

The tests were carried out on a drilling machine PB 501. The processed specimens were fastened on the machine table and the ball-forming tool of the vertical spindle The roughness of the specimens after each experiment was measured with a Mitutoyo Surftest - 4 profiles shaper at two lengths, averaging the arithmetic roughness (Fig. 1). A multifactorial dispersion analysis was performed in order to quantify the influence of the factors and regression analysis of the experimental results obtained from the experimental plan.

Fig. 1. Roughness measurement.

The levels of variability of the control factors are shown in table. 2 and were selected on the basis of experimental pre-planning results.

Print ISSN 1691-5402
Online ISSN 2256-070X
http://dx.doi.org/10.17770/etr2019vol3.4192

TABLE 2 FACTORS, LEVELS

Factors		**Levels of factors**		
	coded			
	-1	**0**	**+1**	
natural	**coded**	**natural**		
Force of pressing of the ball to the part F_b, N	x_1	100	300	500
Radius of the deforming ball tool r, mm	x_2	5	10	15
Feed f, mm / min	x_3	100	900	1500
Number of the cuts N	x_4	1	2	3
*I*nitial roughness R_a^n, μm	x_5	1	3	5

The results of the preliminary experiments show that the models are non-linear. For this reason an optimal composition plan has been chosen.

Since the factors are 5, the number of experimental points increases to $N = 2^5 + 2\times 5 = 42$. To reduce attempts, the centre of the plan is chosen to be a fractional replica with $t = 3$, that is, the number of attempts in the kernel of the plan is $N_{ÿäðî} = 2^{5-3} = 4$. The optimal one-point composite plan was synthesized by QStatIab [8]. The impact of various factors on surface quality was investigated by dispersion analysis. From the experimental studies and the multifactor dispersion analysis, a graphical interpretation of the major factors was obtained (Fig. 2).

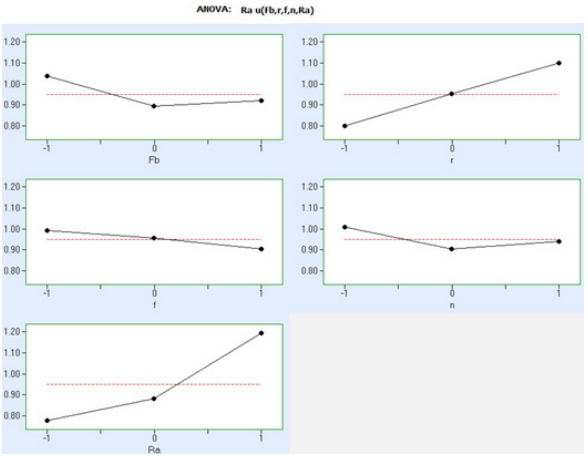

Fig. 2. Overview of the main effects (significance of the factors).

From Fig. 2 it follows that in order to maintain a maximum level of the quality indicator (in this case it is minimal roughness) it is necessary to maintain the 5 factors at the respective levels shown in table. 3. Obviously, reducing the diameter of the ball achieves a reduction in roughness. The impact of the initial roughness is strongest, and the impact of the feed is minimal.

TABLE 3. LEVELS OF FACTORS

Factor	x_1	x_2	x_3	x_4	x_5
Level	lower	upper	lower	lower	upper

Given the fact that the plan is second order (optimal compositional), the regression model is chosen to be a second order polynomial to allow for a correct statistical analysis [7]:

$$Y_{R_a}(x_1,...,x_6) = b_0 + \sum_{i=1}^{k} b_i x_i + \sum_{i=1}^{k-1}\sum_{j=i+1}^{k} b_{ij} x_i x_j + \sum_{i=1}^{k} b_{ii} x_i^2, \quad (1)$$

where Y_{R_a} is the target function of the obtained roughness R_a with the arguments of the coded factors.

Coefficients estimates $b_0, b_1, ..., b_{44}, ...$ are obtained from the matrix multiplications:

$$\{b\} = \left([F]^T [F]\right)^{-1} [F]^T \{R_{a,u}\}, \quad (2)$$

where $\{b\}$ is the vector of the quoted coefficients in the model, $[F]$ is an extended matrix of the plan, $\{R_{a,u}\}$ is the vector of the experimental values of the target function Y_{R_a}.

The resulting regression model is

$$Y_{R_a} = 0.850 - 0.347x_2 + 0.302x_3 - 0.167x_5 - 0.122x_1x_2 + 0.648x_2^2 + 0.234x_3x_5 - 0.475x_4^2 - 0.241x_4x_5$$

The detailed scan of the obtained model indicates the existence of areas with negative values for the roughness, although the polynomial is of the second degree, and the selected coefficients are significant. For this reason, this roughness model can only be used in area of experimental points to predict roughness, but is not suitable for use in optimization procedures.

The visualization of the main effects (Fig. 3) shows that the influence of the individual factors can be linearized. Based on the plan centre and one central point, the following linear regression model was obtained:

$$Y_{R_a} = 0.952 + 0.122x_1 - 0.222x_2 + 0.26x_3 + 0.048x_4 - 0.14x_5 + 0.079x_1x_4 + 0.07x_1x_6 - 0.09x_2x_3 + 0.076x_2x_4 + 0.048x_2x_5 - 0.144x_2x_5 - 0.105x_3x_4 + 0.152x_3x_5 - 0.075x_4x_5 \quad (3)$$

An object of analysis is the model (3).

The relation between encoded (single) x_1 and natural factors $\%$ is

$$x_1 = (\%_1 - \%_{0,1}) / \lambda_1, \quad (4)$$

where

$$\lambda_1 = (\%_{a,1} - \%_{d,1}) / 2 \quad (5)$$

$\%_{0,l}$, $\%_{a,l}$ and $\%_{a,l}$ are respectively the average, upper and lower levels of the l-s natural factor.

After replacing (4) and (5) in (3), the expression of roughness with natural factors is obtained. The results of the analysis are shown in Fig. 3 in the form of three-dimensional graphs.

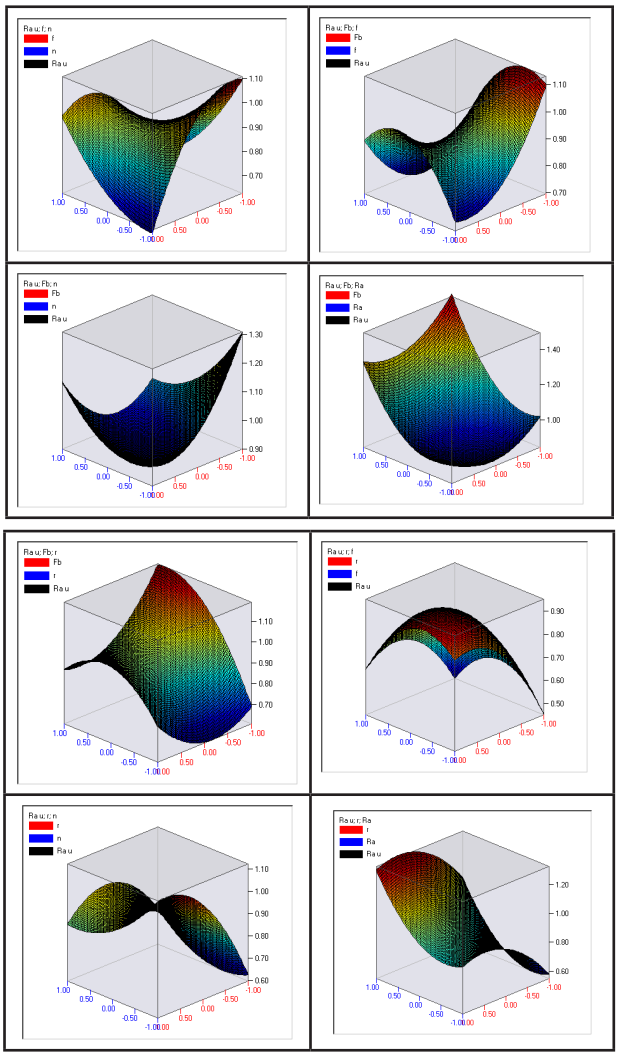

Fig. 3. Three-dimensional graphs of roughness function Y_{R_a} .

III. Conclusions

The resulting graphical visualizations of the roughness pattern model after the SPD of the treated flat surfaces (Fig. 3) confirm the conclusions about the influence, significance and the levels of the factors on the surface qualitative indicators.

The detailed scan of the obtained model indicates the existence of areas with negative values for the roughness, although the polynomial is of the second degree, and the selected coefficients are significant. For this reason, this roughness model can only be used in area of experimental points to predict roughness, but is not suitable for use in optimization procedures.

The implementation of small feeds, a high deformation force and a lower initial roughness lead to an improvement in the qualities of the treated surfaces and greatly reduce the roughness.

References

[1] S N Grigoriev, N M Bobrovskij, P A Melnikov and I N Bobrovskij,"Research of Tool Durability in Surface Plastic Deformation Processing by Burnishing of Steel Without Metalworking Fluids", International Conference on Recent Trends in Physics 2016 (ICRTP2016) IOP Publishing Journal of Physics: Conference Series 755 2016 011001 doi:10.1088/1742-6596/755/1/011001

[2] L. G. Odintsov ,"Uprochnenie i otdelka detalej poverhnostnym plasticheskim deformirovaniem", Spravochnik [Hardening and finishing details by surface plastic deformation. Handbook] / L. G. Odintsov. M.: Mashinostroenie, 1987. 328 p. [in Russian].

[3] T. Kuzmanov, I. Amudzhev, S. Taneva, "Tool equipment for mechanical surface treatment of small holes" , Journal of Machine Building and Machine Science, Varna, Bulgaria, Year. V, No. 2, Vol. 11, pp. 15-18, 2010.

[4] T. Kuzmanov, R. Rachev, S. Taneva, K. Ambarev, "Finishing processing of cylindrical rack-wheels for the transport technique by surface plastic deformation", Journal of Fundamental Sciences and Applications, Plovdiv, Bulgaria, Vol.15, pp. 311- 317, 2009.

[5] A.Y. Lavrentev, E.A. Sursimov, "The application of surface plastic deformation for finishing tunching tools", Международный научно-исследовательский журнал ▪ № 9 (51) ▪ Часть 2 ▪ Сентябрь, стр.55-57, 2016 DOI: 10.18454/IRJ.2227-6017.

[6] T. KALDASHEV, P. HADZHIYSKI, G. I. Nikolcheva, "Study wear tool with high-speed milling", Environment. Technology. Resources. 11th International Scientific and Practical Conference, June, 2017, 3, pp. 117-121 DOI: 10.17770/etr2017vol3.2598.

[7] Ronald Christensen , "Analysis of Variance, Design, and Regression: Applied Statistical Methods", Chapman and Hall/CRC; 2 edition (December22,2015), 636 pages ISBN-10: 1498730140, ISBN-13: 978-1498730143.

[8] И. Н. Вучков, И. И. Вучков, "Програмен продукт QStatLab Professional, версия 5.4. Ръководство за потребителя", София, 2009.

Inductive Linear Displacement Sensor in Active Magnetic Bearing

Sergei Loginov
Department of the electric drive and systems of automation
Pskov State University
Pskov, Russia
lsy1@mail.ru

Dmitriy Fedorov
Department of the electric drive and systems of automation
Pskov State University
Pskov, Russia
dmitriy-fedorov-2012@mail.ru

Igor Savrayev
Department of the electric drive and systems of automation
Pskov State University
Pskov, Russia
igor_savraev@mail.ru

Igor Plokhov
Department of the electric drive and systems of automation
Pskov State University
Pskov, Russia
igor_plohov@list.ru

Andrey Hitrov
Department of the electric drive and systems of automation
Pskov State University
Pskov, Russia
khitrov.aa@gmail.com

Alexander Hitrov
Department of the electric drive and systems of automation
Pskov State University
Pskov, Russia
khitrov-pscov@mail.ru

***Abstract*— Active magnetic bearings are increasingly used in various fields of industry. The absence of mechanical contact makes it possible to use them in ultra-high-speed electric drives. The main trend of active magnetic bearings development is the improvement of the control system. The main problem of the control system is the displacement sensor (most of them has low accuracy and large interference). The sensor must have the following properties: simple in realization, high linearity of the characteristic, high sensitivity and noise immunity, high reliability. At the present time there is no sensor that satisfies all these conditions. Most manufacturers use various kinds of filters to get an accurate position signal. This increases the response time of the control system. Thus, problem of designing and modeling the position sensor, considered in the article is topical.**

Keywords*— active magnetic bearings, inductive sensor of situation, measurement of provision of a rotor.

I. INTRODUCTION

The Active Magnetic Bearings (AMB) receive the increasing application in various fields of the industry. Lack of mechanical contact allows to use them in ultrahigh-speed electric drives (now it is in great demand) [4]. An integral part of AMB is the measuring converter of linear movements (the situation sensor). The sensor measures the shift of a rotor of rather central situation. The sensor of situation is one of the major elements in the AMB control system, stability of system depends on its accuracy and speed. Sensor parameters in many respects are defined by its design. Now in AMB inductive, vortical current based, capacitor and magnetic sensors [11] are used. Besides, sensor-less systems [12] can be applied. For improvement of the AMB technical parameters (stability, quality of transitional characteristics, speed) there is urgent a problem of development of sensors of a new design with the improved technical characteristics [7,8, 9].

II. MATHERIALS AND METHODS

Active magnetic bearings due to lack of mechanical contact between a rotor and the stator except high-speed appendices allow to work in vacuum, in the conditions of radiation, in hostile environment, in superclean technologies and at low and high temperatures at which operation of ordinary bearings is impossible [1], [2]. The principle of action of AMB is shown in fig. 1.

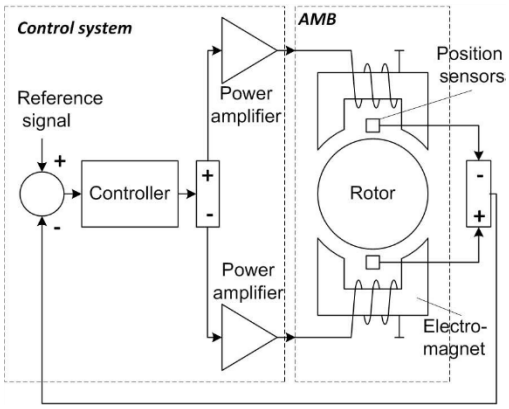

Fig. 1. Principle of action of AMB.

The AMB without control system is unstable system. The correct work is reached only at the expense of feedback by situation and control systems. The provision of a rotor in a gap is defined by situation sensors. By means of a signal of a task it is possible to set micromovements of a rotor in a gap. The controller processes a signal from the sensor on one of laws of management (proportion-differential, proportional-integral-differential-regulators, adaptive management, an algorithm on the basis of neural networks, etc. [3,5,6]). Amplifiers of power set currents in windings of electromagnets. Thus, the electromagnetic forces holding a rotor in a standard position are controlled.

Key element of a control system is the sensor of linear shift of a rotor in radial situation. Properties of all system

Print ISSN 1691-5402
Online ISSN 2256-070X
http://dx.doi.org/10.17770/etr2019vol3.4070

in many respects are defined by its parameters. It has to have high precision of measurements (about several microns), high speed (about several kHz), a high noise stability. There is a big variety of sensors of situation, the main can be considered inductive, induction, capacitor and sensors of measurement of magnetic field.

However there is not enough noise stability of any sensor to use it directly for further processing on the controller. For obtaining value of shift of a rotor filters are used (or on active elements, or digital). The problem is that the better filtration requires the big frequency of a signal, otherwise there is an inadmissible delay when processing a signal.

Let's consider the existing inductive sensor of provision of a rotor.

The function chart of the converter (fig. 2) includes the generator of rectangular voltage of the bearing frequency set by the microcontroller, the transformer with two identical windings for obtaining two voltage in an antiphase, the inductive sensor of shift, with two oppositely concerning the center of a rotor the located windings (for receiving a differential signal), the analog-digital converter and the microcontroller which carries out processing of a signal.

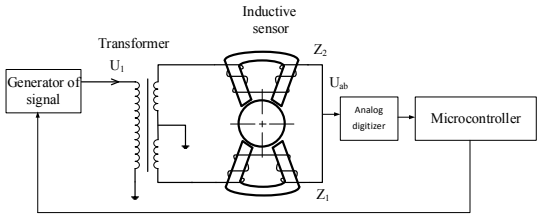

Fig. 2. The function chart of the inductive converter with the transformer bridge.

Secondary windings of the transformer and winding of the sensor form the transformer bridge. In the central provision of a rotor the bridge is balanced also output voltage U_{ab}=0. In the displaced provision of a rotor we have

$$U_{ab} = E\frac{Z_1 - Z_2}{Z_1 + Z_2 + 2Z} \qquad (1)$$

where E - the electromotive force of a secondary winding of the transformer; - complex resistance of a secondary winding, first and second windings of the sensor respectively.

The bearing frequency is usually high therefore active resistance of windings are negligible in comparison with their inductive resistance. Besides the transformer bridge is designed so that inductance of secondary windings of the transformer was much less inductance of windings of the sensor. Then in the displaced provision of a rotor we have

$$U_{ab} = \frac{E(L_1 - L_2)}{L_1 + L_2}, \qquad (2)$$

where L_1, L_2 - inductance of windings of the sensor.

The sensor model in the environment of Ansys is presented in the figure 3

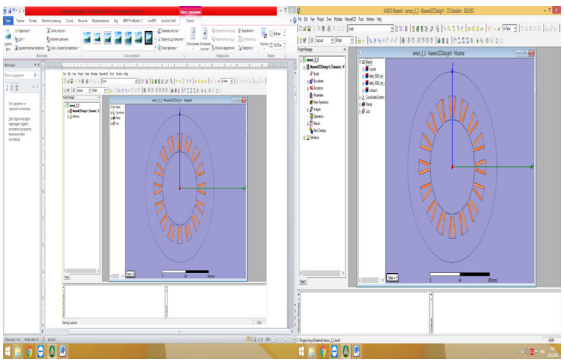

Fig. 3. Shift sensor Model in the environment of Ansys.

The bearing frequency usually is set about 10 kHz. It is caused on the one hand by desire to increase speed, on the other hand restriction of speed of analog digitizer of the microcontroller.

When giving on an entrance of basic voltage of squared Uo (fig. 4), at the exit we receive voltage which sign concerning a sign basic will depend on in what party the rotor concerning sensor windings is displaced.

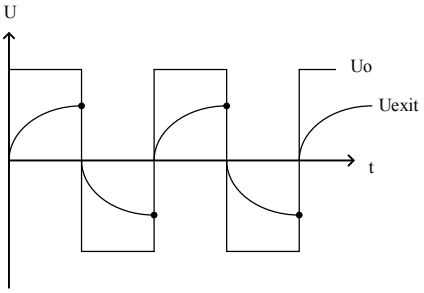

Fig. 4. Basic and output voltage of the sensor of shift.

At low frequencies output voltage has almost rectangular shape. At frequencies about tens kHz vortex currents, despite execution of a from leafs made magnetic conductor of the sensor have significant effect. Therefore we observe exponential increase of current. At such form of a signal it is required to perform measurement in a point of the highest value of voltage, but it is necessary to finish transformation of an analog signal before switching of the front of a basic signal. Taking into account that in full AMB there are 5 sensors of situation, speed of analog digitizer has to be 2 orders more than the frequency of a basic signal.

In the figure 5 results of modeling in the environment of Ansys Maxwell at rotor shift in the direction of an axis y on 0.1 mm are presented.

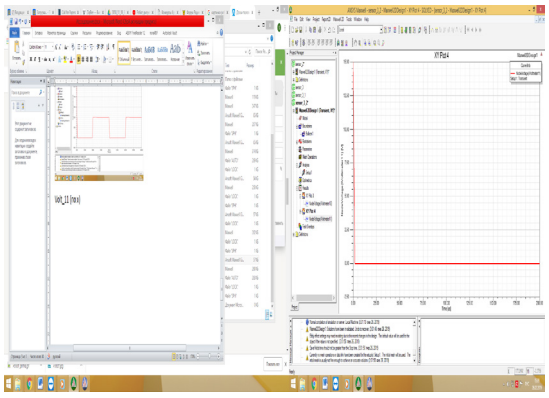

a)

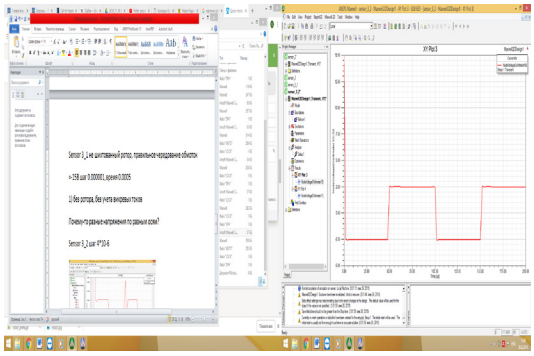

b)

Fig. 5. Results of basic and output modeling in the environment of Ansys Maxwell. a) voltage on axis X coils) voltage on axis Y coils.

Initial value of voltage 15B is caused by entry conditions when calculating model and does not reflect reality

Now speed of analog digitizer of the microcontroller makes about 1 MHz. Thus the frequency of a basic signal is limited to value about 10 kHz.

III. RESULTS AND DISCUSSION

Application of more high-speed analog digitizer is possible, however for them the range of entrance voltage usually decreases that negatively affects on a sensor noise stability.

In modern microcontrollers there is a module of capture and comparison. It allows to perform measurements of intervals of time between digital signals with a big accuracy and speed. Thus, if to receive a situation signal from the sensor which will be proportional to width of an impulse of a digital signal it is possible to increase speed.

In the figure 6 the function chart of the inductive measuring converter with a digital output is shown.

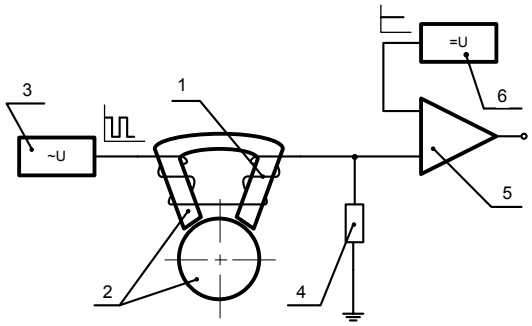

Fig. 6. The functional chart of the upgraded inductive sensor of linear movements.

The inductive measuring converter with a digital output contains the coil of inductance 1 which is put on not closed magnetic conductor with a changeable gap 2, a source of the rectangular voltage 3, the resistor 4, the comparator 5, a source of basic voltage 6. Consistently to the coil 1 are switched on the generator of rectangular voltage 3 and the resistor 4, one of conclusions of which is connected to grounding, and another to the coil 1 and one of comparator 5 entrances, the source of basic voltage 6 is connected to other entrance of the comparator 5.

If in a reciprocal part of a magnetic conductor 2 there are vortex currents, then power failure on the resistor will have the form close to triangular. At change of a gap of the core inductance of the coil and size of vortex currents change, and, therefore, also voltage amplitude on the resistor will change. On entrances of the comparator the constant basic voltage and triangular voltage from the resistor (fig. 7) moves. At the same time at its exit there are impulses which duration the T depends on magnetic conductor gap size.

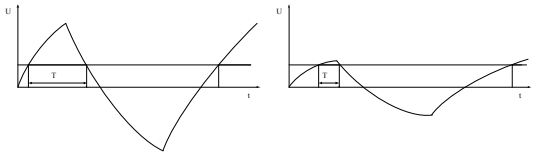

Fig. 7. Formation of impulses on the upgraded sensor.

In the figure 8 results of modeling in the environment of Ansys Maxwell with a frequency of 50 kHz are shown.

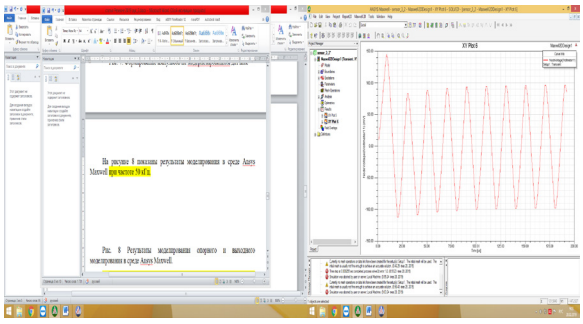

Fig. 8. Results of basic and output modeling in the environment of Ansys Maxwell.

Voltage shift at the initial stage of modeling is caused by entry conditions of calculation. Smaller amplitude value of voltage is caused by the bigger frequency and influence of vortex currents. For increase in sensitivity it is enough to increase sensor supply voltage.

For reduction of losses it is desirable that regarding a magnetic conductor on which the coil is reeled up, there would be no vortex currents, i.e. it needs to be produced from thin sheets of steel or from ferrite.

IV. CONCLUSIONS

Thus, are presented in article result of computer modeling of the inductive sensor of shift, and the upgraded inductive converter of linear movements used now.

Due to more fast measurement an opportunity to increase the frequency of the signal of basic voltage given on a sensor winding is available the T time interval microcontroller, than an analog signal. It positively affects on speed of all system and gives the chance of better processing of the received signal digital filters. Besides, there is an opportunity to avoid processing of analog signals that allows to choose more high-speed digital signal processor which is not containing the analog digitizer block. Still, if to place this converter directly with AMB, the hindrances induced at a transmission line of an analog signal from the sensor to the control unit are excluded.

On this inductive converter of linear movements the patent for the invention is taken out [12].

ACKNOWLEGMENTS

This article is prepared with partial support of the Ministry of Education and Science of the Russian Federation. “Development of Bases of the Theory of the Bearingless Synchronous Electrical Machine” project No. 2014/700

This study was partly supported by the Ministry of Education and Science of the Russian Federation. Project “Development of the Bearingless Synchronous Electrical Machine Theory Foundations” No. 2014/700

REFERENCES

[1] A.Chiba, T.Fykao, O.Ichikawa, M.Oshima, M.Takemoto and D.G.Dorrell, Magnetic Bearings and Bearingsless Drives. ELSEVIER, pp. 127-135.

[2] Y. Zhuravlyov Active Magnetic Bearings: Theort, Design, Aplication. St. Petersburg: Politechnica, 2003, pp. 12-25

[3] Adaptive control of the 1-DOF active magnetic bearing Sergei Loginov, Yuri Zhuravlyov, Yulia Domracheva, Dmitriy Fedorov Environment. Technology. Resources. Proceedings of the 11-th International Scientific and Practical Conference. – 2017. – volume III – p. 188-191. ISSN 1691-5402

[4] G. Schweitzer, H. Bleuler, and A..Traxler, Active Magnetic Bearings. Zurich, VDF Hochschulverlag AG, pp. 31-77 1994

[5] V.S. Polamraju, G.V. Sobhan, K. Nagesh, J. Amarnath and M. Subbarao. “Stabilization of active magnetic bearing system using single neuron PID controller”, ARPN Journal of Engineering and Applied Sciences vol. 9, no. 7, july 2014

[6] Ming-Mao Hsu, Seng-Chi Chen, Van-Sum Nguyen and Ta-Hsiang Hu “Fuzzy and online trained adaptive neural network controller for an AMB system”, Journal of Applied Science and Engineering, vol. 18, No. 1, pp. 47 -58. 2015

[7] AN AXIAL POSITION SENSOR FOR ACTIVE MAGNETIC BEARINGS Alexei V. Filatov Lawrence A. Hawkins Proceedings of ASME Turbo Expo 2010: Power for Land, Sea and Air GT2010 June 14-18, 2010, Glasgow, UK

[8] A low cost eddy current displacement sensor for active magnetic bearings A dissertation presented to The School of Electrical, Electronic and Computer Engineering North-West University In partial fulfilment of the requirements of the degree Master Ingeneriae in Electrical and Electronic Engineering by Andries May 2008

[9] Resonant inductive displacement sensor for active magnetic bearings AngeloBonfittoa RanGabaib AndreaTonolia Luis MiguelCastellanosa NicolaAmatia Sensors and Actuators A: Physical Volume 287, 1 March 2019, Pages 84-92

[10] The patent for the invention No. 2557373 “The inductive measuring converter with a digital output” It is registered on June 24, 2015. Loginov Sergey Yuryevich, Domracheva Yulia Vyacheslavovna, Fedorov Dmitry Sergeyevich

[11] Position Sensor. Waukesha Magnetic Bearings position sensors provide [Online]. Available: <https://www.waukbearing.com/en/magnetic-bearing-systems/system-details/position-sensor/>

[12] Sensorless position control of active magnetic bearings based on high frequency signal injection method Jung-Sik Yim, Jang-Hwan Kim, Seung-Ki Sul, Hyeong-Joon Ahn, Dong-Chul Han Conference: Applied Power Electronics Conference and Exposition, 2003. APEC ‘03. Eighteenth Annual IEEE, Volume: 1

Power Model of Impulse Arc Discharge Generation in Active Media Optical Pumping Xenon Lamps of Solid-State Lasers

Yury Anatolievitch Mandryko
ITMO University
St.-Petersburg
mandryko1@rambler.ru

Aleksander Sergeevitch Chirtsov
Saint-Petersburg Electrotechnical University ETU "LETI"
Herzen State Pedagogical University of Russia
St.-Petersburg
alex_chirtsov@mail.ru

Vladimir Mikhailovitch Mikushev
Saint-Petersburg State University
St.-Petersburg
v.mikushev@spbu.ru

***Abstract*—The semi-empirical model of arc impulse discharge development in impulse xenon lamps for optical pumping of solid-state lasers' active media was considered. Equations of the power balance of supplied electrical power and processes of ionization, plasma heating, heat dissipation and optical radiation generation laid the model's basis. The analytical description of the processes being considered results in an ordinary differential equation which allows a non-resource-intensive numerical solution. The built model enables to evaluate basic electrical and optical parameters of non-local arc discharge plasma at its development stage. Comparison with the results of measurements of electrical and optical plasma parameters which are the most convenient for experimental diagnostics in the modelled non-stationary mode testifies to adequacy of the developed model. Relative simplicity and convenience of the model predetermines its possible usage when solving applied engineering tasks of optimization of operating parameters of impulse pumping lamps and for obtaining initial (zero) approximations for comprehensive modelling of a non-local non-stationary gas discharge plasma in science-intensive calculations taking into account a great combination of elementary collision and radiation processes in a non-equilibrium system.**

Keywords — expanded xenon non-equilibrium plasma channel, impulse direct xenon lamp.

I. Introduction

Current development of technical means of numerical modelling of complex physical systems predetermined emergence of a new low-temperature plasma physics development stage. Emergence of the non-local plasma model [1] at the beginning of a new century and fast popularity growth during description of gas discharge media predetermined quick development of a new low-plasma physics area connected with macroscopic averaged numerical modelling of a large combination of elementary collision and radiation processes as part of hydrodynamically similar approximations [2]. A large number of works dedicated to such an approach during the study of quite a wide set of diverse gas discharge media (for example, [3--7]) enables to formulate a number of major problems which occurred in this area. First of all, they include difficulties of restriction of multiply elementary plasma processes [8] taken into consideration when developing quasi-closed models based on the set of reliable data on their probabilistic characteristics [9] or systematically made quantum-mechanical calculations, resource-intensity of which can be mitigated significantly by means of transitions to different semi-empirical approximations [10, 11]; yet limited experience of comparison of plasma modelling results with the experiment [12]. In this regard, it appears to be expedient to fulfil a series of works for modelling of non-local plasma media of already used or developed technical devices with a view to check the quality of developed theoretical approaches in the non-local plasma physics [13], on the one hand, and to solve applied tasks of optimization of real devices – on the other hand [14 - 16]. The practice of numerical modelling of non-local plasma in a quite popular today medium Comsol [17] shows that the quality and speed of models' convergence largely depend on selection of initial (zero) approximations for non-local plasma parameters, and it turns out to be particularly significant during the analysis of non-stationary processes quickly developed in time [18]. In this respect, the present work was made for development and testing of a simple semi-empirical model for the calculation of obtaining a possibly more qualitative approximation for internal (hardly susceptible to experimental determination) parameters of plasma of the developed discharge in xenon which emerges during generation of impulse arc discharges in xenon pumping lamps used in solid-state lasers.

Pulse stroboscopic direct xenon lamps ISP-200, ISP-250, ISP-600, ISP-2000, ISP-2500, INP-5/75, INP-5/40, INP-5,5/80, INP-7/80, INP-5,5/60) and their foreign analogues IPL-11x75x180, IPL-8.3x40x162, IPL-11x80x180, IPL-14x80x300, IPL-10.5x60x182 and others are widely used: in impulse light sources [19, 20], in solid-state and chemical lasers [21-23], in state-of-the-art electrophysical units, for distance measurement, in alarm, in high-speed photography, for

Print ISSN 1691-5402
Online ISSN 2256-070X
http://dx.doi.org/10.17770/etr2019vol3.4061

welding and cutting, in medicine, cosmetology, light engineering, photochemistry, spectrophotometry, water, air decontamination technologies, medications, solutions, instruments, food products, packing materials [24–34]. A wide spectrum of fields of application of impulse lamps predetermines the need for variation of their radiation parameters. These parameters depend on the dynamics of generation and expansion of an arc discharge plasma channel and, hence, can be adjusted within given limits by varying electrical power modes. For the efficient selection of such modes which assures optimization of optical characteristics, it is expedient to develop above-mentioned semi-empirical models interconnecting external, easily changing in practice, and important for optimum operation internal electrical and optical characteristics of impulse arc discharge non-local plasma. The specified considerations predetermined the choice of impulse xenon gas discharge lamps as an object of study, the first stage of which the present work is dedicated, the objectives of which include:

• development of a macroscopic model initial for microplasma modelling, on the basis of power balance equations for a gas discharge cell in each moment of a channel expansion stage;

• comparison of calculation results with the experiment for electric power supplied in a gas discharge lamp and power of radiation generated by a lamp at the quasi-stationary plasma channel generation stage;

• development of theoretical assessments for internal non-stationary non-equilibrium process parameters: dependences on time of radiation power of an expanded xenon non-equilibrium plasma channel, mean xenon plasma radiation absorption coefficient, power losses for gas ionization, plasma heating in the developed channel, heat transfer in gas surrounding a plasma channel.

• development of semi-empirical data on relations between listed non-stationary arc discharge parameters.

II. Semi-empirical model of the process of impulse arc discharge development in xenon

During the development of the model of arc discharge development processes in impulse xenon lamps, the equation of the power balance at the non-equilibrium plasma channel expansion stage was used. The electrical field power N_Σ supplied per a unit of time in a discharge gap is consumed for ionization of inert gas atoms (N_{ion}) heating of generated plasma (N_{T+}), heat transfer in surrounding non-ionized gas (N_T), and for generation of electromagnetic radiation (Φ_{rad})

$$N_\Sigma = N_{ion} + N_{T+} + N_{N-} + \Phi_{rad}. \quad (1)$$

On the other hand, the power described by the sum (1) can be experimentally determined by a voltage drop in the discharge gap u and the value of discharge current I. The electric power dissipated on a positive discharge column N_+ may be found by discharge current and specific plasma conductivity σ in this discharge field.

The speed of system power loss for radiation of electromagnetic waves Φ_{rad} through the side surface S of expanded plasma channel, which is included in (1) and is of greatest practical interest, may be determined by plasma radiation spectral density $E_{\nu,T}$ at effective radiating medium temperature:

$$\Phi_{rad} = 2\pi S \int_0^\infty E_{\nu,T} d\nu \quad (2)$$

Function $E_{\nu,T}$ standing under integral (2) may be evaluated by the Planck formula for equilibrium radiation spectral density and Kirchhoff optical law connecting radiating capacity ($E_{\nu,T}$) and absorbing capacity of the "grey" body $A_{\nu,T}$:

$$E_{i,T} / A_{\nu,T} = \text{const}. \quad (3)$$

Herewith in evaluation calculations based on the Planck formula of radiation of significantly non-equilibrium (at the arc discharge development stage) medium characterized by different electrons and heavy particles temperatures it is reasonable to use the typical electron kinetic power T_e as effective temperature.

As a result, the expression for plasma channel radiation power Φ_{rad} follows from (2) and (3):

$$\Phi_{rad} = \frac{4\pi}{c^2} h\left(\frac{h}{kT}\right)^3 S \int_0^\infty A_{\nu,T} \frac{\omega^3}{\exp\left(\frac{h\omega}{kT}\right)-1} d\omega \quad (4)$$

The experimentally observed lamp radiation power Φ_{lamp} differs from Φ_{rad} due to partial light absorption by bulb walls. In a restricted spectral frequency range from ν_1 to ν_2 corresponding to the bulb clarity band, the specified effect can be taken into consideration [24] by introducing effective (for a frequency band corresponding to the lamp bulb glass pass band) quartz wall radiation transmission coefficient, $\langle\gamma\rangle$. Its inclusion in (4) where an integration variable is replaced with a dimensionless value $x = h\nu/kT$ results in the following expression for the impulse lamp light flow measured during the experiment:

$$\Phi_{lamp} = \frac{4\pi}{c^2} kT_e S \langle\gamma\rangle \int_{hc/(kT_e\lambda_2)}^{hc/(kT_e\lambda_1)} A_{x,T} \frac{x^3}{\exp(x)-1} dx \quad (5)$$

For evaluation of the mean value of plasma channel absorption coefficient $A_{\nu,T}$ included in (8) the approximate approach based on the Bouguer law was used in [24]:

$$\langle A \rangle \approx 1 - \exp(-Kr) \quad (6)$$

where K [m^{-1}] – mean by spectral interval xenon plasma radiation absorption value, r – plasma channel radius. In its turn, the mean xenon plasma radiation absorption value k included in (6) was evaluated based on classical considerations (Schirmerformula [20]):

$$K \approx B_1 \frac{p}{T_e^3} \exp\left(-\frac{eU_i}{kT_e}\right) \quad (7)$$

where $B_1 = 7.9 \cdot 10^{13}$ K^3/(Pa m), p –xenon pressure in a plasma channel, U_i=11.7 B – xenon atom ionization potential, e – elementary charge. For the calculation of thermodynamic pressure of xenon plasma channel with volume V Van der Waals equation for xenon was used. As a result of insertion of Ratios (6) and (7) in (5) there

appears an approximation convenient for its quantitative evaluations for the effective absorption coefficient:

$$\langle A\rangle \approx 1-\exp\left[B_1\frac{\rho\, R\, T_i\, r}{(\mu-b_{Kr}\,\rho)T_e^3}\exp\left(-\frac{eU_i}{kT_e}\right)\right] \quad (8)$$

included in final expressions for electromagnetic radiation flows by a plasma channel and impulse lamp:

$$\Phi_{rad}=\frac{4\pi h}{c^2}\langle A\rangle\left(\frac{kT_t}{h}\right)S\int_0^\infty\frac{x^3}{\exp(x)-1}dx \quad (9)$$

$$\Phi_{lamp}=\langle\gamma\rangle\frac{4\pi h}{c^2}\langle A\rangle\left(\frac{kT_e}{h}\right)S\int_{hc/(kT_e\lambda_2)}^{hc/(kT_e\lambda_1)}\frac{x^3}{\exp(x)-1}dx \quad (10)$$

Final expressions formulas for calculations (8-10) introduce the following designations:, R – universal gas constant, T_i – plasma channel ion temperature, a_{kr}, b_{kr} – critical constants for xenon, P_{kr}=5.84 – critical xenon pressure and T_{kr}=289.734 K – critical xenon temperature, ρ – gas density, μ – its molecular weight. Quartz wall pass band wave lengths (λ_1=180 nm to λ_2=1100 nm) for lamp types IPL-8.3x40x162, INP-5/40 and ISP250 and the effective radiation transmission coefficient (<γ>) are given in [20, 36].

For accounting power losses N_{T+} spent for heating a gas component from heavy particles (ions in atoms) in the expanded plasma channel it was taken into account that density (ρ) and specific heat intensity (c) of plasma at its expansion stage vary weakly as compared to its volume (V) and ion temperature (T_i):

$$N_{T+}=\frac{d}{dt}cmT_i=\rho c\frac{d}{dt}(VT_i)=\rho c\left(V\frac{dT_i}{dt}+T_i\frac{dV}{dt}\right) \quad (11)$$

For exclusion of ion temperature included in (11) the Shockley formula typical for the classical gas discharge thermal physics connecting the volume variation speed and plasma channel temperature was used:

$$\frac{dT_i}{dt}=\frac{1}{\alpha V}\frac{dV}{dt},\quad T_i-T_{io}=\frac{1}{\alpha}\ln\frac{V}{V_0} \quad (12)$$

where α_{kr}=1.087·10^{-3} K^{-1} – plasma channel volumetric expansion coefficient. Its applicability amidst developed arc discharge was checked based on experimentally obtained dependence of a plasma channel proportional to the cross section area (and, hence, its volume) of discharge current on temperature. Applicability of the relation (12) between the plasma channel volume and temperature for the considered discharge development stage was checked experimentally.

Sizes, volume of a plasma channel and their expansion speed using the Ohm's law recorded in a differential form are easily expressed via electrical discharge parameters convenient for measurement: specific electrical conductivity of plasma channel σ, its variation speed in a positive column with the length of H and current intensity through a plasma interval i. As a result of insertion in (11) of so transformed ratios (12), the relation between heat power N_{T+} and electrical discharge gap parameters convenient for comparison with the experiment is obtained:

$$N_{T+}=\rho c T_i\frac{H^2}{\sigma}\frac{dy}{dt},\quad T_i=T_0+\frac{1+\ln(i/I_0)}{\alpha} \quad (13)$$

The ratio (13) via I_0 and T_0 designates initial (i.e. established during the time of combustion of a pilot arc preceding voltage power pulse arrival) current and ion temperature values of a plasma channel, respectively. Specific conductivity of a positive column is determined by electronic temperature $\sigma = D(T_e)^2$ where D_1=3.2·10^{-5} Siemens/(m·K^2) [24]. The latter at the plasma channel expansion stage can be deemed approximately invariable [24].

Power losses N_{ion} required for providing generation and expansion of a non-equilibrium plasma channel are related to its volume variation speed V through multiplication of charged particles concentration in plasma n_e by power w_i required for ionization of one atom with generation of an electron with power corresponding to electronic temperature of a xenon plasma ("ionization specific power"):

$$N_{ion}=\frac{d(w_i n_e V)}{dt}\approx w_i n_e\frac{dV}{dt},\quad w_i=\left(U_i+\frac{3}{2}kT_{e0}\right) \quad (14)$$

The formula for the calculation of the heat dissipation power N_{T-} from the expanded xenon non-equilibrium plasma channel with time variable ion temperature T_i in the environment at temperature T_0=300K through the boundary area with Δl width has the following form:

$$N_{T-}=\chi\, S\,\frac{T_i-T_0}{\Delta l} \quad (15)$$

where χ=3·10^{-2}·W/(m·K) – xenon heat conductivity coefficient. The side surface area S and radius r of the expanded plasma channel are determined via discharge current I using the differential Ohm's law:

$$r=\sqrt{\frac{HI}{\pi\sigma(u_1-U_a-U_k)}},\quad S=2\pi\, rH \quad (16)$$

Values of near-electrode potential drops U_a and U_k included in (16) in total do not exceed several volts and are low as compared to voltage drop u_1 on a positive column of approximately 40 V in the pilot arc mode and reaching 400 V in the power impulse mode.

Use of (16) for expression of geometrical parameters of the expanded plasma channel included in (14) and (15) via discharge current intensity and plasma channel conductivity easily measured at the experiment y=σs/L enables to obtain the ultimate working formula for calculation of total heat losses and to transform using (4) the initial equation (1) into the differential equation for finding a dependence of current intensity on time:

$$I^2\sigma^{-1}=\left\{\rho c\left[T_0+\frac{1+\ln(I/I_0)}{\alpha}\right]+n_e\left(U_i+\frac{3}{2}kT_{e0}\right)\right\}\frac{H^2}{\sigma}\frac{dy}{dt}+$$
$$+\frac{4\pi h}{c^2}\langle A\rangle\left(\frac{kT_t}{h}\right)S\int_0^\infty\frac{x^3}{\exp(x)-1}\,dx+\chi\, S\,\frac{T_i-T_0}{\Delta l} \quad (17)$$

III. Discharge Numerical Modelling

Equations obtained in the considered power model make up the closed system which enables to calculate

the course of dependences of discharge current on time $i_1(t)$ and other systems characteristics at the non-equilibrium plasma channel expansion stage as part of made approximations.

The built differential equation (17) was solved in the course of its numerical integration for discharge current, via which conductivity y, ion temperature T_i, mean absorption coefficient $< A >$, plasma channel side surface area S were expressed. The integration step did not exceed one hundredth of typical time of the aggregate arc discharge generation process.

Calculations were performed for the case of the value of constant voltage drop between lamp anode and cathode $u_1 \approx$ const, which, in its turn, implied invariability of the potential difference between positive column edges. This feature enables to simplify the equation (17) by transferring in it from conductivity to voltage drop on a positive column U_{colomb}:

$$i_1 U_{colomb} = \left\{ \rho c \left[T_0 + \frac{1+\ln(I/I_0)}{\alpha} \right] + n_e \left(U_i + \frac{3}{2} kT_{e0} \right) \right\} \times \qquad (18)$$
$$\frac{H^2}{\sigma}\frac{dy}{dt} + \frac{4\pi h}{c^2}\langle A \rangle \left(\frac{kT_t}{h}\right) S \int_0^\infty \frac{x^3}{\exp(x)-1}\, dx + \chi\, S \frac{T_i - T_0}{\Delta l}$$

As a result of solution of the power balance equation (18) the time behaviour of the instant current value $I(t)$ of pumping in a discharge lamp was calculated, by means of which time dependences of instant electric power supplied in lamp and its instant radiation power were calculated. Thus, the obtained modelling results were compared with an experiment.

IV. Experiment

The experimental test of the built model was made on lamp types IPL-8.3x40x162 ISP250 for two voltage values at storage capacity (U_{la1}=80 V and U_{la2}=110 V) [37].

Recording of a transitional instant voltage characteristic proportional to instant pumping voltage between electrodes. Recording of the discharge current time behaviour in an impulse lamp is carried out using non-inductive current sensor.

Figure 1 shows experimental and design transitional characteristics of electric powers $N_{el}(t)$ supplied in the expanded xenon non-equilibrium plasma channel in INPKL (ISPKL).

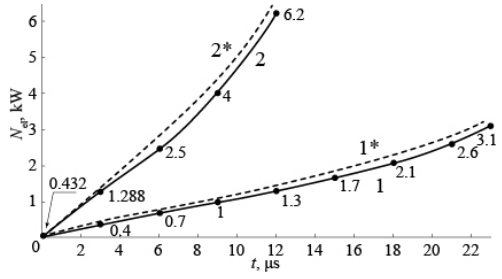

Fig. 1. Transitional characteristics of electric powers supplied in a xenon lamp: 1 and 1*— experimental and calculated characteristics for 80 V and 140 V supply voltage, 2 and 2* — experimental and calculated characteristics for the same voltages.

As it follows from figure 2, calculated and experimental transitional characteristics $N_{el}(t)$ during expansion of a xenon non-equilibrium plasma channel rise and match satisfactorily. It testifies in favour of the proposed physical and mathematical model.

Figure 2 shows design time dependences of common logarithms of rated powers for ionization of an expanded plasma channel $\lg(N^{(i)}_{channel}(t)/N^{(e)}_{pdao})$ (8), for heating a plasma channel $\lg(N^{(T)}_{channel}(t)/N^{(e)}_{pdao})$ (13), for radiation of a plasma channel $\lg(N^{(r)}_{channel}(t)/N^{(e)}_{pdao})$ (24) and heat dissipation from channel $\lg(N^{(\chi)}_{xe}(t)/N^{(e)}_{pdao})$ (27) in respect of electric power supplied in a plasma channel of a pseudo-pilot arc.

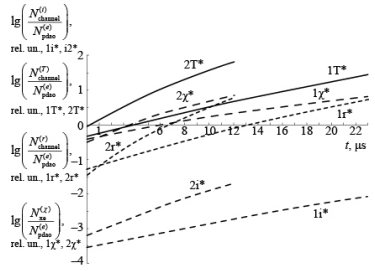

Fig. 2. Timedependences of common logarithms of rated powers for ionization of an expanded plasma channel $\lg(N^{(i)}_{channel}(t)/N^{(e)}_{pdao})$, for heating a plasma channel $\lg(N^{(T)}_{channel}(t)/N^{(e)}_{pdao})$, radiation of a plasma channel $\lg(N^{(r)}_{channel}(t)/N^{(e)}_{pdao})$ and heat dissipation from it into the environment $\lg(N^{(\chi)}_{xe}(t)/N^{(e)}_{pdao})$ in respect of electric power supplied in a plasma channel of a pseudo-pilot arc: 1i*, 2i* — calculated characteristics for powers of plasma channel ionization at supply voltage values on a lamp of 80 V and 110 V respectively, 1T*, 2T* — calculated characteristics for powers of expanded plasma channel heating at supply voltage values on a lamp of 80 V and 110 V, respectively; 1r*, 2r* — calculated characteristics for plasma channel radiation powers at supply voltage values on a lamp of 80 V and 110 V, respectively; 1χ*, 2χ* — calculated characteristics for heat dissipation powers from a channel into the environment at supply voltage values on a lamp of 80 V and 110 V, respectively.

As one could expect, at the xenon non-equilibrium plasma channel expansion stage time dependences of common logarithms of rated powers for ionization of an expanded plasma channel $\lg(N^{(i)}_{channel}(t)/N^{(e)}_{pdao})$, for heating a plasma channel $\lg(N^{(T)}_{channel}(t)/N^{(e)}_{pdao})$, for radiation of a plasma channel $\lg(N^{(r)}_{channel}(t)/N^{(e)}_{pdao})$ and heat dissipation from a channel into the environment $\lg(N^{(\chi)}_{xe}(t)/N^{(e)}_{pdao})$ are increased with time at the same lamp voltage value. Herewith, voltage increase between lamp electrodes results in an increase of rates of power rise for ionization of an expanded plasma channel, for heating a plasma channel, for radiation of a plasma channel and heat dissipation from it into the environment.

Recording of a transitional characteristic of a radiation power surface density INPKL (ISPKL) is made using VD3 photodetector and R_4 current sensor. Based on the experimental transitional characteristic of radiation power surface density INPKL (ISPKL) experimental transitional characteristic of radiation power INPKL (ISPKL) $N_{izl}(t)$ was determined. The latter is given in figure 3 together with numerical modelling results.

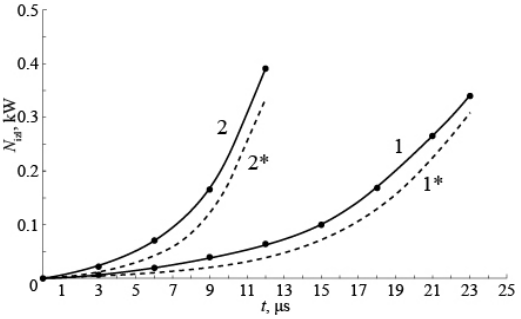

Fig. 3. Transitional characteristics of radiation powers INPKL (ISPKL): 1 and 1*— experimental and calculated characteristics for 80 V and 140 V supply voltage, 2 and 2* — experimental and calculated characteristics for the same voltages.

Satisfactory matching of numerical modelling results with the experiment enables to speak about applicability of the proposed model for rough evaluations of the time course of parameters of non-equilibrium plasma of an impulse arc discharge in xenon pumping lamps at the plasma channel expansion stage.

Development of the numerical expanded plasma channel model based on power balance accounting enables not only to obtain initial evaluations for full-scale plasma modelling taking into account specifics of elementary collision and radiation plasma processes significant for the considered system but also gives a possibility to evaluate a number of internal parameters of non-local non-stationary expanded discharge channel plasma important for optimization of pumping lamps operation.

V. Conclusion

As a result of theoretical and experimental studies, a model for processes of expanded non-equilibrium plasma channel generation in impulse stroboscopic direct xenon lamps and impulse direct xenon lamps for optical laser pumping was built. The accuracy of calculations made within the model being considered is approximately 90%. Thus, the built and tested model may be used for applied calculations and modelling operating modes of devices in which non-stationary arc electrical discharges are used, including - for optimization of operating modes of impulse direct xenon lamps.

References

[1] I.D. Kaganovich, V.I. Demidov, S.F. Adams and Y. Raitses, “Nonlocal collisionless and collisional electron transport in low-temperature plasma (invited paper)”, Plasma Physics and Controlled Fusion, vol. 51, p. 124003, 2009.

[2] A.A. Kudryavtsev, A.S. Smirnov, L.D. Tsendin, Glow discharge physics. SPB: Lan’, 2010.

[3] A. Chirtsov, A. Kudryavtsev, E. Bogdanov, “Fluxes of Charged Particles in Two-Chamber ICP Discharge in Oxygen”, Accepted to EEE Transactions on Plasma Science Special Issue, Images in Plasma Science, v.39, N8, P. 2562-2563, 2011.

[4] E.A. Bogdanov, A.S. Chirtsov, A.A. Kudryavtsev, “Fundamental non-ambipolarity of electron fluxes in 2D plasmas”, Phys. Rev. Lett., Vol. 106, pp. 195001, 2011.

[5] K. Kapustin, A. Kudryavtsev, E. Bogdanov, A. Chirtsov, “Non-local behavior of electron fluxes and excitation rates for “local” EEDF in moderate and high pressures DC positive column plasmas”, Imag. Plasma Sci., Vol. 39, pp.180-183, 2011.

[6] S.I. Eliseev, V.I. Demidov, A.A. Kudryavtsev, V.I. Kolobov, E.A. Bogdanov, A.S. Chirtsov, “Impulse breakdown modelling in helium using adaptive methods”, J. Sci.-techn. Bull. Inf. Techn., Mech. Opt., Vol. 5, pp.139-146, 2014.

[7] A.S. Chirtsov, V.M. Mikushev, E.V. Lebedeva, S.V. Sychov, “Numerical Simulation of Glow Discharge in Air Mixtures under Low Pressure Conditions”, Int. J. Appl. Eng. Res., Vol. 11, pp. 11836-11846, 2016.

[8] H. Mahadevan, L.L.Raja, “Simulations of direct-current airglow discharge at pressures 1 Torr: discharge model validation”, J. Appl. Phys., Vol. 107, pp. 093304, 2010.

[9] T. Makabe, T. Tatsumi, “Workshop on atomic and molecular collision data for plasma modelling: Database needs for semiconductor plasma processing”, Plasma Sources Science and Technology, vol. 20, n.2, 2011. https://doi.org/10.1088/0963-0252/20/2/024014.

[10] L.A. Weinstein, I.I. Sobelman, E.A. Yukov. Atom excitation and widening of spectral lines. M.: Science, 1979.

[11] S.V. Sychov, A.S. Chirtsov “Genetic algorithm as a means of solving a radial Schrödinger equations system” presented at 19th International Conference on Soft Computing and Measurements, SCM, St. Petersburg, Russia, 2016

[12] M.V. Chernysheva, A.S. Chirtsov, D.A. Shvager, “Comparative analysis of plasma chemical models for computer simulation of glow discharges in air mixtures”, Sci.-Techn. Bull. Inf. Techn., mech. Opt., Vol. 16, pp. 903-916, 2016.

[13] Jr. De Joseph “Non-local effects in a bounded low-temperature plasmas with fast electrons”, Phys. Plasmas, Vol. 14, pp. 057101, 2007.

[14] E.A. Bogdanov, K.D. Kapustin, A.A. Kudryavtsev, A.S. Chirtsov, “Comparison of various options of hydrodynamic (fluid) modelling of a longitudinal structure of atmospheric pressure micro-discharge in helium”, Techn. Phys. J., Vol. 80, pp. 41-53, 2010.

[15] E.A. Bogdanov, A.A. Kudryavtsev, N. Ochikova, “Violation of Boltzmann distribution for plasma electron density in two-chamber ICP-discharges”, Techn. Phys. J., Vol. 85, pp. 155-158, 2015.

[16] A.S. Chirtsov, S. Eliseev, A. Kudryavtsev, H.N. Liu, Y.D. Zhongxi, “Transition from Glow Microdischarge to Arc Discharge with Thermionic Cathode in Argon at Atmospheric Pressure”, IEEE Trans. Plasma Sci. Special Iss. – Atmosph. Press. Plasmas Appl., Vol. 44, pp. 2536-2544, 2016.

[17] Comsol 4.0a Plasma module user guide // HUMUSOFT [Web-site] [Online]. URL: https://www.humusoft.com/comsol/ (Accessed January 2019).

[18] S.I. Eliseev, V.I. Demidov, A.A. Kudryavtsev, V.I. Kolobov, E.A. Bogdanov, A.S. Chirtsov, “Impulse breakdown modelling in helium using adaptive methods”, J. Sci.-techn. Bull. Inf. Techn., Mech. Opt., Vol. 5, pp. 139-146, 2014.

[19] ILC Engineering Note No. 152 (Use of Xenon Short Arcs as Pulsed Light Sources), ILC Technology, 399 West Java Drive, Sunnyvale, CA 94089.

[20] G.N. Rokhlin. Discharge light sources. Moscow: Energoatomizdat, 1991.

[21] Xenon Flash Lamps, Technical Literature TLSX1008E04, Hamamatsu Photonics K.K., 1998.

[22] Super Quiet Xenon Lamps, Technical Literature TLSX1002E06, Hamamatsu Photonics K.K, 2000.

[23] W. Koechner Solid-State Laser Engineering. Sixth revised and updated edition. Germany:Springer, 2006.

[24] A.A. Mak, N.L. Soloviev. Introduction in high-temperature laser plasma physics. Leningrad: LSU, 1991.

[25] W.J. O’Brian, G.L. Hunter, J.J. Rosson, R.A. Hulsey, K.E. Carns, “Ultraviolet system design: past, present and future”, in : Proceedings Water Quality Technology Conference, AWWA, New Orleans, LA., 1995, pp. 271-305.

[26] J. Dunn, A. Bushnell, W. Ott. & Clark, “Pulsed white light food processing”, Cereal Foods World, Vol. 42, pp. 510-515, 1997.

[27] J. Dunn, D. Burgess, F. Leo, “Investigation of pulsed light for terminal sterilization of WFI filled blow/fill/seal polyéthylène containers. Parenteral Drug Assoc.”, J. Pharm. Sci. & Tech., Vol. 51, pp. 111-115, 1997.

[28] High-voltage engineering. Gas discharge process physics. St.-Petersburg: SPBSTU, 1999.

[29] S.K. Zhdanov, V.A. Kurnaev et al. Fundamentals of physical processes in plasma and plasma units. Moscow: MSIPI, 2000.

[30] A. G. Grigoryants, I. N. Shiganov. A. M. Chirkov. Hybrid laser welding technologies. Moscow: Publ. Bauman’s MSTU, 2004.

[31] A. Mimouni, “Inactivation microbienne par lampes flash ou lumière pulsée”, La Lettre - Traitements de surfaces, Vol. 10, pp. 21-25, 2004.

[32] F. Fine, P. Gervais, “Efficiency of pulsed UV light for microbial decontamination of food Powders”, J. Food Protection, Vol. 67, pp. 787-792, 2004.

[33] B. Mrabet, H. Elloumi, A. Chammam, M. Stambouli, G. Zissis, “Effect of a pulsed power supply on the ultraviolet radiation and electrical characteristics of low pressure mercury discharge” Plasma Devices and Operations, Vol.14, pp. 249– 259, 2006.

[34] L. Bouslimi, A. Chammam, M. Ben Mustapha, M. Stambouli, J.P. Cambronne, “Simulation and Experimental Study of an Electronic Pulsed Power Supply for HID Lamps Intended for Photochemical Applications”, Int. Rev. Electrical Eng. (IREE), Vol. 4, pp. 799-808, 2009.

[35] L. Bouslimi, A. Chammam, M. Ben Mustapha, M. Stambouli, J.P. Cambronne, “Electric and spectral characterization of a high pressure mercury lamp used in the photochemical treatment”, Int. J. Sci. Techn. Automatic Control Comp. Eng. (IJ-STA), Vol. 3, pp. 1064-1071, 2009.

[36] I.S. Marshak. Pulse light sources. Moscow: Energiya, 1978.

[37] Y.A. Mandryko, “Electrical circuit with switching IGBT-transistors for gas discharge lamps”, Adv. Electronics, Vol. 7, pp. 64-69, 2015.

Environment. Technology. Resources. Rezekne, Latvia
Proceedings of the 12th International Scientific and Practical Conference. Volume III, 160-165

Determining the Positions of the Elements for the 3-2-1 Principle of Location in a Solidworks Add-in

Oleg Mihaylov
Faculty of Industrial Technology
Technical University of Sofia
Sofia, Bulgaria
inj.mihaylov@gmail.com

***Abstract*—This paper presents the methodology behind the positioning of modular fixtures (for the 3-2-1 principle in particular) in a CAFD application (add-in) for SolidWorks. The application is integrated into SolidWorks and it's used to automate the design process of modular fixturing devices. Part of it is a methodology for automated determination of the positions of the modular elements by using rule-based logic and mathematical formulas.**

***Keywords*—add-in, computer-aided fixture design, fixtures, locating, solidworks**

I. Introduction

A fixture is a work-holding or support device used in the manufacturing industry. Fixtures are used to securely locate (position in a specific location or orientation) and support the work, ensuring that all parts produced using the fixture will maintain conformity and interchangeability. Using a fixture improves the economy of production by allowing smooth operation and quick transition from part to part, reducing the requirement for skilled labor by simplifying how workpieces are mounted, and increasing conformity across a production run [1, 2]. In addition to processing, they are also used in experiments at elevated regimes and increased duration of cutting, while retaining accuracy in the measurement [3].

Fixture selection and design takes a significant part of the total time necessary for technical and technological production preparation and the costs associated with fixture design and manufacture can account for 10%–20% of the total cost of a manufacturing system [4]. These costs relate not only to fixture manufacture, assembly, and operation, but also to their design. Hence there are significant benefits to be gained by reducing the design costs associated with fixturing.

Approximately 40% of rejected parts are due to dimensioning errors that are attributed to poor fixturing design [5]. Fixture design work is also tedious and time-consuming. It often heavily relies on fixture design engineers' experience/knowledge and usually requires over 10 years manufacturing practice to design quality fixtures [6]. The design and manufacture of a fixture can take several days to complete when human experience and a try-and-error process is utilized in fixture design. By reducing the subjective influence of the human factor and the try-and-error process the design process can be improved significantly.

Modular fixturing systems are the most widely used flexible fixturing systems in manufacturing. They are based on standardization of their components and they are designed as groups of pre manufactured standard elements and units with relatively tight tolerances. Those elements can be assembled in variety of different fixtures for locating and clamping variety of different parts. Once all the needed processes are completed the fixtures can be disassembled and reassembled in other, completely different configurations [7]. This is the modular systems' biggest difference and biggest advantage over the dedicated fixtures as the latter are usually scraped after completing their task.

For years, applications of modular fixtures have led to significant technological and economical benefits including [8]:

1. Significant reduction of the lead time – applications of modular fixtures can reduce more than 80% of the production preparation time.
2. Reduction of the production cost – modular fixtures are reusable, thus replacing dedicated with modular fixtures leads to a significant reduction of the materials and manufacturing costs of fixtures, especially in job and batch productions.
3. The use of modular fixtures helps ensuring production quality – the standard modular components are manufactured with tight tolerances. Once they are assembled into a configuration, the positions of functional components can be locally adjusted thus providing a potential to improve the production quality.
4. The use of modular fixtures may extend the manufacturing equipment's capability and improve the production rate.

Modular fixtures are composed from baseplate on which are positioned different locating and clamping elements. All the system holds up a workpiece in a strict position during process operations. [9] Generally the design process for modular fixture devices consists of the correct selection of locating, supporting and clamping elements and their precise position on the base plate. The number and position of locating points must be such that a workpiece's six degrees of freedom (Fig.1a) are adequately constrained during machining [10] and there are a variety of conceptual locating point layouts that can facilitate this, such as the 3-2-1 locating principle, plane and pin-hole locating, long-pin locating, V-block locating (Fig.1b).

Print ISSN 1691-5402
Online ISSN 2256-070X
http://dx.doi.org/10.17770/etr2019vol3.4138

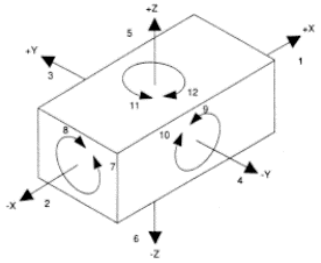

a)

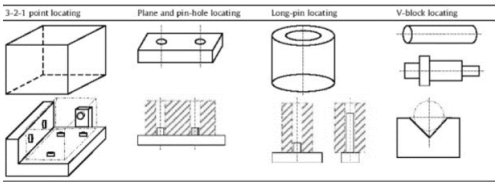

b)

Fig. 1. (a) The six degrees of freedom [11] and (b) methods of constraining them [12].

When separate locating elements are used (e.g. seating pins) their positions have to be such, that they ensure the stable position of the workpiece, i.e. the workpiece should not be moved by its own weight. This is achieved by placing the elements at maximum distance of one another [13]. When a baseplate with pin-hole pattern is used, there are obvious restrictions to that distance, so the positions of the locating elements have to be at maximum distance in contention with the pin-hole pattern and the workpiece's dimensions and form.

The automation of fixture design process is successfully solved by applying the system for Computer Aided Fixture Design (CAFD), which are using various intelligent methods, such as expert system, case based reasoning, and genetic algorithm (GA), etc.

The methodology presented in this paper uses rules of type IF-THEN-ELSE, mathematical formulas and SolidWorks' options to determine optimal positions for the locating elements.

II. Related researches.

In [14] was presented the basis for an application integrated in SolidWorks, whose task is to create fixture design for locating prismatic and cylindrical parts by one of three methods - 3-2-1 locating principle, plane and pin-hole locating or V-block locating. The application is created like an integrated in SolidWorks' environment add-in and was developed by using SolidWorks' API, VB.NET programing language and rules IF-THEN-ELSE.

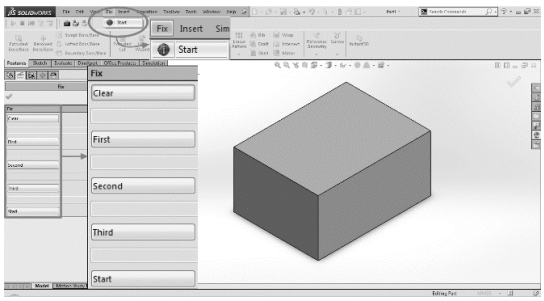

Fig. 2. Interface of the ADD-IN.

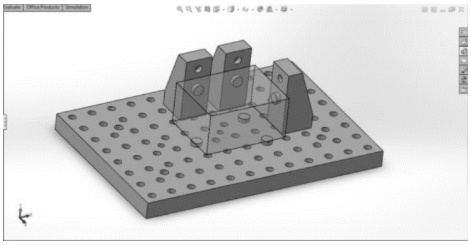

Fig. 3. Assembled fixture with workpiece.

The add-in is started in "PART" file by its own button in the Toolbar. The necessary input data is entered by the user by selecting the locating surfaces and confirming the selection with the buttons in the Property Manager Page (Fig.2.). While the selection is made, the program determines the surfaces' type and dimensions and the locating elements' positions. When the button "Start" is selected by the user the program creates a new assembly file, places the base plate and start inserting and mating operations for the rest of the elements and the part. After concluding all of its actions the program leaves the assembly file open for the user so he can continue working with it (Fig.3.).

III. Selecting surfaces.

To the aforementioned interface (Fig.3.) was added a button for the selection of the machined surface (Fig.4.). Whit this button the user marks the surface(s) that will be machined and therefore cannot be used for locating or clamping. For every surface selected for locating the program have to determine if it is suitable by checking first the selected surface's orientation in relation to the machined surface. This is done by using custom rules of the If-Then-Else variety and SolidWorks' built-in commands through its application programming interface (API). Basically the add-in measures the angle and distance between the two surfaces and, with the help of the rules, decides if the selected surface is suitable. At the moment this means that the angle between the two surfaces have to be between 90° and 270°.

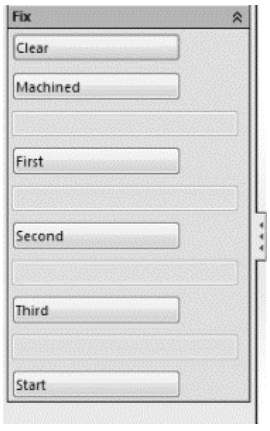

Fig. 4. Property Manager Page.

After successful selection of the to-be-machined surface(s) the text field under the button shows the number of selected surfaces. After successful selection of a locating surface the text field under the button shows "OK". The clamping surfaces are selected by the program and there is

no indications for selection in the Property Manager Page.

IV. Determining the locating elements' positions.

As it was stated before, with the location of parts it is crucial the locating elements to be correctly positioned. Those positions directly depend on the surface's shape (rectangle, circle, polygon), dimensions and if it's solid or not are there holes, steps etc. (Fig.5.)).

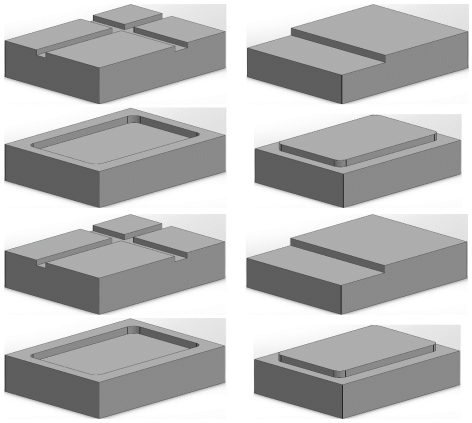

Fig. 5. Surfaces with different features.

When the surface has simple shape (solid square or circle) the positions are easily determent but with complicated shapes and/or additional features the task becomes more and more complicated. The program needs to "understand" what portion of the part it can use for location and that's achieved whit the help of the user and set of rules, which allow the program to find other surfaces in the same plane without the user selecting all of them.

The rules are using SolidWorks' option, available through the application programming interface (API). After the user selects a surface and presses a button, the program determines its orientation by extracting its normal vector data and gets the coordinates of the end points. Then the program checks every surface of the part for others with the same orientation and in the same plane. If there are such surfaces their end points' coordinates are added to those of the selected surface. Example for the used rules:

Automated selection of a surface. Extraction of the normal vector's data.

***IF** the vector data match the vector data of the surface selected by the user **THEN**;*

***IF** the surface lies in the same plane as the surface selected by the user **THEN**;*

Collecting the coordinates of the surface's end points.

ELSE

Automated selection of the next surface;

ELSE

Automated selection of the next surface.

Those and other rules of the same type are included into cycles, which are repeated until every surface is compared to the selected surface.

After the comparison is concluded, a new sketch is created on the selected surface. The coordinates gathered from all end points are transformed to the local coordinate system of the sketch and the maximal and minimal values for each axis are determined -$x_{(1\,max)}$, $x_{(1\,min)}$,$y_{(1\,max)}$,$y_{(1\,min)}$. Those values are used for the calculation of a center point :

$$X10 = \frac{X\,max + X\,min}{2}, Y10 = \frac{Y\,max + Y\,min}{2} \quad (1)$$

The locating points are going to be calculated in a relation to this center point in such manner, that they will imitate the hole pattern on the base plate. Next the distance between the minimal and maximal value for each axis is calculated:

$$\Delta_X = X_{1\,\max} - X_{1\,\min}, \Delta_Y = Y_{1\,\max} - Y_{1\,\min} \quad (2)$$

$$k_x = \left[\frac{\Delta_x}{0{,}050}\right], k_y = \left[\frac{\Delta_y}{0{,}050}\right] \quad (3)$$

The coefficient shows the multiplicity of the distance to the step of the holes on the base plate (50mm) rounded down to an integer (means the floor of , i.e. the largest integer less than or equal to). Those coefficients are used for calculation of the coordinates for the location elements so the round down guaranties that they will be between the endpoints of the surface. The coordinates are calculated as follows:

$$\begin{aligned} u_{13} &= u_{10} + k_u * 0{,}025; \\ v_{11} &= v_{10} - k_v * 0{,}025; \\ v_{12} &= v_{10} + k_v * 0{,}025; \\ v_{13} &= v_{11} + * 0{,}050 \end{aligned} \quad (4)$$

The values for are taken from equations (2) and (3) depending on which value of is greater – for and for . The same logic is applied for the values of . In equations (4) is multiplied by half the step of the holes on the base plate, so the symmetry of the locating points according to is consistent to the symmetry of the holes. On the base plate there are no pin-holes on the axes of the plate that's why in the equation for there is additional round down – without it in the cases when is odd the coordinate comes between the holes.

With the calculated coordinates the program creates points in the sketch and closes it. Next there are checks on whether the points lie on the surface (or surfaces). The task of those checks is to avoid placing a locating element in a hole, grove or outside the surface. If at least one point is not on the surface (or surfaces) (Fig.6.a) the program implements one or series of corrections aiming to get all points on the surface.

The corrections can be:

- mirror reversal of the points to one axis (Fig.6b);
- single or multiple displacement of all points along one or both axes at distance equal to portion of the free space (Fig.6c), i.e. from (2) and (3):
  (6)
- recalculation of the coordinates with coefficient , with the possibility of repetition until ;
- swapping the coefficient (Fig.6d).

The different corrections can be combined in various

ways so after one type of correction to be executed multiple corrections of different type. For example: after recalculation of the coordinates with coefficient to be executed multiple displacements until reaching , after which another recalculation with to be implemented end so on until . Of course any subsequent correction is executed if at least one point doesn't lie on the surfaces.

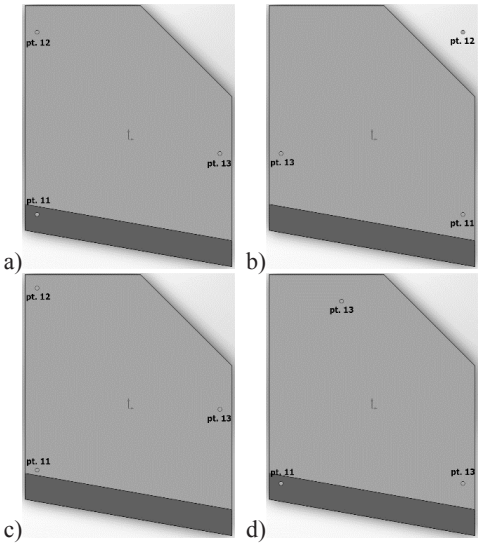

Fig. 6. Locating points – a) calculated coordinates; b), c), d) with corrections.

When all possible corrections are implemented and at least one point doesn't lie on the surfaces the program shows message to the user, stating that the selected surface is not suitable for this type of locating.

The checks and corrections are the same for solid surfaces and surfaces with different features. The program finds the features without the help of the user, however if the user want to use a tiered surface for location he needs to select one surface for each plane. A tiered surface is considered when two or more surfaces have same orientation but lie on different parallel planes. The reason why the user has to select one surface for each plane is to avoid placing locating element on the bottom of any feature (e.g. on the bottom of a blind hole).

When $\left[\frac{0,5 * (v12 - v11)}{0,050}\right]$re lying on the surfaces, the program checks if the center of gravity (its projection on the plane of the surface) lies in the triangle of the three points. If it does, then the determination of coordinates is completed successfully, otherwise additional corrections are implemented. The corrections consist of displacement of one or two points along one or both axes at distance multiple of 50mm (Fig.7.). After each correction all the points are checked whether they still lie on the surface. If there is no way the center of gravity to lie in the triangle the determination of coordinates can't be completed successfully.

After the successful selection of the first surface (i.e. all checks are passed successfully) the user can make selection for second surface. For determining the locating points on the second and third surfaces the center point is projected onto their planes thus ensuring the same symmetry in all planes.

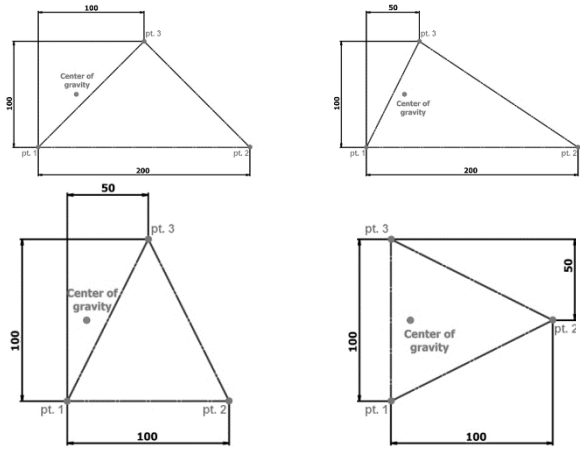

Fig. 7. Positioning the locating points according to the center of gravity.

For the second and third surfaces the coordinates are determined differently than for the first surface. For the second surface the coordinates for one of the axes (the one parallel to the projection of the first surface) are calculated according to :

$$u_{21} = u_{20} - \left(\left[\frac{u_{2max} - u_{2min}}{0,050}\right] * 0,050\right)/2;$$
$$u_{22} = u_{20} + \left(\left[\frac{u_{2max} - u_{2min}}{0,050}\right] * 0,050\right)/2 \quad (6)$$

In (6) are the coordinates on the first axis; is the coordinate of the projected point on this axis. The coordinates on the second axis are selected according to the selected adjustable stops (Fig.8.). The coordinates are equal to the height of the adjustable screw (D, C or B) minus the height of the seating pin's head.

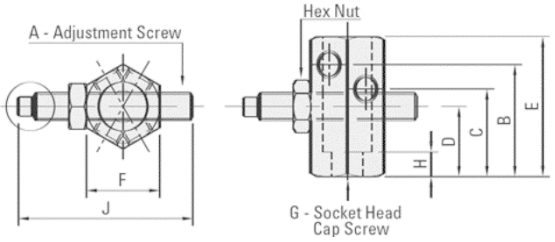

Fig. 8. Adjustable stops. [15]

The height of the adjustable screw is selected so that the center of gravity (its projection on the plane) is between the locating points and the first surface's projection (Fig.9).

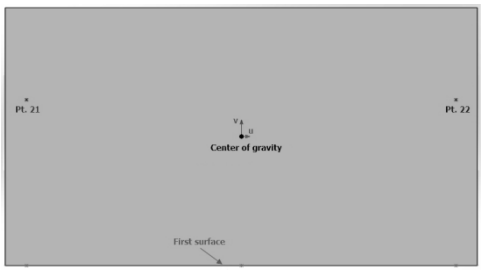

Fig. 9. Position of points 21 and 22 in relation to the first surface and center of mass.

The program creates point with the calculated coordinates and starts checks and corrections, similar to those

for the first surface. The corrections can be mirror reversal or displacement of one or both points by 50mm on each of the axes. If necessary the locating points can be moved below the center of gravity.

For the third surface the coordinate is calculated similar to :

$$u_{31} = u_{30} - \left(\left[\frac{u_{3max} - u_{3min}}{0,050} \right] * 0,050 \right) / 2. \quad (7)$$

The symbol in (7) is replaced with so that the point of center of gravity is between the locating point and the second surface's projection (Fig.10.). For the second axis the coordinate of the point is selected the same way as . The checks and corrections are same as for the second surface.

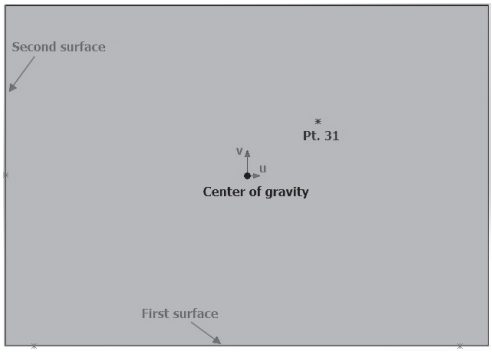

Fig. 10. Position of pt.31 in relation to the first and second surface and the center of mass.

After the successful selection of all three surfaces and all calculations are completed the program transforms all coordinates in global coordinate system and recalculates them so they match the pin-hole pattern on the base plate (Fig.11.). This is done automatically at the end of the user's selection.

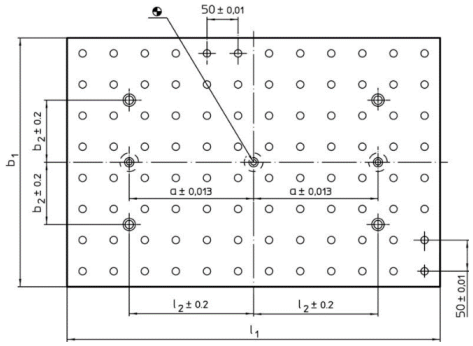

Fig. 11. Base plate [16].

Once the selection process is completed successfully the user can select button "Start" and let the program create a new file of type "ASSEMBLY" (.sldasm). In this file the program places the base plate as fixed part and starts inserting and mating processes for all locating and supporting elements and the part. The program inserts the default configuration of every element and changes it according to the values of coordinates. If it's needed the adjustable stopper's body can be placed on raising elements for additional height. The need, type and dimensions of the raising elements are automatically selected by the system.

All elements are mated together at the calculated positions and the system concludes its work by leaving the new assembly for the user to interact with it (Fig.12.) – to inspect it, to manually correct it if needed, to save the file with selected name and in selected folder etc.

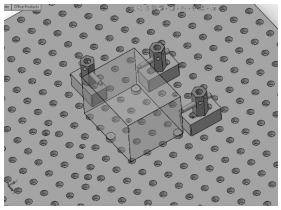

Fig. 12. Assembled fixture with part.

V. Determining the clamping elements' positions.

The determination of positions of the clamping elements is similar to that of the adjustable stops. It is done in relation to the locating surfaces and elements. The program searches for surfaces that are opposite to the locating surfaces but are not selected as to-be-machined. The clamping points are selected by the same equations with a difference for the side clamps – the positon is calculated not for the middle of the clamp but for the socket that will be outermost from the center of the part (Fig.13.).

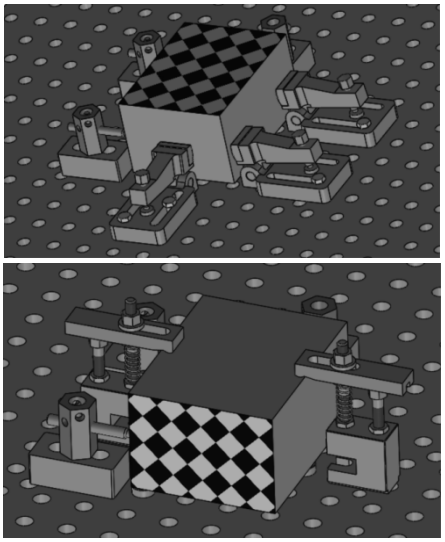

Fig. 13. Clamping (to-be-machined surface in checkered pattern).

VI. Conclusions.

This paper presents a methodology for determining the positions of the locating and clamping elements in modular fixture design for the 3-2-1 principle. The methodology is consisted of mathematical formulas, rules of the If-Then-Else type and SolidWorks' API functions. The result is optimal positions for the elements according to the workpiece's dimensions and form, the pattern of the base plate's holes and the intended machining surfaces (but not taking the type of machining in consideration). This methodology is included into a system for automated fixture design for prismatic and cylindrical parts. The system is integrated in SolidWorks as an add-in and it uses SolidWorks' API.

This methodology allows accurate automated determination of the positions for the elements. It is

developed for the 3-2-1 locating principle, and it allows the selection of surfaces with different geometries and containing multiple features (holes, pockets, steps etc.). The input data is selection of surfaces chosen by the user, and the output data is an assembly file consisted of base plate, locating, supporting and clamping elements and the part.

References

[1] F.H. Colvin and L. L. Haas, Jigs and Fixtures: A Reference Book. New York and London: McGraw-Hill Book Company, 1938.

[2] E.K. Henriksen, Jig and Fixture Design Manual. New York, N.Y.: Industrial Press Inc. 1973.

[3] Ts. Kaldachev, P. Hadziski and G.Nikolcheva, "Study wear tool with high-speed milling", Environment. Technology. Resources. 11th International Scientific and Practical Conference, Vol.3, pp.117-121, June 15-17, 2017.

[4] Z.M. Bi and W.J. Zhang, "Flexible fixture design and automation: review, issues and future direction." International Journal of Production Research, Vol.39 (13), pp.2867–2894, 2001.

[5] F. Nixon, Managing to achieve quality. McGraw Hill, Maidenhead, 1971.

[6] Y.(K.) Rong and S. Huang, Advanced computer-aided fixture design. Boston (MA), Elsevier Academic Press, 2005.

[7] Y. Zhu and S. Zang, Modular Fixturing Systems: Theory and Application. Machinery Press, Beijing.

[8] Y. Rong and Y. Zhu, Computer-Aided Fixture Design. Marcel Dekker, Inc., New York, 1999.

[9] G. Nikolcheva and B.Tomova-Raykova, "Modular fixtures stiffness determining", Fourth International Congress "Mechanical Engineering Technologies'04" Varna, Bulgaria, vol.2, pp.102-106, September 23-25,2004

[10] W.E. Boyes, Handbook of jig and fixture design, 2nd ed.. Michigan: Society of Manufacturing Engineers, 1999.

[11] I. Boyle, Y. Rong and D.C. Brown, A review and analysis of current computer-aided fixture design approaches. Robotics and Computer-Integrated Manufacturing, Vol. 27 pp.1–12, 2011.

[12] G. Peng, G. Chen, C. Wu, H. Xin and Y. Jiang, Applying RBR and CBR to develop a VR based integrated system for machining fixture design. Expert Systems with Applications, Vol. 38, pp. 26–38, 2011.

[13] A. Nedyalkov, P. Sabchev and D. Marov, Processing equipment. Tehnika, Sofia, 1987.

[14] G. Nikolcheva, O. Mihaylov, An integrated add-in for locating parts in SolidWorks, Scientific Proceedings Of the Scientific-Technical Union Of Mechanical Engineering, Vol.3, XII International Congress "Machines. Technologies. Materials 2015", Varna, Bulgaria, pp. 15-18, 2015.

[15] Fixtureworks Workholding Technologies. "Products". Available: www.fixtureworks.net. [Accessed: Nov. 17, 2016].

[16] Erwin Halder KG. "Products". Available: www.halder.com. [Accessed: Nov. 17, 2016].

Environment. Technology. Resources. Rezekne, Latvia
Proceedings of the 12th International Scientific and Practical Conference. Volume III, 166-171

Evaluation of Heartrot Caused Phellinus Pini and Related Yield Loss in Pinus Sylvestris Stands

Ziedonis Miklašēvičs
Rezekne Academy of Technologies.
Atbrīvošanas aleja 90, Rēzekne,
LV-4600, Latvia
z.miklasevics@lvm.lv

Abstract- **Tree wounds are the starting points that may lead to heartwood discoloration and decay caused by invading micro-organisms such as heartrot caused Phellinus pini. Phellinus pini most frequently occurs on douglas–fir (Pseudotsuga menziesii), pine (Pinus sylvestris) and spruce trees (Picea abies). According to investigations made in this area, infection by Phellinus pini entries through felling scars or broken tops when Phellinus pini fruiting bodies (conks) on other trees are realising airbone spores. When spores land on a freshly wounded stem, the infection process starts.**

Internal decay is often difficult to detect because only Phellinus pini conks indicate its presence. In most cases the number of conks doesn't exceed one-two pieces on the surface of inficied Pinus sylvestris stems. When wood poles for power lines are harvested in length from 10 to 16m in wood felling areas where the average height of Pinus sylvestris trees is more than 27m, the local distribution of heartrot doesn't exceed for more than 1.5m above and below each conk, the conk is located in the middle part of the pole length, the speeed of pruning exceeds 4m/sek, the hight level of risk exists that the damaged with heart rot wood pole will be accepted as appropriate to quality requirements toward heartrot because after pruning the presence of conk would be vanished but the top and butt surfaces of pole's won't indicate heartrot. The evidence of heartrot will be checked only in the technological process of debarking before impregnation when Phellinus pini conk place indicates.

The purpose of this study is to predict the influence of Phellinus pini on Pinus sylvestris stems and to provide operational and safety recommendations concerning the risky assessment and management of infected felling areas in harvest planning processes.

Key words- Phellinus pini, Pinus sylvestris, wood poles for power lines

1. INTRODUCTION

Pinus sylvestris is the world's most widespread conifer after *Juniperus communis*. Its native range includes Albania, Andorra, Armenia, Austria, Azerbaijan, Belarus, Bosnia & Herzegovina, Bulgaria, China, Croatia, Czech Republic, Estonia, Finland, France, Georgia, Germany, Greece, Hungary, Italy, Kazakhstan, Latvia, Lithuania, Macedonia, Mongolia, Montenegro, Norway, Poland, Portugal, Romania, Russia, Serbia, Slovakia, Slovenia, Spain, Sweden, Switzerland, Turkey, Ukraine, and the United Kingdom.[3].

Phellinus pini is one of the most common stem and butt decay fungi in conifers. According to investigations [1]; [10], its distribution spreads across the north temperature zone. *Phellinus pini* most frequently occurs on Douglas – fir (*Pseudotsuga menziesii*), pine (*Pinus sylvestris*), spruce (*Picea abies*) and western larch (*Larix occidentalis*) [7].

Decay dynamics and damage will vary with host species and age [12]. According to literature data, the evaluation of *Phellinus pini* has not been studied extensively. Infection through adaxial twigs and branches usually occurs in late fall or early spring when the bark is loose. As the result it causes red ring rot. Developing of heartrot in hardwood can take over 100 years. The early stage of decay appears as a reddish-purple stain in the heartwood. During incipient decay the surrounding wood tends to be discoloured when the wood strenght parameters doesn't significantly changed [1], [10], [16]. Decay is usually confined to the heartwood of mature trees and the most extensive deccay occurs in the trunk [9]; [16]. Decay develops after *Phellinus pini* fungus causes the springwood. The fungi firstly destroying lignin and later cellulose [11]. From this stage fruiting bodies may develop at branch stubs or wound faces along the stem. The appearance of conks are usually brownish, hard, woody and hoof–shaped. According to investigation results [16] only *Phellinus pini* consistently produce the conks that indicate heartrot decay.

Print ISSN 1691-5402
Online ISSN 2256-070X
http://dx.doi.org/10.17770/etr2019vol3.4081

Fig. 1. *Pinus sylvestris* stem with heartrot indicator - *Phellinus pini* conk, where:
a - conk on the growing tree; b-conk place after harvesting; c-conk place after debarking

Pinus sylvestris separate the wound and subsequent decay by forming barrier zones of cells in the pholoem and xylem to prevent fungal spread. Therefore, the wound usually won't exceed the diameter of the tree at the time the damaging happened (Fig.2). *Phellinus pini* may overcame these barriers resulting in canker enlargement [6]. There is no approved information in literature if the amount of decay correlates with the wound size and age [18].

If the tree is unsuccessful to prevent fungal spread, decay will spread further into the heartwood. In trees with advanced decay conks are often seen along the lenght of the stem (Fig.1.)

According to investigation results [9], [14] *Phellinus pini* is one of the most descrustive heartrots in North America, especially in old growth forests [1]. According to investigation results [5] the average loss due to *Phellinus pini* decay is about 10% of the volume of interior stands, less than 5% in stands on Vancouver Islans and the Queen Charlotte Islands and about 15 % of the gross volume of Douglas fir stands western Oregon and Washington state. Unfortunately, the studies addressing *Phellinus pini* investigation is limited in Latvia [2], [3], [4], [13], [17], [19].

Therefore, the risk related to *Phellinus pini* is underestimated when harvesting is managed in old growth forests. The quality problems related to heartrot reveals in manufacturing process of wood poles for power lines in the technological stage of debarking when places of *Phellinus pini* conks reveal visible on wood poles surfaces (Fig.1).

The goal of this study was to evaluate and predict the effects of *Phellinus pini* infection on structural stability of wood poles for power lines. The following objectives were set to achieve the study goal:to verify the presence of *Phellinus pini* by laboratory analysing of wood samples from conks places;

- to correlate the presence of visible indicators-conks of infection by *Phellinus pini* to wood poles structural condition as extend of decay, observed average shell thickness, number of annual rings in sound shell zone, in barrier and hardwood zone, required shell thickness, etc;
- to collect and analyse all measurement results;
- to prepare the technological recomendations concerning risk assessment of felling areas infected by *Phellinus pini* in forestry operations

III. MATERIALS AND METHODS

A field study was carried out at the period May - December of 2017, in Vidzeme region of Latvia and in energy company JSC "Sadales tīkli". Wood poles which were harvested in Vacciniosa and Myrtillosa forest types where the age of pine stands according to the forest inventory description was more than 105 years old were selected in the investigation. The quality control of each of selected 4863 pcs. wood poles was done in each stage of technological process in JSC "Sadales tīkli". Traceability of wood poles was ensured. In order to gather information about impact of *Phellinus pini* on wood pole's strenght parameters, the following approach, methods and data was collected:

- data characterized the wood felling area: coordinates of wood felling area; forest type;
- growing stock; growth conditions; site quality classes; species composition index and the age of species;
- data characterized the wood pole's visual quality parameters: lengh of wood pole; wood pole top and butt diameter; wood pole diameter at a conk positions; a conk possition measured from the wood pole butt and a conk location place dimensions on infected tree surface;
- data characterized wood pole's quality parameters at the position on the wood pole where *Phellinus pini* conk or blid conk was visible: number of annual rings in sound shell zone; number of annual rings in barrier and hardwood zone damaged by *Phellinus pini*; total number of annual rings; mean thickness of annual rings in sound shell zone; mean thickness of annual rings in barrier zone; mean distance of heart rot measured from conk position toward to wood pole butt; mean distance of heartrot measured from conk position toward to the wood pole top; mean distance of internal wood staining area (indicative of incipient decay) measured from conk position toward to the wood pole butt; mean distance of internal wood staining area (indicative of incipient decay) measured from conk position toward to the wood pole top;

Required Shell Thickness; observed Average Shell Thickness and calculation of mean AST/RST ratious.

IV. RESULTS AND DISCUSSION

When wood poles for power lines are harvested in length from 10 to 16m in infected by *Phellinus pini* wood felling areas where the average height of pine trees is more than 27m, the conk is located in the middle part of the pole length, the speed of pruning exceeds 4m/sek, the hight level of risk exists that the damaged with heartrot wood pole will be accepted as appropriate to quality requirements toward heartrot. After pruning the presence of conk would be vanished but the top and butt surfaces of pole's won't indicates heartrot. The evidence of heartrot will be checked only in the technological process of debarking before impregnation when Phellinus pini conk place indicates (Fig. 1)

For the long period, in the process of quality evaluation of wood poles before impregnation, the conk places were evaluated as the unspound knots. Only when the heartrot as a cause of breaking of wood poles was checked, the problem started to be explored.

For investigation of the reason of heartrot, the sample of damaged wood was taken and analysed (Fig.2) in the laboratory of molecural genetics LSFRI Silava.

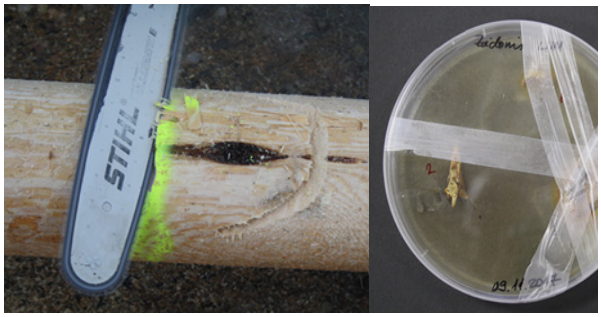

Fig. 2. The example of examined wood taken for molecural genetics analyse

The results of the laboratory analyses revealead the reason of heartrot in infected wood poles - *Phellinus pini.*

According to the investigation objective, the dimensions of *Phellinus pini* conk's location places were measured on infected wood poles surfaces (Fig.3). The measurement results are given in Table 1.

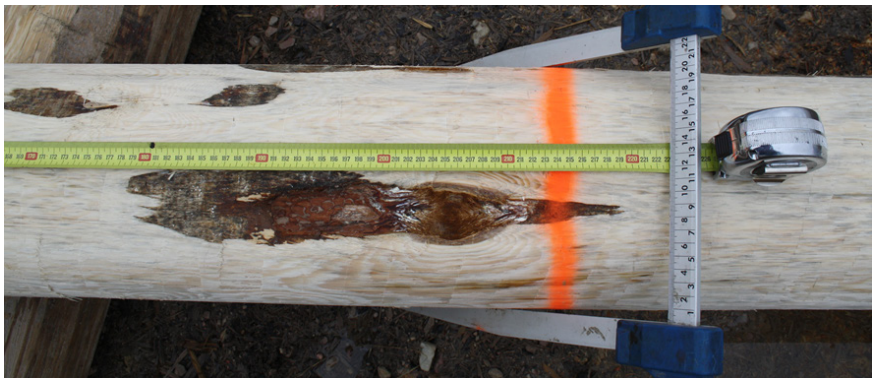

Fig. 3. The measurement of conk location place dimensions on infected wood pole surface

All wood poles on which surfaces were indicated *Phellinus pini* conk's were cross or/and longitudinally sectioned at the position of the visible conk's or blind conk's (Fig.4; Fig.5; Fig.6). In some cases wood poles were cross sectioned above and below the conk's in order to evaluate AST at these positiions. The investigation results is given in Table1.

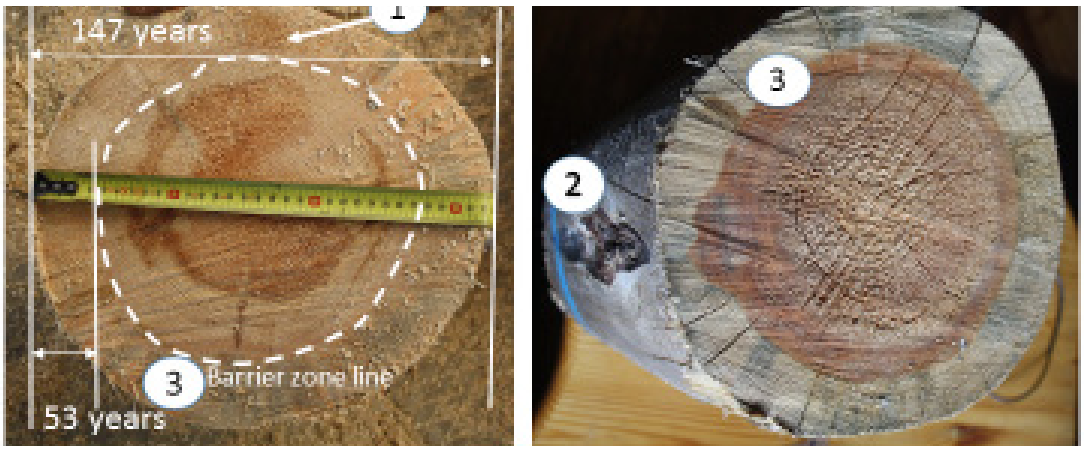

Fig. 4. Cross sections of infected Pine wood poles upper Phellinus pini conks possition where:
1- entry point of fungus at old branch stub, 2- conk possition, 3- barrier zone line which indicates the outer limit that heart rot would have extended in this tree [15], [18]

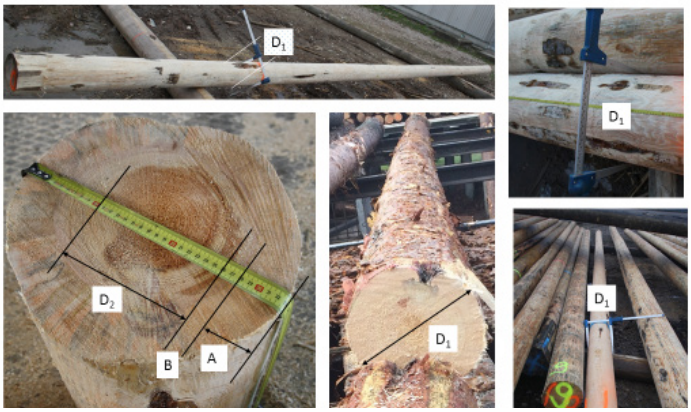

Fig. 5. The analyses example of cross section of infected pine wood pole taken at a conk position, where: **D_1** - wood pole diameter at conk position, mm; **D_2** - diameter of hardwood damaged by Phellinus pini, mm; **B**- number / thickness of annual rings in barrier zone, mm; **A**- number / thickness) of annual rings in sound shell zone, mm

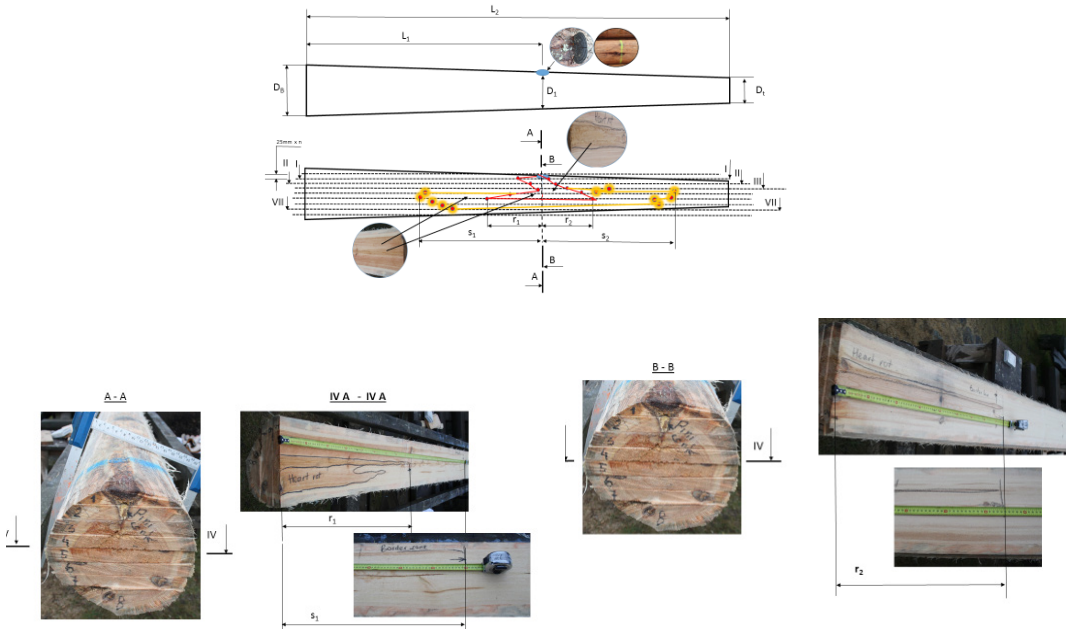

Fig. 6. The analyses example of longitudinal section of infected pine wood pole taken at conk position, where: L_1 - distance of conk possition measured from butt, cm; L_2 - lenght of wood pole, cm; D_1- wood pole diameter at conk positions, mm; r_1- distance of heart rot measured from conk position toward to wood pole butt, mm; r_2- distance of heart rot measured from conk position toward to wood pole top, mm; s_1- distance of wood staining (indicative of incipient decay) measured from conk position toward to wood pole butt, mm; s_2- distance of wood staining (indicative of incipient decay) measured from conk position toward to wood pole top, mm

TABLE 1. THE MEASUREMENT RESULTS CHARACTERIZED DAMAGES OF PINE WOOD CAUSED BY PHELLINUS PINI

Mean conk location place dimensions on infected tree surface, cm^2 (n=128)	24.8 (range 16.3 -28.7)
Mean /Median distance of conk possition measured from wood pole butt, cm (n=83)	4598/4250
Median lenght, cm (73 wood poles)	10000
Mean / Median wood pole diameter at conk positions, mm (n=83)	280/268
Mean /Median wood pole top diameter, mm (73 wood poles)	205/204
Mean /Median wood pole butt diameter, mm (73 wood poles)	310/315
Mean diameter /Median of hardwood damaged by P.pini, mm (n=128)	101/95
Mean thickness of annual rings in sound shell zone, mm (n=128)	0.7
Mean thickness of annual rings in barrier zone, mm (n=128)	1.4
Mean age of trees, years (n=128)	111 (range 105-147)

Mean AST*, mm (n=128) ***AST** - observed Average Shell Thickness. Calculated as the average of actual wood pole sound shell width measured at 3 points around the pole at a given height positiion. This positrion corresponds to the position of the defect indicator (i.e.,conk) above pole height*	35.4 (±SD 5.22) (±SE 0.46)
Mean RST*, mm (n=128) ***RST** - Required Shell thickness. Calculated as a wood pole radius at a conk position (D_1 /2) x 0.30 (Fig.5.)*	30.2 (±SD 9.44) (±SE 0.83)
Overall Mean AST/RST * ratio /(n=128) ***An AST/RST** ratio of 1.00 or grater means that the actulal average stem shell thickness is equal to the required minimum of shell thickness and soundwoood shell ensures columnar strenght and structural stability. When ratio AST/RST<1.00, wood pole have relatively thin stem shell walls and therefore have insufficient sound stemwood shell to maintain columnar strenght and structural stability.*	0.81 (±SD 0.22) (±SE 0.019)
Mean AST/RST ratio of wood poles with blind conks (n=4, 4 wood poles)	1.86
Mean AST/RST ratio of wood poles with multiple conks (n=14, 4 wood poles)	0.72
Mean distance of heart rot measured from conk position toward to wood pole butt, mm (59 wood poles)	875 (±SD 185.43) (±SE 24.14)
Mean distance of heart rot measured from conk position toward to wood pole top, mm (65 wood poles)	850 (±SD 176.31) (±SE 21.87)
Mean distance of internal wood staining area (indicative of incipient decay) measured from conk position toward to wood pole butt, mm (43 wood poles)	2370
Mean distance of internal wood staining area (indicative of incipient decay) measured from conk position toward to wood pole top, mm (65 wood poles)	2240

5. CONCLUSIONS

The results of the study indicated the following:

- About 1.5 % of inspected 4863 pcs wood poles harvested in felling areas in Vacciniosa and Myrtillosa forest types where the mean age of pine trees were 111 years old were infected by *Phellinus pini.*
- Wood poles for power lines are building structure which characterize strenght parameters. Typical minimum characteristic values for *Pinus sylvestris* wood poles by standard EN 14229 are: bending strenght f_m=48.97N/mm^2; modulus of elasticity E=8000 N/mm^2 [17], [21].
  Wood poles strenght parametrs mainly dependent of wood density. When wood pole's structural stability is being impacted by heartrot caused by *Phellinus pini* when Overall Mean AST/RST <1, the expluatation risky will be actual because of low parametrs toward bending limit and modulus of elasticity.
- There are advisable to evaluate the pine trees external quality before harvesting of wood poles for power lines inVidzeme region of Latvia in felling areas in *Vacciniosa* and *Myrtillosa* forest types where the age of pine stands is more than 100 years old (Fig.7). In cases when the *Phellinus pini* are being indicated, wood pole's should be harvested using motor saws.
- To eliminate expluatation risky of wood poles for power lines, new information related to infected by *Phellinus pini* felling areas is required for harvesting planning.

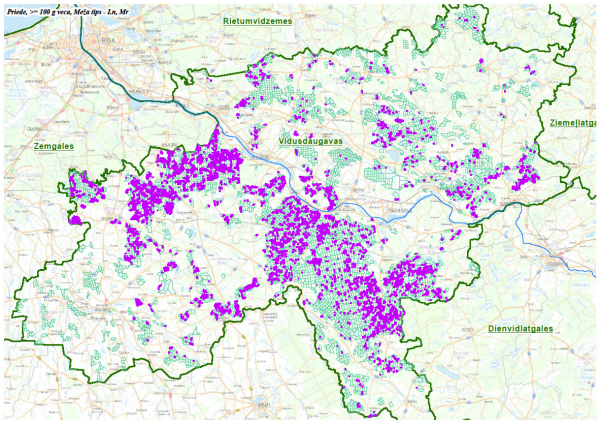

Fig. 7. The felling areas in *Vacciniosa* and Myrtillosa forest types in Vidzeme region of Latvia
where the age of pine trees is more than 100 years old

REFERENCES

[1]. Conference paper-Allen E., Morrison D., Wallis G., 1996. Common Tree Diseases of British Columbia 178p. [Online]. Available: https://www.pfc.forestry.ca/diseases/CTD/index_e.html.

[2]. Journal: Arhipova N., Gaitnieks T., Donis J., Stenlid J., Vasaitis R., 2011. Butt rot incidence, causal fungi and related yield loss in Picea abies stands of Latvia. Canadian Journal of Forest Research, 41(12), pp.2337-2345

[3]. Journal: Baumanis I., 1993. A complex research project: factors in Latvia affecting the health of pine (planting stock and young plantations), and recommended protective measures. Proceedings of the Latvian Academy of Sciences, Section B, 7(552), pp. 79-80.

[4]. Book: Baumanis I., Jansons, Ā., Neimane U., 2014. Selection, genetics and seeding in Latvia. In: Daugavpils, 324 p.

[5]. Journal: Bier, J.E., R.E. Foster and P.J. Salisbury. 1946. Studies in forest pathology. IV. Decay of Sitka spruce on the Queen Charlotte

Islands. Can. Dept. Agric. Publ. 783. Tech. Bull. #56. 35 pp.

[6]. Journal: Blanchette R.A., 1982. Decay and canker formation by Phellinus pini in white and balsam fir. Can. J. For. Res. 12: pp. 538-544.

[7]. Book: Boyce, J.S. 1961. Forest Pathology. 3rd. Ed., McGraw-Hill, Toronto.

[8]. Journal: Earle C.J., 2011. *Pinus sylvestris* (Scots pine) description. In: The Gymnosperm Databaswe. [WWWdokument]. [Online]. Available: http://www.conifers.org/pi/Pinus_sylvestris.php [archived in July, 2014]

[9]. Journal: Etheridge D.E.,1972. True heartrots of British Columbia. Canadian Forest Service, Pacific Forest Research Center, Victoria, BC.Forest Pest Leaflet No. 55. 14 p.

[10]. Journal: Hunt R.S., Etheridge D.E., 1995. True heart-rots of the Pacific Region. Forest Pest Leaflet No.55, Pacific Forestry Centre. 8 p.

[11]. Journal: Kimmey J.W., 1964. Heart rots of Western Hemlock. Forest Pest Leaflet 90, U.S. Dep't of Agriculture. Accessed 5 Mar. 2007. [Online]. Available: https://www.fs.fed.us/r10/spf/fhp/leaflets/Hearotweshem.htm

[12]. Journal: Larsen M.J., Lombard F.F., 1979. A new variety of Phellinus pini associated with cankers and decay in white firs in southwestern Oregon and northern California. Can. J. For. Res. 9: pp.31-38.

[13]. Journal:Lībiete Z., Jansons J., Zālītis T., 2009. Age structure and productivity of conifer stands in Latvia. Mežzinātne / Forest Science 19(52): pp.28-48.

[14]. Book: Scharpf R.F., 1993. Diseases of Pacific Coast Conifers. USDA For. Service, Pacific Southwest Research Station, Albany, CA. USDA For. Serv. Handbook 521, June 1993. 199 p.

[15]. Book: Shigo A.L., 1991. Modern Arboriculture. Shigo and Trees, Associates, Durham, NH. 424 p.

[16]. Conference paper - Zeglen S., 1997. Tree wounding and partial-cut harvesting: A literature review for British Columbia. BC Min. Forests Pest Management Report No. 14, Vancouver Forest Region, Nanaimo, BC. 40 p.

[17]. The technological investigations and ecological evaluation of manufacturing of wood poles for power lines.[Online]. Available: https:// *llufb.llu.lv/dissertation-summary/engineering/Z_Miklasevics_l-a.pdf*

[18]. Evaluation of the effects of heart rot fungi on live tree structural stability. [Online]. Available: *https://www.for.gov.bc.ca/.../WTReport-Effects-of-HeartRotFungi-June.* [Accessed 2007].

[19]. Assessment of the development of the forest industry https://www.zm.gov.lv/public/ck/files/ZM/mezhi/.../1_pielikums.pdf. [Accessed 2011]

[20].. Opinin on the draft guidelines on forest and related development guidelines for 2015-2020. Available: VSS-489 *ldf.lv/sites/default/files/faili/Par_mums/LDF_vestules/80_ldf_msnp_vss489.doc*

[21]. EN 14229. Structural timber-Wood poles for overhead lines

Environment. Technology. Resources. Rezekne, Latvia
Proceedings of the 12th International Scientific and Practical Conference. Volume III, 172-176

Ferroelectric Nanocomposites With Governed Interface on Base of Magnetic Porous Glasses

A.A. Naberezhnov
Ioffe Institute,
26 Polytekhnicheskaya str., St. Petersburg, 194021, Russian Federation

O.A. Alekseeva
Peter the Great St. Petersburg Polytechnic University 29
Politechnicheskaya str., St. Petersburg, 195251, Russian Federation

I.V. Golosovsky
Petersburg Nuclear Physics Institute named by B.P. Konstantinov of NRC
«Kurchatov Institute»
188300, Russia, Leningradskaya Oblast, Gatchina, 1, mkr. Orlova roshcha

A.A. Sysoeva
Ioffe Institute,
26 Polytekhnicheskaya str., St. Petersburg, 194021, Russian Federation

P.Yu. Vanina
Peter the Great St. Petersburg Polytechnic University
29 Politechnicheskaya str., St. Petersburg, 195251, Russian Federation

B. Nacke
Leibniz University of Hannover, ETP,
Wilhelm-Busch-Street, 30167 Hannover, Germany

A. Nikanorov
Leibniz University of Hannover, ETP,
Wilhelm-Busch-Street, 30167 Hannover, Germany

***Abstract* — Two-phase (nonporous) magnetic alkali borosilicate glasses have been produced by induction melting. Their macroscopic properties and crystal structure have been studied and it is shown that in the silica skeleton there are the agglomerates of Fe_3O_4. These agglomerates are formed by monodomain nanoparticles of magnetite and demonstrate the superparamagnetic properties. After special thermal treatment (liquation process) and chemical etching the nanoporous matrices with random dendrite pore structure and magnetic properties have been produced. The channels (porous space) were filled by ferroelectric materials KH_2PO_4(KDP), KH_2PO_4+$(NH_4)H_2PO_4$ (KDP-ADP or KADP), and $NaNO_2$ and the effect of applied magnetic fields on phase transitions in these nanocomposite have been studied. It has also been established that a restricted geometry changed essentially the phase diagram of KADP.**

Keywords – magnetic glasses, nanocomposite materials, restricted geometry, interface, artificial multiferroics

I. Introduction

Mesoporous silica materials, especially alkali borosilicate glasses with magnetic properties, attract steadfast interest because of their unique physicochemical properties such as a low thermal expansion coefficient, perfect chemical and mechanical stability, a large and controllable porosity, a high surface area, tunable pore sizes and volumes, interesting optical and magnetodielectric characteristics [1–14]. The skeleton of these glasses is organized by rigid groups SiO2 and has an amorphous crystal structure. The pores form 3D dendrite random interconnected network, which is very suitable for deposition and incorporation of different guest molecules (substances) to produce multifunctional materials with unique capabilities and properties. The average pore diameter one can controllable change in a wide diapason from units to hundreds nanometers, the porous space achieves 40% from the total volume of glass sample. At present time these nanoporous matrices with magnetic properties use in medicine and in biology [2, 8-13], in magneto-optic devices [3,5,7], as different kinds of sensors [13] et cetera . It is important to note that in all the mentioned above cases the matrices themselves play a passive role providing conditions of a restricted geometry, and the magnetic nanoparticles synthesize into the pore space. However, one can realize another approach: to create the "active" porous media, which participates in modification of embedded material properties. Here the term "active" means that the magnetic properties become intrinsic feature of matrix itself. It is necessary to underline that these matrices can be used as a model object for creation of novel multifunctional materials, for example multiferroics with spatially separated coexisting magnetic and ferroelectric orderings and with a large interface between these subsystems. By acting on the interface (using temperature, external magnetic or electric fields, pressure and so on), we are able to govern the phase state of embedded substances, for example, due to elastic stresses. It should be note that this technology permits to produce artificial multiferroics possessing ferroelectric and magnetic properties at room temperature that is very attractive for application. The principle purpose of this contribution has been to study the properties of porous magnetic glasses and some nanocomposite materials (NCM) on base these matrices containing embedded ferroelectrics..

II. Samples and methods

For the first time the production of alkali borosilicate glasses with magnetic atoms into the matrix skeleton was realized in the paper [15] by melting in a platinum crucible with mechanical stirring. Their macroscopic properties and crystal structure have been studied [6,16]

Print ISSN 1691-5402
Online ISSN 2256-070X
http://dx.doi.org/10.17770/etr2019vol3.4048

and we have proved the existence of magnetic properties of these glasses. Later we have developed a novel method of magnetic glass production – induction melting [17,18]. Magnetic properties of produced magnetic glasses were studied by SQUID. Crystal structure of produced porous magnetic glasses was studied by X-ray diffractometer (Supernova, Agilent Technologies) using $Cu_{K\alpha}$ line. The average pore diameter, which was determined by adsorption poroscopy, was about 54(5) nm (macroporous glasses – MAP). KDP-ADP (KADP) solid solutions were embedded into the pores from an aqueous solution with triple recrystallization. The pore filling achieved 35 % for the 5 % ADP sample and 38 % for the 15 % ADP sample. The dielectric response was studied using a capacitance bridge at 1 kHz in the International Laboratory of High Magnetic Fields and Low Temperatures (ILHMFLT, Wroclaw, Poland). The temperature dependences of the samples capacitances were measured from 40 – 200 K on cooling and heating at different applied magnetic fields. Temperatures of phase transitions were determined from a position of maximum in the capacity vs. temperature dependences. Temperature stability was better 0.1 K at measurements in ILHMFLT. The applied magnetic fields were varied from 0 to 10 T. The filling of MAP glasses by $NaNO_2$ was carried out from melt under vacuum. In a case of NCM MAP+$NaNO_2$ we have studied the temperature evolution of crystal structure of sodium nitrite on heating and cooling at the temperature interval RT- 460 K, i. e. below and above the ferroelectric phase transition (437 K in the bulk material), on the neutron diffractometer E9 (Helmholtz Zentrum Berlin, reactor BER II). The applied magnetic field was change from 0 till 2 T only due to some experimental restriction. Temperature stability was better 2 K.

III. Results and discussion

Magnetic macroporous glasses

The X-ray diffraction pattern of the empty MAP glass and the model spectrum for Fe_3O_4 are presented in Fig.1.

One can see that there are very good agreement between both parts, the additional peaks on the top part correspond to sample environment. The elastic peaks are essentially broaden due to size effect and using this information we have determined the characteristic size of Fe_3O_4 nanoparticles – 18 (3) nm. It means that in the matrix skeleton there are monodomain magnetite nanoparticles [19]. AFM and MSM data have shown that these nanoparticles have been self-organized in large agglomerates [20]. The additional evidence of presence of magnetite in the matrix have been obtained at studies of temperature evolution of magnetic properties of glasses at two regimes: Field Cooling (FC) at H= 100 Oe and Zero Field Heating after Field Cooling (ZFHaFC) – Fig 2. The anomaly at ~ 120 K corresponds to so-called Verwey transition existing in Fe_3O_4 only at this temperature. The difference between FC and ZFHaFC regimes testifies that Fe_3O_4 nanoparticles form a superparamagnetic system with very high irreversibility temperature (near 300 K).

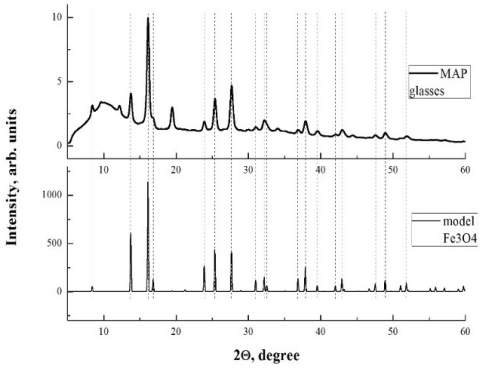

Fig. 1. Diffraction pattern for MAP glasses (top part) and model pattern for magnetite (bottom part) at RT. The vertical lines indicate the position of elastic peaks characterizing magnetite

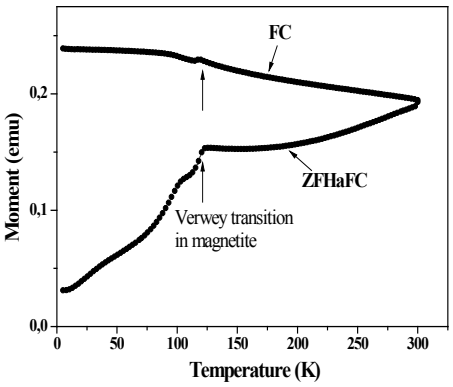

Fig. 2 Temperature dependence of magnetization of MAP glasses at FC and ZFHaFC regimes. Arrows point out the positions of Verwey transition in the bulk Fe_3O_4

Ferroelectric nanocomposites on base of MAP glasses

Initially we have characterized our samples with embedded KADP nanoparticles by X-ray diffraction. Since the embedded materials are the solid solutions of KDP-ADP with a small admixture of ADP, the structures of these nanocomposites have to be close to the structure of KDP and according X-rays diffraction correspond to the spatial group **I-42d**, as well as the bulk KDP at RT, with the unit cell parameters $a = b = 7.459$ and $c = 6.994$ Å. From the broadening of elastic peaks we have estimated the average particle diameters: they are equal to 49 (2) nm for the sample with 5 % of ADP, 46 (2) nm for the sample with 15 % of ADP and 53(5) for NCM with a pure KDP. So the nanoparticle sizes coincide practically with average pore diameter in the MAP glasses. Further we have measured the temperature dependences of sample capacities on heating and cooling and have determined the temperatures (T_C) of ferroelectric phase transition. The obtained T_C values are presented in Table 1. As a reference sample we have used the conventional (nonmagnetic) alkali borosilicate glasses with average pore diameter 46(3) nm. The size of nanoparticles in this case was practically the same.

TABLE I

T_C FOR NCM KADP+MAP GLASS ON HEATING AND COOLING AS A FUNCTION OF APPLIED MAGNETIC FIELDLS

ADP concentration, %				0	5	15
Bulk samples [21, 22]			T_C, K	~ 122	104.2	-
Present work KDP-ADP nanoparticles	Nonmagnetic glass		$T_{C(cooling)}$, K	120.2±0.1	116.7±0.1	112.7±0.1
	$T_{C(heating)}$, K			126.2±0.1	119.8±0.1	114.8±0.1
	$\Delta T_C = T_{C(cooling)} - T_{C(heating)}$, K			6	3.1	2.1
	Magnetic glass	B = 0 T	$T_{C(cooling)}$, K	120.4±0.1	117.3±0.1	113.8±0.1
			$T_{C(heating)}$, K	126.2±0.1	118.9±0.1	116.2±0.1
			$\Delta T_C = T_{C(cooling)} - T_{C(heating)}$, K	5.8	1.6	2.4
		B = 10 T	$T_{C(cooling)}$, K	126.7±0.1	117.4±0.1	114.0±0.1
			$T_{C(heating)}$, K	130.9±0.1	120.4±0.1	117.5±0.1
			$\Delta T_C = T_{C(cooling)} - T_{C(heating)}$, K	4.2	3.0	3.5

It is known that a small admixture of ADP leads to a drastic decreasing of the ferroelectric phase transition temperature T_C [21] (Fig.3), but as it is easy to see in a restricted geometry without an external magnetic field the T_C increases essentially at growth of ADP concentration in comparison with the bulk KADP solutions. Application of magnetic field increases (Table 1) T_C both during heating and cooling. It is necessary to note that the effect of ADP admixture on T_C in confinement becomes less pronounced than in the bulk KADP.

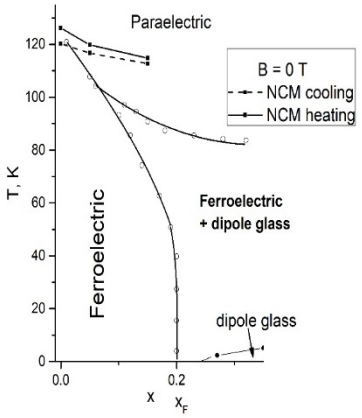

Fig. 3 Dependences of T_C in NCM KADP+MAP glasses on heating and cooling at B = 0 T

The observed shifts of T_C and the appearance of thermal hysteresis can be explained by the multidirectional influences of thermal compression (or expansion) plus positive magnetostriction of MAP glasses [23] on cooling and heating depending on magnetic field and temperature variation of thermal expansion coefficients for KADP or KDP [24]. On cooling the action of a part of these coefficients is compensated by positive magnetostriction. On heating, they act in one direction and in this case T_C becomes slightly higher. As a result, we have observed the temperature hysteresis ΔT between T_C on cooling and on heating. This fact points out that the appearance of additional tensile strains due to application of magnetic field effects really on T_C. The role of the form and tensile strains has been considered in the theoretical paper [25] for NCM on base of two types of porous glasses for $BaTiO_3$ and $PbTiO_3$ nanoparticles and it has been shown that the shift of T_C depends on an asymmetry of nanoparticle form and type of matrix.

The next sample was the magnetic MAP glasses with sodium nitrite embedded into the porous space. In this case we have studied the temperature evolution of crystal structure of this NCM by neutron elastic scattering

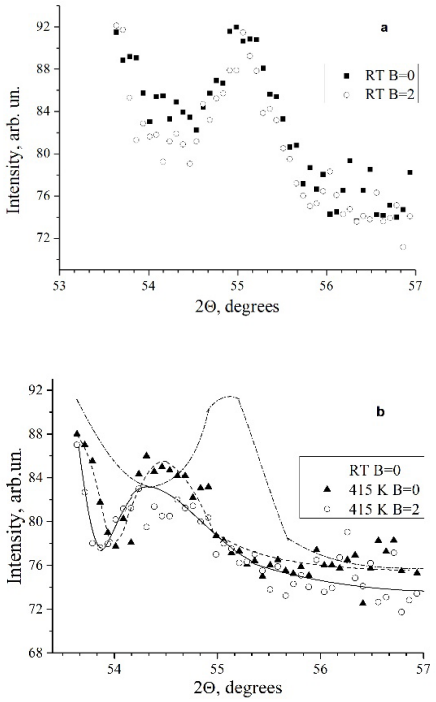

Fig. 4. Intensities of (022) Bragg peak in NCM MAP+NaNO2: (a) - at RT and at B = 0 and B=2 T, (b) – at 415 K and B = 0 and B = 2 T. The dash-dotted line in Fig.4b corresponds to the intensity of (022) peak at RT and B = 0 T.

Sodium nitrite belongs to the order-disorder ferroelectrics and undergoes the first order phase transition at $TC \approx 437$ K. At room temperature (RT) $NaNO_2$ has a body centered orthorhombic lattice (a = 3.57 Å, b = 5.578 Å, c = 5.39 Å) with two molecules per unit cell, and its space group is ***Im2m.*** In the low-temperature ferroelectric phase the spontaneous polarization points along the b-axis and appears due to a partial alignment of NO_2^-

groups along this axis, accompanied by the displacement of sodium ions. At high temperature (above T_C) a mirror plane perpendicular to the b-axis appears and the space group changes to ***Immm.*** The physical realization of the ferroelectric order parameter η in $NaNO_2$ is the difference between the occupations f_1 and f_2 of two crystallography equivalent positions of NO_2^- groups, i.e. $\eta=f_1-f_2$. As it has been shown in the paper [26], the intensity of diffraction peaks is proportional to

$$|F|^2 = F^2_{re} + \eta^2(T) \times F^2_{im} \qquad (1)$$

where F_{re} and F_{im} are the real and imaginary parts of the structure factor F, and η is the order parameter for the ferroelectric phase. In the case of NaNO2 there are two principal distinguishing groups of Bragg peaks. For example, for the (022) peak F_{re} is equal to 0.46 and F_{im} - 2.04 (for neutron scattering [27]). It means that in the equation (1) the value F^2_{re} becomes negligible in comparison with F^2_{im} and the total intensity of the (022) peak is practically proportional η^2.

The size of $NaNO_2$ nanoparticles in this NCM has been about 50(4) nm. In Figure 4a and 4b the temperature and field evolutions of (022) Bragg peak for NaNO2+MAP composite are presented. One can see that the application of magnetic field 2T suppresses the total intensity (the loss is about 30 %) in comparison with the measurement without field. At 430 K and at B = 2 T we have not observed this peak in diffraction pattern. Without magnetic field the phase transition takes place near 435 K [28]. This result means that the application magnetic field shifts the T_C to the lower temperature.

IV. Conclusion

The studies of crystal structure and magnetic properties of magnetic porous glasses produced by induction melting confirm the presence of magnetic agglomerates consisting of magnetite nanoparticles in the matrix skeleton. On base of magnetic MAP glasses the NCM with ferroelectrics KADP and $NaNO_2$ nanoparticles embedded into the pores have been prepared. It is shown that the restriction geometry leads to an essential increase of ferroelectric phase transition in nanostructured KADP. The measurements of dielectric response of nanocomposites KADP+MAP and temperature evolution of crystal structure of NCM $NaNO_2$+MAP in applied magnetic fields prove the possibility to govern by ferroelectric phase transition using magnetic field. It is shown that the interface "matrix-embedded material" plays the important role in modification of microscopic properties of nanocomposites. It open the way to the creation of multifunctional nanostructured materials with governed interface on base of porous magnetic glasses.

V. Acknowledgments

In SPbPU the study was performed in the framework of grant 3.1150.2017/4.6 of RF Ministry of Education and Science. This study was partly supported by the RFBR (grant 19-02-00760).

References

[1] A. Mekki, G. D. Khattak, D. Holland, M. Chinkhota, and L. E. Wenger, "Structure and magnetic properties of vanadiumsodium silicate glasses," *Journal of Non-Crystalline Solids*, vol. 318, no. 1-2, pp. 193–201, 2003.

[2] J. Zhou, W. Wu, D. Caruntu, M. H. Yu, A. Martin, J. F. Chen, C. J. O'Connor and W. L. Zhou, "Synthesis of porous magnetic hollow silica nanospheres for nanomedicine application," *Journal of Physical Chemistry C*, vol. 111, no. 47, pp. 17473–17477, 2007.

[3] S. Tomas, D. Sakthikumar, Y. Yoshida and M. R. Anantharaman, "Spectroscopic and photoluminescence studies on optically transparent magnetic nanocomposites based on sol-gel glass: Fe_3O_4," *Journal of Nanoparticle Research*, vol. 10, no. 1, pp. 203–206, 2008.

[4] C.-C. Chang, L. Zhao and M.-K. Wu, "Magnetodielectric study in SiO_2-coated Fe_3O_4 nanoparticle compacts," *Journal of Applied Physics*, vol. 108, no. 9, Article ID 094105, 2010.

[5] O. Yeshchenko, I. Dmitruk, A. Alexeenko, A. Dmytruk and V. Tinkov, "Optical properties of sol-gel fabricated Co/SiO_2 nanocomposites," *Physica E: Low-Dimensional Systems and Nanostructures*, vol. 41, no. 1, pp. 60–65, 2008.

[6] T. V. Antropova, I. N. Anfimova, I. V. Golosovsky, Yu. A. Kibalin, A. A. Naberezhnov, N. I. Porechnaya, O. A. Pshenko and A. V. Filimonov "Structure of Magnetic Nanoclusters in Ferriferous Alkali Borosilicate Glasses," *Physics of the Solid State*, vol. 54, no. 10, pp. 2110–2115, 2012.

[7] T. Senoy, D. Sakthikumar, Y. Yoshida and M.R. Anantharaman, "Spectroscopic and Photoluminescence studies on optically transparent magnetic nanocomposites based on sol–gel glass: Fe_3O_4 ," *Journal of Nanoparticle Research*, vol. 10, no.1, pp. 203-206, 2008.

[8] S. Huang, C. Li, Z. Cheng, Y. Fan, P. Yang, C. Zhang, K. Yang and J. Lin, "Magnetic Fe_3O_4 - mesoporous silica composites for drug delivery and bioadsorption," *Journal of Colloid and Interface Science*, vol. 376, no. 1, pp. 312-321, 2012.

[9] S. Zhu, Z. Zhou and D. Zhang, "Control of Drug Release through the In Situ Assembly of Stimuli- Responsive Ordered Mesoporous Silica with Magnetic Particles," *Journal ChemPhysChem.*, vol. 8, pp. 2478 – 2483, 2007.

[10] R.K. Singh, A. Srinivasan and G.P. Kothiyal, "Evaluation of $CaO–SiO_2–P_2O_5–Na_2O–Fe_2O_3$ bioglass-ceramics for hyperthermia application," *Journal of Material Science: Materials in Medicine*, vol. 20**,** pp. S147-S151, 2009.

[11] X. Li, F. Qu, W. Li, H. Lin and Y. Jin, "Synthesis of hierarchically porous bioactive glasses using natural plants as template for bone tissue regeneration," *Journal of Sol-Gel Science and Technology*, vol. 63, no. 3, pp. 416–424, 2012.

[12] Y.-H. Won, H.S. Jang, S.M. Kim, E. Stach, M. Ganesana, S. Andreescu and L.A. Stanciuet, "Biomagnetic glasses: preparation, characterization, and biosensor applications," *Langmuir*, vol. 26, no. 6, pp. 4320–4326, 2010.

[13] C.A. Paula, P.C.A. Jerónimo, N. Alberto, A.N. Araújo, M. Conceição, B.S.M. Montenegro, "Optical sensors and biosensors based on sol–gel films," *Talanta*, vol. 72, no. 1, pp. 13-27, 2007.

[14] C.-C. Chang, L. Zhao and M.-K. Wu, "Magnetodielectric study in SiO_2-coated Fe_3O_4 nanoparticle compacts," *Journal of Applied Physics*, vol. 108, article #094105, 5 pp, 2010.

[15] S.V. Stolyar, I.N. Anfimova, I.A. Drozdova and T.V. Antropova, "The new two-phase ferriferous alkali borosilicate glasses for creation of the nanoporous materials with magnetic properties," *Nanosist., Nanomater., Nanotechnol.*, vol. 9, no. 2, pp. 433-440, 2011.

[16] A. Naberezhnov, N. Porechnaya, V. Nizhankovskii, A. Filimonov and B. Nacke, "Morphology and magnetic properties of ferriferous two-phase sodium borosilicate glasses," *The Scientifc World Journal*, vol. 2014, Article ID 320451, 7 pp, 2014.

[17] A.A. Naberezhnov, E.Yu. Koroleva, A.V. Filimonov, A.I. Rudskoy, B. Nacke, V. Kichigin and V. Nizhankovskii, "Production of magnetic alkali-borosilicate glasses by induction melting," *Metal Science and Heat Treatment*, vol. 56, no. 11 – 12, pp. 681-684, 2015.

[18] A.V. Filimonov, A.I. Rudskoy , A.A. Naberezhnov, S.B. Vakhrushev, A.E. Fotiadi , E.Yu. Koroleva, I.V. Golosovsky, Yu.A. Kumzerov, B. Nacke, "Nanocomposite materials on the base of dielectric porous matrices", *St.-Petersburg State Polytechnical University Journal. Physics and Mathematics,* vol. 4 - 2 (182), pp. 9 -29, 2013

[19] W.F. Brown, "Magnetic interactions of superparamagnetic particles," *Journal of Applied Physics*, vol. 38, no. 3, pp. 1017–1018, 1967.

[20] N. Andreeva, M. Tomkovich, A. Naberezhnov, B. Nacke, A.

Filimonov, O. Alekseeva, P. Vanina and V. Nizhankovskii, "SEM and AFM Studies of Two-Phase Magnetic Alkali Borosilicate Glasses," *The Scientific World Journal*, vol. 2017, Article ID 9078152, 9 pp, 2017.

[21] S.A. Gridnev, L.N. Korotkov, S.P. Rogova, L.A. Shuvalov and R.M. Fedosyuk, "Dielectric properties and x-T phase diagram of $K_{1-x}(NH_4)_xH_2PO_4$ crystals," *Ferroelectrcis Letters*, vol. 13, no. 3, pp. 67-72, 1991.

[22] L.N. Korotkov and L.A. Shuvalov, "Transitions to the relaxor and dipole glass states in mixed crystals of the potassium dihydrogen phosphate family," *Crystallography reports*, vol. 49, no. 5, pp. 832-842, 2004.

[23] E.Yu. Koroleva, A.A. Naberezhnov, V.I. Nizhankovskii and N.I. Porechnaya, "Magnetostriction and Magnetization of ferriferous glasses," *St. Petersburg State Polytechnical University Journal. Physics and Mathematics*, vol. 170, no. 2, pp. 144 - 148, 2013. [in Russian]

[24] M.P. Shaskolskaya, "Acoustic crystals," *Moscow. Nauka*, 633 pp, 1982. [in Russian]

[25] A.I. Nikitchenko, A.V. Azovtsev and N.A. Pertsev, "Phase diagrams of ferroelectric nanocrystals strained by an elastic matrix," *Journal of Physics: Condensed Matter*, vol. 30, 015701 (9 pp.), 2018.

[26] A. da Costa Lamas, S.-L. Chang, S. Caticha-Ellis. "On the Use of Powder Difractometry in the Study of Phase Transitions", *Physica Status Solidi (a),* vol. 68, pp. 173-178, 1981

[27] A. Naberezhnov, A. Fokin, Yu. Kumzerov , A. Sotnikov , S. Vakhrushev, and B. Dorner, "Structure and properties of confined sodium nitrite", *Eur. Phys. Jour. E.* vol. 12, pp. s21-s24, 2003

[28] A. I. Beskrovny, S. G. Vasilovskii, S. B. Vakhrushev, D. A. Kurdyukov, O. I. Zvorykina, A. A. Naberezhnov, N. M. Okuneva, M. Tovar, E. Rysiakiewicz-Pasek, and P. Jagus "Temperature Dependences of the Order Parameter for Sodium Nitrite Embedded into Porous Glasses and Opals" *Physics of the Solid State,* vol. 52, no.5, pp. 1092–1097, 2010

Environment. Technology. Resources. Rezekne, Latvia
Proceedings of the 12th International Scientific and Practical Conference. Volume III, 177-183

Analysis of Laser Processing of Artificial Leather

Pavels Narica
Engineering faculty
Rezekne Academy of Technologies
Rezekne, Latvia
Pavels.Narica@rta.lv

Ruta Laizāne
Engineering faculty
Rezekne Academy of Technologies
Rezekne, Latvia
Ruta.Laizane@rta.lv

Antons Pacejs
Engineering faculty
Rezekne Academy of Technologies
Rezekne, Latvia
Antons.Pacejs@rta.lv

Silvija Mežinska
Engineering faculty
Rezekne Academy of Technologies
Rezekne, Latvia
Silvija.Mezinska@rta.lv

***Abstract*—With the development of laser technologies, the field of application of lasers is developing as well. They are capable of processing numerous materials and are still finding their application in unexpected areas. In this case, lasers are studied as a system with which black and white color artificial leather can be processed. This modern material allows you to combine comfort, practicality and reasonable price in a finished product. The manufacturer of artificial leather provides wide possibilities of design. In this study laser beam was used for dark and light laser markings on black and white color artificial leather and in this work, it could be observed how CO_2 and fiber laser processing influence this specific material.**

Keywords*—Artificial leather, CO2 laser, Fiber laser, laser processing.

I. Introduction

A. Marking

Product labeling is an important process in modern production. It provides control over the quantity and quality of the products produced. For the manufacturer, labeling is required for product lobbying and as additional protection against counterfeiting attempts, for the consumer to obtain information on the product and as a guarantee of quality control. Laser labeling is becoming more widespread as a result of the rapid development of this industry and its integration into other industries [1]. Fast and accurate scanning of products on different materials is one of the main advantages of this technology [2].

There are lots of ways how to apply information on the products and some of them are: **pad printing**- indirect printing of paints on the flat and convex surfaces of products made of plastic, wood, cardboard, etc. with a silicone tampon, **direct full-color printing on fabric with water ink** - direct printing on textiles, which does not require preparatory procedures, this method allows you to apply full-color images to T-shirts, polos and hoodies, print on complex surfaces (seams, slats, etc.), getting a stable and colorful raster image with high resolution, **machine embroidery images on textiles and fabric chevrons** - the most persistent type of imaging on textiles, the choice of colors is limited by the color palette of the threads themselves, but the logo on T-shirts, hoodies, hats, jackets and shirts will not be erased and will remain bright [3] as well as **shock-mechanical**, **electro erosion**, **electrochemical**, **powder coating** and **laser marking** etc.

B. Laser processing

Contactless method has high scanning accuracy, fast scanning speed and a clear pattern, the ability to scan all kinds of texts, symbols, patterns on flat and convex surfaces, hard, soft and fragile products. The laser scanning machine integrates all the advantages of laser cutting, marking and engraving, which makes it possible to scan small and complex patterns on numerous materials [1].

Laser scanning has been used for decades, but it has become very common in recent years. Before we start let's remember what were: laser marking, engraving and cutting. The basic schematics view of those processing methods could be observed in Fig.1.

Fig. 1. Schematic view of laser cutting, engraving and marking processes.

The technology of **cutting** materials using lasers are commonly used in industrial production lines. A focused laser beam, usually controlled by a computer, provides a high energy density and allows to cut almost any material, regardless of their thermophysical properties using different laser sources.

When **engraving**, the laser beam changes the structure of the material. Under the influence of a laser, cavities

Print ISSN 1691-5402
Online ISSN 2256-070X
http://dx.doi.org/10.17770/etr2019vol3.4040

Published by Rezekne Academy of Technologies.

open and irregularities form on surfaces, and the impact zone itself is visible to the naked eye. The laser beam creates heat at the point of impact and causes the fibers to evaporate. This is a quick process, and the image is clear, and all the irregularities are well felt during the touch. The more passes, or the higher power and slower speed are set, what causes increasing in energy density, the deeper laser engraving is made during the treatment.

In the process of **marking** under the influence of a laser, the surface of the material slightly changes its properties or appearance. The material itself in the process of marking does not hugely change its original properties, because of the local laser treatment. On the one hand, for metals slight heat provokes oxidation and changing reflectance of the light of the areas of impact, and the surface itself is not damaged, but on the other hand, laser marking of no-conductive materials causes the changes in surface of the material so the spot of the impact causes for material to change color.

II. MATERIALS AND METHODS

A. Material

Currently, the genuine leather industry is facing severe pressure from multiple sources, including scarcity of raw hides, environmental pollution, and growing ethical concern over animal rights. Thus, to meet the escalating demand for leather products worldwide, the design and manufacture of leather substitutes, or artificial leather, are springing up, especially in Southeast Asia [4].

Artificial leather has been used for decades as an essential element of clothing design. The reason for designing faux fabrics are: the lower cost of the material; the ease of cutting and sewing; the fact that they are more available than leather or suede; no irregularities on the fabric surface, common in natural materials; and animal treatment and environment concerns. They are also designing to go beyond the limitations of leather and suede by creating "unnatural" colors and textures. [5].

There are many names for artificial leather: faux leather, fake leather, leatherette, synthetic leather, imitation leather, manmade leather etc. The adjective "artificial", initially subconsciously associated with the phrases "not real", "fake", has long acquired a somewhat different meaning. So, the concept of "artificial leather" over the past decades has absolutely nothing to do with the notion "product of inadequate quality."

The two main differences between the natural material and faux material are: faux leather is nonporous, so the fabric does not allow the air to pass though; fabric backing is required to support the embossed plastic face. Usual fiber content - face: usually polyurethane (PU) or polyvinylchloride (PVC) film; polyester film, which is recyclable may be available; backing depending on the purpose of use: non-woven fabric, 100% polyester interlock knit or polyester/cotton blend square plain weave Weaknesses: not breathable; dry-cleaning chemical may damage or destroy plastic film; cannot be re-sewn, needle holes cannot be repaired; plastic surface may cause "noise" or adhere together easily; extremely heat-sensitive [4].

PVC is the most commonly used polymer in the manufacture of faux leather because of its high durability and low cost. PVC is water-durable, crack resistant at room temperature, and resilient to wear and tear due to its chemical properties. PU feels more like genuine leather and is lighter than PVC, but PU leather is about twice as expensive as PVC leather, making it cost-prohibitive for many producers of low-margin consumer goods [6].

As a new polymeric material, synthetic leather is an important material for making shoes, bags, accessories, jackets, trousers and shirts suitcases and decorations. With the advancement and application of new processes and technologies, synthetic leather develops an advantage unparalleled by natural leather in aspects of variety, design and color, style, price and performance [7].

Various structural effects, colors and thicknesses are produced using PVC and PU. PU skin is considered to be more environmentally friendly compared to vinyl base because it does not produce dioxins. Artificial leather has a wide range of applications in the textile industry for technical textiles, different color material could be observed in Fig.2. There are areas where artificial skin is better suited because it is more resistant to the constant exposure to sunlight and water, which damages the natural skin [8].

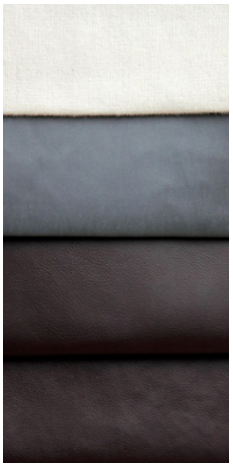

Fig. 2. Different shades of artificial leather.

The structure of the base material and coating layer could be observed in Fig.3. In this study two different color (black and white) artificial leather was used to implement high marking contrast possibilities on the material.

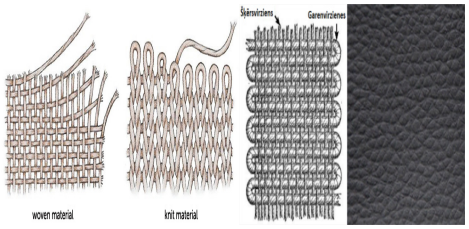

Fig. 3. Polyester interlock knit base fiber structure (with weft and warp fiber direction) and PVC, PU black color coating.

Fabric type - artificial leather: 1) Black color artificial leather composition coating PU 100%, backing 90% polyester,6% Cotton, 4% Viscose, weight - **± 555±5 g/m²,** thickness 0,9-1 mm, width **± 140±2 cm,** fire resistance

BS 5852, Abrasion resistance >45000 ISO 12947-2, resistance on light xenon test 7 (scale 1-8), resistance to sebum good.

2) White color artificial leather -composition coating 95% PVC 5% PU, backing 100% polyester, weight - ± **430±5 g/m²,** thickness 0,7 mm, width 140±2 cm, fire resistance BS 5852, Martindale Abrasion resistance > 100.000 cycles ISO 12947-2, Color Fastness to Light 4 (scale 1-5) ISO 105-B02, resistance to sebum good.

B. Laser systems

Laser radiation is a type of physical energy that is not found in natural light sources. This is achieved by special devices - optical quantum generators of various types and structures. All lasers consist of three basic components: *active medium*, *pumping system* (power source), *optical resonator* (in the case when the laser is working as an amplifier, the optical resonator is not used). Each of these components fulfills the specific functions of laser operation.

The aim of this paper is to achieve potentiality acceptable contrast markings on the material by the laser processing without causing a significant change of the material structure. To operate with a marking laser system mostly the following parameters should be set: power regulation coefficient, scanning speed, line step as well as for the impulse laser systems pulse- repetition frequency can be changed as well. As we know that each set of parameters applied to the material could change the outcome. So, there exist a lot of combination which can be managed.

1) CHANXAN CX-20G laser system specifications are:

- Laser type – Nd:Yag fiber laser;
- Operating mode - impulse;
- Wavelength - 1064 [nm];
- Working range - 300x300 [mm];
- Focal spot diameter ~ 20 [µm].

Laser system technical parameters can be observed in Table 1. and schematic view of experimental set-up could be observed in Fig.4.

TABLE 1 *CHANXAN CX-20G* LASER TECHNICAL PARAMETERS

Symbol	*Name*	*Values range*	*Step*	*Units*
v	Scan speed	1 — 10000	1	mm/s
Δf	Focus shift	-100 — 100	0.1	mm
kP	Power regulation coefficient	0-100	0.1	%
P	Avarege power	0 — 20		W
f	Frequency	20 — 50	1	kHz

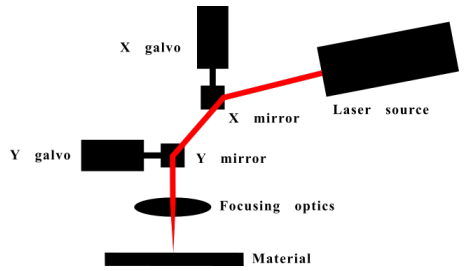

Fig. 4. Schematic view of experimental set-up of *CHANXAN CX-20G fiber laser system.*

In Fig.5 it could be seen that coloration between laser *kP* parameter for average output power *P* for fiber laser is almost linear.

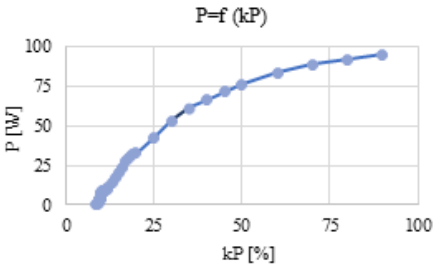

Fig. 5. Mapping of values of power regulation coefficient kP [%] to fiber laser power P [W] with a constant pulse repetition frequency f = 30 [kHz].

2) SUNTOP ST-CC9060 laser system specifications are:

- Laser type – CO2 gas laser;
- Operating mode – continuous wave;
- Wavelength - 10060 [nm];
- Working range – 900x600 [mm];
- Focal spot diameter ~ 80 [µm].

Laser system technical parameters can be observed in Table 2 and schematic view of experimental set-up could be observed in Fig.6.

TABLE 2 SUNTOP ST-CC9060 LASER TECHNICAL PARAMETERS.

Symbol	*Name*	*Values range*	*Step*	*Units*
v	Scan speed	1 — 400	1	mm/s
Δf	Focus shift	-50 — 50	0.1	mm
kP	Power regulation coefficient	0-100	0.1	%
P	Avarege power	0 — 100		W

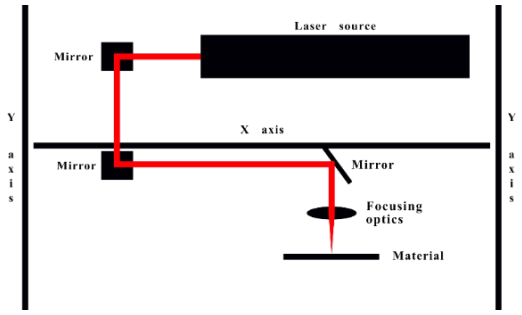

Fig. 6. Schematic view of experimental set-up of SUNTOP ST-CC9060 CO_2 laser system.

In Fig.7. it could be observed that coloration between laser *kP* parameter for average output power *P* is something similar to exponential and one more thing was noted that those kind of CO_2 systems generate laser beam only after specific *kP* value. In this case it was 8 [%].

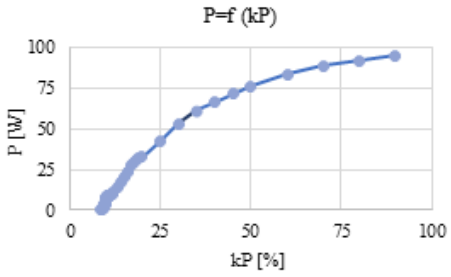

Fig. 7. Mapping of values of power regulation coefficient *kP* [%] to CO2 laser power *P* [W].

C. Output power measurements

The active medium is what determines the wavelength of the lasers itself, that often determines how the material will behave due to laser processing. It has been noted that power regulation coefficient *kP%*. could be set in the laser system software, but for better process understanding and for further optimization of parameters it is better to carry out power measurements of a laser output power (could be used any suitable power measurements system or output power measurements could be defined by the manufacturer) in our case it was power measurement sensor OPHIR F150A-BB-26 that is shown in Fig.8. and its specifications are summed up in Table 3.

Fig. 8. Power measurement sensor OPHIR F150A-BB-26

TABLE 3
POWER MEASUREMENT SENSOR OPHIR F150A-BB-26 SPECIFICATIONS

Name	*Values*
Absorber Type	Broadband
Spectral Range [µm]	0.19 - 20
Aperture diameter [mm]	26
Power Range [W]	0,05 - 150
Power Noise Level [mW]	3
Max Average Power Density [kW/cm2]	12
Max Energy Desnity [J/cm2]	10
Power Accuracy [+/-%]	3
Cooling	fan

During this study from preliminary experiments it was determinate that artificial leather coating is very heat sensitive material, so there are no needs to use high energy density systems to treat this specific material.

D. Process parameters

The upper power limit (and therefore the energy density) of each laser source is preset, and it is necessary to determine the optimal range parameters variation to achieve required results.

However, the **power density** [W/mm^2] is determined by the formula (1), where *S* is the surface of the laser beam working spot [mm^2] and *P* [W] output power.

$$q_{pS} = \frac{P}{S} \tag{1}$$

Considering, that $S = (\pi d^2) / 4$ we get,

$$q_{pS} = \frac{4P}{\pi d^2} \tag{2}$$

where d [mm] is the diameter of the working spot. This formula will help us understand that by changing (defocusing) laser beam, the power density changes as well. So, for precise measurements this study laser processing experiments was made in focus position, where laser beam has smallest working spot.

In this study laser **energy density** was described and it is related to delivered total energy [J/mm^2] to the target material and in this paper, it helped better characterizing the laser processing and beam impact on the material.

$$q_{eS} = \frac{P}{d * v} \tag{3}$$

Where *v* is the scanning speed [mm/s], d is the diameter of the working spot [mm] and *P* output power [W].

The goal of this paper is to determine the limits of energy density [J/mm^2] for artificial leather treatment using CO_2 and fiber laser, where laser processing has:

- Almost imperceptible impact on the material coating layer;
- There is a complete destruction of the material base layer.

Then in that obtained range it will be possible to find the best processing parameters for laser marking of artificial leather using the different values of parameters matrix method.

III. RESULTS AND DISCUSSIONS

A. Outcomes from fiber laser processing on white and black color artificial leather

In Fig. 9., 10. and 11. it could be observed that samples were scanned by the fiber laser in a form of a 4 × 5 matrix with each cell having different combination of laser parameters values.

For both white and black color artificial leather was applied this range of parameters:

- Average power *P* – 1 – 20 [W];
- Scanning speed *v* – 300 – 3000 [mm/s];
- Line distance *dx* – 0.01 [mm];
- Pulse repetition frequency *f* = 30 [kHz];
- Focus shift Δf – 0 [mm].

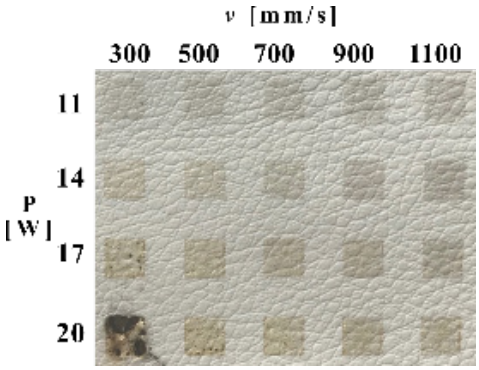

Fig. 9. Outcomes after fiber laser treatment on white color artificial leather material.

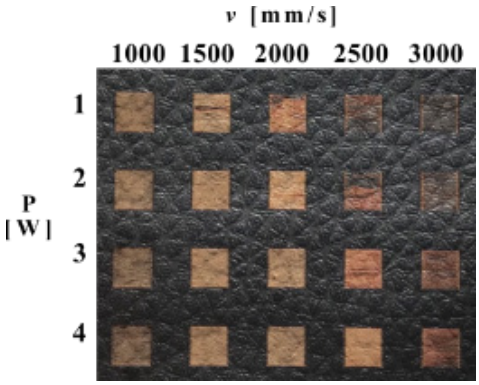

Fig. 10. Outcomes after fiber laser treatment on black color artificial leather material.

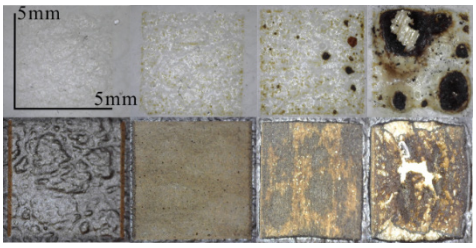

Fig. 11. Material degradation caused by changing energy density applied to the material (Dino-Lite Edge AM7115MZT microscope).

In Table 4 it could be observed the approximate energy density limits using fiber laser system for different material treatment like marking, engraving and cutting on black and white color artificial leather.

Table 4 required approximate energy density for material treatment using fiber laser system

Material degradation	White color artificial leather [J/mm^2]	Black color artificial leather [J/mm^2]
Slightly visible zone of impact, coating marked	0.50	0.017
Material has been engraved	2.83	0.2
Material cut through	3.33	1.33

B. Outcomes from CO_2 laser processing on white and black color artificial leather

Fig. 12., 13. and 14. shows that samples were scanned by the CO_2 laser in a form of a 4 × 5 matrix with each cell having different combination of laser parameters values.

For both white and black color artificial leather was applied same sets of parameters (Fig.2.):

- Average power *P* – 1 - 4 [W];
- Scanning speed *v* – 100 – 300 [mm/s];
- Line distance *dx* – 0.1 [mm];
- Focus shift Δf – 0 [mm].

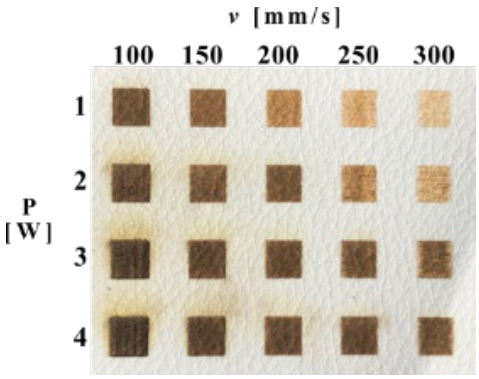

Fig. 12. Outcomes after CO2 laser treatment on white color artificial leather material.

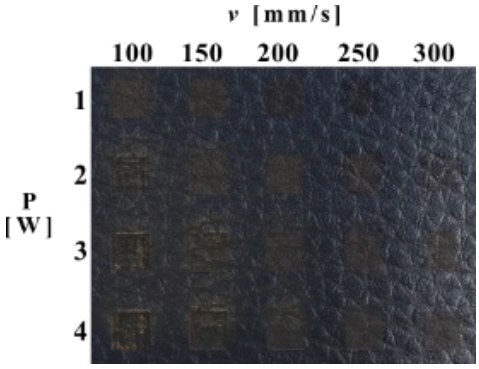

Fig. 13. Outcomes after CO2 laser treatment on black color artificial leather material.

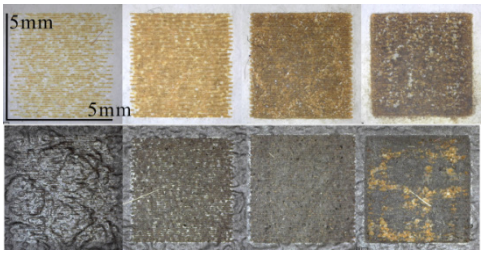

Fig. 14. Material degradation caused by changing energy density applied to the material (Dino-Lite Edge AM7115MZT microscope).

Table 5 demonstrates approximate energy density limits using CO_2 laser system for different material treatment like marking, engraving and cutting on black and white color artificial leather.

Table 5 required approximate energy density for material treatment using CO_2 laser system

Material degradation	White color artificial leather [J/mm^2]	Black color artificial leather [J/mm^2]
Slightly visible zone of impact, coating marked	0.13	0.0083
Material has been engraved	1.25	0.15
Material cut through	1.67	0.70

A. Ultimate tensile strength results and discussions

Ultimate tensile strength is the greatest stress especially

in tension that a material is capable of withstanding without rupture. In this study ultimate tensile strength of artificial leather were tested and results plotted in graphs and tables. The one of the tasks of the article was to observe influence on the specimens by laser processing on the material in weft and warp directions.

During preparation, black color artificial leather was cutted in weft and warp directions of the fibers with dimensions 50 [mm] x 300 [mm], 6 samples in weft and 6 samples in warp. Then fiber laser marking was applied in the middle of prepared samples with dimensions 50 [mm] x 50 [mm] (Fig. 15. and 16.), 3 samples in weft and 3 samples in warp with applied laser scanning as well as 6 samples for both fiber directions remained unscanned. The ultimate tensile strength test was applied to 4 sample sets (Table 6).

TABLE 6 PREPARED SAMPLE SETS

Description	Sample set
3 specimens of artificial leather weft direction	I
3 specimens of artificial leather weft direction with marking applied	II
3 specimens of artificial leather warp direction	III
3 specimens of artificial leather warp direction with marking applied	IV

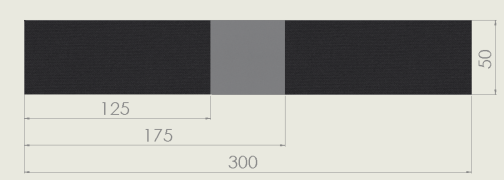

Fig. 15. Schematic drawing of prepaired samples in [mm].

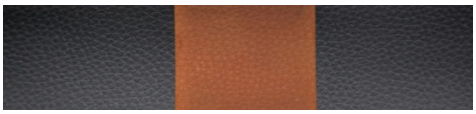

Fig. 16. Obtained laser treatment on artificial leather sample by fiber laser.

In this work was carried the effect of specificly selected input parametrs for laser processing, in this case – marking (contrasted color), on the tensile strength of artificial leather. The aim was to determine how the acceptable contrasted engraving applied to artificail leather impacts on the maximum tensile strength compared to the untreated (control) samples. The test was performed using Zwick / Roell machine (Fig. 17.) and results could be observed in Table 5.

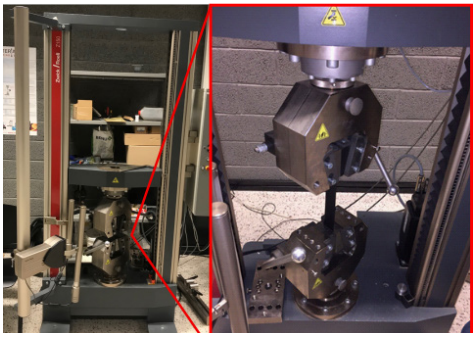

Fig. 17. Ultimate tensile strength testing using Zwick/ Roell machine

TABLE. 7 ULTIMATE TENSILE STRENGTH RESULTS FOR ALL SAMPLE SETS.

Sample set	Average UTS (N)	Maximum (N)	Minimum (N)	Range (N)
I	256.89	265.29	256.89	14.88
II	262.01	266.21	258.93	7.28
III	457.21	496.31	431.76	64.55
IV	466.38	484.69	441.85	42.84

We noted that obtained laser treating parameters has no influence on the artificial leather both in weft and warp directions till the base material has not damaged by the laser beam.

From chart in Fig. 18. and test results in Table 7 we can clearly see how applied laser marking influence the artificial leather. On the one hand it could be observed that chosen material has a bigger ultimate tensile strength in weft direction, than in a warp direction and on the other hand we can clearly observe that applied laser marking is not affect the UTS results, because laser treatment was obtained only on the material coating.

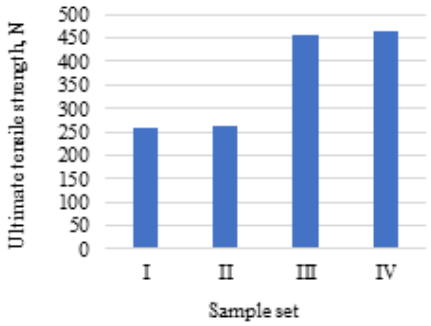

Fig. 18. Average ultimate tensile strength (N) plotted in chart

IV. SUMMARY

Due to different absorbtion, reflection and transmission properties by different IR wavelengts of used material it could be observed (Fig 19. and 20.) that in both cases (using fiber and CO_2 laser) white color artificial leather is more reflective material to specific IR wavelengths used in this study and energy density requested for treatment like marking, engraving and cutting for black color artificial leather is much less than white color artificial leather. From plotted energy density charts it could be observed that in this work used laser system could be used in marking, engraving and cutting processes.

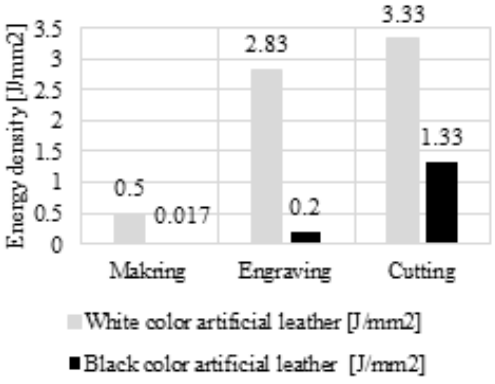

Fig. 19. Values of energy density required for maring, engraving and cutting of black and white color artificial leather using fiber laser plotted in chart.

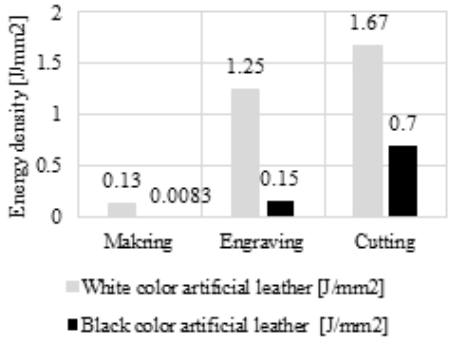

Fig. 20. Values of energy density required for marking, engraving and cutting of black and white color artificial leather using CO_2 laser plotted in chart.

In this study it was noted that until the artificial leather base is not subjected to any change by laser scanning ultimate tensile strength properties remains the same. It means that artificial leather tensile strength fully depends on the mechanical properties of the base layer no matter the condition of PVC/PU coating. Applied study results could be observed in Fig. 19.

Fig. 21. Laser treatement of black and white color artificial leather.

In conclusion, this study is not last in the coming series of future articles where features of laser processing will be studied for such specific material and others. At this moment RTA laser technology laboratory with "Laser technologies" Masters students and students from "Design" faculty are working on very various topics, trying to find more and more applications and optimizing already known processes for coherent, monochromatic laser light and material interaction.

References

[1] "Global and China Industrial Laser Industry Report 2018-2022" Research In China, ID: 4585808, July 2018.

[2] W. M. Steen, Laser Material Processing. Berlin: Springer-Verlag, 1991.

[3] W. C. M. Leslie, Textile Printing. Machester: Department of Textiles, University of Manchester Institute of Science and Technology, 2003.

[4] Ruowang Liu, Yi Chen, Haojun Fan, Design, Characterization, Dyeing Properties, and Application of Acid-Dyeable Polyurethane in the Manufacture of Microfiber Synthetic Leather, Fibers and Polymers, September 2015, Vol.16, Issue 9, pp 1970-1980, [Online]. Available: https://link.springer.com/article/10.1007/s12221-015-5024-4

[Accessed March 7, 2019] https://doi.org/10.1007/s12221-015-5024-4

[5] Gail Baugh, The Fashion Designers Textile Directory. Thames & Hudson LTD, London, 2011

[6] Case Study: Inspires innovation of new, more sustainable faux leather [Online]. Available:

https://www.exxonmobilchemical.com/en/library/asset/bf9707c-29913473d9e48d7691eab2030 [Accessed March 9, 2019]

[7] Xu Xu, Wu Zhiping, Environmental Cost Analysis and Upgrading Research of Synthetic Leather Industry Available online at www.sciencedirect.com Energy Procedia 5 (2011) 1341–1347 [Online]. Available: https://www.sciencedirect.com/science/article/pii/S1876610211011684 [Accessed March 7, 2019]

[8] Artificial leather - Imitation leather, [Online]. Available: https://www.leatherdictionary.com/index.php/Artificial_leather_-_Imitation_leather [Accessed March 10, 2019]

Environment. Technology. Resources. Rezekne, Latvia
Proceedings of the 12th International Scientific and Practical Conference. Volume III, 184-188

Reducing Risk Factors in the Workplace of the Laser System Operator

Pavels Narica
Faculty of Engineering
Rezekne Academy of Technologies
Rezekne, Latvia
pavels.narica@rta.lv

Inese Martinsone
Institute of Occupational Safety
andEnvironmental HealthRiga Stradins
university
Riga, Latvia
inese.martinsone@rsu.lv

***Abstract*—Laser processing of materials takes an increasing place in production processes. Improving the performance, improving the quality of processing is not a complete list of the positive aspects of the introduction of laser processing, but there are a number of points that need to be paid attention to during the operation of laser systems - these are issues related to safety. The following risk factors are specific to laser systems: firstly, the laser beam itself, effects on the organs of vision, direct thermal effects on the skin and tissues, secondly, harmful products resulting from the interaction of the laser beam and the material being processed. Aerosols, smoke and dust have different effects on the human body, especially on the respiratory system and the publication considers the risks associated with the release of harmful products during laser processing and the existing methods for reducing the concentration of harmful substances in the working area with specific examples.**

Keywords — Clean air, Safety, Nano particles, Laser processing.

I. Introduction

Industrial laser systems are becoming more widely used as they have high productivity, production processes become more efficient and largely automated. Increasingly, laser systems appear in educational institutions, in the youth technical creativity centers. On one hand, this is great, but on the other hand, as many years of experience have shown, entrepreneurs and laser system operators often have a low level of awareness of the risks and unwanted by-products which depend on the type of laser source; from the laser process; of the material type.

Depending on the application, these are harmful vapours, gases, aerosols, and solid particles. The negative impact will be not only on the person, but also on the laser equipment as well as the products may be damaged. Laser fume builds up firmly adhering layers of contamination. The danger of laser dust is often underestimated. Only effective air filtration can ensure safe working conditions and protect the health of the personnel of the enterprise in which the laser systems operate. The amount of harmful products during processing depends on the kind of technological process - drilling, cutting, welding, engraving or marking, as well as on the properties and composition of the material being processed, such as plastic, wood or metal. Fine dust and aerosols generated by laser processes are often smaller than 1 ***µm*** [1].

Impact on human health can manifest itself in different ways depending on the concentration of undesirable substances in the work area and on the individual characteristics of the human body. Manifestations of exposure to harmful substances can be expressed in inflammation and changes in the tissues of the respiratory organs, from allergies, and functional disorders of the lungs to lung cancer.

The classification of fine dust is based on the particle size (more precisely: on the aerodynamic diameter). Fine dust with a particle size of 10µm is respirable. These particles reach the bronchial area, as shown in Fig.1. In the case of fine dust, the smaller the dust particles, the more dangerous it is, as it can penetrate further into the lungs. Very fine dust can penetrate into the alveoli and clog them. Particles smaller than 1µm are extremely dangerous as they can penetrate very far into the lungs. [2]

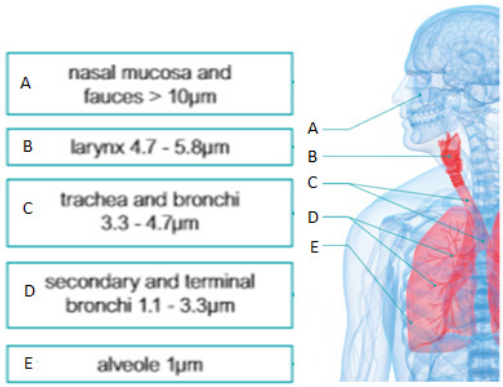

Fig. 1. Penetration of dust particles into the human body, depending on their size. [2]

The nanoparticles during inhalation overcome the lung blood barrier and enter the nervous system [3]. Depending on their chemical composition, they have further harmful effects. The health burden increases linearly proportional to the fine dust concentration. According to the information provided by the Laser Zentrum Hannover in the Laser safety database health burden increases linearly proportional to the fine dust concentration [4]. Information on the amount of emission in the process of laser processing is summarized in table 1. The EU Air Quality Plans aim for a maximum fine

Print ISSN 1691-5402
Online ISSN 2256-070X
http://dx.doi.org/10.17770/etr2019vol3.4153

dust concentration of 40-50µg / m³ in the respiratory air. It should be contrasted with the fact that the fine dust concentration in laser processes is partly 100µg / m³ and more! [5]

The ISO committee who is responsible for the documents in the field of cleaning equipment from air and other gases. prepared new standards in accordance with research in this important area. This first edition of ISO16890-1, together with ISO16890-2, ISO16890-3 and ISO16890-4, cancels and replaces ISO/TS21220:2009, which has been technically revised.

ISO16890 consists of the following parts, under the general title Air filters for general ventilation:

- Part 1: Technical specifications, requirements and classification system based upon particulate matter efficiency (ePM)
- Part 2: Measurement of fractional efficiency and air flow resistance
- Part 3: Determination of the gravimetric efficiency and the air flow resistance versus the mass of test dust captured
- Part 4: Conditioning method to determine the minimum fractional test efficiency

The ISO 16890 series describes the equipment, materials, technical specifications, requirements, qualifications and procedures to produce the laboratory performance data and efficiency classification based upon the measured fractional efficiency converted into a particulate matter efficiency (ePM) reporting system. In Germany, the Technical Rules for Hazardous Substances (TRGS) reflect the state of the safety-technical, occupational-medical, hygienic and occupational-scientific requirements for hazardous substances with regard to marketing and handling. [9], [10]

Table 1. The fine dust concentration in laser processes [5]

	Process	Quantity	Aerodynamic diameter
Aerosols-emission	Removal of plastic	> 30mg / s	<0.12µm
	Welding of metal	> 9mg / s	
	Cutting of metal	> 100mg /s	
	Removal of paint	> 25mg / s	<0,23µm
Fine dust - concentration	Cutting of plastic	> 500µg /m³	<1.7µm
	Cutting of metal	> 300µg /m³	
	Welding of metal	> 2000µg /m³	

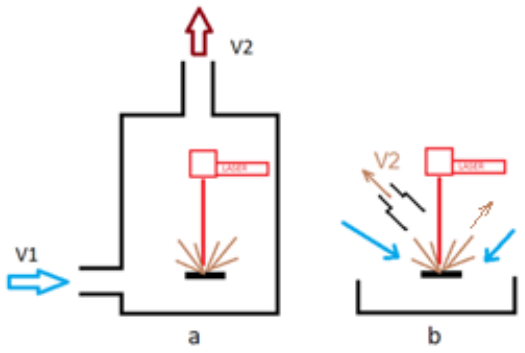

Fig. 2. Variants of the constructive implementation of laser systemsб closed a) and open b) systems

There are open and closed laser systems. Their main difference is that in the case of a closed system, it is possible to direct almost all the air from the laser working area to the filtration system; Fig. 2a, in this case, the flow of incoming air to the filtration system V2 and entering the working area V1 is almost equal, in an open or semi-closed system Fig. 2b, this is very difficult to draw. The air flow V2 that will be directed to the filter system will not be able to catch all the harmful emissions from the treatment zone.

It is necessary to note a few important points and technical solutions extraction systems. There is a relationship between the required air flow and the distance between the suction intake nozzle of the aspiration system and the material processing zone of the laser beam. Fig. 3 clearly shows that by reducing the distance to the treatment area by half, the air flow through the aspiration system can be reduced four times, with the same air cleaning efficiency in the operator's working area. The required air velocity depends on the size and weight of the particles, as well as on the distance from the treatment point to the suction raster. This means that the same result can be achieved at lower cost.

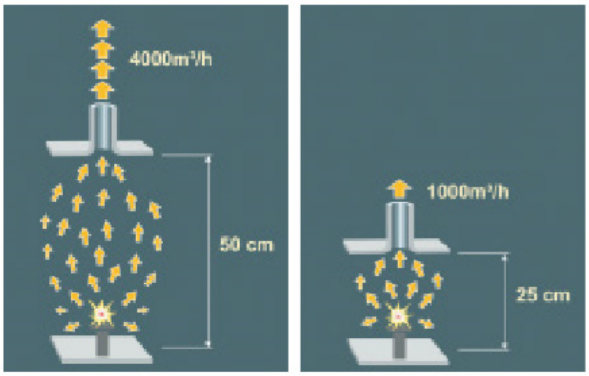

Fig. 3. Influence of distance to the required airflow [6]

The right design for collecting the contaminants is one of the most decisive factors for cost-effective, suitable dimensioning of the overall extraction and filter system this is clearly seen in Fig. 4 [7].

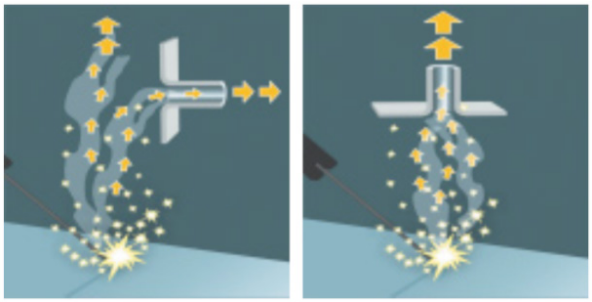

Fig. 4. Influence of hoods flanges forms to the effective extraction area. [7]

Depending on workplace and extraction situation, you can choose among various shapes and sizes of collection elements. The following figures illustrate the most important standard versions, this is seen in figure 6. In addition, the manufacturer designs customer specific versions, up to complete housing of the pollutant source [11]. Through skillful use of physical

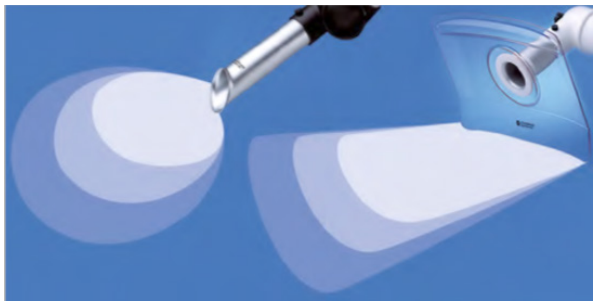

Fig. 5. Examples of the location of the suction raster [8]

laws, the low depth effect of the open detectors can be improved. These include: Most existing heat sources will cause upward thermal currents that can be used for local placement, example in Fig. 5, on the example to the right, the operation of the aspiration system will be more efficient.

Fig. 6. Collection elements [11]

Depending on the laser process, the kind of laser fumes can vary. Therefore, there are various filtering systems. Let us consider these systems on the example of ULT AG products. This is a saturation filter unit and a cartridge filter unit [12]. In both systems, the degree of cleaning allows you to return the purified air back into the work area. The cleaning level is in accordance with the current regulations in the European Union.

Saturation filter units:

- for low laser fume concentration;
- for sticky laser fume;
- for additional odour pollutio.

Cartridge filter units:

- for high laser fume concentration;
- for dry laser fume;
- for high demands on service life. [12]

When using a system consisting of filtering blocks, it must be kept in mind that the filters have a fixed life expectancy and will periodically need changing to ensure effective air filtration. Constructively, the system is visible in Fig. 7. Air filtration occurs gradually, from the beginning of the filters which cleans the air from large particles to the purge from the nano particles.

Cartridge filter units are mainly used to remove dry, intensive laser smoke continuously in fairly large volumes Fig. 8. They have long service life and low operating costs. The pollutants are collected on the surface of the filter cartridge. The filter cartridge is removable. They need to be systematically cleaned after a certain time period, the cartridge is cleaned with compressed air and dust is fully collected in dust collectors. Refined air is returned to the working area.

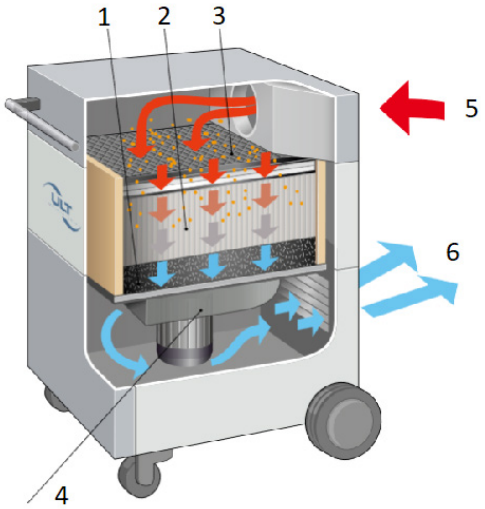

Fig. 7. Functional principle of saturation filter units , 1- activated carbon filter; 2- submicron particulate filter; 3- resublimation filter / spark protection; 4- fan; 5- process exhaust air; 6- purified air[12]

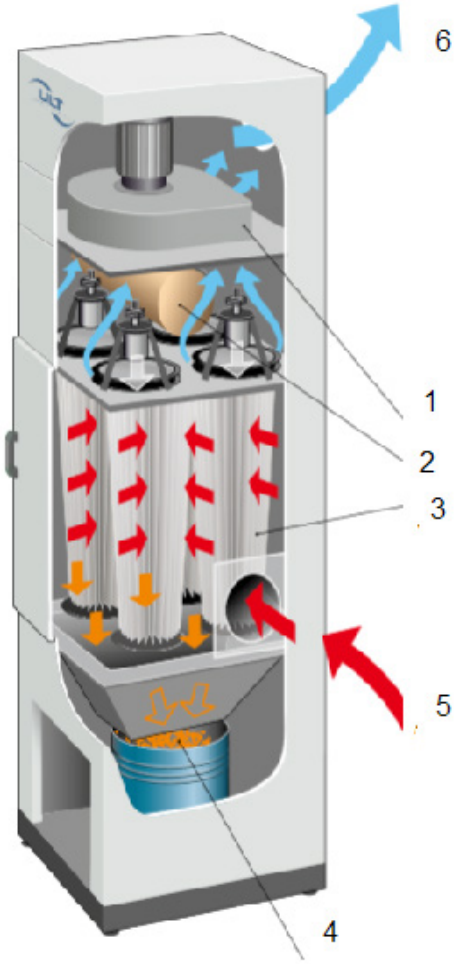

Fig. 8. Functional principle of cartridge filter units; 1- fan; 2- compressed air tank; 3- filter cartridges; 4- dust collector; 5- process exhaust air; 6- purified air [12]

II. Materials and methods

Air samples of fumes in the laser cutting were gathered from the breathing zone of the workers during the active work periods. Cellulose acetate membrane filters (Millipore, 0.45 mm) with a 37-mm open-face cassette were used as collectors. The flow rate was 2 L/min (GilAir sampling equipment was used), and the sample time varied from 55 to 90 minutes. The inhalable dust concentration was then calculated from the weight difference (method of gravimetry) of the filters before and after sampling, and the corresponding of air volume was done, too.

As well particle number measurements were done by "P-Trak Ultrafine Particle Counter" Model 8525 (particles size: 20 - 1000 nm) during metal laser cutting process.

The laser-cutting machine is equipped with closed fume extraction system.

III. Results and recomendations

The concentration of metal fumes in the work place air near by the laser cutting machine fluctuated in range from 0.40 to 0.56 mg/m3. The highest concentration of fumes was detected in the worker breathing zone, respectively 1.03 ± 0.15 mg/m3.

Working with metals makes an large part of the industry and nowadays one cannot imagine such manufacturing processes as metal processing, metallurgy and various manufacture auxiliary processes, for instance, maintenance of production equipment and work equipment without it. Employee who performs metal cutting and welding is subjected to series of harmful factors. Fumes consisting of various metal salts and oxides is released in work environment air; the presence of substances having especially adverse human health effects – cadmium, nickel, manganese, chromium (VI) – is possible. A safe limit value for welding aerosol fumes is 4 mg/m3, it is integrated in the Regulation of the Cabinet of Ministers No. 325/2007 "Work Safety Requirements when Working with Chemical Substances" (adopted on 15.05.2007, published in Latvijas Vēstnesis, 18.05.2007).

Total dust concentrations of metal fumes in work environment do not exceed safe limit value, however concentration in worker breathing zones where people are moving within the workshop is higher than in the work environment near the laser-cutting machine.

The particle concentration measurements were made during the technological process. In the laboratory measurements for clean room before the measurements in the workshop were done. The workshop gate was closed in period of "Conditions 1" and "Conditions 3'" during the working process. The gate was open for finished production transportation needs out of the workshop in the period of "Conditions 2", see measurement results in the table 2. The temperature difference between outdoor (+ 6 C°) and indoor (+ 24 C°) environment leads to air movement inside the workshop and particles from the surfaces, walls and ceiling areas moved down, and cause rapid increase of particle concentration in the breathing zone, see Fig. 9.

Table 2. Number of particles in the operator zone

Conditions	Concentration of particles in the air, pt/cc			
	Min	*Max*	*Average*	*Median*
Clean room	733	791	762	763
Conditions 1	8510	11600	9916	9845
Conditions 2	12100	45700	24548	22500
Conditions 1'	6510	17500	9934	9250

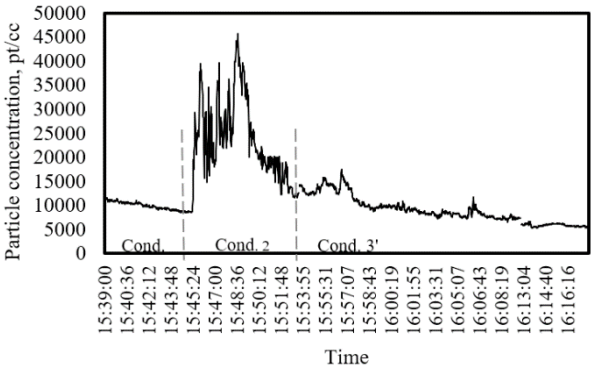

Fig. 9. Particle concentration during working process

According to literature, metal fumes consist predominately of particle agglomerates smaller than 1

μm. This means that most of the fumes are respirable [13]. Lehnert et al. (2012) indicate that the welding process is the major determinant of the exposure to particles in different size fractions, however in welding processes it can be observed that there is a large number of small - sized particles including ultra fine particles [14]. Typical workplace air is usually a mixture of these groups and the convection currents, work equipment and air ventilation systems keep the dust in a mobile state preventing the sedimentation of smallest particles [15].

Inhalation is considered to be the primary route of exposure for dusts with smaller particles, which have greater potential for harmful effects on human health as they reach alveolar level. Special attention should be paid to finding that the smaller fractions of dust from the metal industry contained toxic metals at nano-size (such as Zn, Mn, and Cr) [16,], [17], [15].

It is particularly essential to identify and determine the concentration of the smallest size dust particles with little mass, if there are any, as they could be found in the air in suspended state for prolonged periods and their effects on human health are particularly harmful.

References

[1] Jakschik St., Blei St., Laser fumes in femtosecond laser processes – product, process and environment considerations, ULT AG, ILK Dresden, https://www.ult.de

[2] https://www.tbh.eu/en/shortlinks/downloads.html

[3] https://www.ult.de/images/content/download/02_geraeteserien/LAS_extraction_filtration_laser_fume_2016_en_web.pdf

[4] https://www.lzh.de/de/publikationen/lasersicherheit

[5] Laserbearbeitung,datenblatt/dbl_tb_laserbearbeitung_dbl_deutsch.pdf

[6] Meissner St., Why Extraction and Filtrationn tehnology is important; ULT GmbH https://www.ult.de

[7] https://www.tbh.eu/en/shortlinks/downloads.html

[8] VDMA, Allgemeine Lufttechnik, Erfassen luftfremder Stoffe, www.luftreinhaltung.vdma.org

[9] TRGS 900 Grenzwerte in der Luft am Arbeitsplatz – „Luftgrenzwerte

[10] TRGS 901 Begründungen und Erläuterungen zu Grenzwerten in der Luft am Arbeitsplatz,

[11] https://www.ult.de/images/content/download/03_absaugearme/ULT_extraction_arms_capturing_elements_flextractor_en.pdf

[12] https://www.ult.de/images/content/download/02_geraeteserien/LAS_extraction_filtration_laser_fume_2016_en_web.pdf

[13] Jenkins, N.T., Pierce, W.M.-G., Eagar, T.W. (2005) Journal of Welding, October, 156-163.

[14] Lehnert, M., Pesch, B., Lotz, A., Pelzer, J., Kendzia, B., Gawrych, K., Heinze, E., Van Gelder, R., Punkenburg, E., Weiss, T., Mattenklott, M., Hahn, J.U., Möhlmann, C., Berges, M., Hartwig, A., Brüning, T.; Weldox Study Group. Ann Occup Hyg. (2012), 56(5), 557-567.

[15] Pavlovska, Z., Martinsone, Z., Vanadzins, I., Martinsone, I., Seile, A., Sudmalis, P.,2016. Occupational exposure parameters for characterization of nanoparticu-late matter toxicity: metal versus wood processing. Process Saf. Environ. Prot.102, 230–237.

[16] Peixe, T.S., de Souza Nascimento, E., Schofield, K.L., Arcurid, A.S.A., Bulcão, R.P., 2015. Nanotoxicology and Exposure in the Occupational Setting. Occup. Dis. Environ. Med. 3, 35–48

[17] O'Shaughnessy, P.T., 2013. Occupational Health risk to nanoparticulate exposure. Environ. Sci. Process. Impacts 15, 49–62.

Comparative Study of Industrial Lignosulfonates and Some Their Properties

Brigita Neiberte
Latvian State Institute of Wood Chemistry,
27 Dzerbenes St., Riga, LV-1006, Latvia.

Antons Jablonsky
Latvian State Institute of Wood Chemistry,
27 Dzerbenes St., Riga, LV-1006, Latvia.

Galia Shulga
Latvian State Institute of Wood Chemistry,
27 Dzerbenes St., Riga, LV-1006, Latvia.

Anrijs Verovkins
Latvian State Institute of Wood Chemistry,
27 Dzerbenes St., Riga, LV-1006, Latvia.

Sanita Vitolina
Latvian State Institute of Wood Chemistry,
27 Dzerbenes St., Riga, LV-1006, Latvia.

Julia Brovkina
Latvian State Institute of Wood Chemistry,
27 Dzerbenes St., Riga, LV-1006, Latvia.

***Abstract*—The aim was to compare the chemical composition and some properties of three industrial lignosulfonates produced as a by-product at three pulp and paper mills (Russia). Using the classical methods of lignin chemistry, it was found that there were differences in the elemental composition and the content of functional groups of the industrial lignosulfonates, but in general, they were not very significant. The Kondopoga lignosulfonates contained the highest content of methoxy, aliphatic hydroxyl groups and carbonyl groups. The Vyborg lignosulfonates had the highest degree of sulfonation and the lowest content of carbonyl groups. The content of the functional groups in the chemical composition of the Syassky lignosulfonates was intermediate between the functional composition of the Vyborg and Kondopoga lignosulfonates. The Vyborg lignosulfonates had the lowest values of the viscosity average molecular mass, dynamic viscosity and surface tension at the air-water interface in comparison with these parameters of the Kondopoga and Syassky lignosulfonates.**

***Keywords*—industrial lignosulfonates, chemical composition, viscosity, surface tension**

I. Introduction

According to the strategy and principles of the Circular Economy, great attention has to be drawn to the rational and effective utilization of biomass by-products because this provides a huge secondary resource for producing new materials and reduces their costs.

Lignosulfonates are available on the global market as a by-product of pulp and paper mills producing cellulose. They can be regarded as a special class of industrial lignins that are used for production of materials and chemical applications [1].

Due to their availability, physicochemical properties and low price, lignosulfonates are used for obtaining binders, emulsifiers, dust suppressants, dispersants and soil improvers. Their ability to coagulate and precipitate proteins is used in water purification of wastewater from meat and fish canneries or milk processing plants. As an anti-settling agent, lignosulfonates are used in concrete mixtures, ceramics, gypsum board production and for leather tanning. Lignosulfonates provide flowability and plasticity to cement. Lignosulfonates can be used in polymeric blends as an additive or a filler for obtaining new composite materials [2, 3].

On the other hand, the achievements of remarkable results in application of lignosulfonates require a deeper knowledge of their chemical composition and properties, which may help overcome their drawbacks and exploit their advantages.

The aim of the work was to compare the chemical composition and some properties of three industrial lignosulfonates produced as a by-product at three pulp and paper mills (Russia).

II. Materials and methods

For the study, we used three industrial lignosulfonates, obtained as a result of producing cellulose by the sulfite method at three Russian mills, namely, JSC Kondopoga (Kondopoga Pulp and Paper Mill), JSC Syassky Pulp and Paper Mill and OJSC "Vyborg Cellulose". Industrial lignosulfonates were used in a powder form and were stored in a desiccator with P_2O_5. The content of reducing substances in the lignosulfonates did not exceed 10%. Their main characteristics corresponded to TU 2455-028-00279580-2004 (Russia). Methods for determining the content of functional groups and ash in lignosulfonates are given in a concise form and are described in detail in [4-6].

Determination of methoxy groups by the Zeisel-Vebock-Schwappack method. The content of methoxy groups ($-OCH_3$) is an essential criterion for the characterization of the lignin content in a sample. The methoxy groups' content was determined by the Zeisel-Vebock-Schwappack method using the test sample treatment with 57% concentrated HJ at a temperature of 140 °C during 30 min.

Determination of the sulfo and phenolic hydroxyl groups. The conductometric titration method was applied for the quantitative determination of the sulfo groups ($-SO_3H$) and phenolic hydroxyl groups (OH_{phen}) in lignosulfonate samples. For this purpose, an automatic

Print ISSN 1691-5402
Online ISSN 2256-070X
http://dx.doi.org/10.17770/etr2019vol3.4121

"Radiometer analytical" titration device CDM 210 Meter Lab was used.

Determination of the total acidic hydroxyl groups. The hemosorption method is based on the ion exchange reactions between the substance's acidic groups (OH_{phen}+OH_{COOH}) and $Ba(OH)_2$ or $(CH_3COO)_2Ca$. The tested sample was suspended in 0.1M LiOH (or NaOH) solution and heated at 85 °C; then the relevant amount of $BaCl_2$ solution was added. The chemical equilibrium was shifted, creating insoluble salts. The strong acidic groups were determined by the treatment of the sample with CH_3COOCa.

Determination of the total aliphatic and phenolic hydroxyl groups. A Freudenberg method is based on the quantitative reaction between lignin's hydroxyl groups and acetic anhydride in the presence of pyridine as a catalyst.

Determination of carbonyl groups. Lignin's carbonyl groups are presented as ketone groups $R_2C=O$ or aldehyde groups RHC=O, which, in the reaction with hydroxylamine hydrochloride solution, attract it in an equivalent amount by releasing HCl. The amount of the released HCl was determined by potentiometric or conductometric titration with 0.1M alkaline solution.

Determination of the mineral (ash) content. The tested sample was burnt in a muffle oven at a temperature of 525-600 °C using a previously weighed and heated porcelain crucible. The sample was kept at this temperature during 3-4 hours.

Elemental analysis. The LS elemental composition (C, H, S, N) was determined by an element analyzer Vario Macro CHNS Elementar Analysensysteme GmbH (Germany).

FTIR spectroscopy. Fourier-transform infrared spectroscopy (FTIR) was carried out using a spectrophotometer (Perkin-Elmer Spectrum One, USA) with KBr tablets.

Determination of molecular mass. To determine the average molecular mass of lignosulfonates, the viscometric method was used, using 0.1M NaCl water solution as a solvent. Molecular masses were found using the Mark-Houwink-Kun equation [7]. Three replicates were made for each LS sample.

*Surface tension***.** The surface tension (σ) of LS water solutions at the water-air interface was measured by a Wilhelmy plate, using a tensiometer K100M (KRUSS, Germany) at 25 °C with a circulation thermostat. The preparation of the samples and the measuring procedure were similar to those described in [8]. Three replicates were made for each sample.

Viscometry. Specific viscosity (η) was determined using a capillary viscometer Ubelhode with the flow time of pure water close to 300 ± 0.01 sec at 25.0 ± 0.1 °C similar to that described in [8], as well as a digital viscometer (Brookfield Engineering Laboratory, USA). Three replicates were made for each sample.

III. Results and discussion

Lignosulfonates are water-soluble salts of lignosulfonic acids with impurities of reducing and mineral substances, formed during the sulfite process of wood delignification. It is known that three main reactions occur in the sulfite cooking process – lignin sulfonation, its hydrolysis and condensation, which are accompanied by the oxidation of lignin, its dehydration, sulfidation, etc. In addition, industrial lignosulfonates contain hemicelluloses, which are chemically bonded to lignin due to ester bonds, as well as metal ions that are presented by ash. All these chemical conversions affect the molecular mass, chemical composition and properties of the resulting lignosulfonates.

Tables 1 and 2 show the results of the elemental and chemical analysis of three industrial lingo-sulfonates obtained at the JSC Kondopoga (Kondopoga LS), the JSC Syassky Pulp and Paper Mill (Syassky LS), and the OJSC "Vyborg Cellulose" (Vyborg LS).

TABLE 1.
Content of elements, methoxy groups and ash in lignosulfonates

Ligno-sulfonates	Ash, %	[-OCH_3], %	C, %	H, %	O, %	S, %	N, %
Kondopoga	17.21	8.78	41.53	3.68	47.84	6.95	0.25
Syassky	16.54	7.93	41.65	3.86	47.34	7.15	0.32
Vyborg	19.75	6.98	41.88	3.89	45.65	7.92	0.66

According to the conducted chemical analysis, there are differences in the elemental composition and the content of the functional groups of the studied lignosulfonates, but in general, they are not very significant. It can be seen that Kondopoga LS contain more methoxy groups – 8.78%, aliphatic and phenolic hydroxyl groups – 8.96%, as well as carbonyl groups – 3.48% that is almost 2.3 and 1.5 times higher than their content in Vyborg LS and Syassky LS, respectively. At the same time, Vyborg LS have the highest degree of sulfonation, expressed in a high content of sulfo groups – 5.75%, which is 25% higher than the content of these groups in Syassky LS and Kondopoga LS.

TABLE 2.
Content of acidic hydroxyl, aliphatic and sulfo groups in lignosulfonates

LS	[SO_3H], %	[OH], % aliphatic + phenolic	[OH], % phenolic	[OH], % aliphatic	[OH], % phenolic + carboxyl	[CO] %
Kondopoga	4.56	8.96	2.88	6.08	5.92	3.48
Syassky	4.59	6.35	2.82	3.53	6.41	2.36
Vyborg	5.75	7.24	2.28	4.96	6.97	1.49

The chemical composition of Vyborg LS is characterized by the highest content of acidic hydroxyl groups, represented by phenolic hydroxyl and carboxyl groups, and the lowest content of carbonyl groups of 1.49% compared to the other

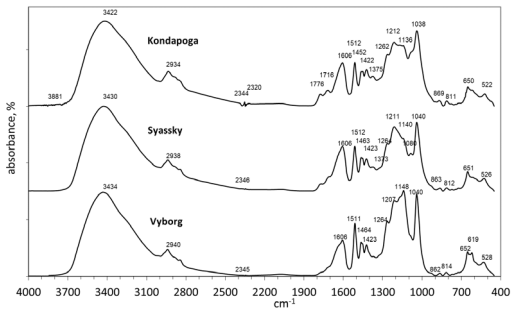

Fig. 1. FTIR spectra of Kondopoga LS, Syassky LS and Vyborg LS

Samples of lignosulfonates. It should be noted that Syassky LS contain the lowest amount of aliphatic hydroxyl groups – 3.53%, while the content of other functional groups in Syassky LS is intermediate between the functional composition of Vyborg LS and Kondopoga LS.

For more information about the functional composition of the technical lignosulfonates, the FTIR method was used. The obtained FTIR spectra of Kondopoga LS, Syassky LS and Vyborg LS are presented in Fig. 1. A qualitative comparison of the spectra shows that the lignosulfonates of various productions have insignificant differences in the functional composition. The presence of two absorption peaks at 1776 cm^{-1} and 1715 cm^{-1} due to the stretching vibrations of carbonyl groups in the aromatic and aliphatic structures of lignin [9] in the FTIR spectrum of Kondopoga LS confirms the increased content of carbonyl groups in their functional composition in comparison with Syassky LS and Vyborg LS, whose FTIR spectra in this region contain weakly pronounced these absorption bands. The absorption bands in the region of 1160-1030cm^{-1} are attributed to the planar deformation vibrations of C-H bonds in syringyl and guaiacyl derivatives of lignin [9]. A different ratio of the intensity of the absorption bands at 1148 cm^{-1} and 1040 cm^{-1} in the FTIR spectrum of Vyborg LS relative to the intensity ratio of the bands at 1140 cm^{-1} and 1040 cm^{-1}, 1136 cm^{-1} and 1038 cm^{-1} in the FTIR spectra of Syassky LS and Kondopoga LS, respectively, may be caused by the different content of these derivatives in the industrial lignosulfonates and may be confirmed by the different amount of methoxy groups in the samples. The presence of two absorption bands at 652 cm^{-1} and 619 cm^{-1}, which are attributed to the sulfo groups in lignosulfonates [2], in the FTIR spectrum of Vyborg LS, is in agreement with the increased degree of sulfonation of this lignin sample.

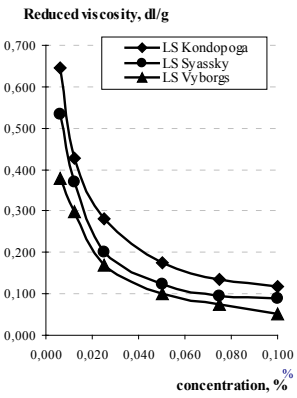

Fig. 2. Reduced viscosity of lignosulfonates depending on their concentration

The effectiveness of the practical application of lignosulfonates is determined by their properties. Fig. 2 shows the curves of the reduced viscosity of the dilute aqueous solutions of lignosulfonates depending on their concentration. It is seen that, with decreasing concentration, the reduced viscosity of lignosulfonates increases dramatically due to the presence of the polyelectrolyte effect that is caused by the ionogenic nature of these industrial lignins containing strong sulfo and weak acidic groups such as phenolic hydroxyl and carboxyl ones in their phenylpropane chains. Determination of the average molecular masses of lignosulfonates by viscometry, using the Mark-Houwink-Kun equation for their calculation, showed that Kondopoga LS with the lowest degree of sulfonation and the highest content of methoxy groups, compared to the same indicators for Syassky LS and Vyborg LS, had the highest viscosity average molecular weight equal to 41,300 Da. Vyborg LS, characterized by the highest content of sulfo groups and the lowest content of methoxy groups, had the lowest molecular mass of 34,700 Da. The value of the viscosity average molecular mass of Syassky LS was close to that of the molecular mass of Vyborg LS, to be 36,500 Da.

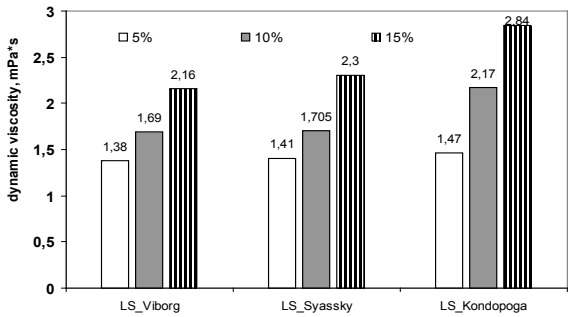

Fig. 3. Dynamic viscosity of lignosulfonates; pH 5.0

Figure 3 shows the dynamic viscosity values of moderately concentrated solutions of the technical lignosulfonates, determined with a rotational viscometer. It can be seen that, with increasing concentration from 5 to 15%, the dynamic viscosity of lignosulfonates increases 1.5-2.0 times and achieves 2.2-2.8 mPa*s. Kondopoga LS are characterized by the highest values of dynamic viscosity. It can be assumed that the higher viscosity average molecular mass of Kondopoga LS, compared with the molecular masses of Syassky LS and Vyborg LS, is the main reason for their higher values of dynamic viscosity. It is known that lignosulfonates are often used to obtain biodegradable and non-toxic emulsifiers and dispersants based on their good surface active properties. The surface activity of technical lignosulfonates from the different pulp and paper mills can be evaluated by measuring their surface tension (σ) against their concentration.

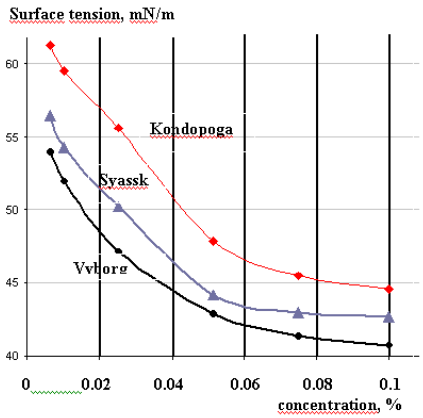

Fig. 4. Surface tension of diluted solutions of lignosulfonates at the air-water interface; pH 5.0; 22 °C

Figure 4 shows the surface tension isotherms at the air-water interface for 0.01-0.1% lignosulfonates water solutions at pH 5.0. As can be seen, surface tension is dependent on the lignin concentration and, with its increasing, the surface tension at the interface decreases. The measured values of the surface tension at the air-water interface vary from 62-54 mN/m to 45-41mN/m for 0.01-0.1% lignosulfonates water solutions, respectively, and are aligned as Kondopoga LS > Syassky LS > Vyborg LS. It is known that the ability to be adsorbed at the air-water interface, along with the solution environment, is determined by the features of the lignin molecular structure, including the molecular mass values and chemical composition, affecting their hydrophilic-hydrophobic balance. Evidently, the highest content of carbonyl groups and a higher dynamic viscosity of Kondopoga LS cause a lower surface activity of these lignosulfonates in comparison with Syassky LS and Vyborg LS. On the other hand, Vyborg LS, containing the lowest content of carbonyl groups and having a lower dynamic viscosity, has the enhanced surface activity at the air-water interface.

IV. Conclusion

The comparative chemical analysis of three industrial lignosulfonates from the Kondopoga, Syassky and Vyborg pulp and paper mills was performed. It was found that the Kondopoga lignosulfonates contained the highest content of methoxy, aliphatic hydroxyl groups and carbonyl groups. The Vyborg lignosulfonates had the highest degree of sulfonation and the lowest content of carbonyl groups. The content of the functional groups in the chemical composition of the Syassky lignosulfonates was intermediate between the functional composition of the Vyborg and Kondopoga lignosulfonates. The Vyborg lignosulfonates had the lowest values of the viscosity average molecular mass, dynamic viscosity and surface tension at the air-water interface in comparison with these indexes of the Kondopoga and Syassky lignosulfonates.

Acknowledgments

The authors have received funding for this study from the Forest Sector Competence Centre of Latvia (P2 project, No. KC/2.1.2.1.1/10/01/003).

References

[1] Qian Y., Lou H., Liu W., Yang D., Ouyang X., Li Y., Qiu X. Lignin - a promising biomass resource, TAPPI JOURNAL, March 2018.
[2] Sarkanen K. V., Ludwig C. H., Lignins, Occurrence, Formation, Structure and Reactions. Wiley Interscience, New York, 1971.
[3] Lignin: Structural Analysis, Applications in Biomaterials and Ecological Significance. Fachuang Lu (Ed), Nova Publishers, New York, 2014.
[4] Zakis G. F**.** Functional analysis of lignins and their derivatives. Atlanta: TAPPI PRESS, GA: 1994.
[5] David N.-S., Shiraishi Hon Nobuo**.** Wood and cellulosic chemistry, second edition. New York: Marcel Dekker, 2001, 931.p.
[6] Fengel D., Wegener G. Wood Chemistry. Verlag Kessel: 2003, 611p.
[7] Yean G.W., Rezanowich A., Goring D.A.I. The molecular weight and configuration of sodium lignosulphonate from spruce wood. In: Chemistry and Biochemistry of Lignin, Cellulose and Hemicelluloses. M.N. Cipkina (Ed). Moscow, 1969, pp.158–169.
[8] Shulga G., Shakels V., Aniskevicha O., Bikova T., Treimanis A. Effect of alkaline modification on viscometric and surface-active properties of soluble lignin. Cell. Chem. Technn., 40, 2006, pp. 383–392.
[9] Ahvazi B., Cloutier É., Wojciechowicz O., Ngo T.D. Lignin Profiling: A Guide for Selecting Appropriate Lignins as Precursors in Biomaterials Development. ACS Sustainable Chem. Eng., 2016, 4 (10), pp 5090–5105.

Grinding Wheel Monitoring System

Igor Nikiforov
Departament of Technology of machinebuilding
Pskov state university
Pskov, Russia
Nikiforov.i.p@mail.ru

Pavel Maltsev
Departament of Technology of machinebuilding
Pskov state university
Pskov, Russia
Inertan@gmail.com

Marina Kulakova
Departament of Technology of machinebuilding
Pskov state university
Pskov, Russia
Kulakovamarinavas@gmail.com

***Abstract*—It has been hypothesized that the change in the micro and macro geometry of the grinding wheel can be determined by a non-contact way by supplying jet of air through the nozzle of a pneumatic-electric-contact converter to the surface of the tool during operation. To confirm this hypothesis an experiment was did on a surface grinding machine. Various samples were machined, that led to self-sharpening of the tool. Grinding wheel monitoring system was developed for the experiments. System includes a device that provides the setting of the necessary working gap between the nozzle and the controlled wheel. A justification is proposed for determining the frequency of grinding wheel grinding during operation by accurately accounting for changes in the state of its surface without stopping the machining process.**

Keywords*—grinding wheel, monitoring system, self sharpening.

I. Introduction

The grinding process of various steels is characterized by self-sharpening and salting of the grinding wheel. In addition, the grains can wear out and break out of the bunch.

Self-sharpening is the process of chipping blunt abrasive grains with the emergence of new cutting edges. This process is positive, however, it leads to an intensive decrease in the dimensional accuracy of processing due to a decrease in the tool diameter and a change in the original shape of the wheel.

Salting is the process of filling the space between cutting abrasive grains with slurry. This process is negative, because the tool loses its cutting ability and cutting is replaced by elastic and plastic deformation. This increases the temperature in the cutting zone, burns and other defects appears on the treated surface.

It is important to know the state of the surface of the grinding wheel during processing, in order to obtain accurate geometrical sizes of the part, to prevent the appearance of defects on the surface and identification of the need to dressing of the wheel.

There are some methods to measure the linear wear of the grinding wheels and to monitor the state of its surface: contact and non-contact, with stopping the grinding process and without stopping. Let's look at main examples.

There is an indirect method to measure the wear of diamond grinding wheels by measuring the cutting force.

The degree of wear of the diamond wheel can be estimated by the level of forces and restore its cutting properties in a timely manner. Many researchers made an experimental determination of value and nature of changes in cutting forces during grinding process by using various measuring tools. Firstly, the cutting force was determined by measuring the power developed by the electric motor during grinding with a wattmeter. The value of the tangential component of the cutting force was determined by calculation. This method is simple, but it does not allow to measure the components of the cutting forces and is not accurate, because it determines the total power, including friction losses in the machine mechanisms. Dynamometric devices can be used to directly measure the component forces. However, this method is valid only when parts are installed in centres [1].

There is a method of contactless determination of the wear of the grinding wheel according to the parameters of the vibration of the machine. The essence of this method is the measurement of the distance between the grinding wheel and the capacitive sensor. Capacity changes with relative fluctuations. Changing the capacitance using a special amplifier is converted into an electrical signal, which is recorded by a recording device. This method almost does not find practical application, because it has low measurement accuracy and it is characterized by the complexity of processing the measurement results and significant errors [5]. Based on the research [2] was found that the wear of the grinding wheel can be determined by the statistical parameters of the signal of vibration acceleration. The appearance of new vibration components in the range of 2000 ... 2200 Hz was revealed from the spectra of vibration accelerations. Obtaining harmonics of vibration accelerations in two directions allow to get rid of

Print ISSN 1691-5402
Online ISSN 2256-070X
http://dx.doi.org/10.17770/etr2019vol3.4107

the noise components in the signal and solve the problem of diagnosing tool wear at any stage of work.

There are several studies on the measurement of wear and the topography of the grinding wheel by examining changes in hydrodynamic pressure during operation. The studies are based on the analysis of the change in pressure of the fluid that was applied between the grinding wheel and the workpiece being processed. To measure the hydrodynamic pressure used several pressure sensors, which are installed directly near the wheel and the workpiece. When the wheel is worn, the gap between it and the sensor increases, which leads to a decrease in pressure. [3]

Also known methods for contactless analysis of the state of the surface of the grinding wheel using the indicator and optical devices, step-by-step photographing and laser projection with 3D-modeling. Most optical methods are based on laser triangulation. The main elements of the installation: a laser diode and a position-sensitive detector with an amplifier and two lenses [4], [6].

II. Materials and methods

One of the most promising is the non-contact pneumatic method for measuring grinding wheels. For this purpose, it is proposed to use bellows-type pneumatic-electric-contact converter, the principle of action of which is based on the change in air pressure in the bellows chamber, when the gap between the nozzle and the measured surface changes. In Fig. 1 shows a diagram of bellows pneumatic-electric-contact converter.

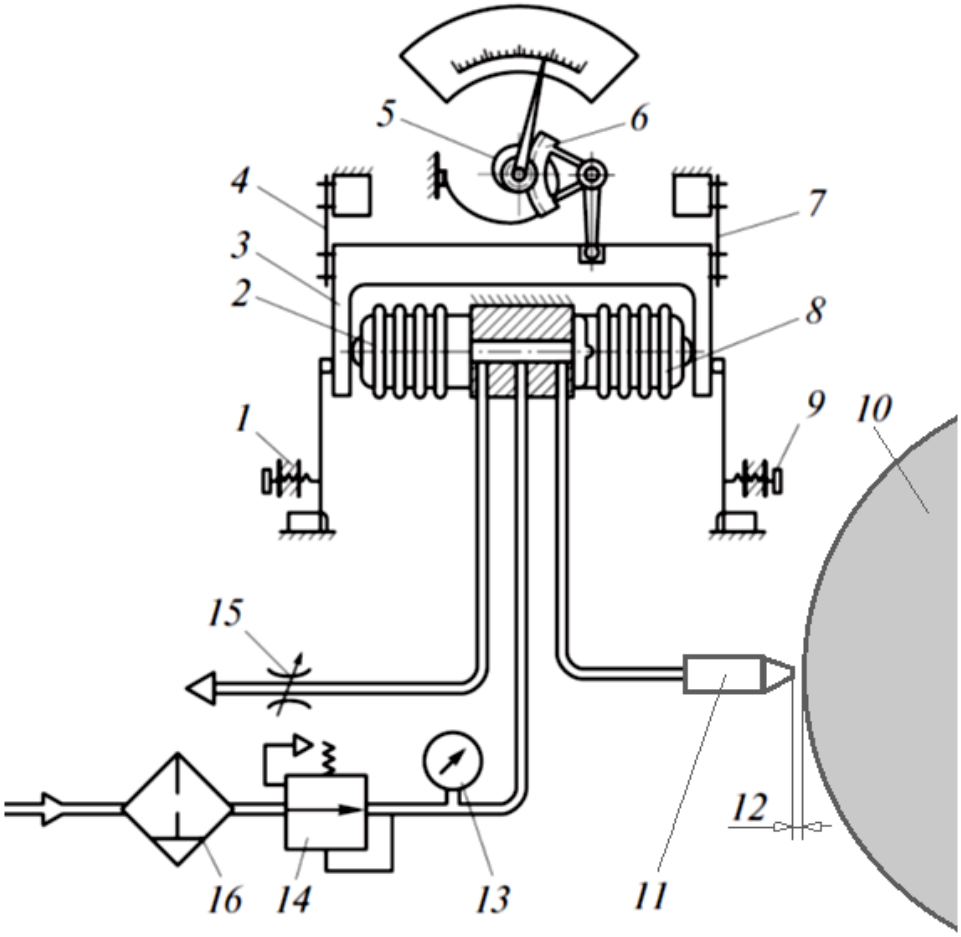

Fig. 1. Scheme of pneumatic-electric-contact convector.

Compressed air is supplied from the compressor through the filter 16 and the reducing valve 14 in the cavity of the left 2 and right 8 bellows (closed brass vessels with corrugated walls). At the same time, the air enters the nozzle 11 and the backpressure valve 15, which is an adjustable air throttle.

The air flow through the valve 15 (at a certain setting) will be constant; the pressure in the left bellows will also remain unchanged. The air flow through the nozzle 11 and the pressure in the right bellows will depend on the actual size of the gap 12 between the surface of the controlled grinding wheel 10 and the end face of the nozzle 11.

When the grinding wheel is worn, the gap 12 between the nozzle 11 and the wheel 10 will increase, the pressure in the right knee of the sensor will decrease, the right bellows will compress, and the left one will stretch. Frame 3, suspended from the sensor body on flat springs 4 and 7, will displacement to the left and close the adjustable contact 1. There can be up to six such contacts in commercially available sensors, which close at a different

value of displacement of the frame 3 in one direction or another. Thus, the whole measurement range can be divided into seven intervals. This allows simplifying the automation of dressing of the grinding wheel.

The use of a differential circuit (with an adjustable backpressure valve) increases the sensitivity of the sensor and reduces requirements for stabilizing the air pressure controlled by a manometer 13. The converter is equipped with a indicating device: the frame 3 turns the toothed sector 6, which is connected to the arrow.

The appearance of the pneumatic-electric-contact converter is shown in Fig. 2, and as a whole grinding wheel monitoring system – in Fig. 3. The system includes the following components: a compressor (not shown in the figure); air preparation unit 1, in which the air is dried and separated from moisture; choke 2; pressure stabilizer 3; pneumatic-electric-contact converter 4; backpressure valve 5; adjusting device 6 with a nozzle (to regulate the size of the gap); grinding wheel 7, connecting pipes.

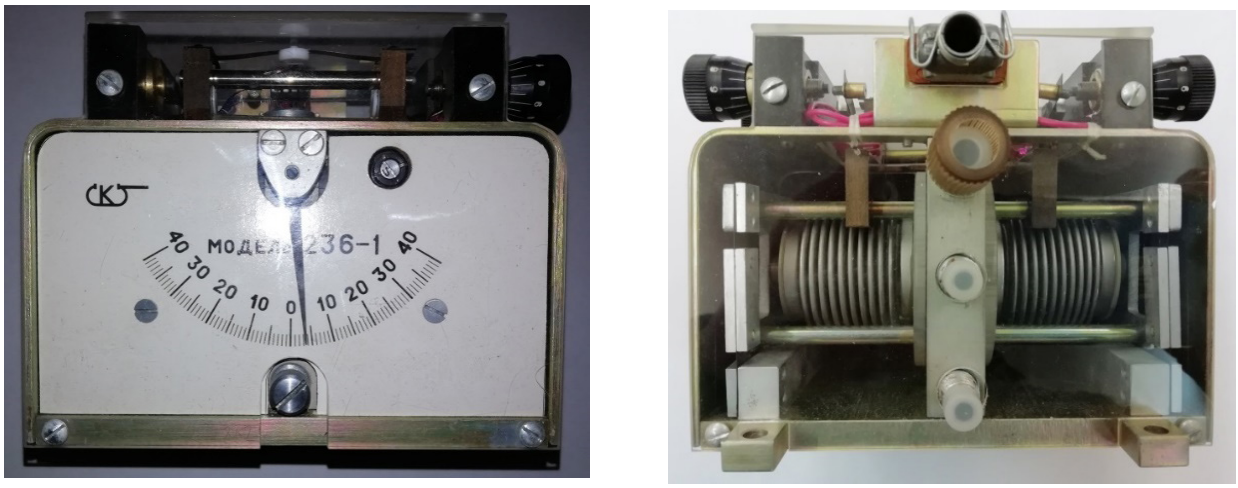

a) b)

Fig. 2. Appearance of pneumatic-electric-contact converter: a — front view; b — rear view.

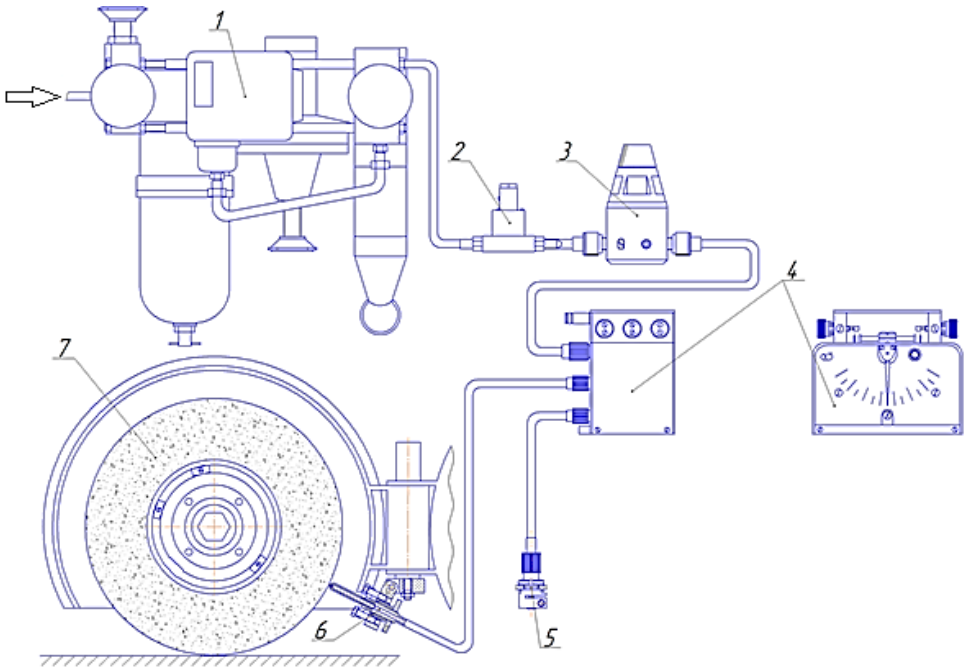

Fig. 3. Grinding wheel monitoring system.

The design of the adjusting device is shown in fig. 4. The adjusting device consists of a bracket 1 mounted on a support 2. A housing 3 is located rotatably around an axis 4 on bracket 1. There is an adjustment screw 5 in the housing 3, which containing a guide screw 6 with a fitting 7. A nozzle 8 is fixed in the guide screw 6.

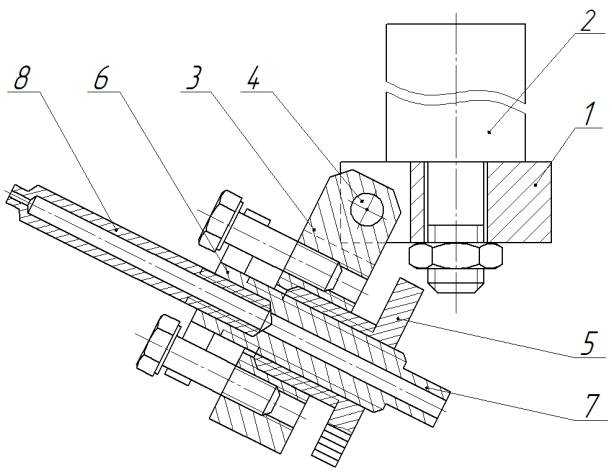

Fig. 4. Adjusting device

The adjusting device operates as follows: support 2 is fixed in the housing protection grinding wheel. The housing 3 with its rotation around the axis 4 positions the axis of the nozzle 8 radially relative to the grinding wheel. The movement of the nozzle 8 to the center of the grinding wheel is carried out by turning the adjusting screw 5, which causes the guide screw 6 to move. The thread pitch on the surface of the adjusting screw 5 is larger than that of the guide screw 6, which makes it possible to feed the nozzle 8 smoothly. Air is supplied through fitting 7.

The calibration was performed before the experiment. Wheel dressing was made by a diamond pencil. Depth of dressing was established by a limb of vertical feed of the grinding head of the machine, with an accuracy of 1 micron. The measurement of the radial size of the circle was carried out continuously in the process of dressing. The value of change in the radial size of the circle is equal to the vertical feed. The graduation of the pneumatic-electric-contact convector is 0.2 – 2 microns. The required pressure (3,6 MPa) was set using a stabilizer (pos. 3 Fig. 3), which provided a change in the position of the convector arrow by 1 mark on the scale when dressing a wheel by 1 micron.

III. Results and discussion

The calibration was performed before the experiment. Wheel dressing was made by a diamond pencil. Depth of dressing was established by a limb of vertical feed of the grinding head of the machine, with an accuracy of 1 micron. The measurement of the radial size of the circle was carried out continuously in the process of dressing. The value of change in the radial size of the circle is equal to the vertical feed. The graduation of the pneumatic-electric-contact convector is 0.2 – 2 microns. The required pressure (3,6 MPa) was set using a stabilizer (pos. 3 Fig. 3), which provided a change in the position of the convector arrow by 1 mark on the scale when dressing a wheel by 1 micron. Setting error is 0,003% on the passport of convector.

Samples made of stainless steel P900 were processed on a surface grinder 3G71 by the grinding wheel 1 250x20x76 WA F30 L6V 50 2 made of aluminum oxide white with using the proposed monitoring system. The cutting conditions are as follows: depth 5 μm per double stroke, longitudinal feed 12 m/min.

The results of this experiment and the graphs shown in Fig. 5. The experiment was conducted with a triple repetition. The homogeneity of the dispersion was evaluated by the Cochren criterion.

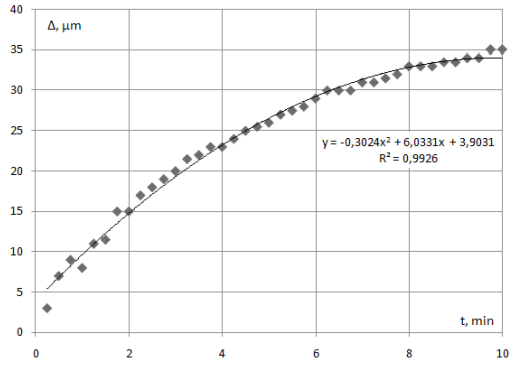

Fig. 5. Plot of dependence wear of grinding wheel on the time

The abscissa axis is the time (t) in minutes; the ordinate axis is the wear (Δ) of the wheel in micrometers. The resulting graph describes the mode of running-in tool and normal wear, and therefore, the proposed system can be used to assess the state of the grinding wheel during processing.

The condition of the surface of the wheel after processing is shown in Fig. 6. A characteristic change in the state of the circle during the processing of the steel is an intensive self-sharpening with grain chipping, accompanied by local salting.

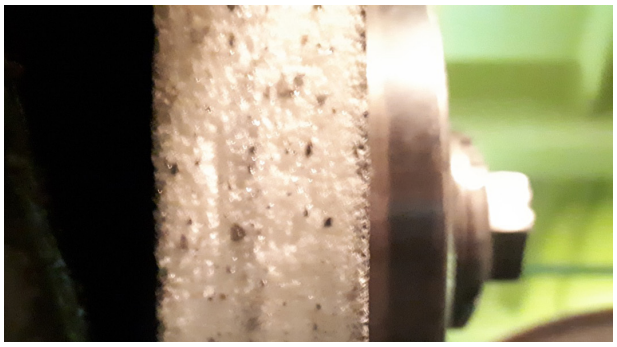

Fig. 6. The condition of the surface of the wheel after processing

IV. Conclusions

The developed system can be used in mass production to determine the frequency of dressing of the grinding wheel when processing small blanks, and to assess the condition of the wheel and to increase dimensional accuracy when processing large-sized blanks. In a single production, the developed system can be used to assess the state of a circle, determine the processes occurring during grinding and the need for dressing.

References

[1] E. N. Maslov, Theory of grinding materials. Moscow, RU: Machinebuilding, 1974.

[2] A. M. Zahezin and T.V. Maluisheva, Determination of grinding wheel wear by machine vibration parameters. Chelyabinsk, RU: Vestnik YUGU, 2007, №11, pp. 48–53.

[3] K. Furutani, N. Ohguro1 and N. Trong, In-process Measurement of Topography of Grinding Wheel by Using Hydrodynamic Pressure. Nagoya, JP: Toyota Technological Institute.

[4] H. K. Toenshoff, B. Karpuschewski, F. Werner, Fast Sensor System for Diagnosis of Grinding Wheel and Workpiece. Cincinatti, Ohio, USA: 5th Intern. Grinding Conf., 1993.

[5] B. E. Bolotov and V. V. Trubnikov, “Method for contactless measurement of grinding wheel vibrations”, SU Patent 444632. September 30, 1975.

[6] A. McDonald, Investigation of Grinding Wheel Wear Using a White Chromatic Sensor, Nova Scotia, CA: Dalhousie University Halifax, 2015.

Environment. Technology. Resources. Rezekne, Latvia
Proceedings of the 12th International Scientific and Practical Conference. Volume III, 197-200

Determination of Chamber and Piston Geometry for a Rotary Type Expansion Machine

Andrey Perminov
Department of Electric Drive and Automation Systems
Pskov State University
Pskov, Russia
alp-mail@mail.ru

Yury Zhuravlev
Department of Road Construction
Pskov State University
Pskov, Russia
drakon426@mail.ru

Yury Lukyanov
Department of Electric Drive and Automation Systems
Pskov State University
Pskov, Russia
luk-yra@mail.ru

Sergey Tikhonov
Department of Mechanics and Motor Trantsport Service
Pskov State University
Pskov, Russia
sit42@rambler.ru

Alexander Ilyin
Department of Electric Drive and Automation Systems
Pskov State University
Pskov, Russia
al.ilyin@yandex.ru

***Abstract*—The article deals with the determination of chamber and piston geometry for a rotary expansion machine. Analytical expressions for the working surface area of piston and for chamber volume are derived. Three defining parameters of the expansion machine were obtained: gas dynamic machine constant Cp; constant M0 connecting torque and Cp; the main dimensionless parameter of the machine Q0, which relates the volume of the chamber and the torque.**

***Keywords*—power generation system, rotary engine, lever-cam motion converter.**

I. Introduction

The subject of this article is the rotary type expansion machine protected by patent RU2619391 [1].

Fig. 1 shows a piston 1 (AB), which is in a fixed position given by the polar angle α=-45° between the interpolar radius $OA=\rho_A=\rho(\alpha)$ and the axis Ox. In this position, the volume of the chamber is maximum, while

$$\rho_A = \rho_B = L \cdot \sin(a + b \cdot \cos 2\alpha) = \frac{\sqrt{2}}{2} L, \quad (1)$$

where L is the distance between the axes of the piston hinges, $a=\pi/4$; $b=\pi/4-\psi_{min}/2$, and where ψ_{min} is the minimum angle between the pistons.

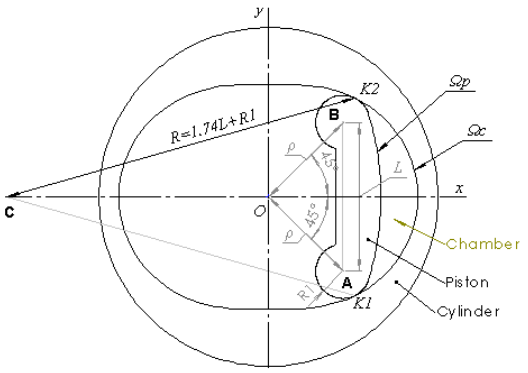

Fig. 1. Piston in a fixed position given by the polar angle

The piston profile Ω_P relates to the equidistant surface of the cylinder Ω_C at two points K_1 and K_2. A chamber is formed between these points and the surfaces, the volume of which V_K with α=-45° should have the specified maximum value V_0, i.e.

$$V_K=V_K(L, R_1, t)=t \cdot S_K(L, R_1)=V_0, \quad (2)$$

where t is the piston thickness; R_1 is the radius of the end curves of the piston; $S_K(L, R_1)$ is the chamber area.

The task is to obtain the specified value of the chamber volume with different variants of the values of three geometric parameters L, R_1, t.

To do this, we need to compile some functional and get values of parameters $L,R_1, t,$ which deliver the extremum to the functional.

II. Analysis of Geometric Constraints

A. Preliminary notes

For the presence of extremum the influence of the three quantities $L,R_1,t,$ must be multidirectional.

We will try to solve the problem of determining the geometric dimensions of L,R_1, t, based on the analysis of the restrictions imposed on the geometry of the machine for one reason or another. Consider three of them: 1) cross section size of cylinder; 2) volume of chamber; 3) torque.

B. Cross section size of cylinder

When making a cylinder from a single piece, the diameter must be available for processing equipment. From this point of view, and also proceeding from economy of metal and reduction in price, the size of the cylinder L_C (Fig. 2) should be as small as possible. Let the upper value of the size of the cylinder L_C be given, which we denote by $L\hat{}_C$.

Print ISSN 1691-5402
Online ISSN 2256-070X
http://dx.doi.org/10.17770/etr2019vol3.4060

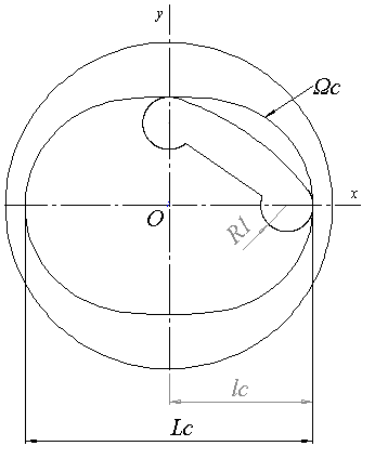

Fig. 2. Piston in a fixed position given by the polar angle α=0°

From Fig. 2 follows

$$\frac{1}{2}L_c = \rho_A(0) + R_1 = L\sin(a+b) + R_1 = 0.819L + R_1. \quad (3)$$

The constraint in question is described by the inequality

$$0.819L + R_1 \le \hat{L}_c/2. \quad (4)$$

C. Volume of chamber

The chamber volume is a pi-periodic function of the angle of rotation of the shaft α, which varies in the range V_{min}... V_{max}. The term "chamber volume" is understood as the value V_{max} , which is described by the approximate expression [2]

$$V_K(L, R_1, t) = (0.15L^2 + 0.54L\,R_1 + 0.49R_1^2) \quad (5)$$

If based on thermal calculations, this volume must be equal to the specified value V_0 , we will have a limitation

$$V_{max}(L, R_1, t) = V_0. \quad (6)$$

D. Torque

The torque M_T is a π/2-periodic function of the angle of rotation of the shaft , which, being expanded in a Fourier series, has a constant component

$$a_0 = \frac{1}{\pi/2}\int_0^{\pi/2} M_T(\alpha)\,d\alpha. \quad (7)$$

For a given nominal power N_N and nominal angular velocity ω_N , the value can be considered known and equal to [3]

$$a_0 = \frac{N_N}{\omega_N} \quad (8)$$

According to [3] for torque

$$M_T(\alpha) = \frac{L}{2}[(F_2 + F_4)(1 - 2b\sin 2\alpha) - (F_1 + F_3)(1 + 2b\sin 2\alpha)]\sin(2b\cos 2\alpha), \quad (9)$$

where $2b=2\cdot0.1749=0.35$. Considering that the gas forces acting on the pistons are $F_3=F_1=p_1(\alpha)S_P$, $F_4=F_2=p_2(\alpha)S_P$, where $p_1(\alpha)$ and $p_2(\alpha)$ are the gas pressure on the pistons 1 and 3, and 2 and 4, respectively, and where S_P is the working surface area of the piston $S_P=2|y_{K1}|t=2(0.5L+0.9R_1)t$, or $S_P=(L+1.8R_1)t$. Expression [9] takes the form

$$M_T(\alpha)=(L^2+1{,}8LR_1)t\,[p_2(\alpha)(1-0.35\sin2\alpha) - p_1(\alpha)(1+0.35\sin2\alpha)]\sin(0.35\cos2\alpha). \quad (10)$$

Substituting (10) into (7) and introducing the designation of a parameter

$$CP = \frac{2}{\pi}\int_0^{\pi/2} p2(\alpha)(1 - 0.35\sin 2\alpha) - p1(\alpha)(1 + 0.35\sin 2\alpha)]\sin(0.35\cos 2\alpha)d\alpha \quad (11)$$

We arrive at a torque-induced geometry limitation.

$$(L^2 + 1{,}8LR_1)t = \frac{a_0}{C_p} \quad (12)$$

Note that the constant C_P is an important gas-dynamic parameter of machine. It depend only on the gas pressure in the chambers and depend on the geometry of the chambers.

III. Determination of basic geometric dimensions

The main dimensions of the machine are three parameters: the inter-joint distance on the piston $AB=L$, the radius of the end curves of piston $R_1$and the thickness of piston t.

A. Initial equations

Three equations (5), (12) and (6), respectively, describing the restrictions on the size of the cylinder L_c , on the torque M_T and on the volume of the chamber V_0 :

$$\begin{aligned} &0.819L + R_1 \le \hat{l}_c, \\ &(L^2 + 1{,}8LR_1)t = m_0, \\ &(0.15L^2 + 0.54LR_1 + 0.49R_1^2)t = V_0. \end{aligned} \quad (13)$$

Here, for the sake of brevity, new notation has been introduced $m_0=a_0/C_P$, $\hat{l}_C=\hat{L}_C/2$, in which a_0 and C_p are defined by (8) and (11), respectively.

If we specify the size of the cylinder $\hat{l}_C=l$, the inequality in (13) becomes equal to $0.819L+R_1=l$.

The formulation of the solution of the problem on the basis of three equations, two of which are non-linear, may be different. There is no guarantee that a solution exists.

It is quite obvious, for example, that with a very small cylinder size $l\hat{}_C$, it is not possible to create the required torque a_0, or the specified volume of the chamber V_0.

B. Common Solution

Let cylinder size $l\hat{}_C=l$ be given. Then we have a system of three algebraic equations.

$$0.819L+R_1=l,$$
$$(L^2+1.8LR_1)t=m_0,$$
$$(0.15\,L^2+0.54\,L\,R_1+0.49\,R_1^2)t=V_0 \quad (14)$$

From the first equation we express R_1 through L : $R_1=l-0.819L$. From the second equation we express t through L:

$$t=\frac{m_0}{L^3+1.8L(l-0.819L)},\ or\ t=\frac{m_0}{1.8Ll-0.474L^2}$$

, or Substituting into the third equation:

$$[0.15L^2+0.54L(l-0.819L)+0.49(l-0.819L)^2]\frac{m_0}{1.8Ll-0.474L^2}=V_0$$

By opening the brackets and grouping the terms, we get the equality

$0.0367L^2-0.263Ll+0.49l^2=V_0/m_0(1.8Ll-0.474L^2)$, from which the quadratic equation follows on the size of L:

$$aL^2+bL+c=0 \quad (15)$$

where $=0.474\,V_0/m_0+0.0367$, b=-(1.8 V_0/m_0 +0.263)l, c=0.49 l^2 , whose solution has a well-known appearance

$$L_{1,2}=\frac{-b\pm\sqrt{b^2-4ac}}{2a} \quad (16)$$

Considering that V_0 is the volume of the camera and $m_0=a_0/C_p$ is a parameter characterizing the torque according to (10) and having the dimension m^3 we introduce the dimensionless machine parameter

$$q_0=\frac{V_0}{m_0} \quad (17)$$

We write the coefficients of equation (15) in the form

$$a=0.474q_0+0.0367,$$
$$b=-(1.8q_0+0.263)l,$$
$$c=0.49\,l^2.$$

C. Common Solution Analysis

It is known that the number of real solutions of equation (15) depends on the discriminant sign $D=b^2-4ac$: *if* $D>0$, then there are 2 solutions (2 real roots); $D=0$, then there is 1 solution (2 matching roots); $D<0$, then there are 0 solutions (2 imaginary roots).

We make the discriminant the coefficients of which are determined by (17):

$$D=l^2(3.24q_0^2+0.016q_0-0.0027) \quad (18)$$

The value of the parameter $q_0=V_0/m_0$, for which $D=0$. Rejecting the negative root, we get

$$q_0=\frac{V_0}{m_0}=0.0265 \quad (19)$$

When $q_0=0.0265$ there is one solution, i.e. two coincident positive roots $L_1=L_2=-b/2a=3.15$l When $q_0<0.0265$ there are no solutions; at $q_0>0.0265$ there is one positive solution for L. At the same time, the presence of a solution for L does not guarantee the presence of positive solutions for R_1 and t.

For convenience, let's move on to the dimensionless variables.

$$L'=\frac{L}{l},\ R_1'=\frac{R_1}{l},\ t'=\frac{t}{l}. \quad (20)$$

values will be positive if the inequality
$l(1-0.819L')>0$ is satisfied, or the condition
$L'<1.22$.
Find the value of q_0, for which ,
$L'<1.22$, $R'=0$.
After the transformations we get the solution
$q_0=0.15$.

Thus, for R_1 to be greater than zero, the machine parameter connecting the chamber volume and torque $q_0=V_0/m_0=V_0/(a_0/C_p)$ must be greater than 0.15.

The results of calculations of dependences L'=L/l, R_1'=R_1/l and t'=t/l multiplied by l^3/m^0, from q_0 are shown in Table 1

TABLE 1

q_0	L'=L/l	$R_1'=R_1/l$	R_1/L	$(t'l^3)/m_0$
0.15	1.22	0	0	0.45
0.175	1.00	0.181	0.181	0.754
0.20	0.996	0.184	0.185	0.756
0.25	0.841	0.311	0.370	0.850
0.30	0.730	0.402	0.550	0.940
0.50	0.475	0.610	1.280	1.340
1.00	0.254	0.792	3.120	2.340

The table has a range of $0.175\le q_0\le 0.3$. This range has practical interest due to the fact that the ratio R_1/L from design considerations should not be greater than 0.5. Graphically, this range is shown in Fig. 3. The dotted line shows the relation R_1/L.

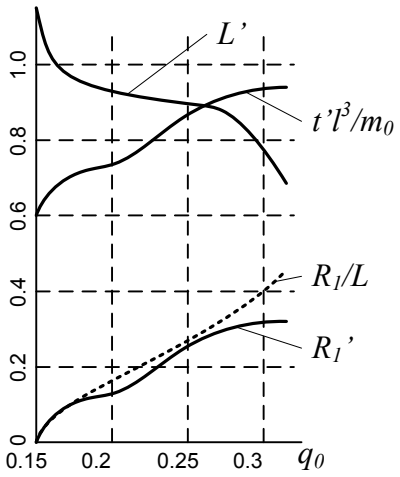

Fig. 3.

IV. Conclusions

The main result is the identification of several important parameters of rotary expansion machine.

First of all, this is the gas-dynamic constant $C_P(H/м^2)$ defined by (11). It depends only on the initial and final pressure of the gas and does not depend on the geometrical dimensions of chamber and piston.

The second parameter is $m_0=a_0/C_P(m^3)$, which relates the torque and the gas dynamic constant.

The third, which can be called the main dimensionless rotary expansion machine parameter, is $q_0=V_0/m_0$, which relates the chamber volume and torque, and, as was established above, its value should be in the range of $0.15<q_0<0.3$.

References

[1] RF Patent 2619391 for an invention. Int. Cl. F01C1/44. Rotary Expantion Machine / Y.N. Lukyanov, Y.N. Zhuravlev et al. Publ. 15.05.2017.

[2] Y.Zhuravlev, A.Perminov, Y.Lukyanov, S.Tikhonov, A.Ilyin, S.Semyonov, Optimization of Mechanical Strength of Rotary-Vane Engine. "Environment. Technology. Resources - Proceedings of the 11th International Scientific and Practical Conference", 2017. DOI: 10.17770.

[3] S.Semyonov, S.Tikhonov, Y.Lukyanov, A.Perminov, Analysis Method of Calculation Parameters of Heat and Mass Transfer Processes in the Stirling Engine. "Environment. Technology. Resources - Proceedings of the 11th International Scientific and Practical Conference", 2017.

[4] Y. N. Zhuravlev, I. V. Plokhov, Y. N. Lukyanov, and others, Calculation and Design of Rotaty-blade Machine with External Heat Supply. Monogrphy. Pskov, 2012.

[5] Y. N. Zhuravlev, I. V. Plokhov, Y. N. Lukyanov, and others, Mathematical Models of Physical Processes in Rotary-blade Engine with External Heat Supply. Monogrphy. Pskov, 2012.

[6] Y. N. Zhuravlev, A. L. Perminov, Y. N. Lukyanov, S. I. Tikhonov, S. N. Semenov, Minimization of Mechanical Strength of Rotary-blade Heat Engine with Cam-and-lever Motion Transformer. Bulletin of Pskov State University. Series: Engineering scinces, 2016. # 4.

[7] RF Patent 2374526 for an invention. Int. Cl. F16H25/04. Mechanism for converting motion / Y.N. Lukyanov, Y.N. Zhuravlev et al. Publ. 27.11.2009. Bull. Number 33.

[8] RF Patent 2387844 for an invention. Int. Cl. F01G1/077, F02G1/044. Rotary-vane engine with an external supply of heat / .N. Lukyanov, Y.N. Zhuravlev et al. Publ. 27.04.2010. Bull. Number 12.

[9] Perminov A., Lukyanov Y., Tikhonov S., Ilyin A. Thermodynamic cycle with two-component working fluid. "Environment. Technology. Resources - Proceedings of the 11th International Scientific and Practical Conference", 2015. DOI: 10.17770/etr-2015vol2.261.

[10] A. L. Perminov, A. A. Khitrov, A. I. Khitrov, Mechatronic System "Magneto-electric Synchro Motor – Active Rectifier" for Autonomous Energy Station Using Rotary-blade Machine with External Heat Supply. "Proceedings of VII International (VIII Russian) Conference on Automotization Electrical Drives AEP-2012", Ivanovo State Energy University, Ivanovo, 2012. P. 330–335

[11] A. L. Perminov, Y. N. Lukyanov, S. I. Tikhonov, Electrogenerators fot Energy Sets. "Electrical Engineering. Electrical Energy. Information Techlogies. Proceedins of I International Research and Prctice Seminar", Pskov. 2018. P. 52–55.

The Model of the Constriction Resistance of a Sliding Electrical Contact

Igor Plokhov
Department of Drive and Automation System
Pskov State University
Pskov, Russia
igor_plohov@list.ru

Igor Savraev
Department of Drive and Automation System
Pskov State University
Pskov, Russia
igor_savraev@mail.ru

Alexander Markov
Department of Drive and Automation System
Pskov State University
Pskov, Russia
markov-am55@mail.ru

Oksana Kozyreva
Department of Drive and Automation System
Pskov State University
Pskov, Russia
ks_33n@mail.ru

Nikita Kotkov
Department of Drive and Automation System
Pskov State University
Pskov, Russia
4ce@goodgame.ru

Yulia Domracheva
Department of Drive and Automation System
Pskov State University
Pskov, Russia
juli-politeh@yandex.ru

***Abstract*—This article is devoted to a theoretical study of the processes in a sliding electrical contact and the derivation of the formula for constriction resistance in the transient layer of electrical sliding contact taking into account the fractal heterogeneity of contact current-transmitting clusters, as well as the verification of the obtained theoretical formulas using a static experimental plant.**

***Keywords*—brush, experimental plant, modeling, sliding contact.**

I. Introduction

Each scale of heterogeneity of the contact zone of a sliding electrical contact (SEC) corresponds to the component of the general constriction resistance [1]. R.Holm proposed to consider two components corresponding to the constriction to the group of spots and corresponding to the constriction within the boundary of this group. Equation for bodies with the same resistivity ρ containing one group of round uniformly distributed spots is derived:

$$R_{rctr} = R_1 + R_2 = \rho \cdot \left(\frac{1}{2na} + \frac{1}{2a_k} \right), \quad (1)$$

where n - the total number of contact spots; a - the radius of the spot; a_k - the radius of the circle within which the contact spots are placed; R1, R2 - the resistance components corresponding to the constriction to the spots and to their groups.

J.A.Greenwod [18] specified clarified the second part of the equation:

$$R_{rctr} = R_1 + R_2 = \left(\frac{1}{2na} + \frac{16}{3\pi^2 a_k} \right) \quad (2)$$

and showed that its value is almost the same for any location of contact spots in the general group.

The Greenwood equation was extended by terms that took into account the asymmetry of the spot groups distribution (clusters) on each other as well as the asymmetry of the groups distribution on the nominal area [2], [8-9], [21].

Theory of the electrofriction interaction is currently at a critical stage which is characterized by a large number of accumulated empirical data, hypotheses and various types of models that can not sufficiently claim the adequacy of the presentation of the studied phenomena. To overcome these contradictions, it is necessary to attract new physical views and ideas to this applied area of knowledge.

The theory of self-organizing systems (synergetics and the fractal theory) is rapidly developing nowadays. These systems are self-similar evolutionary structures which cannot be described using Euclidean geometry.

The synergetics studies the processes of self-organization, of stability and of decay of structures of different nature formed in open systems, the ordered state of which is related to the consistent behavior of the subsystems. It leads to the formation of organized structures as a result of the exchange of energy and matter with the environment, when a certain balance between a production and a reduction of entropy is established [3-4], [11]. The evolution of the system considers as a transition through a number of thermodynamic quasi-equilibrium states. Fractal theory [5-6] was the basis for quantitative description of self-organizing structures using the fractal dimension parameter.

The processes of electrofrictional interaction will be considered from the standpoint of the synergetics and of the fractal theory, because the sliding electrical contact is an open system and evolutionary processes of the origin and decay of conducting clusters, which can be interpreted in the tangential direction as fractal and in the radial direction as percolation clusters, there are in the intermediate layer [6], [12], [17], [19-20].

From told above we can conclude that on the problem of explaining the mechanism of current transfer through sliding contact a one frame of mind has not yet developed. There are different interpretations of the processes of current transfer in the intermediate layer. It leads to the

Print ISSN 1691-5402
Online ISSN 2256-070X
http://dx.doi.org/10.17770/etr2019vol3.4071

Published by Rezekne Academy of Technologies.

fact that the most reliable and frequently used means of studying of the properties and of the characteristics of sliding contact today is an experiment. This situation is also due to the absence of modeling software products for calculating the basic integral characteristics of the sliding contact according to the data containing the parameters of contacting bodies, their surfaces, as well as external energy influences.

Therefore, work aimed at creating computational models that allow one to obtain static and dynamic characteristics of brush-contact device by calculation at the design stage are very relevant.

II. MATERIALS AND METHODS

The direct conductivity in the sliding contact occurs when the microasperities in the intermediate layer of the contacting microreliefs come into direct contact. In addition, we will assume that as a result of fritting, conductivity similar to the direct conductivity also occurs.

The main component of the transient resistance of the sliding electrical contact is the constriction resistance, which is caused by the distortion of the current lines in the region of each individual contact spot of rough surfaces. Many scientific works are devoted to studies of contact conductivity and constriction resistance, for example [7], [10], [23].

To determine the transient resistance in the computational models of the electrofriction interaction it is necessary to define a mathematical expression for the intermediate resistance of an individual contact cluster. Therefore, we will derive mathematical expressions that give a topological and fractal representation of the constriction resistance and compare the obtained results with the known ones.

In the simplified version of the calculation we will set a single round contact spot of radius ro. Such unification in a single area is acceptable with a sufficiently compact placement of conducting clusters. We will divide the surrounding half-space into two zone A and B for determination the constriction resistance. The zone A is bounded by the hemisphere of the spot of the contact with radius r_o, and the zone B is bounded by the hemisphere with radius $r_m >> r_o$. Let's call these areas in accordance with their placement of a relatively small "contact" hemisphere: A – "internal", B – "external".

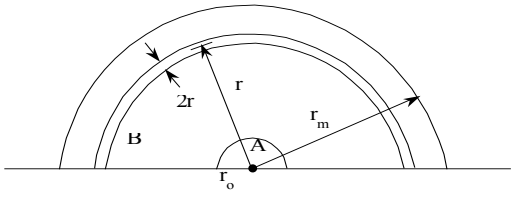

Fig.1. Approximate definition of the constriction resistance of the round spot of contact.

Selecting the volume located between two spheres with radius r+dr/2 and r–dr/2 in zone B we determine the resistance dRB of this layer in the direction of the current lines:

$$dR_B = \rho \frac{dr}{2\pi r^2} \tag{3}$$

The current lines in zone B are directed radially and the specified spherical volume is limited by equipotential surfaces. In this case we assume that the current lines connect the superconducting spheres with radius r_o and $r_m >> r_o$. Then the resistance R_B of the zone B is determined by integrating of the previous formula:

$$R_b = \frac{\rho}{2\pi}\int_{r_0}^{r_m}\frac{dr}{r^2} = \frac{\rho}{2\pi}\left(\frac{1}{r_0} - \frac{1}{r_m}\right) \tag{4}$$

Taking into account that $r_m >> r_o$, we find the "external" component of the constriction resistance by the formula:

$$R_B = \frac{\rho}{2\pi r_0} \tag{5}$$

We define the "internal" component approximately from the consideration of replacing a hemisphere with a cylinder with the equivalent height and the same area of the base and with non-conducting side walls. We find the height of the cylinder by the condition of equality of the volumes of the hemisphere and the cylinder:

$$h = \frac{2}{3}r_0;\ R_A = \frac{\rho}{6\pi r_0} \tag{6}$$

Then the total constriction resistance is

$$R_{rctr} = R_A + R_B = \frac{2\rho}{3\pi r_0} \approx \frac{\rho}{4{,}71 r_0} \tag{7}$$

We calculate the "internal" resistance (hemisphere A) by integrating the conductivities of the elementary ring-shaped areas shown in Fig. 2 to clarify the constriction resistance.

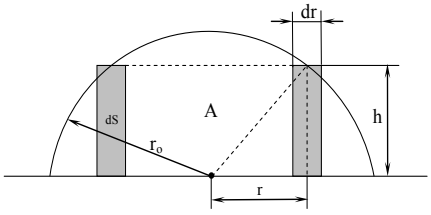

Fig. 2. Clarifying constriction resistance.

The conductivity of the annular region dr is

$$G_h = \frac{ds}{\rho\sqrt{r_0^2 - r^2}} \tag{8}$$

where - the area of the horizontal cross section.

The conductivity of the sphere A is defined as follows:

$$G_a = \int_0^{r_0}\frac{2\pi r}{\rho\sqrt{r_0^2 - r^2}}\,dr \tag{9}$$

After integration within the given limits and after tran-

sition to the inverse value we obtain an equation for the resistance of the zone A

$$R_A = \frac{\rho}{2\pi r_0} \tag{10}$$

Then the constriction resistance is defined as the sum

$$R_{retr} = R_A + R_B = \frac{\rho}{\pi r_0} \tag{11}$$

We obtain an underestimated value in the first version of the calculation and an overestimated value in the second version of the calculation in comparison with the classical formulas.

The most correct result is obtained by integrating of the conductivity in all volume of the half-space. We select for this purpose in the zone B the elementary areas which are the difference of the volumes of two truncated cones with corners at the vertices: 2α и 2(α+dα) (see Fig. 3).

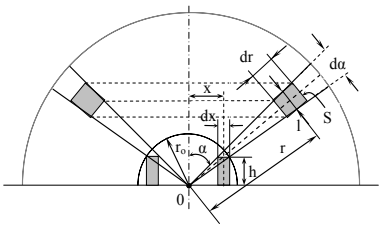

Fig. 3. Clarifying constriction resistance

The conductivity of the ring-shaped volume dx is

$$dG_X = \frac{2\pi x\, dx}{\rho\sqrt{x_0^2 - x^2}} \tag{12}$$

For the zone B area S and a width of the annular volume dr are:

$$S = 2\pi r^2 \sin\alpha\, d\alpha;\ \lambda = r d\alpha$$

Then the resistance of the volume of the angle dα of rotation in the zone B:

$$dR_B = \frac{\rho}{2\pi \sin\alpha\, d\alpha}\int_{r_0}^{r_m}\frac{dr}{r^2} = \frac{\rho}{2\pi \sin\alpha\, d\alpha}\left(\frac{1}{r_0} - \frac{1}{r_m}\right) \tag{13}$$

We express the increment dx and coordinate x through the angle α:

$$dx = r_0\left(\sin\alpha + \frac{d\alpha}{2}\cos\alpha\right)d\alpha = r_0 \sin\alpha\, d\alpha; \tag{14}$$

$$r = r_0 \sin\alpha; \tag{15}$$

$$dR_A = \frac{\rho\cos\alpha}{2\pi r_0 \sin^2\alpha\, d\alpha} \tag{16}$$

The constriction resistance of the element will be found as the sum of the resistances of the elements of zones A and B:

$$dR_{retr}(\alpha) = \frac{\rho\cos\alpha}{2\pi r_0 \sin^2\alpha\, d\alpha} + \frac{\rho}{2\pi \sin\alpha\, d\alpha}\left(\frac{1}{r_0} - \frac{1}{r_m}\right) \tag{17}$$

After transformations and simplifications we obtain

$$dR_{retr}(\alpha) = \frac{\rho}{2\pi \sin\alpha\, d\alpha}\left[\frac{1}{r_0}(1 + ctg\alpha) - \frac{1}{r_m}\right] \tag{18}$$

Taking into account that $r_m >> r_o$ the expression is simplified to

$$dR_{retr}(\alpha) = \frac{\rho(1 + ctg\alpha)}{2\pi r_0 \sin\alpha\, d\alpha} \tag{19}$$

The integration of the elementary volume conductivity dG_{retr} is carried out within the limits giving the full coverage of the considered half-space:

$$G_{retr} = \int_0^{\pi/2}\frac{2\pi r_0 \sin\alpha}{\rho(1 + ctg\alpha)}d\alpha \tag{20}$$

$$G_{retr} = \frac{\pi r_0}{\rho\sqrt{2}}\lambda\nu\left(\frac{\sqrt{2}+1}{\sqrt{2}-1}\right) \tag{21}$$

$$G_{retr} = \frac{r_0}{\rho}\,3{,}916 \tag{22}$$

Then the total constriction resistance approximately is

$$R_{retr} \approx \frac{\rho}{3{,}916\, r_0} \tag{23}$$

The exact formula is as follows:

$$R_{retr} = \frac{\rho}{r_0}\cdot\frac{\sqrt{2}}{\pi}\ln^{-1}\left(\frac{\sqrt{2}+1}{\sqrt{2}-1}\right) \tag{24}$$

As we see, the expression (23) almost coincides with the Holm formula for the constriction resistance of the round contact pad.

Until now it was about the resistance of the continuous contact area. However, in reality, almost always contact spot is a fractal cluster of fractional dimension with imperfect boundaries [13], [15-16], [24]. In this case, the packing density of cluster elements ρкл and its fractal dimension D should be taken into account when determining the constriction resistance. The dimension D is not dependent on the shape of the cluster, or whether the package of its constituent monomers dense, random or slitted. The fractal dimension of a flat cluster is always less than 2, i.e. less than the size of the topological dimension of space. The packing density depends on the shape of the monomers. Thus, for close packed spheres is about , and at a random packing is reduced to 0,637. To cover a flat cluster with squares, and three-dimensional with cubes, we can assume that with an unlimited decrease of monomers, the packing density tends to the one. If the size of the element is r and the characteristic cluster size is r_{kl} then we write:

$$N = \rho_M\left(\frac{r_M}{r}\right)^D \tag{25}$$

in the limit when $\rho_{kl} \to 1$, $N = \left(\frac{r_M}{r}\right)^D$ where from

$$D = \frac{\lg N}{\lg r_{kl} - \lg r} \qquad (26)$$

As the parameter of the cluster size, the radius of gyration is used. It is introduced by the ratio $R_g=(<R^2>)^{1/2}$, where R is the distance from the considered point of the cluster to its center of mass, angle brackets mean averaging over the distribution of particles in the cluster.

Expression (23) defines only half of the constriction resistance, since defined for half space. Therefore, the total resistance in the case of identical density ρ of the half-spaces is determined by the following expression

$$R_{retr} = \frac{\rho}{1,96 \cdot r_0} \approx \frac{\rho}{2r_0} \qquad (27)$$

For the spatial defining of clusters instead of the topological dimension, fractional fractal dimension is used. Therefore, the magnitude of the constriction resistance of the cluster depends on its fractal dimension. In view of the above, we write down the constriction resistance formula for fractional objects in the following form:

$$R_{retr\ kl} = R_{retr} \cdot (r_{kl} \cdot D_f) \qquad (28)$$

where $R_{retr\ kl}$ is the constriction resistance of the fractal cluster, $R_{retr}(r_{kl})$ is the constriction resistance of a circle with a radius equal to the characteristic size of the cluster r_{kl}, for three-dimensional space

$$R_{retr}(r_{kl}) = \frac{\rho}{2r_{kl}},\ R_{retr\ kl} = \frac{\rho}{2r_{kl}D_f}$$

D_f is the cluster's fractal dimension.

The proof of assertion (28) in general form is of considerable complexity. Therefore, a series of experimental studies was carried out to verify the above formula. The results of the experiments, as well as the derivation of the necessary mathematical expressions are given below.

Expression (28) becomes more versatile than the Holm, Ipa, Venart, and Greenwood formulas and makes it quite simple to calculate the constriction resistance of fractal clusters and multifractals. In this aggregation of limited clusters is carried out according to the criterion of their minimum distance from each other (no more than by the size of the characteristic size of the smaller cluster).

To determine the degree of adequacy of formula (28) a series of experiments was carried out on a flat model of current lines. The experimental plant is shown schematically in Fig. 4.

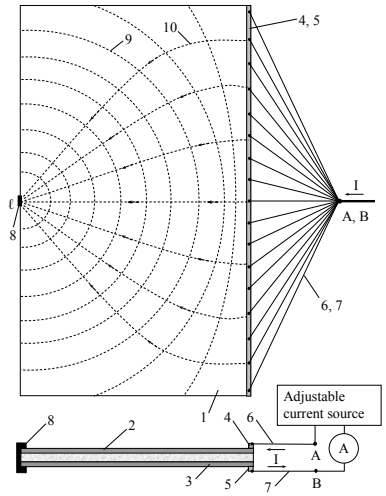

Fig. 4. Experimental setup for measuring the constriction resistance on the conductive plane.

A rectangular sheet of foiled textolite 1 has two copper layers 2 and 3 deposited on both planes. On one side of the sheet, along the edge of the electrically conductive layers, copper buses 4, 5 are soldered, to which two groups of conductors 6, 7 are attached. These groups of conductors are connected by other ends at points A and B, which are connected to an adjustable current source through ammeter A. On the other side of sheet 1, copper jumpers 8 of width ℓ are installed, which may be several at different distances from each other. One jumper shown in the figure is a linear analogue of a flat circular contact spot. The constriction resistance of a single jumper is calculated according to the formulas, which are defined below.

Fig. 5 shows a quarter of the conducting plane, which is divided into two halves of a non-conductive straight line x containing a conducting segment of length $2r_o$.

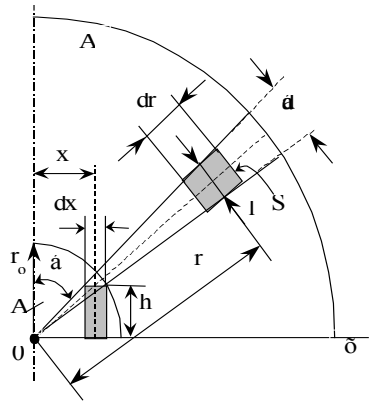

Fig. 5. To determination the constriction resistance on the plane.

The resistance of the flat portion dx of the inner constriction zone A:

$$dR_A = \rho \cdot \frac{h}{dx} \qquad (29)$$

The increment dx and the x coordinate itself is expressed through the angle α:

$$dx = r_0 \cdot \sin\alpha\, d\alpha\ ; \qquad (30)$$

$$h = r_0 \cdot \sin\alpha; \qquad (31)$$

$$dR_A = \frac{\rho}{d\alpha}. \qquad (32)$$

For the "outer" zone B of the half-plane, the width l of the annular volume dr is determined by formula l=r dα , and the resistance of the elementary part dr is

$$dR_r = \rho \frac{dr}{r\, d\alpha}. \tag{33}$$

Then the resistance of the ring sector with the angle dα is

$$dR_B = \frac{\rho}{d\alpha}\int_{r_0}^{R_m}\frac{dr}{r} = \frac{\rho}{d\alpha}\cdot \ln\frac{R_m}{r_0}. \tag{34}$$

We find the resistance of the element as a sum

$$dR_{retr}(\alpha) = \frac{\rho}{d\alpha} + \frac{\rho}{d\alpha}\ln\frac{R_m}{r_0} = \frac{\rho}{d\alpha}\cdot\left(1+\ln\frac{R_m}{r_0}\right). \tag{35}$$

The conductivity of the constriction element is

$$dG_{retr}(\alpha) = \frac{d\alpha}{\rho\left(1+\ln\frac{R_m}{r_0}\right)}. \tag{36}$$

The integration of the conductivity of the elementary volume dG_{retr} will be done within the limits giving the full coverage of the considered plane:

$$G_{retr} = \frac{d\alpha}{\rho\left(1+\ln\frac{R_m}{r_0}\right)}\int_0^{2\pi} d\alpha. \tag{37}$$

$$G_{retr} = \frac{2\pi}{\rho\left(1+\ln\frac{R_m}{r_0}\right)} \tag{38}$$

Then the total constriction resistance is equal to

$$R_{retr} = \frac{\rho}{2\pi}\left(1+\ln\frac{R_m}{r_0}\right) \tag{39}$$

For the cluster, taking into account the fractal dimension , we get

$$R_{retr} = \frac{\rho}{2\pi}\left(1+\ln\frac{R_m}{r_{kl}D_f}\right) \tag{40}$$

The characteristic cluster size r_{kl} is defined as twice the radius of gyration, which is calculated as follows: 1) we find the radius of the mass center of the linear cluster

$$R_c = \frac{1}{n}\cdot\sum_1^n r_i. \tag{41}$$

where r_i is the distance from the origin to the i-th element of the cluster; n is the number of cluster members; 2) calculate the radius of cluster gyration:

$$R_g = \sqrt{\frac{1}{n}\sum_1^n (r_i - R_c)^2} \tag{42}$$

and find the numerical value of the fractal dimension:

$$D_f = \frac{\log(n)}{\log\left(\frac{R_g}{r_0}\right)} \tag{43}$$

From the current source through the flat copper layers 2, 3 and jumper 8 the current I is conducted. Measurements of the potential difference on surfaces 2, 3 by a millivoltmeter allow us to construct equipotentials 9 and current lines 10.

III. RESULTS AND DISCUSSION

We will determine the constriction resistance in two ways. The first method is to use for calculation the measured voltage drops on the plane and the magnitude of the current I. The second method is based on applying formula (28) together with expressions (40–43).

In the second case, in the calculations we use only the geometric dimensions of the model and the magnitude of the resistivity of the electrically conductive layer. The accuracy of the coincidence of the calculation results of the constriction resistance, carried out in two ways for different clusters, determined by the location of the jumpers 8, allows us to view the adequacy of the proposed formula for calculating the constriction resistance.

The specific resistivity of the conductive layer was determined experimentally. For this purpose strap width S from foil-coated textolite was manufactured. Along it, a current was passed through the conducting layer (up to 70 A) and the voltage drop ΔU was measured on a section of a layer of length L. Resistivity was calculated by the formula

$$\rho = \frac{\Delta U\, S}{1\, L} \tag{44}$$

Multiple measurements with averaging gave the result $\rho \approx 57\cdot10^{-3}$ Ом.

Using the same copper jumpers width ℓ = 0.0012 m linear conductive clusters of various configurations were created, for which the formulas (40-43) were calculated constriction resistance. The voltage drop was measured along a straight line perpendicular to the line of separation of the conducting plane and passing through the mass center of the cluster.

Using the same copper jumpers width ℓ = 0.0012 m linear conductive clusters of various configurations were created, for which the formulas (40-43) were calculated constriction resistance. The voltage drop was measured along a straight line perpendicular to the line of separation of the conducting plane and passing through the mass center of the cluster.

Fig. 6-11 shows a the calculated and experimental dependences of the constriction resistance R_{cr} on the distance R_m to the center of mass of the cluster at which the voltage drop was measured.

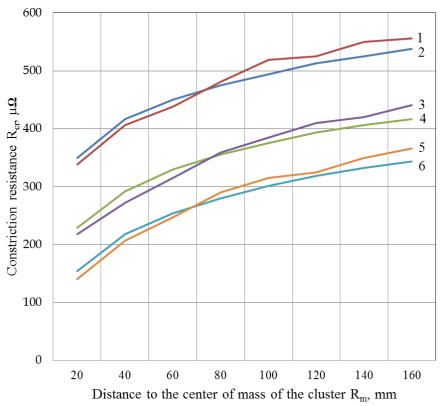

Fig. 6. Dependences $R_{cr} = f(R_m)$(1-3 elements)
1 - 1 element, experiment, 2 - 1 element, calculate,
3 - 2 elements, experiment, 4 - 2 elements, calculate,
5 - 3 elements, experiment, 6 - 3 elements, calculate

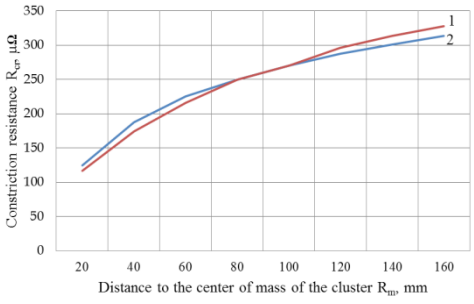

Fig. 7. Dependences $R_{cr} = f(R_m)$(4 elements)
1 - 4 elements, experiment, 2 - 4 element, calculate

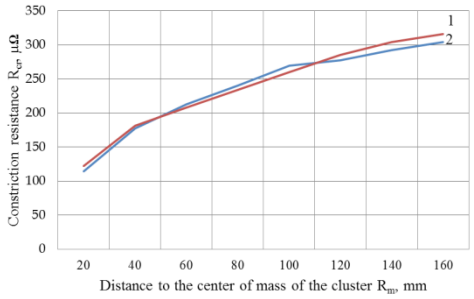

Fig. 8. Dependences $R_{cr} = f(R_m)$(5 elements)
1 - 5 elements, experiment, 2 - 5 element, calculate

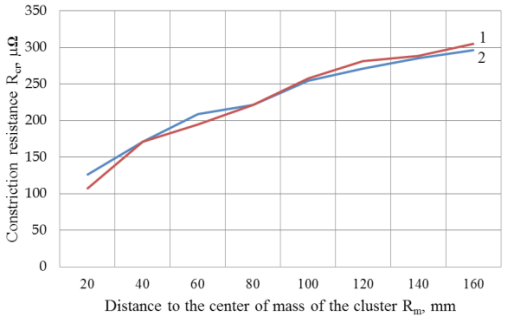

Fig. 9. Dependences $R_{cr} = f(R_m)$(6 elements)
1 - 6 elements, experiment, 2 - 6 elements, calculate

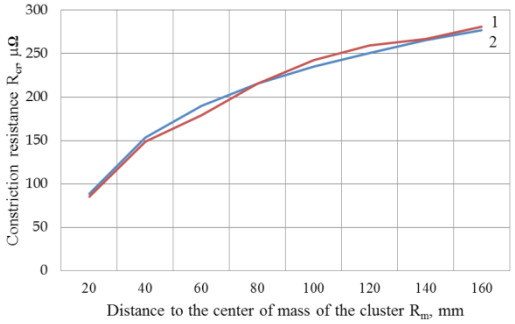

Fig. 10. Dependences $R_{cr} = f(R_m)$(7 elements)
1- 7 elements, experiment, 2 - 7 elements, calculate

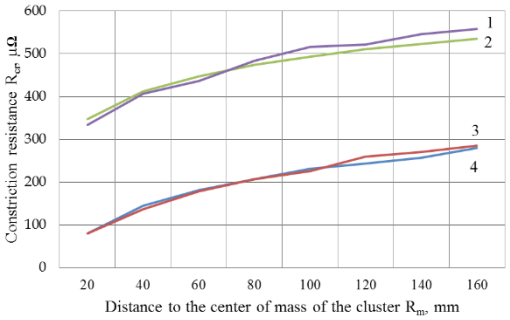

Fig. 11. Dependences $R_{cr} = f(R_m)$(8-9 elements)
1 - 9 elements, experiment, 2 - 9 elements, calculate
3 - 8 elements, experiment, 4 - 8 elements, calculate

First the voltage drops ΔU_o between the bus 5 and the centers of the jumpers 8 was measured. (These voltages are almost equal, since the cluster dimensions are significantly less than the distance to the bus). Then the voltage drops ΔU_i between the bus 5 and selected points on the conductive plane 2 was measured. The following formula was used to calculate the experimental constriction resistance value.

$$R_{cntr\,\exp} = \frac{\Delta U_0 - \Delta U_i}{I} \tag{45}$$

The theoretical value of the constriction resistance was found by the formula (40).

II. CONCLUSION

A comparison of experimental and theoretical data (Fig. 6–15) indicates a satisfactory rate of adequacy of the formula for the constriction resistance of a cluster, which uses the magnitude of the fractal dimension as a scaling factor. The difference between experimental and theoretical results does not exceed 5%.

III. ACKNOWLEDGMENTS

Due to the fact that the verification of this formula was made using a flat experimental model, the conclusion about adequacy was made taking into account the principle of physical similarity. In addition, on the model using this formula, satisfactory qualitative and quantitative correspondences of the experimental and calculated current-voltage attractors were obtained [14].

REFERENCES

[1] Holm R. Electric contacts handbook. Landkof N.S. Foundations of Modern Potential Theory, Berlin, Springer, 1973, 424 p.
[2] Merl W. *Elektricheskiy kontakt* [Electric Contact]. – M.-L., Gosenergoizdat Publ, 1962. (in Russian).
[3] Haken, H. Synergetik. Berlin, Heidelberg, New York, Springer Verlag, 1981. 382 p.
[4] Mandelbrot B.B. The fractal geometry nature. N.Y., Freeman, 1983. 480 p.
[5] Feder J. Fractals. New York, Plenum Press, 1988, 283 p.
[6] Smirnov B.M. *Fizika fraktal'nykh klasterov*. [Physics of fractal clusters]. Moscow, Nauka Publ., 1991. 136 p. (in Russian).
[7] Omel'chenko V.T. *Teoriya protsesov na kontaktakh*. [Theory of processes at the contacts]. Kharkov. KhGU, Vishcha shkola Publ. 1979. 126 p. (in Russian).
[8] Reutt E.K., Saksonov I.N. *Elektricheskie kontakty.* [Electric contacts]. M. Voenizdat. 1971. 126 p. (in Russian).

[9] Konchits V.V., Meshkov V.V., Myshkin V.V. *Tribotekhnika elektricheskikh kontaktov*. [Tribotechnique of electrical contacts]. Minsk: Nauka i tekhnika Publ. 1986. 255 p. (in Russian)

[10] Kim E.I., Omel'chenko V.T., Harin S.N. *Matematicheskie modeli teplovykh prozessov v elektricheskikh kontaktakh*. [Mathematical models of thermal processes in electrical contacts]. Alma-Ata: Nauka Publ. 1977. 236 p. (in Russian).

[11] Ivanova V. S., Balankin A. S., Bunin I. Zh., Oksogoev A. A. Sinergetika i fraktaly v materialovedenii. [Synergetics and fractals in materials science]. Moscow, Nauka Publ., 1994. 384 p. (in Russian).

[12] *Fraktaly v fizike* [Fractals in Physics] Trudy VI mezhdunarodnogo simpoziuma po fraktalam v fizike. Moscow, Mir Publ., 1988. 672 p. (in Russian).

[13] Vaimann T., Rassõlkin A., Gevorkov L., Kallaste A., Kozyreva O., Plokhov I., Kotkov N., Savraev I., Ilyin A. Reducing Sparking in the Transient Layer of the Sliding Electrical Contact Unit. In: L. Radil, J. Macháček, J. Morávek (Ed.). 19th International Scientifc Conference on Electric Power Engineering (EPE) (223−227). Brno: IEEE. 2018

[14] Plokhov I.V. *Kompleksnaya diagnostika i prognozirovanie tekhnicheskogo sostoyaniya uzlov skolzyashchego tokos"ema turbogeneratorov.* Doct.Diss. [Complex diagnostics and forecasting of the technical condition of the sliding electrical contact unit of turbo-generators. Doct. Diss.] Sankt-Petersburg. 2001. 362 p. (in Russian).

[15] Plokhov I.V. *Model' dinamiki tokoperedachi cherez skolzyashchiy kontakt.* [Dynamic model of current transfer through a slipping contact]. *Elektrotekhnika* [Electrical Engineering], 2005, no. 2, pp. 28-33. (in Russian).

[16] Plokhov I.V. Issledovanie soprotivleniya styagivaniya elektricheskogo kontakta. [Investigation electric contact contraction resistance]. *Elektrotekhnika* [Electrical Engineering], 2004, no. 5, pp. 13-18. (in Russian)

[17] Plokhov I.V. *Klasternaya model elektrofriktsionnogo vzaimodeystviya (EFV)*. [Cluster model of electro-friction interaction]. Trudy Pskovskogo politekhnicheskogo instituta. S.-Peterburg/Pskov, SPbGTU Pub., 1997, no. 1. pp. 55-57. (in Russian)

[18] Greenwod J.A. Constriction resistance and the real area of contact. – British Journal off appl. Physics. 1966. V.17. p.1621-1631.

[19] Plokhov I.V., Savraev I.E. И.Е. *Vychislitelnaya model razvitiya perkolyacionnykh klasterov kontaktnoy provodimosti*. [Computational model of development of percolation contact conductivity clusters.]. Trudy Pskovskogo politekhnicheskogo instituta. S.-Peterburg/Pskov. SPbGTU, 1997, no.1, pp.51-54. (in Russian)

[20] Shklovskiy B.I., Efros A.L. *Teoriya protekaniya i provodimost' sil'no neodnorodnykh sred* [Flow theory and conductivity of highly inhomogeneous mediums]. Uspekhi fizicheskikh nauk. [Advances in the physical sciences]. vol.117, no. 3. 1975. pp.401–435. (in Russian)

[21] Yip F.C., Venart J.E.S. Surface topography effects in the estimation of thermal and electrical contact resistance. – In: Proc. Inst. Mech. Eng., 1968. vol. 182. Pt. 3K. p. 81.

[23] Anca Sorana Popa, Veronica Argeşanu. Tribologic aspects concerning the contact surface roughness, in ase of sliding electric contacts. The annals of University "Dunărea de jos " of gala ti fascicle VIII, 2004. ISSN 1221-4590 TRIBOLOGY pp. 127-131.

[24] Ilyin A., Plokhov I., Savraev I., Kozyreva O., Kotkov N. Forming and overlapping microreliefs in sliding contact simulation model – Vide. Tehnologija. Resursi - Environment, Technology, Resources. 2017.

Environment. Technology. Resources. Rezekne, Latvia
Proceedings of the 12th International Scientific and Practical Conference. Volume III, 208-213

Synergetic Model of Electro-friction Interaction

Igor Plokhov
Department of Electric Drive and Automation Systems
Pskov State University
Pskov, Russia
igor_plohov@list.ru

lexander Ilyin
Department of Electric Drive and Automation Systems
Pskov State University
Pskov, Russia
al.ilyin@yandex.ru

Oksana Kozyreva
Department of Electric Drive and Automation Systems
Pskov State University
Pskov, Russia
ks_33n@mail.ru

Igor Savraev
Department of Electric Drive and Automation Systems
Pskov State University
Pskov, Russia
igor_savraev@mail.ru

Nikita Kotkov
Department of Electric Drive and Automation Systems
Pskov State University
Pskov, Russia
4ce@goodgame.ru

***Abstract*—The paper describes algorithms and structure of the electro-friction interaction synergetic model. The results of theoretical modelling and experimental study of sliding electrical contact are given. The comparison of theoretical and experimental results made in the paper proves high validity of the model and its programmatic implementation.**

Keywords—fractal theory , simulation modelling, sliding contact, synergetic.

I. Introduction

The basic approaches to the modern explanation of the physical processes in the sliding electrical contact are the next.

A common surface of two contacting rough bodies divides into many separate spots. When the flow of energy gets through the surface, it overcomes additional constriction resistance because of the nonuniform flow lines. In addition, there is the resistance of the surface films.

The theory of the electro-frictional interaction (EFI) at the time is at a critical time when there are large bulk of experimental data, hypotheses and different models, which could not be adequate to the studied processes. To overcome this conflict the new physical views and presentations must be involved in the applied area.

At present it is developing synergetics, the theory of self-organizing systems, and fractal theory studying self-similar evolutionary structures that cannot be described within Euclidian geometry.

Synergetics is studying the processes of the self-organizing, stability and disintegration of different nature structures forming in the open systems and the ordered state of which is connected to cooperative behaviour of theirs subsystems. This leads to the forming of self-organizing structures as the result of energy and material exchange with the environment when equilibrium has established of the entropy production and reduction [1] – [5]. The evolution of a system is considered as transition through the series of thermodynamic quasi-equilibrium states [6]. Fractal theory [7] – [10] has become the base for quantitative description of the self-organizing structures using the fractal dimension as a parameter.

II. Model Of Sliding Contact Transient Layer

The transient layer of sliding electric contact (SC) is representable as set of the contact elements (CE) placed in nodes of a regular grid on the transitional plane (TP). We will describe each CE with the state vector having components.

Components of the power vector F are independent input influences: pressure force F_p , velocity of relative movement in contact couple of v, external voltage applied to contact U , environment temperature θ_{env}, vector of concentration of environment chemical reagents Z.

We will divide all components of the state vector of a contact element into the following classes. Mechanical V_M: contact stiffness S_C; contact damping K_C; contact approach Y_C; contact force F_C; microhardness q; density ρ; coefficient of boundary friction k_{fr}. Electrical V_E: voltage U (it is identical for all contact elements); fritting voltage U_f; electric conductance g_E or resistance ρ_E; contact capacity C_E; current I through C_E. Thermal V_T: heat capacity C_θ; heat conductivity k; melting temperature θ_m; evaporation temperature θ_{ev}; CE temperature θ. Chemical V_H: vector of chemical composition ħ; intensity of the main chemical reactions of V_h.

Let's determine the state vector by the sum of this four components

$$V=V_M+V_E+V_\theta+V_H \quad (1)$$

Voltage U is identical for all CE, however the value of current will be different for the different types and characteristics of conductivity, different temperatures, approaches, and etc. Besides, the flow of current leads to emitting power in CE and increases temperature θ,

Print ISSN 1691-5402
Online ISSN 2256-070X
http://dx.doi.org/10.17770/etr2019vol3.4072

which significantly affects conductivity of the element and conductivity of the neighbor areas.

In each CE there are substances and compounds of different concentration which can react with each other and with the materials of contact bodies. Either they can be passive or be catalysts and inhibitors for other reactions.

III. Modification Of the State Vector Components

The operations described below provide a basis for the dynamic processes in CE and contain the main computational procedures.

In the transient layer matrix we allocate clusters of direct and film conductivity (α-clusters and β-clusters). For this we use an allocation procedure that translates the elements of each cluster into an additional matrix.

After calculating the number of elements that make up the cluster N_i we calculate the characteristic radius of the cluster r_{cl} as the gyration radius R_g:

$$R_g = \sqrt{\frac{1}{N}\sum_{i=1}^{N} r_i^2} = \sqrt{\frac{1}{N}\sum_{i=1}^{N}\left[(X_c - x_i)^2 + (Y_c + y_i)^2\right]} \quad (2)$$

$$X_c = \sqrt{\frac{1}{N}}\sum_{i=1}^{N} x_i,\ Y_c = \sqrt{\frac{1}{N}\sum_{i=1}^{N} y_i} \quad (3)$$

Determine the fractal dimension of the cluster by the formula

$$D = \frac{\lg N}{\lg r_{cl} - \lg r} \quad (4)$$

Find the resistance of each cluster as the sum of the constriction resistances of the sliding contact upper and lower half-spaces, the resistance of the oxide film and the wear products $R_{cli}=R_{Ci}'+R_{Ci}''+R_{fi}+R_{wi}$, where:

$$R'_{ci} = \frac{\rho E'}{4Dr_{cli}},\ R''_{ci} = \frac{\rho E''}{4Dr_{cli}}. \quad (5)$$

Calculate the contact resistance as a parallel connection of all clusters:

$$R=(\sum R_{cli}^{-1})^{-1} \quad (6)$$

Calculate the full contact current (R_{br} is the resistance of the brush body)

$$I = \frac{U}{R_{br} + R} \quad (7)$$

Find the thermal power emitting in each cluster. Power contains electrical and mechanical components.

Electrical component:

$$P_{Ei} = \frac{\Delta U^2}{2R_{cli}} \quad (8)$$

$$\Delta U = U - IR_{br} \quad (9)$$

where ΔU is the voltage drop at the transient layer; U is the voltage applied to the contact pair; I is the current of SC; R_{br} is the brush resistance.

Mechanical power of friction:

$$P_{Mi} = S_{Ci} + \Delta Y_i k_{fr} v, \quad (10)$$

where S_C is the CE stiffness, N/m; ΔY is the compression of CE, m; k_{fr} is the friction coefficient; v is the velocity of microreliefs displacement, *m/s*.

Then the total power in CE is

$$P_{CEi} = P_{Ei} + P_{Mi}. \quad (11)$$

Determine the CE temperature increment for one step of modelling time. Since the emitting power is went into heating the CE volume to a temperature θ over a time Δt, then using the electrothermal analogy method [11] – [15] an equivalent electrical circuit can be made. The heat source of power P_{CE} will be represented as the current source I_E and the heat capacity of CE C_{CE} as the electrical capacitance C_E, and the voltage U_E corresponds to the temperature θ (Fig. 1).Write in the operator form:

$$U_E(p) = I_E X_C(p) = \frac{I_E}{pC_E} \quad (12)$$

where $X_C = \frac{1}{pC_E}$ is the reactance of the capacitor C_E.

In accordance with the direct analogy:

$$\theta(p) = \frac{P_{CE}}{pC_{CE}},\ C_{CE} = C_{CE} m_{CE}, \quad (13)$$

where c_{CE} is the specific heat; $m_{CE}=\Delta x^2\ \Delta h \rho_{CE}$ is the mass of CE; Δh is the CE height; ρ_{CE} is the average density of the CE materials

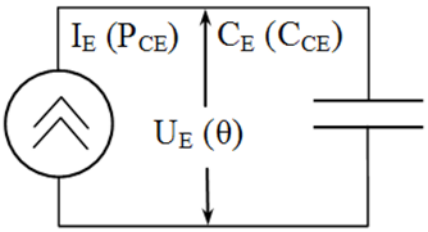

Fig. 1. Equivalent circuit.

After r $\theta(t) = \frac{P_{CE}}{C_{CE}\Delta x^2 \Delta h \rho_{CE}} t$ get:

(14)

Repre: $\Delta\theta = \frac{P_{CE}}{C_{CE}\Delta x^2 \Delta h \rho_{CE}} \Delta t$ rences:

(15)

By the one step of the simulation the CE temperature will be:

$$\theta_{i+1} = \theta_i + \Delta\theta \quad (16)$$

The temperature of the CE has been changed due to heat exchange with the contacting bodies and the neighbour CE. Therefore, after calculating the temperature increment caused by heat emitting in CE, we calculate the temperature distribution in the three-dimensional system of nodes over the same time interval (Fig. 2) using the explicit method [12], [13].

Taking into account the nonuniform distribution of thermal conductivity and heat capacity in the structure of the transition layer, we can write:

$$\theta_{i,j,s}(t+\Delta t)=\begin{Bmatrix}\theta_{i,j,s}(t)+\\ F_{i+1,j,s}(t)\Delta\theta_{i+1,j,s}(t)+\\ F_{i-1,j,s}(t)\Delta\theta_{i-1,j,s}(t)\\ F_{i,j-1,s}(t)\Delta\theta_{i,j-1,s}(t)+\\ F_{i,j+1,s}(t)\Delta\theta_{i,j+1s}(t)+\\ F_{i,j,s+1}(t)\Delta\theta_{i,j,s+1}(t)+\\ F_{i,j,s-1}(t)\Delta\theta_{i,j,s-1}(t)\end{Bmatrix}, \quad (17)$$

where $\theta_{i,j,s}$ *(t)* is the temperature of the node with co-ordinates *i, j, s;* $\Delta\theta_{i+1,j,s}$ *(t)* $=\theta_{i+1,j,s}$ *(t)*-$\theta_{i,j,s}$ *(t),* $\Delta\theta_{i-1,j,s}$ *(t)* $=\theta_{i-1,j,s}$ *(t)*-$\theta_{i,j,s}$ *(t)*, and etc. are the temperature differences of the calculated node and the neighbor nodes; $F_{i,j,s}=\frac{\langle k_{i,j,s}\rangle}{\langle c_{i,j,s}\rangle\Delta x^2\langle\rho_{i,j,s}\rangle}\Delta t$ is Fourier number for the calculated node, where $(k_{i,j,s})$, $(c_{i,j,s})$, $(\rho_{i,j,s})$, are the average values of thermal conductivity, specific heat and density calculated by the nodes of the fragment (Fig. 2).

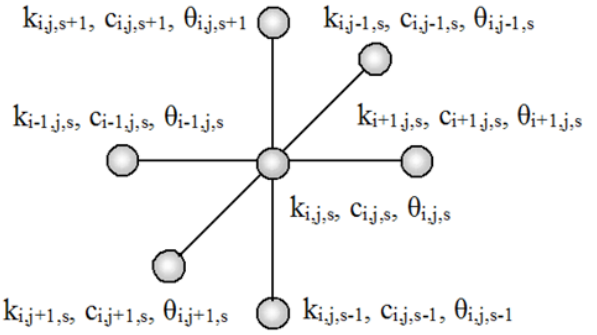

Fig. 2. Calculation of the sliding contact non-stationary temperature field.

The computational procedure has a stable solution if the Fourier number is less or equal 1/6 [12]. This indicator has the greatest value for the zones of direct conduction, therefore the choice of the step *Δt* and the discretization *Δx* are made by CE allocated into the specified zones.

The temperature increment of the CE from electromechanical heat emitting and its change due to the distribution of heat over the three-dimensional grid is not combined into a general procedure, since in this case the principle of simultaneous heat emitting in CE is violated. The calculation of the non-stationary temperature field of the SC is carried out for each *Δt* in two steps and for analysis we use only the final values of the CE temperatures for the second step.

To simplify the algorithm and increase the speed, we introduce the assumption that the temperature of the CE layers adjacent to the contact is defined as the half sum of the average temperature of all calculated CE of the transient layer and the temperatures of the contacting bodies. We also neglect the convective heat transfer at the boundaries of the contact layer setting zero values of the thermal conductivity of boundary CE to the environment.

At each step of calculating the temperature field for all CE, we check the condition for exceeding the critical temperature levels of materials: 1) the recrystallization temperature, 2) melting point, 3) the evaporation temperature. Depending on which interval the temperature of the calculated CE falls within, it is decided how to change its characteristics and parameters.

Up to the temperature θ_m the mechanical stiffness of the CE is considered constant. In the interval $\theta \in [\theta_m,\theta_{ev}[$, the stiffness of the CE is changing in linear dependence. When the temperature θ_{ev} is reached evaporation of the least heat-resistant material of the CE occurs and the distance between the contacting surfaces at this point increases. For this a correction is made in the matrix of micro-reliefs. The approach in CE is changed by the value of *Δh*. As a result at a constant pressing force F_n the equivalent stiffness of the SC Cкэ changes and the approach of the contacting surfaces is:

$$\Delta Y=\frac{F_b}{S_{CE}}, \quad (18)$$

where $S_{CE}=\sum S_{Ci}$.

As the temperature increases the conductivity of the surface films also increases and when the certain temperature $\theta=\theta_{tb}$ is reached thermal breakdown occurs, which is defined as the transition of the CE to the direct conductivity state.

The fritting of oxide films is interpreted as the transition of the CE into the direct conduction state when the electric field strength reaches the threshold value E_f that depends on the voltage at the contact layer and the thickness of the o

$$E=\frac{\Delta U}{d}. \quad (19)$$

If $E>E_f$ *CE* goes into the direct conduction state.

The temperature dependence of the specific resistance, specific heat capacity, thermal conductivity and friction power is taken into account using

$$\rho_E=\rho_{E0}(1+\alpha\Delta T), \quad (20)$$

$$c=c_0(1+\alpha_c\Delta T), \quad (21)$$

(22)

$$P_M(T)=P_{M0}\left(1-\left(\frac{\Delta T}{T_*-T_0}\right)^2\right), \quad (23)$$

where ρ_{E0} is the electrical resistivity at the initial temperature; α is the temperature coefficient of resistance, *1/K;* ΔT is the difference between the current and initial temperatures; c_0 and k_0 are specific heat and thermal conductivity at the initial temperature; α_c and α_k are the temperature coefficients of specific heat and thermal conductivity; coefficient α_k may be, both positive and negative, depending on the materials of the SC; P_{M0} is the

friction power at the initial temperature; T is the current temperature; n and T_* are the parameters which selected from the condition of the best approximation of the empirical dependence $P_M(T)$ in the studying temperature range.

The block diagram Fig. 3 depicts the main procedures of the simulation program. The main loop contains the block "Service input-output operations", which is responsible for the graphical interfaces of the program, the visualization of tables, graphs and color portraits, etc.

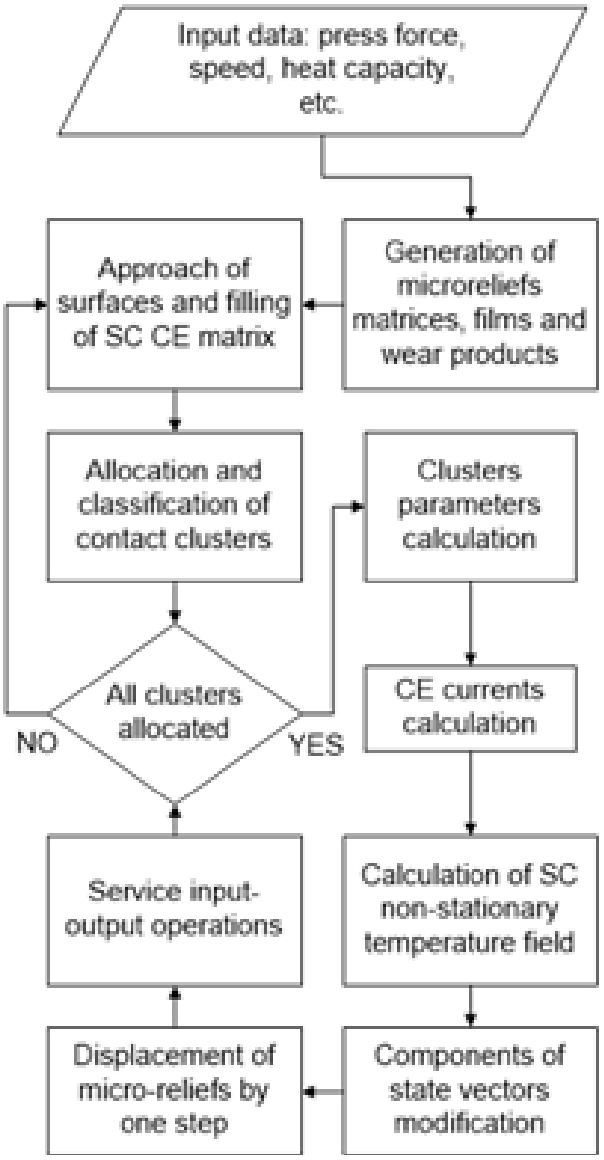

Fig. 3. Generalized block diagram of the EFI simulation model.

IV. Theoretical and Experimantal Study Of EFI Dynamic Processes

Objectives of the study are: 1) determination of the simulation model adequacy, 2) study of the qualitative regularities of the EFI dynamics related to the processes of formation and growth of conducting clusters in the transition layer, thermal processes and voltage-current dependencies generated by various disturbing influences. Similar studies are described in [16] – [22].

Let's compare some model and experimental characteristics.

The calculated voltage-current attractor shown in Fig. 4 is obtained with a sinusoidal modulation of the pressing force in the range from 2 to 25 N at the applied voltage 2 V and the speed of 3000 rpm for the contact pair "brush-steel ring". Under the same conditions the experimental voltage-current limit cycle is shown in Fig. 5. The main difference is that the modulation of the pressing force in the experiment occurred naturally as the result of the interaction of the brush with the irregularities of the contact surface. In addition there was an effect of screw thread of the steel ring on the contact area value. The randomness of the phase trajectory shown in Fig. 5 is explained by the result of the action of these two polyharmonic factors. Despite all its complexity the indicated trajectory was steadily reproduced on each revolution of the ring with the slight stochastic variations.

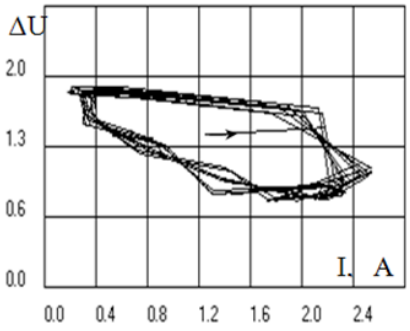

Fig. 4. Calculated voltage-current attractor.

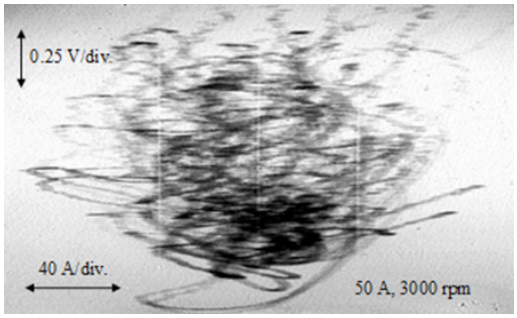

Fig. 5. Experimental voltage-current attractor.

Statistical estimates of these curves is the ranges of current I and voltage drop ΔU are almost match. For I_{exp} the range of variation is about 200 A and for I_{calc} the range is calculated as $2.3 \cdot 89 = 204.3$ V. For ΔU_{exp} and ΔU_{calc} the ranges are quite close.

In the Fig. 6 the model dynamic voltage-current characteristic obtained by high-frequency sinusoidal modulation of the applied voltage is shown.

For comparison to the model the experiment was performed on the collector. Initial data: speed 1000 rpm, press force 20 N, voltage 4 V. Fig. 6 corresponds to the experimental oscillogram in Fig. 7.

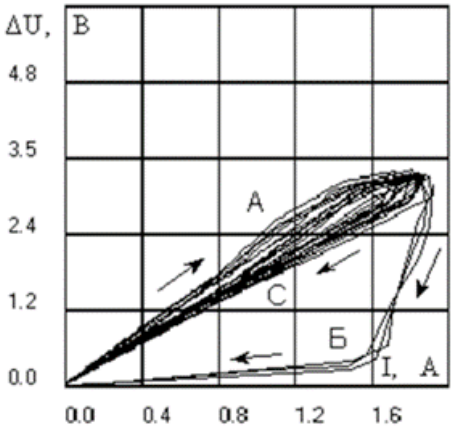

Fig. 6. Theoretical voltage-current attractor.

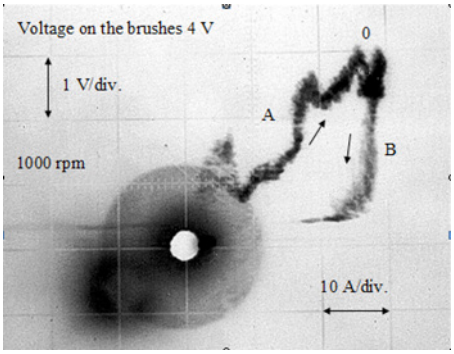

Fig. 7. The voltage-current attractor recorded during the passage of the collector lamella under the brush.

The simulation program allows to observe movement and development of the interacting microreliefs, aggregation of conducting clusters in the contact transition layer and the non-stationary temperature field. Fig. 8 shows examples of images obtained in the modelling process.

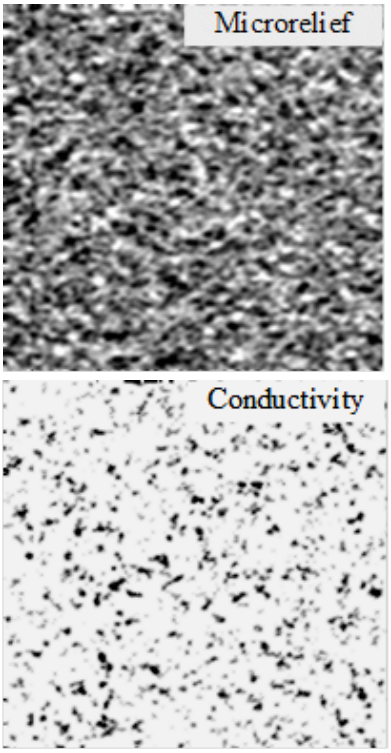

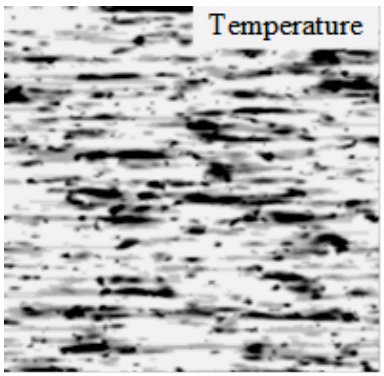

Fig. 8. Typical simulation images of the EFI synergistic model.

Fig. 9 shows enlarged fragments of the conduction in the contact transition layer, which contain characteristic conducting clusters. The shade portraits of the thermal field corresponding to the areas of conductivity show the values of local temperatures in various contact zones.

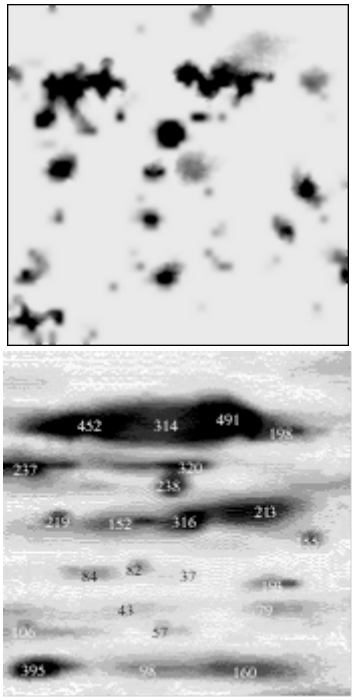

Fig. 9. Enlarged fragments of the conductivity containing characteristic contact clusters, and temperature field with indication of local temperatures (press force 30 N, voltage 2.5 V, velocity 30 m/s, contact is "brush EG-4 – steel").

Many conducting clusters have an oval or circular configuration. Usually they are located in less saturated areas with a relatively low average temperature. In the areas of increased heating a significant part of the clusters has a larger size and a complex configuration characterized by fractional fractal dimension. In addition, thermal zones are strongly elongated by the axis of the contact surface motion.

V. Conclusions

The structure of conductivity and thermal field is significantly influenced by the value of thermal conductivity of contact pair materials.

At low thermal conductivity the heated zones are elongated by the axis of contacting bodies movement and

take the form of diffuse strips.

With high thermal conductivity thermal zones acquire the local forms and at the same time have a lower temperature.

When certain values of the voltage and the press force are reached the temperature of a large number of thermal clusters reaches values at which the melting of the lower-melting material of the contact pair occurs. In practice, such modes of operation should be accompanied by increased sparking caused by the spitting of molten metal particles from the contact zone.

Most conductive clusters located in areas with low average temperature are oval or round in shape.

Clusters located in zones with a high average temperature have a larger size and a complex configuration characterized by fractional fractal dimension.

With an increase in the press force () the current, the saturation of the contact layer with conducting clusters, the number and temperature of the heated spots quickly increase.

Increasing the voltage at increases the density of conductive clusters at a lesser degree, however it affects the temperature field almost the same way as press force.

References

[1] G. Haken, Sinergetika. M.: Mir, 1980.

[2] I. M. Yaglom, Sovremennaya kulytura I kompyutery. M.: Nauka, 1990.

[3] B. R. Fuller, Sinergetics. N.Y.: MacMillan, 1982.

[4] G. Haken Informatsiya i samoorganizatsiya. Makroskopicheskiy podhod k slozhnym sistemam. M.: Mir, 1991.

[5] S. V. Emelyanov, V. I. Utkin V. A. Taran i dr., Teoriya sistem s peremennoy strukturoy. M.: Nauka, 1970.

[6] Г. П. Гладышев, Термодинамика и макрокинетика природных иерархических процессов. М.: Наука, 1988.

[7] B. B. Mandelbrot, The fractal geometry nature. N.Y.: Freeman, 1983.

[8] E. Feder, Fraktaly. M.: Mir, 1991.

[9] B. M. Smirnov, Fizika fraktalynyx klasterov. M.: Nauka, 1991.

[10] Fraktaly v fizike, Trudy VI mezhdunarodnogo simpoziuma po fraktalam v fizike. M.: Mir, 1988.

[11] V. P. Isachenko, V. A. Osipova, A. S. Sukomel, Teploperedacha. M.: Energoizdat, 1981.

[12] F. Kreit, U. Blek, Osnovy teploperedachi. M.: Mir, 1983.

[13] I. M. Tetelybaum, Ya. I. Tetelynaum, Modeli pryamoi analogii. M.: Nauka, 1979.

[14] I. M. Tetelybaum, Yu. R. Shneider, Praktika analogovogo modelirovaniya dinamicheskih sistem. M.: Energoatomizdat, 1987.

[15] V. A. Venikov, G. V. Venikov, Teoriya podobiya i modelirovaniya (primenitelyno k zadacham elektroenergetiki). M.: Vysshaya shkola, 1984.

[16] A. Ilyin, I. Plokhov, I. Savraev, O. Kozyreva, N. Kotkov, "Forming and overlapping microreliefs in sliding contact simulation model," in Environment. Technology. Resources: Proceedings of the 11th International Scientific and Practical Conference, Volume III, Rezekne: Latvia, 2017, pp. 102–106, http://dx.doi.org/10.17770/etr2017vol3.2532

[17] I. Plokhov, I. Savraev, A. Markov, A. Ilyin, O. Kozyreva, N. Kotkov, "Industrial tests of current distribution dynamics in the brush-contact apparatus of the turbo-generator," in Environment. Technology. Resources, Rezekne, Latvia, Proceedings of the 11th International Scientific and Practical Conference, Volume III, Rezekne: Latvia, 2017, pp. 258–268, http://dx.doi.org/10.17770/etr2017vol3.2661

[18] O. Kozyreva, I. Plokhov, N. Kotkov, I. Savraev, A. Ilyin, "Experimental investigations of effect of LC-circuits on sparking and thermal state of sliding electric contact unit," in Environment. Technology. Resources, Rezekne, Latvia, Proceedings of the 11th International Scientific and Practical Conference, Volume III, Rezekne: Latvia, 2017. pp. 150–153, http://dx.doi.org/10.17770/etr2017vol3.2575

[19] O. Kozyreva, I. Plokhov, I. Savraev, A. Ilyin, "Reducing sparking in the transient layer of the sliding electrical contact unit," in 2018 19th International Scientific Conference on Electric Power Engineering (EPE), 16–18 May 2018, Brno, Czech Republic, 2018, pp. 189–193, https://doi.org/10.1109/EPE.2018.8395969

[20] O. Kozyreva, Y. Guravlev, I. Plokhov, I. Savraev, A. Ilyin, "The regions of parametric instability of brush-contact device electromagnetic circuit in unstable working conditions," in Environment. Technology. Resources. Proceedings of the 10th International Scientific and Practical Conference, Volume 1, Rezekne, Latvia, 2015, pp. 84–88, http://dx.doi.org/10.17770/etr2015vol1.218

[21] A. Ilyin, I. Plokhov, I. Savraev, O. Kozyreva, "Modeling of time dependent thermal process in sliding electrical microcontact," in Environment. Technology. Resources. Proceedings of the 10th International Scientific and Practical Conference, Volume 3, Rezekne, Latvia, 2015, pp. 109–113, http://dx.doi.org/10.17770/etr2015vol3.194

[22] I. Plokhov, A. Ilyin, O. Kozyreva, I. Savraev, "The simulation model of sliding contact with three degrees of freedom and distributed parameters of the transition layer," in Environment. Technology. Resources. Proceedings of the 10th International Scientific and Practical Conference, Volume 3, Rezekne, Latvia, 2015, pp. 182–186, http://dx.doi.org/10.17770/etr2015vol1.229

Environment. Technology. Resources. Rezekne, Latvia
Proceedings of the 12th International Scientific and Practical Conference. Volume III, 214-218

Experimental Studing of Mechanical-and- Physical Properties of Rubber during Ageing

Svetlana Polukoshko
Ventspils University College
Engineering Research Institut "VSRC"
Ventspils, Latvia
pol.svet@inbox.lv

Andris Martinovs
Rezekne Academy of Technologies
Rezekne, Latvia
andris.martinovs@rta.lv

Edgars Zaicevs
Rezekne Academy of Technologies
Rezekne, Latvia
edgars.zaicevs@rta.lv

***Abstract*— Elastomeric materials, both natural rubber and synthetic, are widely used in industry and civil engineering, due to their unique properties: high elasticity, low volume compressibility, capability to absorb and dissipate input energy, a linear relationship between stress and strain up to strain of 15% ÷ 20%, resistance to aggressive environmental factors. Different kind of compensation devices, vibration dampers, shock absorbers are fabricated from rubber materials.**

At the same time the elastomeric materials nonreversible change their properties over time, this disadvantage is called ageing.

In given paper the results of experimental studying of the influence of aging on the physical-and-mechanical properties of polyurethane rubber is presented. The samples of cylindrical form were prepared from soft flexible polyurethane rubber Xenias PX30 and subjected to the artificial ageing. Accelerated aging of samples was fulfilled in accordance with European standard ISO 188:2011 (Rubber, vulcanized or thermoplastic - Accelerated ageing and heat resistance tests).

The changing of volume, Shore A hardness, elastic rebound coefficient and static elasticity modulus under compression were investigated. Experiments showed the volume decrease, hardness shore increasing, elastic rebound increase and compression modulus under static loading increasing. This data are necessary for correct designing of the compensation devices to provide their working properties during all service life.

***Keywords*—accelerated ageing, elastomers, hardness, compression static loading, stiffness.**

I. Introduction

Natural and synthetic rubber is very important structural materials, which is widely used in various sectors of the economy and in everyday life: vehicle manufacturing, shipbuilding, cable and electrical industry, building industry, products for contact with food and drinking water, medical, pharmaceutical, hygiene products and products for children.

Such extensive use the elastomeric materials received primarily due to their unique properties: ability to deform significantly at relatively low stresses, restore the original shape after removing the load, absorb and dissipate mechanical energy during deformation. They have high strength, low volume compressibility (change shape under mechanical loading, keeping almost a constant volume); low residual deformation; high wear resistance, resistance to ultraviolet radiation and radiation [1].

Thereby rubbers are widely used in engineering and industry where products operate in "harsh" conditions for such technical products as seals of any type, bushings, plugs, sockets, valves and plugs, shock absorbers, rollers.

The main disadvantage of rubber materials is their ability to change their properties significantly under the influence of external factors of a mechanical and non-mechanical nature. These changing are associated with corresponding changes in the structure and may be reversible and irreversible.

Irreversible changes may be the result of a number of mechanochemical and chemical processes activated by mechanical stress. Irreversible destruction of the structure under the action of mechanical forces is the greater, the lower the rate of relaxation processes. With repeated deformations, this leads to corresponding changes in the structure and properties of rubber.

One of non-mechanical factors affecting the properties of rubber is the effect of heat. It causes reversible changes in the structure and properties associated with an increase in the energy of thermal motion. Along with this, prolonged exposure of rube to heat, especially in a chemically active medium, may lead to irreversible changes, called ageing.

Ageing is the irreversible change in the properties of a rubber under the action of heat, light, oxygen, air, ozone, etc, or corrosive media, i.e. mostly non-mechanical factors. Ageing is activated if the rubber is simultaneously exposed to mechanical loads [2] – [4].

Ageing tests are carried out by withstanding rubber under various conditions. Experiments on accelerated ageing test are regulated by ISO standards [5] – [7]. With atmospheric aging in the open air or thermal ageing in an environment of hot air, the result of the test is assessed by the coefficient of aging, which is the ratio of changes in the performance of some properties, most often tensile strength and relative elongation at break, to the corresponding indicators before aging [8]. The smaller the change in properties during ageing and the coefficient

Print ISSN 1691-5402
Online ISSN 2256-070X
http://dx.doi.org/10.17770/etr2019vol3.4200

of aging, the higher the resistance of rubber to ageing.

As soon scope of our study is application of elastomeric materials for technical products like mechanical seals, joints, etc., in machinery we estimate the change of compression elastic modulus, hardness Shore A, elastic rebound coefficient and volume change during accelerated ageing of polyurethane rubber. The Xencas PX series is a range of industry leading flexible polyurethane rubbers which cure to hardness from 30 to 90 Shore A whilst retaining excellent tear strength and resilience. Xencast PX resins are ideal for product applications requiring a flexible yet durable material including soft-grip handles, protective cases, rests, training weapons, tools, wheels, bushes and much more. PX series resins can also be used to produce durable, flexible molds for concrete casting. Utilizing the latest polymer technology, Xencast PX30 is able to create flexible PU rubber parts with superior tear strength, abrasion and wear resistance and chemical tolerance.

Suggested uses of Xencast PX rubber are soft gaskets and seals, therefore the main goal of this work is the investigation of this product under pure compression and the changing of its property in time.

II. Materials and Methods

A. *Material and specimens*

Material**,** used in research, is Easy Composites Ltd Xencast PX30 soft flexible polyurethane rubber**.** Cured properties of this product: Shore A hardness 30 – 35, tensile strength 0.7 – 1.2 MPa, elongation at break 100 – 155%, maximum operating temperature 80° C. These properties are given by manufacturer, elastic modules at static load E = 3.20±0.10MPa was obtained earlier by compression test with machine Zwick / Roell Z-150 in RTA laboratory.

Test specimens were prepared of cylindrical shape with initial dimensions of a diameter 39 mm and a height 13 mm. Samples were made in accordance to standard ISO 23529, 2010 [9].

B. *Testing methodology and machinery*

All equipment for rubber testing were calibrated accorging to the guide ISO 18899:2004 [10].

The artificial ageing of polyurethane rubber samples was performed according to DIN 53508: 2000 in the thermostat Memmert UNE 400 [11].

The oven Memmert UNE 400 (maximal temperature +250℃) was produced in Germany with the use of high-grade materials and the application of the latest manufacturing techniques. Samples were subjected to heating under 100℃ during 14, 24, 56, 72, 120 and 168 hours. The specimens sizes after heating decrees.

The relative change of volume during heating time is calculated as:

$$\theta = \frac{V - V_0}{V_0} \cdot 100\%, \tag{1}$$

where: V_0 - the volume of the sample before ageing,
V is the volume of the sample after aging.

Shore A hardness measurement was performed in accordance with DIN 53505: 2000 Testing of rubber – Shore A and Shore D hardness test [12] and ISO 48-4:2018 [13].

The rebound elasticity was determined according to DIN 53512: 2000, using Schob pendulum in case of direct central impact shown in Fig. 1 [14].

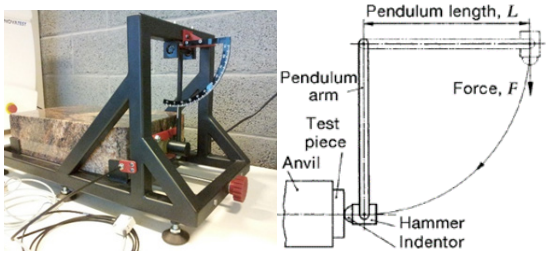

Fig. 1. Rebount resilience test: .(a) testing rig, (b) principle of test

Rebound resilience R is the ratio of energy returned E to energy applied E_0 Rebound resilience:

$$R = \frac{E}{E_0} = \frac{mgh}{mgh_0} = \frac{h}{h_0} = \frac{L \cdot (1 - \cos\alpha)}{L \cdot (1 - \cos\alpha_0)} = \frac{1 - \cos\alpha}{1 - \cos\alpha_0}, \tag{2}$$

where: m – indentoe mass,

g – gravity acceleration,

α –coner of pendulum deviationion.

If α 0 =90 0 R=(1-cosα)·100% in perctntage.

The elasticity modulus is determined using the pure compression test data. The compression test was performed with Zwick / Roell Z-150 universal tensioning machine (Fig. 2 a); strain rate 10mm / min; maximum deformation 18%.

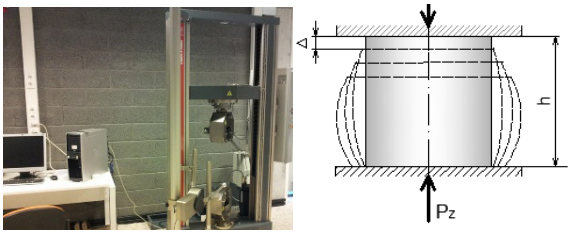

Fig. 2. Compressing testing: (a) Zwick / Roell Z-150 universal testing machine, (b) scheme of sample deformation.

The mechanical stress is to be. calculated in relation to the true cross-section. The deformative behavour of spesimens under compression depend on boundary conditions, i.e. contact friction between steel and rubber (usually friction factor f =0.2 – 0.3) and deformed spesimen will be of barrel-shaped cylinder (Fig. 2b). Straight circular cylider may save its form after compression between two rigid plates only if f = 0.

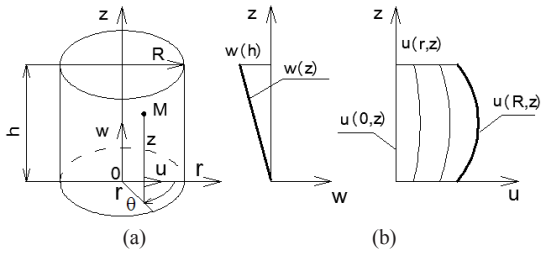

Fig. 3. Cylindrical coordinate system (a); displacement functions *w(z)* and *u(r,z)* (b).

The deformed shape of the cylinder may be defined using displacement fu nctions, which are required for minimization of the total potential energy functional in Ritz method [15]. For axially symmetric problems cylindrical coordinates system are chosen and the sought –for functions of displacement (*u, v, w*) are set as the functions of the coordinates (*r, θ, z*). Coordinate system and scheme of rubber block displacement are shown in Fig. 3.

Displacement functions must satisfy the main boundary conditions, as well as the symmetry and the presence of extremum must be taken into account; in our case for simplicity we choose:

$$u = C_1 f_1(z),\ v = 0,\ w = C_2 f_2(z) \text{ and } f_1 = \frac{\partial f_2}{\partial z} \qquad (3)$$

Contact geometrical boundary conditions are the next:

$$u(r, z = 0) \neq 0,\ u(r, z = h) \neq 0,\ w(r, z = 0) = 0,$$
$$w(r, z = h) = -\Delta. \qquad (4)$$

The displacement functions *u, v, w* along the axis of cylindrical coordinate system *r, θ, z* are chosen as*:*

$$u(r,z)=C_1 r(z^2 - zh - h^2),\quad v(r,z)=0,$$
$$w(r,z) = C_2\left(\frac{z^3}{3} - \frac{z^2 h}{2} - zh^2\right) \qquad (5)$$

Relative deformation functions along cylindrical coordinate axis *r, θ, z* are:

$$\varepsilon_r = \frac{\partial u}{\partial r}, \varepsilon_\theta = \frac{u}{r}, \varepsilon_z = \frac{\partial w}{\partial z}; \qquad (6)$$

For incompressible material (Poisson's ratio μ=0.5):

$$\varepsilon_r + \varepsilon_\theta + \varepsilon_z = 0. \qquad (7)$$

Constants C_1 and C_2 as functions of Δ are determined from the boundary conditions (4) and conditions (7):

$$C_1 = -0.429\frac{\Delta}{h^3},\ C_2 = 0.858\frac{\Delta}{h^3}. \qquad (8)$$

$$D_Z = {}_{0,h} = D\left(1 + 0.429\frac{\Delta}{h}\right),$$
$$D_{Z=\frac{h}{2}} = D\left(1 + 0.536\frac{\Delta}{h}\right). \qquad (9)$$

True cross-section areas for each step of loading are determined with (9).

III. Results and Discussion

The main results of the investigation are given below. In Fig. 4 – 7 the plots of dependence of physical-mechanical properties of elastomer samples on the time of heating under temperature *T*=100° are presented. In Fig. 8 – 12 show compressive stress – strain diagrams for samples without aging and after 1, 3, 5 and 7 days heating.

During heating of the cylindrical samples they decrease in sizes, both height and diameter, shrink and their volume reduce up to 35% (Fig. 4).

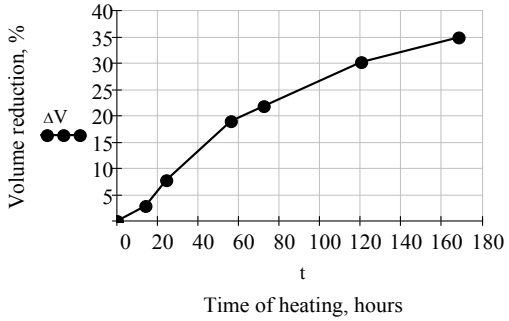

Fig. 4. Volume changing depemdence on time of heating under temperature *T*=100°.

The elasticity of polymers diminish in time, so Shore A hardness of the testing samples increase from 40 to 52.7 (Fig. 5). In accordance to scale type A this material is soft and middle soft.

Rebound resilience value decrease during time heating from 79 to 68 % (Fig. 6).

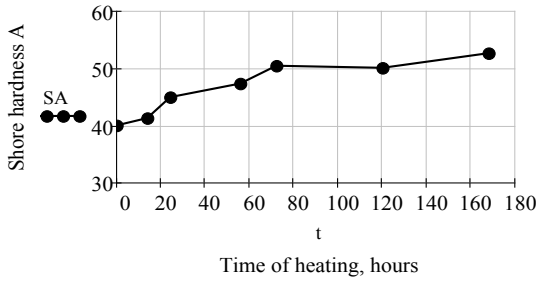

Fig. 5. Shore hsrdness A dependce on the time *t* of heating under temperature *T*=100°.

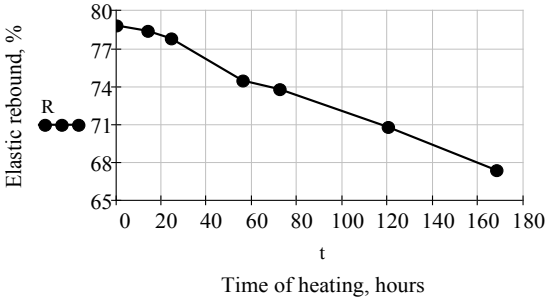

Fig. 6. Rebound resiliens value dependce on the time *t* of heating under temperature *T*=100°C.

In Fig. 7 experimental and approximated curve of the modulus of elastisity *E* and *Eap* are shown as function of time heating. Experimental value of elastisity modulus is calculated taking into account the changing of the cross section area during compression. i.e. *E* is so-called apparent modulus. Approximated curve of modulus of elasticity is represented as a power function (10).

$$E_{ap}(t) = 0.048t^{0.71} + 3.458 \qquad (10)$$

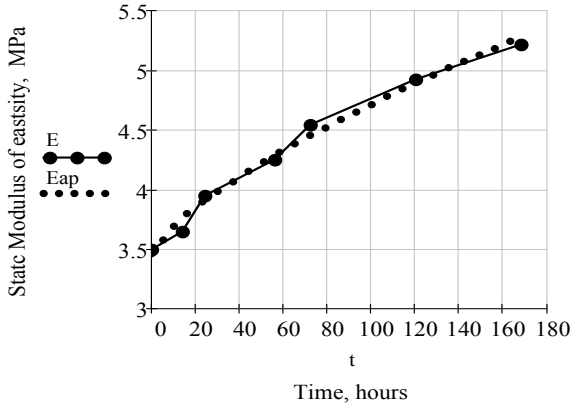

Fig. 7. Static compressive modulus of elasticity dependence on time of heating under T=100°C.

The constants in equation are defined using Mathcad-15 program with help of built-in function for curves adjusting and fitting.

This equation allows easy to estimate elastic modulus value and, consequently, deformation for any time interval.

In Fig. 8 – 12 the plots of compression stress – strain dependence for samples without ageing, samples with 1, 3, 5 and 7 days of heating are presented.

In these plots stress σ_0 with initial cross-section area and stress σ, taking into account cross-section area change, are given. Stress σ_i is approximated by straight lines $f_i(\varepsilon_i)$ in accordance with (11) – (15), given below each plot. These straight lines in the plot show the linear relationship between stress and strain and constant modulus of elasticity. The slope of these straight lines indicate the value of modulus of elasticity; it is seen from the equations that elasticity modulus increase with ageing and remain constant during experiments up to strain 16 – 18%.

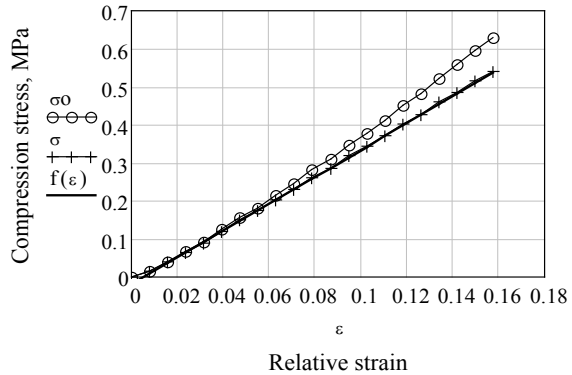

Fig. 8. Static compression stress dependence on relative strain for sample without heating.

$$f(\varepsilon)=3.51\varepsilon1-0.02 \qquad (11)$$

For the samples without ageing dependence "σ – ε" is linear during all period of loading (Fig. 8). This is true for all elastomeric materials up to strain of 15% ÷ 20%.

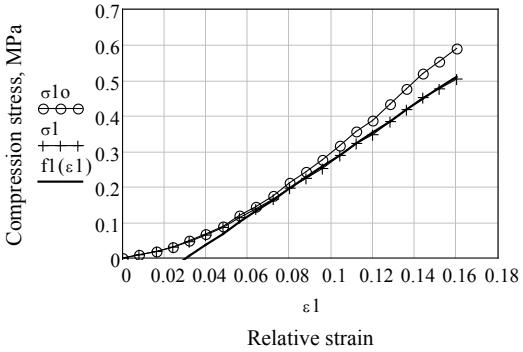

Fig. 9. Static compression stress dependence on relative strain for sample after 1 day heating under T=100°C.

$$f1(\varepsilon1)=3.95\varepsilon1-0.12 \qquad (12)$$

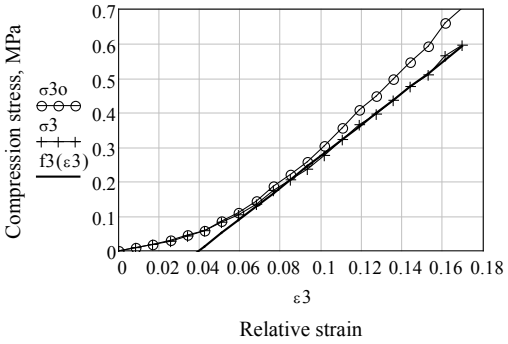

Fig. 10. Static compression stress dependence on relative strain for sample after 3 days heating under T=100°C..

$$f3(\varepsilon3)=4.54\varepsilon6-0.18 \qquad (13)$$

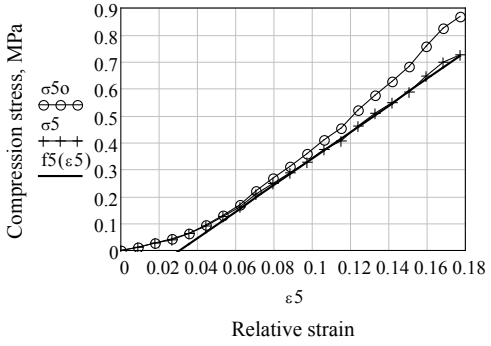

Fig. 11. Static compression stress dependence on relative strain for sample after 5 days heating under T=100°C.

$$f5(\varepsilon5)=4.92\varepsilon5-0.15 \qquad (14)$$

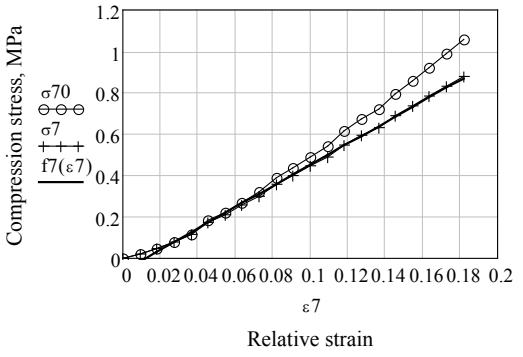

Fig. 12. Static compression stress dependence on relative strain for sample after 7 days heating under T=100°C.

$$f7(\varepsilon 7)=5.12\varepsilon 7-0.07 \quad (15)$$

After 7 days heating the elastic compression modulus reach 5.12 MPa, which is almost 50% increasing from the initial value 3.51 MPa. Cross-sectional area decrease from 1207 mm^2 till 908 mm^2 in undeformed state and from 1408 mm^2 till 1089 mm^2 after deformation of 2 mm.

IV. Conclusions

In this work the experimental studding of the influence of aging on the physical and mechanical properties of rubber is performed. The samples of cylindrical form were prepared from soft flexible polyurethane rubber Xencast PX30 and subjected to the artificial aging. Accelerated aging of samples was fulfilled in accordance with European standard ISO 188:2011 Rubber, vulcanized or thermoplastic - Accelerated ageing and heat resistance tests [5].

The changing of volume, hardness Shore A, elastic rebound coefficient and static elasticity modulus under compression were investigated. Experiments showed the volume decrease, hardness shore increasing, elastic rebound increase and compression static modulus increasing.

Influence of ageing on dynamic characteristics of polyurethane rubber Xenias PX30 will be developed in the next step of this study, based on works [16] – [18].

References

[1] A. N. Gent, Engineering with Rubber: How to Design Rubber Components. Munich, Carl Hanser Verlag, 2011.
[2] Brown R. P., Bulter T. and Hawely S.W. Ageing of Rubber: Acceleration Heat Ageing Test Results, Smither Rapra Publishing, 2001. Available: https://epdf.tips/ageing-of-rubber-accelerated-heat-ageing-test-results.html
[3] Reincke et. all, "Experimental characterization of the ageingr esistanse of elastomers", in: Constitutive Models for Rubber IX, Marvalova & Petrikova, Ed. Taylor & Francis Group, London, UK, 2015, pp. 33-37.
[4] A, Martinovs, "Mechanical properties of elastomers forecasting and principles of accelerated experiment," D.S. thesis, Riga Technical University, Riga, EU, Latvija, 2005.
[5] ISO 188:2011* Rubber, vulcanized or thermoplastic - Accelerated ageing and heat resistance tests.
[6] ISO 11346 Rubber, vulcanized or thermoplastic - Estimation of life-time and maximum temperature of use.
[7] ISO/TR 9272 Rubber and rubber products - Determination of precision for test method standards
[8] ISO 37:2017(E) Rubber, vulcanized or thermoplastic — Determination of tensile stress-strain properties.
[9] ISO 23529: 2010 Rubber — General procedures for preparing and conditioning test pieces for physical test methods.
[10] ISO 18899:2013, Rubber — Guide to the calibration of test equipment.
[11] DIN 53508: 2000. Prüfung von Kautschuk und Elastomeren. Künstliche Alterung. Testing of rubber and elastomers. Artificial ageing of rubber. ISO 18899:2004,
[12] DIN 53505:2000. Prüfung von Kautschuk und Elastomeren. Härteprüfung nach Shore A und Shore D. Testing of rubber - Shore A and Shore D hardness test.
[13] ISO 48-4:2018 Rubber, vulcanized or thermoplastic -- Determination of hardness -- Part 4: Indentation hardness by durometer method (Shore hardness).
[14] DIN 53512: 2000 Determining the rebound resilience of rubber using the Schob pendulum.
[15] S. Polukoshko, V. Gonca, A. Martinovs, S. Sokolova, "Boundary conditions influence on compressive stiffness of elastomeric isolators", Proceedings of the 15-th international scientific conference Engineering for Rural Development 2016, Volume 15 May 25-27, 2016, Jelgava, p. 924-931. Available: http://www.tf.llu.lv/conference/proceedings2016/Papers/N137.pdf
[16] S. Polukoshko, A. Martinovs, S. Sokolova. "Aging, Fatigue and Durability of Rubber Vibration Isolation Elements." Proceeding of the 11th International Scientific and Practical Conference *"Environment. Technology. Resources*.", Volume III, pp. 269-275.
[17] S. Polukoshko, A. Martinovs, E. Zaicevs, "Influence of rubber ageing on damping capacity of rubber vibration absorber", in: *Vibroengineering PROCEDIA*, September 2019, Volume 19, pp. 103-109.
[18] Martinovs A., Polukoshko S., Apeinans E., Zaicevs E. "Determination constants of 4-element rheological model with rebound resilience method." Proceedings of the 16-th international scientific conference Engineering for Rural Development 2017, Volume 16 May 24-26, 2017, Jelgava, p. 924-931.Available: http://tf.llu.lv/conference/proceedings2017/Papers/N189.pdf

Valorized Soda Lignin and Its Possible Application

Galia Shulga
Latvian State Institute of Wood Chemistry,
27 Dzerbenes St., Riga, Latvia

Sanita Vitolina
Latvian State Institute of Wood Chemistry,
27 Dzerbenes St., Riga, Latvia

Brigita Neiberte
Latvian State Institute of Wood Chemistry,
27 Dzerbenes St., Riga, Latvia

Jevgenijs Jaunslavietis
Latvian State Institute of Wood Chemistry,
27 Dzerbenes St., Riga, Latvia

Anrijs Verovkins
Latvian State Institute of Wood Chemistry,
27 Dzerbenes St., Riga, Latvia

Jurijs Ozolins
Riga Technical University,
3 Paula Valdena St., Riga, Latvia

Sandra Livcha
Latvian State Institute of Wood Chemistry,
27 Dzerbenes St., Riga, Latvia

Talrits Betkers
Latvian State Institute of Wood Chemistry,
27 Dzerbenes St., Riga, Latvia

Abstract – The aim was to obtain a valorized soda lignin and to study its properties for the followed treatment of hardwood sawdust as a filler for obtaining a wood-polymer composite. It was shown that the treatment of aspen sawdust microparticles by their immersion into a water solution of the valorized soda lignin, that is a water-soluble soda lignin/polyethylenimine polyelectrolyte complex, leads to hydrophobisation of the sawdust particles, which in turn positively affects the mechanical performance of the obtained wood-polymer composite.

Keywords – soda lignin, valorization, wood polymer composite

I. Introduction

Lignin is a biopolymer being one of the main constituents of all plants, where it performs the role of adhesive of cellulose fibres. The peculiarities of the macromolecular structure of lignin, combined with their renewability, low cost, biocompatibility, and biodegradability, make the design of new lignin-based polymer products a challenge for fundamental and applied researches. Technical lignins as by-products are formed during wood chemical processing, namely, in the paper and bioethanol industry, and their production estimated almost 50 mln tons annually [1]. Unfortunately, 98% of this amount is burnt for energy regeneration at the plants. The rest of the total amount of produced technical lignins have found widespread application as a renewable resource at a competing price level for obtaining various value-added products such as adhesives, surfactants, stiffness enhancers, soil improvers, lignin carbon fibres, chemical, as well as functional additives in polymer blends and polymer composite materials. Due to the fact that technical lignins are available in large amounts and have a relatively low price, the valorization of lignin regardless of application will be beneficial and would result in considerable economical gain.

The major limiting factor for incorporation of technical lignin in polymer blends and composite materials is its limited compatibility with a polymer matrix [2, 3]. The compatibility between lignin and synthetic polymers can be achieved, for instance, via purposeful chemical valorization of lignin. There are many methods for valorization of lignin by complexation with metal ion, hydroxyalkylation, esterification, alkylation, grafting, mixing with reactive polymers, etc. [4, 5].

One of the perspective ways of lignin valorization may be the formation of polyelectrolyte complexes on lignin basis [6, 7]. The polyanionic nature of water-soluble lignin gains spontaneous interaction with polymeric cations in water solutions with the formation of polyelectrolyte complexes that may be regarded as one of the advanced added value lignin products due to the simplicity of their preparation technology and a wide range of their possible applications [8, 9]. Owing to the features of the structure of lignin-based polyelectrolyte complexes formed, their macromolecules can be easily adsorbed at the different surfaces due to the formation of physicochemical and covalent bonds.

The aim of the work was to obtain a valorized soda lignin and to study its effect on the mechanical properties of a wood polymer composite

II. Materials and methods

Materials

Soda lignin. Soda lignin was extracted from hydrolysed aspen sawdust in a laboratory reactor under the following laboratory conditions: hydromodulus – 1/7, NaOH concentration – 4.0 mass %, temperature – 165 ^{o}C and duration – 1.5 h. The hydrolysed aspen soda lignin (HASL) was separated from the cooking solution by precipitation with 20% sulphuric acid. The chemical composition of lignin was studied by elements (Elementar Analysensysteme GmbH, Germany) and functional groups analysis, according to [10]. The purified lignin had the following chemical composition: 62.3% C, 6.5% H, 0.15% N, 0.25% S, 30.8% O; OCH_3 - 19.3%, total

Print ISSN 1691-5402
Online ISSN 2256-070X
http://dx.doi.org/10.17770/etr2019vol3.4122

OH - 5.6%, phenolic OH - 3.5%, aliphatic OH – 2.1%, COOH - 2.1%, CO - 3.9%. The average molecular of the lignin (Mw, Mn) were found by SEC-MALS20 (Malvern, United Kingdom) in DMSO with lithium bromide as an eluent at 60°C and closed to 10.5 kDa and 5.7 kDa, respectively.

Polyethylenimine. High molecular branched polyethylenimine (PEI, Mw = 750 kDa, M_n = 60 kDa, 50% water solution) contains primary, secondary tertiary amine groups was used for obtaining the functional additive. It was supplied from Sigma Aldrich.

Obtaining of the valorized soda lignin. The valorized soda lignin as a water-soluble polyelectrolyte complex (LPEC) was obtained in a reaction mixture by mixing equal volumes of dilute alkaline water solutions of hydrolysed soda lignin and polyethylenimine at a room temperature. The pH value of the obtained lignin/PEI reaction mixture was about 10.5. The mixture was used after 2 hours after its obtaining.

Treatment of sawdust particles with the LPEC. The treatment was performed by immersion of the hydrolysed aspen particles < 100 mkm in a HASL/PEI reaction mixture during 24 h at a constant stirring and a room temperature.

S*awdust*. The aspen sawdust, representing a waste of the mechanical processing of aspen wood (*Populus tremula*), was suppled by a Latvian company. The sawdust was characterised by elemental analysis (Elementar Analysensysteme GmbH, Germany) and wood polymers composition according to chemical procedures for lignin, hemicelluloses, cellulose and extractives [11]. The content of cellulose, lignin, hemicelluloses, extractives and ash in the aspen wood was 50.6%, 18.5%, 28,7%, 4.51% and 0.4%, respectively. The hydrolysis of the sawdust was performed at a low temperature with a hydrochloric acid under mild conditions (60°C, 5 h, mass ratio of wood particles to water of 1/20) with a purpose to decrease the content of hemicelluloses in the sawdust. After the hydrolysis, the sawdust particles were washed to a neutral medium, dried and milled with a planetary ball mill (Retsch, Germany) during 15 min at 300 rpm.

Polymer matrix. Recycled polypropylene (rPP) (0.9 t m^{-3}, 5.2/10 min at 230° C, 2.16 kg) was used as a thermoplastic polymer matrix and supplied from a Latvian polymer recycling plant.

Wood-polymer composite samples. The composite samples were prepared from rPP and the modified aspen microparticles, treated with the LPEC, with a moisture content < 1.0%, using a twin screw extruder and a moulding machine (HAAKE MiniLab II with MiniJet II, Thermo Scientific "HAKKE") at temperatures of 175°C. The extruder screw rotational speed was 130 rpm, while the injection moulding pressure was 600-700 bar. The microparticles content in the composites was 50 %.

Experimental Procedure

*Surface tension***.** The surface tension (σ) of HASL, PEI and LPEC water solutions at the water-air interface was measured by a Wilhelmy plate, using a tensiometer K100M (KRUSS, Germany) at 25° C with a circulation thermostat, according to [12]. Three replicates were made for each sample.

Zeta potential and size. Zeta potential (*Z*) for the sawdust microparticles was measured with a dynamic light scattering device Zetasizer Nano SZ (Malvern, UK) at 25 °C, using 0.1% suspensions of the sawdust particles in distilled water. For circulation of the suspension, autotitrator MPT-2 was used. Three replicates were made for each modified sawdust.

Viscometry. Specific viscosity was determined using a capillary viscometer Ubbelohde with a flow time of pure water closed to 300 ± 0.01 sec at 25.0 ± 0.1° C, according to [12]. Three replicates were made for each sample.

Potentiometric and conductometric titration. The titration curves were obtained using InoLab level 3 Multiparameter Meter (WTW, Germany) at the constant stirring. O.1 M NaOH un 0.1 M HCl were used for adjustment of pH values of the water solutions of polyelectrolytes. Three replicates were made for each sample.

UV-VIS spectroscopy. The UV-spectra were recorded with a Genesys 10UV UV/VIS spectrophotometer (Termo Fisher Scientific).

Mechanical tests. Mechanical properties were determined with a universal machine "Zwick" (Zwick/Roell, Germany) with a load capacity of 0.5 kN at a rate of 50 mm/min "Zwick" (Zwick/Roell, Germany) with a load capacity of 0.5 kN at a rate of 50 mm/min and 2 mm/min for tensile and bending tests, respectively, according to ASTM D638 and EN ISO 178 with the help of a software programme TestXpert. Before testing, the samples were conditioned at 60 °C during 24 h and then placed in a desiccator with phosphorus pentoxide. Five replicates were made for each mechanical testing, and standard deviation for each index was found.

Milling. The milling of wood sawdust was carried out with a planetary ball mill (Retsch, Germany) with the followed sieving, using a mill "Pulverisette" (Fritsch, Germany).

III. Results and discussion

Valorized soda lignin

The polyelectrolyte complex with a mass ratio of HASL/PEI equal to 1 was obtained in the reaction mixture by blending dilute alkaline solutions of the soda lignin and PEI. A content of amine groups of PEI in the obtained LPEC was more then 3-folds higher than the content of phenolic hydroxyl and carboxyl groups in the soda lignin. The pH value of the reaction mixture was about 10.5. The alkaline medium of the reaction mixture was chosen, taking into account a nucleofilic character of interaction of amine groups of PEI with carbonyl and carboxyl groups that were contained in both the soda lignin, milled hydrolysed sawdust and recycled polypropylene. The charged ratio between HASL and PEI were chosen basing on the results of potentiometric and conductometric titration of ionogenic groups of the soda lignin (phenolic hydroxyl and carboxyl groups) (Fig. 1) and amine groups of PEI (Fig. 2). The excess of amine groups was dictated by both the need to compensate for the negative surface charge of the modified lignocellulosic particles in order to increase their hydrophobicity and to form chemical bonds with the lignin and recycled polymer matrix, containing

carbonyl and carboxyl groups [13, 14], the concentration of which are increased during obtaining

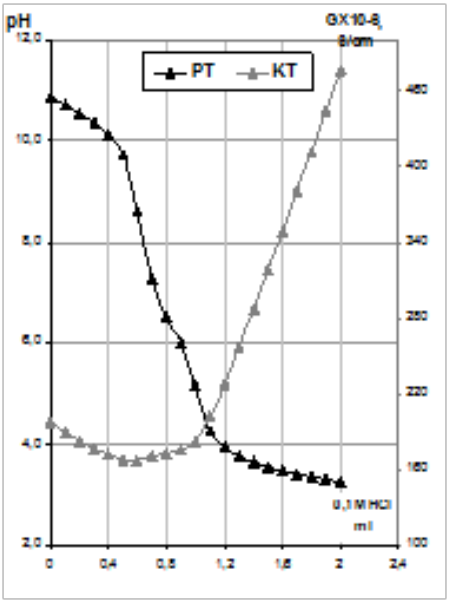

Fig. 1. Curves of potentiometric and conductometric titration of a 0.01% HASL water solution

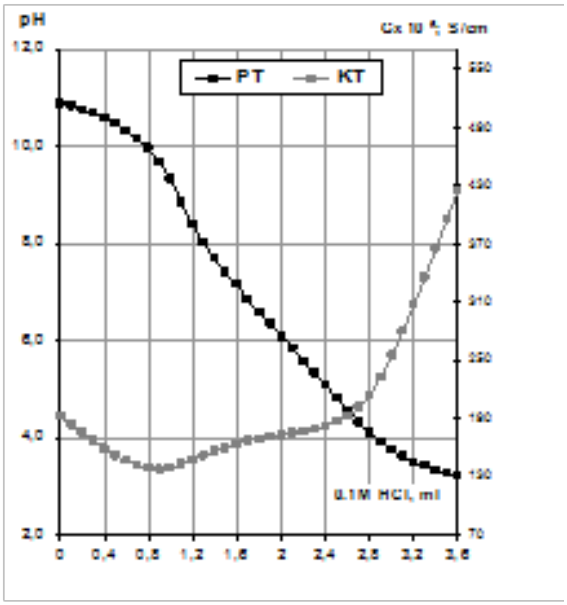

Fig. 2. Curves of potentiometric and conductometric titration of a 0.01% PEI water solution

wood polymer samples. Taking into account the fact that the amino groups of PEI are practically not protonated in a strong alkaline medium, it can be assumed that the LPEC can be formed by H-binding of non-protonated amino groups of PEI with carbonyl (α- and β-ketogroups, aldehyde groups) and hydroxyl groups of the soda lignin. At the same time, a visible increase in the intensity of the absorption curve of the UV spectrum of the alkaline solution of the reaction mixture relative to that of the lignin solution (PEI does not absorb in the UV region) (Fig. 3), pronounced in the range of 260-340 nm, may indicate the presence of electrostatic interaction between the induced protonated amine groups of PEI and lignin's fragments, containing non-conjugated phenol hydroxyl groups (absorption at 280-300 nm), phenol hydroxyl groups conjugated with α-carbonyl groups (absorption at 310 nm), carbonyl and carboxylic groups (absorption at 328 and 345 nm). The presence of the electrostatic interaction in the alkaline medium between the negatively charge groups of the soda lignin and partially positively charged amine groups of PEI, leading to the formation of salt bonds, is also confirmed by a decrease in the zeta potential value of the resulting polyelectrolyte complex relative to the zeta potential of the soda lignin (Table 1).

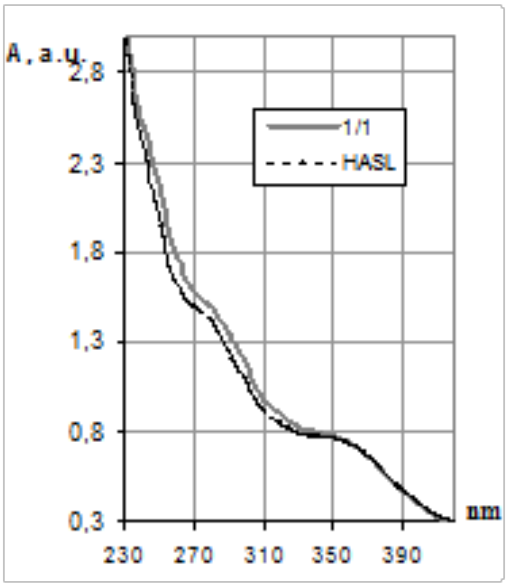

Fig. 3. UV spectra of dilute water solutions of HASL and LPEC

TABLE 1. Characteristics of HASL, PEI and their polycomplex HASL/PEI (1:1), pH 10.5

INDEX	HASL, 0,1%	PEI, 0,1%	HASL /PEI complex
Surface tension, mN/m	60,6	69,8	50,6
Zeta potential, mv	-23,1	-7,5	-19 ,0
Size, nm	134 100%*	95 100%*	98 91%*
Specific viscosity	0.019	0.045	0.056

* relative intensity

Table 1 shows the values of sizes and zeta potential for the LPEC, HASL and PEI, as well as a surface tension and a specific viscosity of aqueous solutions of the water-soluble LPEC and its initial components, having the same concentrations as in the reaction mixture. Lower values of a surface tension of the LPEC at the water-air interface compared with the soda lignin and PEI, and the value of a specific viscosity of the LPEC, which is less than the additive value of the specific viscosities of the soda lignin and PEI, testify the formation of a new polymeric product in the alkaline water solution and indicate its enhanced surface activity in comparison with the lignin and the polycation. According to Table 1, the particles of HASL, PEI and the obtained water-soluble LPEC are characterized by sizes of 108-134 nm. According to Fig. 4, the diameter of the LPEC particles are smaller than the sizes of the soda lignin ones and closed to the size of the PEI particles.

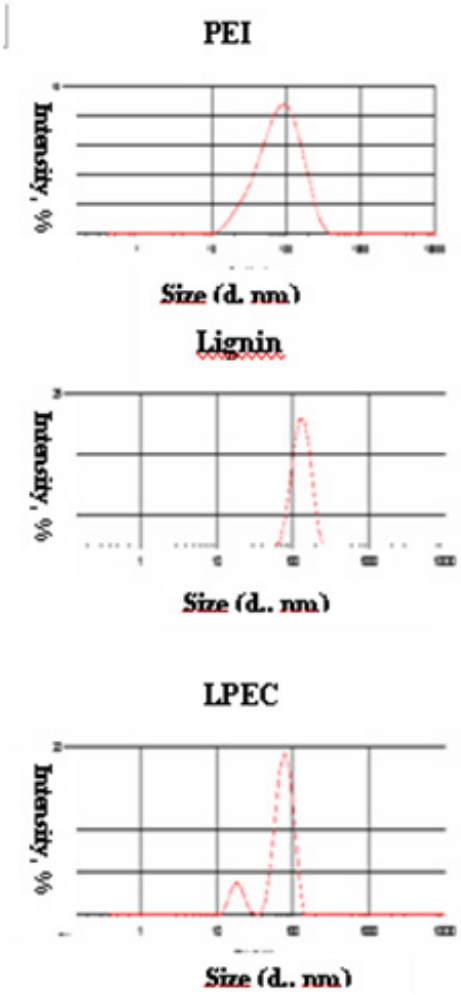

Fig. 4. Particle-size distribution pattern of PEI, HASL and HASL/PEI particles in alkaline solutions with pH 10.5.

Thus, the obtained valorized soda lignin is a water soluble polyelectrolyte complex formed in an alkaline medium as a result of hydrogen and electrostatic interactions between the functional groups of the soda lignin and PEI. The presence of the excess of the amine groups, capable of forming covalent bonds with carbonyl and carboxyl groups, as well as the presence of the salt bonds, forming the hydrophobic sites in the LPEC, indicate the increased surface activity of the valorized soda lignin obtained.

Wood polymer composite

The treatment was performed by immersion of the sawdust particles in an alkaline water solution of the HASL/PEI polyelectrolyte complex. The treated particles were separated from the suspension by a filtration using a Buchner funnel in order to remove the excess of the cationic polymer, and then they were dried. The content of a fixed nitrogen in the treated hydrolysed sawdust was equal to 1.12 %. The wood polymer composite samples with a filling degree 50 % were prepared from a recycled polypropylene powder and the hydrolysed aspen sawdust microparticles treated with the HASL/PEI polyelectrolyte complex. The obtained composite samples are shown in Fig. 5.

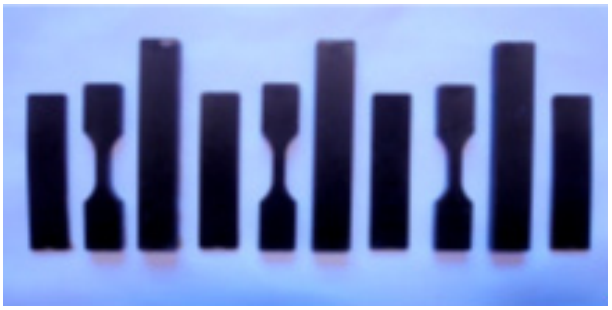

Fig. 5. Wood polymer composite samples obtained for testing

As follows from the Table 2 and Table 3, the presence of nitrogen-containing groups in the hydrolysed sawdust microparticles, treated with the valorized soda lignin, positively affects the mechanical properties of the obtained wood polymer samples.

TABLE 2. Tensile properties of wood polymer composites filled (50%) with the treated sawdust

Filler	Maximal tensile strength, MPa	Tensile modulus, MPa	ε_T, %
Initial	26.2±0.2	725±12	11.5±0.5
Hydrolysed + LPEC	38.5± 0.3	1028±15	5.1±0.6

TABLE 3. Bending properties of wood polymer composites filled (50%) with the treated sawdust

Filler	Maximal bending strength, MPa	Bending modulus, MPa	ε_B, mm
Initial	29.1±0.2	1635±31	5.9±0.2
Hydrolysed + LPEC	41.5±0.4	3455±23	1.8±0.3

According to the presented data, the composite samples are characterised by an essential increase in the mechanical strength and stiffness in comparison with the recycled polypropylene composites reinforced with the untreated sawdust. The maximal tensile strength and the tensile modulus of rupture of the composites incorporating the treated hydrolysed sawdust particles increases 1.46 and 1.42 folds, respectively. The maximal bending strength and the bending modulus of the composites filled with the treated sawdust grows 1.43 and 2.1 folds, respectively. Simultaneously, the deformability of these composites essentially decreases, namely, elongation at break drops more than 2.3 times, but deflection ability diminishes more than 3.2 folds in comparison with the case of the composite filled with the initial sawdust. Evidently, the formation the covalent bonds between the treated sawdust microparticles and the recycled polypropylene leads to the structuring of the interfacial layers and contribute to the increase in interfacial adhesion in the composite. It also may be supposed that the possible formation of a hydrogen bonds network between the functional groups of the treated sawdust and recycled polypropylene can also contribute

to the decreasing of the interfacial free energy. Thus, the treatment of the hydrolysed sawdust microparticles with the valorized soda lignin has a favourable effect on their compatibility with the recycled polymer matrix in the wood polymer composite.

IV. Conclusion

The valorized soda lignin was obtained in the form of a water soluble polyelectrolyte complex formed as a result of hydrogen and electrostatic interactions between the oppositely charged groups of the soda lignin and PEI in an alkaline medium. The presence of the excess of free amine groups as well as the presence of salt bonds, forming hydrophobic sites in the polyelectrolyte complex, indicate an increased surface activity of the valorized soda lignin.

The composite samples, filled with the hydrolysed sawdust microparticles, which are treated with a water solution of the valorized soda lignin, are characterised by better mechanical properties compared with the composite, contained the untreated sawdust. This testifies the enhancement of the interfacial adhesion between the aspen sawdust particles and recycled polypropylene in the wood-polymer composite.

V. Acknowledgments

The authors would like to thank the Ministry of Education and Science of the Republic of Latvia for the financial support of the National Research Programme (ResProd) and the institute's grant "AtkritBiomasKM".

VI. References

[1] Zion Research, Lignin Market (Lignosulfonates, Kraft Lignin and Others) for Concrete Additive, Animal Feed, Dye Stuff, and Other Applications: Global Industry Perspective, Comprehensive Analysis and Forecast 2014 – 2020, Market Research Store, Deerfield Beach, 2015.

[2] J.F. Kadla, S. Kubo, Lignin-Based Polymer Blends: Analysis of Intermolecular Interactions in Lignin–Synthetic Polymer Blends, *Composites Part A*, 35, 2004, pp. 395–400.

[3] B. Košiková, E. Sláviková, Use of Lignin Products Derived From Wood Pulping as Environmentally Desirable Additives of Polypropylene Films, *Wood Research*, 55, 2010, pp. 87–92.

[4] V.K. Thakur, M.K. Thakur, P.Raghavan, M.R. Kessler, Progress in Green Polymer Composites from Lignin for Multifunctional Applications: A Review, *ACS Sustainable Chem. Eng.* 2, 2014, pp.1072−1092.

[5] F. Lu, Lignin: structural analysis, applications in biomaterials and ecological significance. Nova Science Publishers, New York, 2014.

[6] G. Ström, P. Stenius, Formation of complexes, colloids and precipitates in aqueous mixtures of lignin sulphonate and some cationic polymers, *Colloids and Surfaces,* 2(4), 1981, pp. 357-371.

[7] G. M. Shulga, R. I. Kalyuzhnaya, L. N. Mozheyko, F.V. Rekner, A.B. Zezin, V.A. Kabanov, Features of the reactions between lignosulphonates and polymeric bases in aqueous solutions, *Polymer Science,* 26(2),1984, pp. 319-324.

[8] L. Gärlund, L. Wågberg, R. Gernandt**,** Polyelectrolyte complex for surface modification of wood fibres. II. Influence of complexes on wet and dry strength of paper, *Colloids and Surfaces: A Physicochemical and Engineering Aspects*, 218(1): 2003, pp. 137-149.

[9] G. Shulga, F. Rekners, J. Varslavans. Lignin-based Interpolymer complexes as a novel adhesive for protection against erosion of sand soil, *Journal of Agricultural Research Engineering*, 78 (3), 2001, pp. 309-316.

[10] G. F**.** Zakis Functional analysis of lignins and their derivactives. Atlanta: TAPPI Press, GA, 1994.

[11] A.V. Obolenskaya, Z.P. Elnitskaya, A.A. Leonovich, Laboratory Manual on Wood and Cellulose Chemistry, Ecologia, Moscow, 1991.

[12] G. Shulga, V, Shakels, O. Aniskevicha, T. Bikova, A. Treimanis**,** Effect of alkaline modification on viscometric and surface-active properties of soluble lignin. *Cell. Chem*. *Techn*., 40, 2006, pp. 383-392.

[13] G. M. Shulga, L. N. Mozeyko, F.V. Rekner, R.I. Kalyuzhmajya, A.B. Zezin, V.A. Kabanov, Chemical conversions in polyelectrolyte complexes based on lignosulfonates. *Khim. Drev.*, 1, 1982, pp. 87-93.

[14] De La Orden, M.U., Gonzalez Sanchez, C., Gonzalez Quesada, M., Martinez Urreaga, J. Effect of different coupling agent on the browning of cellulose-polypropylene composites during melt processing, *Polymer Degradation and Stability*, 95(2), 2010**.** pp**.** 201-206.

Environment. Technology. Resources. Rezekne, Latvia
Proceedings of the 12th International Scientific and Practical Conference. Volume III, 224-228

Interactive System for Study of Car's Movement with Low and Ultra-low Profile Tires in a Turn

Stiliyana Taneva
Technical University – Sofia, Plovdiv Branch
Department of Transport and Aircraft Equipment and Technologies
Plovdiv, Bulgaria
e-mail: s.taneva@tu-plovdiv.bg

Krasimir Ambarev
Technical University – Sofia, Plovdiv Branch
Department of Transport and Aircraft Equipment and Technologies
Plovdiv, Bulgaria
e-mail: kambarev@tu-plovdiv.bg

Dimitar Katsov
Technical University – Sofia, Plovdiv Branch
Department of Transport and Aircraft Equipment and Technologies
Plovdiv, Bulgaria
e-mail: katsov@abv.bg

***Abstract*— In this paper an interactive system for the study of the movement of a car in a turn is proposed. The interactive system is implemented on a modular principle in the MATLAB environment. The system operates on an algorithm, taking into account the current redistribution of the vertical wheel load and its effect on the characteristics of the lateral slip of wheels with low and ultra-low profile tires. The capabilities of the interactive system are visualized with graphical dependencies.**

***Keywords*—algorithm, slip, car, low and ultra-low profile tires.**

I. Introduction

Movement of cars with pneumatic tires in turns has been the subject of many studies, following the discovery of Broucherit of the lateral slip of elastic wheels phenomenon in 1925 [1]-[6]. The literature states that when moving through a turn with recording the lateral slip, the centre of the turn shifts [1], [2], [6] and [4]. The analysis of the slip of the front δ_1 and rear δ_2 axles in the theory [2] determines three types of automobiles: with a normal inclination to turn $\delta_1 = \delta_2$; with a lowered inclination to turn $\delta_1 > \delta_2$, and with increased inclination to turn $\delta_1 < \delta_2$.

It is known that lateral slip characteristics are determined for one wheel with a pneumatic tire on tire testing machines with different level of complexity [7]. When driving in a turn, the wheels of the car slip in different ways due to the redistribution of their vertical load in the centre of the turn.

The purpose of the present work is to propose an interactive programming system in the MATLAB environment to study the analytically the motion of the cars with low and ultra-low profile tires through a turn, taking into account the redistribution of load on the characteristics of the lateral slip of tires. The interactive system allows a dialogue operational mode with the user and allow for quick and accurate calculation.

The interactive system allows as early as the design stage of the car to determine its inclination to turn with the selected tires.

II. General Regulations

2.1. Analysis of the movement of a car with low and ultra-low profile tires in a turn

Fig. 1 (*a*) presents the motion scheme of a 4x2 car at settled turn with pneumatic wheels slip in a fixed actual centre of the turn p. $\hat{I}_\delta$. For a car with hard wheels the centre of the turn is $\hat{I}_1$. From Fig. 1 (*a*) the radius of the turn can be presented as

$$R_\delta = \frac{L}{tg\left(\theta_{sr} - \delta_1\right) + tg\delta_2} \quad , \tag{1}$$

where δ_1 and δ_2 are respectively the angles of slip of the front and rear axles;
L - wheelbase;
θ_{sr} - the average angle of the steered wheels.

The distance from the centre of the turn p. O_δ to the centre of gravity of the vehicle p. C, according to Fig. 1 (*a*) can be recorded as

$$R_c = \sqrt{R_\delta^2 - \left(b - R_\delta tg\delta_2\right)^2} \quad , \tag{2}$$

where b is the longitudinal coordinate of the centre of gravity of the vehicle.

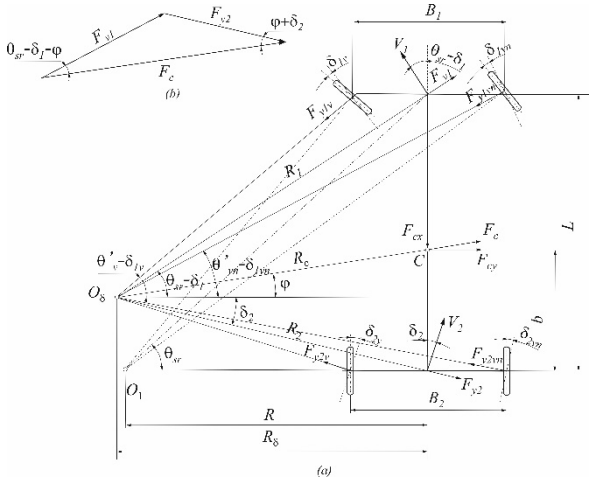

Fig. 1. Scheme of a car in a turn.

From the scheme of Fig. 1 (*a*) the actual centre of turn

Print ISSN 1691-5402
Online ISSN 2256-070X
http://dx.doi.org/10.17770/etr2019vol3.4198

p. $\hat{I}_{\delta}$ determines the lateral slip of the vehicle tires with the following dependencies

$$\delta_{1v} = \theta_v^{'} - arctg\frac{R_\delta tg\left(\theta_{sr} - \delta_1\right)}{R_\delta - \frac{B_1}{2}} \quad (3)$$

$$\delta_{1vn} = \theta_{vn}^{'} - arctg\frac{R_\delta tg\left(\theta_{sr} - \delta_1\right)}{R_\delta + \frac{\hat{A}_1}{2}} \quad (4)$$

$$\delta_{2v} = arctg\frac{tg\delta_2}{1 - \frac{B_2}{2R_\delta}} \quad (5)$$

$$\delta_{2vn} = arctg\frac{tg\delta_2}{1 + \frac{B_2}{2R_\delta}}, \quad (6)$$

where $\hat{A}_1$, $\hat{A}_2$ are respectively the track widths of the front and rear axles of the vehicle;

$\delta_{1v}, \delta_{1vn}$ - the angles of slip, respectively, of the inner and outer front wheels;

$\delta_{2v}, \delta_{2vn}$ - the angles of slip, respectively, of the inner and outer rear wheels.

To determine the reactions on the road, it is necessary to know some of the parameters of the vehicle: vehicle weight G, track widths $\hat{A}_1$, $\hat{A}_2$, wheelbase L, the angles of rotation of the wheels around the steering axis - θ_v, θ_{vn}.

For the centrifugal force applied at the centre of gravity of the vehicle, p. C, Fig. 1 (*a*), we obtain the following dependency

$$F_c = \frac{GV_2^2}{gR_\delta^2} R_c \cos^2\delta_2 \quad (7)$$

where G is the weight of the car;

g - acceleration of gravity;

V_2 - the speed of the rear axle of the vehicle.

The longitudinal and transverse components of the centrifugal force can be presented as

$$F_{cx} = \frac{GV_2^2}{gR_\delta^2} b\cos^2\delta_2 - \frac{GV_2^2}{2gR_\delta}\sin 2\delta_2$$
$$F_\delta = GV_2^2\frac{\cos^2\delta_2}{gR_\delta} \quad (8)$$

Taking into account the static load on the wheels and taking into account the additional redistribution of loading and unloading according to Fig. 1 (*a*) for their normal reactions we obtain:

- for the inner front wheel

$$F_{z1v} = \frac{G.b}{2L} + A\frac{\cos^2\delta_2}{R_\delta^2} - A\frac{\sin 2\delta_2}{2bR_\delta} - B\frac{\cos^2\delta_2}{R_\delta} \quad (9)$$

- for the outer front wheel

$$F_{z1vn} = \frac{G.b}{2L} + A\frac{\cos^2\delta_2}{R_\delta^2} - A\frac{\sin 2\delta_2}{2bR_\delta} + B\frac{\cos^2\delta_2}{R_\delta} \quad (10)$$

- for the inner rear wheel

$$F_{z2v} = \frac{G(L-b)}{2L} - A\frac{\cos^2\delta_2}{R_\delta^2} + A\frac{\sin 2\delta_2}{2bR_\delta} - C\frac{\cos^2\delta_2}{R_\delta} \quad (11)$$

- for the outer rear wheel

$$F_{z2vn} = \frac{G(L-b)}{2L} - A\frac{\cos^2\delta_2}{R_\delta^2} + A\frac{\sin 2\delta_2}{2bR_\delta} + C\frac{\cos^2\delta_2}{R_\delta}, \quad (12)$$

where the coefficients A, B and C are:

$$A = \frac{G.b.h.V_2^2}{2gL};\ B = \frac{G.b.h.V_2^2}{gLB_1};\ C = \frac{G.(L-b)h.V_2^2}{gLB_2} \quad (13)$$

With the sinus theorem and the conversion of trigonometric expressions (Fig. 1 (*b*)) the total lateral forces acting on the front and the rear axle can be presented as

$$F_{y1} = \frac{GbV_2^2\cos^2\delta_2}{gLR_\delta\cos\left(\theta_{ñò} - \delta_1\right)} \quad (14)$$

$$F_{y2} = \frac{G(L-b)V_2^2\cos^2\delta_2}{gLR_\delta}. \quad (15)$$

The proposed interactive system applies an iterative method for determining the centre of the turn of the vehicle p. O_δ.

Dependencies (1) - (15) are valid under the assumption that the centre of the turn p. O_δ in Fig. 1 (*a*) is known. In fact, to find the centre of the turn, the angles of the slip need to be known, i.e. δ_1 and δ_2 of the two axles of the vehicle under the given operating conditions which can be determined experimentally directly on the vehicle or by the lateral characteristics of the wheels obtained on the laboratory equipment.

Specifying the centre of the turn p. O_δ is related, both with the determination of the lateral slip δ_1 and δ_2 of the axles, and the lateral slips of the front and rear wheels. An iterative method is used in this study, initially assuming that the slip of the pneumatic wheels is zero, i.e. $\delta_1 = \delta_2 = \delta_{1v} = \delta_{1vn} = \delta_{2v} = \delta_{2vn} = 0$. In this case, the centre of the turn will be in point $\hat{I}_1$ (Fig. 1 (*a*)).

Formulas (1) and (2) define the radius of the turn R_δ and distance R_c, after which the normal load on the wheels of the vehicle is determined. Using the K. Enke graphical method [9] the characteristics of the lateral slip for the inner wheels are drawn, and the dependencies for the outer wheels are oppositely drawn at the values obtained for the normal wheel load F_{z1v}, F_{z1vn}, F_{z2v}, F_{z2vn}. The charts are positioned so that the axes of the lateral forces F_y to coincide and are oppositely directed, and the ordinate axes on which the lateral slip δ_{1v}, δ_{1vn} of

the wheels are recorded, are displaced at a distance equal to the lateral force of the front F_{y1} and the rear F_{y2} axle. Characteristics for $\delta_v = f\left(F_{yv}\right)$ and $\delta_{vn} = f\left(F_{yvn}\right)$ have a mirror image. The ordinate of the intersection of the characteristics of the lateral slip is the common angle of the slip of the front δ_1 and the rear δ_2 axle (Fig. 2).

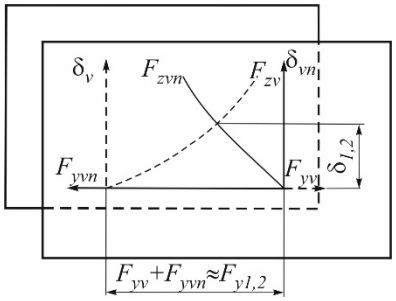

Fig. 2. Determining the lateral slip of the two axles by a mirror image of the lateral forces for the outer and inner wheels displaced at a distance equal to, respectively, the lateral forces of the front and rear axles.

The lack of experimental data on the characteristics of tire slip for normal loads of pneumatic wheels (F_{z1}, F_{z2} ….. F_{zn}), which are obtained when moving in a turn in the range $R_{\min} < R_\delta < \infty$, makes the graphical method in this form, inapplicable for studying the turn.

In this work a software was been developed for the method of K. Enke in specifying the radius of the turn R_δ with the ever changing characteristics of the lateral slip of the front and rear wheels $\delta_{1vy} = f\left(F_{1}\right)$, $\delta_{1vny} = f\left(F_{1}\right)$, $\delta_{2vy} = f\left(F_{2}\right)$, $\delta_{2vny} = f\left(F_{2}\right)$.

Through the mirror images of the slip of the outer wheels, the slips of the front δ_1 and the rear δ_2 axles are determined.

In software modules, non-linear dependencies $F_{yi} = f\left(\delta_i\right)$ for all wheels with the corresponding normal load on each wheel are determined by the proposed in [7], [8] dependencies

$$F_{yi} = k_t k_r \frac{arctg\left[\pi k_{\delta 0i}\delta_i / \left(2\varphi_{yi}F_{zi}\right)\right]}{\pi / \left(2\varphi_{yi}F_{zi}\right)} \quad (16)$$

$$F_{yi} = k_t k_r \frac{arctg\left[\pi k_{\delta 0i}\left(\delta_i - 0{,}026\right) / \left(2\varphi_{yi}F_{zi}\right)\right]}{\pi\left(\delta_i - 0{,}026\right) / \left(2\varphi_{yi}F_{zi}\right)}\delta_i \,, \quad (17)$$

where k_t is the coefficient for taking into account the profile of the tire;

k_r - the coefficient measuring the wheel rim size;

F_{zi} - load on i^{th} wheel in N;

$k_{\delta 0i}$ - coefficient of resistance against lateral slip of i^{th} wheel [7], [8];

φ_{yi} - grip coefficient of lateral direction of i^{th} wheel [7], [8].

From experimental studies in [8] to determine of the coefficient of resistance against the lateral slip $k_{\tilde{a}0i}$ the averaged experimental curves are used for: the referred length of the contact patch a''_{pr}, angular stiffness $\tilde{n}''_{\omega}$ and grip coefficient of lateral direction φ''_y for low and ultra-low profile tires with rim size from 13" to 16". The coefficient $k_{\delta 0i}$ is calculated by the dependency $k_{\delta 0i} = 2c''_\omega / a''_{pr}$, and the grip coefficient of lateral direction by $\varphi_{yi} = k''_{\varphi y}\varphi_y$ [8].

With the obtained values of the slip of the controllable axle δ_1 and the slip of the rear axle δ_2 by formula (1) we calculate the new value of the radius of the turn R_δ, while by formula (2) - the distance R_c. If the deviation of the new R_c^{new} from the old R_c^{old} value of the distance R_c is small, the calculation can be stopped. Deviation is determined by the inequality

$$\left|100\left(\frac{R_c^{new}}{R_c^{old}} - 1\right)\right| < \Delta \,, \quad (18)$$

where Δ is the set accuracy of approximation in %. In this study Δ=0,1%.

If inequality (18) is not satisfied with the received values of the lateral slip of the front axle δ_1 and the rear axle δ_2 and the radius R_δ the new wheel loads are determined F_{z1v}, F_{z1vn}, F_{z2v}, F_{z2vn} and the lateral forces of the front F_{y1} and the rear F_{y2} axle.

Once the inequality is achieved, the actual radius of the turn is specified R_δ and the slip of the front δ_1 and the rear δ_2 axle.

Formulas (3) and (4) are used to determine the difference Δ_1 between the angles of slip of the inner δ_{1v} and outer δ_{1vn} on the front axle by the dependency

$$\Delta_1 = \delta_{1v} - \delta_{1vn} = \left[\theta'_v - arctg\frac{R_\delta tg\left(\theta_{sr} - \delta_1\right)}{R_\delta - \frac{\hat{A}_1}{2}}\right] - \left[\theta'_{vn} - arctg\frac{R_\delta tg\left(\theta_{sr} - \delta_1\right)}{R_\delta + \frac{\hat{A}_1}{2}}\right] \quad (19)$$

Formulas (5) and (6) are used to define the difference Δ_2 between the angles of slip of the inner δ_{2v} and outer δ_{2vn} wheel on the rear axle by dependency

$$\Delta_2 = \delta_{2v} - \delta_{2vn} = arctg\frac{tg\delta_2}{1 - \frac{B_2}{2R_\delta}} - arctg\frac{tg\delta_2}{1 + \frac{B_2}{2R_\delta}} \quad (20)$$

With the latter (after inequality (18) is achieved) values of the normal wheel load F_{zi}, the lateral forces of the front F_{y1} and the rear axle F_{y2}, the displaced lateral slip characteristics are drawn by the K. Enke method (Fig. 3), by drawing also the characteristics of Fig. 2, but

displaced at a distance $\Delta_{1,2}$.

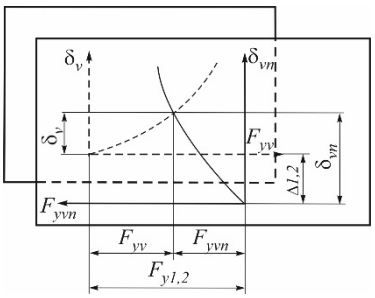

Fig. 3. Determining the lateral reactions and lateral slip of the wheels of the two axles.

The interactive system allows to explore the movement in the turn of 4x2 and 4x4 cars.

2.2. Structure of the interactive system

Based on the analytical dependencies presented above and the iterative method (dependency (18)) a program was developed in the MATLAB environment. The block-scheme of the interactive system is presented on Fig. 4. It also has a number of logical operations required by the specifics of the calculations performed. The programme also uses the obtained experimental results for drawing dependencies $F_{yi} = f(\delta_i)$ [7], [8]. The interactive system allows graphic analysis determination of the slip of the inner δ_{1v}, δ_{2v} and the outer $\delta_{1vn}, \delta_{2vn}$ wheels of the car and the lateral slip in a turn of the front δ_1 and the rear δ_2 axle. All this allows for automated analytical study of the movement in a turn of cars with low and ultra-low profile tires, including the impact of varying initial data on vehicle stability and handling.

The mass and geometric parameters of the vehicle are initially introduced. The initial data are: the mass of the vehicle m, the track width of the front $\hat{A}_1$ and the rear $\hat{A}_2$ axle, the wheelbase L, the coordinates of the mass centre of the car b, h, the angles of rotation of the inner θ_v and outer θ_{vn} wheels and the tire dimensions - B_t, H_t, d_r.

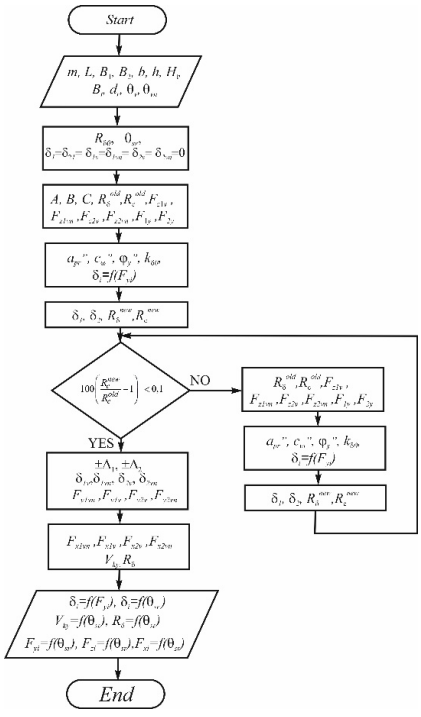

Fig. 2. Block-scheme of the interactive system.

2.3. Results

For visualizing the capabilities of the interactive system, the initial data of a car Honda Civic Aerodeck 1.5iLS were used with tire dimensions 185/60R14. The graphical dependencies shown in Fig. 5 and Fig. 6 are at a given vehicle speed $V = 20\ km/h$, vertical wheel loads, respectively $F_{z1v} = 3{,}164\ kN$, $F_{z1vn} = 4{,}886\ kN$, $F_{z2v} = 3{,}175\ kN$, $F_{z2vn} = 4{,}962\ kN$ and air pressure in the tires $p_b = 0{,}25\ MPa$. Fig. 5 illustrates the graphical dependencies of the characteristics of slip of the front $\delta_{1vn} = f(F_{y1v})$, $\delta_{1vn} = f(F_{y1vn})$ and the rear $\delta_{2v} = f(F_{y2v})$, $\delta_{2vn} = f(F_{y2vn})$ wheels, and Fig. 6 shows the changes of the slips of the front δ_1 and the rear δ_2 axles from the average angle of the steered wheels $\theta_{sr} = 15°$ of the car.

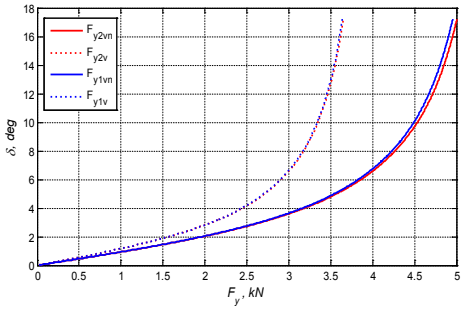

Fig. 3. Characteristics of lateral slip of the car's inner and outer tires.

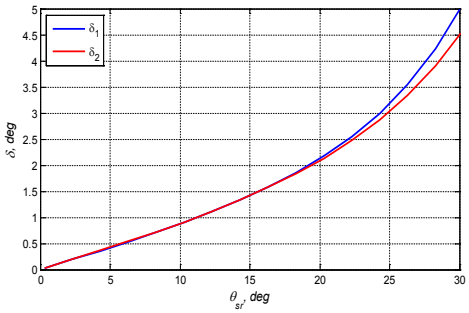

Fig. 4. Lateral slip of the front δ_1 and the rear δ_2 car axle.

III. Conclisions

From the results for the slip of the front δ_1 and rear δ_2 axle, as well as the angles of slip of the outer $\delta_{1vn}, \delta_{2vn}$ and inner δ_{1v}, δ_{2v} wheels under the above conditions, the following conclusions can be drawn:

- The Honda Civic Aerodeck car has a reduced inclination to a turn for the entire steered wheel rotation range.
- The characteristics of the lateral slip of the inner δ_{1v}, δ_{2v} and the outer $\delta_{1vn}, \delta_{2vn}$ wheels are approximately equal which is due to the centre of gravity position in the centre of the car.
- The proposed interactive system for studying the turn of a passenger car with low and ultra-low profiled tires allows to quickly and accurately examine the kinematic and dynamic parameters of the car's wheels as early as the design stage of the vehicle.

Acknowledgements

The authors would like to thank the Research and Development Sector at the Technical University of Sofia for the financial support.

Our research, the results of which are presented in this article have been carried out under the Programme Young Scientists and Postdoctoral Students of the Ministry of Education and Science, Bulgaria.

References

[1] Litvinov A. S, Handling and stability of the car. M., Mechanical Engineering, 1971.
[2] Lyubenov S, Angelov B, Evtimov I, Vehicles and Tractors. Performance properties, Ruse, 2004.
[3] Pacejka H. B, Tyre and Vehicle Dynamics. SAE, Warrendale, 2002.
[4] Pacejka H. B, Tyre and Vehicle Dynamics. Second edition, Amsterdam, Boston, Heidelberg, London, New York, Oxford, Paris, San Diego, San Francisco, Singapore, Sydney, Tokyo, ISBN -13: 980-0-7506-6918-4, 2006.
[5] Katsov D. A., Hlebarski D. A, Dynamics of the turn of wheel vehicle with account of the deformations of the tires and the influence of the suspension. International Journal of Computational and Numerical Analysis and Applications, Vol. 6, No. 2, pp.97-106, 2004, ISSN 1311-6789.
[6] Katsov D. A., Hlebarski D. A, Kinematics of the turn of wheel vehicle with account of the deformations of the tires and the influence of the suspension. International Journal of Computational and Numerical Analysis and Applications, Vol. 25, No. 2, pp. 203-214, 2005, ISSN 1311-8080.
[7] Katsov D., S. Taneva, On obtaining the lateral slip characteristics of low and superlow profile tires of cars. Journal of Machine Building and Machine Science, Varna, Bulgaria, year. X, No. 2, vol. 24, pp. 33-38, 2015, ISSN 1312-8612.
[8] Katsov D., S. Taneva, Investigation of the lateral slip and grip of low and superlow profile tires of cars. Journal of Machine Building and Machine Science, Varna, Bulgaria, year. X, No. 2, vol. 24, pp. 39-45, 2015, ISSN 1312-8612.
[9] Katsov D.A, Study on stabilization of the steered wheels of a wheeled tractor 4x2 - class 14 kN. PhD thesis, “Angel Kanchev” University of Ruse, Bulgaria, 1987.

Surfacing – Technologies and Layer Properties (a Review)

Manahil Tongov
Faculty of Industrial Technology
Technical University of Sofia
Sofia, Bulgaria
tongov@tu-sofia.bg

***Abstract*—The overview includes the basic methods for obtaining surface layers: arc surfacing - submerged arc surfacing (SAS), tungsten inert gas arc surfacing (TIGS), metal gas surfacing (MIG/MAG), plasma surfacing (PS); electron beam surfacing (EBS); laser surfacing (LS); electroless cladding (ELC); friction stir surfacing (FSS). Layers are applied on carbon steels, low alloyed steels, highly alloyed steels, aluminium alloys, titanium alloys or ductile cast iron substrates. The data on the additive materials used are provided and data on the hardness and wear resistance of the layers is given.**

***Keywords*— surface layers; methods; hardness, wear.**

I. INTRODUCTION

The application of layers and the modification of the surface of the parts are widely used in various areas of the industry. This review examines various technological processes that allow for a substantial change in surface properties relative to those of the substrate. Emphasis is placed on the resulting hardness and surface wear. The wear resistance data of the layer is generally compared with that of the substrate metal in the application of layers of homogeneous composition. The wear resistance of the layers in which there is a dispersed phase is compared to layers without dispersive phase. The variants, which demonstrates the best results are shown. The hardness data are given in the way they are published by the authors concerned, indicating the maximum values achieved.

II. TECHNOLOGICAL PROCESSES

The surfacing technological processes are in most cases close to welding processes. However, there are also technological variants that differ significantly from welding and are not applicable to joint parts. Thus, the thickest layers are obtained by electroslag surfacing (ESS) [1]. In this case, as with submerged arc surfacing (SAS) [5], [6], [7], [19], the layer characteristics are obtained depending on the combination of the components contained in the flux and the additive wire. Typically, the additional wires are solid, but core wires [6], [19] is used also. The components added in the flux which leads to increasing of the hardening phases [2] results in similar effects on hardness and wear resistance. The core wire are widely used in another electric arc processes - TIG [11], [12] and [13] and MIG/MAG [3], [10], [15], [16], [17] 20]. The solid wires are applicable in the MIG / MAG process [4], [8], [9], [10], [18] too. Additional impacts such as forced gas cooling [4], longitudinal electromagnetic field [10] and post-surfacing electron beam treatment [3] are also used to improve the characteristics of the applied layer. The heat output of the welding arc is also used for remelting of the pre-deposited layer [14]. The plasma arc can also be used to remelt a deposited layer [21] or apply a layer using the powder injected in the plasma arc [22], [23], [24]. In both cases, the surface of the substrate melts, a welding pool is formed, and during on its crystallization the additive materials participate in the formation of the layer and thus determine its properties. When the aim is to obtain intermetallic compounds with the metal of the substrate in the coating, this can be achieved by adding the second metal in the form of a powder [23]. High cooling rates using heat sources with high energy concentration such as electron beam surfacing (EBS) [25], [26], [27], [28] and [29] or laser surfacing (LS) [30] - [39] creates conditions for modifying the surface layer even without the use of filler materials [25] or after a surfacing process has been performed [3], [26]. The electron beam process is also used for sintering [27] of powder mixture to form layers. Laser surfacing is realized in three ways. The first one involves the introduction of powder material into the heated zone [30], [31], [32], [33], the second assumes the remelting of a precoat [35], [36], [37] [39] and the third uses a gaseous medium to introduce the necessary components [34]. Another possibility to produce the layer is electroless cladding (ELC) from a solution and subsequent thermal treating [40], [41], [42]. The specific in this case is that no heating is required for the deposition of the bed, and the thermal treatment is at relatively low temperatures (2900C). Both in this case and in the friction stir surfacing (FSC) [43], [44], [45], [46], [47], the melting temperatures of the substrate are not reached. Therefore, diffusion processes have a significant effect on the final result. Powders may also be used during friction stir technology [44] and [45].

III. RESEARCH METHODS

The methods used to study layers properties can be

Print ISSN 1691-5402
Online ISSN 2256-070X
http://dx.doi.org/10.17770/etr2019vol3.4180

divided into the following main groups. The microstructure is examined by optical (OM) [1], [9], [17], [21], [23], [27], [30], [31], [36]], [42], [43] and electron microscopy (SEM) [1], [10], [11], [14], [21], [22], [23] , [33], [39], [46], [47]. The phase composition is determined by the X-ray diffractometer [18], [23], [27], [31], [33], [36], [39], [45], the transmission diffraction electron microscopy [18] and energy-dispersive X-ray spectroscopy [14], [22], [30], [33], [39]. The X-ray fluorescence method [7] and the atomic emission spectrometer [7] were used to determine the chemical composition. Image analysis is used to determine the relative share of individual components [1].

IV. SUBSTRATE MATERIALS

In the publications reviewed, the materials used as substrates can be divided into the following main groups: carbon steels [3], [6], [7], [12], [13], [15], [16] 17, 18, 21, 25, 26, 29, 36 and 37; alloyed steels [1], [4], [8], [9], [20], [22], [24], [30], [41] and [42]; highly alloyed steels [5] and [32]; aluminium and aluminium alloys [11], [28], [39], [43], [44] and [45]; titanium and titanium alloys [23], [31], [34] and [35]; ductile cast iron [33] and [40]. The SAS, MIG / MAG, TIG, PST, EBS and LS methods were used to apply the layers to carbon steels. When the substrate is made from alloy steel ESA, MIG / MAG, PST, LS and ELC were used. With a high alloy steel substrate, the SAS and LS methods are listed. The deposition of layers on ductile cast iron is represented by the LS and ELS methods. The TIG, EBS, LS and FSS methods have been used for layers deposited on aluminium or aluminium alloys. To deposit layers over titanium and titanium alloys two methods are presented - PST and LS.

V. FILLER MATERIALS AND LAYER PROPERTIES

Highest thickness layers are obtained using electroslag surfacing. The process for depositing high-chromium cast iron on low-alloy steel is described [1]. The chemical composition of the applied layer is shown in Table 1 [1]. The content of vanadium is varied. Rockwell hardness and wear resistant of the applied layer are measured and data (presented as graphics in [1]) is shown into the same table. The results show that hardness and wear resistance have the highest values for vanadium content of 1.5 wt%.

TABLE I

Layer chemical composition, wt% (Fe-bal.)					HRC	Volume lost, [mm^3]
C	*Mn*	*Si*	*Cr*	*V*		
3.62	2.31	0.86	19.48		58.5	220
3.59	2.25	0.68	20.19	0.83	59	160
3.58	**2.06**	**0.68**	**19.40**	**1.50**	**61**	**80**
3.56	1.91	0.64	19.57	2.32	60	180

The filler materials used with submerged arc surfacing are shown in Table 2 [5], [7] and [20]. In practice, in all cases, the major alloying elements are C-Mn-Si-Cr-Ni-Mo-V. To increase amount of carbides B and Nb are added. Small amounts of cobalt are also registered in [7] and [20]. Filler materials are solid or core wires. The resulting hardness of the specimen surface is also shown in Table 2. In general, it correlates with wear resistance. Experiments with a powder mixture containing (wt%): Al_2O_3 = 21-46.23; F = 18-27; Na_2O = 8-15; K_2O = 0.4-6; CaO = 0.7-2.3; SiO_2 = 0.5-2.48; Fe_2O_3 = 2.1-3.27; C = 12.5-30.2; MnO = 0.07-0.9; MgO = 0.06-0.9; S = 0.09-0.19; P = 0.1-0.18 are carred out [6]. A regression analysis of the obtained results was made and equations for the hardness and wear resistance of the type:

$$y = A_o + A_1C + A_2Si + A_3Mn + A_4Cr + \\ + A_5Ni + A_6Mo + A_7Co + A_8Al + A_9Cu + \\ + A_{10}H \quad (1)$$

The values of the coefficients are given in Table 3.

The method presented in [19] uses two electrode wires for submerged arc surfacing- the first wire is equivalent to steel 30XGCA and second to aluminium alloy AlMg3 [19]. As mentioned, the second wire behind the main arc has a radically different chemical composition. The reached hardness of the layer varies from 28 to 55HRC depend on the conditions of the process - both filler wires ratios and the magnitude of the current.

In MIG / MAG overlaying [3], [9], [14], [15] and [18], core wires are commonly used. Table 4 shows the chemical composition. In [18] the Vickers hardness was also measured. Maximum measured value is 11 [GPa]. The main alloying elements are C-Mn-Si-Cr-Ni. In [14] layers are deposited on an aluminium substrate. Micro particles of SiC are used to increase wear resistance. Particles are coated with nickel using electroless method in salt (NiSO4 and NiCl2) solutions. In addition, the influence of flux (based on cryolite and three salts - sodium chloride, potassium chloride and magnesium chloride) deposited on the nickel coating was investigated. The results are compared with those obtained by the TIG method [11], where micro and nano SiC particles were also used. It has been found that wear resistance is highest when using nanoparticles coated with flux.

TABLE II

Chemical composition (Fe-bal.) (wt%)									HV_{30}	HRC	Wear rate		Remark
C	*Mn*	*Si*	*Cr*	*Ni*	*Mo*	*V*	*B*	*Nb*			*mm^3/(N.m)*	*mg/min*	
0.12	1.0	0.6	12	2.92					400		0.052		filler
0.1	1.0	0.6	12	2.5	0.8	0.15		0.15	550		0.032		
0.25	**1.0**	**0.6**	**9**	**0.25**	**2.0**				**600**		**0.0011**		
0.3	1.0	0.6	12.2		0.75	0.15			675		0.0014		
0.19	0.52	0.74	2.79	0.17	0.26	0.14	0.001			44		0.03	deposit
0.22	0.62	0.35	2.78	0.09	0.25	0.02	0.001			36		0.04	
0.27	0.68	0.49	4.61	0.36	0.42	0.01	0.001			48		0.04	
0.43	**0.84**	**0.37**	**7.04**	**0.42**	**0.49**	**0.03**	**0.001**			**56**		**0.02**	
0.16	0.32	0.62	0.25		0.11	0.19	0.003			37		0.15	
0.10	0.45	0.15	0.23	0.08	0.10	0.11	0.003			28		0.10	
0.23	0.66	0.25	0.95	0.34	0.35	0.29	0.003			44		0.12	

TABLE III

A_i	Hardness		Wear resistance	
	with H	*with no H*	*with H*	*with no H*
			.10^3	
A_0	214.819	535.343	0.260	2.005
A_1	-163.253	168.120	-0.695	1.110
A_2	-307.499	-276.437	-0.973	-0.804
A_3	-353.293	-890.442	-0.597	-3.522
A_4	-21.239	6.037	-0.108	0.040
A_5	33.871	108.851	0.091	0.500
A_6	858.517	445.851	2.707	0.460
A_7	-280.917	-433.688	-0.229	-1.061
A_8		-1014.594		-5.525
A_9	321.784	477.567	2.283	3.132
A_{10}	13.830		0.075	
Appr. error, %	0.01	0.01	10.74	0.32

The TIG method is used to apply layers containing nanoscale particles of Al_2O_3 and TiCN. Nano powder is fed directly into the low-temperature zone of the welding pool. The method of direct nanoscale particle delivery is compared with the method of melting a precoated layer. The wear is compared to a sample without a nanomodifier. The results obtained show an increase in the wear resistance of the layers with modifier (up to 30%) and that direct delivery of the powder in the welding pool gives a better result. The achieved microhardness is up to 350 $HV_{0.1}$. The use of nanoscale particles of TiN, doped with chromium, as a dispersed phase, has been investigated in [13]. Overlayed layers with and without a nano modifier are compared. It has been found that the use of TiN + Cr increases up to 2 times the wear resistance. The hardness reached 282 HV.

TABLE IV

Chemical composition (Fe-bal.) (wt%)										Remark
C	*Mn*	*Si*	*Cr*	*Ni*	*Mo*	*V*	*W*	*Nb*	*Cu*	
1.3	0.9	1.1	7.0				1.4	8.5		filler
0.07	7.03	0.78	19	8.94	0.15				0.1	deposit
0.09	5.32	0.83	14.68	6.62						deposit
1.43	0.81	0.55	5.22	0.1	1.30			5.85		
4.46	0.76	0.77	23.54	0.11						
1.4			7.0			1.0	1.2	8.0		

When plasma surfacing process is used, the filler material is in the form of a powder. It can be fed through the plasma gun or to be pre-applied onto the pad in the form of a paste. Thus, for example, in the use of a powder containing (wt%) C-0.9; Si-2 ÷ 3; Cr-8 ÷ 10; B-2.8 ÷ 3.2 and Fe-bal. a hardness of the 60.6 HRC layer was obtained at the hardness of the 41 HRC matrix [22]. The wear of the layer compared to the substrate in this case is 30% less. In [24] results were obtained using a nickel based composition containing (wt%) of F3-2.5; C-0.3; Cr-7; B-2.2 and Ni-bal. The hardness reached in this case is 754 HV. In [21] we have shown a hardness of 400 ÷ 1800 HK using NiCrBSiC filler material. In [23] unalloyed aluminium powder is used and a layer is applied to titanium. The particle size is 75 to 147 [nm]. A TiAl-based intermetallic layer is obtained on the surface. Electron beam processes are mainly used to improve the properties of the applied layer. Using electron beam scan of the applied layer, the hardness increased 1.7 times and the wear resistance was 70 times higher comparing to substrate [25] and [26]. The main reason for this is the change of structure (a cell structure of 20 ÷ 100μm is obtained) on the surface of the layer due to the high cooling rates. The additive material contained (wt%): C-1.3; Mn -0.9; Si-0.3; Cr-7.0; W-1.4; Nb-8.5 and Fe-bal. In [27] the possibility of sintering of pre-compressed powdered samples containing TiC and Ti was investigated and the titanium content was (vol.%) - 50 and 60. In parallel, mixtures of TiC and 20 ÷ 50 % nickel based self-

fluxing alloy was exanimated. These mixtures could be used as a component of a paste applied to the substrate. The ability to obtain a layer of TiCuN on an aluminium substrate is shown in [28] through process modelling and experimental

verification. The layer was applied by plasma surfacing and subsequent electron beam treatment. Electron beam technology for deposition of layers by surface remelting is described in [29]. The samples was scanned with an electron beam to make specific roughness. On prepared rough surface a paste containing TiN or TiCN is applied. Subsequent remelting of the surface layer was performed. The wear resistance of the layer was 36% higher than that of the base reference sample without coating.

The materials used for deposition of layers by laser technology are given in table. 5. Various techniques are used to obtain the necessary hardening phases. Thus, for example, to obtain titanium nitride into the surface layer in the Ti_6Al_4V substrate, a process is carried out in a pure nitrogen medium [34]. The resulting hardness is in the range 1000 ÷ 2300 $HV_{0.2}$. A mixture of Ti and TiC is introduced directly into the molten metal applying a layer over ductile cast iron [33]. Depending on the process parameters different concentrations of Ti are obtained in the melt layer from 3.0 to 5.9 and TiC - 4.8 ÷ 14.8 vol%. The reached hardness of the layer is 800 $HV_{0.2}$. The wear resistance of the layer is about 10 times higher than that of the substrate. On the same type of substrate (Ti_6Al_4V) using a mixture of Ti_6Al_4V and B_4C is applied a layer by direct feeding of the powder material to the melting zone [31]. The hardness achieved in this case is 480 HV. On pure titanium a layer is applied using a graphite powder mixed with polyvinyl alcohol, dried and applied as a paste [35]. Surface is remelted. The achieved hardness of the layer surface is 300 $HV_{0.3}$. Similarly, a graphite powder blended with Ni, C, V, and Ti is applied in the indicated proportions onto a medium carbon substrate [36] and [37]. The hardness of the resulting layer is 800 $HV_{0.3}$. It has been found that the hardness can be increased to 970 $HV_{0.3}$ by increasing the laser beam scanning speed. Powder-based paste [39] is applied to an aluminium substrate and scanned with a laser beam. The hardness of the layer is 500 HV. When the layer consists mainly of Al_3Ti / TiC its wear resistance increases to 10 times compare to the pad.

When layers are depositing on highly alloyed chromium-nickel steels [32] with the use of nickel and iron-based powders, the Vickers hardness is 460 MPa at the surface of the bed and decreases to 250 MPa at the base metal boundary (layer thickness is 0.5 mm).

TABLE V

Chemical composition (wt%)	remark	Ref.
C-0.2; Si-0.75; Cr-16; Ni-2.5; Mo-0.5; B-1.0; Co-0.5; Fe-bal	powder	[30]
Ti_6Al_4V-80; B_4C-20	powder	[31]
C-0.23; Mn-0.7; Si-0.7; Cr-13; Ni-2.2; Fe-bal	powder	[32]
C-0.34; Mn-0.6; Si-0.5; Cr-13; Ni-0.3; Fe-bal	powder	
Fe-3.7; C-0.5; Si-3.1; Cr-15; Ni-bal	powder	
Fe-4.9; C-0.7; Si-3.1; Cr-16; Ni-bal	powder	
Ti+TiC	powder	[33]
N	gas	[34]
C - graphite powder	paste	[35]
C; Ni=8C; V=4C; Ti=4C	paste	[36]
C; Ti	paste	[37]
Al; Ti; TiB_2; TiC; SiC	paste	[39]

The deposition of layers by electroless method is realized in [40] ÷ [42]. The method consists of depositing a nickel layer followed by deposition of a layer containing a hardening phase - TiN or a detonating nano diamond. The particles of the hardening phase have nanoscale values of 4 ÷ 6 nm. Low alloy steel and ductile cast iron are used as substrates. The hardness reached 720 $HV_{0.3}$ and the wear resistance of the layers containing the hardening phase is up to 10 times higher than the nickel-only coating. Heat treatment (290^0C / 6h) can reduce wear to 36%.

Friction stir surfacing is also used for depositing layers on aluminium alloys [43] ÷ [45]. The additive material may be in the form of a wire or powder containing a hardening phase such as SiC or Al_2O_3. Using a wire with a composition (wt.%): 97.5Al, 1.87Mg, 0.086Si, 0.006Mn, 0.009Cu, 0.27Fe and 0.21Cr a hardness of 85 $HV_{0.2}$ [43] was achieved. When using a hardening phase, wear is reduced to 7 times compare to substrate.

In some of the publications reviewed, there is an indication of the coefficient of friction and its change in the process of the experiment [3] ÷ [5], [33], [35] and [44] ÷ [46]. These values varies from 0.12 to 0.75, and in some cases are averaged only.

VI. CONCLUTIONS

The technologies used to apply surface layers in the reviewed publications are electroslag surfacing, electric arc methods (MIG/ MAG, TIG, submerged arc and plasma surfacing), beam methods (electron beam and laser surfacing), friction stir electroless surfacing. Steel, aluminum and titanium alloys are used as substrates. The hardness (up to 61 HRC and 2300 HV) and wear resistance varies over a wide range depending on the process and the filler materials.

REFERENCES

[1] H. Wang., S. F. Yu, A. R. Khan and A.G. Huang, .,Effects of vanadium on microstructure and wear resistance of high chromium cast iron hardfacing, layer by electroslag surfacing, (2018) Metals, 8 (6), art. no. 458.

[2] N.A. Kozyrev, R. E. Kryukov, A. A. Umanskii, A.R. Mikhno and L. V. Dumova, Investigation and development of welding fluxes with the use of ladle electric-furnace slag and barium-strontium modifier for rolls surfacing, (2018) Izvestiya Ferrous Metallurgy, 61 (4), pp. 274-279

[3] Y. F. Ivanov, V. E. Kormyshev, V. E. Gromov, S. V. Konovalov, E.V. Martusevich, A. D. Teresov and A. P. Semin, The Increase in Wear Resistance of Low Carbon Steel by Flux-Cored Wire Surfacing Followed Be Electron Beam Processing, (2017) IOP Conference Series: Materials Science and Engineering, 253 (1), art. no. 012019

[4] T. Wêgrzyn, J Piwnik, L Wszolek and W. Tarasiuk, Shaft wear af-

ter surfacing with microjet cooling, (2015) Archives of Metallurgy and Materials, 60 (4), pp. 2625-2630
[5] J. Brezinová, A. Guzanová, P. Maruschak and D. Lorincová, Study of wear processes of weld clads, (2014) Acta Metallurgica Slovaca, 20 (2), pp. 167-176
[6] A.I. Gusev, N.A. Kozyrev, I.V. Osetkovskiy, R.E., Kryukov and O.A. Kozyreva, Quality of Metal Deposited Flux Cored Wire with the System Fe-C-Si-Mn-Cr-Mo-Ni-V-Co, (2017) IOP Conference Series: Materials Science and Engineering, 253 (1), art. no. 012008
[7] A. I. Gusev, N.V. Kibko, N.A. Kozyrev, M.V. Popova and I. V. Osetkovsky, A study on the properties of the deposited metal by flux cored wires 40GMFR and 40H3G2MF, (2016) IOP Conference Series: Materials Science and Engineering, 150 (1), art. no. 012033
[8] S. Song, Y. Liu, Q. Ke and Y. Shen,., Overlaying welding technology and performance of axle tube remanufacturing, (2013) Advances in Manufacturing, 1 (2), pp. 143-150.
[9] M. Lomozik and J. Adamiec, Impact of heat treatment on microstructure of steel 30X padded with wire G18 8Mn, (2012) IOP Conference Series: Materials Science and Engineering, 35 (1), art. no. 012021
[10] J. Luo, F. Li and X. Wang, Microstructure and mechanical properties of overlaying specimens in GMAW hybrid an additional longitudinal electromagnetic field, (2011) Yosetsu Gakkai Ronbunshu/Quarterly Journal of the Japan Welding Society, 29 (3), pp. 76s-80s
[11] R. Dimitrova R, M. Kandeva and V. Kamburov, Mechanical and tribological characteristics of TIG hardfaced dispersive layer by reinforced with particles extruded aluminium, JournalTribology in Industry, (2017), Vol.39, (1), pp 9-19, .
[12] T. Petrov, P. Tashev and M. Kandeva, Wear resistance of suface layers modified with Al2O3 and TiCN nanopowders weld overlaid using tig and itig methods, Journal of the Balkan Tribological Association 2016, SciBulCom Ltd., vol. 22, No 1, №1136, ISSN 1310-4772,
[13] P. Tashev, R. Lazarova, M. Kandeva, R. Petrov and V. Manolov, "Tungsten Inert Gas Weld Overlay using Nano-sized TiN Powder", JOURNAL OF THE BALKAN TRIBOLOGICAL ASSOCIATION, Vol. 22, No 3, 2238-2254
[14] V. Kamburov, R. Dimitrova and M. Kandeva, Introduction of nickel coated silicon carbide particles in aluminum metal matrix hardfaced by MIG/TIG processes on precoated flux layer. Tribology in Industry 40(1), pp. 73-80
[15] F. Huang, W. Peng, Y. Zhao and Z. Ren,, Push-off test for measuring the bonding property between surfacing layers and steel base metal and its application, (2017) ISIJ International, 57 (4), pp. 723-729.
[16] V. E. Kormyshev, Y.F. Ivanov, V.E. Gromov, S.V. Konovalov and A.D. Teresov, Surface nanohardness of wear resistant surfacing irradiated by electron beam, (2017) Izvestiya Ferrous Metallurgy, 60 (4), pp. 304-309.
[17] R. Bęczkowski and M. Gucwa1, Defects Appearing in the Surfacing Layers of Abrasion Resistant, (2016) Archives of Foundry Engineering, 16 (4), pp. 23-28.
[18] S.V. Konovalov, V.E. Kormyshev, S.A. Nevskii, Y.F. Ivanov and V.E. Gromov, Formation Wear Resistant Coatings on Martensite Steel Hardox 450 by Welding Methods, (2016) IOP Conference Series: Materials Science and Engineering, 142 (1),
[19] D.N. Makeev, O.V. Zakharov, A.N. Vinogradov and A.V. Kochetkov, Modification of Surface Layers by Surfacing Intermetallic Coatings with Variable Properties, (2016) IOP Conference Series: Materials Science and Engineering, 116 (1), art. no. 012023, .
[20] A.I. Gusev, N.V. Kibko, M.V. Popova, N.A. Kozyrev and I.V. Osetkovskii, Surfacing of details of mining equipment by powder wires of C – Si – Mn – Mo – V – B AND C – Si –Mn – Cr – Mo – V systems, (2017) Izvestiya Ferrous Metallurgy, 60 (4), pp. 318-323
[21] T. Simeonova, M. Tongov and G. Avdeev, Microstructure and properties of NiCrBSiC overlay coatings deposited by plasma scanning process, WIT Transactions on the Built Environment Volume 137, 2014, Pages 553-564 International Conference on High Performance and Optimum Design of Structures and Materials, HPSM/OPTI 2014; Ostend; Belgium; 9 June 2014 through 11 June 2014; Code 105905 , ISSN: 1743-3509, DOI 10.2495/HPSM140511
[22] L. Song, J. Guo, M.A. Xiaolei and J Zhao, Research on Microstructure and Wear Resistance of Fe-Based Hardfacing Layer Using Plasma Surfacing Technology, (2018) IOP Conference Series: Materials Science and Engineering, 409 (1), art. no. 012028, .
[23] T. Owa and T. Shinoda, TiAl surface coating on titanium by plasma transferred arc surfacing and its oxidation behavior, (2006) Materials Transactions, 47 (2), pp. 247-250.
[24] M. Tajoure and A. Tajouri, Characterization of Carbides Composite Surface Layers Produced By PTA , Conference: 4th International Congress in Advances in Applied Physics and Materials Science (APMAS) Location: Fethiye, TURKEY Date: APR 24-27, 2014, 4TH INTERNATIONAL CONGRESS IN ADVANCES IN APPLIED PHYSICS AND MATERIALS SCIENCE (APMAS 2014) Book Series: AIP Conference Proceedings Volume: 1653 Article Number: 020099 Published: 2015, DOI: 10.1063/1.4914290
[25] E.N. Korosteleva, V.V. Korzhova and M.G. Krinitcyn, Sintering behavior and microstructure of TiC-Me composite powder prepared by SHS, (2017) Metals, 7 (8), art. no. 290
[26] V.E. Gromov, V.E. Kormyshev, A.M. Glezer, S.V. Konovalov, Y.F. Ivanov and A.P. Semin, Microstructure and wear properties of Hardox 450 steel surface modified by Fe-C-Cr-Nb-W powder wire surfacing and electron beam treatment, (2018) IOP Conference Series: Materials Science and Engineering, 411 (1), art. no. 012024, .
[27] V.E. Kormyshev, V.E. Gromov, Y.F. Ivanov and S.V. Konovalov, Structure and properties of the wear-resistant facing modified by electron-beam processing, (2017) Uspehi Fiziki Metallov, 18 (2), pp. 111-139.
[28] Yu.F. Ivanov, A.I. Potekaev, E.A. Petrikova, E. A.; et al., Modification of the surface layer of the system coating (TiCuN)/substrate (A7) by an intensive electron beam , Conference: International Scientific Conference on Radiation-Thermal Effects and Processes in Inorganic Materials Location: Tomsk, RUSSIA Date: NOV 03-08, 2014, INTERNATIONAL SCIENTIFIC CONFERENCE ON RADIATION-THERMAL EFFECTS AND PROCESSES IN INORGANIC MATERIALS Book Series: IOP Conference Series-Materials Science and Engineering Volume: 81 Article Number: 012009 Published: 2015, DOI: 10.1088/1757-899X/81/1/012009
[29] P. Tashev, P. Petrov, S. Valkanov, G. Stefanov and E. Balabanova, „Electron Beam Surface Alloying of Low Carbon Steel in Presence of TiN, TiCN Nanopartic" Nanoscience & Nanotechnology, Iss. 14, pp.183-187, (2014) ISSN 1313-8995
[30] J. Ju, Y. Zhou, M. Kang and J. Wang, Optimization of process parameters, microstructure, and properties of laser cladding fe-based alloy on 42CrMo steel roller, (2018) Materials, 11 (10), art. no. 2061, .
[31] M.O. Ogunlana, E.T. Akinlabi, M.F. Erinosho et al., Integrated Experimental Approach for Alloying of Surface Layer Ti6Al4V+B4C Metal Matrix Composites using Laser Treatment ,MATERIALS RESEARCH-IBERO-AMERICAN JOURNAL OF MATERIALS Volume: 22 Issue: 2 Article Number: UNSP e20180368 Published: 2019
[32] S.E. Krylova, S.P. Oplesnin and M.I. Goltyapin, Influence of gas-powder laser cladding's technological parameters on structural characteristics of corrosion-resistant steels' restored surface layer , Conference: 11th International Conference on Mechanical Engineering, Automation and Control Systems (MEACS) Location: Tomsk, RUSSIA Date: DEC 04-06, 2017 INTERNATIONAL CONFERENCE ON MECHANICAL ENGINEERING, AUTOMATION AND CONTROL SYSTEMS 2017 Book Series: IOP Conference Series-Materials Science and Engineering Volume: 327 Article Number: UNSP 042058 Published: 2018
[33] D. Janicki, Microstructure and Sliding Wear Behaviour of In-Situ TiC-Reinforced Composite Surface Layers Fabricated on Ductile Cast Iron by Laser Alloying , MATERIALS Volume: 11 Issue: 1 Article Number: 75 Published: JAN 2018
[34] A. Lisiecki, Mechanisms of hardness increase for composite surface layers during laser gas nitriding of the Ti6A14V alloy, MATERIALI IN TEHNOLOGIJE Volume: 51 Issue: 4 Pages: 577-583 Published: JUL-AUG 2017 DOI: 10.17222/mit.2016.106
[35] T. Yamaguchi, H. Hagino, Y. Michiyama, et al., Sliding Wear Properties of Ti/TiC Surface Composite Layer Formed by Laser Alloying , MATERIALS TRANSACTIONS Volume: 56 Issue: 3 Pages: 361-366 Published: 2015, DOI: 10.2320/matertrans.M2014330
[36] T. Yamaguchi, H. Hagino, M. Takemura, et al., Microstructure of MC-Fe Composite Layer on Carbon Steel by Laser Surface Alloying , JOURNAL OF LASER MICRO NANOENGINEERING Volume: 9 Issue: 2 Pages: 83-87 Published: JUN 2014, DOI: 10.2961/jlmn.2014.02.0001
[37] T. Yamaguchi, H. Hagino, M. Takemura, et al., Microstructure of Fe-TiC Composite Surface Layer on Carbon Steel Formed by Laser Alloying Process , MATERIALS TRANSACTIONS Volume: 54 Issue: 9 Pages: 1755-1759 Published: 2013, DOI: 10.2320/matertrans.MAW201304
[38] S. Zherebtsov, K. Maekawa, T. Hayashi, et al., Laser surface alloying of SUS316 stainless steel with Al-Si - (Effect of substrate temperature on structure and properties of modified layer), Conference: JSME/ASME International Conference on Materials and Processing Location: Seattle, WA Date: JUN 19-22, 2005 ,Sponsor(s): JSME; ASME , JSME INTERNATIONAL JOURNAL SERIES A-SOLID MECHANICS AND MATERIAL ENGINEERING Volume: 48 Issue: 4 Pages: 292-298 Published: OCT 2005, DOI: 10.1299/jsmea.48.292
[39] K. Uenishi and KF. Kobayashi, Formation of surface layer based

on Al3Ti on aluminum by laser cladding and its compatibility with ceramics , INTERMETALLICS Volume: 7 Issue: 5 Pages: 553-559 Published: MAY 1999, DOI: 10.1016/S0966-9795(98)00071-5

[40] J.A. Kaleicheva and Z.K. Karaguiozova, Electroless composite nickel coatings strengthening with TiN nanoparticles plated on ductile cast iron, Materials Science Forum 919, pp. 52-58 https://doi.org/10.4028/www.scientific.net/MSF.919.52

[41] J. Kaleicheva and Z. Karaguiozova, Improvement of the Wear Resistance of Ferrous Alloys by Electroless Plating of Nickel, IOP Conference Series: Materials Science and Engineering 295(1), 012036

[42] Z. Karaguiozova, J. Kaleicheva, V. Mishev and G. Nikolcheva, Enhancement in the tribological and mechanical properties of electroless Nickel-nanodiamond coatings plated on iron. Tribology in Industry, vol. 39, No 4, pp. 444-451, 2017, ISSN: 0354-8996

[43] J.C.Galvis, P.H.F. Oliveira, J. De Paula Martins, J. and A.L.M. De Carvalho, Assessment of process parameters by friction surfacing on the double layer deposition, (2018) Materials Research, 21 (3), art. no. 20180051

[44] R. Srinivasu, A. Sambasiva Rao, G. Madhusudhan Reddy and K. Srinivasa Rao, Friction stir surfacing of cast A356 aluminium–silicon alloy with boron carbide and molybdenum disulphide powders, (2015) Defence Technology, 11 (2), pp. 140-146.

[45] E. Mahmoud, M. Takahashi, T. Shibayanagi, et al., Fabrication of Surface-Hybrid-MMCs Layer on Aluminum Plate by Friction Stir Processing and Its Wear Characteristics , MATERIALS TRANSACTIONS Volume: 50 Issue: 7 Special Issue: SI Pages: 1824-1831 Published: JUL 2009, DOI: 10.2320/matertrans.M2009092

[46] Dema Ba, Fanjun Meng and Xiaoting Liu, Friction and wear behaviors of surface nanocrystalline layer prepared on medium manganese surfacing layer under oil lubrication, Tribology International 80 (2014) p. 210–215

[47] S. Hanke, A.Fischer and J.F.dos Santos, Sliding wea rbehaviour of a Cr-base alloy after microstructure alterations induced by friction surfacing, Wear 338-339 (2015) 332–338, https://doi.org/10.1016/j.wear.2015.07.010

Influence of the Anode and Wehnelt Voltage on the Crossover Position in the Electron Beam Welding

Manahil Tongov
Faculty of Industrial Technology
Technical University of Sofia
Sofia, Bulgaria
tongov@tu-sofia.bg

***Abstract*—Through the numerical modelling methods, the influence of the wehnelt voltage anode voltage on the crossover position of the electron beam welding (EBW) was monitored and analysed. The finite element method (FEM) is used to obtain the simulation results. The formation of the electron beam in the electrostatic part of an electron optic system (EOS) is described by solving the electrostatic task. To obtain the current emitted from cathode, electrical and thermal tasks are solved in the cathode node and Richardson-Dushman equation is used with Schottky correction. By using the results of the electrostatic field, the active emission spot is determined. By simulating the movement of the emitted electrons under the action of the electrostatic field, the shape of the beam is determined and the distance between the cathode and the electrostatic focus is found. The results of the influence of the wehnelt and anode voltage on the magnitude of the emission current and the position of the crossover, as well as the beam dimensions in crossover and anode outlet section at constant cathode heating current are presented.**

Keywords— EBW, modelling, crossover, FEM.

I. Introduction

Welding technological processes are based on the introduction and thermodynamically irreversible transformation of one kind of energy into another [1], [2]. In the electron beam welding (EBW), the kinetic energy of the accelerated electrons is transformed into thermal. The main advantage of the EBW to electric arc methods is the high concentration of energy flux and respectively the high density of the heat flux in the area of interaction between the focused electron beam and weld joint. This causes several times the small energy that is introduced into the welding area, and hence a significantly lower heat influence in the heat affected zone and the weld. A keyhole shape of the penetration is obtained and allows the welding of large thicknesses while at the same time achieving high welding speeds. The ratio between the width b and the depth h of the weld profile reaches 1:30 and more. The process of electron beam welding with the keyhole formation in the welding pool is possible at densities of the heat flow above a certain critical value [3], [4]. The electron beam area in which this density exceeds the critical is defined in [4] as the active zone, and in [5] it is shown that the quality of the weld is determined by the shape and position of the active zone relative to the welded sample. To achieve a high concentration of energy flow, the quality of the inputted to the electromagnetic focusing system electron beam is of particular importance. This beam quality is achieved in the electrostatic part of the welding apparatus. That is why the study and analysis of the processes in this part of the electron beam gun (EBG) is highly important. In this study the processes in the electrostatic part of the electron beam gun were examined and the position of the crossover was determined. The simulation modelling methods [9] and [11] provide a good opportunity to analyse the influence of the technological parameters on the physical processes. The modelling of beam-forming processes creates conditions for modelling the heat source [14]. In turn, heat sources are the basis for the modelling of the heating processes of the welded structure [13].

II. FEM MODELLING

To provide numerical experiments an electrostatic part of EBG, illustrated schematically in Fig. 1, is used [6] ÷ [8] and [10]. The cathode is a strip of thickness of 0.1 [mm] and an active surface size of 2x2 [mm].

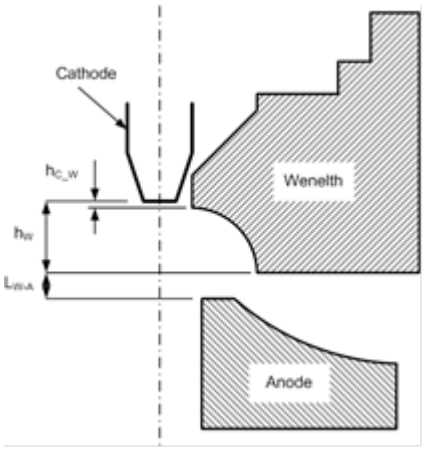

a)

Print ISSN 1691-5402
Online ISSN 2256-070X
http://dx.doi.org/10.17770/etr2019vol3.4183

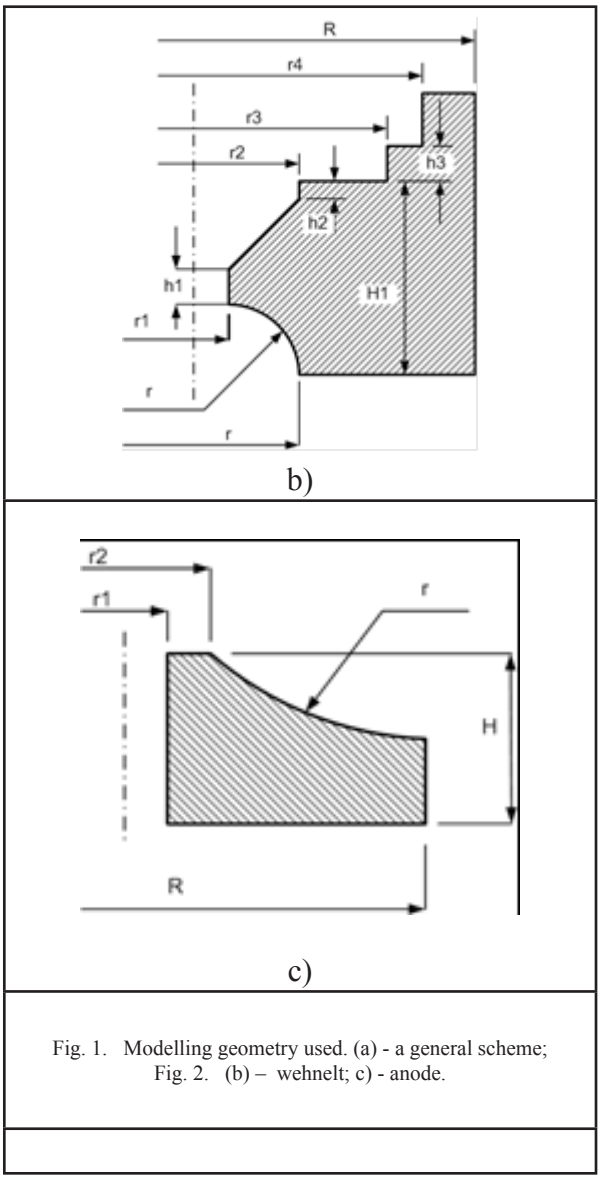

Fig. 1. Modelling geometry used. (a) - a general scheme;
Fig. 2. (b) – wehnelt; c) - anode.

Electrons are emitted from the cathode surface. The Richardson equation describes the thermionic emission process. According to this equation, the current density of the emission is defined as:

$$j_R = \beta A T^2 \exp\left(-\frac{\varphi}{kT}\right) \quad (1)$$

Here β is a material-dependent coefficient (for tungsten the value is 0.38 ÷ 0.40 [10], [12]); ***T*** - the absolute temperature; ***k*** - Boltzmann constant; φ - work function (for tungsten φ = 4.3 [eV]) and ***A*** - quantum coefficient, defined as $A = \left(4\pi m_e k^2 e\right)/h^3$. Here $\boldsymbol{m_e}$ and ***e*** are the electron mass and charge, and ***h*** is Planck's constant. Under the EBW conditions, the electrostatic field intensity ***E*** in front of the cathode has a significant effect on the emission of electrons, which makes it necessary to include the Schottky effect by using the dependence ($\boldsymbol{E_n}$ is the normal to the cathode surface component of the electric field intensity):

$$\Delta\varphi = \sqrt{\frac{e^3 E_n}{4\pi\varepsilon_0}}$$

and (1) may be written as:

$$j_{R-S} = \beta A T^2 \exp\left(-\frac{\varphi}{kT}\right).\exp\left(\frac{1}{kT}\sqrt{\frac{e^3 En}{4\pi\varepsilon_0}}\right) \quad (2)$$

It is also noted that the emission of electrons is only performed by the active spot located on the active surface of the cathode. The condition of this is that the normal component of the electric field is directed to the cathode (Fig.2).

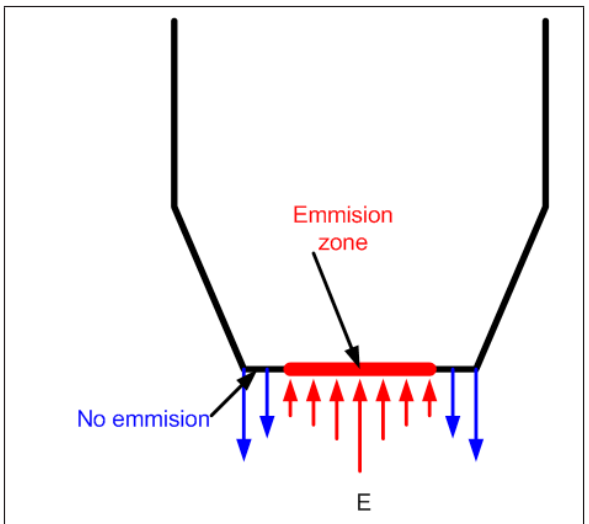

Fig. 3. Determination of active spot on cathode active surface

It is also possible to emit from other parts of the cathode, but these electrons fall into an electrostatic field, which returns them to the cathode. Once the electrons fall into the space between the cathode and the anode they are accelerated by the electrostatic field. The velocity vector has three components - axial, radial and orbital. The radial component leads to the formation of the crossover, and the axial has the main merit of electron energy at the anode outlet. Thus, for the simulation modelling of the beam formation, it is necessary to determine the surface temperature of the cathode and the electric field in the space between the cathode, the wehnelt and the anode. In the case in question, the cathode is directly heated (by running current). To model these processes the tasks to be solved are: electrical and thermal in the cathode and the cathode node; electrostatic and motion (of electrons) in the space between the cathode and the anode. To solve the thermal task in the cathode node, the differential equation of the heat conduction is used, and for the electric field equations for the potential and the current density in the conducting medium. For the electrostatic task, the Laplace equation was used and the potential and electric field were determined. These tasks are solved as stationary for different combinations of control and anode voltages. The control voltage is negative for the cathode and its absolute value is changed from 650 to 1150 [V]. The anode voltage is positive for the cathode and is changed from 30 to 60 [KV]. Since the parameters defining these processes do not change over time, these tasks are solved as stationary and fully coupled.

To model the electron movement in the electrostatic field, a transient task is solved and the following equations are used for each electron in the electron beam:

$$\frac{d\left(m_{er}\mathbf{v}_i\right)}{dt} = \mathbf{F}_i \quad (3)$$

$$m_{er} = \frac{m_e}{\sqrt{1 - \mathbf{v}_i \cdot \mathbf{v}_i / c^2}} \quad (4)$$

Here m_{er} is the relativistic mass of the electron, and F_i is the force acts on it. This force has two components - one resulting from the interaction with the electrostatic field and the second is electron - electron interaction. This is how it gets

$$\mathbf{F}_i = -e\mathbf{E} - \frac{e^2}{4\pi\varepsilon_0} \sum_{\substack{j=l \\ j \neq i}}^{N} \frac{\boldsymbol{r}_i - \boldsymbol{r}_j}{\left| \boldsymbol{r}_i - \boldsymbol{r}_j \right|^3} \quad (5)$$

To solve this task, the emission of electrons from the cathode is generated. Their initial distribution in space is based on the separation of the active spot in a number of areas. For this purpose, the mesh on the active surface of the cathode is used. The number of electrons emitted from each of these areas is proportional to the emission current of the respective area.

Factors that affect beam quality in terms of physical processes are: temperature distribution on the active surface of the cathode; the shape and dimensions of the spot through which the electrons are emitted; the structure of the electrostatic field that defines the beam section in the crossover and the anode outlet; the electron velocity components (axial, radial and orbital) of the anode outlet. We only look at the influence of two of these factors on the position of the crossover, as well as the beam dimensions in crossover and anode outlet section.

III. RESULTS AND DISSCUTION

In our case, the heating current is 37 [A]. Thus, the magnitude of the electron beam current is determined by the wehnelt and the anode voltage. (Fig. 3). It is calculated by integrating the current on the active surface emission:

$$I_{beam} = \int_{S_{active}} j_{R-S}(T, E_n)\, dS \quad (6)$$

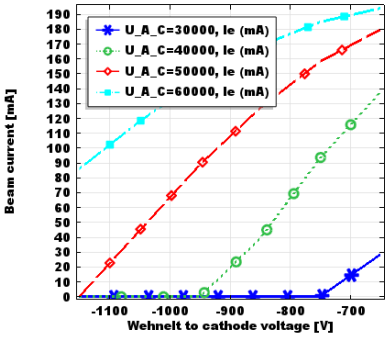

Fig. 4. . Beam current vs wehnelt voltage for different anode voltage

In calculating this integral, the current density is determined in accordance with (2). This graph shows that at low anode voltage a relatively low control voltage value is sufficient to stop the electron emission. The task of moving the electrons in the electrostatic field is solved only for the cases where a cathode emission is realized. For these cases the beam formation is monitored and the distance between the cathode and the crossover is determined. The overall shape of the beam is shown in Fig. 4. It narrows to reach the crossover and expands later. This process depends on the components of the intensity of the electric field. In Fig. 5 are given examples illustrating the influence of the anode and wehnelt voltage.

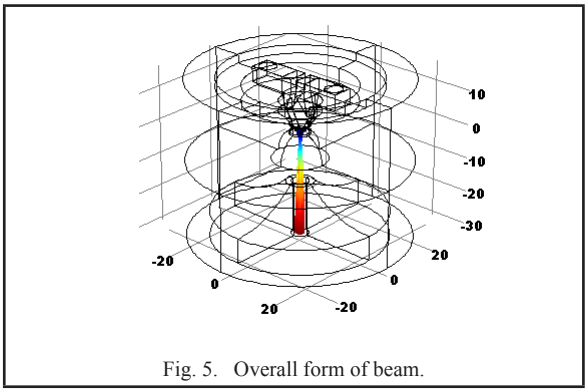

Fig. 5. Overall form of beam.

The measured values (all are in millimeters) of the distance from the cathode to the electrostatic focus are given in *Table I*. As the anode voltage increases, the electrostatic focus shifts to the anode. At the same time, increasing the control voltage leads to the opposite effect. The reason for this is the change in the structure of the electrostatic field with the application of these two voltages - the increase of the anode voltage leads to higher axial electron speeds and the increase of the control voltage generates higher centripetal forces. Higher axial electron velocities lead to less time to pass through the area in which the focal force acts and the focus shifts to the anode.

TABLE I. DISTANCE FROM CATHODE TO CROSSOVER

U_A [KV]	Wehnelt voltage U_w [V]					
	650	*750*	*850*	*950*	*1050*	*1150*
30	0.8	-	-	-	-	-
40	2.4	1.8	1.0	-	-	-
50	4.2	3.1	2.3	1.6	1.0	-
60	5.7	5.0	4.2	2.9	2.2	1.7

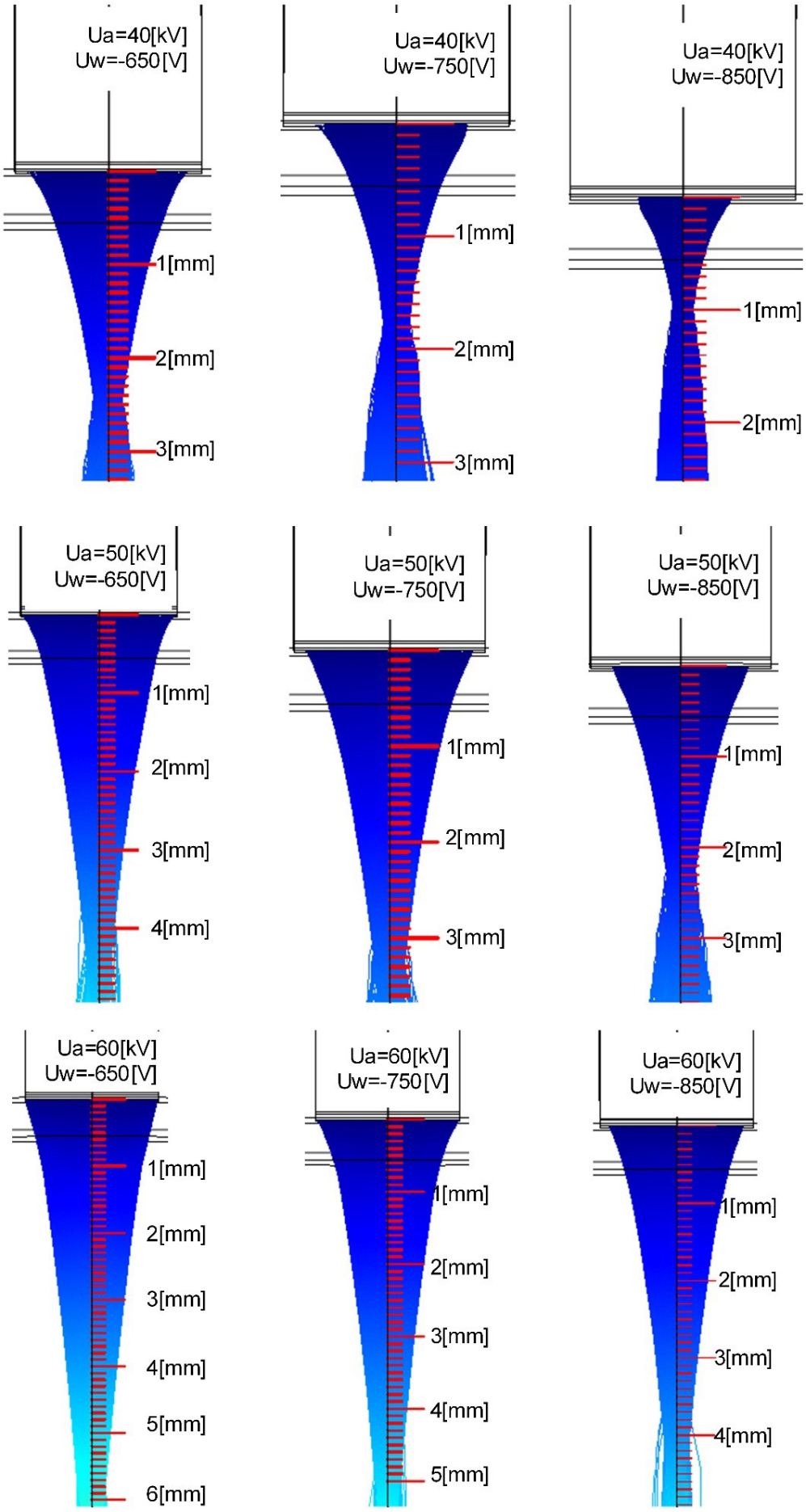

Fig. 5. Influence of anode (Ua) and wehnelt (Uw) voltage on the electron beam.

The beam shape is examined in two sections - in the section of the crossover (blue) and the anode outlet (red) (Fig. 6). In most of the cases examined, the shape of the beam in crossover section is elliptical or oval. With the change in the parameters studied, this shape changes. Similar is the situation with regard to the shape of the beam of the anode outlet. The measured values of the beam dimensions in the indicated sections are shown in *Table II* and *Table III*. The deviation from central symmetry is mainly due to the absence of one for the cathode's active surface. These data show that with the increasing of the absolute value of the control voltage, the beam dimensions in the section decrease. The acceleration voltage influences over these dimensions in similar way. At the same time, the magnitude of the current is also decreasing (Fig. 1). To link these values, we determine the current density in the relevant sections. The magnitude of the current I_b [mA] represented in Fig. 3 is given in *Table IV* for the different combinations of accelerating and control voltage. The effective radius of the beam in the crossover r_{Ceff} and on the anode outlet r_{Aeff} is calculated as:

TABLE II. BEAM DIMENSIONS IN CROSSOVER SECTION

Uw [V]	Anode voltage, [KV]							
	30		40		50		60	
	a	b	a	b	a	b	a	b
650	0.6	0.55	0.82	0.7	0.86	0.85	1.0	0.8
750	-	-	0.76	0.62	0.86	0.79	0.85	0.85
850	-	-	0.63	0.6	0,8	0.7	0.6	0.9
950	-	-	-	-	0.74	0.6	0.88	0.78
1050	-	-	-	-	0.7	0.58	0.8	0.7
1150	-	-	-	-	-	-	0.7	0.63

TABLE III. BEAM DIMENSIONS IN ANODE OUTLET SECTION

Uw [V]	Anode voltage, [KV]							
	30		40		50		60	
	c	d	c	d	c	d	c	d
650	0.95	0.8	2.55	2.35	2.8	2.8	2.8	2.8
750	-	-	2.0	1.8	2.8	2.6	2.8	2.8
850	-	-	1.1	0.9	2.4	2.2	2.85	2.65
950	-	-	-	-	1.9	1.7	1.6	2.4
1050	-	-	-	-	1.2	1.02	2.3	2.1
1150	-	-	-	-	-	-	1.84	1.64

$$r_{Ceff} = \sqrt{a.b} \tag{7}$$

$$r_{Aeff} = \sqrt{c.d} \tag{8}$$

TABLE IV. BEAM CURRENT

U_A [KV]	Wehnelt voltage U_w [V]					
	650	750	850	950	1050	1150
30	28.4	0	0	0	0	0
40	137.8	93.7	39.0	0	0	0
50	180.1	158.2	127.0	88.8	44.8	0
60	194.3	184.8	168.7	146.0	117.9	86.1

The calculated values for the current density j [mA/mm^2] in the sections considered are given in *Table V* and *Table VI*. Current density in crossover increases with anode voltage increasing. When the absolute value of the control voltage increases, this density decreases, due to the dominant decrease in beam current. At the current density of the anode outlet the influence of the two voltages is more complicated. The reasons for this are the change in the distance between the two sections, the twisting of the electron beam and the deformation of the section. This issue will be discussed in a separate publication.

TABLE V. CURRENT DENSITY IN CROSSOVER SECTION

U_A [KV]	Wehnelt voltage U_w [V]					
	650	750	850	950	1050	1150
30	27.4	0	0	0	0	0
40	76.4	63.3	32.8	0	0	0
50	78.4	74.1	72.2	63.7	35.1	0
60	77.3	81.4	99.4	67.7	67.0	62.1

TABLE VI. CURRENT DENSITY IN ANODE OUTLET SECTION

U_A [KV]	Wehnelt voltage U_w [V]					
	650	750	850	950	1050	1150
30	11.9					
40	7.3	8.3	12.5			
50	7.3	6.9	7.7	8.8	11.6	
60	7.9	7.5	7.1	7.4	7.8	9.1

IV. CONCLUTIONS

The conclusions reached relate only to the case under consideration and cannot be said to be of a universal nature because of geometrically attached to a particular EBW installation. The main conclusions that can be drawn are the following.

1. The results of simulation modelling of the processes in the electrostatic part of EBG are presented. The influence of the anode and wehnelt voltages on the position of the crossover, the beam dimensions in crossover and anode outlet sections is determined.
1. By simulation modelling of the processes in the electrostatic part of the EBG it was found that with increasing the anode voltage the crossover moves to the anode while the increase of the control voltage leads to the opposite result.
2. In the cases considered, the distance between the cathode and the crossover varies from 0.8 to 5.7 [mm] depending on the control and anode voltages.
3. The current density in the crossover increases with increasing the anode voltage. When the absolute value of the control voltage increases, this density decreases, due to the dominant decrease in beam current.
4. Density of beam current in the crossover in the combinations of control and anode voltages ranged from 27 to 77 [mA/mm^2].
5. The beam size of the anode outlet changes from 0.8 to 2.8 [mm] depending on the value of the variable parameters.

References

[1] S. David, T. Debroy, "Current Issues and Problems in Welding Science", Science Vol.257 Issue 5069, pp. 497-502, (1992), DOI: 10.1126/science.257.5069.497

[2] S. Kou "Welding Metallurgy" A John Wiley&Sons, Inc.Publication, (2002), 460p., ISBN 978-0-471-28496-3

[3] G. Mladenov "Electron and ion technologies", Prof. Marin Drinov Publishing House of Bulgarian Academy of Scienses, 2009, 387p., ISBN 978-954-322-345-9.

[4] Y.Arata "Plasma, Electron and Laser Beam Technology" American Society for Metals, (1986) 630p., ISBN-13: 978-0871702548

[5] Y. Arata, K. Terai and S. Matsuda, Transaction of JWRI, Vol. 2, n.1(1973)103.

[6] S. Shiller U. Heisig and S. Panzer "Elektronenstrahltechnologie" Forschungsinstitut Manfred von Ardene, Dresden, VEB Verlag Technik, (1972)528p

[7] V. Adam et al.: "Elektronenstrahlschweißen". pro-beam AG & Co. KgaA, München (2011).

[8] P. Petrov and S. Sabchevski "Parameters used for electron beam welding - A comparative study" Proc. 8th Int. Conf. Beam Technology, Halle, pp. 92-94, (2010).

[9] M. Dulău and L. David, "Modeling and simulation of electron's trajectory inside of electron beam gun", CEAI, Vol. 9, No. 1, pp. 27-32, 2007.

[10] M. Tongov and P. Petrov, "Study of physical processes in optical system for electron beam welding", TEMEL-ij, Valume 1, issue 2, oct. 2017. pp 85-94, ISSN 2545 – 4390

[11] V. Shcherbakov, M. V. Ivashchenko, A. S. Kozhechenko, and M. S. Gribkov, "Parametric Analysis in the Design of Technological Electron Beam Guns", ISSN 1068-3712, Russian Electrical Engineering, 2016, Vol. 87, No. 1, pp. 41–45. © Allerton Press, Inc., 2016, doi.org/ 10.3103/ S1068371216010089.

[12] E. Lassner and W. Schubert, "Tungsten Properties, Chemistry, Technology of the Element, Alloys, and Chemical Compaunds", ISBN 978-1-4613-7225-7, Springer Science+Business Media New York, 1999

[13] P. Lacki, K. Adamus, K. Wojsyk, M. Zawadzki and Z. Nitkiewicz, "Modeling of heat source based on parameters of electron beam welding process", ARCHIVES OF METALLURGY AND MATERIALS Volume: 56 Issue: 2 Pages: 455-462 DOI: 10.2478/v10172-011-0049-1

[14] Y. Seregin, A. Murygin, V. Laptenok and V. Tynchenko, "Modeling of electron beam distribution in electron beam welding", IOP Conference Series: Materials Science and Engineering, Volume 450, Issue 3, 30 November 2018, Article number 03203, doi:10.1088/1757-899X/450/3/032036

Acknowledgements:

This work was supported by the Bulgarian National Scientific Fund under Grant DN 07/26

Environment. Technology. Resources. Rezekne, Latvia
Proceedings of the 12th International Scientific and Practical Conference. Volume III, 241-248

Analysis of the Power Drives of Terrain Forklifts

Georgi Valkov
Department of Design and Technology
Balkancar Record Co.
17 Kuklensko Shose str., 4004, Plovdiv, Bulgaria
techno@balkancar-record.com

Valyo Nikolov
Department of Transport and Aviation Equipment and Technologies, Technical University of Sofia, Plovdiv Branch
25 Tsanko Dyustabanov str., 4000
Plovdiv, Bulgaria
vnikolov@tu-plovdiv.bg

***Abstract*—The main subject of this publication is to provides a description of terrain forklifts, their design and specific features. The main mechanical, hydrodynamic and hydrostatic types of power drives and their application in terrain forklifts are presented herein. This article includes an analysis of the power transmissions drive systems of terrain forklifts. The most important trends in the development of the terrain forklifts have also been presented.**

***Keywords*—Terrain forklifts, mechanical, hydrodynamic and hydrostatic power drives.**

I. Introduction

The boom in the development and deployment of terrain forklifts which has lasted for several decades continues to be one of the current trends in the design of forklifts worldwide. These forklift trucks are designed to carry out lifting and transport operations in agriculture and forestry, in construction, at open storage sites, waste recycling sites, ports, military fields, etc. Terrain forklifts are designed to operate on both hard and soft roads characterized by significant unevenness and different physical and technical properties of the soil (structure, humidity and density). These conditions determine the nature of the interaction between the forklift drive system and the road and significantly influence its traction properties, which has a direct impact on the productivity and fuel economy of the forklift.

The towing-traction properties of the forklift truck characterize its traction capability and its passability when moving on different types of roads.

Substantial influence on the towing-traction properties and sustainability of forklift trucks is the weight of the machine, the load and its distribution on the axles, the engine power, the forklift truck composition design, the kinematic power transmission design, the wheel formula, the type and the technical characteristics of the wheel drive [1], [2], [4] - [7].

The great variety of composition designs and constructive developments of these machines and their use in different soil conditions require the search for optimum conditions in the compilation of mathematical models and the development of an optimization program.

Terrain forklifts or "high passability forklifts" and "off-road forklifts".as are frequently mentioned in literature.

The production of terrain forklifts and special work equipment for them has shown a continuous tendency for increasing the volumes in recent years. The reason for that is the constant increas in the need for mechanization of loading and unloading and some other types of work, as well as the need of increased productivity in construction, forestry and agriculture and other specialized terrains.

Geographically, the production of these vehicles, except in Europe and North America, where the major suppliers of this equipment are the well-known "Manitou", AUSA, "Case", JSB, "Agrimac" and other ones, has been transferred to Asia in recent years. Companies such as "Maximal", "Heli", "Hangcha" and others have very successfully entered this market.

On the territory of the Republic of Bulgaria to this date the companies that produce this type of equipment are "Balkancar Record" Co., IPO and "Herku - Milko Tanev".

The main type of mass-produced forklift trucks feature a working body of lifting mast unit [1], [5].

Since the technical and advertising literature often refers to the concepts of „high passability forklifts" and „off-road forklifts", it should be borne in mind that there are significant differences between these two types of forklifts.

II. High Passability Forklift Trucks

The most common feature of these trucks is the classic computational design - engine, gearbox and front drive axle. The front wheels are large in size and the rear wheels are with considerably smaller size – see Fig. 1 [9].

Fig. 1. Forklift with the "classic" design – engine, gearbox and front drive wheels.

Print ISSN 1691-5402
Online ISSN 2256-070X
http://dx.doi.org/10.17770/etr2019vol3.4197

Forklifts produced according to this design primarily feature wheel formula 4x2. The capacity of these forklifts ranges from 1,000 to 10,000 kg. Machines featuring wheel formula 4x4 are also produced. Using this wheel formula the transmission ratio of the front and rear drive axles varies due to the different diameters of the front and rear wheels. In addition to this computational design, a splitting distribution gearbox can also be included, and the rear steering axle can also be a drive axle.

All standardized attachments, which can be mounted on the forklifts with universal forklifts mast may also be used for terrain forklifts with the main working body of lifting mast unit. In addition, the following specialized working units are also produced: various types of baskets - sand, ballast, concrete, for various agricultural production and others. An excavator can also be used, which is reversed in the direction of movement above the engine bonnet at the back of the machine with a separate workspace for the operator [5].

Due to the high unification of the forklift trucks of the 4x2 family with industrial forklift trucks, their power transmission design is the same: a rear-end engine, a hydrodynamic gearbox, a twin cardan coupling joint, a front drive axle and a rear steering axle. The difference only involves the use of a larger diameter wheels and low-pressure wide-profile tires.

For forklifts with wheel formula 4x4, the distribution gearbox is rigidly mounted to the transmission or to any of the drive axles. There are two cardan coupling between the distribution gearboxes and the front and back drive axles. The rear wheels are smaller in size than the front wheels to achieve better maneuverability. All of the above-mentioned specialized mast attachments used on forklift with 4x2 wheel formula can also be used for this type. The advantage of these machines is lower vibration activity at driver's seat and compact operating parameters and dimensions. Mostly hydrodynamic and hydrostatic transmissions are used with this wheel formula.

The most important features of the above- mentioned forklift trucks are:

- In most computational design, the drive and steering axles are of the portal type – to enhance road clearance and their being stronger;
- In many forklift truck models, inter-wheel differentials are not blockable.
- Wheel forklifts featuring wheel formula 4x2 are without splitting distribution gearboxes.
- Regarding forklift trucks with 4x4 wheel formula, most often have a 100% front drive axle locking ability and a 45% automatic locking on the rear drive axle.
- In the most gearbox designs for forklift trucks with wheel formula 4x4 wheelbase differentials are not placed;
- In the latest models one of the cardan couplings is removed by attaching a distribution box to the front or rear axles;
- In recent years, the hydrostatic transmission has been increasingly used with a hydro-motor coupled to the gearbox.

Fig. 2. Off-road forklift.

Insufficient passability of the above-described types of vehicles due to the relatively small and narrow rear wheels and insufficient universality when working with a lifting equipment, regardless of the specialized changeable mast attachments, entailed the development and production of three new types of terrain forklifts with wheel formula 4x4 at the end of the last century. They feature identically sized front and rear wheels that are fitted with wide-profile tires of low air pressure therein. Such machines are shown in Fig. 2 [9].

III. Off-road Forklifts

The first type forklift trucks is with two frame joints connected (articulated forklift trucks), a lifting mast and rapidly changing different types of lifting mast attachments.

The second type is complete frame forklifts, two drive axles (of which two or one is used for steering) and a lifting mast.

The third type are complete frame forklifts, two drive axles (of which two or one is for steering) and one specialized working equipment unit – a telescopically extending boom, but with greater capabilities for using different attachments.

The turning of articulated forklift trucks (those of the first type) is done by turning the wheels on the front of the frame to the rear. Axles are only drive axles, which are at lower cost than the drive axles with steering wheels. The frame is more complicated and consists of three parts – front, rear and articulation. Adjustment of the machine on uneven terrain occurs in two ways.

The first one, which is also most commonly used, is an articulation with only one degree of freedom (rotation around the vertical axis and a swinging rear axle /rotation around the horizontal axis).

The second way is through an articulation with two degrees of freedom – one turning around the vertical axis and one turning around the horizontal axis. In this case, the entire rear end of the frame rotates in relation to the front. Forklift trucks pivoted articulated 4x4 were launched for the first time by the company "Omfort", UK. They received a wide distribution for a short time. The most typical thing concerning this type of machine is the use of a large number of different work attachments, that can be changed only by the driver for a short time using built-in quick-ly changeable devices. The following working equipments are placed on the chassis: a mast, a loader with forks, an excavator, a dump, a bulldozer, a hydraulic hammer - breaker, a screwdriver (for drilling

holes in the soil), etc. In addition to them, all of the above-mentioned removable work attachment equipment can be fitted.

The power drive transmission of articulated machines is as described above: an engine featuring mounted transmission box, a distribution gearbox, and a cardan joint between it and the drive axles.

Turning of forklift trucks with a full frame, with lifting equipment or telescopic-extending boom (those of the second and third type) is done by turning the wheels of the rear drive axle. Due to the constraints imposed by the cardan couplings and the large wheel sizes, the turn radius of this type of machine is relatively large. Due to the need for increasing their maneuverability, forklifts with both axles constitutes driving and steering units have been developed. The adjustment of the machines on the uneven ground is done by a swinging rear axle (rotation around the longitudinal axis). The main advantage of this type of forklift trucks is expressed in two aspects: when using a boom, its pulling forward allows for the most appropriate loading and unloading of means of transport with large loading platforms. The boom makes it possible to achieve high lifting heights of the load - up to 12-13 m. This allows building materials to be delivered up to 3-4 storey buildings in farm yards or out-of-town settlements. The boom can be fitted with all attachments such as those for articulated forklifts, except for the excavator.

The power drives of forklift trucks with a full frame, a lifting unit or a telescopic-exiting boom in most models feature distribution boxes coupled to one of the axle.

Articulated and complete frame forklift trucks are mainly produced with hydropower transmissions, with a hydro motor attached to the transmission box or with a hydro-dynamic transmission and distribution gearbox. The axles are mainly portal type with locking inter-wheel differentials and multi-disc brakes operating in oil on both sides of the first stage of the main transmission. Wheelbase differentials are rarely incorporated in some models.

Off-road forklifts are available at the following lifting capacity: 1,500; 2,500; 3,500; 4,000; 5,000; 6,000; 7,000; 8,000, and 10,000 kg.

In summary, the main concepts on which the off-road forklift trucks are developed are the following:

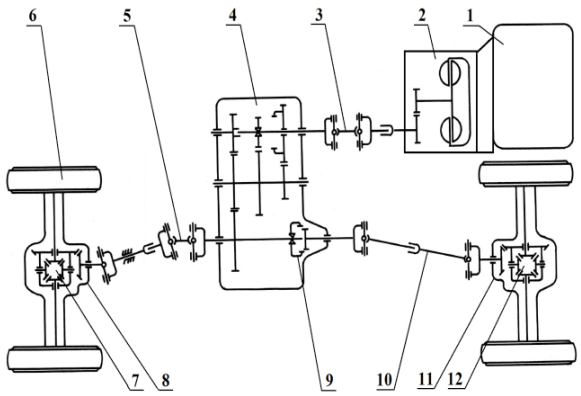

Fig. 3. Power drive design of the articulated forklift family with two drive axles, where: 1. Internal combustion engine (ICE); 2. Hydrodynamic gearbox; 3. Cardan coupling; 4. Two-stage distribution gearbox; 5. Cardan coupling with intermediate bearing; 6. Wheel drive; 7. Differential of front drive axle; 8. Front drive axle; 9. Coupling for enabling/disabling of the rear drive axle; 10. Cardan coupling; 11. Rear drive axle; 12. Differential of the rear drive axle.

The power (engine), transmission, and drive axle design of articulated frame and complete frame trucks have virtually no difference. The power drive design of the articulated forklift range is shown in Fig.3 [9].

The power drive design of the complete frame forklift family with two drive and steering axles is shown on Fig. 4 [9]. It is essentially the same as the one regarding articulated forklifts. The main differences are – the cardan coupling /8/ to the front axle, which is two-carded without intermediate bearing, the presence of synchronous cardan couplings /9/ in both drive and steering axles, as well as their construction.

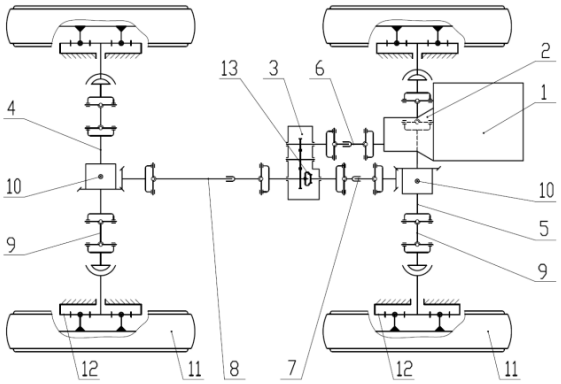

Fig. 4.Power drive design of the complete frame forklift family with two drive and steering axles, where: 1. ICE; 2. Hydrodynamic gearbox; 3. One-stage distribution gearbox; 4. Front drive axle; 5. Rear drive axle; 6. Cardan coupling; 7. Cardan coupling; 8. Cardan coupling ; 9. Synchronous cardan coupling; 10. Differential of front and rear drive axles; 11. Wheel drive; 12. Endwheel reduction gearbox; 13. Coupling for enabling/disabling of the rear drive axle.

Transmission hydrodynamic gearboxes are usually produced with two forward gears and two rear gears or three forward and three reverse gears.

The distribution gearboxes are single-stage or two-stage in most cases without a wheelbase differential. They only have a coupling to shut off torque transmission transfer to the rear axle at the driver‘s request.

The use of cardan couplings with telescopic extension similar to the one used in many lorries.

The wheels of all the above-mentioned forklifts feature wide-profile, large diameter and lower pressure. The frames of the three types of forklift trucks differ considerably in their construction.

The hinged articulated forklift’s frames consist of three parts - front, rear and articulation. The front part is a frame construction of steel profiles. Attached to it is the work body, the front axle, the cab with the controls and the protective roof. The axle is rigid handing to the front of the frame with bolts. The rear part is a box-like structure made of thick sheets of steel and profiles. The engine with transmission gearbox, distribution gearbox, the rear axle and the fuel and oil tanks are attached to it. The rear axle is rigid handing also to the frame. The fitting of a forklift on the ground is done by swinging the rear frame to the front by using an articulation with one or two degrees of freedom.

The frames of the forklift trucks with two drive and steering axles are considerably simpler. They are two longitudinal sheets of thick steel, connected with 3 or 4 cross beams. The front axle is rigid handing to the frame

and the rear of the swing by means of 2 metalrubber bearings and two rubber springs or an axle.

The servosteering of off-road forklifts is hydrostatic.

Their service brakes are drum brakes for some of the machines. Nowadays, oil-friction discs are predominant, acting like the others on all wheels. The brake systems feature a brake booster for trucks with a load capacity of over 4,000 kg. The hydraulic braking of lower capacity loaders does not differ from that of universal forklifts and is carried out with unified components.

The parking brakes of all machines are located on the front drive axle. The braking action is mechanical. In the newer axles the handbrake is negative, it is released by an electro-hydraulic unit.

A hydraulic unit is used to trigger all the specific working equipment and operations. Also, it is used for the steering of the forklift truck. Hydraulic distributors for this purpose are multi-sectional, with manual or joystick control.

Off-road forklifts are designed to work with several types of quick-ly changeable work attachments. For the quick change, by the driver only, of the different operating organs, special attachment devices have been developed.

For articulated forklifts, quick-ly change able attachments are used: a dumper, pliers, a bulldozer, a hydraulic hammer, a screwdriver, a bucket, a grapple - manure loader, a grapple for lengthy materials.

For the whole frame forklift family with two drive and steering axles, a telescopically extending boom has been developed for reaching high lifting heights.

IV. Power Drives of Terrain Forklifts

Since the power transmission design for type 4x2 forklifts is the same as the one of the universal forklift trucks, we will look at the power drive only of the 4x4 wheel formula forklifts.

In the forklift trucks featuring wheel formula 4x4, a variety of construction designs is used for their power transmissions. Regardless of their large variety depending on how the torque is transmitted to the front and rear drive wheels, power transmissions can be subdivided into mechanical, hydrodynamic and hydrostatic. In the analysis of existing constructions, the main attention is focused on the kinematic and power links between the individual drive motors and their mutual influence on the design and performance of the machines.

A. Mechanical power transmissions

Mechanical power transmissions are widely used in cars, tractors, trucks, dumpers and other transport machines. Compared with other types of power transmissions, they are characterized by simplicity, reliability in operation and high efficiency, because they do not convert energy from one type to another. In contemporary technological development, however, due to such drawbacks as stepping, manual gear shifting, large number of levers and pedals, large size and weight, etc., they increasingly fall back on other types of power transmissions or are used in combination with them.

Concerning vehicles featuring the 4x4 wheel formula, there is a wide variety of composition designs which are determined by the design of the machines, the adopted construction of other elements and systems such as suspension, steering system, etc. The most important aspect of the passability and traction properties of the machines is the distribution of the engine's power between the individual wheels and the axles.

Mechanical power transmission is mainly used in high passability forklift trucks. The most commonly used composition design is the so-called "I-shaped".

I-shaped power transmissions (Fig. 5) [2] have been more widely manufactured on 4x4 machines due to the smaller number of cardan couplings and gearboxes and their cheaper production. In this case, the torque from the engine /1/ via the transmission box /2/ and the distribution gearbox /3/ is transmitted to the main differentials of the front and rear axle /4/ and by inter-wheel differentials to the drive wheels /5/

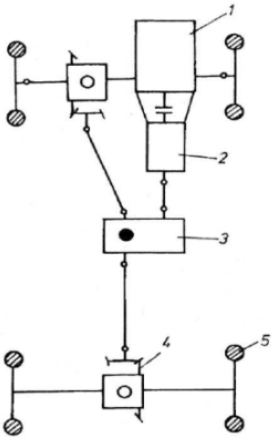

Fig. 5. Design of I–shaped power transmissions.

The design of Fig. 5 is most common in high passability forklift trucks with a small lifting capacity of 1,000 to 1,500 kg. The front and rear axles are permanently connected via a symmetrical differential lock with a manual locking capability. Between the wheels of the two axles there is almost always a differential connection.

In order to avoid the drawbacks of mechanical power transmission and its limited use in terrain forklifts featuring low lifting capacity, it is necessary to use other power transmissions in the machines with higher lifting capacity – hydrodynamic power transmission.

B. Hydrodynamic power transmissions.

Hydrodynamic power transmissions are used in both rough terrain and off-road vehicles. They are used in forklifts with a lifting capacity of over 2,500 kg. For all machines in the hydrodynamic transmission boxes, after the hydrotransformer, a mechanical gearbox featuring 1, 2 or 3 forward and reverse gears is used.

Fig. 3 shows a hydrodynamic power transmission design of off-road forklifts with a single-speed hydrodynamic gearbox, two-stage distribution box and articulated chassis produced in the 1980s in "Balkancar Record" Co. [9].

Fig. 6 [9] show the diagram of the highway DV80/40 4x4 HD forklift with lifting capacity of 8,000 kg produced by "Balkancar Record" Co. The transmission box /2/ is

coupled to the distribution gearbox /3/. The distribution box is of the T12000 type and has three stages. It can enable/disable the torque transmission to the rear axle via the coupling /8/. The main transmission consists of the cone pair /4/, the end wheel gearboxes /5/ are exported to the wheel drive /6/. There is one output for PTO /7/ which is used for a power output for propulsion of hydraulic pumps on the gearbox /2/. There is no differential connection between the front and rear axles. The front differential /9/ has the option of 100% forced locking, and the rear axle /10/ is 45% self-locking. A feature of the design is the adopted construction with two driving and one rear steering axle. The front axle is rigid handing to the frame and the rear axle is swinging on a specially designed shaft.

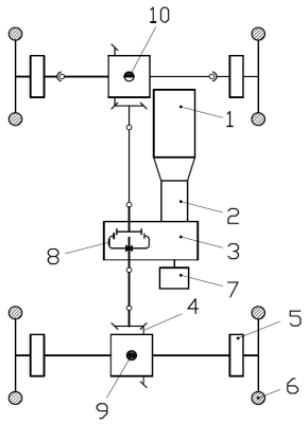

Fig. 6. Design of power transmissions of DV80/40 4x4 HD forklift with lifting capacity of 8,000 kg.

From the schematic view of the mechanical and hydrodynamic power drive transmissions of 4x4 forklifts it is evident that the most applications are I-shaped using different types of wheelbase and inter-wheel differentials. With the use of regular inter-wheel differentials and the same road traction conditions of the left and right wheels, the best performance and patency characteristics of the machine are provided both in lineal motion and when turning. When using forced manual or hydraulic locking, the most complete adhesion of the wheels to the road can be achieved. Under various traction conditions of the left and right wheels, it is sometimes difficult for the driver to determine the optimal solution and often requires the locking to be switched on and off. Inter-wheel differentials are also used in self-locking, which have a common lock factor ranging from 1.6 to 6, which provides some automaticity, but worsens the steering control during turns.

Wheelbase differentials are rarely used and they are common with option for manual locking. Most popular are gearboxes with coupling for manual or hydraulic enabling and disabling of the lock of the rear axle when wheelbase differential is not used.

C. Hydrostatic power transmissions.

A great interest in the hydrostatic power transmissions of terrain forklifts is shown by all the design teams dealing with this technique. This is determined by the rapid development of scientific and technological progress, the implementation of modern technologies, the incorporation of a number of types of hydromachines in serial production, on the one hand, and the need for high-performance transport machines allowing for complex mechanization and automation of the basic loading and unloading work they perform, on the other hand.

The most important advantages of hydrostatic power transmissions for terrain forklifts that can be highlighted involve:

1. Possibility for stepless adjustment of the speed of movement in quite a wide range.
2. High compactness, small mass and overall dimensions, which reduce the machines weight.
3. Low inertia, ensuring good dynamic properties of the machines, including fast reverse movement.
4. Easy automation of power transmission.
5. Independent location of the power transmission individual elements, which enables to be placed in the most convenient positions for the composition design. Great structural flexibility for design engineers.
6. Reliable protection of the motor and transmission from overloading by incorporating safety valves.
7. Use of unified assembly units (pumps, hydromotors, valves, distributors, filters, etc.) to reduce production cost and to facilitate the operation and repair of machines.

It should be taken into account that in practice the effective implementation of the advantages of the hydrostatic power drive transmission is hampered by the following disadvantages:

1. Significant dependence on the performance and reliability of the power transmission from the ambient temperature and the viscosity of the working fluid, respectively.
2. Existence of internal and external leakage due to airtightness of the system, requiring compensation and causing volume losses.
3. Increased requirements for the operational properties of working fluids – the need for constant filtration to remove the dirt. The periods between machine servicing are reduced.
4. Increased requirements for the used materials, quality of workmanship and assembly of the part of the hydraulic equipment.
5. Need for highly qualified personnel and personal responsibility in operating and servicing machinery.

There is a wide variety in the hydrostatic design of hydropower transmissions for terrain forklifts. It should be noted that they are used in both rough terrain and off-road vehicles, whether the wheel formula is 4x2 or 4x4. For example, Fig. 7 [10] shows the hydropower driving of a high passability forklift model MSI 40 of "Manitou" featuring a wheel formula of 4x2 and a lifting capacity of 4,000 kg.

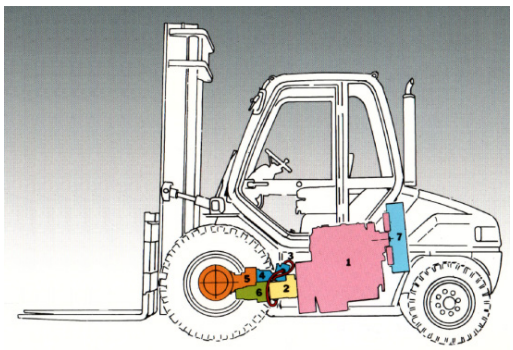

Fig. 7. Hydropower drive of a forklift, where: 1. ICE; 2. Hydrostatic axial pump; 3. Flexible high pressure hoses; 4. Hydraulic motor; 5. Drive axle; 6. Operating hydraulic toothed pump; 7. Cooler.

Adjustment of the speed of movement can be done smoothly by varying the pump productivity or the working volume of the hydromotor, or both together, and also stepwise by using composite hydromotors, switching the same from sequential coupling to parallel, etc.

Using an adjustable hydromotor and a non-adjustable pump, a transmission with a characteristic close to the ideal is obtained, but an increase in the volume and size of the hydromotor is necessary, making this circuit inadequate.

Regarding terrain forklifts, the most common hydrostatic design is the following: one adjustable pump and one adjustable high-speed motor shown in Fig. 8. [9] This design has been successfully realized in the DV80/ 4x4 off-road forklift truck of "Balkancar Record" Co., shown in Fig. 2.

With such a movement speed control, the range of high-efficiency operation of the machine is expanded, but since the mechanical part of the transmission is retained, the internal losses from friction, and other, inside the transmission are also included. This design achieves complete unification with mechanical power transmissions since they achieve it by replacing the transmission box with a hydraulic power transmission.

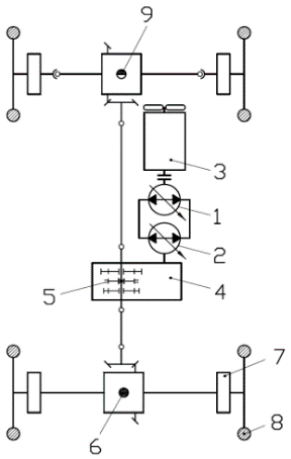

Fig. 8. Design of hydrostatic power transmissions of a forklift, where: 1. Adjustable hydrostatic pump; 2. Adjustable hydromotor; 3. ICE; 4. Two-stage distribution gearbox with hydraulic gearshift; 5. Coupling clutches for shifting quick and slow speed; 6. Front differential with possibility for 100% forced locking; 7. Endwheel reduction gearbox; 8. Wheel drive; 9. Rear differential 45% self-locking.

Another variation of the hydrostatic driving for a forklift 4x4 is shown in Figure 9 [9]. It is distinguished by its simplicity, a small number of composite units (hence low cost) and high efficiency. The ICE /1/ is traditionally located at the rear part of the machine, but its fan does not blow back to the radiator like all forklift trucks – it sucks air through the radiator in front of it similar to cars and tractors. The adjustable pump /2/ is connected via an elastic coupling to the engine flywheel and the direction of movement of the machine is to be considered. The adjustable hydromotor /3/ is connected to the rear side of the main transmission /5/ of the rear axle via a gearbox /4/. The main gear distributor is a worm – worm gear and is connected to the main transmission of the front axle by means of a cardan coupling shaft /7/. Both axles are drive and steering axles with inter wheels lockable differentials /6/.

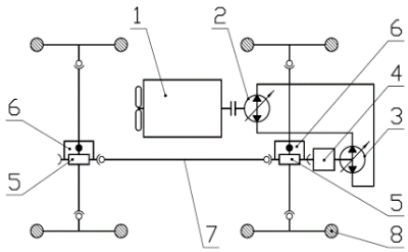

Fig. 9. Design of hydrostatic power transmissions of a forklift.

In this design there is no wheelbase differential, the axels do not have end wheel reduction gearbox and it is used on terrain forklift trucks with telescopic boom and small load capacities of 1,000 to 1,500 kg.

Fig. 10 shows a diagram with 4 traction motors and one adjustable pump, used accidentally in terrain forklifts, mainly in the forestry industry [2].

Hydromotors /3/ are mounted in the wheel drive /1/ together with the wheel gearboxes /2/. The moving speed control is effected smoothly by varying the pump output /4/. The hydromotors are connected in parallel by a pilot-controlled flow divider /5/ between the front and rear axles. This type of connection, ensures synchronization of the peripheral speeds of the front and rear axles and locking of the differential link between the axles. The flow distribution between the two axles depends on the divider characteristic. An ideal divider is the one in which the ratio of front and rear axles flows is a constant value under all operating conditions. This composition design, as well as the independent suspension of the wheel drive, provides a high passability for all road conditions. A major drawback is its high cost.

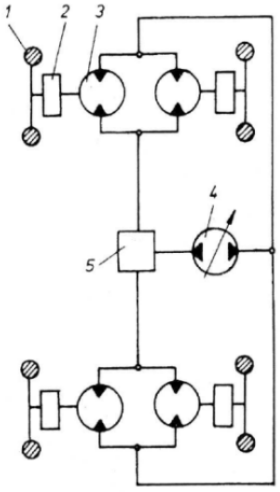

Fig. 10. Design of hydrostatic power transmissions of a forklift.

From the analyzed hydro power transmissions for 4x4 wheel formula forklift trucks, the following characteristic trends can develop:

1. Use high-performance and high-speed hydromotors that are integrated into the distribution gearboxes or embedded in the wheels of the machines and contribute to the simplification of the computational design.
2. Wide application finds mass-produced high-speed hydromotors that are built into the wheels via gearboxes. They are preferred because of the higher reliability and techno-economic performance compared to the high-volume ones, which are still considered special purpose products.
3. Maximum unification of mechanical transmissions – Hydrostatic transmissions are performed with a monolock hydraulic power transmission mounted instead of a gearbox.

V. Analysis of the Power Drive Transmissions of Terrain Forklifts

The analysis of power transmissions in modern 4x4 terrain forklifts shows that widespread distribution finds the differential driving between the wheels and its locking to a certain extent. Differential driving between the axles is more rarely used.

Differential driving is characterized by the use of differentials in all units of division of power flow from the transmission in the forklift truck with wheels [3].

Differential drive can be symmetrical and asymmetrical. The condition to be satisfied by the symmetrical drive is in the absence of internal friction, the torque distribution should be equal between the drive shafts, and regarding the case of cartridge locking and forced rotation of one of these shafts, the other shaft should be rotating in the reverse direction at the same angular velocity. The symmetrical drive ensures the equality of provided torque on all wheels regardless of the moving conditions.

The asymmetric drive provides unequal torque distribution along the shafts. In practice, the non-symmetric differential distributes the torques in proportion to the traction weight of each drive axle, and when the cartridge is locked, the drive shafts rotate at a different angular velocity.

The locked drive is characterized by a rigid mechanical connection between all of the drive wheels. The condition to be fulfilled with it is equality of the angular speeds of all wheels.

The differential driving to the two wheels does not allow for the full utilization of the potential driving torque force of drive axle to be fully utilized, thereby reducing the towing-cohesion properties of the machine. This is observed when the load on the wheels is redistributed when the machine is operating on a transverse slope.

In 4x4 terrain forklifts inter-wheel and lesser wheelbase differentials are used with forced or automatic locking. Wheelbase differentials are mounted in distribution boxes which mainly feature differential or locked action.

Inter-wheel differentials enable the drive wheels on one axle to rotate at different angular speeds, which provide motion during turning, on uneven road or when wheels feature different radiuses. This removes the slipping and skidding of the wheels. But, as it is known, the differential divides the torque evenly between the two semi-axis. This property of the differential when driving on a transverse slope, as well as under other conditions, reduces the propelling force of the machine. Various devices for locking the differential are used to overcome this disadvantage.

Wheelbase differentials are used in the 4x4 forklift for inter-wheel drive of the drive wheels. In the differential drive between the angular speeds of the axle of the wheeled forklift, there is no definite variable ratio similar the locked drive. However, in the case of a locked drive, it is possible to generate parasitic circulating power due to the presence of a closed power loop and a kinematic inconsistency in the different modes of movement of the machine.

Parasitic circulating power in closed power flow occurs under construction and operational factors. The construction factors include the type of drive system and type of wheel drive, different rolling radiuses, the type of power transmission, the vertical load on the drive wheel and its distribution, the size of the longitudinal and transverse base, etc. The operational factors include varying wear of tire treads, varying tire pressure, the different road traction due to the diverse physical and mechanical properties of the soil, etc.

The resulting parasitic circulating power results in deterioration of the traction-coupled properties of the forklift, the possibility of breakage in the power drive transmission and the wear of the drive wheels.

The wheelbase axle distributes the torque between the front and rear drive wheels in proportion to the traction weight of the respective axle and enables the wheels to rotate at different angular speeds. As a result of which there is no kinematic discontinuity and the occurrence of parasitic circulating power. But the wheelbase differential is inherent in the same shortcomings that were pointed out in the inter-wheel differential. For this reason, it also provides for the incorporation of devices for forced or automatic locking of the differential. The construction of a self-locking wheelbase, installed in the distribution gearbox of a CH200-CH250 series forklift of AUSA, is

marketed as "COMPEN System" [8].

In practice, it is a self-locking conical differential with friction discs, the crown is driven by a chain, which in turn is driven by a chain gear connected to the hydromotor.

In recent developments of terrain forklifts, an ever-wider application finds the use of "Smart Drive CT" modules similar to those shown in [11].

This module provides an electronic solution for controlling the entire power transmission drive of terrain forklifts, most commonly hydrostatic or hydro-dynamic. It selects the most optimal drive motion mode and manages the traction efforts at any moment of the vehicle [11].

VI. Conclusions

From the study of the kinematic designs and constructions of forklift power transmissions, the following conclusions and suggestions could be pointed out:

1. Power transmissions of forklifts are mechanical, hydrodynamic and hydrostatic with a wide variety of kinematic and power drive transmission to the individual drive wheels.
2. Depending on the drive design (locked, unlocked and differential) of the drive wheels, 4x4 forklift trucks could feature the following motion modes: drive, driven, brake, neutral or free travel drive.
3. The most of existing power drive transmissions of 4x4 terrain forklifts are implemented using distributor gearboxes with locking action, which enables the occurrence of circulating parasitic power in the power transmission or incomplete use of potential traction-cohesion properties on the machine.
4. In the power transmission design of forklifts featuring wheel formula 4x4, different mechanisms and devices are incorporated between the two drive axles (inter axle differentials with or without locking devices, distribution gearboxes, cardan coupling shafts, etc.), part of which are permanently working without locking and others include manual or automatic locking depending on the load and movement modes.
5. The great variety of 4x4 terrain forklift composition designs and the power transmissions thereof, as well as their operation in various road and production conditions, require that optimal solutions be sought by developing mathematical models and programs to optimize their parameters.

Acknowledgments

This work was supported by the European Regional Development Fund within the OP "Science and Education for Smart Growth 2014 - 2020", Project Competence Centre "Smart Mechatronic, Eco- And Energy Saving Systems And Technologies", № BG05M2OP001-1.002-0023.

References

[1] I. Evtimov, Electric and motor forklift trucks. University of Ruse, Ruse, Bulgaria, 2014.
[2] D. Katsov and Y. Dimitrov, Wheeled and tracked machines. Technical University of Sofia, Plovdiv Branch, Plovdiv, Bulgaria, 2005.
[3] K. Stepanova and A. Lafarov, Blocking differentials of trucks. Mashgiz, Moscow, Russia, 1960.
[4] D. Katsov, D. Hlebarski and S. Taneva, Transmissions of automobiles. Arena Print, Plovdiv, Bulgaria, 2018.
[5] G. Valkov and V. Nikolov, „Classification of terrain forklifts". 7th international scientific conference TECHSYS 2018, 17-19 May 2018, Plovdiv, Bulgaria, Proceedings, pp. 253-257, [Online]. Available: http://techsys.tu-plovdiv.bg/files/TECHSYS_2018_Proceedings.pdf, [Accessed: July 15, 2018].
[6] I. Iliev and V. Nikolov, "System for automatic stability of forklift trucks". Patent BG 62225 B1, November 15, 2007.
[7] I. Iliev and V. Nikolov, "System for control of the operations of forklift trucks". Patent BG 62226 B1, November 15, 2007.
[8] https://www.ausa.com/en-gb/forklifts/ [Accessed March 19, 2019]
[9] https://balkancar-record.com/en-US/Products/Forklifts, [Accessed March 19, 2019].
[10] https://www.manitou.com/en/ [Accessed March 19, 2019].
[11] https://www.poclain-hydraulics.com/_upload/ressources/media/pdf/A51874K.pdf, [Accessed June 13, 2017].

The Analysis of Stochastic Processes in Unloadingthe E*nergyw*illow Cuttings from the Hopper

Serhii Yermakov
Educational and scientific laboratory "DAK GPS"*State Agrarian and Engineering University in Podilia*
Kamianets-Podilskyi, Ukraine
dakgps@pdatu.edu.ua

Hutsol Taras
Vice Rector for Educational, Scientific and Pedagogical Affairs
State Agrarian and Engineering University in Podilia
Kamianets-Podilskyi, Ukraine
pro-gp@pdatu.edu.ua

Krzysztof Mudryk
Department of Mechanical Engineering and Agrophisics
University of Agriculture in Krakow
Krakow, Poland
krzysztof.mudryk@ukr.edyu.pl

Krzysztof Dziedzic
Department of Mechanical Engineering and Agrophisics
University of Agriculture in Krakow
Krakow, Poland
krzysztof.mudryk@ukr.edyu.pl

Liudmyla Mykhailova
Department of Electrical Machinery and Electrical Equipment Operating in Agriculture
State Agrarian and Engineering University in Podilia
Kamianets-Podilskyi, Ukraine
mihajlovaimesg@gmail.com

***Abstract*—The paper deals with the theoretical and experimental investigation of the main characteristics of woody crop cuttings unloading from the hopper. To create a variety of automated systems for material feed there is a need to ensure high performance selecting and unloading the material, in particular, it is of vital importance in designing machines for energy willow planting. The analysis of existing theories in mechanics of loose materials motion made it possible to identify the features of unloading the cuttings that narrowed the area of discussion. We will consider two half-planes located at angles to the horizontal plane as a model for hopper in pilot testing.**

It is analytically and experimentally determined that woody crops cuttings flow occurs according to dry friction laws and inverse-square law and the flow is normal in nature. The statically stable formation and dynamic arches that prevent the uniform and continuous unloading are in evidence.

For the theoretical validation of results, we present a set of cuttings as the pseudo liquid that consists of two phases: a discrete phase formed by cuttings and the continuous phase (gaseous medium, air). Each of these phases in terms of the mechanics of multiphase systems is represented as a solid medium with certain characteristics. According to these assumptions, the process unloading of such structure from the hopper can be modelled on the basis of methods of hydrodynamics of multiphase systems. In such a case the field speeds of such pseudo liquid must satisfy the Navier-Stokes equation type.

The analytical and empirical analysis of unloading the energy willow cuttings helps to prove theoretically the possibility of enhancing the process of planting till its full automation. As a result, the study gives the theoretical formula that evaluates the velocity of energy willow cuttings flow, the adequacy of which is partially tested in pilot experiments conducted by the authors of the paper in the process of creating the planting machine.

Using the received data for further research will make it possible to take into account all the factors involved *in unloading* and bridging, which is important for examining and improving this process.

Keywords — wood cuttings, bridging, hopper, automatic planting, pseudo liquid.

I. Introduction

The production of alternative renewable energy sources is a priority direction in the development of the nation's economy, and the use of bio-feedstock, including energy crops, as fuel, is one of the strategic path ways. Therefore, it is important to ensure high-performance of machines for plantings of such crops. It is well-known that machines for energy willow or poplar planting use, primarily, hand supply of planting material that significantly limits both quantitative and qualitative characteristics of this device. Therefore, the development of the planting machine for such crops is a significant engineering challenge.

Willow and Poplar are cloned for energy purposes by planting cuttings with the diameter of 15-20 mm and the length of 20-30 cm. The features of such material determine the main complexity in its loading. If the studies on the mechanics of small lump granular materials movement are frequent [2, 3, 4, 5, 6], the research on this kind of materials lack.

The necessary part of machines and units (both mobile and stationary) that are designed for the bulk materials are tankers of different shapes and sizes. Obviously, to develop the automated system of cuttings flow we should consider the issue hopper. Therefore, the aim of this research is the study of stochastic processes in pouring

Print ISSN 1691-5402
Online ISSN 2256-070X
http://dx.doi.org/10.17770/etr2019vol3.4159

the woody crops cuttings out that will provide continuous and uniform flow, transportation, navigation and setting in place ofplanting.

Materials and methods

The material for study is the rod-like body (the cuttings of woody crops). The lack of roots and relative identity of cuttings according to form size, allow us to find the solutions in the existing theories of granular material flow and to determine the peculiarities that can be applied to hardened cuttings. Moreover, such phenomena as adhesion and strength of clutches between cuttings will not influence the movement. That is why when we unload such material it will act as a free-flowing and bulk material that is characterized by dry friction determined by inverse-square law. Taking into account the mentioned information we can use the mathematical models of the discrete granular body (for example, the theory of L. Hiachev, V. Bohomiahkykh) for examining the cuttings flow from the tanker.

The models of the tanker for cuttings unloading in our experimental research will be two half-planes set at the angles **α** and **β** to the horizontal plane (fig. 1).

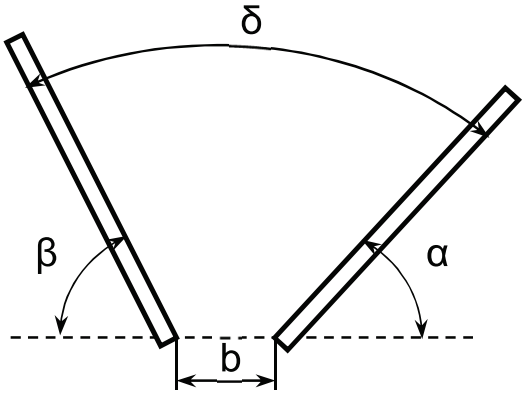

Fig. 1.
Hopper model for unloading the energy willow cuttings.

To process data, the conclusions of the various theories on free-flowing material flow and empirical studies conducted at the laboratory installation in State Agrarian and Engineering University in Podilia were used.

II. Results and discussion

The productivity of machines and technological lines of various industrial complexes in general and agriculture in particular, depends, primarily, on the bandwidth of the feed items – the tankers. In addition, tankers not only receipt and issue the material, they often work as transporting units, dosing devices. It, consequently, gives the reason to consider them as an important link in terms of automatic or automated functioning of machines, as well as the differential regulation of control systems.

The features of the shapes and sizes of such material as energy crops cuttings influence also the mechanics of their flowing terms of their gravity discharging from the tanker. The explanation of the process of the movement of such material can be found in the theories of granular materials flow in terms of dry friction.

As far as scientific theories are concerned, starting from the end of the 19th century scientists explore the mechanics of granular bodies that is shown in the following conclusions:

- the pressure on the bottom of reservoirs is significantly lower than the weight of the material. Besides, at some height of material layer, this pressure remains unchanged. And therefore the flow rate and speed of granular materials do not depend on the height of backfill over the exhaust opening (Roberts, Fried, Delakroa, Bernstein);
- the pressure of the granular material depends on its density and the parameters of cross-sectional mortice of unloading hole (Jansen, Zenkov);
- The bulk material can be regarded as a discrete environment (Dzhenkìn);
- thespeed and the consumption of leakage under normal flow are larger than hydraulic, due to different frequency formation of arches (Keneman);
- The phenomenon of "dynamic bridging" takes place in the process of granular materials flow (Protodiakonov, Pokrovskyi, Arefiev, Platonov, Banìt);

Such conclusions for different types of granular materials are frequent. We presented only some of the patterns that can be applied to study the movement of woody crops cuttings.

The mechanical model of granular body motion designed by L. Hiachev, V. Bohomiahkykh are widely used today. The study of the scientists is an attempt to develop the first combined model for granular materials that combined its discrete and continuous properties. The authors took into consideration such physical and mechanical properties like the size of the particles, the angle of the installation, the coefficients of friction, etc. [5] L. Hiachev, for example, in his research accepts that the friction of particles of the material between each other and the walls of the tanker are dry, that allows to use these ideas for wood cuttings. V. Bohomiahkykh, in his turn, used the idea of bridging to identify the impact of unsustainable arches on the movement of grain flows in tankers and determined the frequency of formation and destruction of riveting [4]. The phenomenon described by the author were applied in our experimental research on cuttings flow [6].

The mentioned statements and theories give grounds to consider unloading energy crops cuttings as of the flow of incompressible bulk material, and the patterns of material movement in the gravitational discharge is accompanied by various phenomena that prevent movement (first of all arching) and have the stochastic nature.

On the basis of the accepted model of the tanker and the material and on the basis of the carried out analyses and laboratory experience, the process of discrete bulk material flow from the tankers can be described as follows.

At the moment of opening the damper of exhaust outlet of the hopper, the flow of loose material in it some short period of time will be transient (before the moment of destruction of the most remote from the exhaust outlet of a dynamic arch, generated in the process of unloading).

Under certain conditions, the dynamic arches become statically stable. This occurs when a polygon of forces acting on this arch, is closed. That is, in this case, the resultant of all forces acting on this arch is zero. If it is not

zero, then statically stable set becomes unstable (dynamic) and, finally, collapses.

Statically stable arches stop the process of flow, but the probability of their development depends on the width of the discharge opening. We can always find a value for the width of the discharge opening, where such stops can be avoided. Adopting empirically this window width we can fix the material flow from the tanker in different periods of time after the start of unloading (opening the unloading window). Because the process of unloading from the symmetrically inclined walls follows the same principles, let's have a look at the phase of flow when the form of a tanker has one vertical wall (fig. 9)

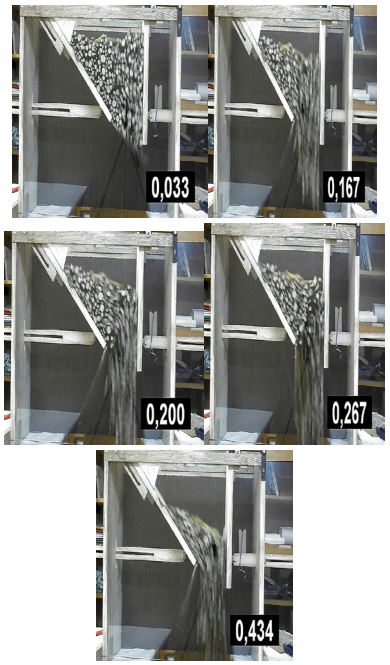

Fig. 2. Theflowphaseof energy willow cuttings from the hoppers if theslanted corners ofhalf-planesare$\alpha=90°$ и $\beta=40°$

Periodic stochastic arches and destruction of statically stable arches over the entire height of the moving stream in the tanker determine the periodic stochastic 3-d loosening and sealing of loose material and, therefore, causes its throbbing exit from the hopper outlet. This was confirmed by the experiments in boundary value of discharge opening width.

Consequently, the process of bridging the bulk materials that are in the boundary conditions is a natural phenomenon peculiar to loose bodies. Stochastic process of origin and fracture of arches is observed with any kind of discrete bulk material flow from the discharge opening of tankers.

This process is both discrete and continuous. Its discretion is evident in beating nature of flowing the loose material and its continuity - in laminarity (uniformity) of flow in a tanker since the moment of its inception and until its complete exit from the hopper.

Another aspect of selection the theories for studying the mechanics of unloading the granular material is a kind of material from the banker.

Taking into accountthe physical and mechanical properties of wood cuttings, as well as the form, design options, and frictional properties of walls of possible hoppers the hydraulic motion is unlikely. The normal movement of the flow, when the material over the slit window is uploaded first and then the material from the inclined walls of the hopper (fig. 3). As a result, on the surface of the material a funnel, or in our case a wedge is formed.

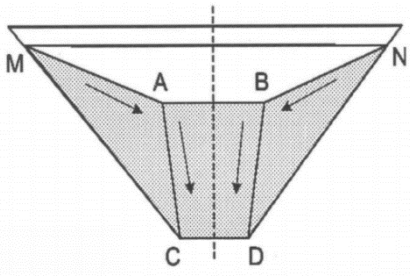

Fig. 3. The diagram of the normal motion of the material in the hopper.

The appropriate nature of cuttings flow, was confirmed by research conducted in State Agrarian and Technical University in Podilia, where the motion of energy willow cuttings in the track hopper with wooden walls [1; 2].

The detailed analysis of cuttings movement made it possible to characterize the features of their flow. So, if you unload such material from the hopper with one vertical wall the first cuttings that are above the discharging window and along a vertical wall (fig. 2-1 and 2). On a sloping wall angled at 40° the cuttings form the inactive layer. As a result of cuttings flow a wedge like hole visible from the second frame is formed in the upper layers which is clearly visible from picture 2 (fig. 2-2). In a period of time, the material falls down into the emptiness (fig. 2-4 and 5). We should mention that the material was non-mobile before (upper layers above the sloping wall). As a result, a collision between the layers is formed (fig. 2-4) that "strike" with layers of normal pouring out that have not yet had time to leave the hole. From our point of view, it is the moment when the static arch and delay of unloading (or even stop) take place. The hopper leaves the last layer of cuttings that were near the sloping wall (fig. 2-5).

It can be stated that the cuttings in the hopper move erratically: first of all, the cuttings over the unloading window move, and in the end the cuttings on the sloping wall move. Respectively, the speed of cuttings movement of the over the unloading window is always the biggest and speed of cuttings over the sloping wall is smaller and depends on the angle of its inclination. It can be concluded that the cuttings flow follows the normal rules of material flow when the pillar falls over the hole at the beginning, and then the layers from the sides start to move. Continuing the experiments different angles of installation at α and β half-planes, it is possible to determine approximately the same patterns (fig. 4).

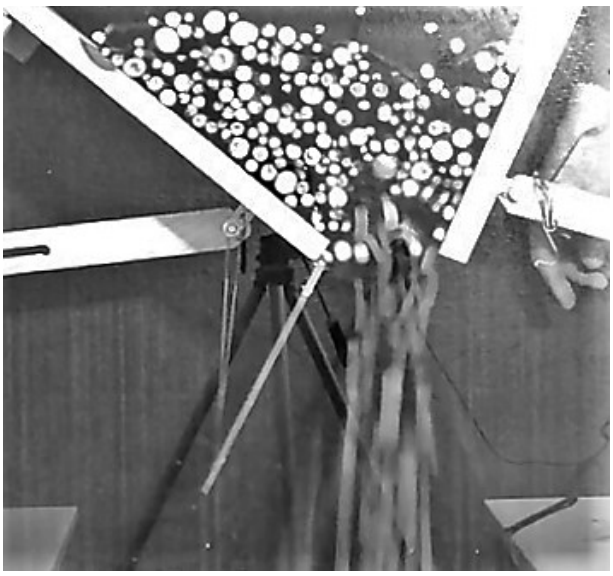

Fig. 4. .The normal character of energy willow cuttings flow inSAE-UP research.

For the theoretical substantiation of the specified processes, we propose to review the mechanics of cuttings motion in terms of the gravitational unloading from the point of view of dynamics of multiphase systems [10, 13]. The set of cuttings is regarded as the double phase pseudo liquid, where the cuttings form the discrete phase and the second phase is the gaseous medium that fills the spaces between the cuttings. Taking into account the fact that the volume concentration of cuttings (discrete phase) is significantly larger than the similar values of continuous phase, the movement of the discrete components (aggregate cuttings) can be logically modelled as a movement of viscous incompressible pseudo liquid, velocity field of which satisfies the Navier-Stokes equation [12].

III. Conclusions

It follows from the above that the process of grain materials flow from the hopper is the natural process of frequent in time formation and destruction of dynamic arches over the entire height of the moving discrete stream. This process is stochastic according to both the time of formation and destruction of arched structures and the location of their formation and destruction in the volume of boundary conditions (e.g., the volume of the hopper).

The analysis of the unloading process and the form of the arches shows that such material as woody crops cuttings, besides the common causes of arches formation and patterns of their origin have some more peculiarities. One of the features of these cuttings is their rod-like form that makes the bridging difficult and invokes such additional conditions and factors as distortions of cuttings in the layer, the irregular shape of the cuttings, their uneven pinching in length, etc.

It is possible to analyze the patterns of cuttings unloading from the hopper if we create the conditions when there is no occurrence of static arches. In this case, the flow follows the principles of normal flow.

We are able to theoretically justify the results with the help of modelling the mechanics of cuttings movement based on the dynamics of multiphase systems. The material is supposed to be a two-phase incompressible pseudo liquid, the flow of which would correspond to the Navier-Stokes equation.

Using the received data in further research will make it possible to take into account all the factors involved in unloading and formation of arches that is important in examining and improving this process.

References

[1] S.V. Yermakov, Perspektyvy udoskonalennia konstruktsii dlia sadinniazhyvtsiv enerhetychnykh kultur [Perspectives of improvement of constructions for energy crop planting]. Bulletin of State Agrarian and Engineering University in Podilya, V. 2 (26), 2017, p. 37-45. Available: http://188.190.33.56:7980/jspui/bitstream/123456789/296/1/PB-26-29.pdf. [Accessed: Feb. 09, 2019].

[2] S.Yermakov, M.Tulej, W.Tulej, I. Shevchuk,Analiz konstruktsiy avtomativ sadinnia [Construction analysis means of plantingi automation]. Materialy XXXIV Mizhnarodnoi naukovo-praktychnoi internet-konferentsii «Tendentsii ta perspektyvy rozvytku nauky i osvity v umovakh hlobalizatsii». Vypusk 34. Pereiaslav-Khmelnytskyi, 2018, p.615-619.

[3] V.A. Bohomiahkykh, A. P. Pepchuk, Intensifikaciya razgruzki bunkernyx ustrojstv v usloviyax svodoobrazovaniya zernistyx materialov [The improvement of unloading of bunker devices in terms of grain bridging]. Zernohrad, 1985, 162 p. Available: https://elibrary.ru/item.asp?id=24577674. [Accessed: Feb. 09, 2019]

[4] L.V. Gyachev, Osnovy teorii bunkerov [Fundamentals of bunker theory]. Novosibirsk: izd-vo novosibirskogo universiteta, 1992, 312 p.

[5] L.N. Tyshchenko, (2004) Intenifikaciya separirovaniya zerna [Identification of grain separation]. Kharkov: Osnova, 224 p. Available: https://elibrary.ru/item.asp?id=19507459. Access: 25th November, 2018.

[6] L. N.Tyshchenko, V. N. Olshanskyi, Vibroreshotochnaya separaciya zernovyx smesej. [Vibro latticed separation of grain mixes]. Kharkov: Misruk, 2011, 280 p.

[7] N.N. Boholiubov, J.A.Mytropolskyi, Asimptoticheskie metody v teorii nelinejnyx kolebanij [Asymptotic methods in the theory of nonlinear oscillations]. Moscow: Nauka, 1974, 504 p. Available: http://books.e-heritage.ru/book/10081090. Access: 25th November, 2018.

[8] M.A. Lavrentev,; B.V. Shabat, Metody teorii funkcij kompleksnogo peremennogo [Methods of the theory of functions of a complex variable]. Moscow: Izd-vo Physics and Mathematics Lit, 1958 674 p.

[9] R. L. Zenkov,; G. P. Grinevich,; V. S.Isaev, Bunkernye ustrojstva [Bunker devices].Moscow: Mashinostroenie, 1966, 234 p. Available: http://science.totalarch.com/book/3939.rar. Access: 25th November, 2018.

[10] S. Sous, Gidrodinamika mnogofaznyx sistem [Hydrodynamics of multiphase systems]. Moscow: Mir, 1971, 536 p.

[11] K. Dziedzic, B. Łapczyńska-Kordon, K. Mudryk, M. Wróbel Decision support systems to establish plantations of energy crops on the example of willow (Salix Viminalis L.). Scientific achievements in agricultural engineering, agronomy and veterinary medicine polish ukrainian cooperation. Vol. 1, No. 1, 2017, p.150-160. Available: http://188.190.33.56:7980/jspui/bitstream/123456789/858/1/SCIENTIFIC%20ACHIEVEMENTS.pdf#page=150. Access: Feb. 09, 2019.

[12] S.Yermakov, T. Hutsol. Features of the heterogeneous rod-like materials outflow. Technological and methodological aspects of agri-food engineering in young scientist research.Krakow, 2018, pp. 55-68.

[13] R.I. Nyhmatulin, Osnovy mexaniki geterogennyx sred [The basics of mechanics of heterogeneous mediums]. Moscow: Nauka, 1978 336 p.

[14] K, Dziedzic, K. Mudryk, T. Hutsol, B. Dziedzic; "Impact of grinding coconut shell and agglomeration pressure on quality parameters of briquette, Engineering for rural development", 2018, pp. 1884-1889.

Professional Competence as a Key Factor in Improving the Quality of Engineering Education

Lesia Zbaravska
Department of Physics and Engineering Discipline
State Agrarian and Engineering University in Podillia
Kamianets-Podilskyi, Ukraine
olzbaravska@gmail.com

Olha Chaikovska
Department of Social and Humanitarian State Agrarian and Engineering University in Podillia
Kamianets-Podilskyi, Ukraine
olgachaikovskaya@ukr.net

Hutsol Taras
Vice Rector for Educational, Scientific and Pedagogical Affairs
State Agrarian and Engineering University in Podillia
Kamianets-Podilskyi, Ukraine
pro-gp@pdatu.edu.ua

Sergii Slobodian
Department of Physics and Engineering Discipline
State Agrarian and Engineering University in Podillia
Kamianets-Podilskyi, Ukraine
dakgps@pdatu.edu.ua

Oleksandr Dumanskyi
Department of Agricultural Machinery and Mechanization Technology
State Agrarian and Engineering University in Podillia
Kamianets-Podilskyi, Ukraine
dakgps@pdatu.edu.ua

***Abstract*—The integration of Ukraine into the European community is impossible without changes in the education sphere. The implementation of such projects of the European Union as "Horizon 2020" provides the collaboration between experts in Agriculture and Engineering. The results of the questionnaire conducted by "Agro Survey" agency showed the lack of student's practical knowledge in Ukrainian Engineering and Agricultural universities. It is obvious that the quality of education in Ukrainian technical universities doesn't meet the requirements of the European labour market. Getting theoretical knowledge has no value until students can apply it for practical purposes. We suggest that a subject like Physics should be practice-oriented. If the Physics course at technical universities integrates theory with practice, students will be better prepared for their future career.**

The purpose of the study is to define the basic principles of professional competence as the key factor for improving the quality of future engineer's training in the process of studying Physics.

To select and interpret the factual material, concepts and theories the theoretical analysis of philosophical, psychological and pedagogical literature on research was used in the paper. The pedagogical experiment was carried out on the basis of 4 universities in different regions of Ukraine and involved 159 respondents (151 students and 8 university teachers). To determine the strategies for implementation of the profession-based tasks in Physics course we carried out specially designed questionnaires for students majoring in Agrarian Engineering and university teachers.

One of the necessary conditions for future engineer training is professional orientation in studying. We suppose that to consider the relationship between a comprehensive Physics course and the disciplines of professional and practical training the in-depth analysis should be performed. First of all, it will help to determine Physics knowledge, abilities and skills that should be used in student's further professional training. Second of all, it will enable the most effective use of engineering-based tasks in Physics classes. However, knowledge of basic Engineering and General Theoretical subjects is not applied by the students of Technical High School for a long-period of university study. The results of the survey have shown that studying major subjects at a later stage doesn't motivate students to learn Natural Science and Engineering disciplines.

We can conclude that profession-based tasks in Physics class contribute to the formation of a system of natural knowledge, practical skills and abilities. They stimulate the students' cognitive interest in Physics as a science, help to better absorb material of other disciplines, develop creative abilities and influence the formation of persistent motifs for obtaining knowledge of professional disciplines.

Keywords*— *professional competence, practice-oriented, Physics, professional training, agrarian engineering.

I. Introduction

High School is a background to the future of most students. Yet many students finish universities unprepared for a career. Professional competence training of graduates should be one of the priorities in Higher Education that provides a perfect final result, i.e. an expert who has mastered the necessary knowledge, abilities, has higher order of creative skills, the appropriate worldview and erudition, intellectual level, who acquired the skills of self-study and formed the professional qualities and moral, aesthetic, ecological culture. Consequently, the

Print ISSN 1691-5402
Online ISSN 2256-070X
http://dx.doi.org/10.17770/etr2019vol3.4118

development of the professional competence model for High School is one of the most urgent issues today.

The academics examined the characteristics of specialist professional training in international affairs [16], medicine [1], the border guard servicing [18] on the basis of an interdisciplinary approach [13], [14]. Some studies on the professional competence training, its basic principles and the impact on the career of a future engineer [15] [2], [4], [5], [9], have been done by Ukrainian [3], [11], [12] and foreign academics [6], [7], [8], [10], [17]. However, there is a number of questions that was not discussed at all. Moreover, the research on the development of profession-based Physics teaching methods with the students of Agricultural and Technical High Schools is still lacking.

The review of regulatory literature, plans and curriculum, standards for engineering training, educational characteristics of experts in agriculture engineering allowed us to state that:

- there is a disagreement between the content of new standards of education and outdated teaching-methodological, instructive and normative support and pedagogical strategies;
- the principle of professional orientation in teaching Physics with the students of Agricultural and Technical Universities is not fully implemented;
- there is a tendency for student mastering a vast amount of educational material and for systematical reducing the hours for in-class studying Physics;

As a result, a significant number of students doesn't realize the goal of studying Physics. During the period of their learning, they don't fully acquire the basic knowledge in Physics and have no experience of its applying to perform the tasks associated with the future professional activity [12].

To develop the profession-based model for teaching Physics in High School the authors identified the following tasks: to determine the basic principles of professional competence and to identify the most effective professional competence strategies for preparing experts in engineering; to describe the specifics of implementing the vocational-oriented technologies in Physics for students majoring in agricultural engineering; to test the effectiveness of implementation of profession-based tasks in Physics course.

II. Materials and methods

The pedagogical experiment was aimed at testing the effectiveness of professional competence approach for the systematization of Physics course learning in Agricultural and Technical High School, at improving the content and forms of education, at developing means for intensification of the educational process and the complex of knowledge diagnostics.

The research was carried out on the basis of State Agrarian and Engineering University in Podillia, National University of Life and Environmental Sciences of Ukraine and Nizhyn Agrotechnical Institute. The study involved 151 students majoring in Agrarian Engineering. The pedagogical experiment also included the questionnaire for 8 lecturers who teach Physics for students majoring in Agrarian Engineering at Lviv National Agrarian University and State Agrarian and Engineering University in Podillia.

The experiment had the following stages:

- the organization of experimental and research training;
- the analysis of organizational, structural and contextual changes in the process of studying Physics and their influence on the level of student's knowledge in Agricultural and Technical High School;
- the evaluation of teaching activity. Physics teachers who participated in the pedagogical experiment followed the original Physics guides, recommendations and other educational and teaching materials in their teaching practice.

A testing system for learning achievements that performed diagnostic, control, motivational and educational functions was designed in the process of pedagogical experiment. The pedagogical monitoring was carried out on the basis of standard tools (tests, reference works, surveys, etc.). We should admit, it was simple, convenient and effective. On the one hand, the pedagogical control determined the level of students' progress in Physics, and, on the other hand, the results of the monitoring showed the effectiveness of discipline teaching and studying.

During the pedagogical experiment the following methods were used:

- the observation of the educational process and the analysis of Physics and Engineering disciplines teaching methods during attending the classes;
- the questionnaire and the interview.

III. Results and discussion

The observation showed low student participation in the Physics classroom, the absence of motivation and interest in the training material, low grades.

The questionnaires contained several survey questions focused on expressing the idea according to certain supposition.

The following questions were used in the survey:

1. What is the role of Physics in your future profession?
2. Does Physics lay the groundwork for studying the professional disciplines?
3. What is the role of Physics in completing professional tasks?
4. Does Physics help you to write a Diploma Thesis?
5. Does Physics help to improve your intellectual potential?
6. Does Physics help to form logical thinking?
7. Does Physics help to form creative thinking?
8. Does Physics assist the training of agrarian engineer?
9. Is it possible to do profession-based teaching and research work without the knowledge and skills in Physics?

Almost 95% of the students stated that Physics in Agricultural and Technical University doesn't influence

the study of professional disciplines. More than 60% of the respondents associate Physics with such Engineering disciplines as "Electronics", "Theoretical mechanics", "Machine Parts". However, the students agree that "Theory of Mechanisms and Machinery», «Mechanics of Materials and Structures" have no relationship to Physics.

The exam grades in professional disciplines showed that the students don't use the issues and the laws of Physics in the process of studying the disciplines of professional and practical training. What is more, about 87% of the students don't associate Physics with the disciplines of professional and practical training.

The student's answers to the question "What should be done to increase the level of student professional training in the process of studying Physics" were the following:

- to improve the financial and logistical support of the educational process (the percentage index of all interviewed students is 15.2%, where 19.3% of students are from National University of Life and Environmental Sciences of Ukraine, 3.7% of students are from Nizhyn Agrotechnical Institute and 6.7% of students are from State Agrarian and Engineering University in Podillia.
- To improve teaching methodology of Physics (the percentage index of all interviewed students is 23.85%, where 15.6% of students are from National University of Life and Environmental Sciences of Ukraine, 48.2% of students are from Nizhyn Agrotechnical Institute and 40% are students from State Agrarian and Engineering University in Podillia;
- to provide profession-based tasks in different types of training activities in Physics (the percentage index of all interviewed students is 21,9%, where 25.7% of students are from National University of Life and Environmental Sciences of Ukraine, 11.1% of students are from Nizhyn Agrotechnical Institute and 13.3% are students from State Agrarian and Engineering University in Podillia);
- To increase the hours for Physics classes (the percentage index of all interviewed students is 17.9%, where 16.5% of students are from National University of Life and Environmental Sciences of Ukraine, 25.9% of students are from Nizhyn Agrotechnical Institute and 13.3% are students from State Agrarian and Engineering University in Podillia);
- To increase the level of teacher professional training (the percentage index of all interviewed students is 13.9%, where 13.8% of students are from National University of Life and Environmental Sciences of Ukraine, 11.1% of students are from Nizhyn Agrotechnical Institute and 20% of students are from State Agrarian and Engineering University in Podillia);
- to create the conditions for the development of students' ability to self-study (the percentage index of all interviewed students is 3.3%, where 3.7% of students are from National University of Life and Environmental Sciences of Ukraine, 6.7% of students are from State Agrarian and Engineering University in Podillia and no respondents have chosen this variant of answer in Nizhyn Agrotechnical Institute);
- Six students have offered their own answer: the implementation of new information technologies in studying the profession-based material.

Physics teachers had to determine the strategies for the implementation of profession-based principle in the educational and methodical supply of Physics course. The results of teachers' survey questions are shown in Fig. 1

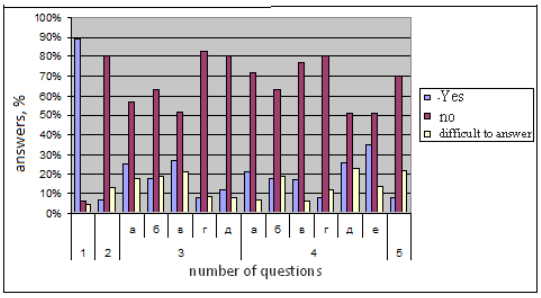

Fig. 1. The diagram of teachers' questionnaire results

More than 50% of the teachers answered that Physics course content is not connected with the future engineering specialization of students. In addition, teaching Physics with the students of Agricultural and Technical Universities doesn't differ from the content of the Physics course in Technical High School, except the number of curriculum hours.

The teachers-respondents confirm that laboratory workshops in Physics and practical training are not related to the future profession. Teachers of professional disciplines highlight that students don't have the skills to apply Physics knowledge in disciplines of professional and practical training.

The obtained results make it possible to confirm that:

- the majority of students doesn't experience the close relationship between Physics, General Technical disciplines and disciplines of professional and practical training;
- the content of the lectures and practical classes sometimes contains abstract material and laboratory classes don't differ from Physics classes at Pedagogical Universities.

The analysis of the research results proves the fact that Physics curriculum in Ukrainian Technical High Schools doesn't integrate disciplines of professional and practical training. The traditional system of teaching Physics in Agricultural and Technical Universities doesn't benefit from the implementation of professional orientation in teaching Physics and doesn't allow to significantly affect the professional development of the students.

IV. Conclusions

To sum up, the use of interdisciplinary links and applied Physics tasks in the educational process will allow forming the student's perceptual unity in Physics structure and content of Physics. The integration of Physics and profession-based disciplines will help students to realize the importance of Physics for their future career and to form the basic professional knowledge and skills.

The implementation of the gradation system of professional education in Ukraine determines the need for further research on the teaching strategies for the profession based learning in Agricultural and Engineering

High Schools. It's very important to adopt the most appropriate scheme for implementation of profession-based learning. It will help to coordinate the teaching, to avoid the duplication of educational material, to reduce inefficient time costs, to provide future experts with deeper and stronger knowledge.

References

[1.] A. El-Moamly, "Medical Education in the New Millennium". New York: Nova Science Publishers.

[2.] A.I. Hurev,"Status of interdisciplinary links in the system of modern education". Science and school, 2, 2002, pp.41-45.

[3.] A.V. Konysheva and E.N. Ibragimova, "Training of Engineers in Mathematics at University on the Basis of the Information Cybernetic Approach". EURASIA Journal of Mathematics, Science and Technology Education, 2017, v. 13, n. 8, pp. 4379-4391.

[4.] A.V. Hutorskoi, "Pedagogical Innovations: Methodology, Theory and Practice". Moskow: «UNZ DO» publishing house, 2005.

[5.] B.A. Ermeling and J. Yarbo, "Expanding instructional horizons: A case study of teacher team-outside expert partnership". Teachers Colleges Record, 2016, v.118(2), pp. 1–48.

[6.] C. Lyall, A. Bruce, J. Tait and L. Meagher, "Interdisciplinary Research" Journeys: Practical Strategies for Capturing Creativity. London: Bloomsbury, 2011.

[7.] D. Kaittani, V. Derri, and E. Kioumourtzoglou, "Interdisciplinary: a focus on physics and physical education". Sports Science, 2016, n. 9, pp. 22-28.

[8.] F. King, "Teacher professional development to support teacher professional learning: Systemic factors from Irish case studies". Teacher Development, 2016, v.20(4), pp. 574–594.

[9.] H. Timperley, "Realizing the power of professional learning". London: McGraw-Hill Education, 2011.

[10.] L. Marcu, "Science education: the need for an interdisciplinary approach". Oradea University, 2007, v. XIV, pp. 53-56.

[11.] L. Zbaravska and S. Slobodyan, "Interdisciplinary communication in teaching physics for students of agricultural universities". Central European journal for science and research, Praha, 2016, pp. 97-101.

[12.] L. Zbaravska, I. Bendera, and S. Slobodyan, "Problem book in profession-based Physics". Kamianets-Podilskyi: PP Zvoleyko D.G., 2010.

[13.] M. Borrego and L. Newswander, "Definitions of interdisciplinary research, toward graduate-level interdisciplinary learning outcomes". The Review of Higher Education, 2010, v. 34(1), pp.61–84.

[14.] S. Aboelela, E. Larson, S. Bakken, O. Carrasquillo, A. Formicola, S. Glied, et al. "Defining Interdisciplinary Research: Conclusions from a Critical Review of the Literature". Health Research and Educational Trust, 2007, v.42(1), pp.329-346.

[15.] V.A. Bolotov, "The Competence Model: From an Idea to a Curriculum". Pedagogics, 10, 2003, p.8–14.

[16.] V. Tretko, "Interdisciplinary approach to teaching of Masters in international affairs". Adult education: theory, experience and practice Journal, 6 (13), 2013, pp.194–202

[17.] X. Cheng and L.-Y. Wu, "The affordances of teacher professional learning communities: A case study of a Chinese secondary school". Teaching and Teacher Education, 2016, v.58, pp. 54 –67.

[18.] Yu. Kuz, "Border guides training methodology in automated complexes and border control devices". Extended abstract of candidate's thesis. Khmelnitskyi: Khmelnitskyi National Academy of Border Guard Service, 2015.

[19.] L. Zbaravskaya, T. Hutsol, V. Melnyk, "Improvement of professional knowledge of students through the use of interdisciplinary connections and applied physical tasks" Bulletin of the Ukrainian Branch of the International Academy of Agrarian Education, 2014, pp. 230-237.

[20.] I. Bendera, L. Zbaravskaya, T. Hutsol, T. Dudar, "Professional orientation in the lecture course of physics for students in the direction of the preparation "Transport technologies"", Bulletin Sevastopol National Technical University. Series: Machinery and equipment and transport, 2011, pp. 133-137.

[21.] K. Dziedzic, K. Mudryk, T. Hutsol, B. Dziedzic; "Impact of grinding coconut shell and agglomeration pressure on quality parameters of briquette, Engineering for rural development", 2018, pp. 1884-1889.

[22.] T. Hutsol, N. Kosulina "Biophysical bases of radiometric receivers application for there mote diagnostics of the animals health situation", Bulletin of State Agrarian and Engineering University in Podilya, 2016, pp. 73-79.

Environment. Technology. Resources. Rezekne, Latvia
Proceedings of the 12th International Scientific and Practical Conference. Volume III, 257-260

Construction of Piston Outer Profile for Rotary Type Expansion Machine

Yury Zhuravlev
Department of Road Construction
Pskov State University
Pskov, Russia
drakon426@mail.ru

Andrey Perminov
Department of Electric Drive and Automation Systems
Pskov State University
Pskov, Russia
alp-mail@mail.ru

Yury Lukyanov
Department of Electric Drive and Automation Systems
Pskov State University
Pskov, Russia
luk-yra@mail.ru

Sergey Tikhonov
Department of Mechanics and Motor Trantsport Service
Pskov State University
Pskov, Russia
sit42@rambler.ru

Alexander Ilyin
Department of Electric Drive and Automation Systems
Pskov State University
Pskov, Russia
al.ilyin@yandex.ru

***Abstract*—The article discusses methods for constructing piston outer profile for the rotary type expansion machine in order to reduce unwanted (parasitic) volumes and offers options for constructing outer profile of piston using analytical and geometric methods.**

***Keywords*—lever-cam motion converter, power generation system, rotary engine.**

I. Introduction

The subject of this article is the rotary expansion machine (patent RU2619391) published by the authors in 2017 [1].

The machine contains four pistons, forming an equilateral four-link mechanism in the form of a mobile rhomboid. The ends of pistons are in full sliding contact with inner surface of chamber, the profile of which is the external equidistant, spaced by a distance of radius R_1 of ends of piston from reference curve, described in polar coordinates ρ and α with equation

$$\rho(\alpha)=L\sin\left[a+b\cos 2\alpha\right], \quad (1)$$

where L is the distance between the axes of the piston hinges; a=π⁄4; b=π⁄4-ψ_{min}/2, and where ψ_{min} is the minimum angle between the pistons.

The optimal value of this angle is $\psi_{опт}$=1.221 rad, at which a = 0.7854 rad, b = 0.1749 rad. The outer surface of each piston has the shape of an arc of a circle of radius R, the value of which is chosen in such a way that in the position α=π⁄4=45°, in which the four-link mechanism is square, the surface of piston touches internal cavity of chamber at three points. Therefore, in this position, two working volumes are formed, isolated from the rest of chamber space.

The task is to determine outer surface of the piston, in which in the position α=π⁄4, the working volumes will be absent, i.e. piston profile will coincide completely with inner surface of chamber, which is equidistant.

II. First option

The initial position of piston AB with α=π⁄4 is shown in Fig. 1.

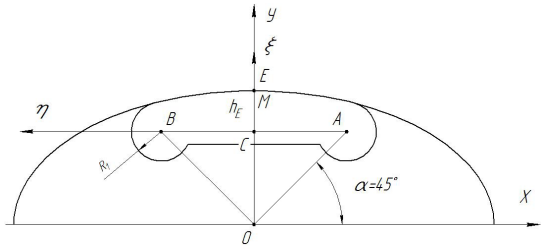

Fig. 1. Initial position of piston

Point E belongs to equidistant, and point M coinciding with it belongs to piston. We introduce a fixed coordinate system xOy with the beginning at the point O of the worker in the center of the cylinder. We introduce the following notation: *AB = L, OC = L/2, yE = L sin(a+b)+R_1*. When *a = 0,7854, b = 0.1749,* we get *yE = 0.573L+R_1*. Then the segment *CE = h_E =y_E – 0.5L, or h_E= 0.079L +R_1*.

Fasten with the piston the moving coordinate system *Cξη* with the origin at point *C* (Fig. 2).

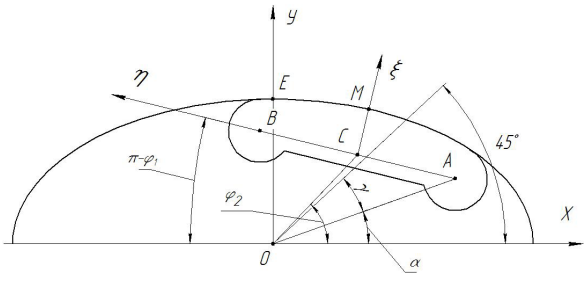

Fig. 2. Arbitrary position of piston

In moving axes, point M will have coordinates $\xi_M=h_E,\eta_M=0$. Determine the trajectory of point *M* when the piston moves from the position α = π/4. That the angle

Print ISSN 1691-5402
Online ISSN 2256-070X
http://dx.doi.org/10.17770/etr2019vol3.4059

α decreases by the value determined by the angle γ, i.e. $\alpha = \pi/4 - \gamma$. Then the coordinates of the point *M* are defined as

$$\begin{cases} x_M = x_C + \xi_M \cos(\hat{x,\xi}) + \eta_M \cos(\hat{x,\eta}) = \\ \qquad \frac{L}{2}\cos\varphi_2 + h_E \sin\varphi_1 \\ y_M = y_C + \xi_M \cos(\hat{y,\xi}) + \eta_M \cos(\hat{y,\eta}) = \\ \qquad \frac{L}{2}\sin\varphi_2 - h_E \cos\varphi_1 \end{cases} \quad (2)$$

where φ_1 is the angle between axes ηx; φ_2 is the angle between axes ξx.

Express the angles φ_1 and φ_2 through the angle γ:

$\varphi_1 = \pi - \gamma + b \sin 2\gamma;$
$\varphi_2 = \pi/2 - \gamma - b \sin 2\gamma.$ (3)

Then the trajectory of the point M in a parametric form is $x_M = x_M(\gamma), y_M = y_M(\gamma)$.

For known coordinates of the point MX_M and Y_M in a fixed coordinate system, we find the coordinates ξ_M, η_M in the moving coordinate system. Using equation (2) we get

$$\begin{cases} \eta_M \cos\varphi_1 + \xi_M \sin\varphi_1 = x_M - x_C \\ \eta_M \sin\varphi_1 - \xi_M \cos\varphi_1 = y_M - y_C \end{cases}. \quad (4)$$

Solving the system of equations (4) with respect to ξ_M, η_M and taking into account that $x_C = L/2 \cos\varphi_2$, $y_C = L/2 \sin\varphi_2$, $\varphi_1 - \varphi_2 = \pi/2\ 2b \sin 2\gamma$ we get.

$$\begin{cases} +y_M \cos(\gamma \quad b \sin 2\gamma) \quad \frac{L}{2}\cos(2b \sin 2\gamma) \\ \eta_M = \quad x_M \cos(\gamma \quad b \sin 2\gamma) + \\ +y_M \sin(\gamma \quad b \sin 2\gamma) + \frac{L}{2}\sin(2b \sin 2\gamma) \end{cases}. \quad (5)$$

The solution of this system of equations has a parametric form: $\xi_M = \xi_M(\gamma)$, $\eta_M = \eta_M(\gamma)$

In the position $\alpha = \pi/4 - \gamma$ the point *M* of the piston must coincide with the point *E* of the equidistants having the coordinates $x_E = x_M = 0$, $y_E = y_M = 0.573L + R_1$.

Then, by expression (5) the point *M* must have coordinates

$$\begin{cases} \xi_M = y_E \cos(\gamma \quad b \sin 2\gamma) \quad \frac{L}{2}\cos(2b \sin 2\gamma) \\ \eta_M = y_E \sin(\gamma \quad b \sin 2\gamma) + \frac{L}{2}\sin(2b \sin 2\gamma) \end{cases}. \quad (6)$$

The system of equations (6) gives the coordinate values $\xi_M = \xi_M(\gamma), \eta_M = \eta_M(\gamma)$ with decreasing angle α, i.e. when $\alpha = \pi/(4 - \gamma)$, where it is considered $\gamma > 0$.

In the case of increasing α, i.e. when $\alpha = \pi/(4 + \gamma)$, in the formula (6) it is necessary to change the sign of γ to the opposite taking $\gamma < 0$. Given the parity of trigonometric functions, the equation for ξ_M remains unchanged and in the equation for η_M both terms will change sign. Therefore, equation (6) is valid in the range of the angle $-\gamma_{max} \le \gamma \le \gamma_{max}$, where the value of γ_{max} should correspond to the contact of the obtained curve with the circle of the end curve of the piston of radius R_1. Obviously, this tangency is possible when $\gamma_{max} = \pi/4$.

Computer simulation made in SolidWorks has shown that if the piston profile is given exactly the profile of the equidistant chamber in the position α=45°. This will jam when moving from this position. Obviously, the profile synthesis problem is multivariate.Second option

Fig. 3 shows the piston in an arbitrary position.

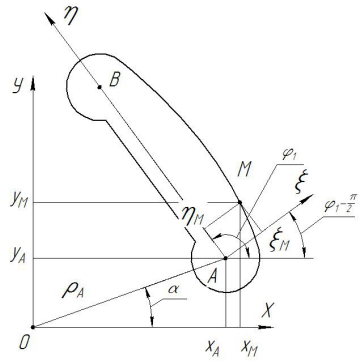

Fig. 3. Arbitrary position of piston

The current position of the piston *AB* in the fixed coordinate system *Oxy* is determined by the coordinates x_A and y_A of the hinge *A*, as well as by the angle φ_1 of the inclination of the axis of the piston *AB* to the axis *Ox*.

Where: $x_A = \rho_A \cos\alpha$, $y_A = \rho_A \cos\alpha$, $\rho_A = \rho(\alpha) = L \sin(a + b \cos 2\alpha)$, $\varphi 1 = \frac{3\pi}{4}\cos 2\alpha$.

Let us introduce the moving coordinate system ξη fixed to the piston with the beginning at point *A*. We choose an arbitrary point *M* on the piston profile, which has coordinates ξ_M and η_M in the moving coordinate system Aξη. The coordinates of this point in the fixed coordinate system *Oxy* are determined by the coordinate transformation formulas:

$$\begin{cases} x_M = x_A + \xi_M \cos(\hat{x,\xi}) + \eta_M \cos(\hat{x,\eta}) \\ y_M = y_A + \xi_M \cos(\hat{y,\xi}) + \eta_M \cos(\hat{y,\eta}) \end{cases}$$

or

$$\begin{cases} x_M = x_A + \xi_M \sin\varphi_1 + \eta_M \cos\varphi_1 \\ y_M = y_A \quad \xi_M \cos\varphi_1 + \eta_M \sin\varphi_1 \end{cases}. \quad (7)$$

Consider the same piston in the position α=45° (Fig. 4)

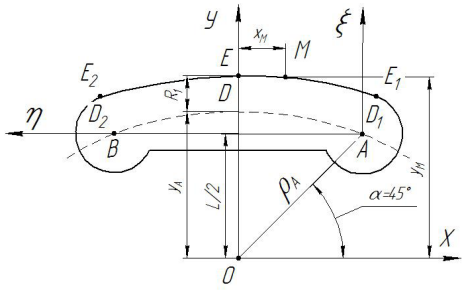

Fig. 4. Position of the piston at α=45°

In this position, the three points of the piston profile *D, D1, D2* touch the equidistants of the chamber at points *E, E1, E2*. The highest point of the piston profile *D* has the following coordinates

$$x_D = x_E = 0,$$

$$y_D = y_E = \rho\left(\frac{\pi}{2}\right) + R_1 = L \sin(a \quad b) + R_1. \quad (8)$$

When the piston moves from the position to the position $\alpha=45°+\Delta\alpha$, the points D_1, E_1 and D_2, E_2 change their position, but the contact between them remains. The upper point of the piston D will also leave the point of the chamber *E*. We will find such a profile of the piston, at which the contact of the points of the profile *M* and the point E of the chamber will remain in a certain range of the increment of the angle $\Delta\alpha$. This means that it is necessary to determine the coordinates ξ_M and η_M of the point M so that in the position $\alpha=45°+\Delta\alpha$, the coordinates of this point x_M and y_M are equal to the coordinates x_E and y_E of point *E*.

$$x_M(45° + \alpha) = x_E,$$
$$y_M(45° + \alpha) = y_E = L\,sin(a \quad b) + R_1. \qquad (9)$$

As a result, we arrive at the following system of equations for ξ_M and η_M

$$\begin{cases} \xi_M \sin\varphi_1(\beta) + \eta_M \cos\varphi_1(\beta) = x_A(\beta) \\ \xi_M \cos\varphi_1(\beta) + \eta_M \sin\varphi_1(\beta) = \quad , \\ y_A(\beta) + L\sin(a \quad b) + R_1 \end{cases} \qquad (10)$$

where $\beta = 45° + \alpha$, $x_A(\beta) = \rho_A(\beta)\cos\beta$,

$y_A(\beta) = \rho_A(\beta)\sin\beta$, $\rho_A(\beta) = L\sin(a + b\cos 2\beta)$,

$\varphi_1(\beta) = \beta + \frac{3\pi}{4} + b\sin 2\beta$.

Solving system (10) according to Kramer's rule $\xi_M = \xi/\ , \eta_M = \eta/$ we get:

$$= \begin{vmatrix} \sin\varphi_1(\beta) & \cos\varphi_1(\beta) \\ \cos\varphi_1(\beta) & \sin\varphi_1(\beta) \end{vmatrix} = 1,$$

$$\xi = \begin{vmatrix} x_A(\beta) & \cos\varphi_1(\beta) \\ y_A(\beta) + L\sin(a \quad b) + R_1 & \sin\varphi_1(\beta) \end{vmatrix}, \qquad (11)$$

$$\eta = \begin{vmatrix} sin\,\varphi_1(\beta) & x_A \\ cos\,\varphi_1(\beta) & y_A(\beta) + L\,sin(a \quad b) + R_1 \end{vmatrix}.$$

Then

$$\begin{matrix} \xi_M = x_A(\beta)\sin\varphi_1(\beta) \\ [\ y_A(\beta) + L\sin(a \quad b) + R_1]\cos\varphi_1(\beta) \\ \eta_M = x_A(\beta)\cos\varphi_1(\beta) + \\ [\ y_A(\beta) + L\sin(a \quad b) + R_1]\sin\varphi_1(\beta) \end{matrix} \qquad (12)$$

Varying the value of the increment of the angle α in the range $0 \le \alpha \le 45°$, or the same as the angle $\beta = 45° + \alpha$ in the range $45° \le \alpha \le 90°$, from equation (12) we obtain the desired piston profile.

In the process of movement each point $M(\xi_M, \eta_M)$ of the synthesized piston profile will move along its own trajectory of the form $x_M = x_M(\alpha)$ and $y_M = y_M(\alpha)$, defined by equation (7). It is important to check the absence of the intersection of these trajectories with the equidistant curve defined by the equations $x_E = x_E(\alpha)$ and $y_E = y_E(\alpha)$. Otherwise, the piston will jam in the housing.

If there is an intersection of the trajectories with equidistant, the wording of the problem should be changed. We require that in the position $\alpha = 45° + \alpha$, the coordinates x_M and y_M of the point *M* should be equal to the coordinates of $x_{E'}$ and $y_{E'}$ of point E' (Fig. 5, a) located on the axis Oy below point *E* at some distance $= (\alpha)$. Then we have

$$x_M(45° + \alpha) = x_{E'},$$
$$y_M(45^0 + \alpha) = y_{E'} = y_E \quad (\alpha) =$$
$$L\,sin(a \quad b) + R_1 \quad (\alpha).$$

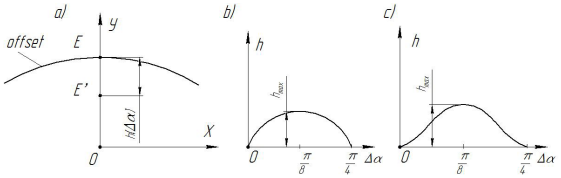

Fig. 5. Types of functions

In this case equation (12) is somewhat modified and takes the form

$$\begin{cases} \xi_M = x_A(\beta)\,sin\,\varphi_1(\beta) \\ [\ y_A(\beta) + L\,sin(a \quad b) + R_1 \quad (\alpha)]\,cos\,\varphi_1(\beta) \\ \eta_M = x_A(\beta)\,cos\,\varphi_1(\beta) + \\ [\ y_A(\beta) + L\,sin(a \quad b) + R_1 \quad (\alpha)]\,sin\,\varphi_1(\beta) \end{cases}.$$

The type of the function h(Δα), which varies in the range $0 \le \Delta\alpha \le 45°$, should be specified. It is known that this function should be equal to zero at two extreme points Δα=0 and Δα=45°. It can be offered two types of this function:

sinusoidal (Fig. 5, b): $(\alpha) = {}_{max}\sin 4(\alpha)$

cosine (Fig. 5, c): $(\alpha) = \frac{h_{max}}{2}(1 \quad \cos 8(\alpha))$.

In both cases it is possible by varying the value of h_{max} to achieve the absence of jamming of the piston in the housing. The decision on which option is preferable can be made based on the results of calculations.

References

[1] RF Patent 2619391 for an invention. Int. Cl. F01C1/44. Rotary Expantion Machine / Y.N. Lukyanov, Y.N. Zhuravlev et al. Publ. 15.05.2017.

[2] Y.Zhuravlev, A.Perminov, Y.Lukyanov, S.Tikhonov, A.Ilyin, S.Semyonov, Optimization of Mechanical Strength of Rotary-Vane Engine. "Environment. Technology. Resources - Proceedings of the 11th International Scientific and Practical Conference", 2017.

[3] S.Semyonov, S.Tikhonov, Y.Lukyanov, A.Perminov, Analysis Method of Calculation Parameters of Heat and Mass Transfer Processes in the Stirling Engine. "Environment. Technology. Resources - Proceedings of the 11th International Scientific and Practical Conference", 2017.

[4] Y.Zhuravlev, A.Perminov, Y.Lukyanov, S.Tikhonov, A.Ilyin, et al. Calculation and design of a rotary vane machine with external heat supply. Monograph. Pskov, 2012.

[5] Y.Zhuravlev, A.Perminov, Y.Lukyanov, S.Tikhonov, A.Ilyin, et al. Mathematical models of physical processes in a rotary-blade engine with external heat supply. Monograph. Pskov, 2012.

[6] Zhuravlev Y.N., Perminov A.L., Luk'yanov Y.N., Tikhonov S.I., Semonov S.N. Minimizatsiya mekhanicheskoy napryazhennosti rotorno-lopastnogo teplovogo dvigatelya s rychazhno-kulachkovym preobrazovatelem dvizheniya. Vestnik Pskovskogo gosudarstvennogo universiteta. Seriya: Tekhnicheskiye nauki. 2016. № 4.

[7] RF Patent 2374526 for an invention. Int. Cl. F16H25/04. Mechanism for converting motion / Y.N. Lukyanov, Y.N. Zhuravlev et al.

Publ. 27.11.2009. Bull. Number 33.

[8] RF Patent 2387844 for an invention. Int. Cl. F01G1/077, F02G1/044. Rotary-vane engine with an external supply of heat / .N. Lukyanov, Y.N. Zhuravlev et al. Publ. 27.04.2010. Bull. Number 12.

[9] Perminov A., Lukyanov Y., Tikhonov S., Ilyin A. Thermodynamic cycle with two-component working fluid. "Environment. Technology. Resources - Proceedings of the 11th International Scientific and Practical Conference", 2015. DOI: 10.17770/etr-2015vol2.261.

[10] Perminov A. L., Khitrov A. A., Khitrov A. I. Mekhatronnaya sistema «magnito-elektricheskiy sinkhronnyy dvigatel' - aktivnyy vypryamitel'» dlya avtonomnoy sistemy elektrosnabzheniya na baze rotorno-lopastnoy mashiny s vneshnim podvodom tepla. Trudy VII Mezhdunarodnoy (VIII Vserossiyskoy) konferentsii po avtomatizirovannomu elektroprivodu AEP-2012: "Ivanovskiy gosudarstvennyy energeticheskiy universitet". - Ivanovo, 2012. - 708 p. pp. 330-335.

[11] Perminov A.L., Luk'yanov YU.N., Tikhonov S.I., Il'in A.V. Elektrogeneratory dlya energoustanovok. Elektromekhanika. Elektroenergetika. Informatsionnyye tekhnologii Sbornik materialov 1-go Mezhdunarodnogo nauchno-prakticheskogo seminara. 2018. pp. 52-55.